Characterising Microstructural Grey Matter Pathology in Acute Mild Traumatic Brain Injury: A Quantitative Susceptibility Mapping Approach

---

Author:
Christi A. Essex

Supervisors:
A/Prof. Mangor Pedersen
Prof. Alice Theadom

A thesis submitted to Auckland University of Technology in fulfilment
of the requirements for the degree of
Doctor of Philosophy (PhD)

Department of Psychology and Neuroscience
Faculty of Health and Environmental Sciences
School of Clinical Sciences

Auckland University of Technology
Auckland, New Zealand

2025

Author:
Christi A. Essex

Supervisors:
A/Prof. Mangor Pedersen
Prof. Alice Theadom

Institute:
Auckland University of Technology, Auckland, New Zealand

ABSTRACT

Mild traumatic brain injury (mTBI) is a heterogeneous injury characterised by complex pathophysiological cascades. Brain iron dyshomeostasis is increasingly recognised as a driver of secondary injury including cytotoxicity and inflammation following mTBI, and alterations to myelin integrity, calcification, and proteinopathy have been implicated in post-injury pathology. However, standard radiographic methods are often insensitive to these microscopic alterations to brain tissue. This limitation necessitates the use of advanced magnetic resonance imaging (MRI) techniques to detect the subtle structural changes associated with this condition.

This thesis applied quantitative susceptibility mapping (QSM), an advanced MRI post-processing method, to elucidate differences in the distribution and concentration of magnetisable tissue constituents between male sports athletes (aged 16–33) with acute (<14 days) mTBI and age-matched male controls. QSM data were first thresholded to generate separate maps of positive (iron-related) and negative (protein-, calcium-, and myelin-related) voxel-wise susceptibility to enable targeted analyses of cerebral grey matter. Extensive segmentations of the basal ganglia and hippocampal formation were used to investigate deep grey matter, while column-based analyses sensitive to cortical depth and curvature were leveraged to approximate the location of tissue dyshomeostasis within the cortical laminae and account for the effect of gyrification. Variables such as injury severity, time since injury, and age were also used in statistical models to elucidate the influence of these factors on tissue pathology.

Bilateral, between-group analyses were first conducted across all regions of interest (ROIs) to identify signatures of tissue dyshomeostasis that may represent common features of mTBI. However, traditional group-wise statistical approaches may obscure subtle, yet clinically relevant, inter-individual variability. To address this limitation, subsequent studies constructed healthy population templates for each ROI using standardised z-scores, against which the z-scores of mTBI participants were analysed.

Group-wise analyses revealed significantly decreased negative susceptibility in the cornu ammonis 4 region of the hippocampus among mTBI participants, suggesting the presence of injury-related effects on myelin content or cell loss. Cortical analyses indicated a trauma-induced increase in positive susceptibility, a marker of iron deposition, localised to the superficial depths of the parahippocampal sulcal bank and fundus. Decreased negative susceptibility values in distinct voxel populations within the same region suggested a dual pathology of neural substrates.

Individualised analyses of deep grey matter identified significantly elevated z-scores indicative of abnormal iron profiles relative to the healthy population, primarily in regions proximal to the hippocampal head and in the mammillary nucleus. Individual-level cortical analyses revealed abnormal iron markers predominantly localised to the temporal

lobe. mTBI participants with abnormal cortical iron markers exhibited significantly higher injury severity scores than their iron-normal counterparts, suggesting a link between potential iron deposition and symptom burden.

The findings of this thesis converge to underscore the vulnerability of the temporal lobe region to tissue dyshomeostasis following mTBI. This highlights the need for enhanced anatomical specificity in QSM-based investigations and suggests that the current emphasis on major basal ganglia substructures and an over-reliance on group-wise analysis is limiting. Collectively, the works contained within this thesis not only advance the current understanding of grey matter micropathology in mTBI and its clinical relevance, but provides both a compelling rationale for refining future QSM methodologies and a framework by which this can be achieved.

CONTENTS

LIST OF FIGURES

LIST OF TABLES

ACRONYMS

T_1**w**	T_1-weighted
T_2**w**	T_2-weighted
Aβ	Amyloid-Beta
ACC	Anterior Cingulate Cortex
ACRM	American Congress Of Rehabilitation
AD	Alzheimer's Disease
AIDS	Acquired Immunodeficiency Syndrome
ALS	Amyotrophic Lateral Sclerosis
ANOVA	Analysis Of Variance
ANTs	Advanced Normalisation Tools
APP	Amyloid Precursor Protein
ATP	Adenosine Triphosphate
AUTEC	Auckland University Of Technology Ethics Committee
BBB	Blood-Brain Barrier
BET	Brain Extraction Tool
BIDS	Brain Imaging Data Structure
BIST	Brain Injury Screening Tool
Ca	Caudate
CA	Cornu Ammonis
CAMRI	Centre For Advanced MRI
CIT168	California Institute Of Technology's 168 Brain Atlas
CNS	Central Nervous System
COSMOS	Calculation Of Susceptibility Through Multiple Orientations Sampling
CSF	Cerebrospinal Fluid
CT	Computed Tomography
CTE	Chronic Traumatic Encephalopathy
DAI	Diffuse Axonal Injury
DBS	Deep Brain Stimulation
DICOM	Digital Imaging And Communications In Medicine
dMRI	Diffusion Magnetic Resonance Imaging

DMT1 Divalent Metal Transporter 1
DNA Deoxyribonucleic Acid
DoF Degrees Of Freedom
DSI Days Since Injury
DTI Diffusion Tensor Imaging
DWI Diffusion-Weighted Imaging
EXA Extended Amygdala
FA Flip Angle
FDR False Discovery Rate
FID Free Induction Decay
FLIRT FMRIB's Linear Image Registration Tool
fMRI Functional Magnetic Resonance Imaging
FoV Field Of View
FRDA Friedrich's Ataxia
FSL FMRIB Software Library
GABA γ-Aminobutyric Acid
GCS Glasgow Coma Scale
GM/WM Grey Matter/ White Matter (interface)
GPe Globus Pallidus (Externus)
GPi Globus Pallidus (Internus)
GRAPPA Generalised Autocalibrating Partially Parallel Acquisitions
GRE Gradient Recalled Echo
GXE Gradient Difference Error
HATA Hippocampal-Amygdala Transition Area
HC Healthy Control
HD Huntington's Disease
HDEC Health And Disabilities Ethics Committee
HFEN High-Frequency Error Norm
HN Habenular Nuclei
HP High-Pass
HTH Hypothalamus
IQR Interquartile Range
LBV Laplacian Boundary Value
LOC Lateral Occipital Cortex
LSMR Least Squares Minimal Residual
LTP Long-Term Potentiation

MAD	Mean Absolute Deviation
MEDI	Morphology Enabled Dipole Inversion
MEGRE	Multi-Echo Gradient Recalled Echo
MFC	Magnetic Field Correlation
mIP	Minimum Intensity Projection
MN	Mammillary Nucleus
MNI152	Montreal Neurological Institute's 152 Brain Atlas
mPFC	Medial Prefrontal Cortex
MPRAGE	Magnetisation-Prepared Rapid Acquisition Gradient Echo
MRI	Magnetic Resonance Imaging
MS	Multiple Sclerosis
ms-TBI	Moderate-to-Severe Traumatic Brain Injury
mTBI	Mild Traumatic Brain Injury
NAC	Nucleus Accumbens
NFT	Neurofibrillary Tangle
NIfTI	Neuroimaging Informatics Technology Initiative
NMDA	N-methyl-D-aspartate
NMI	Normalised Mutual Information
NMR	Nuclear Magnetic Resonance
NRMSE	Normalised RMSE
OFC	Orbitofrontal Cortex
p-tau	Phosphorylated Tau
PBP	Parabrachial Pigmented Nucleus
PD	Parkinson's Disease
PDF	Projection Onto Dipole Fields
PET	Positron Emission Tomography
ppm	Parts Per Million
PRELUDE	Phase Region Expanding Labeler For Unwrapping Discrete Estimates
Pu	Putamen
PVE	Partial Volume Effect
QSM	Quantitative Susceptibility Mapping
RF	Radiofrequency
RMSE	Root Mean Square Error
RN	Red Nucleus
RNA	Ribonucleic Acid

ROI	Region Of Interest
ROMEO	Rapid Open-source Minimum Spanning TrEe AlgOrithm
ROS	Reactive Oxygen Species
RTS	Rapid Two-Step Dipole Inversion
SEGUE	Speedy REgion-Growing Algorithm For Unwrapping Estimated Phase
SHARP	Sophisticated Harmonic Artifact Reduction For Phase Data
SNc	Substantia Nigra Pars Compacta
SNr	Substantia Nigra Pars Reticulata
SNR	Signal-to-Noise Ratio
SPUN	Seed Prioritized UNwrapping
sr-mTBI	Sports-Related Mild Traumatic Brain Injury
STH	Subthalamic Nucleus
STI	Susceptibility Tensor Imaging
STS	Superior Temporal Sulcus
$Sv0_2$	Cerebral Venous Oxygen Saturation
SWI	Susceptibility-Weighted Imaging
TBI	Traumatic Brain Injury
TE	Echo Time
TfR1	Transferrin Receptor 1
TGV	Total Generalised Variation
TR	Repetition Time
TV	Total Variation
VeP	Ventral Pallidum
VTA	Ventral Tegmental Area
XSIM	QSM-Specific Structural SIMilarity Index

ATTESTATION OF AUTHORSHIP

I hereby declare that this submission is my own work and that, to the best of my knowledge and belief, it contains no material previously published or written by another person (except where explicitly defined in the acknowledgements), nor used artificial intelligence tools or generative artificial intelligence tools (unless it is clearly stated, and referenced, along with the purpose of use), nor material which to a substantial extent has been submitted for the award of any other degree or diploma of a university or other institution of higher learning.

Christi A. Essex

ACKNOWLEDGEMENTS

This project was funded by a grant from the Health Research Council of New Zealand (HRC) (Reference: 21/622). The research in this thesis was approved by the Health and Disabilities Ethics Committee (HDEC) (Date: 18/02/2022, Reference: 2022 EXP 11078) and institutional approval was obtained from the Auckland University of Technology Ethics Committee (AUTEC) (Date: 18/02/2022, Reference: 22/12).

During my tenure as a doctoral candidate at Auckland University of Technology, I have been privileged to work alongside many fantastic people; thank you for making my time enjoyable. There are, however, a few individuals who have made significant contributions by either providing academic supervision, support, and guidance or emotional support, love, and understanding (and, in some cases, both). This achievement is as much yours as it is mine.

I would first like to acknowledge my primary supervisor, **A/Prof. Mangor Pedersen**. Your contributions are beyond count, but in particular, thank you for sharing your knowledge and believing in me. Your trust in my work and encouragement to think both critically and creatively have been invaluable in allowing me to grow as a researcher and hone my skills. I couldn't have asked for a better supervisor, and I couldn't have done it without you!

I also extend my gratitude to my secondary supervisor **Prof. Alice Theadom** whose expertise greatly enhanced the quality of my research. Thank you for always making yourself available for discussions when needed, for your encouragement, and for your unerring warmth and understanding.

There are many other members of the academic community who have enriched my research, skills, and thinking along the way, and I am deeply grateful to you all. However, my thesis and research contributions would not be what they are without **Dr. Jenna Merenstein**, to whom I owe a debt of gratitude. Your mentorship, friendship, and guidance, which you were never required to give but did so without restraint, will continue to inspire me throughout my academic career. Thank you for reading and critiquing my work, for your encouragement throughout this process, and for your investment in me as an emerging researcher.

I also extend my thanks to **Dr. Helen Murray**; your work and achievements are matched only by your willingness to share your expertise and guidance. Thank you for your con-

tributions to this research and for providing opportunities for learning outside of my field.

Thank you to **Auckland University of Technology** and the **Traumatic Brain Injury Network** for providing both a community and a doctoral scholarship, both of which enabled me to flourish. I am also grateful for the support of the **Kate Edger Foundation** whose Dame Dorothy Winstone Doctoral Completion Award allowed me to finish this thesis strong.

Thank you to my friends and family, old and new. To my first parents, **Késhav** and **Selina**, thank you for teaching me how to think, to question everything, and to always look from new perspectives different to my own; you have been instilling the virtues of a scientist and teaching me the scientific method from the time I was a child. Thank you for always championing my dreams. To the parents I have acquired along the way, **Olga** and **Craig**, thank you for raising me and loving me like your own, and now **Jenny**, too. I am blessed to have parents like you all. **Lucean**, my partner in crime, I love you to the moon and back! Thank you for all the encouragement, conversations, and your pride in me no matter what I choose to do with my life. To my friends, but especially to **Luca**, **Adarra**, **Ayu**, **Beth**, **Lily**, **Abbey**, and **Edith**, thank you for your understanding and encouragement. To **Minnie**, and now **Margaux (a.k.a. Tiny)**, my littlest loves, thank you for your companionship. Your love and your big personalities (especially for such small cats) have brought me endless joy and comfort.

And last, but certainly not least, my love, **Simon**. It hardly seems fair to condense everything I want to say into a few sentences, but here goes. Thank you for the love, support, and unwavering faith. Thank you for being with me through the laughter, and through the tears, for being there every single day, ready and willing to help, or just sit with me, without the slightest hesitation. Thank you for your calm steadfastness and for filling every day with the little joys that make life beautiful: the morning coffees in bed, the beach walks, sunrise in the garden together, feeding and watching the birds with Minnie, Margaux, and I, not to mention the greasy hands, gritty fingernails, and the world's most mischievous grin as you demonstrate precisely how an engine is put together (whether I want to know, or not!). Thank you for holding my hand, both literally and figuratively, for every step of this journey, and for all the adventures still to come. I love you. This is just the beginning!

DEDICATION

To those who came before me, thank you for paving the way;
To those still yet to come, may you find the inspiration and courage to start the journey;

And finally, to Simon, for accompanying me on this one. *Thank you.*

"The Brain—is wider than the Sky—
For—put them side by side—
The one the other will contain
With ease—and You—beside—

The Brain is deeper than the sea—
For—hold them—Blue to Blue—
The one the other will absorb—
As Sponges—Buckets—do—

The Brain is just the weight of God—
For—Heft them—Pound for Pound—
And they will differ—if they do—
As Syllable from Sound" [1]

1 Emily Dickinson. *The Brain is Wider than the Sky.*

BACKGROUND

1 INTRODUCTION

"The brain is the last and grandest biological frontier, the most complex thing we have yet discovered in our universe."

James D. Watson
Foreword: *Discovering the Brain*

1.1 BIOLOGICAL SUBSTRATES AND MTBI: AN INTRODUCTION

The quote above from renowned molecular biologist and geneticist James D. Watson encompasses the enigma that the human brain presents to science. This organ belies its own complexity; weighing about 1.5 kilograms and comprising just 2% of the body's total mass (Herculano-Houzel, 2009), it not only maintains homeostasis and runs the systems of the body below the level of conscious awareness, but acts as the central processor of sensory input, motor output, emotion, and cognition (Morgane et al., 2005; Venkatraman et al., 2017). From within the dark confines of the cranial vault protecting this vulnerable organ, the brain constructs the subjective experience of both the internal and external world, giving rise to embodied experience as well as subjective consciousness and the phenomenology of *being*.[1] Nerve cells (neurons), the computational units of the brain, are estimated to number approximately 86 billion (Herculano-Houzel, 2009) and amass hundreds of trillions of connections between them (Drachman, 2005). To put this in perspective, next time you look up on a clear night and observe the vastness of the Milky Way stretching across the sky, consider this: the number of connections between neurons in your brain is greater than the number of stars in this galaxy (Howell, 2022). Our connection to the stars extends in a more material sense, too; the elements of our brain tissues were forged in the hearts of these cosmic furnaces. The life-sustaining particulates which trace their origins back to stellar nucleosynthesis include hydrogen, oxygen, carbon, nitrogen, sodium, magnesium, potassium, calcium, and iron, among others (Fox, 2004), and account for not only the con-

1 Although whether the subjective experience of consciousness is inherently *meaningful* (see, for example, Chalmers, 1996), or simply an epiphenomenon of the biological system (Dennett, 1993) is a continuing matter of debate.

stituent elements of the cell (Alberts et al., 2002) and brain tissue, but cellular metabolites (Grochowski et al., 2019) and related byproducts (Rink et al., 2011).[2]

For all the astonishing capabilities of the brain, its central role in preserving life, and its cosmic origin, it is nonetheless fragile. The very elements that make cognition and consciousness possible are tightly regulated within the brain, and any deviation from homeostasis, such as that which occurs when the head is subjected to even minor mechanical forces, can damage the neurons and initiate cascades of biochemical and metabolic changes (Giza et al., 2001, 2014). These cascades can further injure the cells, disrupting structure and function, which can have life-altering consequences. Thus, sustaining a traumatic brain injury (TBI), even a mild traumatic brain injury (mTBI), can significantly affect quality of life in both the short- and long-term, disrupt the sense of *self*, contribute to the development of neurodegenerative conditions, and even diminish life expectancy (Guskiewicz et al., 2007; Mackay et al., 2019; McInnes et al., 2017; Mckee et al., 2015; Rosenbaum et al., 2012).

Whilst the fundamental building blocks of our cells are beautiful and celestial, in injury, the elemental compositions can metamorphose into something far more sinister; iron is one such compound. This vital element is involved in many cellular processes, however, dysregulated iron homeostasis in the brain can have profound effects on neuronal function and cognitive health, and is increasingly recognised as a contributor to cellular pathology following mTBI (Gozt et al., 2021a; Huang et al., 2021; Lu et al., 2015; Nisenbaum et al., 2014; Raz et al., 2011).

Despite significant advancements in neuroscience and neuroimaging techniques that allow visualisation and quantification of neural substrates via surrogate markers, including distributions of iron, calcium, myelin (the fatty sheath surrounding neurons), and protein aggregates, the role of these brain tissue components in mTBI remains a complex puzzle that is only partially understood. Quantitative susceptibility mapping (QSM), an advanced magnetic resonance imaging (MRI) post-processing technique, generates scalar maps representative of biological substrates by leveraging the inherent magnetic properties, such as paramagnetism (iron-related positive susceptibility) and diamagnetism (myelin-, calcium-, and protein-related negative susceptibility), in response to the applied magnetic field of an MRI machine (Duyn et al., 2017; Gong et al., 2019; Jang et al., 2021; S. Kim et al., 2020; Y. Wang et al., 2017; Z. Zhao et al., 2021). However, many of these tissue components, and QSM as a specialised MRI imaging technique, remain under researched and under utilised within the domain of mTBI. This gap underscores the need for more widespread adoption of QSM to better understand the subtle pathological changes occurring after injury; a gap this thesis aims to address.

2 To quote the great Carl Sagan (1980), *"The cosmos is within us. We are made of star stuff. We are a way for the universe to know itself."*

1.2 THESIS AIMS AND OBJECTIVES

In this thesis, thresholded QSM is used to quantify and compare spatial distributions of magnetic substrates across the brain, from the deep grey matter of the basal nuclei to the grey matter of the cerebral cortex, between mTBI participants and healthy controls (HC). The primary focus is on positive magnetic susceptibility values, as iron is the best-characterised and most dominant source of paramagnetism detected by QSM (a comprehensive discussion of this is provided in Chapter 3). As a secondary approach, negative susceptibility values are investigated. Diamagnetic substrates are less well characterised within the literature, and their relatively weaker signal contributions pose a greater challenge to identify using QSM, complicating their relationship with mTBI effects (again, these are reviewed in Chapter 3).

Only a limited number of studies have applied QSM to assess changes in brain tissue composition following mTBI. Most of these studies have focused on relatively coarse segmentations of the basal ganglia, with only two studies exploring iron distribution in the cortex but naïve to cortical architectonics known to influence damage localisation in brain tissue (these studies are discussed in detail in Chapter 3). Furthermore, no studies have yet used QSM to investigate the separate divisions of the hippocampal formation, despite the vulnerability of the temporal lobe and hippocampal subregions to injury in mTBI. Extant research has exclusively relied on the analysis of aggregate QSM, which may introduce confounds related to inter-voxel averaging during analysis (this is also discussed in Chapter 3).

This thesis addresses these research gaps by thresholding QSM into separate maps of dominant voxel-wise net susceptibility sign to assess the effects of mTBI on brain tissue composition across:

a) The extended subregions of the basal ganglia and associated nuclei, representing the most detailed segmentation to date;

b) The hippocampal formation, whose subfields remain unexplored in QSM studies of mTBI; and

c) The cerebral cortex, using column-based analyses to identify the effects of variation in cortical depth and curvature on tissue dyshomeostasis.

This thesis also seeks to recognise the heterogeneity of injury in mTBI and the limitations of group-level statistical approaches, which may preclude inference at the individual level. To date, individualised approaches to QSM in mTBI have been overlooked; a research gap that will be addressed by leveraging z-tests to generate individual profiles of mTBI effects. Due to the well-established relationship between paramagnetism and iron, all individual profiling is conducted specifically for positive susceptibility. Here, the research objective is to:

d) Build the first individualised profiles of mTBI-related deviations in regional positive susceptibility values across all aforementioned brain structures, relative to a healthy normal population.

These research objectives converge into the three overarching aims of this thesis:

1. Advance the current understanding of mTBI-related changes to brain tissue composition: by investigating the spatial distributions of magnetic substrates within the cerebral grey matter.
2. Refine and apply techniques that enhance sensitivity to injury-related changes in the brain: by incorporating advanced methodologies and segmentations that account for anatomical complexities, including extended investigations of basal nuclei, differentiation of the hippocampal subfields, and cortical column-based analyses sensitive to the effects of cortical morphology.
3. Leverage traditional group-level analyses versus individualised profiling: to assess the utility of standard versus individual-specific approaches for understanding mTBI-related tissue content differences.

1.3 THESIS OUTLINE

The remainder of this thesis is organised as follows:

Chapter 2 is the **first background chapter** of this thesis and provides a **comprehensive overview of mTBI** to establish the foundational knowledge necessary to parse the content of subsequent chapters. The chapter begins with a definition of mTBI and diagnostic criterion, before exploring its epidemiological underpinnings. A key focus of this chapter is the underlying pathophysiology of mTBI, including primary and secondary injury, and the associated neurometabolic cascades. Finally, the role of brain iron in the maintenance of normal cellular processes is explored, which facilitates a discussion of its involvement secondary injury cascades in mTBI. This chapter, in essence, communicates why an understanding of brain iron dyshomeostasis, and disruption to other biological substrates, may contribute to understanding mTBI effects and advance the field closer to establishing an objective marker of injury.

Chapter 3 is the **second background chapter** of the thesis and explores the fundamental concepts related to MRI and thereby QSM, highlighting its imaging capabilities, applications, and utility in detecting and characterising brain tissue content in the context of mTBI with the aim of answering the question, ***"why use QSM to study mTBI?"*** This chapter provides a review of the sparse extant literature on the use of QSM to investigate mTBI and notes key gaps that this thesis' *research aims* were developed to address. This chapter serves as a transition into the research studies comprising this thesis, adds context for the novelty of the work presented herein, and elucidates how this research will contribute to advancing this developing field.

Chapter 4 presents the **first research project**. This chapter serves as an **evidence-based rationale** and **methodological justification** for the QSM reconstruction method used in the proceeding *major contributions*. A comparative analysis of the performance of two different QSM reconstruction algorithms, with and without two-pass artefact reduction, is conducted using an existing realistic *in silico* phantom. Reconstructions are analysed relative to a ground-truth susceptibility map across a variety of signal-to-noise (SNR) and image quality metrics. The discussion contextualises the results, synthesising across the current literature and recent recommendations for best-practice QSM reconstruction. Ultimately, this chapter aims to enhance the methodological rigour and validity of the works comprising this thesis.

Chapter 5 contains the **second research project** and **first major contribution**. This study presents an in-depth analysis of differences in positive and negative susceptibility values between mTBI participants and HC across 16 bilateral segmentations of the **basal ganglia** and 10 **hippocampal subfields**. Despite the vulnerability of the temporal lobe and hippocampus to damage following mTBI and the prevalence of associated symptomatology (for example, memory impairment), detailed analyses of this brain region have been excluded from QSM studies of mTBI. By addressing this gap and extending previous seminal work in the field, this study provides a novel and significant contribution to the literature.

Chapter 6 contains the **third research project** and **second major contribution**. The cortex, with its complex layer-specific structure and gyrification (i.e., grooves and ridges), presents significant challenges for study and has been largely overlooked in mTBI-related QSM research. In this chapter, **column-based analyses sensitive to cortical architectonics** are used to assess bilateral patterns of voxel-wise positive and negative susceptibility across 34 cortical regions of interest (ROIs). The analyses in this chapter are sensitive to variations in cortical depth, measured across 21 depths from the pial surface to the grey matter/white matter (GM/WM) boundary, and cortical curvature, including the crown, bank, and fundus. This detailed assessment provides novel insights into how mTBI affects the cortex, and how microstructural changes in brain tissue content may be modulated by cortical architecture and cranial-dural morphology.

Chapter 7 and Chapter 8 present the **fourth and fifth research projects** and **third and fourth major contributions**. In these chapters, I address the inter-individual heterogeneity of mTBI and the loss of subtle, but clinically relevant, information that may occur when using traditional group-wise statistical approaches. These research projects aim to acknowledge the need for more precise, individualised methods. In these chapters, I construct **individualised profiles** of positive susceptibility values by leveraging z-tests for each ROI to build healthy population templates from the z-scores of HC participants. Z-scores of an extended mTBI participant sample are then analysed against the normalised HC z-distribution. Chapter 7 pertains to individualised analyses of the basal nuclei and hippocampal formation. Chapter 8 examines 34 cortical

parcels for the primary analysis, which is followed by exploratory analyses across six depths and three curvatures (crown, bank, and fundus) for each cortical ROI. These two studies represent the first dedicated individualised analyses of mTBI effects using QSM, marking a significant advancement in our approach to, and understanding of, the microstructural brain changes associated with mTBI and their relevance at the individual and clinical level.

Chapter 9 synthesises the five research projects contained within this thesis, and **provides a general discussion**. Here, the works are summarised prior to a discussion regarding the implications of the findings and methodological approaches. This chapter highlights the contribution of this thesis to the QSM and mTBI literature, identifies key general limitations, and provides suggestions for future research. This chapter, and the thesis broadly, is concluded with some final thoughts and closing remarks.

2

MILD TRAUMATIC BRAIN INJURY: DEFINITIONS, EPIDEMIOLOGY, AND PATHOPHYSIOLOGY

To appreciate the societal and personal costs associated with mTBI, an understanding of the epidemiological and pathophysiological landscape is essential. Investigating the incidence, prevalence, risk factors, and burden of mTBI contextualises not only the impetus to address this condition, but also the challenges associated with doing so. In this section, an up-to-date definition and a comprehensive review of the current epidemiological trends is presented. This lays the groundwork for understanding the heterogeneous and complex pathophysiological processes induced by mTBI, including the role of brain iron dyshomeostasis and other biological substrates in the secondary injury cascade central to this thesis. The key points are summarised in § 2.5.

2.1 DEFINITIONS AND DIAGNOSTIC CHALLENGES

TBI is the most common neurological disorder with an annual estimated incidence of 50-60 million cases worldwide, representing a ∼$400 USD billion global economic burden (Howe et al., 2022; Maas et al., 2022). Far from a binary condition, TBI exists along a continuum from mild to severe, with mTBI accounting for 90% of all cases (Maas et al., 2022). While severe TBI is characterised by the presence of lesions readily identifiable on conventional clinical imaging, such as computed tomography (CT) and MRI, the presentation of mTBI is more subtle. Standard radiographic methods fail to detect mTBI-related brain alterations (Hier et al., 2021; Lunkova et al., 2021) in 90-95% of cases (Maas et al., 2022). As a result, mTBI diagnosis and prognosis relies almost exclusively on clinical assessment and self-reported symptoms (Lefevre-Dognin et al., 2021).

Over the last three decades, the criteria for diagnosing mTBI have undergone significant refinements. Seminal definitions, such as those from the Head Injury Interdisciplinary Special Interest Group of the American Congress of Rehabilitation (ACRM) (1993), have provided a foundation from which the current classifications evolved. However, the proliferation and variability of criteria have led to definitional and diagnostic inconsistencies, complicating cross-study comparisons and validation efforts, and leading to drastic inequities in access to care (Silverberg et al., 2023). Indeed, a single study that compared 17 distinct definitions of mTBI, applied to a cohort aged between 3 and 16 years, found that the proportion of the sample classified as having sustained an mTBI ranged from 7.1% to 98.7%, underscoring the level of ambiguity introduced by differing diagnostic criteria (Crowe et al., 2018).

Ultimately, these issues culminated in a recent revision published by the ACRM in 2023 aimed at standardising the operational and diagnostic criterion for mTBI (Silverberg et al., 2023). According to this revision, a mTBI is induced by the transfer of mechanical energy to the brain from either the head striking or being struck by an object or surface, inertial forces such as acceleration/deceleration, and/or exposure to blast impacts. Clinical diagnosis of mTBI requires that:

1. A loss of consciousness lasts less than 30 minutes;
2. A Glasgow Coma Scale (GCS) score is between 13 and 15;
3. Post-traumatic amnesia is not present for more than 24 hours.

In addition, signs and symptoms of mTBI indicative of acute brain dysfunction must be present and should not be accounted for, but may accompany, confounds related to pre-existing or co-occurring health conditions. Clinical signs of mTBI include, but are not limited to, altered mental states including confusion and disorientation; physical symptoms include headache, vertigo, vestibular issues, and sensory sensitivities; cognitive symptoms include impaired concentration and memory, and; emotional disturbances present as lability or irritability. If a focal lesion is present on CT or MRI, a qualifier denoting the presence of structural intracranial injury via imaging should be used (Silverberg et al., 2023).

Here, it is important to note that the term "concussion" is often used interchangeably with mTBI. The ACRM suggests that concussion can be applied to cases of mTBI where conventional MRI returns normal findings (Silverberg et al., 2023). This is largely congruent with the conceptual definition accepted by the recent 6th International Consensus Conference on Concussion in Sport, with the caveat that while standard neuroimaging (CT/MRI) must be normal for diagnosis of concussion, in a research setting changes to brain function, blood flow, or metabolism may be revealed by advanced neuroimaging methods (Patricios et al., 2023). Although the definition offered by Patricios et al. (2023) is broader than the one established by the ACRM, the literature generally accepts the interchangeable use of these terms whereby, broadly, mTBI is used in clinical contexts and concussion is applied to sporting incidents. For the purposes of this thesis, however, mTBI will be used as an umbrella term encompassing the sports-related mTBI (sr-mTBI) investigated herein.

2.2 EPIDEMIOLOGY

Common mechanisms for sustaining a mTBI include sports participation (particularly contact sports), falls, road traffic accidents, instances of domestic or interpersonal violence, military-related exposures such as to blast forces, and the head striking or being struck by an object (Naumenko et al., 2023). Beyond causes, however, epidemiological research is fraught with challenges, primarily due to methodological variability and significant underreporting as many individuals with mTBI do not seek medical attention (Setnik et al., 2007). Indeed, recent injury surveillance data from a United States population suggest that over half of all mTBI are untreated in a medical setting (Waltzman et al., 2025). While hospital-based studies typically report incidence rates of 200–300 cases per 100,000 persons per year (Cassidy et al., 2004), population-based data indicate that the true incidence may be at least twice that, with numerous studies citing incidence rates in excess of 600 cases per 100,000 persons per year (Gardner et al., 2015; Lefevre-Dognin et al., 2021). Within the New Zealand context, a population-based study reported an incidence of 790 TBI cases per 100,000 persons per year, with approximately 749 per 100,000 of these classified as mild (Feigin et al., 2013).

The epidemiology of sr-mTBI is even more complex. This can be attributed, at least in part, to well-documented underreporting among athletes (Kroshus et al., 2015; Meier et al., 2015). In addition, incidence rates vary considerably between countries (Theadom et al., 2020), which is exacerbated by the reliance on the subjective experience for diagnosis of injury, and current surveillance methods are estimated to capture only 1 in 9 cases (Pierpoint et al., 2021). Inconsistencies in how incidence is quantified, whether in terms of player-seasons, player-games, player-minutes, or other metrics (Wasserman et al., 2018), also serve to confound cross-study comparisons. Notwithstanding these complexities, a recent systematic review suggests that up to approximately 30% of all TBI cases may be attributed to sports participation (Theadom et al., 2020).

While for some, mTBI-related symptoms are transient and resolve within two weeks (Gozt et al., 2021b), between 15% (Walker et al., 2013) and 30% (Rosenbaum et al., 2012) of individuals experience significant, and in some cases life-changing, long-term clinical sequelae which can persist for up to three decades post-injury (De Beaumont et al., 2009; Guskiewicz et al., 2005; Hellewell et al., 2020). Numerous factors contribute to differences in injury severity, symptom burden, *in vivo* brain tissue pathology, and even autopsy findings. These include individual differences prior to injury such as genetic predispositions, age, gender, IQ, ethnicity, psychiatric history, prior exposure to mTBI, and substance use history, as well as differences in the mechanisms and loci of injury (Rosenbaum et al., 2012). For example, in sr-mTBI variability in the sport and even player position can affect injury severity, lead to diverse effects on brain structure and function, and divergence in symptom burden and cluster (Rosenbaum et al., 2012; Scopaz et al., 2013).

Age and sex are key risk factors for both sustaining mTBI and experiencing adverse outcomes, including prolonged recovery. Epidemiological data reveal a bimodal distribution in mTBI prevalence, with incidence peaking in adolescence/young adulthood (15–24 years) and again in individuals over 65 (Shukla et al., 2010). Younger individuals, in particular, tend to experience a significantly extended symptom burden (Rosenbaum et al., 2012), suggesting distinct recovery trajectories across the lifespan. Being of female sex is associated not only with an increased risk of sustaining mTBI (Pierpoint et al., 2021; Zech et al., 2022) but also with more severe symptom presentation and longer recovery times, including a heightened likelihood of developing post-concussion syndrome, defined as persistent mTBI symptoms beyond three months (Mavroudis et al., 2024; Preiss-Farzanegan et al., 2009). This disparity may be attributable to sex-based differences in the temporal dynamics of the neuroinflammatory response (Flavin et al., 2023), fluctuations in sex hormone levels (Wunderle et al., 2014), variations in oral contraceptive use (Gallagher et al., 2018), and differences in neck muscle morphology (Tierney et al., 2005). It is also important to recognise that, in addition to biological risk factors, these data may be influenced by sex differences and sociocultural factors that shape attitudes toward reporting injury occurrence and symptom severity (Hardaker et al., 2024).

Lastly, the role of repetitive mTBI and head impacts that do not produce overt clinical symptoms (i.e., "sub-concussive events"), which are common in sports participation, are noteworthy. These events are increasingly recognised as key drivers of long-term neuropathological changes, whereby a clear dose-response relationship is evident in the cumulative burden of such impacts (Bailes et al., 2013; Maas et al., 2017; McKee et al., 2023). These chronic effects extend beyond cognitive deficits to include an increased susceptibility to mental health disorders and neurodegenerative conditions, such as chronic traumatic encephalopathy (CTE), Alzheimer's disease (AD), and Parkinson's disease (PD), as well as premature morbidity (Bieniek et al., 2021; De Beaumont et al., 2009; Graham et al., 2022; Guskiewicz et al., 2007; Khan et al., 2024; Mackay et al., 2019; McInnes et al., 2017; McKee et al., 2023). The mechanisms underlying these neurodegenerative trajectories are discussed in greater detail below.

The persistent difficulties in defining and identifying mTBI illustrates the limitations inherent in relying primarily on clinical assessment by subjective self-report. As demonstrated here, such reliance contributes to diagnostic ambiguity and confounds efforts to delineate or compare epidemiological factors. Developing objective markers, whether using advanced imaging techniques or biomarker assays, is thus critical to ameliorating many of these issues and advancing the current understanding of mTBI. The next section examines the pathophysiological cascades induced by mTBI, exploring how acute mechanical forces trigger a temporally-mediated interplay of cellular, metabolic, and inflammatory processes.

2.3 PATHOPHYSIOLOGY AND MARKERS OF INJURY

The challenges inherent in characterising and classifying mTBI span multiple domains, and this complexity is equally evident in the heterogeneity of its pathophysiological manifestations. Although GCS scores are conventionally employed as an initial metric for categorising TBI severity (Laskowski et al., 2015), they offer limited insight into the physiological processes that drive symptomatology; here, classification by pathophysiology is necessary (Saatman et al., 2008). The initial mechanical energy transmission to the brain precipitates two distinct yet interrelated injury categories, primary and secondary injury, which are characterised by unique temporal dynamics and distinct neurobiological processes (Giza et al., 2014; Gozt et al., 2021a). Although no definitive biomarker for mTBI currently exists, many of these pathophysiological mechanisms can be identified *in vivo* via surrogate markers.

2.3.1 *Primary injury*

Primary injury occurs at the time of the incident when the brain is displaced within the skull, damaging the neurons, glia, and blood vessels of the cerebral tissues (Prins et al., 2013). This initial insult can be further subdivided into focal and diffuse injuries, which frequently co-occur across the broader spectrum of TBI. A focal brain injury arises from contact between the brain and the skull during impact and may manifest as a gross focal lesion or haemorrhage, particularly in severe TBI. These mechanisms of focal injury also apply to mTBI, however, due to the more subtle nature of this injury the degree of tissue damage is comparatively less extreme. Nonetheless, susceptibility-weighted imaging (SWI) can detect small, localised microvascular disruptions (i.e., microhaemorrhages or microbleeds) typically measuring less than 10 mm in diameter (Hageman et al., 2022; Lunkova et al., 2021).

The presence of microhaemorrhage is also associated with diffuse injury process, specifically diffuse axonal injury (DAI) (Lunkova et al., 2021), which is a primary pathologic feature of mTBI (Hellstrøm et al., 2017; Laskowski et al., 2015). Unlike focal lesions, diffuse primary injury is a global phenomenon triggered by rapid inertial forces such as acceleration, deceleration, or rotation, that generally stretch, and in severe cases shear, axonal

processes. This mechanical strain induces microstructural cytoskeletal damage predominantly within white matter (Saatman et al., 2008; Seifert et al., 2015), a pathology most frequently identified using diffusion MRI (dMRI) (Lunkova et al., 2021). DAI has long been implicated in the clinical manifestations of mTBI, and imaging studies have reported associations between DAI and cognitive, somatic, and emotional symptoms up to one year post-injury (Hellstrøm et al., 2017).

2.3.2 *Secondary injury*

Secondary injury refers to the resultant dynamic physiological processes catalysed by the primary injury; this complex, self-perpetuating cascade of ionic and metabolic disturbance unfolds over acute, subacute, and chronic phases, each marked by distinctive cellular events that can influence clinical symptomatology (Giza et al., 2014; Gozt et al., 2021a; Walker et al., 2013). Although the precise mechanisms of secondary injury remain incompletely understood, seminal contributions by Giza and colleagues (2001, 2014) have provided the foundation for elucidating many components of this neurometabolic cascade.

2.3.2.1 *Acute phase (hours to days)*

Excitotoxicity: Stretch-induced mechanoporation of the plasmalemmal membrane causes an immediate efflux of potassium and influx of sodium and calcium, which depolarises cells and activates both voltage- and ligand-gated ion channels (Farkas et al., 2006; Giza et al., 2001, 2014). This depolarisation prompts the release of excitatory neurotransmitters, most notably glutamate, that bind to N-methyl-D-aspartate (NMDA) receptors, further exacerbating ionic imbalances and intensifying cellular depolarisation (Giza et al., 2001). This positive feedback loop of depolarisation and hyper-excitability creates a rapid “spreading depression." As a result, ATP-dependent ion pumps are activated to restore homeostasis, resulting initially in glucose hypermetabolism; however, the heightened energy demand eventually culminates in a cellular energy crisis. The initial phase of hyperglycolysis is followed by a period of glucose hypometabolism and altered cerebral blood flow (lasting up to 10 days); a state that increases vulnerability to additional injury and second impact syndrome (Romeu-Mejia et al., 2019). MRI-based studies have documented regional reductions in cerebral blood flow in the frontal and temporal lobes, areas particularly vulnerable to impact, and decreased global connectivity in the visual and sensorimotor cortices (Churchill et al., 2017).

These events are further compounded by acute sequestration of intracellular calcium in mitochondria, which can lead to mitochondrial dysfunction (for a review, see S. Kim et al., 2017), impaired oxidative metabolism, cell damage, and cell death (Giza et al., 2001, 2014). Alterations to the intracellular redox state can generate free radicals that disrupt metabolic pathways and heighten the risk of long-term impairments (Giza et al., 2014). Additionally, cytoskeletal damage and intra-axonal calcium flux degrades structural integrity via microtubule and neurofilament damage and phosphorylation (Nixon, 1993), which can im-

pair signalling capacity and result in an accumulation of amyloid precursor protein (APP) (Giza et al., 2014; Romeu-Mejia et al., 2019).

The initial glutamate increase is also followed by region-specific decreases up to two weeks post-injury. Inhibitory neurotransmitters, including γ-aminobutyric acid (GABA), also demonstrate region-specific decreases following injury (Romeu-Mejia et al., 2019).

2.3.2.2 *Subacute and chronic phase (days to years)*

Axonal changes and demyelination: In the days to weeks following injury, particularly in cases of repetitive mTBI, alterations in white matter and axonal integrity are increasingly evidenced by the literature. Initially, an acute phase of axonal swelling is observed, as indicated by increased fractional anisotropy on diffusion tensor imaging (DTI), a phenomenon hypothesised to reflect cytotoxic oedema (Wilde et al., 2008). In the subacute phase, decreased fractional anisotropy has been reported, which is consistent with axonal degeneration and demyelination within white matter regions and has been linked to impaired cognitive processing (Wozniak et al., 2007). More recently, demyelination in the intracortical white matter has been identified via analysis of T_1-weighted (T_1w) to T_2-weighted (T_2w) MRI image volume intensity ratios (Mahoney et al., 2022). These effects were most pronounced in the temporal cortex and persisted up to six months post-mTBI. Together with primary DAI, these findings suggest that significant and lasting alterations to axonal structures, including myelin, may contribute to adverse mTBI symptomatology.

Neuroplasticity and LTP: Following mTBI, alterations in receptor function and expression disrupt synaptic plasticity, particularly impairing long-term potentiation (LTP), a key process that mediates learning and memory (Romeu-Mejia et al., 2019). In murine models, hippocampal LTP disruption has been identified after mTBI, with partial recovery typically observed by seven days post-injury (Sick et al., 1998). However, this recovery appears to be delayed in female mice, extending up to 28 days (White et al., 2017); a protracted impairment that may exacerbate cellular vulnerability and contribute to neuron loss (Reeves et al., 1995). This is supported by data from human studies of sr-mTBI, where disruptions in neuroplasticity also correlated with deficits in motor learning (De Beaumont et al., 2012), highlighting the role of impaired synaptic mechanisms in the pathophysiology of mTBI and learning-dependant symptomatology.

Blood-brain barrier disruption: The blood-brain barrier (BBB) is a selectively permeable interface composed primarily of endothelial cells that form tight junctions regulating paracellular transport (Ballabh et al., 2004; Sahyouni et al., 2017). This barrier is reinforced and maintained by the neurovascular unit, including astrocytes, microglia, and pericytes (Broux et al., 2015) and prevents the passage of pathogens, neurotoxins, and blood cells into the brain (Z. Zhao et al., 2015). This protective barrier is essential to the preservation of central nervous system (CNS) homeostasis (Abbott et al., 2010), however, evidence indicates that BBB disruption can occur following a season of sports participation, with up to 52% of young athletes exhibiting signs of compromised barrier integrity (O'Keeffe et al., 2020). In the context of sports participation, this finding is particularly concerning given identification of BBB dysfunction as a feature of CTE (Doherty et al., 2016; Tagge et

al., 2018). In murine models of mTBI, increased BBB permeability has also been observed, often accompanied by atypical astrocytic responses that impede the restoration of BBB integrity (George et al., 2022; Shandra et al., 2019). Such alterations to this critical barrier may last for years after injury, are related to extended neurological symptomatology (Shlosberg et al., 2010), and may be implicated in gliosis and neuroinflammation (Y. Wu et al., 2020).

The astrocytic calcium-binding protein S100B, detectable in blood, has emerged as the primary assay-based marker for mTBI. While elevated serum S100B levels have been attributed to BBB disruption there is debate regarding the precise mechanisms, which remain incompletely understood (see Oris et al., 2023). Despite its status as the most widely utilised and clinically valuable blood biomarker for mTBI, its application is complicated by a narrow sampling window of three hours post-injury and confounds such as extra-neural sources and relationships with age and skin pigmentation (Backus et al., 2024; Oris et al., 2023; Sapin et al., 2021).

Inflammatory pathways: Neuroinflammation is increasingly recognised as a critical factor in both the initial neuronal pathology and the subsequent development of symptoms following mTBI (Rathbone et al., 2015). In the aftermath of injury, neuroinflammation is primarily mediated by the activation of resident immune cells, particularly microglia, which release a cascade of pro-inflammatory cytokines such as interleukin-6 (IL-6), interleukin-1β (IL-1β), and tumour necrosis factor-alpha (TNF-α) (Rathbone et al., 2015). While the initial inflammatory response is neuroprotective, extended inflammation can contribute to neuron loss and degeneration of brain tissue (Hinson et al., 2015; M. S. Kim et al., 2023). Murine models have demonstrated that these inflammatory responses can persist for up to eight weeks post-injury (Shultz et al., 2013). Sustained neuroinflammation has also been implicated in a broad spectrum of clinical sequelae, including headache, irritability, post-concussion syndrome, depression, sleep disturbances, fatigue, and cognitive dysfunction (Rathbone et al., 2015).

2.3.3 *mTBI and neurodegeneration:*

Exposure to mTBI, and in particular repeated mTBI, is associated with an increased risk of neurodegenerative diseases (Butler et al., 2022; McKee et al., 2023), constituting one of 12 modifiable factors (Livingston et al., 2020). In particular, mTBI has been associated with progressive tauopathies such as AD (Mahoney et al., 2022) and CTE (Murray et al., 2022). Central to these pathologies is tau, a microtubule-associated protein that normally supports cytoskeletal integrity but becomes phosphorylated (p-tau) and aggregates into neurofibrillary tangles (NFTs) under pathological conditions (Goedert et al., 2017). In CTE, a pathognomonic lesion is characterised by perivascular accumulation of p-tau in the fundus of the cortical sulci, generally in the frontal and temporal cortices, with additional aggregations in hippocampal subfields (e.g., cornu ammonis (CA) regions 1 and 4) (Bieniek et al., 2021). CTE remains a post-mortem diagnosis and its underlying pathophysiology is still under investigation (for a recent review, see Murray et al., 2022), impeding early identification and intervention.

Understanding the acute-to-chronic neurometabolic cascades is critical to identifying the trajectory from mTBI to later-life neurodegeneration. Recent systematic reviews have underscored the central role of vascular pathology, BBB leakage (Doherty et al., 2016; Tagge et al., 2018), and neuroinflammation, particularly reactive astrogliosis and microglial activation (Murray et al., 2022; Osterman et al., 2025), in the development of CTE and other tauopathies including AD (Hardy et al., 2023). Axonal injury has been implicated in pathological tau phosphorylation and the increased expression of amyloid-beta (Aβ) (Johnson et al., 2013; Katsumoto et al., 2019; Tran et al., 2011). In addition, reactive astrocytes exhibit impaired clearance of these proteins, further exacerbating their accumulation (Cherry et al., 2020; Iliff et al., 2014).

Additional candidate hypotheses such as Blaylock's immunoexcitotoxicity model propose that initial mTBI events, coupled with environmental exposures including to neurotoxic metals like iron, prime microglia such that subsequent traumas elicit an exaggerated excitotoxic, inflammatory, and immune response (Blaylock et al., 2011). This disrupts glutamate clearance, induces oxidative stress, lipid peroxidation, and mitochondrial dysfunction, and may ultimately lead to dendritic retraction, synaptic injury, neuron loss, and tau hyperphosphorylation, which are posited to contribute to the progressive neurodegeneration observed in CTE.

2.4 BRAIN IRON IN THE ACUTE-TO-CHRONIC NEUROMETABOLIC CASCADE

The preceding background on injury mechanisms and temporally-mediated biological cascades is essential for understanding the role of iron in mTBI, particularly its contribution to secondary injury and potential involvement in long-term neurodegenerative processes. This foundation underscores why iron, and related biophysical substrates, may represent a promising target for elucidating mTBI pathophysiology and have been selected as the primary focus of this thesis.

Iron, the most abundant trace metal in the brain, is essential for numerous neuronal processes including neurotransmitter-, myelin-, and DNA-synthesis, cellular metabolism, oxygen transport, mitochondrial respiration, and oxidative phosphorylation (Gozt et al., 2021a; Madden et al., 2023; Stephenson et al., 2014; R. J. Ward et al., 2014). Cellular concentrations are tightly regulated within neural tissue and iron overload, particularly in non-haem forms (i.e., iron bound to proteins like ferritin and transferrin rather than haem groups), is increasingly recognised as a driver of secondary neurotoxic events (Gozt et al., 2021a; Nisenbaum et al., 2014) and cognitive dysfunction after mTBI (Huang et al., 2021; Lu et al., 2015; Raz et al., 2011).

The precise mechanisms leading to iron overload after mTBI remain unclear, however, the extant literature indicates that under normal conditions, one mechanism by which non-haem iron enters the brain is via active transport across the BBB through vascular endothelial cells. The putative mechanisms have been recently reviewed by Levi et al. (2024) and are summarised here. The apical surface of the endothelial cells, which interfaces with the bloodstream, express the transferrin receptor 1 (TfR1), serving as the primary pathway

for transferrin-bound iron uptake (see Fig. 2.1). Non-transferrin-bound iron likely crosses the BBB via endocytosis when bound to ligands such as citrate, ATP, or albumin, or following reduction to ferrous iron by ferrireductases, after which it is transported by divalent metal transporter 1 (DMT1) or other dimetal transporters. Ferritin-bound iron can cross the BBB via ferritin receptors such as Tim-2. Once on the basal side of the BBB, iron is taken up by most cells, which express a range of iron-handling proteins in varying ratios; any excess iron is sequestered in ferritin to mitigate oxidative stress.

However, injury-induced microvascular dysfunction, microbleeds, and increased BBB permeability likely increase iron transport (Gozt et al., 2021a; Huang et al., 2021; R. J. Ward et al., 2014); processes which have been linked to significantly increased non-haem brain iron content (Xiong et al., 2014). When iron accumulates to pathological levels, it can exceed the capacity of storage proteins, increasing the labile iron pool and initiating auto-toxic circuits that drive secondary injury cascades (Gozt et al., 2021a; Huang et al., 2021; Nisenbaum et al., 2014) and neurodegenerative processes (Levi et al., 2024; Rouault, 2013; R. J. Ward et al., 2014).

Specifically, iron overload triggers redox reactions that generate reactive oxygen species (ROS) via the Haber–Weiss reaction, which occurs as a two-part process (see Kruszewski, 2003; Levi et al., 2024). In the first phase, ferric ions (Fe^{3+}) are reduced to ferrous ions (Fe^{2+}) by reacting with superoxide (O_2^-):

$$Fe^{3+} + O_2^- \rightarrow Fe^{2+} + O_2 \tag{2.1}$$

The second phase is the Fenton reaction whereby ferrous ions (Fe^{2+}) react with hydrogen peroxide (H_2O_2) to regenerate ferric ions (Fe^{3+}) and produce hydroxide ions (OH^-) and highly reactive hydroxyl radicals ($\cdot OH$):

$$Fe^{2+} + H_2O_2 \rightarrow Fe^{3+} + OH^- + \cdot OH \tag{2.2}$$

Iron overload and the highly reactive species generated by redox cycling can lead to cytotoxic oxidative stress, lipid peroxidation, increased cell membrane permeability, increased expression of pro-inflammatory cytokines, demyelination, damage to DNA, RNA, carbohydrates, lipids, and proteins, impaired repair mechanisms, mitochondrial dysfunction, glutamate excitotoxicity, proteinopathy, and iron-regulated cell death (ferroptosis) (Daglas et al., 2018; Gozt et al., 2021a; Kruszewski, 2003; Levi et al., 2024; H. Ma et al., 2022; Mackenzie et al., 2008; Nisenbaum et al., 2014; Stephenson et al., 2014; Tang et al., 2020; R. J. Ward et al., 2014). Iron deficiency has also been implicated in neuronal cell death (Levi et al., 2024).

Evidence suggests iron overload also contributes to tau hyperphosphorylation (Nisenbaum et al., 2014; Yamamoto et al., 2002), thus playing a role in the neurodegenerative processes that culminate in tauopathies. Histologically-validated co-localisation of iron

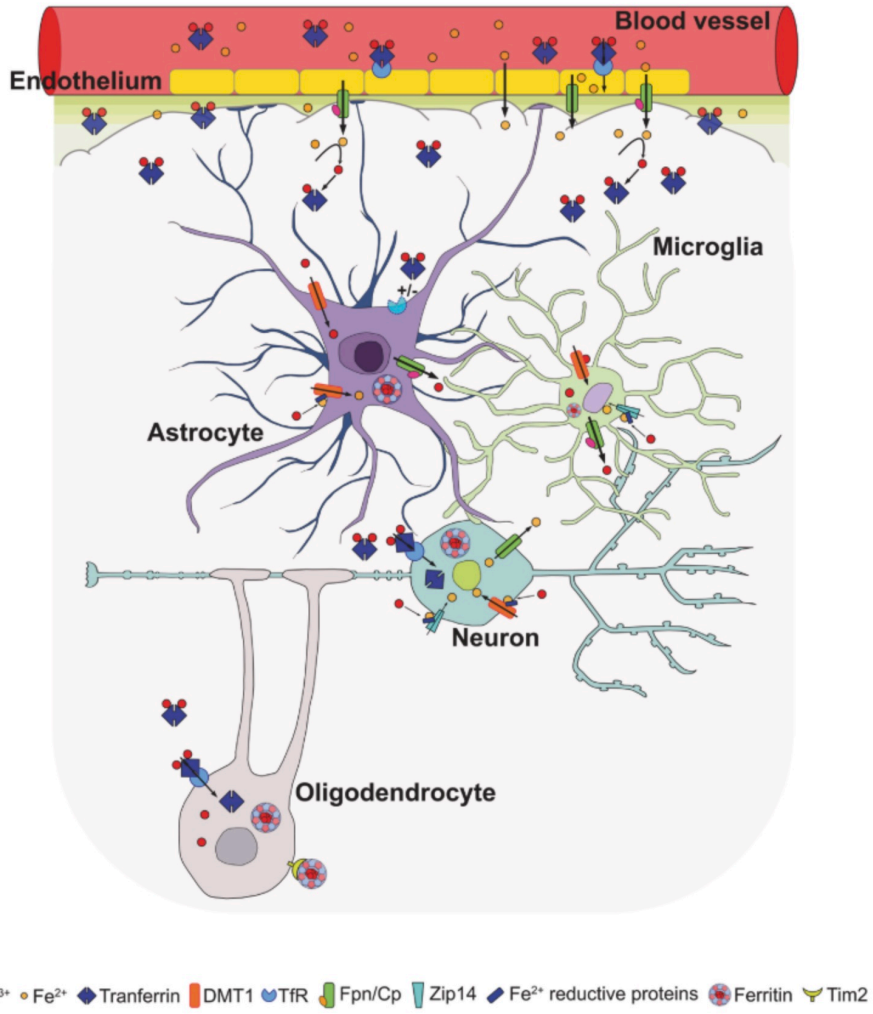

Figure 2.1: Mechanisms of iron transport across the BBB and cellular uptake in the CNS

Iron is transported across the BBB and into the CNS via receptors on the apical surface of endothelial cells. Once on the basal side, iron is taken up by astrocytes via DMT1, by oligodendrocytes via Tim-2 or DMT1, and by neurons through both the Tf-TfR1 pathway and DMT1. Figure reproduced from Levi et al. (2024) under the terms of the Creative Commons CC BY license.

with abnormal protein accumulations has established brain iron as a pathologic feature of AD and PD (Lassmann et al., 2012; Stankiewicz et al., 2007; R. J. Ward et al., 2014; Zecca et al., 2004). Iron dysregulation has also been noted in the pathogenesis of Huntington's disease (HD), Friedrich's ataxia (FRDA), and amyotrophic lateral sclerosis (ALS), as well as in chronic haemorrhage, cerebral infarction, anaemia, thalassaemia, haemochromatosis, Hallervorden-Spatz, down syndrome, and AIDS (Haacke et al., 2005; Rouault, 2013; Y. Wang et al., 2017). Identification of iron within NFTs in histological samples of CTE tissue also suggests involvement of iron in TBI-related degenerative processes (Bouras et al., 1997). Here, the sulcal fundus' heightened susceptibility to mechanical strain (Bakhtiarydavijani et al., 2021; Ghajari et al., 2017) and microhaemorrhage (Kornguth et al., 2017), coupled with dysregulated iron transport across the BBB under injury conditions and evidence implicating iron in tau phosphorylation is particularly intriguing given that pathognomonic CTE lesions manifest as perivascular clusters of p-tau in the sulcal fundus.

A recent histological study provides support for the involvement of iron and subsequent oxidative stress in CTE pathology (Osterman et al., 2025). In this study, L-ferritin–positive astrocytes were observed in close proximity to CTE lesions, suggesting that astrocytic reactivity may be a response to excessive iron accumulation and compromised BBB regulation. While the spatial convergence of these mechanisms undoubtedly warrants further investigation, the precise relationship remains under investigation.

Tauopathies notwithstanding, altered iron levels have been linked to demyelination in ageing (Biel et al., 2021) and in demyelinating disorders such as multiple sclerosis (MS), where dysregulated iron homeostasis may adversely affect myelin maintenance and repair (Bradl et al., 2010; Stephenson et al., 2014; R. J. Ward et al., 2014).

Finally, iron has also been implicated in the development of intracranial calcifications following infections in humans (Snyder-Keller et al., 2020) and seizures in murine models (Aggarwal et al., 2018). Murine models of TBI also support the presence of well-developed calcifications chronically (Laitinen et al., 2015; Lehto et al., 2012), which may also be present as smaller, more diffuse entities at earlier injury stages (Gayoso et al., 2003). Here, reasonable speculation suggests calcifications could be linked to injury-induced iron dyshomeostasis at multiple stages of injury.

Taken together, the literature on brain iron homeostasis identifies that deviations from normal levels not only indicate iron-related pathology but may also reflect broader changes in neural tissue, such as alterations to myelin, tau phosphorylation, and calcification. Despite evidence linking head trauma to elevated brain iron post-mTBI (Gozt et al., 2021a; Huang et al., 2021; Lu et al., 2015; Nisenbaum et al., 2014; Raz et al., 2011), the association between brain iron accumulation and the pathophysiology of acute sr-mTBI remains unclear. This thesis aims to address this gap by applying QSM, an advanced post-processing technique of MRI data that can map and quantify magnetisable neural substrates including iron, calcium, myelin, and certain proteins.

2.5 SUMMARY

This review serves a multidimensional purpose. First, it highlights the significant inter-individual variability in symptom presentation, injury burden, pathophysiology, and both short- and long-term impacts of mTBI. Second, it demonstrates how these factors can substantially degrade quality of life and daily functioning (McInnes et al., 2017), resulting in persistent disability for many individuals (Carroll et al., 2020); burdens that challenge the notion of this injury as "mild" (Zetterberg et al., 2016). Third, it provides an overview of the current state of mTBI research, emphasising the heterogeneity that complicates its study and diagnosis, and how these issues may be further exacerbated by a lack of standardised definitions. Collectively, this underscores the critical need for reliable, objective markers of injury; however, despite considerable efforts, current approaches have yet to yield a definitive biomarker of mTBI.

Lastly, the examination of the role of brain iron in the neurometabolic cascade of mTBI, its interplay with other biological substrates, and its potential contribution to neurodegen-

erative processes, provides a rationale for investigating brain iron as a promising target. The purpose of this thesis is to contribute to this essential research domain by elucidating the potential for mapping and quantifying brain iron accumulation, and other biological substrates, as objective markers of *in vivo* grey matter pathology in mTBI. The next section will outline the methodological underpinnings of QSM, and how this post-processing technique of MRI data can be leveraged in pursuit of this goal.

3

QSM: FROM PRINCIPLES TO APPLICATIONS

The following section provides an overview of the fundamental principles of MRI and the biophysical basis of magnetic susceptibility. The discussion is then extended to QSM and briefly touches on its precursor, SWI. This is followed by a review of the current clinical and research applications of QSM broadly, before examining the relatively few studies that have leveraged this technique to investigate tissue dyshomeostasis following mTBI. Collectively, this serves to contextualise the novel contributions of this thesis to the field, from post-processing thresholding techniques to enhanced anatomical precision that have, until now, been absent from the QSM-mTBI literature. The key points are summarised in § 3.10.

3.1 AN INTRODUCTION TO NUCLEAR MAGNETIC RESONANCE AND MAGNETIC RESONANCE IMAGING

MRI exploits the principles of nuclear magnetic resonance (NMR); a phenomenon first described by Bloch (1946) and Purcell et al. (1946). Azhar et al. (2023) provide a high-level overview of the fundamental principles of MRI relevant to clinical research, which are summarised below. MRI leverages *spin*, an intrinsic property of atomic nuclei that possess an odd number of neutrons or protons, such as hydrogen (^{1}H) which is abundant in biological tissues. Spin is analogous to the movement of a spinning top rotating around its own axis. However, it is important to parse the distinctions between this analogy and the fundamental properties of spin; the elements of the nucleus do not literally rotate but instead generate a local dipolar field, called a *magnetic moment*. Under normal physiological conditions, ^{1}H nuclei in the body are randomly orientated such that the magnetic contributions of each nuclei do not generate a net magnetic field (see Fig. 3.1B). However, the application of an external magnetic field, such as the main magnetic field of an MRI scanner (B_0), causes the ^{1}H nuclei to align either parallel (spin-up) or antiparallel (spin-down) along the longitudinal (z) axis of B_0. These ^{1}H nuclei occupy one of two distinct nuclear energy states: a lower energy state for nuclei oriented parallel to B_0 and a higher energy state for those oriented antiparallel. Due to the energy differential between spin-up and spin-down orientations, a slight excess of nuclei in the lower energy spin-up state produces a small net magnetisation vector, M, along the z-axis in the direction of B_0, known as the longitudinal magnetisation $\left(M_z\right)$ (see Fig. 3.1C and Fig. 3.2). These nuclei rotate (*precess*) with an angular momentum around the B_0 z-axis (see Fig. 3.1A) at a velocity directly proportional to the field strength termed the Larmor frequency (ω_0). This relationship is quantitatively described by the Larmor equation:

$$\omega_0 = \gamma B_0 \tag{3.1}$$

where ω_0 is the angular frequency of the protons; γ is the gyromagnetic ratio constant for specific nuclei, and; B_0 is the magnetic field strength.

This small net magnetisation forms the fundamental source of the MRI signal, and is leveraged to generate image contrast. However, receiver coils used to encode image information are sensitive only to *transverse* magnetisation, which, at equilibrium, is zero. The application of a second radiofrequency (RF) magnetic field (B_1), applied perpendicular to B_0 (generally at 90°) and in short pulses at the Larmor frequency, excites the ^{1}H spins and tips the net magnetisation from its alignment along the z-axis into the transverse plane $\left(M_{xy}\right)$ perpendicular to B_0 (see Fig. 3.2), where the spins begin to precess coherently (i.e., in-phase at the same angular frequency). This phase coherence results in a non-zero net magnetisation in the transverse plane that can be detected and spatially encoded by the receiver coils. The resulting time-dependent signal, the free induction decay (FID) signal, has both a magnitude and a phase component. At the same time, the population differ-

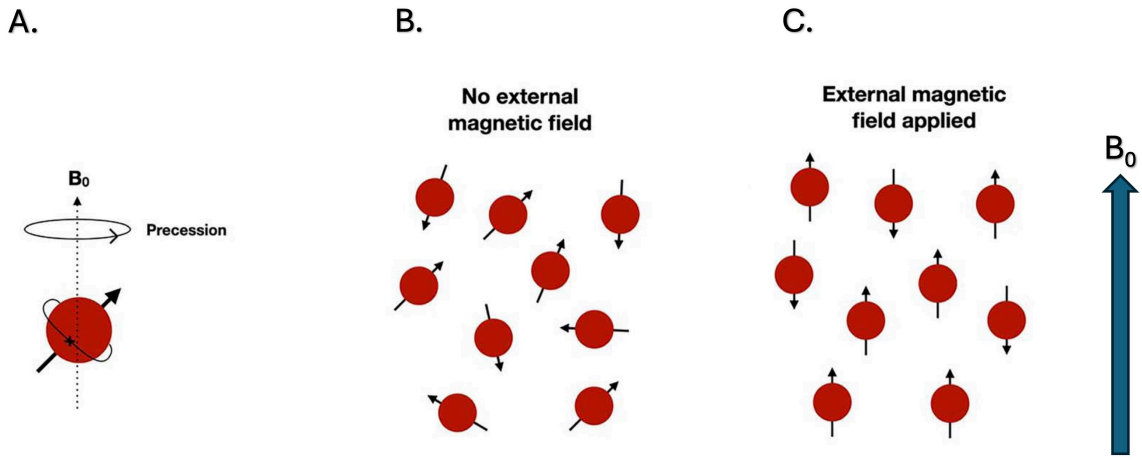

Figure 3.1: Nuclear spin precession, random orientation, and alignment in B_0

A. Depicts the precession of a nuclear magnetic moment of a nucleus (black arrow) precessing about the external magnetic field B_0 (green arrow) at the Larmor frequency ω_0. B. Illustrates the random orientation of the magnetic moment under normal physiological conditions. C. Shows the alignment of these nuclei either parallel (spin-up) or antiparallel (spin-down) along the longitudinal (z) axis of B_0. More nuclei occupy the lower energy spin-up state than the higher energy spin-down state. Figure adapted from Azhar et al. (2023) under the terms of an Oxford University Press license.

ence between the spin-up and spin-down states is reduced, decreasing the longitudinal magnetisation.

Once the RF *excitation* pulse is switched off, the nuclei relax back toward equilibrium. This *relaxation* involves two key processes. First, T_1 relaxation (the recovery of longitudinal magnetisation), also known as spin-lattice relaxation, occurs as protons release absorbed energy to their surroundings (the lattice), returning to a lower energy state. Second, T_2 relaxation (the swift decay of transverse magnetisation) results from spin–spin interactions that cause a loss of phase coherence among spins in the transverse plane. Here, it is important to note that inhomogeneities in the magnetic field lead to additional dephasing, resulting in a faster signal decay termed T_2^* (or *observed*) relaxation. Differences in these relaxation rates across tissues form the basis for image contrast in MRI.

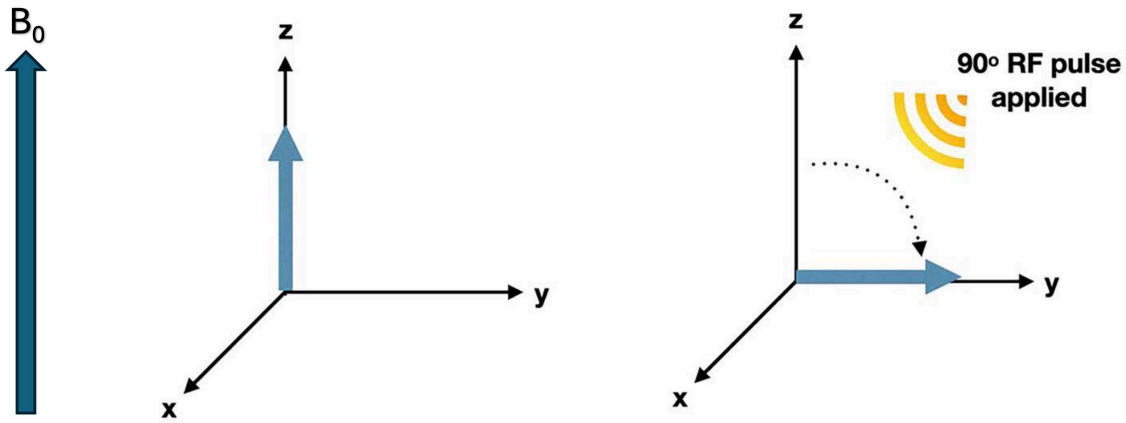

Figure 3.2: Net magnetisation vectors and radiofrequency excitation

This figure shows how the net magnetisation initially aligns along B_0. When a 90° radiofrequency pulse (B_1) is applied, the net magnetisation is tipped into the transverse plane, where the signal can be detected by the receiver coils. Figure adapted from Azhar et al. (2023) under the terms of an Oxford University Press license.

A second rephasing RF pulse applied at 180° (as in a T_2w spin-echo sequence) or via gradient-mediated rephasing (as in a T_2^*-weighted gradient-recalled echo (GRE) sequence), reverses the dephasing of spins in the transverse plane, causing them to regain phase coherence. At the echo time (TE), when the magnitude of the transverse magnetisation is at its peak, the signal is sampled to generate an image.

Additional gradient (G) coils apply weak magnetic field gradients along the three orthogonal Cartesian axes, leading to spatial variations in the precessional frequency and phase of the spins and enabling the encoding of spatial information. G_z (parallel to B_0) is used for slice selection, while G_x and G_y (perpendicular to B_0) enable in-plane frequency and phase encoding. The resulting time-domain signal is then converted to the frequency domain via Fourier transformation for spatially resolved image reconstruction.

The repetition time (TR), which is the interval between two successive RF pulses, mediates the degree of T_1 relaxation while TE determines the extent of T_2 relaxation. Adjusting these parameters, among others, emphasises different relaxation characteristics of biological tissues, enabling the acquisition of images weighted by T_1, T_2, or T_2^* relaxation. For the purposes of this thesis, it is important to highlight that GRE sequences are especially prone to T_2^* dephasing, making them sensitive to magnetic field inhomogeneities and susceptibility effects.

This section has detailed how acquisition of T_1w, T_2w, or other contrast-weighted images, depends upon variations in relaxation characteristics, specific signal sampling, and user-selected pulse sequence parameters. In the next section, the biophysical basis of magnetic susceptibility will be explored, including how this can be leveraged in SWI and QSM as an indirect marker of tissue composition.

3.2 BIOPHYSICAL BASIS OF MAGNETIC SUSCEPTIBILITY

Magnetic susceptibility (χ) is a fundamental, dimensionless, physical property that represents the degree to which a material becomes magnetised when placed in an external magnetic field, such as B_0 (Deistung et al., 2017; Duyn et al., 2017; Schweser et al., 2016). In MRI χ is the bulk magnetic susceptibility of each voxel (Reichenbach, 2012), rather than the individual molecular contributions to susceptibility. The additional magnetic field generated by the magnetisation of a material is known as the *demagnetising* field (L. Li et al., 2004). Although the MRI signal predominantly originates from the ^{1}H protons in water, magnetic susceptibility is determined by the configuration of electrons in surrounding molecules, which have a magnetic moment far stronger ($\sim 10^3$) than that of protons (C. Liu et al., 2015b; Y. Wang et al., 2017).

The quantised spin and orbital angular momentum of unpaired electrons generate a net magnetic moment that aligns with the external field, leading to a positive (paramagnetic) susceptibility (C. Liu et al., 2015b), which is given by:

$$\mu_s = -g_s \mu_B \frac{S}{\hbar} \approx \mu_B \tag{3.2}$$

$$\mu_L = -g_L \mu_B \frac{L}{\hbar} \tag{3.3}$$

where μ_s is the magnetic moment of an electron from its spin and μ_L is the magnetic moment related to angular momentum; g represents the Landé g-factor; s and L denote spin and orbital angular momentum quantum numbers, respectively; $\hbar$ is the reduced Planck constant; and μ_B is the Bohr magneton (see Fig. 3.3A). The probability of finding an electron with a given set of quantum numbers follows the Boltzmann distribution, which in turn yields an effective magnetic moment, μ_{eff}. The more unpaired electrons present, the larger μ_{eff}, as the contributions from paired electrons largely cancel out (C. Liu et al., 2015b). For linear materials, assuming an isotropic response, the magnetisation (M) is directly proportional to the applied magnetic field (H), giving:

$$M = \chi H \tag{3.4}$$

thus, the magnetic susceptibility is approximately given by:

$$\chi \sim \frac{\mu_{\text{eff}}^2}{T} \tag{3.5}$$

where the temperature coefficient T is the Curie temperature C (see Fig. 3.3A).

As orbital electrons in a paired configuration precess about the external magnetic field, the circular current generates a magnetic moment that opposes the applied field. The result is a diamagnetic susceptibility (C. Liu et al., 2015b). In Langevin theory the magnetic moment of the induction current is given by:

$$\mu = -\frac{N e^2 \mu_0 H}{4 m_e} \rho^2 \tag{3.6}$$

where, N is the number of electrons per unit volume; e is the electron charge; m_e is the electron mass; μ_0 is the vacuum permeability; and ρ^2 represents the mean square distance of the electrons perpendicular to the direction of H (see Fig. 3.3B). Therefore, the diamagnetic susceptibility is:

$$\chi = -\frac{N e^2 \mu_0}{4 m_e 2} \tag{3.7}$$

which shows that the susceptibility is negative and indicates that non-spherical molecules possess an anisotropic magnetic susceptibility due to the orientation-dependent cross-

sectional area (C. Liu et al., 2015b). In this way, variations in the magnetic susceptibility depending on chemical composition can be understood.

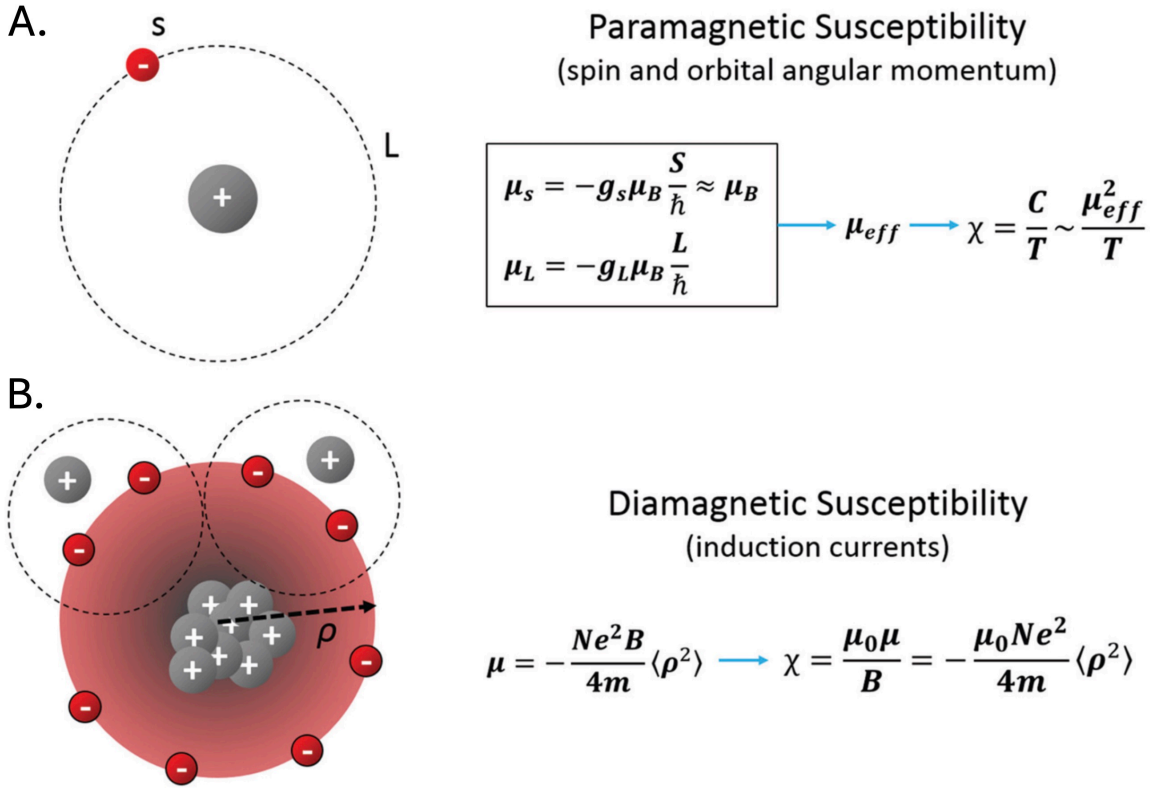

Figure 3.3: Atomic origins of magnetic susceptibility

A. Depicts paramagnetic susceptibility arising primarily as a result of the magnetic moments from both the spin and orbital angular momentum of electrons (μ_s and μ_L, respectively) in an applied magnetic field. Electrons occupy discrete energy levels according to a Boltzmann distribution, which leads to an expected magnetic moment, μ_{eff}, and a paramagnetic susceptibility inversely proportional to the temperature T. B. Shows diamagnetic susceptibility originating from the precession of orbital electrons in an applied magnetic field, modelled as a circular current. The current induces a secondary magnetic field that opposes the applied field, resulting in diamagnetic susceptibility. Figure reproduced from C. Liu et al. (2015b) under the terms of the Creative Commons CC BY-NC-ND license.

At the elemental level, the human body is predominantly composed of oxygen, carbon, hydrogen, nitrogen, calcium, phosphorus, magnesium, potassium, sulphur, sodium, chlorine, iron, and zinc (Y. Wang et al., 2017). The primary constituents of cells include water, proteins, lipids, minerals, and carbohydrates. Most naturally-occurring substrates of brain tissue have paired electrons, and as such are diamagnetic (Duyn, 2013). However, iron in ferritin, haemosiderin, and deoxyhaemoglobin contain unpaired electrons and have a paramagnetism orders of magnitude greater than most diamagnetic tissue constituents (Duyn, 2013; Y. Wang et al., 2017).

The bulk magnetic susceptibility of most biological tissue is relatively small, generally within $\pm$ 10-20% the χ of water, which itself has a weak diamagnetic susceptibility of approximately -9.05 parts per million (ppm) (Schenck, 1996). Because human brain tissue is ~70-85% water, the total tissue susceptibility in grey and white matter is generally within the range of -9.2 to -8.8 ppm, depending on its chemical concentrations (Duyn et al., 2017). While water forms the baseline for tissue magnetic susceptibility, the primary sources of susceptibility in the human brain are iron and myelin (Duyn, 2013; Reichenbach,

2012; Y. Wang et al., 2015) with additional contributions from calcium and certain proteins such as Aβ and tau (Gong et al., 2019; O'Callaghan et al., 2017; Z. Zhao et al., 2021).

Approximately 65% of the body's iron exists in the ferrous (Fe^{2+}) state, incorporated within the haem groups of haemoglobin, which typically contain four unpaired electrons per haem (Pauling et al., 1936). The electronic configuration of haemoglobin varies with its oxygenation state. When oxygen binds to haemoglobin (forming oxyhaemoglobin), electron splitting and pairing occurs, leading to a weak diamagnetic susceptibility (Pauling et al., 1936; Y. Wang et al., 2017). In contrast, deoxyhaemoglobin retains unpaired electrons, rendering it paramagnetic; a property that is exploited in susceptibility-sensitive MRI to differentiate venous blood from the surrounding tissue (Y. Wang et al., 2017). Over 97% of cellular iron is stored in the ferric (Fe^{3+}) state, predominantly as ferrihydrite within ferritin (Y. Wang et al., 2017). This storage form, which is especially abundant in grey matter (Hallgren et al., 1958), constitutes the primary source of paramagnetic susceptibility contrast. As such, the presence of non-haem iron enables highly accurate visualisation of grey matter structures, such as the iron-rich basal ganglia which contain two to three times more iron than the cortical grey matter (Haacke et al., 2005).

In contrast, myelin, calcium, and certain proteins exhibit diamagnetic properties relative to water (Duyn, 2013; Gong et al., 2019; W. Li et al., 2012; O'Callaghan et al., 2017; Schweser et al., 2010; Schweser et al., 2011b; Z. Zhao et al., 2021). However, it is important to note that susceptibility in white matter is anisotropic and orientation-dependent, primarily due to the presence of myelin, whereby the layered, lipid-rich structure results in a magnetic susceptibility dependent on the angle relative to B_0 (Duyn, 2013; W. Li et al., 2012). Air also has paramagnetic properties owing to the presence of molecular oxygen which can induce susceptibility artefacts on MRI that are particularly strong at air-tissue interfaces (Azhar et al., 2023).

The variations in χ induced by tissue constituents create local magnetic field perturbations that lead to inhomogeneities in the phase maps of GRE sequences (De Rochefort et al., 2010; Deistung et al., 2017; Langkammer et al., 2015; Marques et al., 2005) and modulate the T_2^* signal decay (Y. Wang et al., 2015). Historically regarded as a source of artefact and discarded (Deistung et al., 2017), these variations can now be exploited to generate contrast that reflects underlying biological components and cellular architecture of tissue (C. Liu et al., 2015b; Y. Wang et al., 2015). This information can be leveraged as an indirect marker of dysregulated iron metabolism, the presence of calcifications (hydroxyapatite crystals), myelin pathology, and proteinopathy; for example, in mTBI (Gozt et al., 2021a; Huang et al., 2021; Lu et al., 2015; Nisenbaum et al., 2014; Raz et al., 2011). However, the specificity and nature (qualitative versus quantitative) of the final output are determined by the post-processing technique employed. Below, two different approaches to post-processing of magnitude and phase images derived from the complex signal of T_2^*-weighted GRE acquisitions (see Fig. 3.4) are explored.

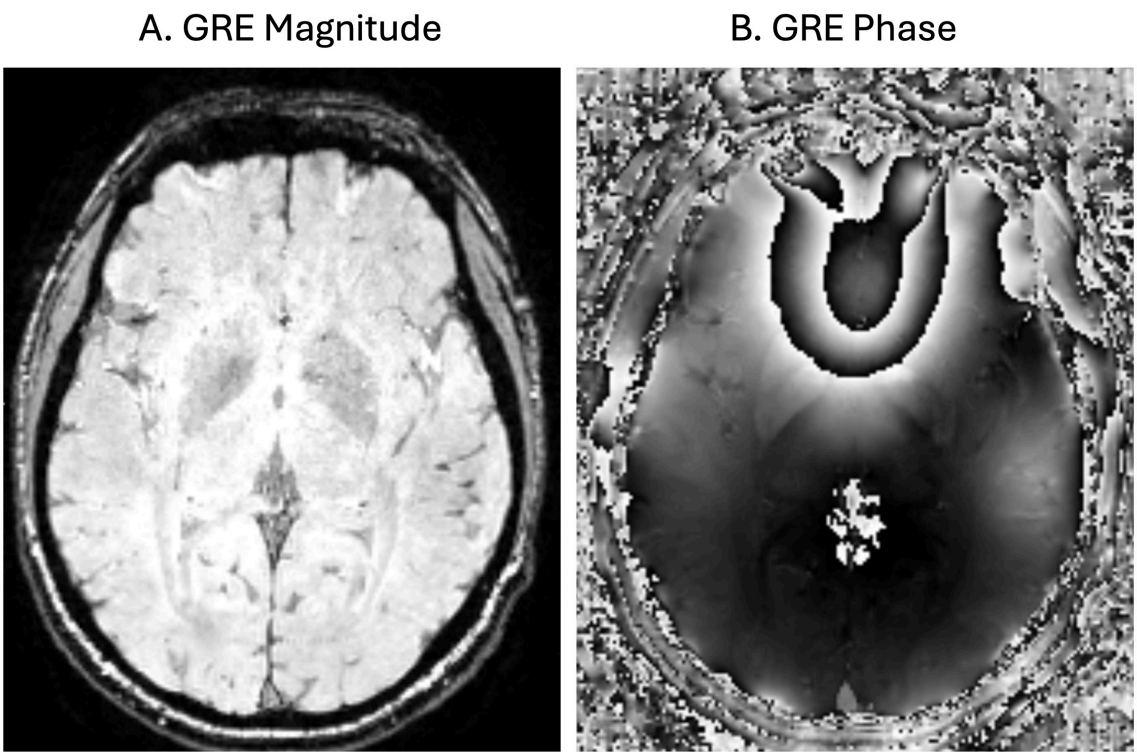

Figure 3.4: Magnitude and phase images

Magnitude (A.) and raw, unwrapped phase (B.) images from a T_2^*-weighted GRE acquisition.

3.3 SUSCEPTIBILITY-WEIGHTED IMAGING

SWI (Haacke et al., 2004) is a high-resolution venographic technique that leverages spin dephasing and frequency shifts induced by various paramagnetic and diamagnetic sources of susceptibility, and the resultant T_2^* signal loss, to enhance image contrast (Haller et al., 2021; Y. Wang et al., 2015). Magnitude and phase images are typically derived from complex data acquired using a T_2^*-weighted 3D GRE sequence with long TEs. The phase data are then filtered, usually with a homodyne high-pass (HP) filter, and transformed into a phase mask with amplitude normalised between 0 and 1. This mask is multiplied, often repeatedly, with the corresponding magnitude image, thereby enhancing phase-based contrast and accentuating paramagnetic susceptibility effects (e.g., deoxyhaemoglobin in venous structures, haemosiderin in microbleeds, iron sequestered in ferritin) as well as diamagnetic features, such as calcium and white matter (Duyn, 2013; Haller et al., 2021). A minimum intensity projection (mIP) across multiple sections can then be applied to further improve the conspicuity of venous structures and other susceptibility-related features (Haller et al., 2021).

SWI has been in clinical use for more than two decades (Haller et al., 2021) and has found utility in a range of diagnostic applications both inside and outside of the brain, including stroke (Elnekeidy et al., 2014; Luo et al., 2015), TBI (Spitz et al., 2013), PD (Schmidt et al., 2017), cerebral amyloid angiopathy (Haacke et al., 2007), siderotic nodules in cirrhotic liver (Dai et al., 2011), prostate cancer and prostatic calcification (Bai et al., 2013), and

spinal cord injury (M. Wang et al., 2011). Despite the broad range of applications, however, SWI remains a qualitative technique, and paramagnetic and diamagnetic susceptibility sources often appear hypointense on SWI and SWI-like images due to the convoluting effect of the dipole fields, rendering differentiation unreliable (i.e., between a calcification and a haemorrhage) (Haller et al., 2021; C. Liu et al., 2015a; Schweser et al., 2010). These limitations, along with the potential for blooming artefacts that can over represent the spatial extent of susceptibility sources, and the inability of SWI to resolve the non-local nature of phase variations (Schäfer et al., 2009; Yablonskiy et al., 1994), prompted the development of QSM (C. Liu et al., 2015a).

3.4 QUANTITATIVE SUSCEPTIBILITY MAPPING

The measured magnetic field results from the cumulative contributions of all susceptibility sources, thus the phase does not represent the local magnetic properties of isolated voxels. Instead, each voxel is a weighted sum of the susceptibilities from surrounding tissues (Y. Wang et al., 2015) (see Fig. 3.7A). Estimation of local magnetic susceptibility necessitates deconvolving the magnetic field to extract the local tissue magnetic properties; a process termed QSM (see Fig. 3.6).

Early attempts to measure the magnetic field perturbations generated by arbitrary bulk susceptibility distributions laid the groundwork for the development of QSM (Koch et al., 2006; Marques et al., 2005; Salomir et al., 2003). This post-processing technique derives scalar maps from GRE phase data to represent the spatial distribution and relative concentrations of paramagnetic and diamagnetic substances in tissue (Deistung et al., 2017; C. Liu et al., 2015a). Through a process of dipole inversion to recover the susceptibility distribution, voxel-wise numerical values of susceptibility are generated which provide both the magnitude and sign (positive or negative) of the magnetic susceptibility and are generally quantified in ppm. In QSM positive values indicate paramagnetism (iron-related), whereas a negative values indicate diamagnetism (myelin-, calcium-, and protein-related). Thus, QSM overcomes the non-quantitative nature and lack of specificity associated with SWI (Reichenbach, 2012) (see Fig. 3.5). However, there are inherent challenges associated with dipole inversion to generate QSM, which are discussed below.

3.4.1 *The ill-posed inverse problem in QSM*

One of the primary challenges in QSM arises from the ill-posed nature of its inverse problem, or deconvolving the measured tissue field, ΔB_t, with the dipole kernel (Bilgic et al., 2024; L. Li et al., 2004; C. Liu et al., 2015b). Each voxel contributes a magnetic field that extends beyond its own voxel; as such, the local magnetic field experienced by any given voxel is a superposition of the dipole fields of surrounding voxels (see Fig. 3.7.1A) (C. Liu et al., 2015a; C. Liu et al., 2015b). Since the superposition of the magnetic field is linear and the dipole field of a unit dipole is shift-invariant (does not change from one voxel to another), the relationship between the susceptibility distribution (proportional to mag-

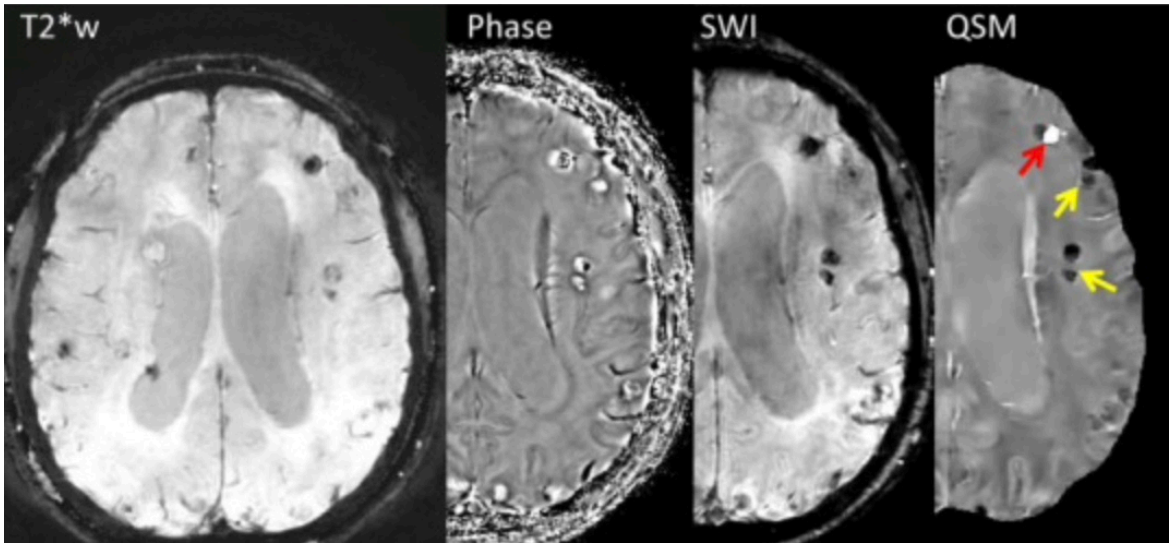

Figure 3.5: Comparative specificity of T_2^*-weighted imaging and post-processing techniques

This figure depicts a comparison of the appearance of calcified and active lesions in neurocysticercosis for T_2^*-weighted magnitude, filtered phase, SWI and QSM images. The ability of QSM to differentiate an active lesion with a positive susceptibility (red arrow) and calcified lesions with negative susceptibilities (yellow arrows) is exemplified. Figure reproduced from Y. Wang et al. (2015) under the terms of an Creative Commons Attribution license.

netisation) and the measured frequency distribution (proportional to local magnetic field) can be expressed as a convolution of neighbouring susceptibility values with the dipole response function (C. Liu et al., 2015a; Vinayagamani et al., 2021; Y. Wang et al., 2015). This convolution can be performed as a relatively straightforward point-wise multiplication in the Fourier domain (k-space):

$$\Delta B_z(\mathbf{k}) = B_0 \left(\frac{1}{3} - \frac{k_z^2}{k_x^2 + k_y^2 + k_z^2} \right) \chi(\mathbf{k}) \tag{3.8}$$

where $\mathbf{k} = (k_x, k_y, k_z)$ is the k-space vector, and k_z its z-component; B_0 is the main magnetic field oriented along the z-axis; $\Delta B_z(\mathbf{k})$ is the Fourier transform of the z-component of the magnetic field perturbation, and; $\chi(\mathbf{k})$ is the Fourier transform of the unknown susceptibility distribution. QSM attempts to invert this Fourier-domain equation to retrieve and quantify the underlying susceptibility (C. Liu et al., 2015b, 2015a; Salomir et al., 2003); see Fig. 3.6.

Although this inversion resolves the non-local property of phase data, challenges remain due to noise susceptibility in ΔB_z and the inherent ill-posedness of the dipole kernel (C. Liu et al., 2015b). The dipole exhibits zero-crossings along a double cone surface at the magic angle (54.7°) relative to the B_0 z-axis in the Fourier domain (De Rochefort et al., 2008; Haacke et al., 2005; C. Liu et al., 2015b; T. Liu et al., 2009; Y. Wang et al., 2015). As such, the kernel exhibits zero-crossings at $\frac{k_z^2}{k^2} = \frac{1}{3}$ (or $k^2 = 3k_z^2$). This defines a conical surface in k-space on which the coefficient becomes zero (see Fig. 3.7.1B), rendering $\chi(\mathbf{k})$ indeterminate and leading to instability, noise amplification, and a loss of information in

certain directions (C. Liu et al., 2015b, 2015a). This can manifest as streaking artefacts and spurious voxel values in the final susceptibility map (L. Zhou et al., 2017).

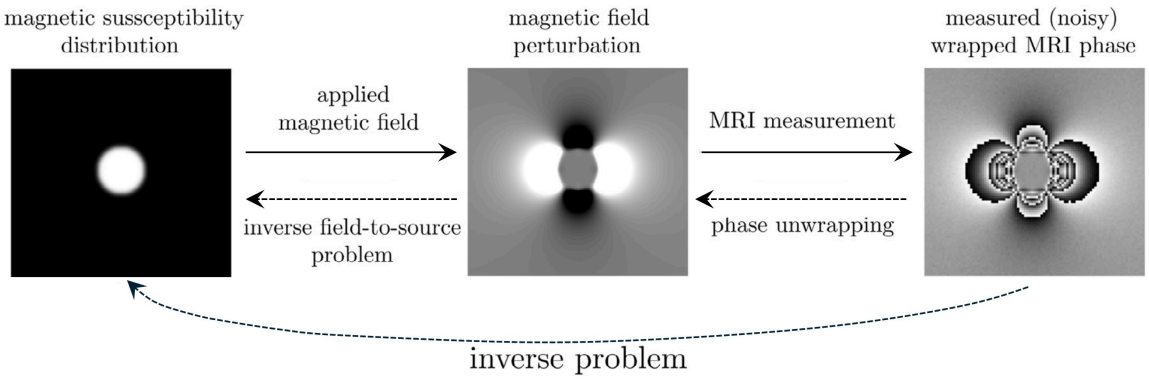

Figure 3.6: The inverse problem in QSM

This schematic shows how the magnetic susceptibility distribution (left image) perturbs the magnetic field (centre image) and leads to wrapped phase images (right). The inverse problem, or quantifying the magnetic susceptibility from the measured phase, is indicated with dashed arrows. Figure reused with permission from Schweser et al. (2016).

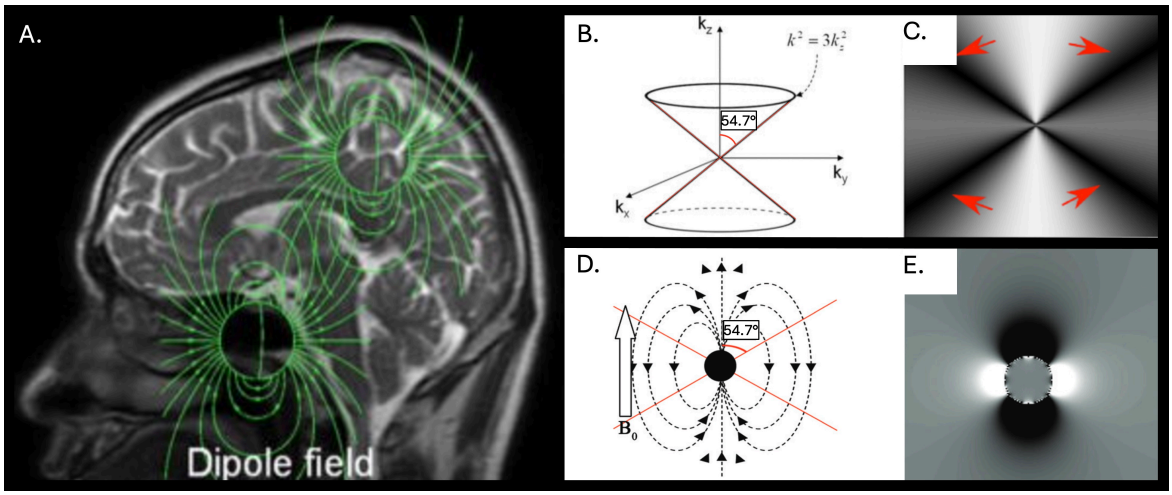

Figure 3.7: The ill-posed nature of the dipole kernel

A. Shows a sagittal MRI slice overlaid with dipole field lines, illustrating the non-local nature of the dipole field where each voxel's magnetisation extends beyond its own boundaries. The superposition of these fields is a convolution in the image domain that can be expressed as a simple multiplication in k-space relating field and susceptibility. B. This inverse problem is ill-posed because the dipole kernel vanishes on a double-cone surface in k-space when $k^2 = 3k_z^2$ (the "magic angle"). C. The unit dipole response is simulated in k-space, with red arrows highlighting the conical region of small absolute values. D. Shows the corresponding illustration of the dipole field and magic angle in real space, alongside a simulation of the dipole response in the spatial domain (E.). Figures in panel A. and B. reused with permission from C. Liu et al. (2015a). Figure in panel C. reused with permission from Schweser et al. (2016). Figure in panels D. and E. reused with permission from Harada et al. (2022).

As a result, directly performing this inversion is impossible without additional constraints and regularisation techniques to mitigate artefacts and enhance robustness. These include coil combination, phase unwrapping, combining multi-echo data (where applicable), masking, background field removal, and, finally, regularised dipole inversion (see Bilgic et al., 2024). Each step is critical for accurate deconvolution and estimation of tissue magnetic susceptibility; the central considerations are briefly reviewed below.

3.4.2 *Phase unwrapping*

In MRI the phase is wrapped every 2π radians, meaning that any signal exceeding the range $-\pi$ and π is folded back, which can introduce aliasing artefacts that distort the true phase information (C. Liu et al., 2015a). Here, phase unwrapping is essential to retrieve the actual phase from the measured phase (W. Li et al., 2011). Common approaches include spatial unwrapping algorithms such as path-based Rapid Open-source Minimum spanning trEe algOrithm (ROMEO) (Dymerska et al., 2021), region-based Phase Region Expanding Labeler for Unwrapping Discrete Estimates (PRELUDE) (Jenkinson, 2003), Speedy rEgion-Growing Algorithm for Unwrapping Estimated Phase (SEGUE) (Karsa et al., 2019b), and Seed Prioritized UNwrapping SPUN (Ye et al., 2019), and Laplacian unwrapping (Schofield et al., 2003), as well as temporal unwrapping for multi-echo acquisitions (Feng et al., 2013; Robinson et al., 2014).

3.4.3 *Background field removal*

Accurate dipole inversion depends on the effective removal of background fields. The measured field map, ΔB_0, not only contains contributions from brain tissue but also includes external sources, such as air-tissue interfaces and hardware imperfections, that must be eliminated to ensure that only brain susceptibility effects are inverted, enhancing the fidelity of dipole inversion (Bilgic et al., 2024). This background field removal is typically performed through an iterative masking process using a brain mask generated from the skull-stripped corresponding GRE magnitude image. Skull-stripping is typically performed using the Brain Extraction Tool (BET) (S. M. Smith, 2002) from the FMRIB Software Library (FSL) (Jenkinson et al., 2012; S. M. Smith et al., 2004; Woolrich et al., 2009) to remove non-brain tissues, air, and skull from the magnitude images. The mask is then used to suppresses unwanted field components outside of the mask boundaries (Bilgic et al., 2024). Several popular methods exist, including Projection onto Dipole Fields (PDF) (T. Liu et al., 2011a), Sophisticated Harmonic Artifact Reduction for Phase data (SHARP) (Schweser et al., 2011b) and its variants, and the Laplacian Boundary Value (LBV) method (D. Zhou et al., 2014). This removal of background field from the total field enables dipole inversion to be constrained to susceptibility variations induced by brain tissue only (Bilgic et al., 2024).

3.4.4 *Dipole inversion and regularisation*

Dipole inversion is the final step in sequential QSM reconstruction algorithms, and generates a susceptibility map from a local tissue field map after background field removal. To overcome the ill-posed nature of dipole inversion, regularisation techniques, typically incorporating priors such as smoothness or sparsity, are employed during dipole inversion to obtain a stable and physically meaningful solution (Y. Wang et al., 2015). The application of regularisation algorithms to approximate solutions for ill-posed problems is

well-established (Tikhonov et al., 1995). These algorithms enable close (though not exact) approximations of the susceptibility source and distribution during dipole inversion.

Differences in these approaches involve imposing constraints on the susceptibility gradients, either promoting sparsity through traditional ℓ_1 norm-based penalisation (least absolute error) or Total Variation (TV) regularisation, or promoting smoothness through the penalisation of large coefficients via Tikhonov/ℓ_2 norm (least squares error) regularisation, or a combination of the two (Bilgic et al., 2014; Milovic et al., 2022; Tikhonov et al., 1995). Smoothing can also be achieved by applying ℓ_1 penalisation to higher-order derivatives rather than only to the first-order gradient domain. For example, Total Generalised Variation TGV (Langkammer et al., 2015) applies ℓ_1 penalisation to both the first-order and higher-order derivatives. This smoothness-promoting method seeks to extend classical TV methods to balance edge-preservation with smoothing in an effort to eliminate staircasing artefacts that can occur with sparsity-only methods (Langkammer et al., 2015). While smoothness-promoting methods can perform well, sparsity-based ℓ_1 methods are considered more effective at producing high-quality images (Bilgic et al., 2014; Bilgic et al., 2024). Popular sparsity-based regularisation methods include TV, Morphology Enabled Dipole Inversion (MEDI) (J. Liu et al., 2012; T. Liu et al., 2011b; T. Liu et al., 2012b) and Rapid Two-Step Dipole Inversion (RTS) (Kames et al., 2018), which use ℓ_1 norm regularisation to produce stable, physically meaningful solutions and enhance edge preservation. The output from this final step is tissue magnetic susceptibility, quantified relative to a specific reference value.

3.4.5 *Reference selection*

Since QSM provides susceptibility values that are inherently relative rather than absolute, selecting a consistent reference region is crucial for robust comparisons across measurements, subjects, and scanners (Bilgic et al., 2024). Whilst the optimal reference region for susceptibility estimation remains debated, with each option necessitating different trade-offs in accuracy and stability (see Straub et al. 2017a), consensus guidelines recommend quantifying QSM relative to a defined reference region or structure (Bilgic et al., 2024). Larger reference regions, such as the whole brain, are preferred as smaller regions can be more vulnerable to artefacts, distortions, and field inhomogeneities which can affect the final map. This is particularly important when assessing certain pathologies whereby the presence of local lesions may affect accurate referencing. While this is less frequently encountered in mTBI, larger reference regions nonetheless produce maps that are stable, reproducible, and clinically meaningful (Bilgic et al., 2024).

3.5 METHODS TO ADDRESS BULK MAGNETIC SUSCEPTIBILITY AND ANISOTROPY

The presence of orientation-dependent and anisotropic myelin remains a challenge in traditional QSM (Denk et al., 2011; C. Liu et al., 2015b). In addition, various substrates of differing magnetic susceptibility sign within a single voxel may also inhibit the reliable quantific-

ation of QSM (Langkammer et al., 2012). To address these limitations, advanced techniques such as acquiring data at multiple orientations, tensor fitting, intra-voxel source separation methods for multi-echo data, and more rudimentary post-processing techniques for inter-voxel thresholding of single-echo data, have been developed and are discussed below.

3.5.1 *Magnetic source separation*

Each individual voxel is an ensemble of different molecules and may thus contain contributions from both paramagnetic and diamagnetic sources (C. Liu et al., 2015b), however, QSM represents the bulk magnetic susceptibility of each voxel (Reichenbach, 2012). This presents several challenges for quantitative MRI and the validation of results. Firstly, the relative magnetic susceptibility of these tissue compounds is not equivalent. Iron exhibits a strong paramagnetic response, whereas most diamagnetic components produce comparatively weaker signals (Ravanfar et al., 2021). Secondly, discrete brain regions are composed of a heterogeneous array of neural substrates. To provide a simplified example; the deep grey matter nuclei, despite their high iron concentrations, also contain some myelinated axons (Branson, 2013; Hametner et al., 2018). The cerebral cortex, on the other hand, is characterised by a complex laminar structure within which contributions from both iron and myelin vary (Möller et al., 2019; Stüber et al., 2014; Sui et al., 2022). Because each voxel represents the average susceptibility of all underlying sources, dominant signals can overshadow weaker, opposing contributions within a voxel, while the latter simultaneously dilutes the stronger signal (J. Chen et al., 2021). This has been demonstrated in AD where diamagnetic Aβ changes sign on QSM due to paramagnetic iron accumulating around the plaque (Telling et al., 2017; Tuzzi et al., 2020). Thirdly, when magnetic susceptibility is estimated within a given ROI, the typical practice of inter-voxel averaging to obtain regional mean susceptibility further masks the contributions of individual tissue elements, reducing specificity. In isolation, each of these factors can result in a less robust characterisation of the ground truth magnetic susceptibility; in combination, the effect is manifold.

3.5.1.1 *Intra-voxel magnetic source separation*

Multi-echo GRE (MEGRE) sequences can address both the problem of intra- and inter-voxel susceptibility averaging via magnetic source separation (see Ahmed et al., 2023; J. Chen et al., 2021; Dimov et al., 2022; Emmerich et al., 2021; J. Lee et al., 2024; Z. Li et al., 2023; Shin et al., 2021; Zhu et al., 2024). Using a multitude of different approaches, these new methods essentially compartmentalise the bulk susceptibility into sub-voxel sign-wise components, yielding separate maps (J. Lee et al., 2024).

These techniques have been applied to characterise the heterogeneity of iron accumulation/iron loss and demyelination/remyelination in relapsing and remitting MS (Zhu et al., 2024) as well as the paramagnetic rim and demyelinated lesion core in the same condition (Dimov et al., 2022). The diamagnetic component has also demonstrated potential for identifying susceptibility-specific protein aggregation and demyelination in AD relative to

traditional QSM (Ahmed et al., 2023). However, these methods cannot fully resolve the orientation-dependent, anisotropic nature of white matter fibers (Shin et al., 2021).

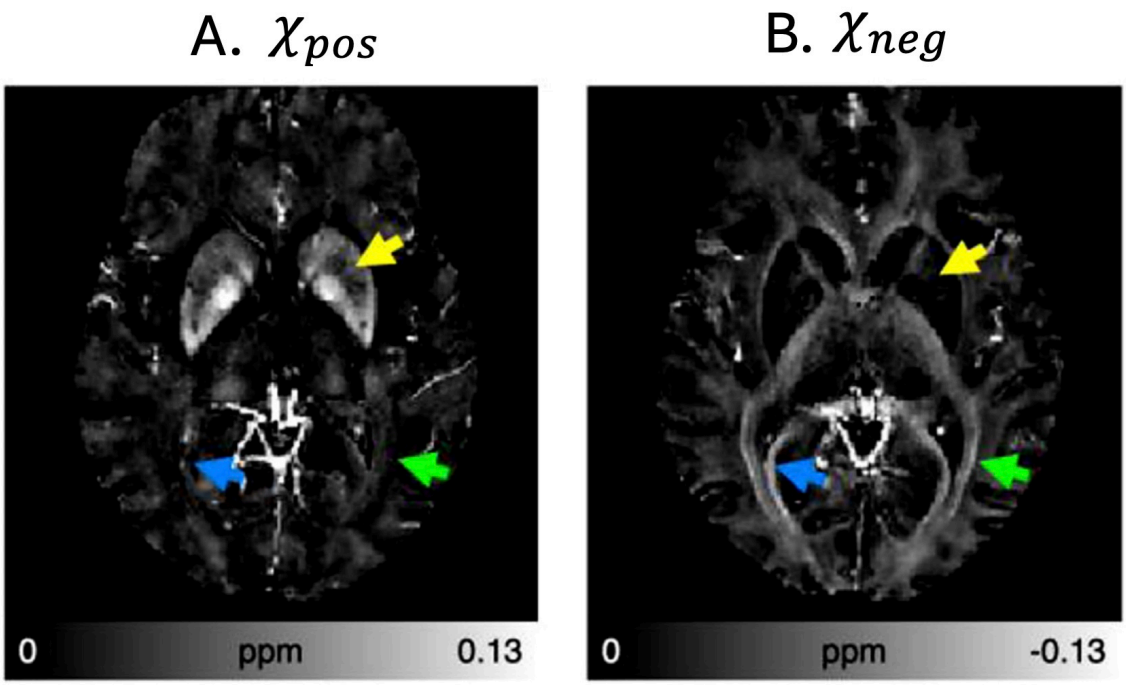

Figure 3.8: Magnetic source separation using χ-separation

This figure depicts the positive (A.) and negative (B.) maps yielded via application of χ-separation to QSM reconstructed from multi-echo data. These distinct maps illustrate the ability of magnetic source separation methods to isolate the well-characterised iron distributions in the deep grey matter (yellow arrows) and myelin in the white matter (green arrows = optic ratiation; blue arrows = forceps major). Susceptibility is measured in ppm. Figure reproduced from Shin et al. (2021) under the terms of the Creative Commons CC BY-NC-ND license.

3.5.1.2 *Inter-voxel thresholding*

While intra-voxel susceptibility source separation necessitates the acquisition of multi-echo data, a more rudimentary inter-voxel thresholding approach can be applied with single-echo data. This approach isolates voxels of net negative susceptibility from voxels of net positive susceptibility, i.e., thresholding above and below zero, thereby producing two separate maps of dominant voxel-wise sign. Thresholding single-echo QSM maps, where intra-voxel magnetic source separation is inhibited, may address some confounds related to *inter-voxel* averaging, providing a cleaner estimation of dominant ROI-wise susceptibility values during analysis. This may enable biologically informative data to be captured that would otherwise be lost. Inter-voxel thresholding has been applied to investigations of AD (Merenstein et al., 2024) and healthy ageing (Merenstein et al., 2025) with meaningful results.

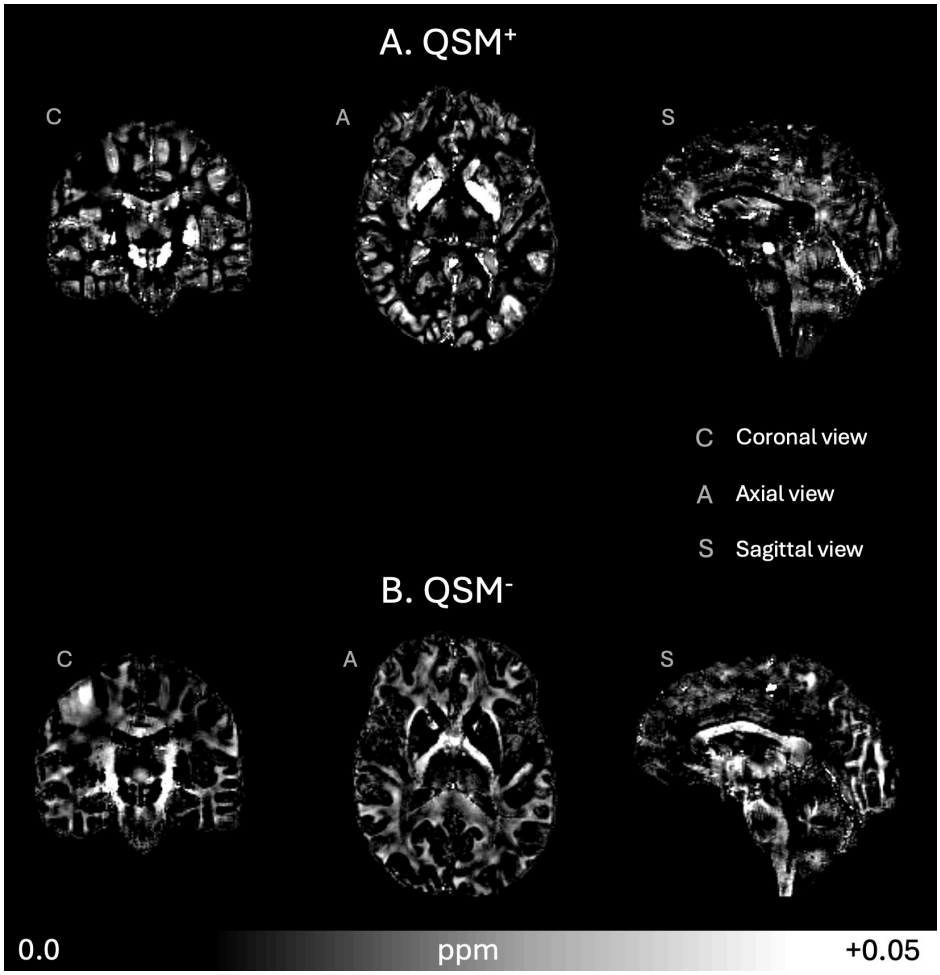

Figure 3.9: Inter-voxel thresholding of QSM

This figure depicts QSM thresholded for inter-voxel net susceptibility sign above (A. QSM^+) and below (B. QSM^-) zero. Negative maps were multiplied by -1 to aid visualisation. Images are shown in coronal (C), axial (A), sagittal (S) planes. Susceptibility is measured in ppm.

3.5.2 *Single- vs multiple-orientation methods*

Most QSM reconstructions and algorithms are based on single-orientation data. These methods assume that all frequency shifts in MRI phase images are solely due to bulk magnetic susceptibility variations within tissues (Marques et al., 2021). While this assumption simplifies the inversion process, it can overlook other contributing factors to the magnetic field distribution, such as anisotropic effects, which may compromise accuracy for specific biological substrates and, by extension, certain brain regions such as the white matter (J. Lee et al., 2010).

Susceptibility tensor imaging (STI), a method analogous to DTI, models magnetic susceptibility as a symmetric rank-2 tensor (i.e., a 3×3 matrix) (W. Li et al., 2017; C. Liu, 2010). STI enables mapping of anisotropic white matter fibre orientations and characterisation of myelin-related susceptibility anisotropy by explicitly quantifying individual magnetic susceptibility tensor elements, as well as deriving scalar metrics such as the mean magnetic susceptibility and magnetic susceptibility anisotropy (W. Li et al., 2017).

Multiple-orientation techniques (e.g., Calculation of Susceptibility Through Multiple Orientation Sampling [COSMOS]) (T. Liu et al., 2009) combine data from images acquired at multiple angles relative to B_0, rotating the dipole kernel and its ill-defined surfaces at each orientation. This approach enables the entirety of k-space to be sampled (C. Liu et al., 2015b).

However, both approaches involve rotating the patients' head to several different orientations (typically ∼5-6), leading to significantly increased total acquisition times (∼40 minutes) that are not typically feasible in clinical or research settings. In lieu of these time-intensive and participant-burdening approaches, optimisation of the previously described processing steps and adherence to best-practice guidelines (Bilgic et al., 2024) can improve susceptibility source localisation and significantly reduce artefacts (see Chapter 4).

3.5.3 *Standardisation*

Standardisation of QSM is paramount as variations in scanner hardware, acquisition parameters, and reconstruction algorithms can affect the measurement of susceptibility values (Bilgic et al., 2021; Langkammer et al., 2018). These issues underscore the need to apply consensus-based protocols to enhance clinical use, the reliability of research findings, and to facilitate cross-study comparisons. Thus, the identification and adoption of best-practice methods is also increasingly essential in this context (Bilgic et al., 2024).

3.6 VALIDATION

QSM has been validated as a robust marker of iron content via *in vivo* and *ex vivo* studies. For example, an ultrahigh-field *in vivo* imaging study has demonstrated both the sensitivity of QSM to iron content and its ability to delineate anatomical structures congruent with anatomical atlases derived from post-mortem histology (Deistung et al., 2013a). In this study, the same level of anatomical precision was largely absent from magnitude, frequency, and R_2^* maps (which reflects the degree of magnetic field inhomogeneity induced by intra-voxel spin dephasing). Post-mortem analyses have demonstrated a strong correlation between bulk magnetic susceptibility measured by QSM and chemically-determined iron concentrations via inductively coupled plasma mass spectrometry (Langkammer et al., 2012). This study confirmed non-haem ferritin as the primary iron storage form in grey matter and the dominant source of positive susceptibility on QSM. A recent *ex vivo* study comparing QSM to Perls iron-stained histological samples as a reference reported a 100% positive predictive value for detecting the paramagnetic, iron-laden rim in chronic active MS lesions; far exceeding the 63% predictive value reported for HP filtered phase images (Gillen et al., 2025). In addition, an ultrahigh-field investigation identified strong agreement between *in vivo* QSM and Perls stained histological samples for identification of iron-related nigral pathology in PD (Lewis et al., 2018). Here, QSM showed stronger associations with iron than did R_2^*.

Beyond iron, ultrahigh-field QSM of *ex vivo*, *in situ* human brain samples, despite orientation-dependent anisotropy, has demonstrated negative correlations between magnetic susceptibility and Luxol fast blue (myelin) intensities in subsequent histology (Hametner et al., 2018). In this study, myelin intensities in the thalamus were higher than those in the basal ganglia. Supporting these findings, investigations using both *in vivo* and *ex vivo* murine models have identified significant reductions in magnetic susceptibility in the striatum and thalamus relative to the cortical and hippocampal grey matter regions (O'Callaghan et al., 2017). This study concluded that the presence of diamagnetic myelin reduces susceptibility values quantified by QSM (O'Callaghan et al., 2017).

While the prevailing consensus is that iron and myelin are the primary contributors to paramagnetic and diamagnetic susceptibility, respectively (C. Liu et al., 2015b), QSM for the identification of proteins and calcifications has also been investigated. *In vivo* studies have demonstrate the performance of QSM relative to GRE phase imaging in distinguishing intracranial haemorrhage from calcification confirmed via CT (W. Chen et al., 2014b). Averaged across reports from two independent neuroradiologist examiners, QSM achieved 89.5% sensitivity and 94.5% specificity for haemorrhage, and 80% sensitivity and 93.5% specificity for calcification; all higher than sensitivity and specificity achieved with GRE phase.

In addition, a multi-modal *in vivo* and *ex vivo* investigation inclusive of QSM has demonstrated its sensitivity to low and intermediate tau burdens in AD (O'Callaghan et al., 2017). This finding has been reinforced by a similar study, which identified not only the diamagnetic nature of tau but also of$A\beta$ (Gong et al., 2019). Here, $A\beta$ and tau diamagnetism was first confirmed via phantom. Following confirmation, a transgenic murine model of AD was utilised to track longitudinal $A\beta$ accumulation *in vivo* with high fidelity. Subsequent *ex vivo* examinations indicated that the contrast induced by $A\beta$ extended to visualisation of individual $A\beta$ plaques, in addition to confirming high spatial correspondence between *in vivo* and *ex vivo* QSM for $A\beta$ localisation. Here, the authors noted that co-localisation of paramagnetic iron with diamagnetic substances, particularly weakly diamagnetic proteins, could reduce contrast and affect accurate quantification of tissue constituents. Finally, an *ex vivo* study conducted by Z. Zhao et al. (2021) found that both $A\beta$ and tau exhibited negative correlations with negative-signed QSM as well as traditional aggregate susceptibility values. However, the associations were less consistent for positive QSM values, where variance in the direction of relationships was observed for both tau and $A\beta$ depending on the sample.

Collectively, these studies demonstrate the ability of QSM to provide reliable delineation and quantitative measures of both paramagnetic and diamagnetic tissue constituents, including iron, myelin, calcium, tau, and $A\beta$. This capability has proved invaluable to investigating both normal development and pathological conditions, which are reviewed below.

3.7 APPLICATIONS

3.7.1 *Regional brain iron and ageing*

The ability of QSM to detect brain iron has rendered this post-processing technique central to studies of normative brain ageing. A seminal histological investigation conducted by Hallgren et al. (1958) has provided the foundation for many subsequent *in vivo* QSM investigations. Hallgren et al. (1958) reported a progressive accumulation of iron across the lifespan, spanning infancy to 100 years of age, in both cortical and subcortical grey matter. Their findings revealed that deep grey matter regions, particularly those of the extrapyramidal motor system, contained substantially higher iron concentrations (4.76–21.30 mg/100 g tissue) compared to cortical regions (2.92–5.03 mg/100 g tissue). More specifically, the globus pallidus exhibited the highest regional iron content, followed by the red nucleus, substantia nigra, putamen, dentate nucleus, caudate nucleus, and thalamus. In the cerebral cortex, the highest iron concentrations were localised to the motor cortex, with progressively lower concentrations in occipital, sensory, parietal, temporal, and prefrontal cortices. Iron in many of these brain regions demonstrated a significant relationship with age. Here, iron content in the red nucleus and substantia nigra increased until about 20 years of age and pallidal iron until approximately 30 years of age following which it plateaued, however, the putamen and caudate showed protracted accumulation into the fifth and sixth decade of life. Motor and sensory cortices displayed a similar trend for age-related increases that persisted until approximately 50 years of age, while the prefrontal cortex plateaued at age 30.

A number of QSM-based studies have subsequently corroborated these findings. For example, Persson et al. (2015) identified variability in the distribution of magnetic susceptibility values in deep grey matter consistent with Hallgren et al. (1958), citing the highest values in the globus pallidus and the lowest values in the thalamus. Many other authors have also reported considerable overlap between age-related QSM measurements and trends described by Hallgren et al. (1958), particularly in the deep grey matter (Gong et al., 2015; G. Li et al., 2023; Treit et al., 2021) and cortical grey matter (Acosta-Cabronero et al., 2016). One large-scale study of 498 individuals aged five to 90 years reported steep increases in QSM values in the caudate, putamen, and globus pallidus in childhood. In this study, susceptibility increases plateaued at 30 years of age in the caudate, but increased in the putamen and globus pallidus throughout adulthood (Treit et al., 2021). In addition, a recent review of 47 investigations has highlighted the general congruence between *in vivo* magnetic susceptibility values, regional tissue iron content, and relationships with age identified by Hallgren et al. (1958) (see Madden et al., 2023). Taken together, these investigations and reviews underscore utility of QSM for accurate localisation of tissue iron content and assessing the temporal biodynamics of brain iron in the context of normative ageing.

3.7.2 *Neurodegeneration*

Abnormal iron homeostasis has been implicated in a number of neurodegenerative diseases (see Chapter 2). Investigations of disease pathogenesis have established QSM as a useful tool for *in vivo* tissue characterisation. For example, several recent reviews have noted the consistent use of QSM for identifying and localising pathology in PD and AD or mild cognitive impairment. In addition, these reviews have highlighted its promise across a broad spectrum of disorders, including HD, FRDA, ALS, primary latereral sclerosis, Lewy body dementia, progressive supranuclear palsy, multiple system atrophy, neurodegeneration with brain iron accumulation, Wilson's disease, and spinocerebellar ataxia, among others (Ghaderi et al., 2024; Mohammadi et al., 2024b; Nikparast et al., 2022a; Paul et al., 2024; Ravanfar et al., 2021; Uchida et al., 2022). Across these conditions, iron deposition is most frequently observed within subcortical nuclei, though some studies also report disease-dependent cortical involvement (Ravanfar et al., 2021). In investigations of AD, for example, the putamen, caudate, and amygdala have been identified as regions of increased susceptibility across multiple studies, whereas the substantia nigra appears to be particularly implicated in PD (see Ravanfar et al., 2021). Elevated regional magnetic susceptibility has also been correlated with the severity or duration of a number of neurodegenerative diseases, including AD (L. Du et al., 2018), PD (G. Du et al., 2016; He et al., 2015), and ALS (Contarino et al., 2020; J. Y. Lee et al., 2017). These associations exemplify both the utility of QSM as an early diagnostic imaging biomarker and as a viable tool for clinical monitoring (Paul et al., 2024).

3.7.3 *Multiple sclerosis*

MS is an inflammatory and demyelinating disorder of the CNS characterised not only by white matter demyelination, grey matter lesions, and BBB impairment (Jakimovski et al., 2024), but also by iron dyshomeostasis which is posited to play a central role in its pathogenesis (Stüber et al., 2016; Zecca et al., 2004). Lesions in MS are typically classified by stage (preactive, active, chronic active, and chronic inactive), based on the degree of microglial activation and demyelination (Absinta et al., 2019; Jonkman et al., 2015; Kuhlmann et al., 2017). Preactive lesions appear myelin-normal but display microglial clusters indicative of an impending immune response, whereas active lesions are bordered by demyelination and myelin-phagocytosing macrophages. Chronic active lesions feature a fully demyelinated core with a *smouldering rim* of activated, iron-laden macrophages and microglia (Absinta et al., 2019; Wisnieff et al., 2015). Finally, chronic inactive lesions show complete demyelination with minimal immune cell presence. Pathological alterations in both iron and myelin content within lesions (Hagemeier et al., 2018), combined with the ability of QSM to differentiate diamagnetic from paramagnetic sources, have led to its widespread adoption for lesion identification and monitoring of lesion stage (see, for example, Absinta et al., 2019; W. Chen et al., 2014a; Hagemeier et al., 2018; Langkammer et al., 2013; Stüber et al., 2016; Wisnieff et al., 2015; S. Zhang et al., 2018; Zivadinov et al., 2018b).

3.7.4 *Neurovascular disorders*

Beyond its role in neurodegeneration, QSM significantly enhances diagnostic accuracy by distinguishing hyperintense, paramagnetic haemorrhage from hypointense, diamagnetic calcification (W. Chen et al., 2014b), as reviewed above in *Validation*. This capability is also particularly valuable for detecting and tracking cerebral microbleeds (T. Liu et al., 2012a; Subramanian et al., 2020; Q. Wu et al., 2017), monitoring recent haemorrhage in cerebral cavernous malformations (Girard et al., 2017; Zeineddine et al., 2018), identifying cerebral aneurysms (Nakagawa et al., 2019), and localising silent cerebral infarcts common to sickle cell anaemia (Murdoch et al., 2022). In addition, QSM can be used to identify and track changes in iron deposition and myelin in infarct and stroke (Han et al., 2023; Kataike et al., 2024; Uchida et al., 2024; Yang et al., 2024).

3.7.5 *Tumour*

Tumours often exhibit abnormal vasculature and angiogenesis. In aggressive malignant tumours, these vascular abnormalities can lead to haemorrhage, whereas in benign tumours, apoptosis may lead to calcification (Bandt et al., 2019). These distinct pathologies, along with their contrasting magnetic susceptibility signatures, render QSM an effective tool for identifying tumour characteristics and tumour grading via *IntraTumoural Susceptibility Signal*, exemplified in a recent case-series (Bandt et al., 2019). In addition, Deistung et al. (2013b) have applied QSM to characterise glioblastoma and identified regions of hyperintense positive susceptibility related to intratumoral blood products. Of particular interest, three patients in this study exhibited hypointense foci of negative susceptibility related to calcification, which was confirmed as an oligodendroglial component in subsequent histology for one patient (Deistung et al., 2013b).

3.7.6 *Venous oxygen saturation*

Due to the linear relationship between magnetic susceptibility values and deoxyhaemoglobin, QSM has been explored for estimating cerebral venous oxygen saturation ($Sv0_2$), from which the cerebral metabolic rate of oxygen consumption and the tissue oxygen extraction fraction can also be derived (Fan et al., 2014; Harada et al., 2022; Vinayagamani et al., 2021; J. Zhang et al., 2015). Alterations in oxygen saturation are observed in a range neurological disorders, thus assessing oxygen saturation provides valuable insight into the underlying pathophysiological disturbances. This capability has broad implications for understanding the pathophysiology of neurodegenerative and cerebrovascular disorders. For example, it has been applied to studies of hypercapnia (Fan et al., 2015a), steno-occlusive cerebrovascular disorders (Kudo et al., 2016; Uwano et al., 2015), ischaemic stroke (Probst et al., 2021), cerebral hyperperfusion following carotid endarterectomy (Nomura et al., 2017), arteriovenous malformations (Biondetti et al., 2019), systemic lupus erythematosis (Miyata et al., 2019), AD (Y. Liu et al., 2021), and MS (Fan et al., 2015b).

3.7.7 *Image-guided procedures*

Due to its high contrast-to-noise ratio, QSM has also been used to facilitate precise electrode placement for deep brain stimulation (DBS), where accurate anatomical localisation is crucial for treatment efficacy and safety (Bandt et al., 2019; W. Chen et al., 2014b; Harada et al., 2022; Vinayagamani et al., 2021). Here, QSM has been applied to presurgical planning for DBS of the subthalamic nucleus (Dimov et al., 2019; T. Liu et al., 2013; Rasouli et al., 2018), globus pallidus internus (Wei et al., 2020), and centromedian thalamic nucleus (J. Li et al., 2020).

3.7.8 *Extra-cerebral QSM*

Although QSM has been most extensively applied to intra-cerebral investigations, its use for body imaging is an active area of research. While several factors can confound the accurate characterisation of susceptibility maps, such as respiratory motion, cardiac pulsation, and the high susceptibility of fat, a number of mitigation strategies have emerged for body-compatible QSM where necessary. These include breath holds, adjustments to TR, flow compensation, and water/fat separation via multi-echo acquisitions (see Dimov et al., 2023). The applications of QSM in the body extend to imaging the liver and hepatic iron load (Jafari et al., 2021; Jafari et al., 2019; J. Li et al., 2018; Qu et al., 2021; Sharma et al., 2017; Sharma et al., 2015; Tipirneni-Sajja et al., 2021; R. Zhao et al., 2023), cardiac performance via blood oxygenation differentials between the left and right ventricles (Wen et al., 2019), imaging atherosclerotic plaques (Azuma et al., 2020; Ikebe et al., 2020; Ruetten et al., 2020; C. Wang et al., 2020), osteoporosis in menopause (Guo et al., 2019), calcifications in both the prostate (Kan et al., 2022; Straub et al., 2017b) and breast tissue (Schweser et al., 2011a), as well as renal fibrosis (Bechler et al., 2021).

3.8 QSM IN MTBI

Chapter 2 demonstrated that cellular components including iron, myelin, calcium, and proteins, are vulnerable to injury-related disruption in mTBI (Daglas et al., 2018; Giza et al., 2014; Gozt et al., 2021a; Nisenbaum et al., 2014). In the present chapter, the magnetic properties of these tissue elements were examined alongside an evaluation of QSM for localising and quantifying their spatial distribution within neural tissue. Collectively, these chapters converge to emphasise the value of QSM for elucidating the microstructural pathophysiology associated with mTBI, thereby addressing the question, *"why use QSM to study mTBI?"*

Despite its wide-ranging applications, the use of QSM to investigate mTBI micropathology remains relatively limited. To date, only a small number of studies have employed QSM to quantify magnetic susceptibility within white matter and/or grey matter (Bell et al., 2024; Brett et al., 2021; Gong et al., 2018; Koch et al., 2018; Koch et al., 2021; Pinky et al., 2022; Weber et al., 2018; Wright et al., 2022; Zivadinov et al., 2018a) or as a marker of

$Sv0_2$ (Chai et al., 2017; To et al., 2024; Wright et al., 2022). Studies pertaining directly to the focus of this thesis, namely the disruption of grey matter constituents, further constrains the number of relevant investigations.

A broad continuum of mTBI-related traumatic insults have been assessed across the seven studies investigating susceptibility-based grey matter alterations. To this end, a variety of research designs have been leveraged. Longitudinal studies have attempted to elucidate the cumulative effect of sub-concussive events over a football season (Gong et al., 2018) and track tissue disruption from the acute to the chronic injury phase (Koch et al., 2018). Cross-sectional designs have explored both acute (Koch et al., 2021; Pinky et al., 2022; Wright et al., 2022) and chronic injury profiles (Pinky et al., 2022; Zivadinov et al., 2018a), in addition to investigating susceptibility profiles in chronic persistent post-concussion syndrome (Bell et al., 2024) (see Table 3.9).

3.8.1 *Gaps in the literature and insufficient anatomical specificity*

Despite the diversity in study design, the extant literature has focused almost exclusively on susceptibility differences in deep grey nuclei as a proxy for injury effects and cellular dyshomeostasis. Most analyses are limited to total deep grey matter (Koch et al., 2021; Wright et al., 2022), basal ganglia segmentations (Bell et al., 2024; Gong et al., 2018; Pinky et al., 2022), or a combination of the two (Koch et al., 2018; Zivadinov et al., 2018a). Where segmentations have been employed, the analyses are typically confined to major subcortical structures such as the caudate, putamen, thalamus, and globus pallidus (see Table 3.9).

The rationale for focusing on these subcortical regions is the abundance of iron relative to other grey matter structures (Hallgren et al., 1958) which supports the high metabolic demand related to signal processing (Gozt et al., 2021a). Dense concentrations of iron are particularly noteworthy in the globus pallidus, red nucleus, substantia nigra, putamen, caudate, and thalamus (Hallgren et al., 1958) and may predispose these regions to iron-mediated disorders (Haacke et al., 2005). Additional vulnerability to shear and strain damage in mTBI (Raz et al., 2011) due to axons originating from, terminating in, or intersecting with these nuclei (Gozt et al., 2021a; Lifshitz et al., 2007; Ropper et al., 2007), for example thalamo-cortical projections (Shaw, 2002), may further increase the risk of iron-driven secondary injury. The high regional iron load confers the added benefit of enhanced contrast on QSM; it is thus hardly surprising that studies have limited their focus.

Nonetheless, the net result has been in an incomplete characterisation of other potentially vulnerable grey matter regions; a gap in the literature that has not escaped the notice of a recent review (see Gozt et al., 2021a). The cerebral cortex and hippocampus, for example, are prone to mechanical strain, excitotoxicity (including iron dyshomeostasis), and impact with the skull base (Arciniega et al., 2024; Bakhtiarydavijani et al., 2021; Bigler, 2007; Bigler et al., 2002; Bigler et al., 2012; Bouras et al., 1997; Ghajari et al., 2017; Kornguth et al., 2017; Mckee et al., 2015; McKee et al., 2023) yet remain under-researched in this context. To date, only three studies have extended their analyses to include additional subcortical structures, select cortical regions, or the cerebellar grey matter (Gong et al., 2018;

Pinky et al., 2022; Zivadinov et al., 2018a). Even these more comprehensive examinations have lacked the anatomical specificity needed to identify distinct structural and functional subregions that may be differentially affected by mTBI.

For example, while some studies have included structures such as the amygdala, hippocampus, and nucleus accumbens (Pinky et al., 2022; Zivadinov et al., 2018a), other deep nuclei of potential interest have nonetheless been overlooked. In addition, the treatment of the hippocampus as a single ROI has neglected the distinct characteristics of its subfields. Given the hippocampus' vulnerability to injury (Arciniega et al., 2024; Geddes et al., 2003), inflammatory processes, impaired LTP (Sick et al., 1998; White et al., 2017), and increased expression of APP (Wilde et al., 2007), such oversimplification may mask pathology. This issue is particularly salient given the high expression of TfR1 on the apical BBB endothelium in the hippocampi (Rouault, 2013), which may exacerbate abnormal iron transport across this barrier following injury. Indeed, both *in vivo* SWI (Lu et al., 2015) and histological analyses (Bouras et al., 1997) have identified hippocampal iron accumulation after mTBI. In addition, temporal regions, including the hippocampus, also exhibit region-specific atrophy and tau hyperphosphorylation in CTE (Bieniek et al., 2021; Cherry et al., 2021; McKee et al., 2023), which may be related to iron dyshomeostasis (Bouras et al., 1997; Nisenbaum et al., 2014; Yamamoto et al., 2002). Macroscopic methods may thus be unable to capture subtle hippocampal pathologies at the acute injury stage.

Pathological changes in these deep brain structures responsible for motor control (Calabresi et al., 2014; Lanciego et al., 2012), emotional regulation (Pessoa, 2017), learning (Seger, 2006), and memory (Bird et al., 2008), may also drive the heterogeneity of mTBI symptomatology. Alterations to the hippocampus, a crucial memory hub (Raslau et al., 2015), may underlie the cognitive deficits seen in mTBI (Mckee et al., 2015). Similarly, iron overload in the substantia nigra has been linked to significant cognitive impairment post-mTBI (Lu et al., 2015), but has yet to be explored using QSM. The convergent evidence indicates that more comprehensive assessments of the subcortical nuclei are warranted.

The limitations of the current literature also extent to the cerebral cortex; the two QSM-mTBI studies to include cortical grey matter ROIs were either constrained by a macroscopic voxel-wise approach (Gong et al., 2018), or limited to gross segmentations of a small number of cortical ROIs (Pinky et al., 2022). To date, no studies have accounted for cortical morphology, despite the cortex's convoluted structure characterised by ridges (gyri) and grooves (sulci) and a complex laminar architecture, both of which render it particularly vulnerable to mTBI-related damage. The base (fundus) of the sulci, for example, are exposed to the greatest mechanical force during mTBI, including shear stress (Bakhtiarydavijani et al., 2021; Ghajari et al., 2017) and movement of non-compressible cerebrospinal fluid (CSF) in a phenomenon referred to as the "water hammer effect" (Kornguth et al., 2017). The sulcal fundus is also a primary loci of degeneration and perivascular tauopathy in CTE (McKee et al., 2023; D. H. Smith et al., 2013) which may be linked to abnormal iron accumulation (Bouras et al., 1997; Osterman et al., 2025). Specific depths of the cortical laminae also appear to accumulate iron in a topographically heterogeneous in both ageing

(Merenstein et al., 2023; Northall et al., 2023) and AD (Merenstein et al., 2024). Similar effects are also evident for cortical myelin content across the lifespan (Sui et al., 2022).

This susceptibility of the cortex to injury and degeneration coupled with the role of iron in secondary injury cascades (Gozt et al., 2021a; Huang et al., 2021; Lu et al., 2015; Nisenbaum et al., 2014; Raz et al., 2011) and evidence of intracortical demyelination after mTBI (Mahoney et al., 2022) exemplifies the need for for analyses sensitive to cortical architectonics. Taken together, the prevailing lack of anatomical specificity constitutes a critical oversight in the current QSM-mTBI literature; a gap this thesis aims to address.

3.8.2 *Null findings are a pervasive feature of existing research: reasons and limitations*

The insufficient anatomical specificity of existing studies may explain why most QSM-based investigations have failed to detect significant grey matter susceptibility changes in mTBI (see Table 3.9). In fact, only two studies have reported significant findings in grey matter: a single instance of decreased susceptibility in the total grey matter sub-compartments (Koch et al., 2021), and a finding of increased susceptibility in the cerebellum (Pinky et al., 2022), constituting the only investigation of this structure to date.

Selection of control groups may further confound the literature. Most studies have used either healthy sport-matched athlete controls (Koch et al., 2018; Koch et al., 2021; Pinky et al., 2022; Wright et al., 2022) or non-contact sport athlete controls (Zivadinov et al., 2018a) (see Table 3.9). However, athletes are likely to have experienced sub-concussive events or multiple mTBI episodes in their sporting career, which could independently alter susceptibility measures and compromise the reliability of between-group comparisons. Similarly, using pre-season assessments as an internal baseline, particularly in adolescent cohorts (15–17 years; see Gong et al., 2018), may not adequately account for known developmental changes in magnetic susceptibility (Hallgren et al., 1958). Only one study (Bell et al., 2024) used healthy controls drawn from the general population, thereby minimising these confounds. This underscores the need for more carefully considered comparison groups to accurately isolate mTBI-related susceptibility alterations.

A further limitation is the use of supra-millimetre or anisotropic voxel resolutions in most studies (Bell et al., 2024; Gong et al., 2018; Koch et al., 2018; Koch et al., 2021; Zivadinov et al., 2018a) (see Table 3.9). These acquisition protocols reduce contrast, introduce errors in susceptibility mapping, and increase partial volume effects (PVE) (Karsa et al., 2019a). Such suboptimal spatial resolutions are thus not recommended by current consensus guidelines on best-practice QSM (Bilgic et al., 2024) and may have hindered the detection of subtle variations in susceptibility and microstructural integrity in previous investigations.

As discussed earlier this chapter, biomagnetic substrates exhibit opposing susceptibility profiles such that paramagnetic iron and diamagnetic myelin, calcium, and protein may co-exist within individual voxels. The effect of mTBI across a range of cellular compartments means that isolation of distinct susceptibility sources, within the constraints of the data at hand, may be critical to identifying the subtle biodynamics and injury cascades occur-

ring shortly after injury. While multi-echo data have been acquired in many studies (Bell et al., 2024; Gong et al., 2018; Koch et al., 2018; Koch et al., 2021; Wright et al., 2022), techniques for intra-voxel source separation remain unused. In addition, despite the promise of inter-voxel thresholding approaches to differentiate net voxel-wise susceptibility signals in single-echo data (Merenstein et al., 2025; Merenstein et al., 2024), they have not yet been applied to QSM analysis in studies that have used single-echo acquisitions (Pinky et al., 2022; Zivadinov et al., 2018a). A few studies have averaged susceptibility images across control subjects and applied a threshold (e.g., >0.05 ppm) to create basal grey matter masks or refine atlas-based segmentations (Koch et al., 2018; Koch et al., 2021; Wright et al., 2022). This method, however, only identifies ROIs and does not yield separate maps of voxel-wise susceptibility sign. As a result, analyses may include voxels with mixed susceptibility signs, obscuring subtle individual differences between positive and negative susceptibility values or diluting the net concentration. This limitation could plausibly account for the inability of most studies to identify significant results.

3.8.3 *Clinically- and individually-relevant investigations are missing from the literature*

Despite advances in inline reconstruction pipelines by scanner vendors (Borzage et al., 2022), QSM remains predominantly confined to research settings rather than seeing incorporation into routine clinical use (Haller et al., 2021). The translation of advanced imaging techniques into clinical diagnostic and prognostic tools may be further hindered by current methodological and statistical approaches. While group-level investigations are valuable for identifying signatures associated with specific disorders, such as structural alterations in the amygdala and hippocampus in anxiety (Łoś et al., 2021), and altered rostral anterior cingulate activity in depression (Pizzagalli, 2011), these standard statistical models may mask inter-individual variability (Marquand et al., 2019).

Analyses insensitive to individual variation may not only limit the generalisability of findings (Marquand et al., 2019), but could compromise the effectiveness of clinical intervention, rehabilitation strategies, and return-to-play guidelines derived from aggregated data in mTBI. An understanding of this injury and its effects predicated on group-level data may thus under serve the very population such research is intended to support. Individual-level investigations may better characterise mTBI-related neuropathology, and are increasingly recognised as for offering biologically informed and clinically relevant insights, particularly for populations where targeted interventions are both useful and necessary (Marquand et al., 2019; Mito et al., 2024), such as mTBI.

This issue remains largely unaddressed in QSM-based studies of tissue changes following mTBI. For example, while Koch et al. (2021) computed z-scores for individual participants in the bilateral thalamus, caudate, putamen, and globus pallidus, these measures served only as covariates in regression analyses, rather than being assessed for statistical significance as independent measures. This gap highlights the need for dedicated, clinically meaningful individual-level investigations of alterations to biomagnetic substrates following mTBI.

3.9 REVISITING THESIS AIMS AND OBJECTIVES

The primary aim of this thesis is to characterise microstructural grey matter pathology in acute mTBI using QSM. To achieve this, the studies presented here employ extensive, anatomically-informed segmentations of the deep grey matter and hippocampus as well as depth- and curvature-specific column-based analyses across the cortex to identify microstructural susceptibility differences at both the group- and individual-level (see Table 3.9). This approach addresses critical gaps in the current QSM-mTBI literature related to insufficient anatomical precision and the lack of clinically and individually relevant investigations.

To enhance methodological rigour and mitigate confounds, healthy participants from the normal population are used as a control group and data are acquired with 1 mm isotropic resolution for QSM reconstruction. Additionally, Chapter 4 presents a comparative analysis of two prominent QSM reconstruction methods to determine the most robust pipeline, which is subsequently used in the research presented in Chapter 5 to Chapter 8. For each study, QSM is thresholded into separate maps of inter-voxel susceptibility sign to differentiate between net positive and net negative voxels during analysis.

Ultimately, this thesis aims to refine and extend current QSM-based methodologies for mTBI research, thereby enabling the detection of significant effects observed in complementary imaging and histological studies yet largely undetected in the current literature. It is hoped that the culmination of these enhanced, comprehensive investigations will validate the utility of QSM for identifying mTBI-related grey matter pathology.

Table 3.1: The current state of the QSM-mTBI literature

Investigators	**Koch et al. 2018[b]**	**Gong et al. 2018[c]**	**Zivadinov et al. 2018[d]**	**Koch et al. 2021[b]**	**Wright et al. 2022[b]**	**Pinky et al. 2022[b]**	**Bell et al. 2024[a]**	**Thesis research[a]**
Timepoints, Analytic Approach, and Voxel Resolution	24 hours, 8 days, 45 days; group; 0.75 × 0.94 × 2 mm	Pre- and post-season (median 2 days prior and 10 days post); group; 0.76 × 0.76 × 2mm	Chronic, not specified; group; 0.5 × 1.0 × 2mm	48 hours; group, z-scores not independently assessed; 0.75 x 0.96 x 2mm	Day 13; 0.83mm isotropic	Within 15 days; additional cohort at 41 ± 16 days; group; 1.0 mm isotropic	Between 3 months and 5 years post with PPCS; group; 0.94 × 0.94 × 1.9mm	Within 14 days post-injury; group and independent individual assessments; 1.0mm isotropic
Basal Ganglia and Associated Nuclei								
Total deep grey matter / subcompartments				↓				
Cerebellar grey matter						↑		
Thalamus								
Caudate								
Putamen								
Undifferentiated Globus Pallidus								
Globus Pallidus internus								
Globus Pallidus externus								
Nucleus Accumbens								
Ventral Pallidum								
Substantia Nigra pars compacta								
Substantia Nigra pars reticulata								
Parabrachial Pigmented Nucleus								
Subthalamic Nucleus								
Ventral Tegmentum								
Hypothalamus								
Red Nucleus								
Mammillary Nucleus								
Habenular Nuclei								
Amygdala								
Extended Amygdala								
Hippocampus and Subfields								
Undifferentiated Hippocampus								
Parasubiculum								
Presubiculum								
Subiculum								
CA1								
CA3								
CA4								
HATA								
Fimbria								
Hippocampal Fissure								
Hippocampal Tail								

Cortical ROIs								
Voxel-wise								
Frontal Pole								★
Medial OFC								★
Lateral OFC								★
Pars Orbitalis								★
Pars Triangularis								★
Rostral mPFC								★
Caudal mPFC								★
Pars Opercularis								★
Superior Frontal								★
Paracentral								★
Precentral								★
Superior Parietal								★
Inferior Parietal								★
Postcentral								★
Supramarginal								★
Precuneus								★
Bank, STS								★
STS								★
Middle Temporal								★
Temporal Pole								★
Transverse Temporal								★
Parahippocampal								★
Entorhinal								★
Fusiform								★
Inferior Temporal								★
LOC								★
Pericalcarine								★
Lingual Gyrus								★
Cuneus								★
Insula								★
Rostral ACC								★
Caudal ACC								★
Posterior Cingulate								★
Isthmus, Cingulate								★

⋆ = depth- and curvature-specific investigations of cerebral cortex; [a] = healthy normal control population; [b] = healthy athlete control population; [c] = internal control group; [d] = non-contact sport athlete control group.

Note. Summary of the methodological approaches and results from the extant QSM-mTBI literature investigating susceptibility effects in grey matter. Most studies have identified no significant difference (grey cells). Two studies have identified significant effects (orange cells) and the direction of change is indicated by arrow direction (↓ = decrease, ↑ = increase). Green cells indicate regions investigated in this thesis to address gaps in the literature. PPCS = persistent post-concussion syndrome; CA = cornu ammonis; OFC = orbitofrontal cortex; mPFC = medial prefrontal cortex; STS = superior temporal sulcus; LOC = lateral occipital cortex; ACC = anterior cingulate cortex.

3.10 CHAPTER SUMMARY

This chapter elucidated not only the fundamentals of MRI, QSM, and the biophysical basis of magnetic susceptibility but provided a complement to the biological cascades of mTBI reviewed in Chapter 2. Together, these background chapters have underscored the potential utility of using QSM as a method to investigate susceptibility changes induced by mTBI. A review of the current QSM-mTBI literature and methodological shortcomings, including the pervasive lack of anatomical specificity, outlined the rationale for the thesis aims, study designs, and analytic approaches used in the subsequent research. The studies that comprise the body of this thesis are presented in the following chapters.

Research Projects Part I: Optimising QSM Methodology

4

SPARSITY-BASED REGULARISATION: A ROBUST APPROACH FOR QSM RECONSTRUCTION

4.1 MOTIVATION

In Chapter 4, I provide an evidence-based rationale for selecting the QSM reconstruction algorithm used in the subsequent research projects. A comparative analysis of the performance of a sparsity-based and a smoothness-promoting regularisation technique is conducted across eight SNR and image quality metrics, and benchmarked against ground truth data. Results from this chapter are presented alongside a discussion of best-practice recommendations for selection of QSM reconstruction algorithms, from phase unwrapping to dipole inversion, ensuring alignment with current consensus guidelines. The findings are summarised in § 4.7.

4.2 INTRODUCTION

Differences in *a priori* mathematical assumptions and regularisation techniques aimed at addressing the ill-posed nature of dipole inversion, as well as different algorithms for coil combination (Robinson et al., 2017), phase unwrapping (Schweser et al., 2017), multi-echo combination where applicable (Robinson et al., 2017), and background field removal (Schweser et al., 2017), can affect the accuracy of dipole inversion (Haacke et al., 2015; Kee et al., 2017; Y. Wang et al., 2015), as discussed in Chapter 3. The algorithms necessitate trade-offs, the inherent strengths and weaknesses of which can lead to deviations in proximity to the ground truth susceptibility distribution. For example, sparsity-based regularisation methods produce stable, physically meaningful solutions and enhance edge preservation through first-order ℓ_1 norm penalisation or by using similar TV methods (Bilgic et al., 2024). In contrast, smoothness-promoting reconstructions seek to balance edge-preservation with smoothing to eliminate staircasing artefacts that can occur with sparsity-only methods, either by using ℓ_2 norm penalisation or ℓ_1 norm penalisation of higher-order derivatives for smoothing such as with TGV (Langkammer et al., 2015). It is important to note that the choice of regularisation involves balancing noise suppression with the preservation of fine anatomical details, which is an ongoing area of research in the field of QSM (Bilgic et al., 2024; Reichenbach et al., 2015).

This variability means susceptibility maps reconstructed from the same phase and magnitude images can regularly identify different effects, erode or omit sections of brain tissue, and the complexity of image reconstruction is rife with opportunities for user error. Artefacts introduced at any of these stages can carry through the process and affect the accuracy of the final map (Marques et al., 2021). Indeed, recent research has highlighted that the fidelity of research outcomes may be determined by algorithm selection (Robinson et al., 2017; Schweser et al., 2017; Y. Wang et al., 2015), reinforcing the importance of selecting a robust technique suitable for the intended research.

Reconstruction challenges held within the QSM community have been devised to improve the accuracy of QSM reconstruction and identify the best methods for susceptibility calculation (Bilgic et al., 2021; Marques et al., 2021; Milovic et al., 2020). Recently, a realistic *in silico* head phantom was developed to eliminate unaccounted-for effects when using real-world, *in vivo* data as a ground truth (Marques et al., 2021). This phantom is available as an open-access data set (Marques, 2021) and can be used to evaluate QSM algorithms and reconstructions.

In addition, a recent consensus statement was issued detailing guidelines for best-practice QSM reconstruction, which, among other recommendations, endorsed sparsity-based regularisation for dipole inversion, for example, RTS (Kames et al., 2018) and MEDI (J. Liu et al., 2012; T. Liu et al., 2011b; T. Liu et al., 2012b), as well as methods like PDF (T. Liu et al., 2011a) and SHARP (Schweser et al., 2011b) (or SHARP-based variations) for background field removal. They also recommend using exact phase unwrapping methods like PRELUDE (Jenkinson, 2003), SEGUE (Karsa et al., 2019b), SPUN (Ye et al., 2019),

and ROMEO (Dymerska et al., 2021), and susceptibility quantification relative to a specific (preferably large) reference structure (Bilgic et al., 2024).

Due to inherent variations in voxel-wise susceptibility estimation arising from differences in scanner hardware, acquisition protocols, and reconstruction algorithms (Bilgic et al., 2021; Langkammer et al., 2018), the development of consensus guidelines and standardisation processes is critical for enhancing the fidelity of QSM-based research. These issues are particularly endemic to mTBI, where the tissue response to injury is inherently subtle. In this context, identifying the most robust reconstruction algorithm is essential as even minimal deviations in the accuracy of susceptibility estimation may result in spurious conclusions.

To address these issues, the comparative analysis conducted in this chapter reconstructs QSM maps using the QSM Reconstruction Challenge 2.0 data with the aim of identifying the most accurate method and ensuring alignment with recent consensus guidelines. Here, two popular pipelines are compared: sparsity-based RTS (Kames et al., 2018) and a smoothness-promoting TGV (Langkammer et al., 2015). Additionally, two-pass, artefact-reduced QSM maps (Stewart et al., 2022b) are generated for both pipelines, yielding four final maps for assessment. Proximity to ground truth is analysed across eight SNR and image quality metrics. The findings contained in this chapter guide the selection of the most appropriate reconstruction approach for the research studies detailed in Chapter 5, Chapter 6, Chapter 7, and Chapter 8, ensuring methodological rigour, accuracy, and consistency throughout this thesis.

4.3 MATERIALS AND METHODS

4.3.1 *Data simulation*

A realistic *in silico* head phantom (Marques et al., 2021) developed for the QSM Reconstruction Challenge 2.0 (Bilgic et al., 2021) was used to generate a ground truth against which different QSM reconstruction algorithms could be evaluated. This high-resolution (0.64 mm isotropic voxel size) head phantom is derived from ultrahigh-field (7T) data and includes a phantom χ-model, tissue property maps (M_0, R_1, R_2^*), and data masks. The head phantom was designed to simulate MRI data under realistic conditions, providing a high-fidelity representation of the human head whilst preserving tissue classes such as grey matter, white matter, and CSF. The phantom also features manually-segmented representations of deep grey structures, allowing for accurate simulation of brain tissue, substructures, and magnetic susceptibility distributions (Marques et al., 2021). A high-susceptibility site of calcification is also present in the longitudinal fissure.

To generate a ground truth susceptibility map and MRI data designed to simulate the local field maps of MEGRE MRI acquisitions for QSM reconstruction, the *in silico* head phantom was forward-modelled and transformed into a Brain Imaging Data Structure (BIDS) compliant (Gorgolewski et al., 2016) directory using the qsm-forward package. This process produced a separate magnitude and phase image, as well as the ground truth

susceptibility map, with a downsampled voxel size of 1 mm isotropic resolution (TR = 50 ms; TEs = 4, 12, 20, 28 ms; flip angle (FA) = 15°; slice thickness = 2.5 mm; matrix size = 164 x 205 x 205). Magnitude and phase images were then used for QSM reconstruction.

4.3.2 *QSM reconstruction*

The simulated field maps generated with qsm-forward were reconstructed into QSM using a containerised version of the QSMxT toolbox (Stewart et al., 2022a; Stewart et al., 2022b) via Docker (Merkel, 2014). QSMxT supports many reconstruction algorithms and regularisation techniques, including sparsity-based and smoothness-promoting methods. QSMxT also automates a two-pass combination method for hole-filling and artefact reduction (Stewart et al., 2022b). Both single-pass and two-pass QSM reconstructions were generated using a sparsity-based and a smoothness-promoting pipeline. The first reconstruction method used ROMEO for phase unwrapping (Dymerska et al., 2021), PDF for background field removal (T. Liu et al., 2011a), and sparsity-based RTS for dipole inversion (Kames et al., 2018), which aligns with recent consensus recommendations for best-practice QSM reconstruction (Bilgic et al., 2024). The second set of QSM maps were reconstructed using TGV (Langkammer et al., 2015), a smoothness-promoting regularisation method that integrates phase unwrapping, background field removal, and dipole inversion into a single step. To comply with recent consensus guidelines and enable meaningful comparisons between sparsity-based and smoothness-promoting methods, all QSM maps were referenced to whole-brain susceptibility (Bilgic et al., 2024).

4.4 ANALYSIS

The QSM-CI package, designed to work with data derived using qsm-forward, was used to evaluate all four QSM maps (single- and two-pass RTS; single- and two-pass TGV). This package automates the computation of eight SNR and quality metrics, each assessing different aspects of data fidelity and providing a comprehensive measure of the algorithms' performance relative to the ground truth. These metrics include: 1) Root Mean Square Error (RMSE): an image quality metric that quantifies the absolute error between the reconstructed QSM map and the ground truth susceptibility map (lower values are better); 2) Normalised RMSE (NRMSE): a scaled version of RMSE that provides a standardised measure (lower values are better); 3) High-Frequency Error Norm (HFEN): quantifies image reconstruction quality, in particular edges and fine details (lower values are better); 4) Mean Absolute Deviation (MAD): measures the average deviation of the reconstructed values from the ground truth (lower values are better); 5) QSM-specific Structural SIMilarity Index (XSIM): a perceptual metric that identifies structural fidelity by considering luminance, contrast, and structure (higher values are better); 6) Pearson correlation (r): assesses the linear relationship between the reconstructed map and the ground truth (higher values are better); 7) Normalised Mutual Information (NMI): quantifies the spatial agreement between the reconstructed image and the ground truth (higher values are better), and; 8)

Gradient Difference Error (GXE): the gradient RMSE, to assess differences between first derivatives of the reconstructed and ground truth data (lower values are better) (see Bilgic et al., 2021; Fiscone et al., 2024; Horé et al., 2010, Knops et al.; 2006, Langkammer et al., 2018; Milovic et al., 2025; Z. Wang et al., 2004; Yager et al., 2014).

4.5 RESULTS

Results indicated that two-pass RTS outperformed all other reconstructions on RMSE (0.0257146), NRMSE (80.711628), HFEN (0.999962), Pearson's r (0.591999), and GXE (0.6562497). Single-pass TGV excelled in MAD (0.0180557), XSIM (0.2176036), and NMI (1.0858868). Two-pass TGV generally performed the worst, exhibiting the highest RMSE (0.0264505), NRMSE (83.0215107), HFEN (0.9999569), as well as the lowest XSIM (0.1752620) and Pearson's r (0.5650767), followed by single-pass RTS which had the highest MAD (0.0190182) and GXE (0.6562504), along with the lowest NMI (1.0682507); see Table 4.1.

Table 4.1: QSM reconstruction evaluation results

Reconstruction Method	RMSE	NRMSE	HFEN	MAD	XSIM	Pearson's r (p-value)	NMI	GXE
RTS: Single-pass	0.0260673	81.8187089	0.9999580	0.0190182$^{\times}$	0.1960915	0.5760515 (0.0)	1.0682507$^{\times}$	0.6562504$^{\times}$
RTS: Two-pass	0.0257146$^{\checkmark}$	80.7116278$^{\checkmark}$	0.9999623$^{\checkmark}$	0.0186949	0.1780462	0.5919990$^{\checkmark}$ (0.0)	1.0715837	0.6562497$^{\checkmark}$
TGV: Single-pass	0.0262987	82.5449381	0.9999604	0.0180557$^{\checkmark}$	0.2176036$^{\checkmark}$	0.5828528 (0.0)	1.0858868$^{\checkmark}$	0.6562529
TGV: Two-pass	0.0264505$^{\times}$	83.0215107$^{\times}$	0.9999569$^{\times}$	0.0184135	0.1752620$^{\times}$	0.5650767$^{\times}$ (0.0)	1.0785821	0.6562529
Optimal Values	low	low	low	low	high	high (low)	high	low

$^{\checkmark}$best performing; $^{\times}$worst performing

Note. Evaluation metrics and results for single- and two-pass QSM reconstructions using both sparsity-based RTS and smoothness-promoting TGV pipelines. Lower values for RMSE, NRMSE, HFEN, MAD, and GXE indicate better performance, while higher values for XSIM, Pearson's r, and NMI reflect better reconstructions. Results are reported to seven decimal places to preserve the detail necessary for comparing between reconstruction methods. Abbreviations are as follows: RMSE = Root Mean Square Error; NRMSE = Normalised RMSE; HFEN = High-Frequency Error Norm; MAD = Mean Absolute Deviation; XSIM = QSM-specific Structural Similarity Index; Pearson's r = Pearson's correlation coefficient; NMI = Normalised Mutual Information; GXE = Gradient Difference Error.

Qualitative visual assessments revealed a significant reduction in streaking artefacts for two-pass QSM, particularly at the high susceptibility interhemispheric calcification (see Fig. 4.1). Visual representation of the QSM reconstructions suggests that a two-pass method reduces unwanted artefacts and is more robust against image distortions, enhancing the accuracy and reliability of the given susceptibility values (L. Zhou et al., 2017).

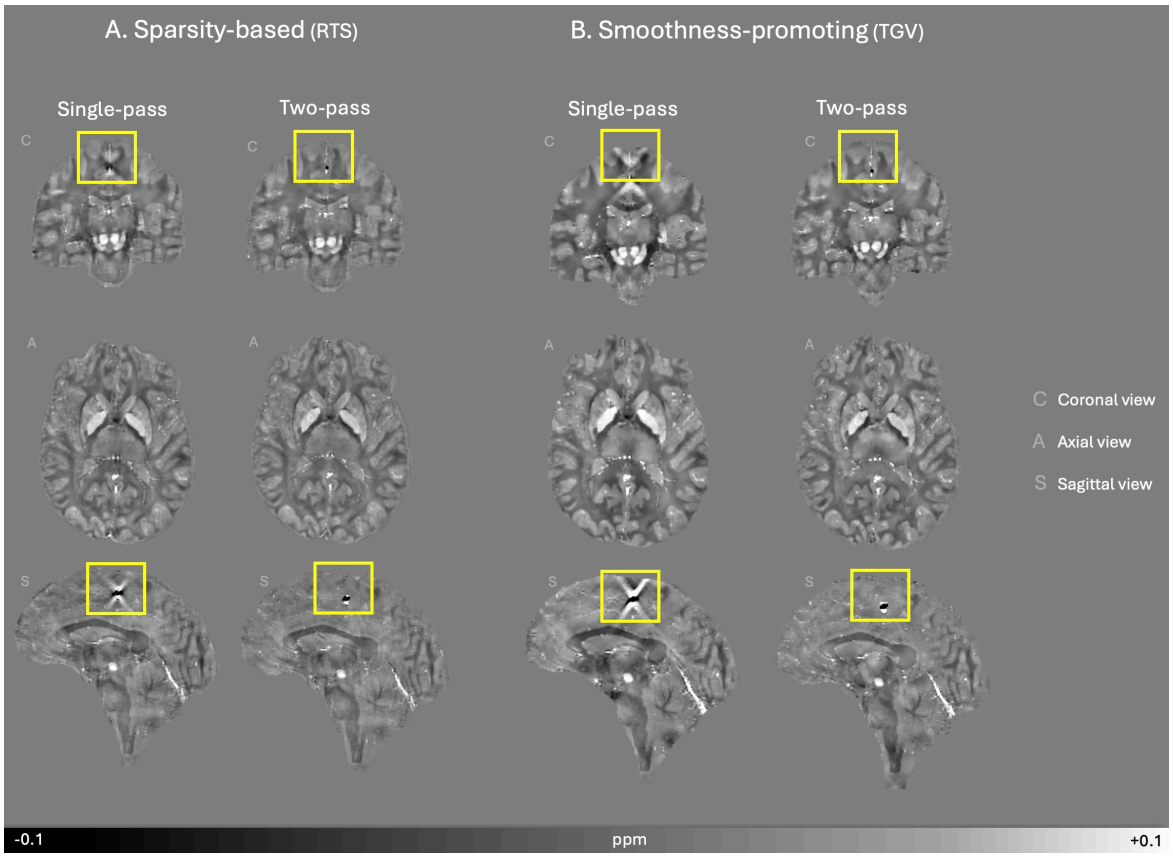

Figure 4.1: Comparison of QSM reconstructions

Visual representation of the susceptibility maps produced using sparsity-based RTS (A.) and smoothness-promoting TGV (B.). Both single- and two-pass reconstructions are displayed for each algorithm for coronal (C), axial (A), and sagittal (S) slices. Single-pass reconstructions are less robust against streaking artefacts at the interhemispheric calcification (yellow boxes) than their two-pass counterparts. Susceptibility is quantified in ppm.

4.6 DISCUSSION

SNR and image quality analyses identified two-pass RTS as the most robust reconstruction method overall, outperforming single-pass RTS and both single- and two-pass TGV on five of the eight reconstruction quality metrics including RMSE, NRMSE, Pearson's r, HFEN and GXE. The performance of single-pass TGV was superior on three of the eight metrics (MAD, XSIM, and NMI). Neither single-pass RTS nor two-pass TGV were superior to the other methods for any metric. Qualitative visual assessments of the reconstruction methods highlighted the utility of two-pass reconstruction methods for streaking artefact reduction (see Fig. 4.1). In contrast, significant streaking artefacts were apparent at the interhemispheric calcification for QSM reconstructed using a single-pass method. These quantitative and qualitative assessments support two-pass RTS as an effective method for maintaining anatomical features and gradient-encoded information while minimising unwanted artefacts which are known to affect image quality, voxel values, and confound analyses (Bilgic et al., 2024; W. Li et al., 2015; Marques et al., 2021).

4.6.1 *Smoothness- vs. sparsity-based regularisation*

Various QSM reconstruction methods seek to address the field-to-susceptibility inverse problem while accounting for incomplete tissue field data and noise (Kee et al., 2017). This necessitates using complex algorithms and regularisation techniques to address the ill-posed nature of dipole inversion (see Chapter 3). Here, TGV and RTS methods differ in several fundamental ways. TGV integrates the individual processing steps of phase unwrapping, background field removal, and dipole inversion into a unified step (Langkammer et al., 2015), and was developed to extend prior work that used only the more traditional ℓ_1-based TV penalty methods. In isolation, ℓ_1-based penalty methods can lead to piecewise staircasing artefacts during map reconstruction; hence, the incorporation of higher-order derivatives helps to promote smoothness in the model (Langkammer et al., 2015). Integrating all reconstruction steps into a single step also aims to mitigate the opportunities for error at each independent step of QSM reconstruction.

In contrast, RTS takes an incremental, two-step approach to dipole inversion, where k-space is divided into well-conditioned and ill-conditioned regions (Kames et al., 2018). In the first step, RTS uses a Least Squares Minimal Residual (LSMR) method but constrains this to a few iterations to reduce reconstruction errors, including streaking artefacts and noise, providing only a first-pass approximation (Kames et al., 2018). This step leverages the implicit regularising properties of Krylov subspace methods to emphasise smoothness and reduce noise artefacts. The second step addresses the ill-conditioned k-space regions by employing a binary mask for priors and using sparsity-based TV for signal estimation, helping to recover ill-conditioned regions while preserving edges (Kames et al., 2018). This two-step approach enables RTS to balance noise reduction and edge preservation effectively.

Both RTS and TGV methods attempt to enhance the fidelity of susceptibility estimation while decreasing computational load. While over-smoothing can pose a problem for structural detail and recovery of small ROIs (Kames et al., 2018), relying solely on ℓ_1 norm regularisation may encourage artefacts. As such, sparsity and smoothness should be carefully managed by the algorithm and regularisation methods, either in isolation or in combination, must be well considered. Recent recommendations for best-practice QSM reconstruction favour sparsity-based methods, whilst concomitantly acknowledging that some sparsity-based algorithms may lead to staircasing in the reconstructed map, with additional recommendations to mitigate these through effective background field removal techniques (Bilgic et al., 2024).

Taken together, smoothness-promoting TGV appears to be less well supported for use in the subsequent research projects. The single step approach also inhibits the manual application of optimal phase unwrapping and background field removal steps. In contrast, the sparsity-based RTS reconstruction aligns with consensus guidelines, as does the use of PDF for background field removal (T. Liu et al., 2011a) and “exact" phase unwrapping via ROMEO (Dymerska et al., 2021). The ability to select a method for each individual step

confers the added benefit of enabling modifications to the pipeline as consensus recommendations evolve.

4.6.2 *Two-pass artefact reduction*

The present investigation demonstrated that a two-pass artefact reduction method is significantly more effective at mitigating streaking artefacts and enhancing image quality, particularly in regions with high susceptibility, such as the interhemispheric calcification (see Fig. 4.1). This enhanced effectiveness is due to the hole-filling, artefact reduction method which performs parallel QSM masking and reconstruction on susceptibility sources identified as reliable and less reliable. These dual QSM images are then combined into a final integrated image that is more robust to reconstruction errors and streaking artefacts than images produced using a single-pass approach. In doing so, this approach improves the accuracy of statistical analysis (Stewart et al., 2022b).

Streaking artefacts present a significant problem for QSM, typically emerging near high susceptibility regions such as air-tissue interfaces, calcifications, and areas in close proximity to blood vessels (Bilgic et al., 2024; W. Li et al., 2015). These bright distortions radiate around the site of high contrast, distorting voxel values within and around the affected area. This can compromise quantitative analysis by yielding inaccurate susceptibility measurements and obscuring anatomical structures, particularly smaller structures such as the subthalamic nucleus and substantia nigra (Bilgic et al., 2024; W. Li et al., 2015; Marques et al., 2021). The studies in this thesis focus on regions with complex microstructural features, including the hippocampus, basal ganglia, and cerebral cortex. Given that these areas also border tissue boundaries and that cortical regions are highly vascularised (Bollmann et al., 2022), reducing artefacts is imperative.

In addition, minimisation of errors or noise is particularly relevant to the study of mTBI, where the associated pathology is subtle and artefacts can obscure small, but clinically relevant, changes in susceptibility or lead to erroneous voxel value calculations and misidentification of tissue pathology. Methods to reduce artefacts are critically important for research broadly, but particularly when assessing conditions where accurate identification of micropathology is essential. Here, preserving anatomical features, maintaining image quality, and mitigating distortion of susceptibility values is paramount. This is particularly relevant to certain analytic approaches, such as the individualised studies presented in Chapter 7 and Chapter 8, which are inherently sensitive to small, individual-level variations in magnetic susceptibility that could, with enough research, be used to inform clinical decision making.

Indeed, a recent individual-level investigation of moderate-to-severe TBI (ms-TBI) conducted by Domínguez et al. (2024) demonstrated the capabilities of a two-pass QSM approach. Their findings indicated that two-pass QSM can substantially reduce reconstruction errors, particularly dark and streaking artefacts near large lesions and at tissue boundaries. These artefacts have been a persistent challenge in TBI studies (Stewart et al., 2022b) and may be a contributing factor to the limited use of QSM in this context (Domínguez

et al., 2024). In addition, Domínguez et al. (2024) identified significant differences in the z-scores of ms-TBI participants in both deep grey and cortical grey matter compared to the HC z-distribution. These findings underscore not only the sensitivity and potential clinical utility of the two-pass artefact reduction method but also its relevance to the work presented in this thesis.

4.6.3 *Signal-to-noise and image quality*

The superior performance of two-pass RTS on RMSE, NRMSE, and Pearson's r indicates that it is the most accurate reconstruction method for error minimisation and represents a close approximation of the true susceptibility distribution. These results suggest that mTBI-related grey matter micropathology identified via two-pass RTS is likely to reflect actual tissue content dyshomeostasis and will be less prone to spurious voxel values from reconstruction artefacts or errors. The preservation of fine detail and gradient-encoded information in two-pass RTS is reflected in the superior performance on the HFEN and GXE metrics which can likely be attributed to sparsity-based regularisation. This capability is valuable when studying detailed substructures, such as the hippocampal subfields, basal ganglia, and associated nuclei (see Chapter 5 and Chapter 7), and for complex, column-based investigations sensitive to cortical architectonics (see Chapter 6 and Chapter 8). In contrast, microstructural abnormalities and subtle deviations in the tissue response may be less identifiable with methods that perform relatively poorly for detail and gradient preservation. On aggregate, the results of this investigation identify two-pass RTS as the optimal choice for high-quality QSM for use in the following research studies. This conclusion is supported by its superior performance on most SNR metrics, competitive outcomes on the remaining measures, and its effective reduction of artefacts.

4.6.4 *Limitations*

Several limitations should be noted. First, consensus recommendations suggest that data should be acquired using a MEGRE sequence, which can enhance SNR (Bilgic et al., 2024; Deistung et al., 2017). While the *in silico* phantom reflects best-practice acquisition in this regard, the data used in this thesis were acquired using a single-echo sequence. Consequently, the QSM *reconstruction* pipeline selected for this thesis represents gold-standard algorithm implementation, however, the data *acquisition* is not aligned with consensus recommendations (Bilgic et al., 2024).

Since ground truth data were necessary for establishing the most robust method for QSM reconstruction, optimal methods identified using the *in silico* phantom are assumed to be generalisable to the data acquired for QSM reconstruction in this thesis. While this is not an exact one-to-one match due to differences in acquisition parameters and the nature of the source images, the agreement between the results of this investigation and best-practice recommendations mitigates some concerns regarding extrapolation to the data acquired for use in Chapter 5 to Chapter 8.

Lastly, because QSM is an indirect measure of magnetic susceptibility, it serves as a surrogate marker for tissue components such as iron, calcium, protein, and myelin, and does not reflect their absolute values. While careful attention has been paid to the wording throughout the following research investigations, the reader is advised to keep this caveat in mind when interpreting the results.

4.7 CONCLUSIONS

This study systematically compared two QSM reconstruction methods, one employing sparsity-based regularisation (RTS) and the other emphasising smoothness (TGV), for both single- and two-pass susceptibility maps. This chapter aimed to identify the most robust method based on eight SNR and image quality metrics. Two-pass RTS outperformed all other reconstructions, particularly in metrics related to error minimisation and feature preservation, including edges and fine anatomical details. In addition, two-pass RTS effectively suppressed artefacts, likely enhancing the reliability of susceptibility values. The superior performance across quantitative and qualitative assessments renders this method particularly suited to investigations of the cortex, hippocampal subfields, and basal ganglia. As a result, the two-pass RTS pipeline was selected for use in the research projects presented in this thesis. Its alignment with consensus guidelines established by experts in the QSM community further validates this choice, ensuring that the research described in the subsequent studies is methodologically sound.

Research Projects Part II: Subcortical Alterations in Brain Tissue Microstructure Following mTBI

5

INVESTIGATING POSITIVE AND NEGATIVE QUANTITATIVE SUSCEPTIBILITY VALUES IN THE HIPPOCAMPAL FORMATION AND BASAL GANGLIA

5.1 MOTIVATION

In Chapter 5 I implement the QSM reconstruction algorithm detailed in Chapter 4 to investigate the effects of mTBI on subcortical brain structures, focusing on 16 sub-regions of the basal ganglia and 10 segmentations of the hippocampal formation. Prior research has predominantly examined major basal ganglia structures as ROIs in QSM-based investigations of mTBI, but no prior studies have systematically explored the hippocampal subfields, despite the well-established vulnerability of the hippocampus and temporal lobe to damage in mTBI, as well as their involvement in mTBI symptomatology. In this chapter, I extend the current literature by conducting a granular investigation of these subcortical regions. In addition, I threshold QSM into separate maps of dominant positive and negative susceptibility values to enable the analysis of distinct magnetic susceptibility distributions that may otherwise be obscured by inter-voxel averaging during analysis. Key discussion points are reviewed in § 5.6.

5.2 INTRODUCTION

The current focus on total deep grey matter or segmentations of major subcortical structures such as the caudate, putamen, thalamus, and intact globus pallidus (Bell et al., 2024; Gong et al., 2018; Koch et al., 2018; Koch et al., 2021; Pinky et al., 2022; Wright et al., 2022; Zivadinov et al., 2018a) or the undifferentiated hippocampus (Pinky et al., 2022; Zivadinov et al., 2018a) may overlook the susceptibility of other regions or subfields to mTBI-induced micropathology (see Chapter 3). Here, investigations differentiating between distinct subcortical brain regions and their substructures may be necessary to better understand the micropathology of mTBI and assist in elucidating the genesis of specific injury-related deficits.

To contribute to the sparse extant literature, this chapter outlines the first QSM analysis of mTBI effects in the hippocampal subfields alongside the most detailed segmentation of the basal ganglia to date. This study aimed to: 1) assess the effects of mTBI on positive (iron-related) and negative (myelin-, protein-, calcium-related) net magnetic susceptibility to better understand acute pathology in, a) 16 segmentations of the basal ganglia, and b) 10 segmentations of the hippocampal subfields, and; 2) elucidate the relationship between magnetic susceptibility in these regions and potentially moderating variables including age, and injury latency and severity. Although many of these regions are both high in iron and susceptible to mTBI-related pathology, the limited prior literature has produced mixed results regarding the direction of iron-related effects, if any. Furthermore, the absence of QSM thresholded for inter-voxel sign in previous studies precludes the development of robust hypotheses regarding the directionality of negative susceptibility effects in grey matter. As such, there were no specific *a priori* hypotheses related to either susceptibility sign, nor secondary correlational analyses.

5.3 MATERIALS AND METHODS

Ethical approval for this research was obtained from the Health and Disabilities Ethics Committee (HDEC) (Date: 18/02/2022, Reference: 2022 EXP 11078) and institutional approval was also obtained from the Auckland University of Technology Ethics Committee (AUTEC) (Date: 18/02/2022, Reference: 22/12). In accordance with the Declaration of Helsinki, all participants provided written informed consent prior to data collection. To recognise their contribution, each participant received a $50NZD food voucher, along with a $20NZD fuel voucher or taxi chit to cover the travel costs associated with attending the MRI scan.

5.3.1 *Participants*

Data from 25 male contact sports players (M = 21.10 years old [16-32], SD = 4.59) with acute sr-mTBI (< 14 days; M = 10.40 days, SD = 3.03) and 25 age-matched male controls (M = 21.10 years old [16-32], SD = 4.35) were used for this observational study (see Table 5.1).

Ages were not significantly different between groups ($t(48) = 0.00$, $p = 1.00$) to mitigate any potential confounding effects due to the known linear relationship between brain iron content and age (Ashraf et al., 2018; Bilgic et al., 2012; Hagemeier et al., 2012; Hallgren et al., 1958; Madden et al., 2023; Treit et al., 2021; Zecca et al., 2004), particularly in this young cohort. Clinical sr-mTBI participants were recruited through three Axis Sports Medicine clinics (Auckland, New Zealand), via print and social media advertisements, word-of-mouth, and through community-based pathways including referrals from healthcare professionals and sports team management. Each clinical participant was required to have a confirmed sr-mTBI diagnosis by a licensed physician as a prerequisite for study inclusion, and symptom severity was assessed using the Brain Injury Screening Tool (BIST) (Theadom et al., 2021) either upon presentation to Axis clinics or electronically following recruitment. HC participants were recruited through print and social media advertisements, and word-of-mouth. Exclusion criteria for all participants included a history of significant medical or neurological conditions unrelated to the study's objectives, and contraindications for MRI. Additionally, controls were excluded if they had any recent history of mTBI events (< 12 months) or were living with any long-term effects of previous mTBI. All participants completed a brief demographic questionnaire and attended a 1-hour MRI scan at The Centre for Advanced MRI (CAMRI), Auckland, New Zealand. All scans were reviewed by a certified neuroradiologist consultant for clinically significant findings. While some incidental findings were identified, none were considered to be clinically significant and no further follow up action was needed (see Table 5.1).

It should be noted that all information regarding ethics, participant acknowledgements, recruitment, inclusion and exclusion criteria, data collection, and clinical radiological review specified here are also applicable to the research conducted in the chapters following this one (i.e., Chapter 6, Chapter 7, and Chapter 8). However, whilst the participant sample detailed in this chapter is identical to the research detailed in Chapter 6, the studies presented in Chapter 7 and Chapter 8 further extend the sample to facilitate comprehensive individualised investigations.

Table 5.1: Summary of sr-mTBI participant clinical characteristics

ID	Age	DSI	BIST Score	MOI	Radiological MRI Findings
mTBI-01	< 20	5 days	140	Rugby	None
mTBI-02	< 20	5 days	12	Rugby	None
mTBI-03	20s	6 days	78	Rugby	None
mTBI-04	< 20	13 days	18	Rugby	Small fluid signal spaces in R peritrigonal WM - normal. R caudate cleft along ventricular surface – possibly developmental or from old ischaemic insult
mTBI-05	< 20	12 days	61	Rugby	None
mTBI-06	20s	13 days	42	Rugby	None
mTBI-07	20s	13 days	13	Football	Minor artefactual T_1 signal in pons
mTBI-08	20s	12 days	6	Hockey	None
mTBI-09	20s	6 days	56	Rugby	Minor R orbital fracture (old)
mTBI-10	< 20	12 days	54	Rugby	None
mTBI-11	20s	10 days	52	Rugby	None
mTBI-12	30s	13 days	13	Football	None
mTBI-13	< 20	5 days	79	Rugby	None
mTBI-14	20s	13 days	2	Rugby	Small focus of susceptibility in L superior frontal gyrus possibly vascular or nonspecific haemosiderin
mTBI-15	< 20	13 days	22	Rugby	None
mTBI-16	< 20	8 days	117	Futsal	Tiny cleft of fluid signal in R cingulate gyrus - minor developmental anomaly or mature gliosis
mTBI-17	20s	13 days	*	Rugby	None
mTBI-18	20s	10 days	34	Gymnastics	None
mTBI-19	20s	13 days	28	Jiu-jitsu	Some artefactual DWI signal in pons
mTBI-20	20s	11 days	69	Surfing	Tiny susceptibility site in R temporal lobe - may be vascular
mTBI-21	< 20	7 days	14	Rugby	Minor susceptibility in transverse sulcus in R mid temporal lobe - nonspecific, may be vascular or reflect haemosiderin deposition from prior small volume haemorrhage
mTBI-22	< 20	13 days	39	Judo	None
mTBI-23	< 20	9 days	34	Rugby	None
mTBI-24	< 20	12 days	68	Rugby	None
mTBI-25	20s	12 days	17	Rugby	7mm pineal cyst - normal limits. Some T_1 hyperintensity in R cerebellum - artefact compatible
Mean mTBI	21.10 (4.59) years	10.4 (3.03) days	44.5 (35.0) /160		No findings considered clinically relevant
Mean HC	21.10 (4.35) years				No findings considered clinically relevant

* = missing data (BIST incomplete on the Axis Sport Medicine Clinic patient portal, reason unknown)

Note. Diagnostic assessment is limited to the volume T_1, SWI and DWI sequences with only limited interpretation of the multi-echo T_2 stack. Clinical assessments are relevant to the identification of micro-haemorrhages, areas of siderosis, T_1 appearance, gliosis, volume, ventricular volumes and non-neurological findings. Age is given in a range to prevent re-identification of participants. The possible range of BIST scores is 0 (min) to 160 (max). Clinical group data correspondent to date at MRI only with the exception of the BIST acquired >24 hours post-injury prior to MRI scanning (< 14 days post). mTBI = mild traumatic brain injury; HC = healthy control; ID = unique identifier; DSI = days since injury; DWI = diffusion-weighted imaging; BIST = Brain Injury Screening Tool; MOI = mechanism of injury; WM = white matter; MRI = magnetic resonance imaging; L = Left; R = right.

5.3.2 *Neuroimaging*

5.3.2.1 *Acquisition*

MRI data were acquired on a 3T Siemens MAGNETOM Vida Fit scanner (Siemens Healthcare, Erlangen, Germany) equipped with a 20-channel head coil. A 3D flow-compensated single-echo GRE sequence was used to obtain magnitude and unfiltered phase images suit-

able for QSM reconstruction. Data were collected at 1 mm isotropic voxel size with matrix size = 180 x 224 x 160 mm, TR = 30 ms; TE = 20 ms; FA = 15°; field of view (FoV) = 180 mm (LR) × 224 mm (AP); bandwidth = 101 Hz/px, in a total acquisition time of ∼3.43 minutes. Additional acquisition parameters included a transversal orientation with right-to-left phase encoding. Wave-CAIPI acceleration was applied (in-plane = 2, 3D = 2) with 30 calibration reference lines in both phase-encode and 3D directions. For each participant, a high-resolution 3D T_1w anatomical image volume was acquired for coregistration, parcellation, and segmentation using a Magnetisation-Prepared Rapid Acquisition Gradient Echo (MPRAGE) sequence (TR = 1940.0 ms; TE = 2.49 ms, FA = 9°; slice thickness = 0.9 mm; FoV = 230 mm; matrix size = 192 x 512 x 512 mm; Generalised Autocalibrating Partially Parallel Acquisitions (GRAPPA) = 2; voxel size 0.45 x 0.45 x 0.90 mm) for a total acquisition time of ∼4.31 minutes. Digital Imaging and Communications in Medicine (DICOM) files were converted to Neuroimaging Informatics Technology Initiative (NIfTI) images and organised in BIDS format (Gorgolewski et al., 2016) for further processing using *Dcm2Bids* (Boré et al., 2023) version 3.1.1, which is a wrapper for *dcm2niix* (X. Li et al., 2016) v1.0.20230411.

5.3.2.2 *QSM processing*

QSM images were reconstructed using QSMxT (Stewart et al., 2022a) v6.4.2 available as a container via NeuroDesk (Renton et al., 2024) (v2024-03-27), a lightweight virtual environment. In keeping with the most robust reconstruction method identified in Chapter 4 and recent consensus statement guidelines (Bilgic et al., 2024), ROMEO was used for phase unwrapping (Dymerska et al., 2021), PDF for background field removal (T. Liu et al., 2011a), and sparsity-based RTS for dipole inversion (Kames et al., 2018), with whole-brain susceptibility referencing. Two-pass, artefact-reduced susceptibility maps were used in all studies described in this thesis (Stewart et al., 2022b). A brain mask was also generated using FSL's BET (S. M. Smith, 2002) to improve masking and hole-filling of the threshold-based selection algorithm (Otsu, 1979) used for two-pass QSM.

Subsequent processing was performed using FSL (Jenkinson et al., 2012; S. M. Smith et al., 2004; Woolrich et al., 2009). For each subject, the raw magnitude image was skull-stripped using FSL's BET (S. M. Smith, 2002) with robust brain centre estimation and a fractional intensity threshold between 0.3 and 0.6. Binary masks were derived from the skull-stripped magnitude image and applied to the susceptibility maps to erode non-brain signal around the brain perimeter using *fslmaths*. Skull-stripped magnitude images were linearly registered to the California Institute of Technology's 168 (CIT168) T_1w template in Montreal Neurological Institute 152 (MNI152) space (see Pauli et al., 2018) using FMRIB's Linear Transformation Tool (FLIRT) (Greve et al., 2009; Jenkinson et al., 2002; Jenkinson et al., 2001) with 12 degrees of freedom (DoF) suitable for atlas-based registration. The resulting transformation matrix was then used for spatial normalisation of the QSM images using FLIRT (Greve et al., 2009; Jenkinson et al., 2002; Jenkinson et al., 2001). In line with prior research that has used a binary inter-voxel thresholding approach (Merenstein et al., 2025; Merenstein et al., 2024), QSM data were thresholded into separate maps of dominant voxel-wise sign with *fslmaths*. This approach separates values across voxel bound-

aries above (QSM^+) and below (QSM^-) zero, thereby isolating predominantly positive (iron-related) voxels from predominantly negative (myelin-, calcium-, and protein-related) voxels prior to ROI-wise analysis (Duyn et al., 2017; Gong et al., 2019; Jang et al., 2021; S. Kim et al., 2020; O'Callaghan et al., 2017; Y. Wang et al., 2017; Z. Zhao et al., 2021).

5.3.2.3 *Basal ganglia segmentation*

The CIT168 basal ganglia mask, available in MNI152 space, provides a detailed 16-part probabilistic atlas of the basal nuclei (Pauli et al., 2018). Derived from T_1w and T_2w *in vivo* structural images of 168 participants from the Human Connectome Project (Van Essen et al., 2013), this atlas is openly accessible via the NeuroVault Collection (No. 3145). The segmentations included: the striatum, comprised of the putamen (Pu), caudate (Ca), and nucleus accumbens (NAC); the pallidum, which includes the globus pallidus externus (GPe), globus pallidus internus (GPi), and ventral pallidum (VeP); and the substantia nigra, including the substantia nigra pars compacta (SNc) and substantia nigra pars reticulata (SNr). Additional segmentations covered the extended amygdala (EXA) and other limbic structures including the hypothalamus (HTH) and mammillary nucleus (MN), the mesolimbic ventral tegmental area (VTA) and the associated parabrachial pigmented nucleus (PBP), the epithalamic habenular nuclei (HN), the subthalamic nucleus (STH), and the red nucleus (RN) (see Fig. 5.1 for reference).

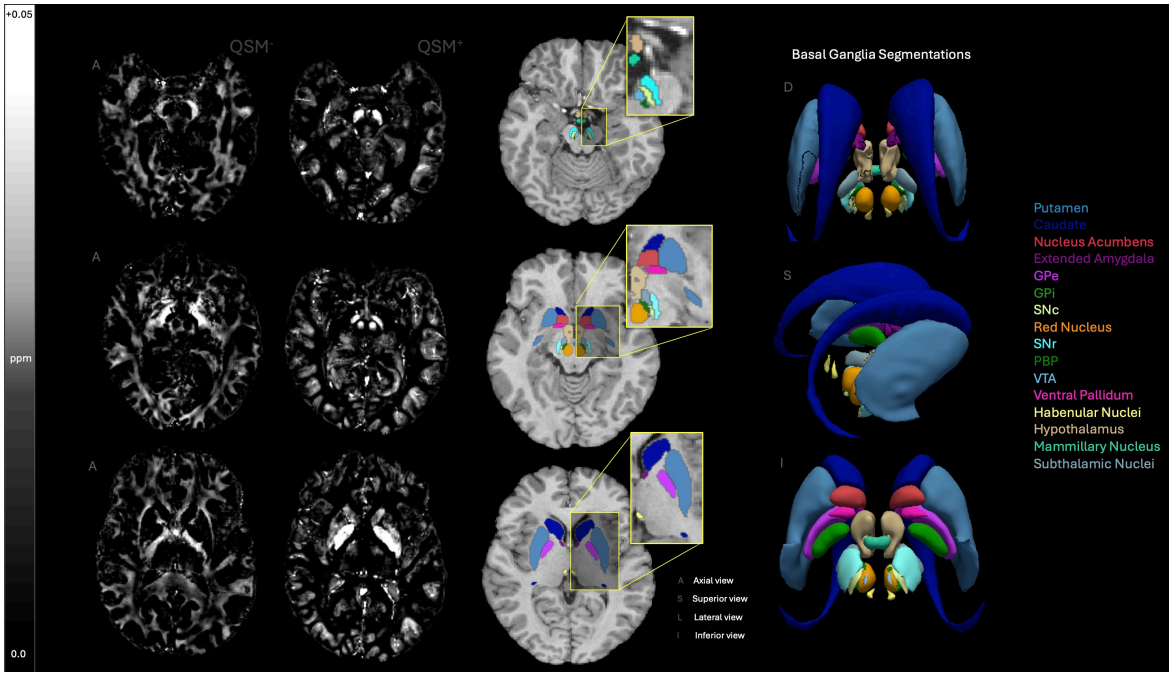

Figure 5.1: Segmentations of the basal ganglia

Sixteen bilateral segmentations of the basal ganglia are displayed across axial (A) slices of the T_1w CIT168-MNI152 brain template, as well as 3D renderings of the basal ganglia mask depicted from a superior (S), inferior (I), and lateral (L) perspective. The key for each basal nuclei is provided in the respective colour of that region. Axial slices for signed maps (QSM^- and QSM^+) are shown at comparable depths for visual reference. Susceptibility values are expressed in ppm ranging from 0.0 to +0.05, and negative maps are multiplied by -1 for better visualisation. GPe = globus pallidus externus; GPi = globus pallidus internus; SNc = substantia nigra pars compacta; SNr = substantia nigra pars reticulata; PBP = parabrachial pigmented nucleus; VTA = ventral tegmental area.

5.3.2.4 *Hippocampal segmentation*

Prior to hippocampal segmentation, bias field correction was applied to each participants' T_1w images using the *N4* algorithm (Tustison et al., 2010) from the Advanced Normalisation Tools (ANTs) library (Avants et al., 2011). The bias field-corrected T_1w images were then processed with FreeSurfer's *recon-all* pipeline (Fischl, 2012). Subsequent unilateral segmentation of the hippocampal subfields was conducted using an automated, FreeSurfer-based pipeline (Iglesias et al., 2015). This hippocampal segmentation leverages a probabilistic atlas derived from ultrahigh-field, *ex vivo* MRI data with approximately 0.1 mm isotropic voxel resolution to automate the delineation of hippocampal substructures for each hemisphere. Three resulting hippocampal segmentation schemes were produced, including a macroscopic head/body/tail segmentation (denoted as "HBT"), a detailed scheme where molecular subregions are merged with the nearest neighbours, specifically the CA subfields (labeled "CA"), and a detailed segmentation where molecular subregions are not merged (referred to as "FS60"). Of these, the mid-detail segmentation (the "CA" scheme) was selected for use in statistical analysis, balancing the level of segmentation detail with the need to mitigate the multiple comparisons problem. The hippocampal subregion masks included in this segmentation: the parasubiculum, presubiculum, subiculum, CA regions CA1, CA3 (which includes CA2), and CA4, the hippocampal-amygdala transition area (HATA), fimbria, hippocampal tail, and hippocampal fissure (see FreeSurfer Documentation). For full details on the segmentation used in this thesis, refer to Table 5.2, and for visual representation see Fig. 5.2.

Table 5.2: Hippocampal subfields and their closest anatomical structures in "CA" segmentation

Parasubiculum	Parasubiculum
Presubiculum head	Presubiculum
Presubiculum body	
Subiculum head	Subiculum
Subiculum body	
CA1 head	CA1
CA1 body	
CA3 head	CA3
CA3 body	
CA4 head	CA4
CA4 body	
GC-ML-DG head	
GC-ML-DG body	
Molecular layer HP-head	Closest structure*
Molecular layer HP-body	
HATA	HATA
Fimbria	Fimbria
Hippocampal tail	Hippocampal tail
hippocampal fissure	hippocampal fissure

* = voxels in the molecular layer are assigned the label of the closest voxel that is neither molecular layer nor background.

Note. This table details the unilateral segmentations of hippocampal subfields within the volume labelled as "CA", along with associated hippocampal structures. Subfield CA2 is incorporated into CA3. Table is also available at the FreeSurfer Wiki.

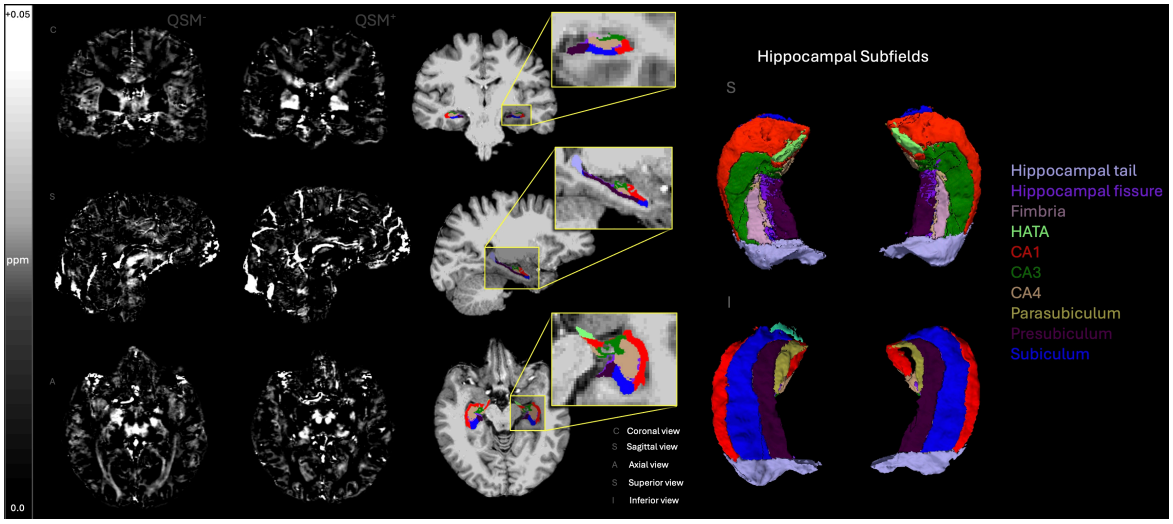

Figure 5.2: Segmentations of the hippocampal formation

Visual representation of the unilateral hippocampal segmentations provided by FreeSurfer under the "CA" scheme, displayed across coronal (C), axial (A), and sagittal (S) views as well as a 3D rendering from the inferior (I) and superior (S) views. The key for each hippocampal region is provided in the respective colour of that region. Signed maps (QSM^- and QSM^+) from which susceptibility values are sampled for each hippocampal region are shown for each orientation (C, A, S). Susceptibility values are expressed in ppm ranging from 0.0 to +0.05, and negative maps are multiplied by -1 for better visualisation. HATA = hippocampal-amygdala transition area; CA 1-4 = cornu ammonis regions 1-4 (Note: CA2 is included in CA3).

To standardise each hippocampal subfield mask for data analysis, each participants' skull-stripped T_1w brain image and left and right hemisphere hippocampal masks were converted from FreeSurfer's .mgz format to NIfTI format (.nii.gz) using MRtrix3 *mrconvert* (Tournier et al., 2019). Skull-stripping automated by the FreeSurfer *recon* was re-run with additional arguments, including *-gcut* and adjustments to the watershed threshold as needed, to improve the accuracy of the original skull-strip. After format conversion, each participants' skull-stripped T_1w brain image was registered to the CIT168 T_1w template in MNI152 space (Pauli et al., 2018) using FLIRT (Greve et al., 2009; Jenkinson et al., 2002; Jenkinson et al., 2001) with 12 DoF. The resulting transformation matrix was then applied to both the left and right hemisphere hippocampal masks using nearest-neighbour interpolation to maintain the integrity of discrete hippocampal label boundaries during transformation. These steps ensured spatial alignment between each of the hippocampal masks, the signed susceptibility maps, and the CIT168 segmentations of the basal ganglia provided in MNI152 space (Pauli et al., 2018).

5.3.3 *Statistical analyses*

Statistical analyses were conducted at the bilateral level using MATLAB (2024a). Average positive and negative net susceptibility values from both QSM^+ and QSM^- maps were extracted from the 16 bilateral segmentations of the basal ganglia. For the 10 hippocampal regions, left and right hemisphere susceptibility values were extracted and averaged to yield a bilateral measure. Any ROIs in which indeterminate values were present for any participant were omitted from subsequent analysis (the PBP for QSM^- analyses, and the HN for QSM^+ analyses). There were no missing values for any participants for any hip-

pocampal ROIs. To evaluate the effects of sr-mTBI compared to HC, two-tailed independent samples t-tests were performed for each subcortical ROI, assessing group differences in susceptibility values. To control for multiple comparisons, a Benjamini-Hochberg false discovery rate (FDR) correction (Benjamini et al., 1995) was applied separately to the 15 p-values corresponding to the remaining basal nuclei (all nuclei except the PBP for QSM^{-} and HN for QSM^{+}) and the 10 p-values for the hippocampal regions, for each signed susceptibility map. Since participants were precisely age-matched, age was not treated as a covariate or confounding factor in between-group comparisons. However, to examine the associations between QSM values and age across the entire cohort, partial Pearson correlation coefficients were computed. These analyses assessed the potential linear relationship between age and both positive and negative susceptibility values across all subcortical ROIs, controlling for group status. Additional relationships were explored between susceptibility values and sr-mTBI-related variables using Pearson correlation coefficients, including BIST scores and injury latency (days since injury; DSI), for clinical participants only. Due to missing BIST data, mTBI-17 was excluded from analyses related to injury severity (see Table 5.1). Negative susceptibility values were multiplied by -1 to convert them to absolute values, ensuring a consistent directional interpretation in all correlational analyses and more intuitive visualisation. Correlations were also corrected for 15 and 10 ROI-wise comparisons, respectively, using FDR procedures (Benjamini et al., 1995). Given the limited sample size and the need to conserve DoF in this exploratory study, regression analyses were deliberately omitted.

5.4 RESULTS

5.4.1 *Regional analyses*

Using two-tailed independent samples t-tests, differences in bilateral regional net susceptibility (positive and negative) were examined for each of the hippocampal subfields and basal nuclei. P-values were corrected for 10 and 15 comparisons, respectively, using FDR procedures (Benjamini et al., 1995) (*p*FDR).

5.4.1.1 *Basal nuclei*

Results showed no significant differences in positive or negative susceptibility between sr-mTBI participants and HC for any of the basal nuclei (*p*FDR > 0.05; see Fig. 5.3).

5.4.1.2 *Hippocampal subfields*

There were no significant differences in positive susceptibility between groups for any of the 10 hippocampal subfields (see Fig. 5.3). Negative susceptibility values were significantly less negative for sr-mTBI participants (M = -0.007, SD = 0.002) than HC (M = -0.008, SD = 0.001) in the CA4 only ($t(48)$ = -2.99, *p*FDR = 0.04). No significant differences between groups in negative susceptibility values were found for any other hippocampal ROI.

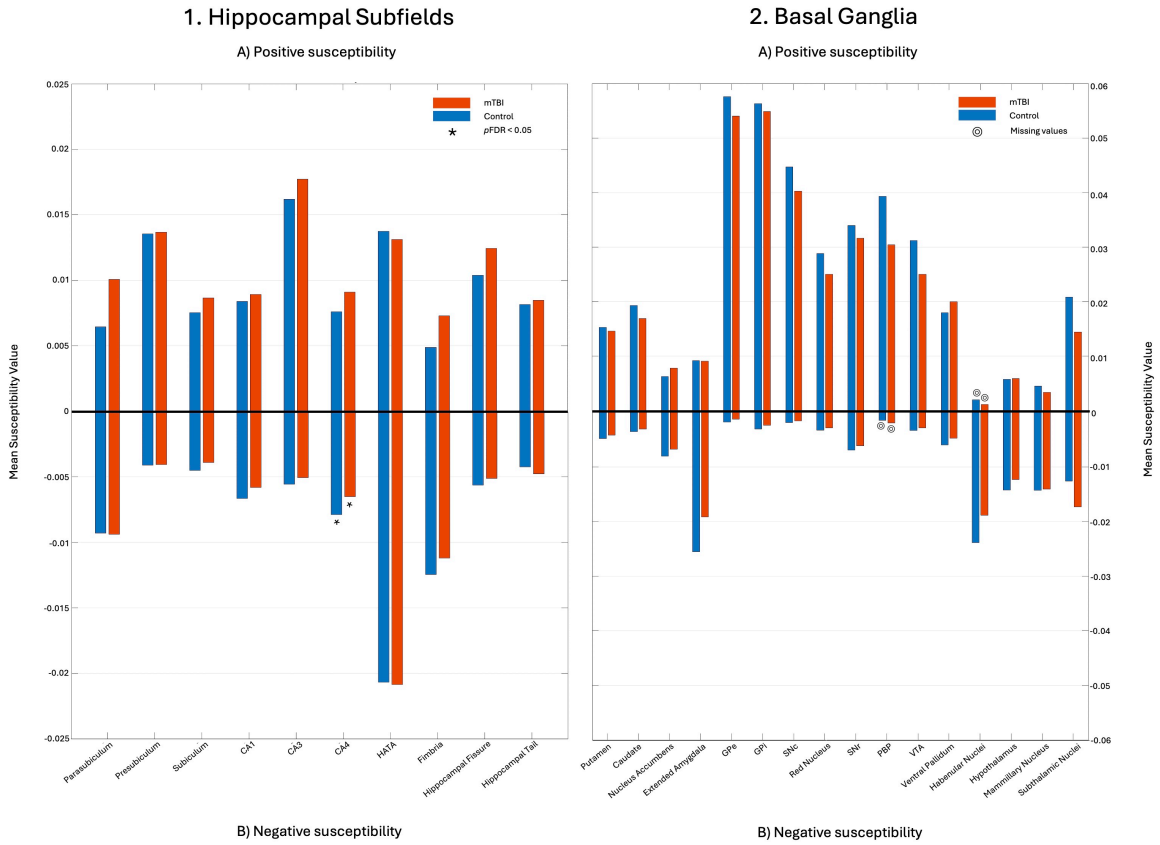

Figure 5.3: Mean susceptibility values in the hippocampal and basal ROIs

⋆ = significant differences between groups; ⊙ = regions omitted from further analysis due to indeterminate ROI-wise values for any participant.

Bar plots showing the mean susceptibility values for mTBI (red bars) versus HC (blue bars) for: 1. Hippocampal subfields, and; 2. Basal ganglia, for both A) positive and B) negative susceptibility maps. Susceptibility is measured in ppm. *p*FDR = statistical significance (*p*-value) after false discovery rate (FDR) correction.

5.4.2 *Bilateral regional correlations*

Partial Pearson correlation coefficients were used to assess the relationship between age and both positive and negative susceptibility for the 10 hippocampal and 15 basal segmentations, controlling for group status. Additionally, correlations between both susceptibility signs and 1) BIST scores as an indicator of injury severity, and; 2) DSI at the time of the MRI scan as a marker of injury latency, were conducted for the mTBI sample only. Negative susceptibility was transformed to absolute values to better represent relationships between variables. P-values were adjusted separately for the 10 hippocampal subfields and 15 segmentations of the basal nuclei using FDR methods (Benjamini et al., 1995).

5.4.2.1 *Age*

No statistically significant correlations were observed between age and positive susceptibility values for any hippocampal ROI, however, a significant positive correlation between age and absolute negative susceptibility in the fimbria ($r(48) = 0.42$, pFDR = 0.03) was observed, suggesting age-related increases in negative susceptibility (i.e., susceptibility becomes more negative with age) (see Fig. 5.4).

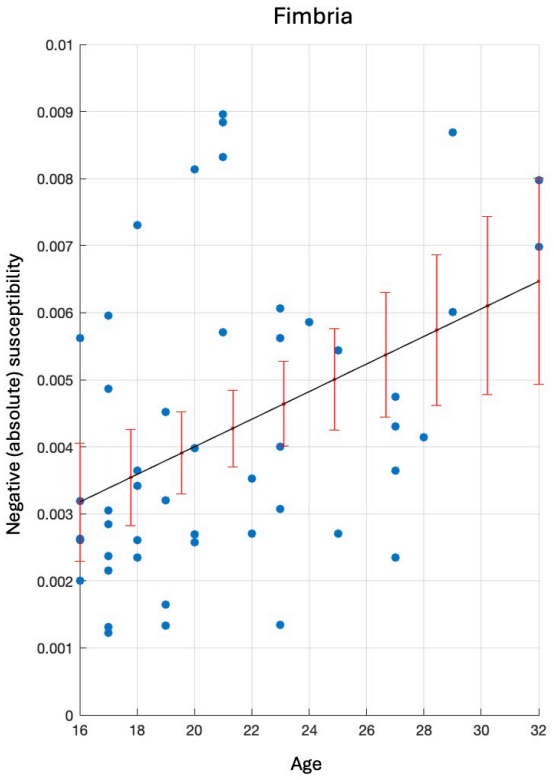

Figure 5.4: Significant correlations: Age and susceptibility values in the Fimbria

Scatter plot illustrating the statistically significant correlation between negative (absolute) susceptibility values in the hippocampal fimbria and age. A line of best fit (black) highlights the trend. 95% confidence interval bars (red) indicate the predicted range for true values, providing a measure of uncertainty in the model.

Results indicated significant age-related increases in positive susceptibility values in several basal regions, including the putamen ($r(48) = 0.64$, pFDR < 0.001), caudate ($r(48) = 0.50$, pFDR $= 0.001$), red nucleus ($r(48) = 0.66$, pFDR < 0.001), PBP ($r(48) = 0.40$, pFDR $= 0.02$), and ventral pallidum ($r(48) = 0.35$, pFDR $= 0.04$) (see Fig. 5.5).

Significant positive correlations were also evident between age and absolute negative susceptibility in the caudate ($r(48) = 0.39$, pFDR $= 0.04$) and extended amygdala ($r(48) = 0.51$, pFDR $= 0.002$) suggesting that susceptibility in these regions tends to increase (become more negative) with age. Significant negative correlations were also observed between age and absolute negative susceptibility values in the ventral pallidum ($r(48) = -0.37$, pFDR $= 0.04$), suggesting that susceptibility tends to decrease (become less negative) with age (see Fig. 5.5).

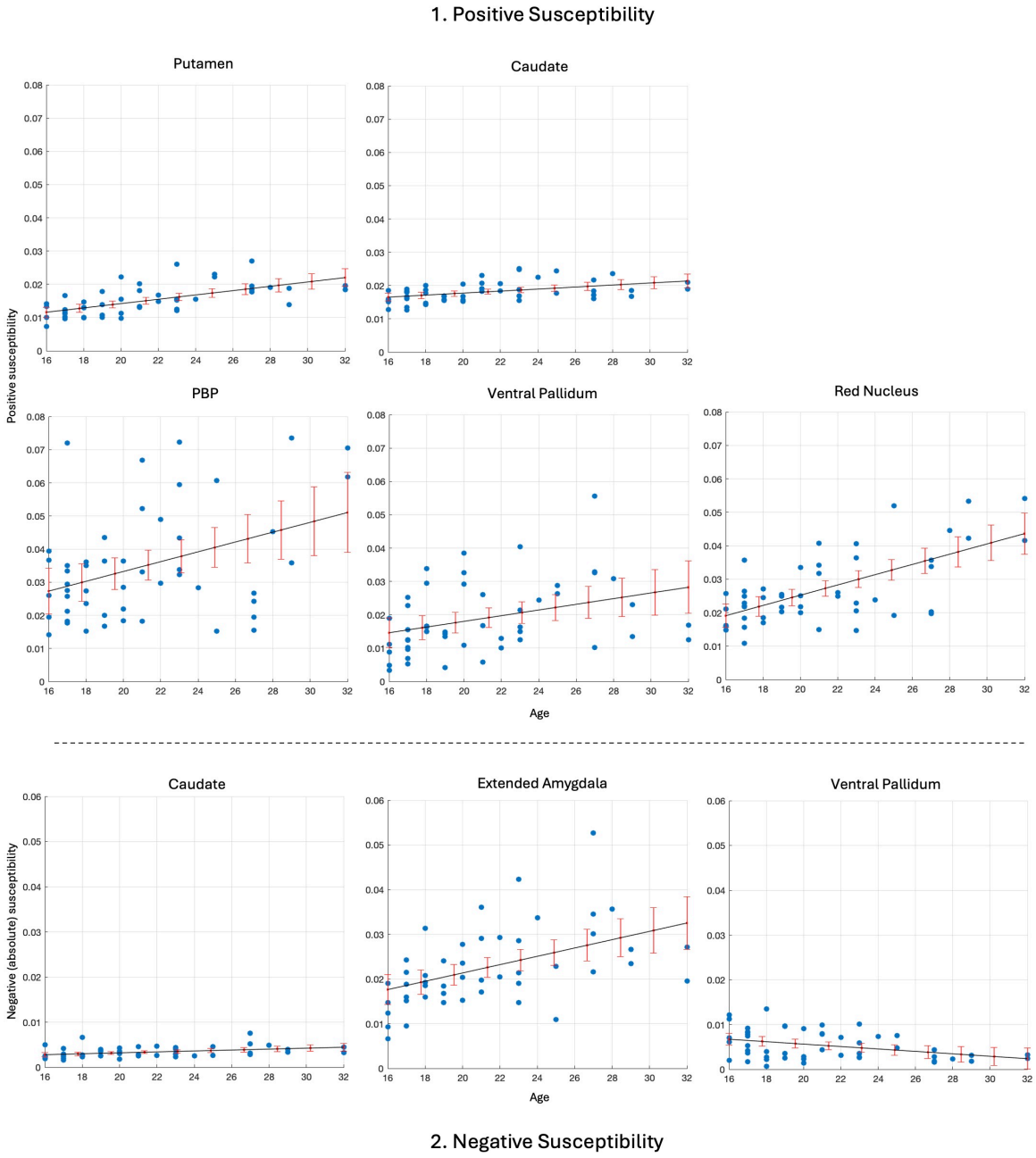

Figure 5.5: Significant correlations: Age and susceptibility values in the Basal Ganglia

Scatter plots illustrating the statistically significant correlations between both 1. Positive and 2. Negative absolute susceptibility values and age in basal ROIs. A line of best fit (black) highlights the trend. 95% confidence interval bars (red) indicate the predicted range for true values, providing a measure of uncertainty in the model.

5.4.2.2 *Injury severity and injury latency*

No statistically significant correlations were observed between both positive and negative absolute susceptibility values and either DSI or BIST scores, for any basal nuclei or hippocampal subfield.

5.5 DISCUSSION

Despite the vulnerability of the striatum and other deep nuclei to mechanical strain, cytoskeletal damage, and secondary metabolic disruptions after mTBI, all of which are risk factors for iron accumulation, previous QSM research has not yet achieved the anatomical specificity necessary to extensively characterise mTBI-related alterations to tissue content in the subcortical grey matter. To address this limitation, I performed a highly detailed segmentation of the basal ganglia alongside the first QSM analysis of the distinct hippocampal subfields in mTBI. QSM images were thresholded for inter-voxel sign prior to analysis. Between-group comparisons showed no significant differences between mTBI participants and controls for either susceptibility sign in the basal ganglia, or for positive sign in the hippocampal subfields. However, the hippocampal CA4 region exhibited significantly decreased (less negative) negative susceptibility values for the mTBI group relative to HC. Correlational analyses also revealed no significant associations between either susceptibility sign and injury latency or severity in the mTBI group within any ROI. Congruent with expected age-related trends, positive susceptibility values in the putamen, caudate, parabrachial pigmented nucleus, ventral pallidum, and red nucleus increased with age. Age-related increases in negative susceptibility were also apparent in the hippocampal fimbria, the caudate, and the extended amygdala, but decreased with age in the ventral pallidum.

5.5.1 *Negative susceptibility is decreased in CA4 after mTBI*

The hippocampal CA4 region is particularly susceptible to both tau pathology in CTE (Cherry et al., 2021; Murray et al., 2022) and associated local dendritic swelling which are considered supporting features for diagnosis (Bieniek et al., 2021; McKee et al., 2016). As a microtubule-associated protein, tau is a promising early indicator of axonal injury in mTBI (Flavin et al., 2023). While focal accumulation of tau would likely result in increased negative susceptibility on QSM (O'Callaghan et al., 2017; Z. Zhao et al., 2021), the observation of decreased negative susceptibility in CA4 reported here nonetheless supports an axonal-injury model. This type of injury is characteristic of both TBI (Johnson et al., 2013) and mTBI (Inglese et al., 2005), and is associated with disruptions of the myelin sheath (Maxwell et al., 2003b; Maxwell et al., 1999) or demyelination as demonstrated in both animal models (Bramlett et al., 2002) and human QSM studies investigating sr-mTBI (Weber et al., 2018). Although density of myelinated fibers is relatively low in the hilus (CA4) (Ábrahám et al., 2010), disruptions to myelination in this region could plausibly account for localised decreases in negative susceptibility, suggesting this area could be vulnerable to axonal damage during mTBI and could speculatively represent an acute component of the injury cascade that culminates in tauopathy as a downstream pathological event later in life for some people.

Other plausible explanations for decreased negative susceptibility after mTBI could be related to phagocytosis of stressed cells and their components, including myelin. Microglia

and macrophages are known to target and phagocytose distressed but still viable cells, even in the absence of cell death (Yu et al., 2022). This could result in a reduction in negative susceptibility if cells within a ROI are particularly sensitive to even mild injury and resultant distress signalling. Indeed, research suggests that the CA4 region is selectively vulnerable to sustained cell loss after head injury (Lowenstein et al., 1992; Maxwell et al., 2003a). Of particular relevance to this hypothesis, the hilus contains glutamatergic mossy cells and GABAergic somatostatin-expressing hilar interneurons which are highly vulnerable to damage and excitotoxicity in temporal lobe epilepsy, TBI, and mTBI (Grovola et al., 2020; Santhakumar et al., 2000; Scharfman, 2016). Indeed, murine models demonstrate irreversible loss of somatostatin-expressing hilar interneurons within just four hours of injury (Lowenstein et al., 1992).

In addition, mossy cells, unique to the hilus, are especially predisposed to metabolic disruptions and excitotoxicity, as well as premature neurodegenerative processes (Scharfman, 2016). Murine models also demonstrate the link between TBI and damage to hilar mossy cells, the “irritable mossy cell" hypothesis, which may account for the memory-related impairments observed after TBI (Santhakumar et al., 2000; Scharfman, 2016). Mossy cells also express proteins that may be implicated in depression, and reductions in mossy cells may increase levels of anxiety (Scharfman, 2016); both of which are mood-related symptoms of mTBI (Rosenbaum et al., 2012). Whilst speculation is interesting, in the absence of histological analysis, the precise pathological mechanisms cannot be accurately characterised. However, at minimum the results presented here support prior research noting the vulnerability of the hippocampus, and in particular the CA4, to mTBI-related pathology.

5.5.2 *Exploring null results: mechanisms of tissue susceptibility changes and evidence from the literature*

5.5.2.1 *Positive susceptibility in subcortical grey matter*

This, and other (Bell et al., 2024; Gong et al., 2018; Koch et al., 2018; Koch et al., 2021; Pinky et al., 2022; Wright et al., 2022; Zivadinov et al., 2018a), QSM investigations have found no significant evidence of increased susceptibility indicative of iron accumulation in the basal nuclei or hippocampus after mTBI. However, iron accumulation as a pathologic feature of mTBI in many of these regions is well documented, contradicting the lack of iron-related findings reported here. For example, an iron-sensitive magnetic field correlation (MFC) study (Raz et al., 2011) reported iron accumulation in the globus pallidus and thalamus following mTBI. Investigations using SWI have also identified iron deposition in the caudate, thalamus, right substantia nigra, red nucleus, lenticular nucleus, splenium of the corpus callosum, and hippocampus in chronic mTBI, concomitantly linking accumulations in the substantia nigra with cognitive dysfunction (Lu et al., 2015). Studies using T_2^* imaging have identified iron deposition in cortical, subcortical (left putamen, bilateral hippocampal), and brainstem regions (Nikolova et al., 2022), along with reports of accumulation in the lateral geniculate nucleus of the thalamus (Chong et al., 2023), with both studies citing associations between elevated iron and post-mTBI headache symptomatology.

Additionally, animal models of controlled cortical impact TBI have demonstrated iron deposition in the thalamus ipsilateral to the impact site upon histological examination, with focal depositions co-localising T_2 hypointensity on MRI (Onyszchuk et al., 2009). Murine models also report the vulnerability of the hippocampus to oxidative stress and synaptic protein modification, underscoring not only the regional susceptibility to traumatic injury mechanisms, but also identifying a potential role of iron in the generation of cytotoxic free radicals (Ansari et al., 2008). Post-mortem studies have also provided evidence of iron accumulation in hippocampal NFTs in CTE (Bouras et al., 1997), as well as abnormal haemosiderin-laden macrophages near small vessels in the frontal and temporal lobes less than one year post-injury, indicating ferritin-bound non-haem iron deposition (Bigler, 2004) which is corroborated by recent research noting the presence of L-ferritin-positive astrocytes proximal to CTE lesions (Osterman et al., 2025). Despite these studies highlighting the vulnerability of the basal nuclei and hippocampus to iron-mediated pathology at multiple stages post-injury, an absence of significant group differences in positive susceptibility observed in this study may suggest a general protective effect conferred by the deep subcortical location of these regions.

It is also reasonable to suggest that the absence of between-group differences in iron markers may reflect the influence of normal age-related increases in iron (for a review, see Madden et al., 2023), which could obscure subtle mTBI-specific effects. Age-related iron deposition is particularly pronounced in the basal nuclei and most evident within the age range of participants in this study, as discussed in more detail further below. This shared characteristic among younger individuals may explain the lack of significant group differences in iron-related markers. In contrast, the general lack of age effects in hippocampal regions and the resultant sensitivity to disruptions in negative susceptibility in the CA4 region supports the hypothesis that changes to biomagnetism which are common to all participants may obscure injury-related susceptibility effects. Consequently, the unique alteration to negative susceptibility values in the hippocampal CA4 thus likely reflect specific pathological consequences of mTBI.

In keeping with these observations, thresholding bulk magnetic susceptibility may have enabled the isolation and identification of weaker negative susceptibility effects, which could otherwise have been diluted or overshadowed by stronger positive susceptibility signals during analysis (Ravanfar et al., 2021). This could also account for the lack of significant differences reported in previous studies where neither more rudimentary thresholding or true magnetic source separation techniques were employed to generate separate sign-wise maps (Bell et al., 2024; Gong et al., 2018; Koch et al., 2018; Koch et al., 2021; Pinky et al., 2022; Wright et al., 2022; Zivadinov et al., 2018a), providing support for intra- or inter-voxel susceptibility separation techniques, depending on the data acquisition parameters.

5.5.2.2 *Negative susceptibility in subcortical grey matter*

There was no evidence of increased negative susceptibility in the subcortical grey matter following mTBI. However, alterations to varying biomagnetic substrates following TBI have previously been characterised in murine models using QSM and R_2^* imaging along-

side histological examinations to assess changes not only to iron, but also myelin and calcium (Chary et al., 2021). These models have demonstrated concurrent iron and calcium accumulation, as well as demyelination after impact. These findings are reinforced by additional *in vivo* and *ex vivo* murine models of TBI also reporting significant calcifications, which are proposed as an indirect measure of inflammation (Lehto et al., 2012) and microglia activation (Gayoso et al., 2003) following injury. Of particular interest, studies have noted that calcifications often co-localise with paramagnetic iron in TBI (Chary et al., 2021). This finding underscores the complex interplay of tissue components affected by mTBI and highlights the contribution of both paramagnetic and diamagnetic substrates to injury pathology. This further validates the need for either source separation, if data are acquired with multi-echo sequences (Ahmed et al., 2023; J. Chen et al., 2021; Emmerich et al., 2021; J. Lee et al., 2024; Z. Li et al., 2023; Shin et al., 2021), or single-echo-compatible voxel-wise thresholding (Merenstein et al., 2025; Merenstein et al., 2024), in QSM research to differentiate these overlapping effects and better elucidate underlying biological mechanisms.

Aβ and tau, two proteins with diamagnetic properties (Gong et al., 2019; O'Callaghan et al., 2017; Z. Zhao et al., 2021), have been associated with both acute injury pathology and later neurodegenerative processes, and are known to co-localise with iron in AD (Madden et al., 2023) and CTE (Bouras et al., 1997). Tau is a promising fluid biomarker for axonal injury in mTBI (Flavin et al., 2023), and both fluid tau (Ost et al., 2006; Rubenstein et al., 2017) and Aβ can accumulate at the acute stage of TBI (Johnson et al., 2010). Focal accumulations may be present in the entorhinal cortex, hippocampus, and striatum (caudate and putamen) as evidenced by positron emission tomography (PET) studies of TBI (Dybing et al., 2023). The aggregation of both proteins would likely produce differences in negative susceptibility. However, systematic reviews have noted inconsistencies between studies regarding the presence or absence of Aβ as a pathologic feature of TBI (Dybing et al., 2023), and similar conflicting evidence exists regarding the biodynamics of tau in mTBI, with some studies suggesting elevations within hours-to-days, and others indicating no difference between individuals with mTBI and controls acutely after injury (Flavin et al., 2023). These factors may have contributed to the absence of quantifiable increases in negative susceptibility in the present study. Alternatively, and perhaps more plausibly, the results presented here indicate that Aβ and tau are not present in this young cohort imaged at the acute stage of a mild head injury (Rodrigue et al., 2009; Schöll et al., 2016).

5.5.3 *Age-related alterations in subcortical biomagnetic substrates are region-specific*

5.5.3.1 *Temporal biodynamics of subcortical positive susceptibility*

Iron increases throughout the lifespan as a function of normal ageing (Ashraf et al., 2018; Gong et al., 2015; Hallgren et al., 1958; G. Li et al., 2023; Madden et al., 2023; Persson et al., 2015; Treit et al., 2021). Particularly steep increases in brain iron content are present in the red nucleus and substantia nigra within the first 20 years of life, the globus pallidus at approximately 30 years, with maximal values reached in the putamen and caudate at

approximately five to six decades after birth (Hallgren et al., 1958). This histological study is supported by extensive QSM investigations (Madden et al., 2023), for example, QSM and R_2^* mapping have demonstrated susceptibility increases in the putamen and globus pallidus throughout adulthood, with values in the caudate peaking in the third decade (Treit et al., 2021). Other QSM studies have evidenced increased susceptibility values in the caudate, putamen, globus pallidus, red nucleus, and substantia nigra in healthy older populations relative to younger samples (Bilgic et al., 2012). Both imaging and histological studies support the biological plausibility of correlational results presented here, particularly within the caudate, putamen, and red nucleus (Madden et al., 2023). This study also extends the existing literature through the observation of additional age-related positive susceptibility increases in the parabrachial pigmented nucleus and ventral pallidum. The correlational findings presented here, and evidence from the literature more broadly, suggest that a younger cohort is particularly prone to iron deposition as a shared characteristic, irrespective of mTBI status. For hippocampal regions, on the other hand, age-related iron accumulation apparent in previous research (Ashraf et al., 2018; Hagemeier et al., 2012; Madden et al., 2023; Zecca et al., 2004) was not reflected in the results of this study, potentially due to a likelihood of more subtle effects in these regions, coupled with the limited age range of this sample.

5.5.3.2 *Temporal biodynamics of subcortical negative susceptibility*

The temporal dynamics of diamagnetic substrates are relatively under-investigated in QSM, making inferences far less substantive than those related to paramagnetism and iron. Although myelin is the main source of negative susceptibility on QSM (Deh et al., 2018), it is unlikely that increases in negative susceptibility reflect age-related increases in myelin content. Whilst developmental myelination of axons is apparent up until approximately 30 years of age, this protraction of normal processes is generally restricted to prefrontal cortical regions (Moulson et al., 2008). In other brain regions, steep increases in myelin content are most apparent in the first months of life, after which time any disparities between age groups are unlikely to produce noticeable differences in tissue contrast on MRI (Branson, 2013). Age-related kinetics of Aβ and tau aggregation point toward similar conclusions. While deposits of Aβ have been detected in the brains of individuals as young as 20 years old (Baker-Nigh et al., 2015), it is typically a feature associated with older age, and has been noted in both the presence and absence of cognitive dysfunction (Rodrigue et al., 2009); a similar pattern to that observed in tau accumulation (Schöll et al., 2016). As such, trends for increasing negative susceptibility with age are unlikely to be related to proteinopathy. Here, reasonable speculation suggests that the positive relationship between negative susceptibility and age in the caudate, extended amygdala, and hippocampal fimbria may be related instead to calcifications in these regions. This is supported by a body of work highlighting age-related calcifications in the basal ganglia (Monfrini et al., 2023; Saade et al., 2019) and hippocampus (Wegiel et al., 2002) in healthy individuals. However, the paucity of granular segmentations in the wider literature makes drawing parallels with the present research more difficult.

Conversely, the decrease in negative susceptibility as a function of age in the ventral pallidum may be related to myelin changes. The ventral pallidum contains both neuronal cell bodies and myelinated axons for rapid signal transmission (Heimer et al., 2006; Kupchik et al., 2017; Root et al., 2015). Although literature related to age-induced demyelination specific to this region does not abound, investigations of myelin biodynamics more broadly suggests a 10% decrease per decade between the ages of 20 and 80 (Marner et al., 2003), which may account for the moderate effects evident here.

5.5.4 *Injury latency and severity do not affect subcortical tissue magnetic susceptibility*

While research suggests a negative correlation between iron deposition and cognitive ability following mTBI (Lu et al., 2015), self-reported injury severity is often misaligned with objective markers of pathology, including on neuroimaging (McCrea et al., 2017; Shenton et al., 2012). Alongside the under-reporting of symptoms that often occurs following a sr-mTBI (Kroshus et al., 2015; Meier et al., 2015), these factors could confound results and contribute to the lack of correlation between positive or negative susceptibilities and both BIST scores and injury latency variables observed here. However, the use of an inter-voxel thresholding approach applied to traditional QSM maps may still be insensitive to the more subtle changes in tissue composition, which are better estimated using contemporary susceptibility source separation techniques (see, for example, Emmerich et al., 2021; Shin et al., 2021). Additionally, the lack of correlation between positive or negative susceptibilities and injury latency suggests that mTBI-related neuropathology may be time-dependent and more evident at subacute and chronic stages. Additional longitudinal research may be needed to better represent associations between injury latency and alterations to brain tissue content.

However, this may also be related to a generalised protective effect conferred by the surrounding cerebrum. The cortex is vulnerable to a diverse range of injury mechanisms and downstream pathology in mTBI, including acute mechanical deformation and sulcal “water hammer" injury, which may be implicated in cortical atrophy and tauopathy in CTE (Kornguth et al., 2017; McKee et al., 2023; D. H. Smith et al., 2013). It is therefore not unreasonable to suggest that cortical, rather than subcortical, brain tissue content changes may be more predictive of adverse symptomatology after mTBI; a hypothesis addressed in Chapter 6 and Chapter 8.

5.5.5 *Limitations and future research*

The absence of elevations in positive or negative net susceptibility following mTBI suggest that iron deposition, calcifications, or focal aggregation of proteins such as tau and Aβ may not be present at the acute stage of injury. However, aforementioned research provides strong evidence that head injury more broadly, and even mild instances, can lead to diverse changes across biomagnetic substrates. This suggests that several factors may have inhibited the detection of changes in this research. Firstly, focal accumulations of

iron, calcium, or proteins may better characterise chronic or later-life effects rather than acute pathophysiology, as evidenced by neuroimaging studies where differences in iron deposition were apparent at an average of 559 days post-injury (Raz et al., 2011). Secondly, tau elevations are most commonly reported in cases of repeated exposure to head injuries (Flavin et al., 2023) and tau oligomer polymorphisms are expressed differently in single versus repetitive mTBI (Bittar et al., 2019). However, in the absence of prior injury data, the study design precluded stratification of mTBI participants according to prior mTBI exposure. Without this information, detection of negative susceptibility changes and the potential relationship with tau pathology may be inhibited. Future studies should consider longitudinal research designs tracking athletes' exposure to head injury to better elucidate the cumulative and temporal effect of mTBI on biomagnetic substrates.

Notwithstanding the detail of the segmentations used in this study relative to previous more macroscopic investigations, the spatial resolution of the susceptibility maps may still limit detection of microstructural alterations. Because the susceptibility value at each voxel in a QSM image is obtained by convolving the susceptibilities of neighbouring voxels with a dipole kernel, each voxels susceptibility value is influenced by the surrounding susceptibility distribution (Y. Wang et al., 2015), and thus resolutions of 1 mm and above may hinder the detection of the subtle pathophysiological changes associated with mTBI (Karsa et al., 2019a). However, a 1 mm isotropic voxel resolution still meets the minimum criteria for best-practice QSM (Bilgic et al., 2024) and the confounding effects related to resolution may not be as severe as other QSM-based investigations (Bell et al., 2024; Gong et al., 2018; Koch et al., 2018; Koch et al., 2021; Zivadinov et al., 2018a).

The use of single-echo QSM restricted voxel thresholding to an inter-voxel approach. As a result, the presence of multiple biological substrates with opposing magnetic properties *within* voxels may have confounded results by representing an aggregate of all susceptibility sources. These bipolar contributions within voxels cannot be disambiguated, and thus analysed, without multi-echo acquisitions (Ahmed et al., 2023; J. Chen et al., 2021; Emmerich et al., 2021; J. Lee et al., 2024; Z. Li et al., 2023; Shin et al., 2021). This was also a likely cause of missing values in certain ROIs comprised primarily of either positive or negative susceptibility sources, such as the habenular nuclei or parabrachial pigmented nucleus (see Fig. 5.3). Thresholding these extremely polarised regions may result in indeterminate values for the non-dominant sign for some participants, which may be further exacerbated by the size of ROIs, like the relatively small habenular nuclei. The use of multi-echo acquisitions would likely also resolve this limitation.

In addition, while the hippocampal (Iglesias et al., 2015) and basal ganglia (Pauli et al., 2018) atlases offer robust segmentations, several limitations are associated with these approaches. First, the hippocampal segmentations provided via FreeSurfer (Fischl, 2012) were developed from a small number of donors (10 for HC, up to 15 when including mild cognitive impairment and AD subjects), with advanced age at death (60–91 years), which may result in hippocampal atrophy influencing the delineations. Furthermore, even with ultrahigh resolution MRI, some regional boundaries are not clearly visible in the training data. Similarly, for the basal ganglia atlas, some fine anatomical details may be lost, po-

tentially leading to inaccuracies in boundary delineation. Although manual delineation is considered the gold standard, it requires extensive anatomical expertise and is prohibitively time-consuming (Morey et al., 2009). Recent advances in deep-learning-based hippocampal segmentation have shown promise (Schell et al., 2023); however, given that the current cohort is unlikely to exhibit gross hippocampal atrophy or other dramatic structural alterations, these advanced approaches may be more beneficial in samples where such abnormalities are expected.

Lastly, group-level analyses may obscure individual neuropathology and inter-individual heterogeneity in mTBI (Bedggood et al., 2024; Domínguez et al., 2024); a limitation addressed with the individualised analyses presented in Chapter 7 and Chapter 8.

5.6 CONCLUSIONS

This research builds upon previous QSM studies of mTBI by presenting the first assessment of mild injury effects specifically in the hippocampal subfields, and offers the most detailed segmentation of the basal ganglia to date. Here, both positive (iron-related) and negative (myelin-, calcium-, and protein-related) net susceptibility maps were utilised to better understand the impact of mTBI on biological substrates with differing biomagnetic profiles. Results revealed mTBI-related decreased negative susceptibility in the hippocampal CA4, indicating potential disruption to myelin or vulnerable cell populations in this region which may represent a component of the degenerative injury cascade. The absence of significant increases in either susceptibility sign as a marker of mTBI pathophysiology may reflect a general protective effect of subcortical location within the brain, the confounding effect of age-related susceptibility changes common to all participants, or the potential loss of clinically relevant information in the current group-wise statistical approach, which may obscure heterogeneous microstructural tissue alterations. Finally, results from correlational analyses support and extend prior literature regarding age-related iron deposition in subcortical grey matter and contributes to the sparse literature on the relationship between negative susceptibility values and age.

Research Projects Part III: Cortical Alterations in Brain Tissue Microstructure Following mTBI

6

CHARACTERISING POSITIVE AND NEGATIVE QUANTITATIVE SUSCEPTIBILITY VALUES IN THE CORTEX FOLLOWING MTBI: A DEPTH- AND CURVATURE-BASED STUDY

6.1 MOTIVATION

The previous chapter demonstrated a general lack of significant findings within the subcortical grey matter regions, with the exception of the hippocampal CA4, aligning with a similar deficit of significant results characteristic of the QSM-mTBI literature. However, the limited findings may also reflect an overemphasis on deep grey matter structures, potentially overlooking other brain regions that could be crucial for identifying loci of grey matter micropathology following mTBI. In Chapter 6, the investigation is extended beyond traditional subcortical regions to the cerebral cortex; a region highly vulnerable to mTBI-related damage, yet largely neglected in QSM-based studies. Where cortical ROIs have been included, study designs have lacked the anatomical specificity required to investigate cortical architectonics, which may contribute to focal tissue disruption. In this chapter, I use depth- and curvature-specific column-based analyses to characterise susceptibility variations in the cerebral cortex, providing more precise localisation than a traditional whole-ROI framework. This chapter not only elucidates the role of biomagnetic substrates in cortical micropathology following mTBI and the vulnerability of this region, but also has implications for understanding the longer-term effects of mTBI. A summary of this chapter is presented in § 6.6.

6.2 INTRODUCTION

Studies using QSM to investigate mTBI effects have largely overlooked the cortex (see Chapter 3). Where this structure has been investigated, the use of voxel-wise comparisons (Gong et al., 2018) or gross segmentations (Pinky et al., 2022) have been naïve to the architectonics and potentially heterogeneous distributions to cellular elements within the cortical layers. Significantly more anatomical precision is needed to detect depth- or curvature-specific differences in magnetic susceptibility within the cortical mantle after mTBI.

More sophisticated analysis of the cortex is likely excluded from investigation due to several methodological challenges primarily related to complex cortical architectonics. Differentiating myeloarchitecture, cytoarchitecture, and cortical laminae using ultrahigh-field, high resolution MRI (such as that acquired at 7T or higher) is a developing area in neuroimaging research (Waehnert et al., 2016). Currently, however, 7T MRI is not as widely available, and clinical MRI data are more typically acquired on scanners of lower field strengths such as 3T or 1.5T (Straub et al., 2019). At magnetic field strengths of 3T or lower, and supra-millimetre voxel resolutions, analysis of specific cortical laminae is inhibited. However, column-based analytic techniques (Y. Ma et al., 2023; Merenstein et al., 2025; Merenstein et al., 2024; Northall et al., 2023; Sui et al., 2022; Waehnert et al., 2014) enable depth-wise investigations of magnetic susceptibility in the cerebral cortex and are already producing promising results in AD research (Merenstein et al., 2024).

To address these research gaps, this chapter presents the first architectonically-motivated QSM analysis of cortical mTBI effects via depth- and curvature-specific column-based analysis. This study aimed to: 1) assess regional patterns of positive (iron-related) and negative (myelin-, protein-, calcium-related) magnetic susceptibility as a marker of acute cortical pathology after sr-mTBI, and; 2) understand the relationship between magnetic susceptibility in the cerebral cortex and variables such as age, injury latency, and severity. Based on prior literature, I hypothesised that differences in susceptibility would likely be evident in the frontal and temporal cortices, which are reported to be susceptible to injury in mTBI and are among the first to show degenerative effects of brain injury. This distribution should be most prominent in the sulcal fundus due to increased vulnerability to trauma-induced deformation. Based on known effects of age on cortical iron deposition in this age range (Hallgren et al., 1958), positive susceptibility values were hypothesised to show a positive relationship with age. However, due to the novel nature of this approach within the domain of QSM for mTBI, analyses remained largely exploratory and without specific *a priori* hypotheses.

6.3 MATERIALS, METHODS, AND PARTICIPANTS

For details on ethical approval, recruitment, inclusion and exclusion criteria, data collection, radiological clinical scan review, and participant sample characteristics, refer to Chapter 5 and Table 5.1. Image acquisition and sequence details are provided in Chapter 5.

6.3.0.1 *Anatomical image processing*

Bias field-corrected T_1w images were processed using FreeSurfer's (Fischl, 2012) *recon-all* pipeline to 1) delineate pial and GM/WM boundary meshes, and; 2) generate estimates of cortical thickness and curvature for each vertex (Merenstein et al., 2024). To enhance the accuracy of both the initial FreeSurfer skull-strip (Fischl, 2012) and the automatically generated pial surface mesh, skull-stripping was re-run with *-gcut*, and watershed threshold adjustments were applied as needed (see Chapter 5).

6.3.0.2 *QSM processing*

QSM image reconstruction, skull-stripping of the raw magnitude images, thresholding of QSM images, and erosion of non-brain signal around the brain perimeter do not deviate from those summarised in Chapter 5. In this study, as well as the one presented in Chapter 8, erosion is particularly important for mitigating noise and PVE, which can otherwise confound the accuracy of cortical susceptibility measurements close to the cortical surface. For this cortical study, skull-stripped T_1w images were used for the linear coregistration of the magnitude image to T_1w native space using FLIRT (Greve et al., 2009; Jenkinson et al., 2002; Jenkinson et al., 2001) with 12 DoF. Due to variability in acquisition parameters, FoV, and matrix size between participants' T_1w and magnitude images (see Chapter 5), the 12 DoF linear registration provided more accurate alignment compared to the 6 DoF alternative, allowing for better compensation of non-rigid anatomical variations upon visual inspection. The resulting transformation matrix was used for spatial normalisation of the QSM images to T_1w space, effectively upsampling the QSM images. As the analyses are based on cortical depth rather than voxel-wise comparisons, upsampling was not considered a concern. QSM maps were then thresholded into separate maps of dominant sign voxel-wise sign with *fslmaths* for analysis.

6.3.0.3 *Cortical column generation*

To generate cortical columns and sample signed susceptibility values, I used a pipeline previously applied to diffusion-weighted imaging (DWI) data analysis (Y. Ma et al., 2023) and recently adapted for use with QSM (Merenstein et al., 2024). First, the T_1w FreeSurfer (Fischl, 2012) recon served as an input into the *easy_lausanne* tool. This stripped-down fork of the open-source Connectome Mapper (Daducci et al., 2012) separates the cortex into five atlases, ranging from 34 to 250 ROIs per hemisphere, according to the Lausanne multiscale atlas (Cammoun et al., 2012). For subsequent analyses, we focused on the atlas with 34 ROIs per hemisphere, which is equivalent to the Desikan-Killiany atlas (Desikan et al., 2006) native to FreeSurfer (Fischl, 2012).

Cortical columns were created for each hemisphere in T_1w space with *write_mrtrix_tracks* (Tournier et al., 2019) in MATLAB (version R2024a), which was used to connect vertex pairs between the pial and GM/WM boundary surface meshes. As such, use of the term "column" in this context denotes a straight line orthogonal to the cortical surface (Merenstein et al., 2024), extending from the pial surface to the GM/WM boundary, rather than

implying distinct cortical cytoarchitecture (Brodmann, 2005). Each cortical column was segmented into 21 equidistant depths, each with a step size of 5% of the cortical thickness (Waehnert et al., 2016; Waehnert et al., 2014), from the pial surface to the GM/WM boundary using MRtrix3 *tckresample* (Tournier et al., 2019). It is important to distinguish results produced using this approach from ultrahigh-field investigations of cyto- and myeloarchitecture in the cerebral cortex; results described herein are related to cortical *depth*, rather than *layer*. The columns were categorised based on cortical curvature, derived from FreeSurfer's (Fischl, 2012) Gaussian curvature values at each GM/WM boundary vertex (Pienaar et al., 2008) and quantified in units of $1/mm^2$. The categories included the gyral crown (curvature values: -0.6 to -0.1), sulcal bank (-0.1 to 0.1), and sulcal fundus (0.1 to 0.6), as well as a combined measure (-0.6 to 0.6) (Merenstein et al., 2024). Positive curvature values indicated sulci, while negative values indicated gyri, with higher values corresponding to deeper curvatures (Merenstein et al., 2024). Only columns ranging from 0.5 mm to 6 mm in length were included in the analysis to capture plausible cortical morphology (Fischl et al., 2000) while reducing some PVE. Depth was measured in percentage of cortical thickness rather than absolute metrics (mm) to mitigate any variability between mTBI participants and controls. The pipeline for image processing and generation of cortical columns is summarised in Fig. 6.1.

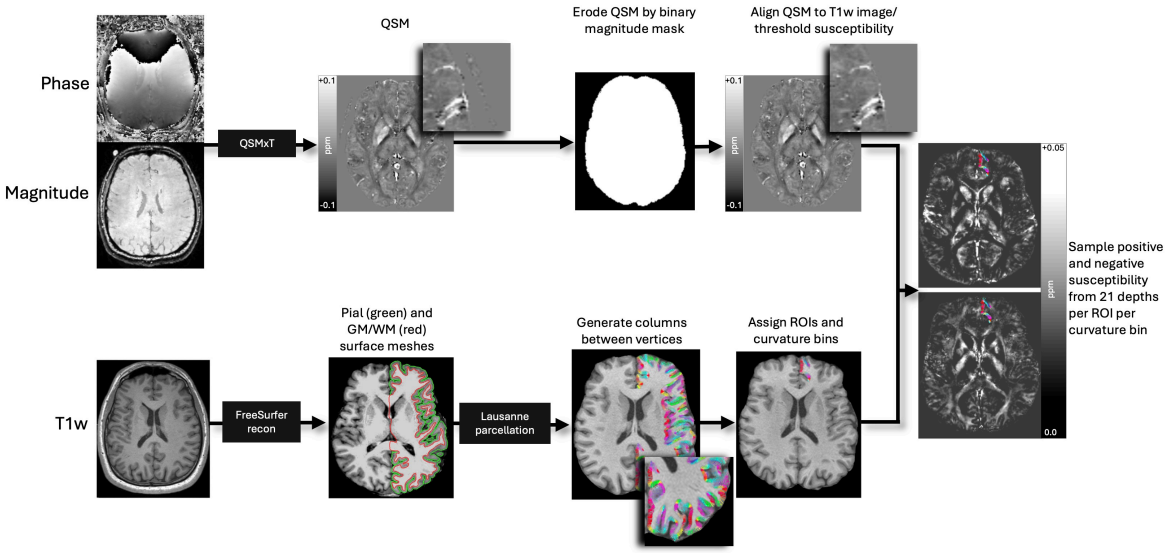

Figure 6.1: Image processing pipeline

Steps are performed independently and in parallel for each participant. Quantitative susceptibility maps were reconstructed from magnitude and phase images using QSMxT, and eroded by the skull-stripped, binarised magnitude image mask to remove non-brain sources of susceptibility. QSM images were then aligned to T_1w images, and thresholded into positive and negative susceptibility maps. FreeSurfer recon was used on bias field-corrected T_1w images to produce pial and GM/WM boundary surface meshes, and vertex pairs were then joined to create cortical columns. Parcellations of the cortical grey matter were estimated by feeding the T_1w FreeSurfer recon into *easy_lausanne*. Columns were then assigned specific ROIs and curvature bins, and used to sample susceptibility from thresholded QSM maps. Susceptibility is measured in ppm. QSM = quantitative susceptibility mapping; GM/WM = grey matter/ white matter boundary; ROI = region of interest.

6.3.1 *Statistical analyses*

To provide a detailed analysis of microstructural differences associated with sr-mTBI while maintaining result granularity, analyses were performed at the bilateral regional level using MATLAB (2024a). Average positive and negative susceptibility values were extracted from 21 cortical depths for all 34 ROIs. Each ROI was analysed by independent curvature bin (gyral crown, sulcal bank, and sulcal fundus) as well as combined curvature as a whole-ROI measure. Between-group analyses were conducted using two-tailed independent samples t-tests. To control for multiple comparisons and align with prior research (Merenstein et al., 2024), FDR correction (Benjamini et al., 1995) was applied to the p-values for 21 comparisons (one for each depth) for each ROI/curvature profile. Due to precise age-matching of participants, age was not considered a covariate or confounding variable of interest for between-group comparisons. However, to explore the relationship between QSM values and age in the entire sample, two-tailed partial Pearson correlation coefficients were calculated between age and both positive and negative susceptibility values independently for all 34 curvature-combined ROIs, at each depth, whilst controlling for group effects. To explore the relationship between susceptibility values and other sr-mTBI-related variables, two-tailed Pearson correlation coefficients were also calculated between BIST scores and DSI and both positive and negative susceptibility values independently for the sr-mTBI sample only. In keeping with Chapter 5, negative susceptibility values were multiplied by -1 to convert them to absolute values, ensuring a consistent directional interpretation in all correlational analyses and more intuitive visualisation. mTBI-17 was excluded from correlations between BIST and both susceptibility signs due to missing data. Correlations were also corrected for 21 depth-wise comparisons using FDR procedures (Benjamini et al., 1995). Given the limited sample size and the need to conserve DoF in this exploratory study, regression analyses were deliberately omitted.

6.4 RESULTS

6.4.1 *Bilateral depth and curvature*

Using two-tailed independent samples t-tests, depth- and curvature-specific between group differences in bilateral regional susceptibility (positive and negative) were examined for each of the 34 ROIs (see Fig. 6.2). P-values were corrected for 21 cortical depths for each ROI/curvature combination using FDR procedures (Benjamini et al., 1995).

6.4.1.1 *Positive susceptibility*

Across bilateral depth profiles, participants with sr-mTBI exhibited significantly higher positive susceptibility than controls in the temporal lobe only (see Fig. 6.2A), specifically in superficial depths of the sulcal bank and fundus of the parahippocampal gyrus, a finding that was conserved when curvature was combined as a whole-ROI measure (see also Fig. 6.3.1A and Fig. 6.3.2A). Susceptibility was decreased following sr-mTBI in the super-

ficial gyral crown of the rostral medial prefrontal cortex (mPFC) and superficially in the frontal pole when curvature was combined. No significant differences between groups were found in bilateral susceptibility values in parietal, occipital, or insular lobes (pFDR > 0.05).

6.4.1.2 *Negative susceptibility*

Across bilateral depth profiles, participants with sr-mTBI exhibited significantly less negative susceptibility than controls in the temporal lobe only (see Fig. 6.2B). This finding was focal to the superficial depths of the fundus in the parahippocampal gyrus, as well as when curvature was combined (see also Fig. 6.3.1B and Fig. 6.3.2B). Negative susceptibility was more negative for participants with sr-mTBI deep in the supramarginal gyral crown of the parietal cortex only. No significant differences between groups for curvature were found in the sulcal bank (see Fig. 6.3B). No significant differences were found in bilateral frontal, occipital, or insular lobes.

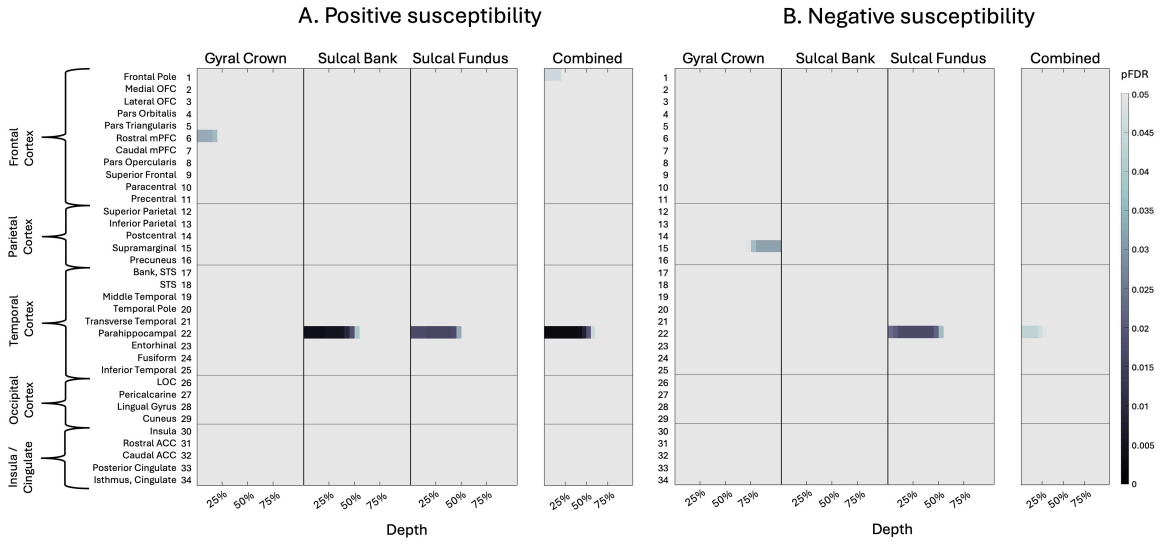

Figure 6.2: Depth- and curvature-specific cortical susceptibility differences

Colour maps demonstrate differences in magnetic susceptibility at each cortical depth (where 0% depth is proximal to the pial surface and increases toward the GM/WM boundary at 100% depth), separately for each curvature bin (crown, bank, fundus) as well as combined curvature as a whole-ROI measure. Two-tailed independent samples t-tests examined group differences in susceptibility at each depth, for each curvature, at each ROI. P-values were corrected for multiple comparisons across 21 cortical depths using FDR implementations. A. Positive susceptibility values were significantly more positive for participants with sr-mTBI than HC in temporal ROIs and significantly less positive in frontal regions only. B. Susceptibility values were significantly less negative for sr-mTBI participants than controls in temporal ROIs and significantly more negative in parietal ROIs. OFC = orbitofrontal cortex; mPFC = medial prefrontal cortex; STS = superior temporal sulcus; LOC = lateral occipital cortex; ACC = anterior cingulate cortex. Figure based on Merenstein et al. (2024).

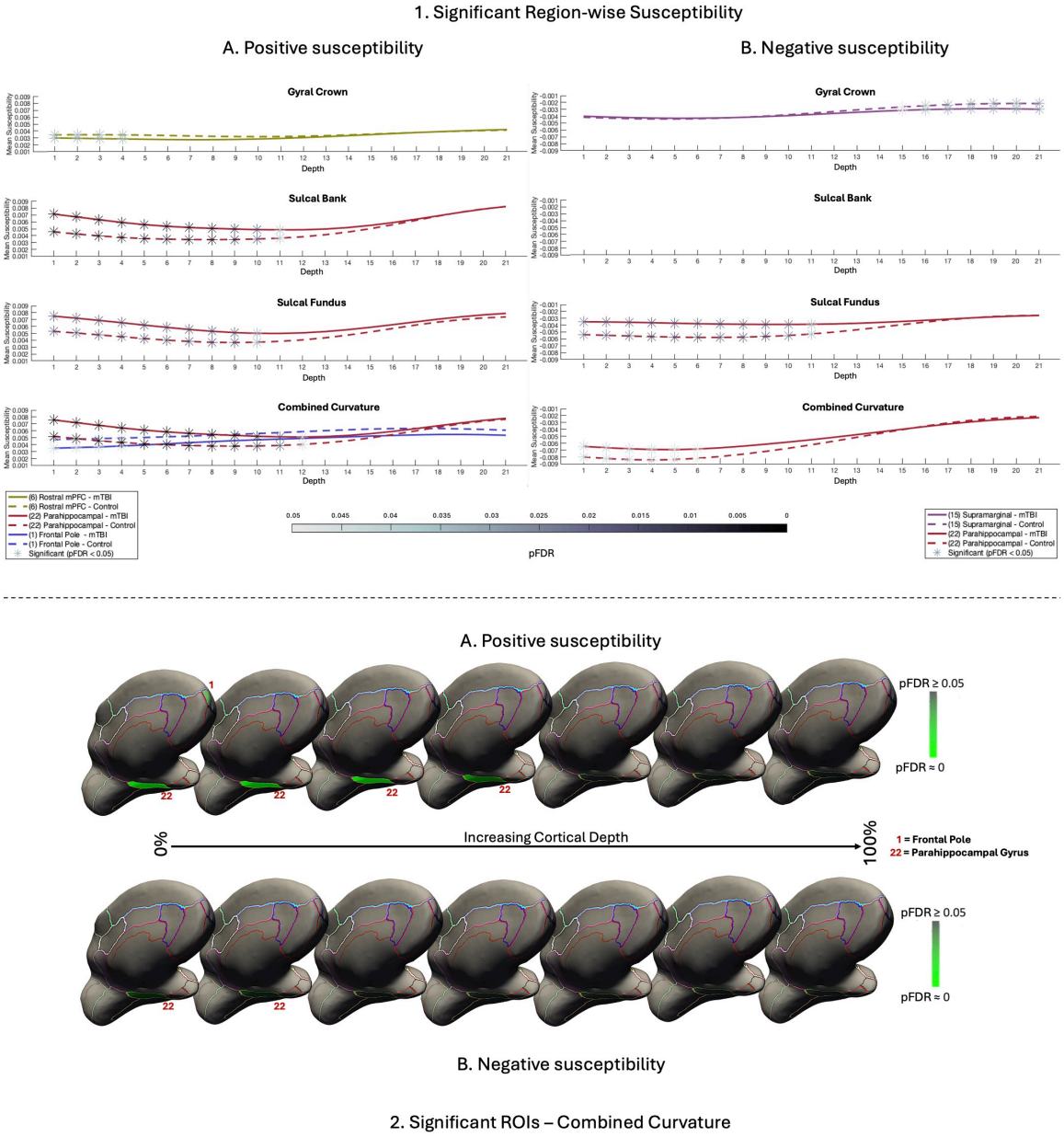

Figure 6.3: Significant depth- and curvature-specific susceptibility differences

1. Differences in susceptibility values between mTBI participants and controls for significant regions of interest only. A. Positive susceptibility values were significantly higher for participants with mTBI than HC in superficial depths of the sulcal bank and fundus of the parahippocampal gyrus, as well as when curvature was combined. Values were significantly less positive for mTBI participants superficially in the gyral crown of the rostral mPFC and the superficial frontal pole when curvature was combined. B. Susceptibility values were significantly less negative for mTBI participants than controls in the superficial depths of sulcal fundus in the parahippocampal gyrus, as well as when curvature was combined. Values were significantly more negative after mTBI deep in the supramarginal gyral crown. Susceptibility is measured in ppm. mPFC = medial prefrontal cortex. 2. Medial visualisation of significant ROIs after mTBI for both positive (A) and negative (B) susceptibility maps when curvature was combined as a whole-ROI measure. Surface lines demarcate borders between ROIs, projected onto an inflated surface. Significant ROIs are filled; intensity values relate directly to *p*FDR significance level. For visualisation purposes, depth was reduced from 21 to 7 by averaging *p*FDR values every 3 consecutive depths where 0% is proximal to the pial surface and 100% to the GM/WM interface. *p*FDR = statistical significance (*p*-value) after false discovery rate (FDR) correction.

6.4.2 *Correlations*

Partial Pearson correlation coefficients were used to examine the relationship between age and regional depth-wise susceptibility (positive and negative) for combined curvature at each ROI across the entire sample, whilst controlling for group status. Additionally, correlations between susceptibility values and 1) BIST scores as an indicator of injury severity, and; 2) DSI at the time of the MRI scan as a marker of injury latency, were explored in the mTBI sample only (see Fig. 6.4). Negative susceptibility was transformed to absolute values to better represent relationships between variables (see Fig. 6.4B). P-values were adjusted for 21 cortical depths within each ROI using FDR methods (Benjamini et al., 1995).

6.4.2.1 *Age and bilateral regional susceptibility*

Significant positive correlations between age and iron-related positive susceptibility distributions were observed exclusively at deeper cortical depths near the GM/WM interface (see Fig. 6.4A(i)). In the frontal cortex, regions with statistically significant age-related increases in positive susceptibility values included the pars orbitalis, pars triangularis, superior frontal gyrus, paracentral lobule, and precentral gyrus. In the parietal cortex, significant regions were the superior and inferior parietal lobules, supramarginal gyrus, and precuneus. In the temporal lobe, significant positive correlations were found in the parahippocampal gyrus and inferior temporal gyrus. The only cingulate region to exhibit a positive age-related correlation was the isthmus. No significant positive correlations with age were identified in any ROIs within the occipital cortex. Conversely, significant negative correlations between age and positive susceptibility were identified exclusively at superficial cortical depths near the pial surface, demonstrating an inverse pattern to the positive correlations. In the frontal cortex, the areas showing significant negative correlations were the pars orbitalis, pars triangularis, superior frontal gyrus, paracentral lobule, and precentral gyrus. In the parietal cortex, the postcentral region exhibited significant negative correlations. No significant negative correlations between positive susceptibility and age were apparent in temporal, occipital, or insular ROIs.

Significant positive relationships were also observed between absolute negative susceptibility values and age, primarily in the superficial depths of ROIs across all lobes, which at times extended to the GM/WM border (see Fig. 6.4B(i)). In the frontal lobe, ROIs exhibiting significant positive correlations between age and negative susceptibility included the frontal pole, rostral mPFC, caudal mPFC, pars opercularis, superior frontal gyrus, and precentral gyrus. All examined ROIs in the parietal cortex exhibited significant positive relationships, namely, in the superior parietal lobule, inferior parietal lobule, postcentral gyrus, supramarginal gyrus, and precuneus. In the temporal cortex, significant positive correlations were found in the middle temporal gyrus and temporal pole. All occipital ROIs showed significant positive correlations, including the LOC, pericalcarine cortex, lingual gyrus, and cuneus. Within the insular cortex, only negative susceptibilities in the insula demonstrated a significant positive relationship with age. In contrast, significant

negative correlations with age were observed only in the deeper cortical layers closer to the GM/WM junction of parietal regions, specifically in the superior parietal lobule and precuneus.

6.4.2.2 *Injury severity and bilateral regional susceptibility*

Significant positive correlations between BIST scores and positive susceptibility values were observed in the mid-depths of the frontal pole and in superficial depths of the bank of the superior temporal sulcus (STS) (see Fig. 6.4A(ii)). No significant correlations were observed between negative susceptibility and BIST scores (see Fig. 6.4B(ii)).

6.4.2.3 *Injury latency and bilateral regional susceptibility*

No significant correlations between DSI at time of MRI and positive susceptibility values were observed for any ROI (see Fig. 6.4A(iii)). Negative susceptibility and DSI were positively correlated in superficial depths of the bilateral paracentral gyrus in the frontal cortex only (see Fig. 6.4B(iii)).

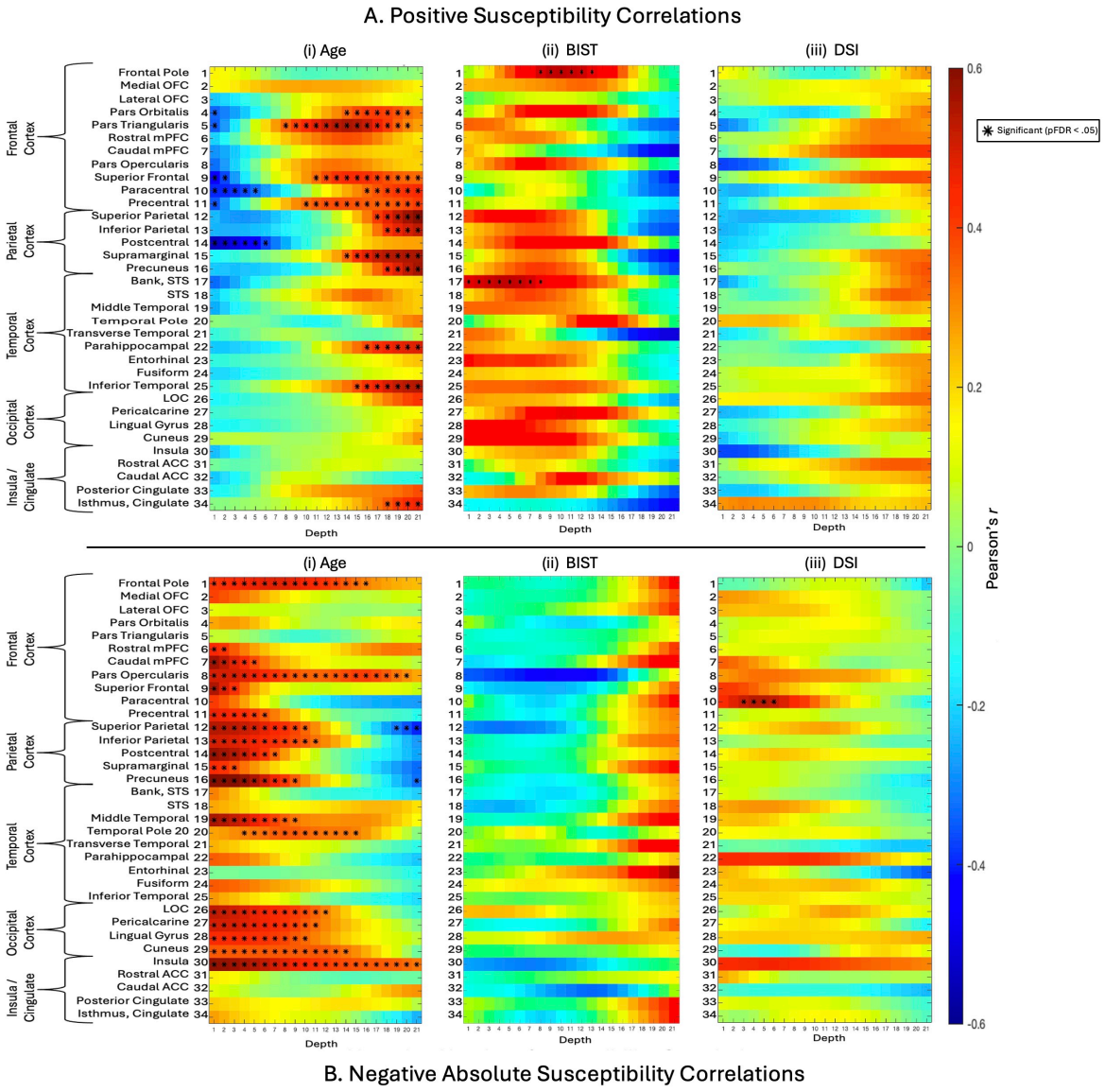

Figure 6.4: Depth-wise correlations between positive or negative susceptibility and variables of interest

i: The relationship between age and positive (A) and negative (B) susceptibility values was assessed for each depth for combined curvature as a whole-ROI measure using partial correlations to control for the effects of group status. ii: the relationship between BIST scores as a marker for injury severity and susceptibility sign values was explored, along with; iii: the relationship between susceptibility sign values and DSI at the time of MRI scan as a marker of injury latency. Negative (B) susceptibility was transformed into absolute values to better represent the relationship between variables. BIST = Brain Injury Screening Tool; DSI = days since injury (at time of MRI scan). *p*FDR = statistical significance (*p*-value) after false discovery rate (FDR) correction.

6.5 DISCUSSION

Previous research seeking to understand the role of brain iron dyshomeostasis in grey following mTBI has focused primarily on susceptibility distributions in subcortical or global grey matter (Bell et al., 2024; Brett et al., 2021; Gong et al., 2018; Koch et al., 2018; Koch et al., 2021; Pinky et al., 2022; Wright et al., 2022; Zivadinov et al., 2018a), largely neglecting the vulnerability of cortical regions to microstructural damage following an mTBI. The two investigations inclusive of cortical ROIs (Gong et al., 2018; Pinky et al., 2022) were constrained either by macroscopic voxel-wise techniques or a limited number of gross segmentations, which lack the anatomical precision necessary to detect depth- or curvature-specific differences in magnetic susceptibility. To address this gap in the literature, I adapted a column-based analytic technique already demonstrating efficacy in AD research (Merenstein et al., 2024) to perform the first investigation of sr-mTBI-related differences in magnetic susceptibility as a function of cortical depth and curvature. In line with prior QSM research (Merenstein et al., 2025; Merenstein et al., 2024), susceptibility maps were thresholded into separate maps of dominant voxel-wise sign for analysis.

Results revealed increased positive susceptibility exclusive to the temporal lobe, specifically in the superficial depths at sulcal curvatures in the bilateral parahippocampal gyrus. This pattern was conserved when curvature was aggregated as a whole-ROI measure. In contrast, age-related positive susceptibility indicative of iron deposition was observed at deep cortical depths, closer to the interface with the white matter, in the overall sample. These findings suggest that increases in positive susceptibility close to the cortical surface indicate abnormal, injury-related iron accumulation after mTBI. Results corresponded with analyses of negative susceptibility, which were less negative in the superficial depths of the sulcal parahippocampal gyrus after mild brain trauma. In addition, negative susceptibility was positively correlated with age in superficial depths only, suggesting possible age-related calcification processes occurring in superficial cortical layers; a pattern opposite to mTBI-related negative susceptibility effects. Fewer correlations were found between subjective injury status or time elapsed since injury and susceptibility, supporting a body of research demonstrating little relationship between objective injury measures and subjective self-report.

6.5.1 *Depth-specific alterations in cortical magnetic susceptibility*

Histological studies have demonstrated variations in iron distribution relative to specific cortical laminae (e.g., Perls iron staining), where concentrations are lowest at the pial surface and increase progressively through grey matter toward its junction with the white matter (Fukunaga et al., 2010). These findings were corroborated by iron-sensitive R_2^* mapping of *ex vivo* tissue samples using ultrahigh-field (7T) MRI (Fukunaga et al., 2010), which also exhibit high congruence with *in vivo* QSM (Shin et al., 2021). Taken together, these studies suggest that iron density in the cortex reflects distinct cyto- and myelo-architecture, with variance between layers. In healthy populations, iron density should be sparse at the pial

surface and increase with depth. Conversely, the findings presented here indicate an abnormal distribution pattern of positive susceptibility related to iron deposition exclusively in superficial depths of the parahippocampal gyrus in temporal cortex following injury (see Fig. 6.2A, Fig. 6.3.1A and Fig. 6.3.2A). This increased positive susceptibility at the acute stage of mTBI is directly inverted for depth comparative to healthy layer-specific variation (Fukunaga et al., 2010; Shin et al., 2021) and patterns related to normal ageing in this range of the lifespan (see Fig. 6.4A(i)), suggesting an injury-specific model of cortical microstructural trauma (see Fig. 6.5).

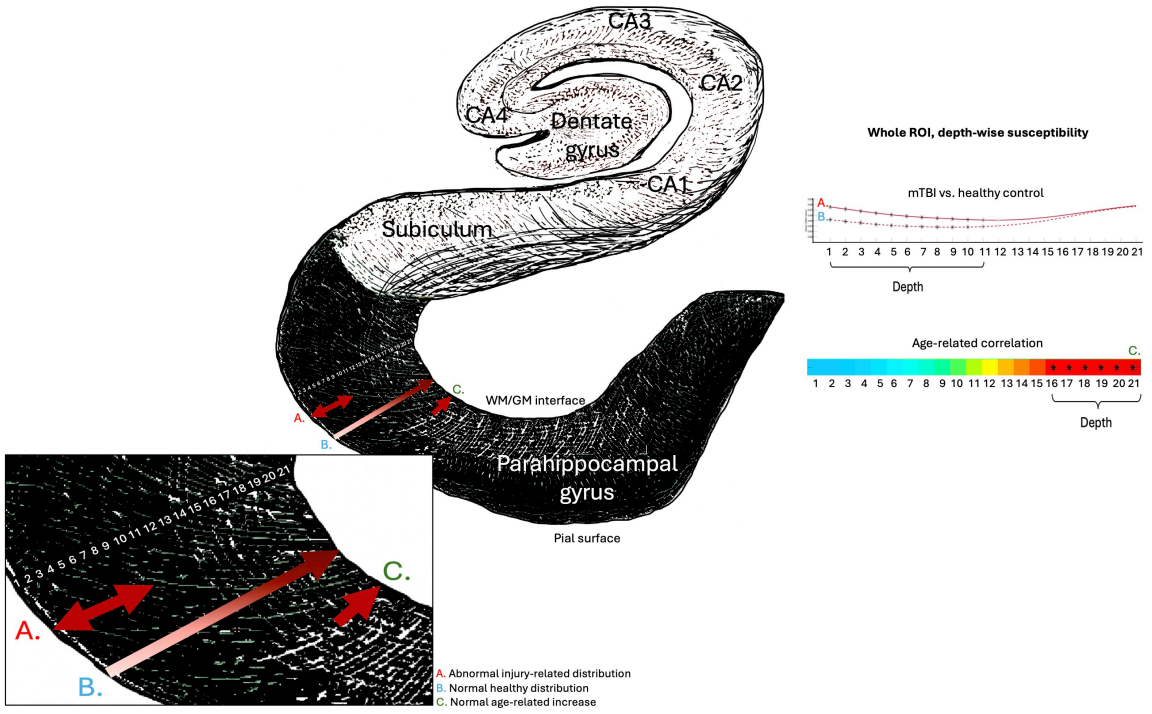

Figure 6.5: Iron and positive susceptibility distributions in the parahippocampal gyrus

Visualisation of depth-specific positive (iron-related) susceptibility distributions. (A.) Depicts increased positive susceptibility following mTBI relative to HC restricted to superficial depths of the parahippocampal gyrus. This pattern does not overlap with (B.) validated patterns of lower iron concentration proximal to the pial surface, and increasing towards the GM/WM interface as a pattern of normal layer-specific distributions, or; (C.) normal age-related increases in positive susceptibility in this population (16-32 years) restricted to the deeper cortical depths closer to the GM/WM boundary. Depiction of the hippocampal formation inspired by illustration in Ranson et al. (1995).

The focal nature of increased positive susceptibility in superficial depths suggests iron accumulation near small blood vessels (McKee et al., 2013). Concordantly, microhaemorrhage and aggregation of activated microglia around perivascular sites are well documented after mTBI (Huang et al., 2021; Mckee et al., 2015; Nisenbaum et al., 2014) and haemosiderin-laden macrophages have been evidenced in post-mortem histopathological studies in the perivascular spaces after mTBI (Bigler, 2004). Here, it is tempting to speculate about the potential mechanisms of iron overload following mTBI. Microvascular dysfunction and increased transport of non-haem iron across the BBB (Sandsmark et al., 2019; Y. Wu et al., 2020) may increase iron content in superficial cortical layers (Levi et al., 2024; R. J. Ward et al., 2014) which could result in a perivascular accumulation of iron and in-

creased magnetic susceptibility of these compromised perivascular regions on QSM (see Chapter 2).

A modest decrease in positive susceptibility was observed at superficial depths in the gyral crown of the rostral mPFC, suggesting dyshomeostatic processes distinct from those identified in the parahippocampal gyrus. While iron overload has been associated with cell death (H. Ma et al., 2022; A. M. Ward et al., 2014), iron deficiency has also been linked to neuronal loss (Levi et al., 2024). These findings collectively indicate that iron dyshomeostasis, through various mechanisms, may serve as a promising early marker of acute cellular damage and mTBI-related neuropathology. This dysregulation has the potential to drive neural tissue degeneration or death both in the acute phase and over the longer term. However, as the precise mechanisms by which iron is released in the brain are still under investigation (Gozt et al., 2021a; Zecca et al., 2004), these mechanisms cannot yet be disambiguated.

Conversely, the results presented here suggest that negative susceptibility is decreased in the parahippocampal gyrus at superficial depths following mTBI. Although the cerebral cortex is not well known for high myelin content (Northall et al., 2023), decreased negative susceptibility at these superficial depths could indicate changes to surface axons. Myeloarchitecture studies indicate that Layer I of cerebral cortex consists primarily of axons, dendrites, and axon terminals, the cell bodies of which are located in deeper layers (Miyashita, 2022), however the cytoarchitectural topography of the parahippocampal cortical laminae is not as homologous. The parahippocampal gyrus is marked by verruca-like protuberances on its cortical surface (termed verrucae) and houses large multipolar and pyramidal neurons in layer II and reticulated axons in layers I and II that contribute to the light appearance of this region (Van Hoesen et al., 2000). Indeed, the temporal lobe is particularly vulnerable to chronic demyelination after mTBI and this phenomenon has been linked to inflammatory and excitotoxic secondary injury events (Mahoney et al., 2022). This lends support to the likelihood of myelin alterations in these superficial regions that may occur alongside increases in inflammatory mediators such as iron.

The pattern of increased positive susceptibility in the superficial parahippocampal gyrus thus alludes to a dual model of perivascular microstructural trauma focal to this region. A substantial portion of the iron present in the human brain parenchyma is stored as non-haem iron within myelin-maintaining oligodendroglia (Connor et al., 1995) and pathological iron levels have been known to damage both oligodendrocytes and myelin (Bradl et al., 2010; Hametner et al., 2013; Lassmann et al., 2012). Mechanisms leading to concurrent increases in positive susceptibility and decreases in negative susceptibility in distinct voxel populations within the same ROI, as observed in this study, are further supported by research into pathogenesis of MS, which indicates that neuroinflammation and altered BBB permeability can result in iron accumulation in macrophages and other iron-related cytotoxic events, such as oxidative stress, causing degradation of oligodendrocytes and axons (Bradl et al., 2010; Lassmann et al., 2012; R. J. Ward et al., 2014). Research leveraging multi-echo QSM and contemporary magnetic source separation to investigate cortical pathology in MS has also linked decreased negative susceptibility to demyelination,

reinforcing the potential role in disease pathology (Straub et al., 2023). Conversely, increased negative susceptibility was mostly observed at deeper cortical depths closer to the GM/WM junction, which might reflect aggregation of Aβ or p-tau inherent to AD (Braak et al., 1991) and CTE (McKee et al., 2023), or calcifications known to negatively affect cognition (Thibault et al., 2007). Notably, the injury-related accumulation patterns did not overlap with age-related changes in negative susceptibility, which increased at superficial depths (see Fig. 6.4B(i)). This suggests that both decreased negative susceptibility in superficial depths and increased negative susceptibility at deeper cortical depths may result from abnormal, injury-related, neuropathological processes.

6.5.2 *Region- and curvature-specific alterations in cortical magnetic susceptibility*

The inferior medial temporal lobe is a notable site of injury in sr-mTBI (Mckee et al., 2015). These observations are supported by investigations of gross pathology in TBI indicating that proximity of the anterior aspect to the sphenoid ridge of the skull base constitutes a risk factor for contusion during impact (Bigler, 2007). The parahippocampal gyri are particularly vulnerable due to the curved alignment with the middle cranial fossa, creating a cocoon that brings portions of the cortical surface into contact with the skull base. The parahippocampal area, which provides direct input into the hippocampus, is adjacent to the free edge of the tentorium cerebelli and may not benefit from the same degree of structural reinforcement from dura matter (for a comprehensive discussion, see Bigler, 2007), further compounding focal injury. Because TBI exists on a spectrum from mild to severe, correspondent pathologies exist on a similar continuum (Bigler et al., 2012) enabling translation of findings from gross TBI to more mild versions. It is therefore not unreasonable to suggest that these risk factors could cause focal tissue disruption and cellular distress signalling, providing a plausible explanation for abnormal tissue susceptibility markers in the parahippocampal region. Indeed, previous research has highlighted the associations between sr-mTBI and loss of cortical thickness in the parahippocampal gyrus along with reductions in parahippocampal volume (Arciniega et al., 2024) providing support for this region-of-risk hypothesis.

Risk factors congruent with the results observed in the present study can be extended past cranial-dural morphology to CSF dynamics, which also serve to exacerbate anatomical vulnerability. The current study supports a sulcus-specific model of damage in mTBI (Bakhtiarydavijani et al., 2021; Ghajari et al., 2017; Kornguth et al., 2017; McKee et al., 2023; D. H. Smith et al., 2013), with the only persistent differences between groups in both positive and negative susceptibility values observed in sulcal regions of the bilateral parahippocampal gyrus (positive susceptibility: sulcal bank and fundus; negative susceptibility: sulcal fundus [see Fig. 6.2 and Fig. 6.3]). The focal nature of injury to these concave regions extends prior work noting increased mean cortical curvature in the sulcus (J. B. King et al., 2016) and sulcal widening (Kornguth et al., 2017) after mTBI. Results are also consistent with observations of mTBI-related vascular injury and microhaemorrhage in the sulcal fundus on SWI (Kornguth et al., 2017).

Co-occurrence of potential iron dyshomeostasis with possible myelin changes within the temporal parahippocampal gyrus is consistent with the memory impairments symptomatic of sr-mTBI (Mckee et al., 2015). Contextually, the parahippocampal cortex acts as a hub region in a network connecting areas of the frontal, parietal, and temporal lobes (Raslau et al., 2015) and represents a vital link between the default-mode network and the medial temporal lobe memory system, as evidenced by resting-state functional magnetic resonance imaging (fMRI) studies (A. M. Ward et al., 2014). As such, it is integral to various cognitive processes including visuospatial processing and episodic memory (Aminoff et al., 2013) and the facilitation of contextual associations fundamental to higher order cognitive performance (Raslau et al., 2015). These processes may be disrupted by cellular distress or damage, leading to altered signalling capacity; an observation that is particularly aligned with magnetic susceptibility alterations in superficial depths and the role of superficial cortical layers in integrating information from different brain regions (Rolls et al., 2017).

6.5.3 *Depth- and curvature-specific tissue dyshomeostasis: a potential early indicator of pathological processes?*

The role of iron in acute responses following cytotrauma, as well as its co-localisation with, and involvement in, misfolded proteins in neurodegenerative diseases, including CTE, identifies it as a potential marker of early degenerative processes (Bouras et al., 1997; Zecca et al., 2004). Interestingly, the temporal lobe and hippocampus are primary loci of atrophy and tau deposition in CTE (McKee et al., 2023; Murray et al., 2022), and iron has been found in NFTs within these regions (Bouras et al., 1997). A pathognomonic CTE lesion is characterised by the presence of p-tau in the cortical sulcus and, while this is not restricted to the subpial regions, supportive features of CTE include the presence of NFTs in superficial cortical layers (II/III), primarily in the temporal lobe (Bieniek et al., 2021; McKee et al., 2023). This laminar predilection is not seen in other tauopathies, like AD, where tau phosphorylation generally occurs in deeper layers (V/VI) (Pearson et al., 1985). Indeed, research shows that different types of head impacts can result in varying brain deformations and injury patterns, with sulci being particularly vulnerable to mechanical strain, which is consistent with, and can be predicted by, patterns of tauopathy in neurodegeneration (Ghajari et al., 2017).

Notwithstanding the short-term effects of iron overload, which have been linked to secondary injury in mTBI (Huang et al., 2021; Nisenbaum et al., 2014), the association between iron-mediated oxidative stress and hyperphosphorylation of tau (Yamamoto et al., 2002; Zecca et al., 2004), and their co-localisation in CTE (Bouras et al., 1997), coupled with the similarity of iron distributions observed in this study to hallmark distributions of tauopathy and degeneration in CTE raises important questions about the disease path from acute injury to eventual tissue degeneration. The precise mechanisms underlying CTE remain an active area of research, but these findings suggest that iron may serve as a candidate biomarker, warranting further investigation. Until such a time, any parallels drawn

between the pattern of iron distribution in this study and the hallmark features of CTE tauopathy can, at this stage, only be speculative.

6.5.4 *Age-related alterations in cortical biomagnetic substrates are depth-specific*

6.5.4.1 *Temporal biodynamics of cortical positive susceptibility*

Increasing iron in deep grey matter nuclei and some regions of the cortex is a hallmark of normal ageing (Hallgren et al., 1958; Zecca et al., 2004). Research indicates that age-related iron increases occur primarily in the motor and premotor cortices, as well as the superior prefrontal and parietal cortices (Acosta-Cabronero et al., 2016; Hallgren et al., 1958). Additionally, these increases have been reported in the insula (Acosta-Cabronero et al., 2016) and hippocampus (Hagemeier et al., 2012). Histological evidence suggests that normal increases in cortical non-haem iron may be especially pronounced in younger individuals, sharply increasing during childhood and plateauing at around 30 to 50 years of age, depending on region (Hallgren et al., 1958; Schenck et al., 2004). These observations are supported by some (Acosta-Cabronero et al., 2016; Callaghan et al., 2014) but not other (Rodrigue et al., 2011) cross-sectional iron-sensitive MRI findings in adjacent age groups.

The findings presented here support age-related cortical iron increases in a youthful population. In line with prior research, ROIs with age-related increases in positive susceptibility values were most dense in frontal and parietal lobes, in addition to two loci in the temporal lobe and one in the insular cortex (see Fig. 6.4A(i)). Of all cortical regions, the motor system is particularly affected by age-related iron deposition (Acosta-Cabronero et al., 2016; Hallgren et al., 1958), a pattern mirrored in these findings which show notable age-related positive susceptibility increases in the primary motor cortex. The results suggest that age-related increases are restricted to deeper cortical depths closer to the GM/WM junction, which are known to naturally express higher iron levels in the healthy population (Fukunaga et al., 2010; Shin et al., 2021). These deeper layers contain large pyramidal cells (Miyashita, 2022), which could speculatively accumulate iron differently. Indeed, previous research (Merenstein et al., 2024) has suggested that because age is more predictive of delayed response time rather than difficulties in decision-making (Madden et al., 2020; Merenstein et al., 2023; Ratcliff, 2008), age-related iron accumulation should show a preference for deeper layers responsible for output, rather than more integrative superficial regions (Rolls et al., 2017).

6.5.4.2 *Temporal biodynamics of cortical negative susceptibility*

Age-related increases in negative magnetic susceptibility were observed exclusively close to the pial surface. Previous studies utilising negative QSM have shown similar distributions at superficial depths (Northall et al., 2023). This pattern aligns well with research indicating more common occurrences of calcifications in areas with high vascularisation and metabolic activity (Jang et al., 2021), such as the cortical surface serviced by the pial arterial vasculature (Bollmann et al., 2022). Taken together, these findings indicate that

age-related increases in iron are likely restricted to deep cortical depths, while diamagnetic calcifications may be more likely to occur at superficial depths. Both observations are supported by strong biological plausibility and well-documented scientific evidence. This reinforces the conclusion that observed differences in both positive and negative susceptibility following sr-mTBI reflect pathological processes distinct from those associated with normal ageing.

6.5.5 *Effects of injury latency and severity on cortical tissue magnetic susceptibility*

Congruent with the findings outlined in Chapter 5, the general lack of correlation between positive or negatives susceptibilities and BIST scores may be related to symptom underreporting (Kroshus et al., 2015; Meier et al., 2015), the well-supported incongruence between subjective self report and objective brain changes or neuroimaging signatures (McCrea et al., 2017; Shenton et al., 2012), or the more rudimentary approach to thresholding necessitated by the acquisition of single-echo data. However, some significant correlations between injury severity and positive susceptibility were observed at mid-depths in the frontal pole and superficial depths in the superior temporal sulcus, suggesting that possible excitotoxic mechanisms in these regions driving more severe symptom presentation. The superior temporal sulcus, for instance, plays a key role in social cognition (Basil et al., 2017; Beauchamp, 2015; Deen et al., 2015) and audiovisual integration (Hein et al., 2008). It is also active in sensory perception, including visual, auditory, and vestibular processing (Dieterich et al., 2008). The frontal pole, which is particularly vulnerable to contusion during TBI (Mckee et al., 2015), is associated with critical functions such as action planning, problem-solving, reasoning, social cognition, working memory, perception, and emotional processing (Bludau et al., 2014; Braver et al., 2002). Of particular relevance to these potential relationships, all of these symptoms are consistent with the effects of mTBI and are collectively assessed by the BIST (Theadom et al., 2021). Lastly, the overarching lack of correlations with injury latency further reinforces speculation that longitudinal studies, or investigations of chronic, rather than acute or subacute injury, may be necessary to understand temporally-modulated variance in biomagnetic substrates.

6.5.6 *Regional depth- and curvature-specific susceptibility alterations in mTBI: elucidating biomechanical influences for a structural biomarker?*

The most striking result from this investigation is the localisation of acute dyshomeostatic processes in the superficial sulcal regions of the parahippocampal gyrus. The observed increase in positive susceptibility in the bank and fundus suggests mTBI-related secondary injury and cytotoxicity (Huang et al., 2021; Nisenbaum et al., 2014). Similar spatial patterns of decreased negative susceptibility reinforce evidence of cellular damage, possibly reflecting changes to axonal components, such as the myelin sheath (Bradl et al., 2010; Hametner et al., 2013; Lassmann et al., 2012). These findings are corroborated by biomechanical models of mTBI that highlight both the heightened susceptibility of the

inferior medial temporal lobe, and in particular the parahippocampal gyrus, to impact forces (Bigler, 2007; Mckee et al., 2015) alongside the vulnerability of sulcal fundus to damaging fluid dynamics (Kornguth et al., 2017). Taken together, these observations suggest that QSM-based susceptibility changes can be mapped to recognised injury mechanisms, representing a step toward bridging the gap between injury biodynamics and focal tissue pathology.

This provides a contrast to the general paucity of significant results that appear to characterise the QSM-mTBI literature (Bell et al., 2024; Gong et al., 2018; Koch et al., 2018; Koch et al., 2021; Pinky et al., 2022; Wright et al., 2022; Zivadinov et al., 2018a). This raises the possibility that focusing predominantly on susceptibility estimation in total basal grey matter or its sub-compartments may be overly narrow; expanding investigations to include additional ROIs, such as the cortex, may provide more significant advances toward understanding mTBI-related tissue pathology. Here, it is important to note that the two investigations to include cortical (Gong et al., 2018), and even parahippocampal (Pinky et al., 2022), ROIs did not find any significant results using voxel-wise analyses and regional parcellation, respectively. Juxtaposed against the results of the present study, it is hard to overlook the implication that the subtle tissue changes associated with mild head injury may require more sensitive and targeted approaches than have historically been employed. This would not only extend to more granular investigations, but also speaks to the utility of separating sources of magnetic susceptibility, whether by more rudimentary thresholding (Merenstein et al., 2024) or contemporary magnetic source separation (Ahmed et al., 2023; J. Chen et al., 2021; Emmerich et al., 2021; J. Lee et al., 2024; Z. Li et al., 2023; Shin et al., 2021).

It is precisely these challenges, alongside the inherent heterogeneity of mild head injuries, that may be confounding efforts to identify a universal MRI-based signature of structural tissue damage. This underscores the importance of conducting more detailed, site-specific analyses. It is possible that susceptibility changes observed in the superficial depths of the sulcal fundus and bank in medial temporal parahippocampal gyrus represent a hallmark of acute mTBI, mirroring the specific loci and patterns considered features tau pathology in CTE (McKee et al., 2013; McKee et al., 2023; Murray et al., 2022). Progress toward establishing a robust tissue biomarker may thus have considerable clinical implications not only for understanding acute pathological processes, but also for elucidating the potential disease path toward neurodegeneration in some cases. Here, additional cross-sectional or longitudinal studies replicating this methodology will be crucial for determining whether these localised susceptibility changes are consistent across differing participant populations, and whether there is a mechanistic link between patterns of neuronal pathology in acute mTBI and hallmarks of tauopathy in CTE.

6.5.7 *Limitations and future research*

While QSM offers valuable insights into iron content and distribution, at lower field strengths (i.e., 3T) voxel resolution is restricted and does not reflect specific architecton-

ics of cortical tissue. The 1 mm isotropic voxel resolution thus inherently restricts depth-wise analysis of the ∼1-4.5 mm thick cerebral cortex (Fischl et al., 2000). As such, cortical column analyses were constrained to investigations of depth rather than susceptibility distributions specific to cortical laminae. However, studies employing comparable depth-specific methodologies have utilised data from QSM (Merenstein et al., 2024), DTI (Y. Ma et al., 2023), T_1w/T_2w imaging (Sui et al., 2022), and quantitative T_1 and QSM (Northall et al., 2023), to sample between 10 and 21 cortical depths with meaningful results. In addition, the DTI-based study (Y. Ma et al., 2023) reported the identification of features with 0.9 mm isotropic resolution, single-shell data similar to those found with 92 μm isotropic, high-angular-resolution data (Aggarwal et al., 2015), underscoring the ability of these technique to conserve features even at coarser resolutions. Future research could nonetheless benefit from applying cortical column analysis to images with higher resolutions, for example those collected on high field scanners, or by pushing images to sub-1 mm resolutions insofar as SNR and acquisition times correspondent to increased participant burden are not overly compromised (for a comparison of data acquired at 3T and 7T, see Straub et al., 2019).

In addition, because analyses related to cortical thickness involve sampling multiple tissue types across a small cross-section, higher resolutions become particularly important for surface mesh-based and voxel-wise analyses (Tohka, 2014). Although $\leq$ 1 mm isotropic resolution is recommended to mitigate PVE (Bilgic et al., 2024), such artefacts may be problematic at the cortical surface and GM/WM tissue interface. While erosion steps were used to reduce non-brain signals around the outer cortex, acquiring higher-resolution images, assuming an adequate field of view (Merenstein et al., 2024), may further reduce PVE at all tissue borders. It is worth noting that QSM studies conducted at similar resolution found that discarding the outer depths did not significantly alter susceptibility measurements (Merenstein et al., 2024), suggesting that the influence of partial volume-induced distortions may be relatively modest under these conditions.

Future studies should also aim to include a broader age spectrum to further explore the interaction between age and susceptibility in mTBI. Here, it should be noted that age-related regional cortical iron accumulation is generally most pronounced up until the third decade of life (Hallgren et al., 1958) and research using cohorts with a broader age range should incorporate statistical modelling that accounts for differential iron deposition with age. Finally, the limitations associated with obscuring subtle and heterogeneous mTBI effects in group-wise statistical analyses, which were briefly alluded to in Chapter 5, are relevant to the research presented in this chapter. These shortcomings of the current macroscopic statistical approach are addressed in the subsequent chapters.

6.6 CONCLUSIONS

To better characterise the mechanisms of mTBI at the acute stage, I conducted the first QSM study to assess depth- and curvature-specific regional patterns of positive (iron-related) and negative (myelin-, calcium-, and protein-related) magnetic susceptibility in

the cerebral cortex following injury. The concurrent instances of increased positive susceptibility with decreased negative susceptibility in discrete voxel populations within the parahippocampal gyrus indicate a possible accumulation of iron and changes to myelin integrity after injury. This distribution pattern was observed in the superficial depths of the sulcus, suggesting trauma due to mechanical forces. The pattern appeared distinct from age-related differences in positive and negative susceptibility and was reminiscent of supporting features of tau pathology in CTE, which is known to co-localise with iron. These results support a complex, dual-pathology model of trauma after mild head injury and have implications for understanding microstructural brain tissue damage following mTBI.

Research Projects Part IV: Precision Analysis and Individual-level Insights in mTBI

7

SUBCORTICAL IRON MARKERS AND REGIONS-OF-RISK: INSIGHTS FROM INDIVIDUALISED ANALYSIS

7.1 MOTIVATION

In Chapter 5 and Chapter 6 I conducted group-wise statistical analyses to compare the effects of mTBI on cortical and subcortical regions between clinical participants and an HC group. Although group-level studies have dominated the quantitative MRI literature, there is increasing emphasis on individual-level analyses. One criticism of group-level analyses is that they may fail to account for the inherent heterogeneity of mTBI, and risk losing critical individual-level information to group-wise averaging. The following chapters of the thesis extend the methodologies described in Chapter 5 and Chapter 6, adapting the respective techniques and segmentations for use in individual-level analyses. Here, two studies are presented: one focusing on subcortical regions (Chapter 7) and the other on cortical regions (Chapter 8). These studies leverage z-tests to characterise individual-level deviations in positive susceptibility relative to a HC distribution within each ROI. The following chapters focus solely on positive susceptibility maps given the stronger theoretical basis surrounding the relationship between iron accumulation and mTBI-induced secondary injury. A summary of key points and concluding statements are provided in § 7.7 and § 8.6 for each chapter, respectively.

7.2 INTRODUCTION

In Chapter 2, I underscored the subtle and diffuse nature of mTBI pathophysiology that complicates investigations of this heterogeneous injury (Giza et al., 2001, 2014; Romeu-Mejia et al., 2019). However, in the absence of specific biomarkers, macroscopic morphological brain abnormalities, and clinic-ready MRI techniques sensitive to subtle mTBI-related neuropathology, the pathophysiology of mTBI remains poorly understood (Hier et al., 2021; Lunkova et al., 2021). These limitations not only necessitate the use of advanced MRI techniques not typically employed in conventional medical settings, such as QSM, but also further highlight difficulties associated with the ability of MRI-based techniques to identify the subtle changes in the brain characteristic of this injury (Cook et al., 2014; Wintermark et al., 2015). Integrating advanced MRI modalities into routine patient care requires further validation and the establishment of clinically- and individually-relevant biomarkers for mTBI diagnosis and treatment.

However, the vast majority of clinical research employs analytic techniques that assess group averages and treat individual variability primarily as noise (Marquand et al., 2019). The rationale for these methodological choices is underpinned by an attempt to identify signatures representative of the “average patient", yet these macroscopic approaches likely obscure the individual-level heterogeneity that characterises clinical cohorts; variation that is central to identifying appropriate and effective intervention. Group-level analytic strategies remain the most common method used in QSM investigations of mTBI (Bell et al., 2024; Gong et al., 2018; Koch et al., 2018; Koch et al., 2021; Pinky et al., 2022; Wright et al., 2022; Zivadinov et al., 2018a), and the potential loss of data to averaging effects could plausibly explain the general lack of significant effects across the extant literature.

Personalised profiles can be generated by leveraging z-tests to compare the results of individual quantitative measures to the distribution of a healthy normative population. This approach allows for a clearer understanding of where the individual falls relative to normal ranges for selected metrics (Domínguez et al., 2024; Marquand et al., 2019). Individual analytic approaches have been successfully applied in the context of mTBI using T_2 relaxometry as a marker of neuroinflammation (Bedggood et al., 2024), and DWI to investigate white matter fiber tracts (Attyé et al., 2021). Under the TBI umbrella more broadly, individual analyses have been applied to fixel-based analysis of dMRI (Clemente et al., 2023) and DTI (Jolly et al., 2021) to investigate white matter integrity, as well as structural connectomics in ms-TBI (Imms et al., 2022). One study has used QSM to generate individualised profiles of iron deposition in ms-TBI (Domínguez et al., 2024), however, dedicated investigations of potential iron deposition at the individual level following *mild* TBI are yet to be conducted.

To address these research gaps, I conducted the first dedicated individual-level investigation of subcortical mTBI effects on iron-related positive susceptibility. This study aimed to: 1) generate individual profiles of potential subcortical iron deposition following sr-mTBI, and; 2) use these results to facilitate more targeted statistical analyses of the relationship between subcortical iron markers and injury severity. Previous group-level human research

has reported elevated iron markers in the globus pallidus, thalamus, caudate, substantia nigra, red nucleus, and within gross hippocampal segmentations following mTBI (Chong et al., 2023; Lu et al., 2015; Nikolova et al., 2022; Raz et al., 2011). However, given the lack of significant findings in the group-level subcortical analyses related to positive susceptibility values presented in Chapter 5, along with challenges in translating group-level research to the individual level and the exploratory nature of this study, no specific *a priori* hypotheses were made regarding the direction of effects across all basal nuclei and hippocampal subfields.

7.3 MATERIALS AND METHODS

Refer to Chapter 5 for details on ethical approval, recruitment, inclusion and exclusion criteria, and data collection methods. Image acquisition, sequence details, QSM image reconstruction, post-processing, thresholding, and segmentation of the basal ganglia and hippocampal subfields also follow the methodology outlined in Chapter 5. However, given the exploratory nature of this research, as well as the more robust theoretical basis related to both sources of paramagnetism on QSM and the role of iron in secondary injury, only QSM^{+} maps were used in all individualised analyses, including those in Chapter 8.

7.3.1 *Participants*

For the two individualised analyses comprising the remainder of the research studies in this thesis (reported here and in Chapter 8), data from 35 male contact sports players (M = 21.60 years [range: 16-33], SD = 4.98) with acute sr-mTBI and 25 age-matched male controls (M = 21.10 years [range: 16-32], SD = 4.35) were used. The mTBI sample is an extension of the cohort analysed in Chapter 5 and Chapter 6. In the previous group-level investigations, equal sample sizes maximised statistical power and satisfied the assumptions made by between-group comparisons (T. K. Kim et al., 2019). In contrast, the individualised analyses reported in the subsequent studies compute each mTBI participants' ROI-wise z-score relative to the HC mean and standard deviation. As such, including a larger mTBI sample carries no statistical cost and improves clinical representativeness (Marquand et al., 2019). All mTBI participants were scanned within 14 days of injury (M = 10.40 days, SD = 3.01). The control group remains identical to the sample used in the last two research studies. To once again minimise the potential interference of age-related iron deposition (Ashraf et al., 2018; Bilgic et al., 2012; Hagemeier et al., 2012; Hallgren et al., 1958; Madden et al., 2023; Treit et al., 2021; Zecca et al., 2004), there were no significant difference in age between the groups ($t(58)$ = -0.44, p = 0.66). Sample characteristics for the extended mTBI participant cohort are detailed in Table 7.1 below.

Table 7.1: Summary of sr-mTBI participant clinical characteristics for individualised studies

ID	Age	DSI	BIST Score	MOI	MRI findings
mTBI-01	< 20	5 days	140	Rugby	None
mTBI-02	< 20	5 days	12	Rugby	None
mTBI-03	20s	6 days	78	Rugby	None
mTBI-04	< 20	13 days	18	Rugby	Small fluid signal spaces in R peritrigonal WM - normal. R caudate cleft along ventricular surface – possibly developmental or from old ischaemic insult
mTBI-05	< 20	12 days	12	Rugby	None
mTBI-06	20s	13 days	42	Rugby	None
mTBI-07	20s	13 days	13	Football	Minor artefactual T_1 signal in pons
mTBI-08	20s	12 days	6	Hockey	None
mTBI-09	20s	6 days	56	Rugby	Minor R orbital fracture (old)
mTBI-10	< 20	12 days	54	Rugby	None
mTBI-11	20s	10 days	52	Rugby	None
mTBI-12	30s	13 days	13	Football	None
mTBI-13	< 20	5 days	79	Rugby	None
mTBI-14	20s	13 days	2	Rugby	Small focus of susceptibility in L superior frontal gyrus possibly vascular or non-specific haemosiderin
mTBI-15	< 20	13 days	22	Rugby	None
mTBI-16	< 20	8 days	117	Futsal	Tiny cleft of fluid signal in R cingulate gyrus - minor developmental anomaly or mature gliosis
mTBI-17	20s	13 days	*	Rugby	None
mTBI-18	20s	10 days	34	Gymnastics	None
mTBI-19	20s	13 days	28	Jiu-jitsu	Some artefactual DWI signal in pons
mTBI-20	20s	11 days	69	Surfing	Tiny susceptibility site in R temporal lobe - may be vascular
mTBI-21	< 20	7 days	14	Rugby	Minor susceptibility in transverse sulcus in R mid temporal lobe - nonspecific, may be vascular or reflect haemosiderin deposition from prior small volume haemorrhage
mTBI-22	< 20	13 days	39	Judo	None
mTBI-23	< 20	9 days	34	Rugby	None
mTBI-24	< 20	12 days	68	Rugby	None
mTBI-25	20s	12 days	17	Rugby	7mm pineal cyst - normal limits. Some T_1 hyperintensity in R cerebellum - artefact compatible
mTBI-26	20s	12 days	25	Rugby	Mildly prominent cisterna magna
mTBI-27	30s	7 days	30	Football	A few mildly prominent biparietal and L cerebral peduncle perivascular spaces - normal variant
mTBI-28	30s	12 days	51	Swimming	None
mTBI-29	20s	5 days	6	Rugby	None
mTBI-30	< 20	12 days	2	Rugby	Some DWI signal disturbance anterior to pons - likely artefactual
mTBI-31	< 20	14 days	22	Rugby	2-3 tiny foci of susceptibility in R frontal lobe - nonspecific, possible site of prior microhaemorrhage. A punctate focus of T_1 hypointensity/T_2 hyperintensity superolateral to the frontal horn of R lateral ventricle
mTBI-32	20s	8 days	58	Football	Bifrontal developmental venous anomaly noted - normal variants
mTBI-33	< 20	8 days	8	Rugby	Minuscule foci of susceptibility in R cerebellar hemisphere /posterior to R aspect of the splenium of CC - nonspecific. Minor susceptibility in R sylvian fissure - vascular
mTBI-34	20s	14 days	47	Rugby	None
mTBI-35	< 20	12 days	28	Football	None
Mean mTBI	21.60 (4.98) years	10.4 (3.01) days	38.1 (32.0) /160		No findings considered clinically relevant
Mean HC	21.10 (4.35) years				No findings considered clinically relevant

* = missing data (BIST incomplete on the Axis Sport Medicine Clinic patient portal, reason unknown)

Note. Diagnostic assessment is limited to the volume T_1, SWI and DWI sequences with only limited interpretation of the multi-echo T_2 stack. Clinical assessments are relevant to the identification of micro-haemorrhages, areas of siderosis, T_1 appearance, gliosis, volume, ventricular volumes and non-neurological findings. Age is given in a range to prevent re-identification of participants. The possible range of BIST scores is 0 (min) to 160 (max). Clinical group data correspondent to date at MRI only with the exception of the BIST acquired >24 hours post-injury prior to MRI scanning (< 14 days post). mTBI = mild traumatic brain injury; HC = healthy control; ID = unique identifier; DSI = days since injury; DWI = diffusion-weighted imaging; BIST = Brain Injury Screening Tool; MOI = mechanism of injury; WM = white matter; MRI = magnetic resonance imaging; L = Left; R = right.

7.3.2 *Personalised QSM profiles*

Individual QSM^{+} profiles for each of the 10 hippocampal subfields and 16 basal ganglia segmentations (see Fig. 7.2.1A and Fig. 7.2.1B) were generated at the bilateral level using MATLAB (2024a). To achieve this, mean positive susceptibility values were extracted from each of the 16 bilateral basal ROIs and 10 unilateral hippocampal segmentations. To yield a bilateral measure, left and right hemisphere susceptibility values were averaged for each hippocampal subfield. In keeping with Chapter 5, the HN was omitted due to zero values in this ROI for a subset of participants. No zero values were present for any participant within any hippocampal ROI. Z-scores were calculated for all participants (HC and mTBI), by subtracting the HC group mean from each individual's susceptibility value and dividing by the HC group standard deviation; a method commonly used in prior research (Bedggood et al., 2024; Domínguez et al., 2024; Imms et al., 2022; Jolly et al., 2021). To bring the HC data closer to a normal distribution, outlier scores for the HC group were filtered (Domínguez et al., 2024) if they fell outside 2 times the interquartile range (IQR), a more stringent criterion than the methods used to identify mild outliers 1.5 times the IQR, but less extreme than the more conservative filter of 3 times the IQR (Tukey, 1977). As a result, outliers in the HC group were filtered in the hippocampal parasubiculum (n = 2), presubiculum (n = 2), and subiculum (n = 1). For basal ROIs, n = *1* HC participant was excluded in the EXA and VeP, n = *2* participants were excluded in the STH, and n = *6* participants were excluded in the MN. Despite the more extensive filtering applied to the MN region, the reduced HC sample size for this region (n = 19) is larger than comparable individualised QSM studies investigating ms-TBI that have used an n of 12 (Domínguez et al., 2024). After filtering, the Shapiro-Wilk normality test yielded an average W value of M = 0.95 (SD = 0.02) across hippocampal ROIs and an average W value of M = 0.94 (SD = 0.03) across basal nuclei, indicating that the data distribution within each ROI was close to normal. The final equation for deriving regional z-scores for individual mTBI participants was as follows:

$$z_{\text{mTBI}} = \frac{X_{\text{mTBI}} - \mu_{\text{HC}_{\text{norm}}}}{\sigma_{\text{HC}_{\text{norm}}}} \tag{7.1}$$

where z_{mTBI} represents the ROI-wise z-score for each individual mTBI participant; X_{mTBI} is the ROI-wise mean QSM value for each mTBI participant; $\mu_{\text{HC}_{\text{norm}}}$ is the mean ROI-wise QSM value of the HC group after outlier filtering to normalise the distribution, and; $\sigma_{\text{HC}_{\text{norm}}}$ is the ROI-wise standard deviation of the HC group QSM values after outlier filtering. This approach ensures that mTBI participants' susceptibility values are directly comparable to the healthy range reflecting a normalised distribution, allowing the detection of deviations that might reflect underlying pathology (see Fig. 7.1 for visualisation of the individualised analysis pipeline).

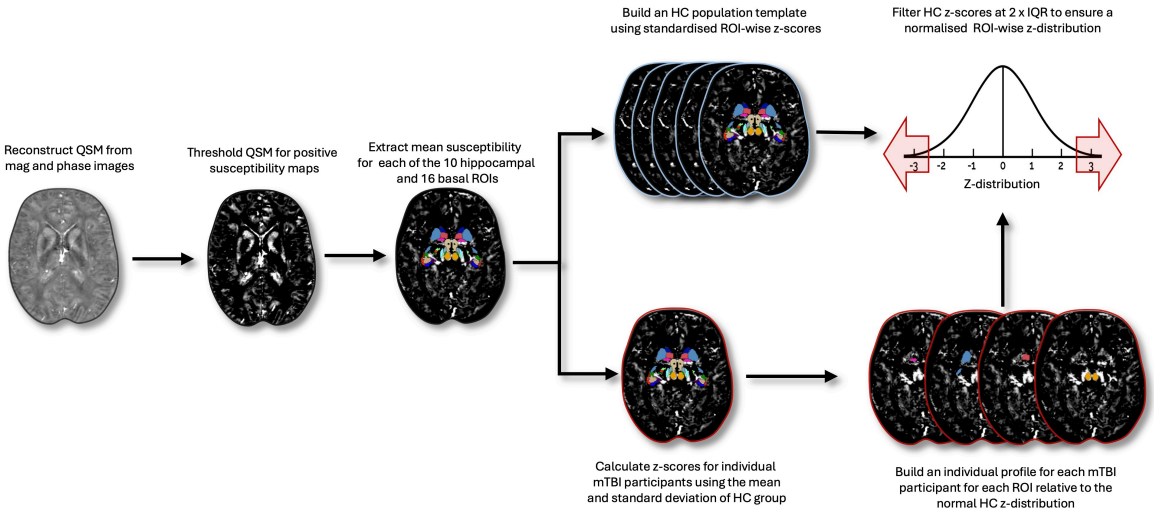

Figure 7.1: QSM post-processing and generation of individual subcortical iron profiles

Steps are performed after QSM image reconstruction using QSMxT. QSM images were thresholded to create a positive sign map, and mean susceptibility values were extracted for each hippocampal and basal ROI. Z-scores were calculated using the mean and standard deviation of the HC group, and standardised around a mean of zero. The HC distribution was then filtered to remove outliers exceeding two times IQR, normalising the distribution. Individual profiles for mTBI participants were constructed by comparing each mTBI participants' z-scores to the healthy normal distribution, while controlling for multiple comparisons across ROIs. QSM = quantitative susceptibility mapping; ROI = region of interest; mTBI = mild traumatic brain injury; HC = healthy control; IQR = interquartile range.

7.4 STATISTICAL ANALYSES

To assess statistical significance for mTBI z-scores, two-tailed p-values were calculated from the z-scores using the cumulative distribution function of the standard normal distribution. A FDR correction (Benjamini et al., 1995) was applied separately to the p-values for the 10 hippocampal or 15 basal nuclei ROI-wise comparisons.

To conduct secondary exploratory statistical tests, the mTBI group was divided into two subgroups: those whose z-scores significantly deviated from the HC normal distribution for any hippocampal or basal ROI (i.e., iron-abnormal) and those whose scores did not (i.e., iron-normal). Although preliminary analyses indicated no statistically significant difference in age between mTBI and HC participant groups, an analysis of variance (ANOVA) was performed between these three new subgroups (iron-normal, iron-abnormal, and controls) to confirm that age was not driving the identification of abnormal z-scores. Iron deposition in subcortical nuclei is a recognised feature of healthy ageing, particularly in individuals of a similar age range to this cohort (Ashraf et al., 2018; Hallgren et al., 1958; Madden et al., 2023), thereby necessitating further analysis to ensure that observed results were not confounded by normative, age-related tissue changes. Additionally, a nonparametric Mann-Whitney U test was used to assess whether injury severity (BIST scores) differed significantly between iron-abnormal and iron-normal mTBI participants, excluding mTBI-17 for this analysis only due to missing BIST data (see Table 7.1).

7.5 RESULTS

To investigate the effects of mTBI on iron markers on an individual basis, personalised profiles of iron-related positive susceptibility values were generated across subcortical regions, encompassing the 10 hippocampal and 15 basal nuclei ROIs. Z-scores, derived from these data, were compared to the normalised HC z-distribution to identify significant outliers among mTBI participants.

7.5.1 *Regional individualised subcortical iron profiles*

Of the 35 total mTBI participants, 15 (43%) exhibited significantly higher z-scores than the healthy population in at least one ROI (see Table 7.2, Fig. 7.2.2A and Fig. 7.2.2B). Among these "iron-abnormal" participants, 87% expressed abnormal iron markers inclusive of hippocampal ROIs, which frequently involved the parasubiculum. In contrast, only 60% of participants had abnormal iron markers inclusive of basal ganglia subregions. These abnormal markers were characterised by a relatively narrow distribution of z-scores across the available basal ganglia segmentations, with abnormal z-scores most commonly observed in the mammillary nucleus.

In addition to the high incidence of elevated z-scores in the hippocampal parasubiculum and basal mammillary nucleus, both of which were affected in close to half of the 15 participants with abnormal iron markers (47%), relatively lower incidences of iron-related abnormalities were apparent in the hippocampal fimbria (27%), presubiculum and HATA (20% each) (see Fig. 7.2.2A and Fig. 7.2.2B). Less frequently affected ROIs included the hippocampal CA4 region and hippocampal fissure, as well as the basal nucleus accumbens and ventral pallidum, each with a 13% incidence rate. The basal SNc, PBP, hypothalamus, VTA, subthalamic nucleus, and hippocampal subiculum exhibited only isolated instances of elevated susceptibility across the whole iron-abnormal cohort. Only two hippocampal ROIs exhibited no significant deviations from the healthy normal distribution for any mTBI participant; the hippocampal tail and CA3. In contrast, no abnormal iron profiles were identified for several major basal subregions, including the putamen, caudate, globus pallidus (both internus and externus), red nucleus, SNr, and extended amygdala.

Only one participant (mTBI-18) had a z-score below the HC range, showing a z of -2.0 in the CA1 region. This case also represents the sole instance of CA1 involvement (see Table 7.2, Fig. 7.2.2A and Fig. 7.2.2B).

Table 7.2: Summary of significant ROI-wise z-scores and symptomatology for iron-abnormal sr-mTBI participants in the basal ganglia and hippocampal subfields

ID	Segmentation	ROI	z-score	Presenting symptoms
mTBI-01	Hippocampus: Basal Ganglia:	Parasubiculum Mammillary Nucleus	+3.7 +4.3	Initial emesis, followed by severe tinnitus and phonophobia, vertigo, cephalalgia, cervicalgia, photophobia, visual disturbance, cognitive impairment, confusion, concentration issues, memory deficits, irritability, restlessness, fatigue, and sleep disturbance. Moderate vestibular dysfunction and ataxia were also noted
mTBI-04	Hippocampus:	Parasubiculum	+2.4	Moderate cervicalgia and photophobia. Mild cephalalgia, ataxia, cognitive impairment, confusion, concentration issues, memory deficits, sleep disturbance. Additional clinical notes include vertigo and confusion at onset
mTBI-10	Hippocampus:	Parasubiculum	+5.8	Moderate cephalalgia, photophobia, vertigo, visual disturbance, fatigue, sleep disturbance. Mild cervicalgia, phonophobia, vestibular dysfunction, ataxia, cognitive issues, memory deficits, confusion, concentration issues, irritability, and restlessness. Additional clinical notes include hand numbness, pins and needles
mTBI-11	Hippocampus: Basal Ganglia:	Parasubiculum Mammillary Nucleus	+2.9 +4.1	Severe photophobia. Moderate cervicalgia, restlessness, fatigue, and sleep disturbance. Mild cephalalgia, phonophobia, vertigo, vestibular dysfunction, ataxia, visual disturbance, cognitive impairment, concentration issues, memory deficits, confusion, and irritability
mTBI-12	Hippocampus:	Presubiculum CA4 Fimbria Hippocampal Fissure	+2.8 +2.1 +3.1 +3.6	Mild cephalalgia, cervicalgia, photophobia, phonophobia, cognitive dysfunction, concentration issues, irritability, fatigue
mTBI-17	Hippocampus: Basal Ganglia:	Parasubiculum Mammillary Nucleus	+4.0 +11.0	No BIST. Clinical notes include transient mental fog, bradyphrenia, indecisiveness, and vestibular dysfunction
mTBI-18	Hippocampus: Basal Ganglia:	Presubiculum Subiculum CA1 CA4 Fimbria Hippocampal Fissure Mammillary Nucleus	+3.1 +2.5 -2.0 +2.9 +13.1 +4.0 +3.4	Moderate phonophobia, photophobia, visual disturbance, concentration issues. Mild cephalalgia, vertigo, vestibular dysfunction, ataxia, cognitive impairment, memory deficits, irritability, fatigue, and sleep disturbance. Additional clinical notes include disorientation, nausea, and impaired thought
mTBI-19	Basal Ganglia:	Nucleus Accumbens	+3.4	Moderate cognitive impairment, concentration issues, fatigue, and sleep disturbance. Mild cephalalgia, photophobia, memory deficits, and confusion. Additional clinical notes include being dazed at time of injury
mTBI-21	Hippocampus:	Fimbria	+4.4	Mild cephalalgia, photophobia, vertigo, cognitive impairment, memory deficits, concentration issues, fatigue, and sleep disturbance
mTBI-24	Hippocampus:	Parasubiculum	+6.1	Moderate cervicalgia, photophobia, phonophobia, vertigo, vestibular dysfunction, ataxia, cognitive impairment, memory deficits, confusion, concentration issues, irritability, restlessness, and fatigue. Mild cephalalgia, visual disturbance, sleep disturbance
mTBI-27	Hippocampus: Basal Ganglia:	HATA Nucleus Accumbens Ventral Pallidum	+2.7 +3.2 +2.8	Severe fatigue and sleep disturbance. Moderate cognitive impairment. Mild cephalalgia, photophobia, phonophobia, vestibular dysfunction, memory deficits and concentration issues. Additional clinical notes include anxiety
mTBI-28	Hippocampus: Basal Ganglia:	HATA Mammillary Nucleus	+4.6 +3.3	Moderate cephalalgia, photophobia, phonophobia, restlessness, fatigue and sleep disturbance. Mild cervicalgia, vertigo, vestibular dysfunction, ataxia, cognitive impairment, concentration issues, and memory deficits. Additional clinical notes include nausea, reduced tolerance to physical and cognitive exertion, and impaired coordination
mTBI-30	Basal Ganglia:	Ventral Pallidum Mammillary Nucleus	+2.9 +2.7	Fatigue
mTBI-31	Hippocampus:	Presubiculum HATA Fimbria	+3.3 +2.8 +5.2	Moderate fatigue and sleep disturbance. Mild cephalalgia, photophobia, cognitive impairment, concentration issues, irritability and restlessness
mTBI-32	Hippocampus: Basal Ganglia:	Parasubiculum SNc PBP VTA Hypothalamus Mammillary Nucleus Subthalamic Nuclei	+4.5 +2.9 +3.9 +3.1 +5.2 +3.5 +3.0	Moderate cephalalgia, cervicalgia, phonophobia, cognitive impairment, confusion, concentration issues, memory deficits, restlessness, and fatigue. Mild photophobia, vertigo, vestibular dysfunction, visual disturbance, ataxia, irritability, and sleep disturbance. Additional clinical notes include being dazed

Note. Presenting symptoms are primarily derived from BIST injury severity assessments and supplemented with additional clinical patient notes made upon presentation of participants to Axis Sports Medicine clinics. Only participants with abnormal iron profiles are included for brevity and relevance. ID = unique identifier; ROI = region of interest; CA = cornu ammonis; HATA = hippocampal-amygdala transition area.

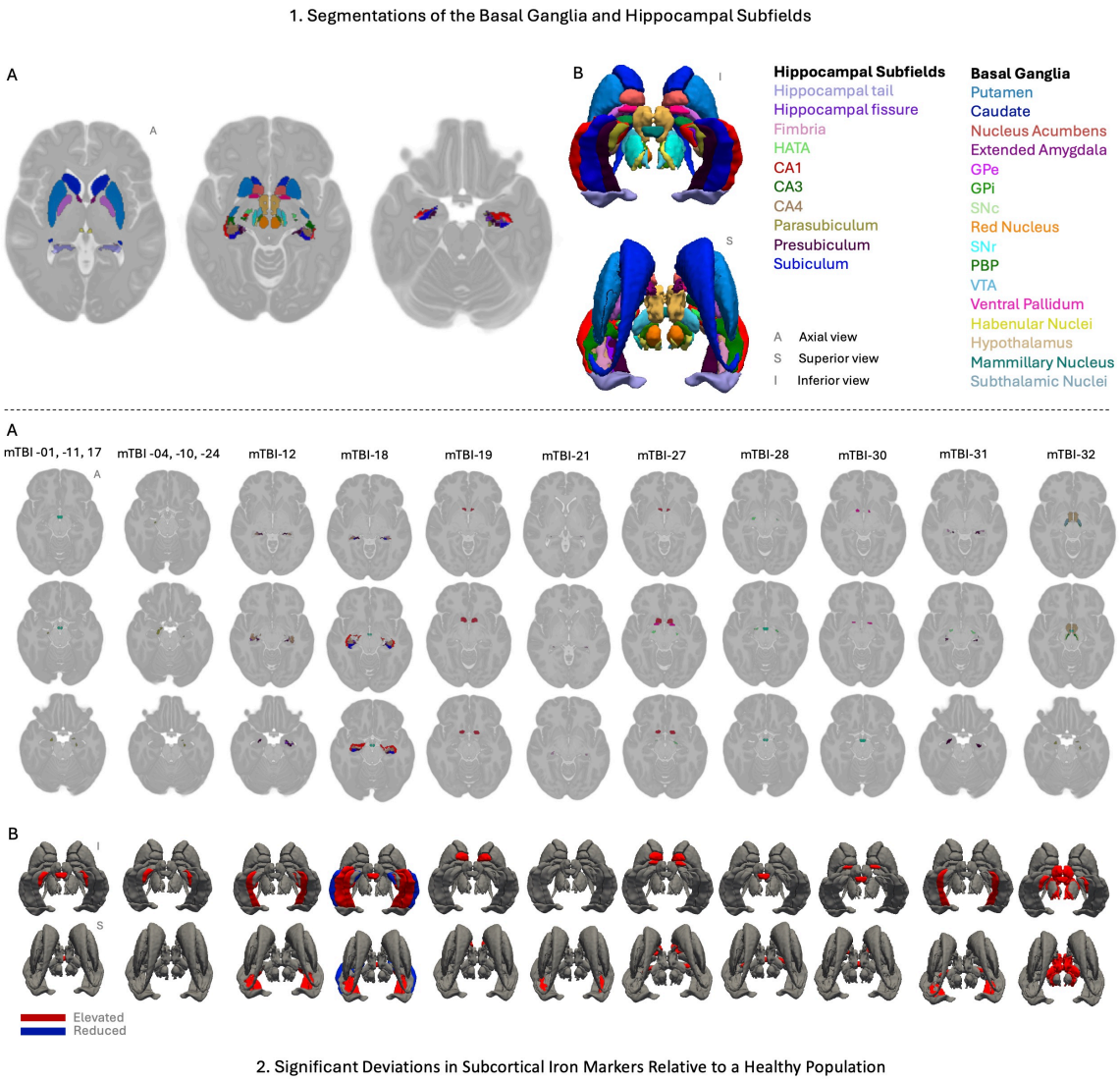

Figure 7.2: Segmentations and individualised profiles for abnormal subcortical iron markers

1. Visualisation of basal ganglia and hippocampal subfield segmentations. A. Axial (A) slices of the CIT168-MNI152 T_1w brain template depict segmentations of the basal ganglia and hippocampal subfields, selected to optimise structural visualisation. B. 3D renderings show superior (S) and inferior (I) views of the segmented regions, with key subcortical structures labelled in their respective colours. 2. Significant deviations in subcortical iron markers for each sr-mTBI participant relative to the HC population. A. Axial views of the CIT168-MNI152 T_1w template highlight significant subcortical ROIs for each participant, shown in the segmentation colours. B. 3D renderings highlight regions with significantly elevated (red) or reduced (blue) z-scores to show regions with abnormal iron profiles; all other regions are greyed out. CA = cornu ammonis; GP = globus pallidus (GPi = internus; GPe = externus); SN = substantia nigra (SNc = pars compacta; SNr = pars reticulata); PBP = parabrachial pigmented nucleus; VTA = ventral tegmental area.

On aggregate, incidence rates of abnormal iron markers tended to cluster around the midline, in commissural nuclei, and inferior regions (see Fig. 7.3). A particularly high concentration was observed in the hippocampus, which is located inferior to the basal ganglia. Within the hippocampus, prevalent abnormal iron markers were observed near the anteromedial aspect of the hippocampus (the hippocampal head), decreasing in frequency laterally and toward the distal tail. In contrast, more superior regions, including the dorsal aspect of the hippocampus and the basal ganglia (excluding the mammillary nucleus) appeared to be less affected.

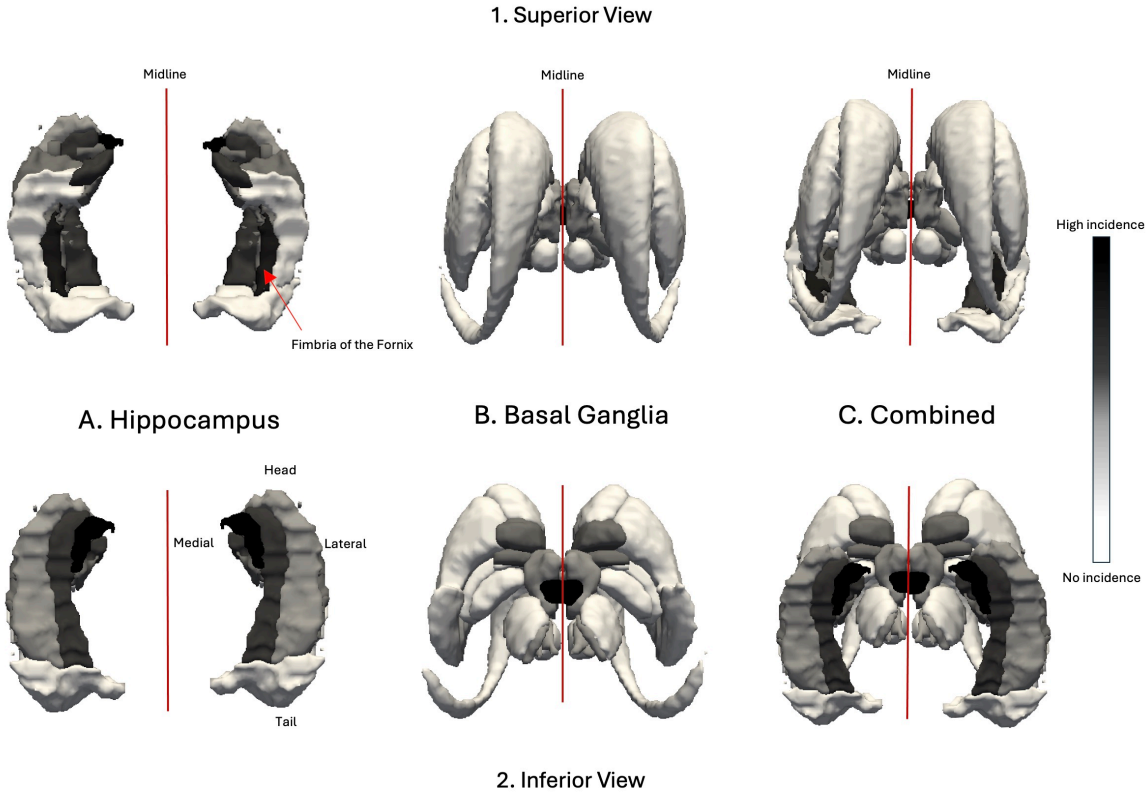

Figure 7.3: Aggregated regional incidence of abnormal iron markers

This figure presents a 3D model of relative incidence rates aggregated across the "iron-abnormal" mTBI population from a superior (1) and inferior (2) view. Incidence rates are represented in grey scale (high: black; low: white). A. Depicts the hippocampus in isolation. Anteromedial and commissural (i.e., the fimbria) structures of the more inferior hippocampus show a higher incidence of abnormal z-scores than more superior or lateral structures. The medial aspect of the anterior hippocampal head is more frequently affected than lateral regions or the more distal tail. B. Depicts the basal ganglia in isolation. Substructures of the superiorly-situated basal ganglia show relatively lower rates of abnormal iron markers than the underlying hippocampal formation, with affected regions also primarily located in relatively more inferior and structures near the midline. C. Provides a combined view integrating both hippocampal and basal ganglia regions. The CA1 region has been omitted due to a negative z-score.

After subdividing the mTBI participants into iron-normal (20/35; 57%) and iron-abnormal (15/35; 43%) sub-groups based on their individual profiles, a one-way ANOVA showed no significant differences in age between the three groups (iron-normal mTBI, iron-abnormal mTBI, and controls), $F(2, 32) = 1.12$, $p = 0.3$. A Mann-Whitney U test revealed no significant difference in BIST scores between iron-normal ($M = 35.6$, $SD = 30.8$) and iron-abnormal ($M = 41.7$, $SD = 34.5$) mTBI participants, $U = 120$, $p = 0.5$.

7.5.2 *Patterns between symptoms and subcortical iron-related markers*

This section is included for descriptive purposes, and relates to observations rather than results of inferential statistics. Elevated iron markers with hippocampal involvement presented alongside self-reported cognitive symptoms (including cognitive impairment, memory deficit, concentration issues, confusion, and clinical notes related to mental fog and bradyphrenia). Disturbances in arousal (fatigue and sleep) and sensory sensitivit-

ies (including headache, photophobia, and phonophobia) were reported by 92% of participants with hippocampal abnormalities. Vestibulo-ocular dysfunction (including vestibular symptoms, vertigo, ataxia, and visual disturbance) were slightly less common in this cohort (85%), followed by mood disturbances (77%). Participants with elevated hippocampal iron markers that included the parasubiculum reported cognitive impairment and vestibulo-ocular symptomatology at a 100% incidence rate. Elevated iron markers in the mammillary nucleus, which almost invariably co-occurred with hippocampal regions and rarely with other basal regions, were also associated with high incidences of cognitive symptoms and vestibulo-ocular disturbances, as well as issues related to arousal (86% each). In contrast, relatively lower frequencies of all symptom clusters were observed across participants with abnormal iron markers inclusive of basal ganglia subregions. Cognitive impairment and arousal disturbances occurred in 89% of these participants, vestibulo-ocular and sensory dysfunctions in 78% each, and mood disturbances in 67% (see Table 7.2 for all symptom/region information).

7.6 DISCUSSION

Group-level analytic methods currently dominate the field of clinical research. However, the suitability of this approach for comprehensive understanding of neuropathology, particularly in the context of mTBI, may be limited. By focusing on population-level effects, subtle, yet clinically meaningful, inter-individual differences in pathophysiology may be overlooked. This could limit our understanding of this injury and hinder the implementation of individualised rehabilitation strategies and treatments. I believe, therefore, that research incorporating comparisons of individual clinical participant data to healthy normative ranges can play a key role in informing targeted neural and pharmacological interventions. To advance the understanding of iron aggregation in acute mTBI, I conducted the first QSM-based, dedicated individualised analysis of subcortical brain regions. Here, detailed segmentations of the basal ganglia were integrated with comprehensive delineation of the hippocampal subfields; an approach designed to overcome the anatomical limitations of previous group-level QSM investigations (see Chapter 3). Iron markers across 15 basal ganglia segmentations and 10 hippocampal subfields for individual mTBI participants were assessed relative to a normative control population using z-scores, enabling identification of subcortical regions where iron markers significantly deviated from a healthy reference range.

Results revealed abnormal subcortical iron profiles in approximately half of the mTBI sample, most of which involved at least one hippocampal subfield. Hippocampal abnormalities were not only observationally linked to a high incidence of cognitive symptoms, but were also associated with more frequent occurrence of all symptom clusters relative to participants whose abnormal profiles involved the basal nuclei. Among the hippocampal subregions, the parasubiculum was both the most prevalent ROI to be affected, and universally accompanied self reported cognitive and vestibulo-ocular symptoms. For iron-abnormal mTBI participants with basal ganglia involvement, elevated iron markers in the

mammillary nucleus were also prevalent, occurring at the same incidence rate as markers in the parasubiculum across the entire iron-abnormal cohort. Significant z-scores in the mammillary nucleus most often co-occurred with hippocampal abnormalities or in isolation, rather than concomitant with abnormal z-scores in other basal nuclei. Symptoms related to cognitive, arousal, and vestibulo-ocular dysfunction were the most frequently reported symptoms among mTBI participants with mammillary nucleus involvement. Statistical analysis of injury severity scores between iron-normal and iron-abnormal mTBI participants revealed no significant differences, suggesting that although abnormal subcortical iron profiles may be observationally associated with specific symptom phenotypes, they may not be directly related to injury severity on aggregate.

7.6.1 *Regional injury vulnerability in the hippocampus*

The basal ganglia remain the most commonly targeted subcortical regions of interest in QSM investigations of mTBI due to their high iron load in the brain (Bell et al., 2024; Gong et al., 2018; Koch et al., 2018; Koch et al., 2021; Pinky et al., 2022; Wright et al., 2022; Zivadinov et al., 2018a) and extensive white matter connections with both cortical and subcortical structures (Lifshitz et al., 2007; Ropper et al., 2007) which increase vulnerability to shear and strain in mTBI (Raz et al., 2011). This excessive biomechanical loading may alter iron expression via secondary injury mechanisms (Gozt et al., 2021a). In addition, the naturally high levels of iron in these nuclei, which under normal conditions support metabolic functions (Gozt et al., 2021a; Hallgren et al., 1958; Levi et al., 2024), may exacerbate risk of trauma-induced cytotoxicity mediated by iron (Haacke et al., 2005). This high regional iron content also render the basal ganglia particularly amenable to imaging methods sensitive to tissue magnetic susceptibility, such as QSM. Collectively, these factors underscore the rationale for selecting the basal ganglia as logical targets in QSM-based mTBI research. However, the higher incidence rates of iron-related abnormalities observed in hippocampal regions compared to the basal ganglia in this individualised study suggest that the prevailing focus on basal structures may represent a critical oversight. Results presented here indicate that the underlying hippocampus and surrounding cerebrum may instead afford the basal ganglia a relative degree of structural protection from injury (see Fig. 7.4).

Despite the medial temporal lobe's known vulnerability to traumatic insult (Bigler et al., 2002; Christidi et al., 2011), the hippocampus remains under-studied in QSM-based investigations of mTBI. Viewed in the context of the broader literature, the general predilection for hippocampal iron-related abnormalities across participants in this study indicate local changes to magnetic susceptibility that may be related to iron-driven secondary injury mechanisms (Daglas et al., 2018; Gozt et al., 2021a) congruent with regional vulnerability of the hippocampus to mechanical deformation in TBI (Bigler et al., 2002). Both acute and chronic pathophysiological sequelae associated with hippocampal regions following mild-to-severe traumatic injury can include cytotoxic secondary injury, disruptions to vascular and metabolic function, DAI of afferent and efferent fibers, and even CTE-associated tauopathy and focal atrophy as a downstream pathological event (Bieniek et al., 2021; Christidi

et al., 2011), for which iron overload may be a mediating factor (Gozt et al., 2021a; Huang et al., 2021; Nisenbaum et al., 2014; Orr et al., 2024). On aggregate, the results of the present study suggest that the hippocampus is a primary site of mTBI-related pathophysiological processes.

7.6.2 *Towards a region-of-risk model of mTBI*

The distinct, subfield-specific patterns that emerged when abnormal iron markers were aggregated across participants highlights not only the hippocampus but also specific subfields and spatial locations as regions with heightened vulnerability to injury. Injury biomechanics and morphology of the skull base may contribute to increased mechanical loading and strain, focal tissue damage, and a resultant dynamic cascade of secondary injury mechanisms which may include altered iron signalling in select vulnerable, and interconnected, regions (see Fig. 7.4). Specifically, the concentration of iron markers in the parasubiculum, mammillary nucleus, and fimbria support and extend findings from the group-wise study of cortical iron markers presented in Chapter 6 which demonstrated localisation of abnormal positive susceptibility values to the adjacent cortical region; the parahippocampal gyrus.

Anatomically, the head of the hippocampus is situated approximately 2 cm from the irregular sphenoid ridge at the junction of the anterior and middle cranial fossa, and is particularly susceptible to mechanical deformation over this bony protrusion during impact (Bigler, 2007). The parasubiculum, as part of this region (Poeta et al., 2022), may thus be more vulnerable to injury than hippocampal substructures located peripherally to this region of heightened injury risk (e.g., the subiculum) or in the more distal hippocampal tail. This observation is supported by a high degree of spatial overlap between areas of varying injury vulnerability, as informed by cranial-dural architecture and injury biomechanics, and the relative incidence rates of abnormal z-scores observed here which cluster at the anterior aspect of the hippocampus (the hippocampal head), and diminish with proximity to this region (see Fig. 7.4). These results further refine the anterior medial temporal lobe-centric (Bigler, 2007; Mckee et al., 2015) region-of-risk model posited in Chapter 6. Data from investigations of temporal lobe epilepsy suggests that parasubicular neurons are hyper-excitable (Sullenberger et al., 2019), which may contribute to iron accumulation as a consequence of excitotoxicity in mTBI (Huang et al., 2021), further exacerbating regional risk. Additionally, the contribution of iron deficiency to neuron loss (Levi et al., 2024) provides a plausible explanation for the abnormally low z-score observed in the hippocampal CA1 region of a single participant in this study, reinforcing a hippocampus-specific model of tissue disruption.

Beyond the medial temporal lobe, midline and commissural structures, including the fornix, are increasingly recognised as regions prone to excessive biomechanical loading during sports-related mTBI impacts, and have been associated with memory and cognitive impairments in 30-50% of cases and removal from play in 30% (Viano et al., 2005). Damage to midline structures has also been cited as a risk factor for subsequent mTBI (Churchill

et al., 2021), and although these observations were not directly related to the structures under investigation in the present study, the incidence of abnormal iron markers in the mammillary nucleus and fimbria observed in this sample is nonetheless noteworthy. The fimbria is a key component of the fornix; a commissural tract not only connecting the bilateral hippocampus, but the hippocampus to the mammillary bodies (Bigler, 2007; Senova et al., 2020). Evidence of dyshomeostatic mechanisms focal to this region may be related to head kinematics during impact, whereby rotational forces are a likely cause of strain-related diffuse injury (A. I. King et al., 2003; Kleiven, 2013), which may be particularly damaging to the fornix (Viano et al., 2005) and related nuclei. In addition, the mammillary bodies, located on the inferior aspect of the diencephalon, are paired structures that sit on either side of the midline and are connected by the intermammillary sulcus (Meys et al., 2022). These nuclei are also related to the commissural fornix, forming the terminals of its anterior pillars (Rich, 2018).

Degeneration of both the fornix and mammillary bodies has been extensively documented in TBI, which is attributed to medial temporal lobe trauma and disruption of these regions as downstream targets (Bigler, 2007). The mammillary bodies receive projections from the parasubiculum (Rich, 2018), and abnormal iron markers in this region may represent a more subtle, but pathologically significant, manifestation of degenerative excitotoxic processes that exist on a continuum with more severe TBI. The interconnection of these two regions may not only explain equivalent incidences of iron-related abnormalities in these regions, but their frequent co-occurrence within individual participant results (see Table 7.2). Taken together, these data not only reinforce the importance of subfield-specific investigations of the hippocampus and granular segmentations of the basal anatomy, but also provide evidence that sites of cellular distress signalling can be mapped to potential injury mechanisms via quantification of positive susceptibility and the use of individualised analytic techniques. This lends support to the utilisation of individualised study designs to detect heterogeneous changes in brain tissue content, and contributes to the current understanding of the relationships between potential iron overload, injury dynamics, and mTBI pathophysiology.

7.6.3 *Regional iron dysregulation, symptom cluster, and Papez circuit integration*

Disruption to cellular integrity can impede function, resulting in changes to cognition and behaviour that may be related to specific injury biodynamics and loci of neuronal injury (Orr et al., 2024). Although elevated subcortical iron markers were not associated with greater self-reported symptom *severity*, and causal inference is precluded in this sample, the universal incidence of symptom clusters within the cognitive domain among participants with abnormal hippocampal iron markers is consistent with extant literature linking memory and cognitive deficits to medial temporal lobe damage (Christidi et al., 2011) and iron dyshomeostasis (Huang et al., 2021; Lu et al., 2015). In addition to the general concentration of abnormal iron markers within the hippocampal subfields broadly, the

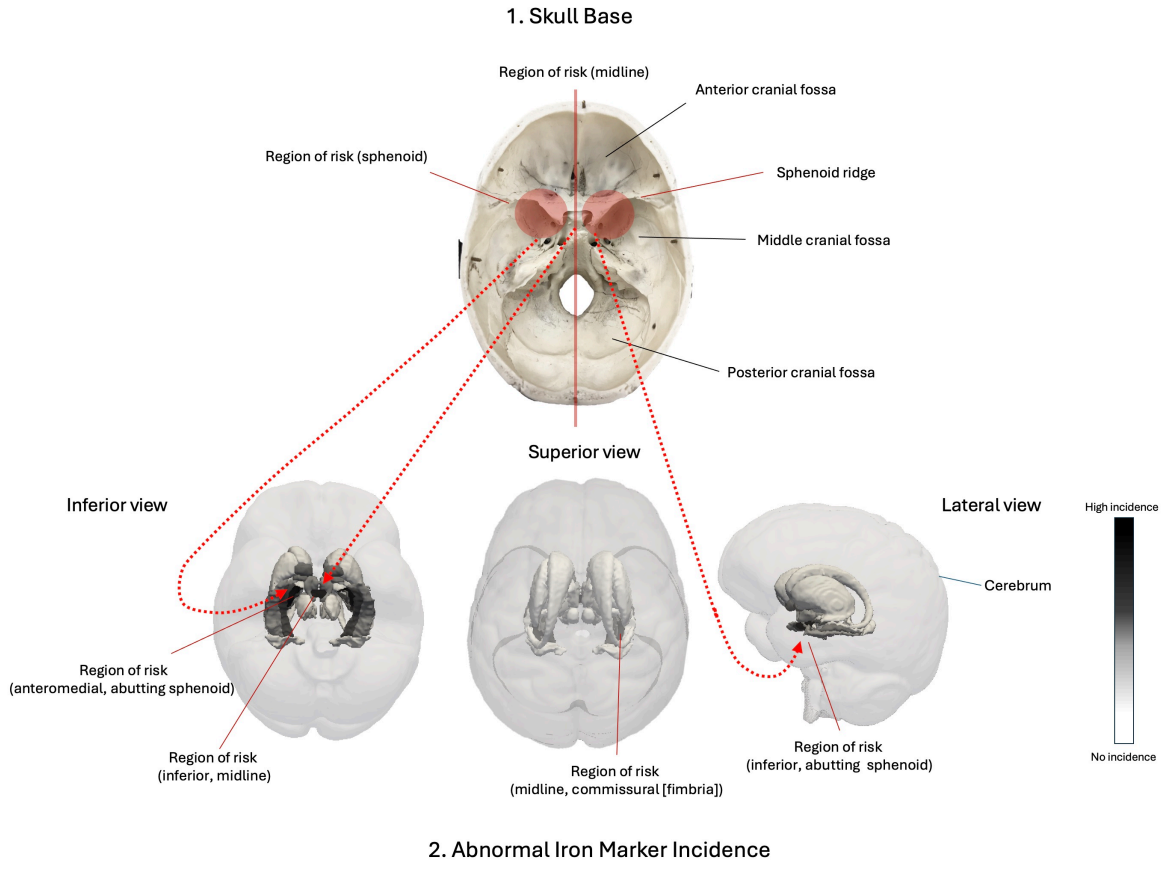

Figure 7.4: Spatial alignment between regions of heightened injury risk and abnormal iron markers

This figure highlights the anatomical alignment between structural vulnerability and impact biomechanics with aggregate iron markers in subcortical brain regions across "iron-abnormal" mTBI participants. 1. Visualises the cranial base from a superior view. Key regions of mechanical risk, including the sphenoid ridge and midline zones, are highlighted in red. 2. Provides a 3D render showing spatial alignment between regions of risk and incidence rates of abnormal iron markers across the sample. This model provides a visualisation of the vulnerability of inferior structures, particularly in the anterior aspect proximal to the sphenoid ridge, as well as midline and commissural regions, to cranial impact, strain, and force transmission. The basal ganglia, shielded from below by the hippocampus and from above by the cerebrum, may be afforded more protection from injury. The CA1 region has been omitted due to a negative z-score.

mammillary nucleus and parasubiculum emerged as consistent sites of abnormal iron loading which could speculatively be related to symptom phenotype.

Although the specific role of the parasubiculum in mTBI-induced pathology and associated symptomatology remains under explored, its involvement in key pathways mediating cognitive and vestibulo-ocular functions may offer a plausible explanation for clinical deficits reported by participants presenting with abnormal iron profiles in this region. Participants with elevated iron markers in the mammillary nucleus also reported similar symptoms, with an additional high incidence of arousal disturbances (see Table 7.2). Functional and structural connectivity between these two regions (Rich, 2018; Swanson et al., 1975) may account not only for the overlapping symptomatology, but also for the frequent co-occurrence of abnormal iron markers.

As part of the subicular complex, the parasubiculum occupies a central position in the medial temporal lobe memory system, supporting memory formation (Ding, 2013; Kerr et al., 2007). This is exemplified by observations of pyramidal cell loss and the formation of severe NFTs in the parasubiculum in AD (Van Hoesen et al., 1990) with memory loss as

a central feature (Jahn, 2013). The parasubiculum also plays a critical role in spatial information processing (Boccara et al., 2010; Sammons et al., 2019). This region is anatomically and functionally connected to the area prostriata, which projects to visual, motor, and auditory regions (Ding, 2013), and interfaces with the entorhinal cortex, a region critical for both memory formation and integration of vestibular and directional cues in spatial navigation (Kerr et al., 2007; Taube, 2007). Directional and spatial orientation signals are further modulated by connections to the mammillary bodies. "Head-direction" cells responsive to head orientation and spatial encoding in the presubicular and parasubicular cortices (Boccara et al., 2010; Cacucci et al., 2004; Sammons et al., 2019) transmit signals to the lateral mammillary nucleus to facilitate navigation and orientation (Vann et al., 2004).

The mammillary bodies also serve as a central pathway for memory processes. In addition to receiving hippocampal outputs via the fornix (Senova et al., 2020), the mammillary bodies relay these signals to the anterior thalamic nuclei through the mammillothalamic tract (Miyashita, 2022). This relay function is a critical component of the Papez circuit central to emotion and memory (Aggleton et al., 2016). Damage to this fundamental network has been associated with a variety of neurological disorders that have cognitive impairment as a defining feature, including AD, PD, semantic dementia, and global amnesia (Aggleton et al., 2016; Bhattacharyya, 2017). Atrophy of the mammillary bodies is also distinguishing feature of Korsakoff syndrome, a degenerative neurological disorder related to chronic alcohol abuse which is characterised by episodic memory deficits (Vann et al., 2004), and linked to dysfunction within Papez circuit (Bhattacharyya, 2017).[1] Within the context of mTBI, pathology of the mammillary bodies has been cited as an antecedent of memory impairment stemming from Papez circuit disconnection in retired athletes with a history of repetitive mTBI (Miyata et al., 2024). By extension, it is plausible that similar symptoms reported by participants with evidence of iron accumulation in these key, highly interconnected, regions might arise from dysfunction of these central circuits.

Finally, the high incidence of issues related to arousal also reported by participants with abnormal iron markers in the mammillary nucleus could speculatively be attributed to disruption of histaminergic neurons within the mammillary bodies that regulate arousal and wakefulness. Damage to these neurons has been identified as a mediating factor in sleep dysregulation following mTBI (Piantino et al., 2022), corroborating this hypothesis.

7.6.4 *The potential of an individualised approach for enhancing research and clinical care*

Collectively, the distribution of abnormal iron markers across subcortical nuclei suggests a region-of-risk model informed by injury biomechanics and a complex interplay with cranial and dural architecture (see Fig. 7.4). It is well-established that different biomechanical forces give rise to heterogeneous and dynamic injury cascades, complicating the study of mTBI pathophysiology (Orr et al., 2024; Rosenbaum et al., 2012). The results presented here suggest that characterising dyshomeostatic iron signalling at the individual level may

1 Renowned neurologist Dr. Oliver Sacks portrays the memory deficits related to Korsakoff syndrome through the case of "Jimmie G", featured in his classic book, *The Man Who Mistook His Wife for a Hat*; a text I highly recommended to interested readers.

serve as a viable proxy for secondary injury mechanisms occurring in a subset of individuals, and at specific spatial locations. These data indicate that mTBI induces iron overload in at least one subcortical region for 43% of participants with mTBI. Taken together with the lack of identifiable differences in positive susceptibility between mTBI participants and controls in the previous group level investigation (see Chapter 5) and in the literature more broadly (Bell et al., 2024; Gong et al., 2018; Koch et al., 2018; Koch et al., 2021; Pinky et al., 2022; Wright et al., 2022; Zivadinov et al., 2018a), this finding suggests that iron dyshomeostasis in the deep grey matter may not constitute a feature of mTBI generalisable to all cases. However, the use of individualised modelling likely enables identification of instances at the single-subject level where iron accumulation may be occurring, providing biologically informative results that are otherwise lost to averages. This suggests that targeted interventions, for example iron chelation therapies (Jia et al., 2023; Khalaf et al., 2019; Long et al., 1996; Panter et al., 1992; J. Zhao et al., 2014), may be beneficial for some individuals, emphasising importance of identifying individual variation that could inform the development of future clinical trials and specific treatment strategies (Marquand et al., 2019). In addition, leveraging inherent tissue susceptibility variations has the potential to identify not only specific injury patterns but also individuals at elevated risk of suboptimal recovery, subsequent injury, or localised tissue pathology, provided that study designs are suitably responsive. Furthermore, the observed relationships between loci of abnormal iron markers and symptom clusters alludes to the potential of individualised approaches to elucidate how distinct patterns of cellular disruption may be related to specific clinical phenotypes.

This study also underscores inherent limitations of the standard methodological focus prevalent in contemporary QSM-based mTBI research. Specifically, identifying hippocampal subfields and the mammillary nucleus as primary loci of acute, iron-related mTBI pathophysiology suggests that prior research concentrated only on major basal ganglia structures (Bell et al., 2024; Gong et al., 2018; Koch et al., 2018; Koch et al., 2021; Wright et al., 2022), or using gross hippocampal segmentations (Pinky et al., 2022; Zivadinov et al., 2018a), is likely insensitive to discrete regions differentially affected by injury. At minimum, the results highlight the need to incorporate both individualised analyses and detailed segmentations into future research designs to improve understanding of regional, inter-individual tissue content changes following mTBI, and provides evidence that calls for the scientific community embrace new paradigms that account for injury heterogeneity (Rosenbaum et al., 2012) and more detailed segmentations (Gozt et al., 2021a) are well-founded.

Lastly, the congruence between dominant spatial distributions of abnormal iron markers in this sample and diagnostic features of CTE are concerning given the putative relationship between the two (Bouras et al., 1997; Yamamoto et al., 2002; Zecca et al., 2004). In particular, the presence of NFTs in the hippocampus and mammillary bodies is diagnostic of CTE and CTE burden (high versus low) (Bieniek et al., 2021). Identifying these specific regions as common locations of potential iron dyshomeostasis in mTBI raises further ques-

tions about the interrelatedness of acute cascades that may present as later-life pathology in a subset of individuals.

7.6.5 *Limitations and future research*

In addition to the limitations described in Chapter 5 that apply equally here, several further constraints specific to this individualised approach remain. There is a lack of any widely established best-practice method to normalise the HC z-distribution. For example, other individualised QSM research has employed less stringent filtering at three times IQR to detect more severe TBI pathology (Domínguez et al., 2024). Future research would benefit from standardised practices for outlier detection. The mammillary nucleus, in particular, was more extensively filtered than other regions. This may have contributed to a greater proportion of abnormal z-scores in this region, despite a residual sample size that is still more robust than other comparable studies (Domínguez et al., 2024). In addition, the use of nonparametric approaches for between-group comparisons of iron-normal and iron-abnormal mTBI participants is limited by the inherent challenges associated with small and unequal sample sizes, which may compromise the statistical power and reliability of these findings and results should be interpreted with caution.

Natural age-related increases in subcortical (and cortical) iron can also be particularly pronounced within this specific age range (Hallgren et al., 1958), and although the ages of the HC and mTBI participants were closely matched with no statistically significant differences between groups, some confounding effects may still be introduced. For example, the relative under representation of abnormal iron markers in the basal substructures (with the exception of the mammillary nucleus) may be related to the potential confounding effects of age-related increases in iron. These effects may be particularly relevant in regions known to exhibit elevated iron content during normal ageing such as the red nucleus, substantia nigra, globus pallidus, putamen, and caudate (Ashraf et al., 2018; Bilgic et al., 2012; Hallgren et al., 1958; Madden et al., 2023; Treit et al., 2021). In Chapter 5, evidence of significant age-related increases in positive susceptibility were observed in the putamen, caudate, parabrachial pigmented nucleus, ventral pallidum, and red nucleus across the entire sample. Many of these substructures showed no evidence of abnormal individualised iron markers compared to the HC population. Despite the lack of statistically significant age differences between groups in all relevant analyses, it is still possible that age-related variability in regional iron content may yield an inherently broader normative distribution, thereby confounding identification of abnormal iron markers in the mTBI cohort. In principle, within a sample so closely age-matched, the normal distribution reflects typical variation in susceptibility values, but age effects may not be fully accounted for. The power of z-scores to regress out the effects of these variables is limited, particularly at small sample sizes, and future research should thus consider recruiting large control cohorts that enable more robust approaches, such as normative modelling (Marquand et al., 2016).

Although this study used detailed segmentations, some structural limitations remain. For instance, the mammillary bodies comprise functionally and structurally distinct subregions. Evidence from murine models suggests that head-direction cells are present in the lateral, but not medial, mammillary nuclei (Vann et al., 2004). Future investigations should consider additional segmentation granularity, whilst balancing the need to detect subregion-specific pathophysiology and challenges related to multiple comparisons. In addition, individualised approaches should integrate additional MRI imaging modalities, for example, to investigate white matter pathway integrity as a marker of axonal injury (e.g., by dMRI) and/or functional connectivity via fMRI. A multi-modal approach would facilitate a deeper understanding of how specific tracts, networks, and nodes are implicated in injury-related pathophysiology and symptomatology, and how this may relate to patterns of cellular disruption in grey matter on QSM.

Lastly, it should also be noted that any inferences made about the relationship between abnormal regional iron markers and symptomatology here and in the following chapter (Chapter 8) are observational only; the small sample size and some ambiguity in self-reported symptoms precludes the use of inferential statistics. Additional intra-individual overlap in abnormal z-scores in basal and hippocampal ROIs also inhibits precise delineation of the relationship between basal versus hippocampal z-score clusters and clinical symptom phenotype. The reader should bear in mind that any inferences made are speculative, and do not represent a one-to-one symptom-to-ROI mapping.

7.7 CONCLUSIONS

This chapter presents the first comprehensive, individualised QSM investigation of iron-related tissue content changes in subcortical grey matter regions following mTBI. Whilst the results of this research highlight inter-individual differences in regions with abnormal iron markers, the general concentration of elevated z-scores in specific hippocampal subfields allude to a region-of-risk model aligned not only with results from Chapter 6, but regional vulnerability, anatomical and functional connectivity, injury biodynamics, and cranial–dural morphology that is well established in the existing TBI literature. Abnormal markers, particularly in hippocampal subfields and mammillary nucleus, may also be related to distinct clinical phenotypes, as evidenced by observational relationships between loci of abnormal z-scores and specific symptom clusters. As an extension of the group-wise analyses described in Chapter 5 where few significant between-group differences were identified in these subcortical regions, this individualised study supports the use of analytic techniques sensitive to inter-individual variation to more accurately characterise potential injury-induced grey matter micropathology.

8

MTBI INCREASES CORTICAL IRON MARKERS: INSIGHTS FROM INDIVIDUALISED ANALYSIS

8.1 INTRODUCTION

This thesis has underscored the general scarcity of QSM-based investigations examining the role of brain iron in microstructural grey matter tissue damage induced by mTBI. However, this gap is especially pronounced for the cerebral cortex, a region known to be highly susceptible to mechanical strain and "water hammer" injury (Bakhtiarydavijani et al., 2021; Ghaderi et al., 2024; Kornguth et al., 2017), yet one that has been almost entirely overlooked. As discussed in Chapter 3 and Chapter 6, the two studies investigating the cortex were insufficiently sensitive to variation in depth and curvature (Gong et al., 2018; Pinky et al., 2022). In addition, these studies relied on group-level statistical analyses, which can obscure individual brain changes due to the subtle nature of cell damage associated with mTBI. Chapter 7 highlighted how this analytic approach may limit our understanding of this heterogeneous injury and inhibit the identification of personalised injury profiles, hindering the implementation of individualised rehabilitation strategies, guidelines for safe return-to-play, and the application of precision medicine. It is therefore essential that research incorporates comparisons of clinical participant data to healthy normative ranges as a component of best-practice research, and to inform individualised neural and pharmacological interventions.

To address this gap, and extend the individualised investigations described in Chapter 7 to include *cortical* ROIs, I conducted the first investigation of individual differences in cortical magnetic susceptibility after mTBI. To achieve this, I applied the techniques outlined in Chapter 7 to: 1) generate personalised profiles of potential cortical iron deposition following sr-mTBI; and 2) enhance these findings by deriving profiles sensitive to cortical architectonics, specifically depth and curvature, as a complementary secondary approach. The results of this individualised study were also used to enhance the accuracy of statistical analyses for elucidating the connection between significant positive susceptibility values in the cortex and self-reported injury severity. Employing this targeted approach to both subcortical and cortical investigations separately enables differentiation between the unique contributions of iron accumulation patterns via positive susceptibility values across superficial and exposed regions relative to those in deeper brain structures. In turn, this differentiation may elucidate how distinct spatial profiles of abnormal iron markers may contribute to risk factors for adverse outcomes. Evidence from Chapter 6 suggests that

elevated magnetic susceptibility should be most evident in ROIs in the temporal lobe (see Fig. 6.2). However, given the preliminary and exploratory nature of this study, no specific *a priori* hypotheses were made about the direction of effects for all cortical regions.

8.2 MATERIALS AND METHODS

Ethical approval, recruitment details, inclusion and exclusion criteria, and data collection methods are reported in Chapter 5. Participant sample characteristics and radiological clinical scan review are detailed in Chapter 7 and Table 7.1. Image acquisition, QSM reconstruction, and thresholding details are provided in Chapter 5. In keeping with the individualised research study outlined in Chapter 7, only QSM^{+} maps were used in the subsequent analyses due to the more reliable and robust biological interpretation offered by positive QSM values.

8.2.0.1 *Cortical column generation*

Cortical column generation and cortical curvature details are provided in Chapter 6. However, in this investigation, each cortical column was segmented into six equidistant depths extending from the pial surface to the GM/WM boundary using MRtrix3 *tckresample* (Tournier et al., 2019). This approach differs both from the research outlined in Chapter 6 and some previous investigations utilising this technique, where 21 equidistant depths were employed (Y. Ma et al., 2023; Merenstein et al., 2024). Here, six depths were used to decrease the number of depth-wise comparisons, and to better approximate the structure of the intracortical layers (Waehnert et al., 2016; Waehnert et al., 2014). These depths represent equidistant segmentations rather than specific cellular laminae (layers I–VI) of the cortex.

8.2.1 *Personalised QSM profiles*

To generate individual QSM^{+} profiles for each ROI at the bilateral level, mean positive susceptibility values were extracted across the whole ROI (curvature and depth combined), as well as three curvature bins (gyral crown, sulcal bank, and sulcal fundus) and six cortical depths independently for all 34 ROIs using MATLAB (2024a). For the whole-ROI profiles, z-scores were calculated using the formula provided in Chapter 7. An abbreviated and adapted processing pipeline has been included below for accessibility and relevance (see Fig. 8.1). In brief, z-scores were calculated for HC and mTBI participants by subtracting the HC group mean from each individual's susceptibility value and dividing by the HC group standard deviation (see Eqn. 7.1 for full equation). HC outliers were filtered at 2 times IQR, resulting in the exclusion of data from $n = 1$ HC participants in three of the 34 ROIs, and data from $n = 2$ HC participants in one of the 34 ROIs. After filtering, the Shapiro-Wilk normality test yielded an average W value of $M = 0.96$ ($SD = 0.02$) for all cortical ROIs, indicating that the data distribution within each ROI was close to normal.

The same process was repeated for each depth at each curvature bin, however, the IQR filter was omitted due to the number of comparison points.

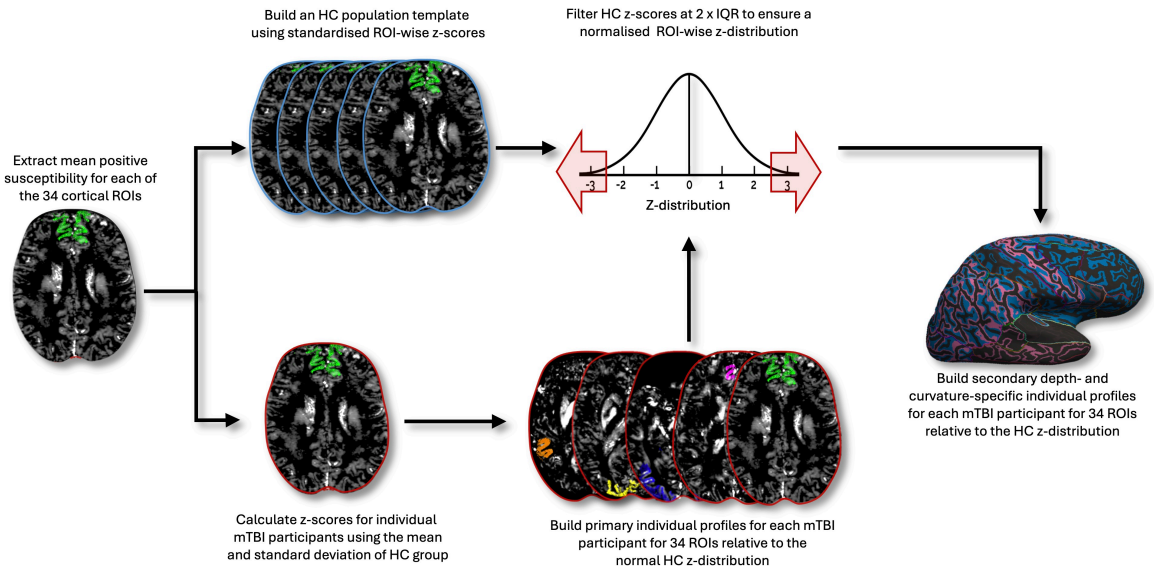

Figure 8.1: Abbreviated and adapted pipeline for generation of individual cortical iron profiles

After QSM images were thresholded to create a positive sign map, mean positive susceptibility values were extracted for each of the 34 cortical ROIs. Z-scores were calculated using the mean and standard deviation of the HC group, and standardised around a mean of zero. The HC distribution was filtered to remove outliers exceeding two times IQR for a normalised distribution. Individual profiles for mTBI participants were constructed by comparing each mTBI participants' z-scores to the healthy normal distribution, while controlling for multiple comparisons across ROIs. Secondary profiles were generated to map abnormal cortical iron markers across 6 cortical depths and three curvatures (crown, bank, and fundus). QSM = quantitative susceptibility mapping; ROI = region of interest; mTBI = mild traumatic brain injury; HC = healthy control; IQR = interquartile range.

8.3 STATISTICAL ANALYSES

To assess statistical significance for whole-ROI mTBI z-scores, two-tailed p-values were calculated from the z-scores using the cumulative distribution function of the standard normal distribution. A FDR correction (Benjamini et al., 1995) was applied to the p-values for 34 ROI-wise comparisons. The same process was repeated for each depth and curvature bin as a secondary, exploratory measure.

In keeping with Chapter 7, additional statistical tests were conducted. A two-tailed, nonparametric, Mann-Whitney U test was used to assess differences in injury severity (BIST score) between mTBI participants whose z-scores significantly deviated from HC norms (i.e., iron-abnormal) and those whose scores did not (i.e., iron-normal) as identified via primary and exploratory analyses, respectively. An ANOVA was also conducted to assess whether age was significantly different between each iron-normal, iron-abnormal, HC grouping to ensure that age was not confounding individualised results, particularly in so young a cohort. As with Chapter 7, mTBI-17 was excluded from these analyses only due to missing BIST information (see Table 7.1 in Chapter 7).

8.4 RESULTS

To understand the effects of mild brain trauma at the level of the individual, personalised profiles of iron-related differences in positive susceptibility were generated across 34 cortical ROIs for each mTBI participant. Secondary analyses sensitive to cortical depth (one through six, from the pial surface to the GM/WM interface) and curvature (crown, bank, and fundus) were conducted to assess more subtle effects that may be influenced by cortical morphology and otherwise lost in whole-ROI susceptibility estimation. Differences in cortical iron markers between mTBI participants with normal and abnormal iron profiles identified in both primary and secondary individualised analyses were also assessed.

8.4.1 *Regional individualised cortical iron profiles*

Of the 35 mTBI participants, 11 (31%) exhibited significantly elevated positive susceptibility for at least one ROI relative to the HC population template (see Table 8.1), likely indicating elevated iron. No clinical participants' z-scores were significantly lower than the HC population.

In these 11 clinical participants, injury-related elevated susceptibility was evident across all cortical lobes, however, elevated iron markers were predominantly localised to either a single lobe (45%) or two lobes (45%). Only one participant (9%) exhibited widespread, multi-focal abnormalities across the cortex (see Table 8.1). Notably, a high density of affected ROIs was observed in the temporal lobe for 82% (9 out of 11) of participants with abnormal iron profiles. In contrast, 45% (5/11) had abnormal iron in occipital ROIs, 27% (3/11) in frontal ROIs, 18% (2/11) in the insula or cingulate, and only one participant (9%) had an abnormal profile inclusive of parietal ROIs. This variability reflects the diverse regions impacted by exposure to mild brain trauma (see Fig. 8.2).

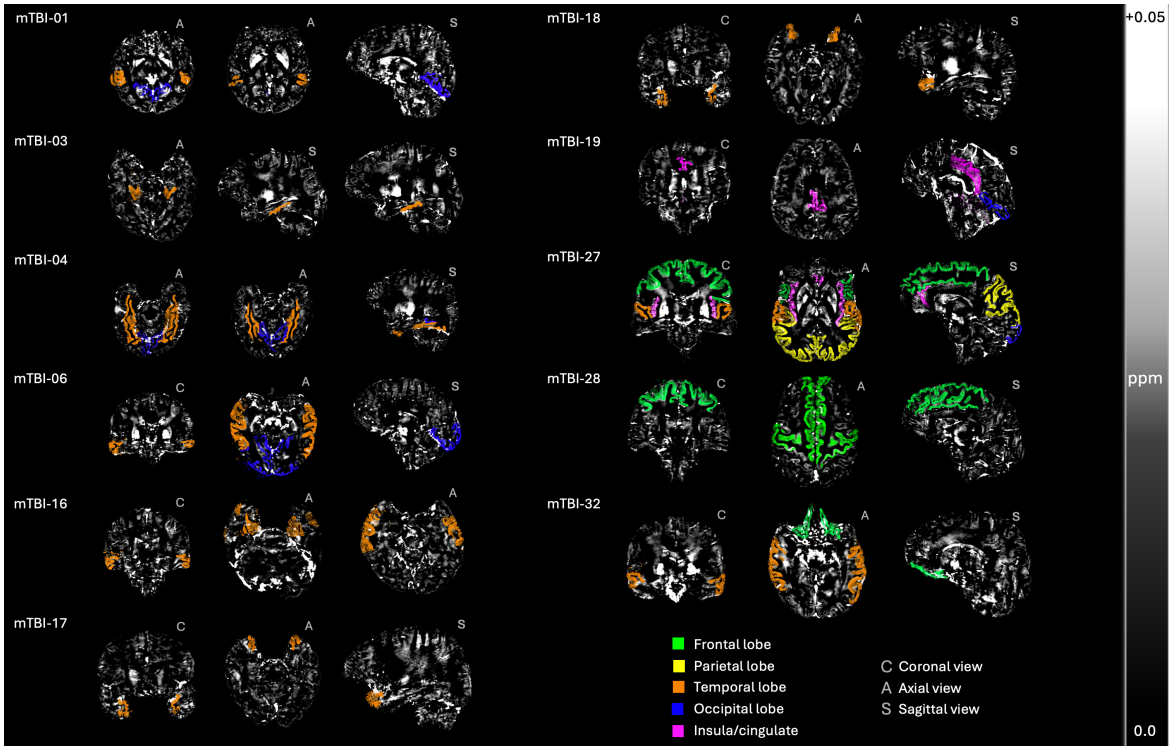

Figure 8.2: Individualised profiles of abnormal iron accumulation sites following mTBI

Visualisation of the specific ROIs and lobes affected in each mTBI participant, highlighting regions where z-scores significantly deviate from the HC population, highlighting the individualised profiles of iron accumulation following mTBI. The lobes are colour-coded as follows: frontal lobe (green), parietal lobe (yellow), temporal lobe (orange), occipital lobe (blue), and insula/cingulate (purple). The selected orientations (C: coronal, A: axial, S: sagittal) are for best visualisation of each participants' result. These maps have been thresholded for positive susceptibility values (iron-related) and are expressed in ppm from 0.0 to +0.05. Z-scores are detailed in Table 8.1.

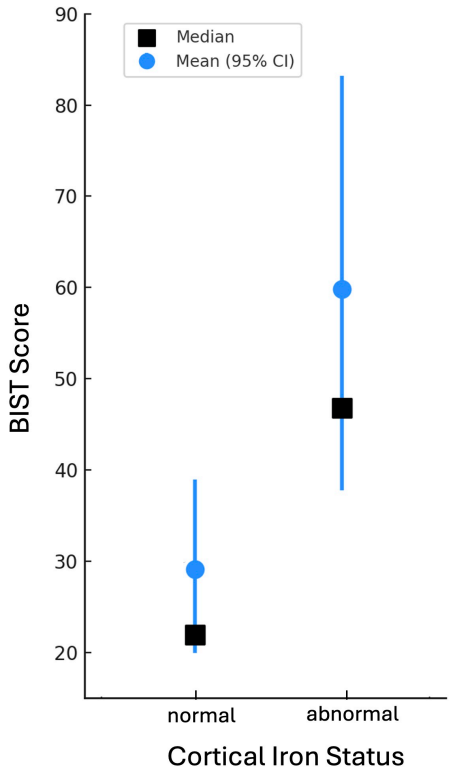

Figure 8.3: BIST scores by cortical iron status

BIST scores as a function of cortical iron marker status (normal vs. abnormal) in mTBI participants. Median (black squares) and mean (blue circles) BIST scores were both higher for iron-abnormal mTBI participants. 95% confidence intervals are indicated using blue bars for each group.

After subdividing the mTBI participants into iron-normal (24/35; 69%) and iron-abnormal (11/35; 31%) based on their individual ROI-wise profiles, a one-way ANOVA showed no significant effect of age between the three new groups (iron-normal mTBI, iron-abnormal mTBI, and controls), $F(2, 26) = 2.0$, $p = 0.2$. The Mann-Whitney U test revealed that injury severity (BIST scores) were significantly worse for the iron-abnormal mTBI group ($M = 59.6$, $SD = 40.5$) than the iron-normal mTBI group ($M = 29.2$, $SD = 23.3$), $U = 57$, $p = 0.02$, suggesting a link between injury severity and elevated regional cortical iron markers (see Fig. 8.3).

Table 8.1: Summary of significantly elevated ROI-wise z-scores and symptomatology for iron-abnormal sr-mTBI participants in the cerebral cortex

ID	Lobe(s)	ROI	z-score	Presenting symptoms
mTBI-01	Temporal: Occipital:	Bank, STS Lingual Gyrus	+3.1 +4.1	Initial emesis, followed by severe tinnitus and phonophobia, vertigo, cephalalgia, cervicalgia, photophobia, visual disturbances, cognitive impairment with confusion, concentration issues, memory deficits, irritability, restlessness, fatigue, and sleep disturbances. Moderate vestibular dysfunction and ataxia were also noted
mTBI-03	Temporal:	Parahippocampal	+3.7	Moderate cervicalgia, cephalalgia, photophobia, phonophobia, vertigo, vestibular dysfunction, cognitive impairment with confusion, concentration difficulties, memory deficits, irritability, restlessness, fatigue, and sleep disturbances. Mild visual disturbance and ataxia were present. Additional clinical notes include myalgia.
mTBI-04	Temporal: Occipital:	Fusiform Lingual Gyrus	+3.0 +6.0	Moderate cervicalgia and photophobia. Mild cephalalgia, ataxia, mild cognitive impairment with confusion, concentration issues, memory deficits, sleep disturbance. Additional clinical notes include vertigo and confusion at onset
mTBI-06	Temporal: Occipital:	Middle Temporal LOC Lingual Gyrus	+3.5 +3.5 +3.2	Moderate cognitive impairment, concentration issues, memory deficits, fatigue, and sleep disturbance. Mild cephalalgia, phonophobia, photophobia, visual disturbance, ataxia, and confusion. Additional clinical notes include mild vertigo with visuomotor sensitivity and light cranial pressure
mTBI-16	Temporal:	Middle Temporal Entorhinal	+3.0 +5.7	Severe phonophobia, photophobia, vestibular dysfunction, cognitive impairment with confusion, concentration issues, memory deficit, irritability, fatigue, and sleep disturbance. Moderate cephalalgia, cervicalgia, vertigo, and restlessness. Mild visual disturbance and ataxia.
mTBI-17	Temporal:	Temporal Pole	+3.7	No BIST. Clinical notes include transient mental fog, bradyphrenia, indecisiveness, and vestibular dysfunction
mTBI-18	Temporal:	Temporal Pole	+3.4	Moderate phonophobia, photophobia, visual disturbance, concentration issues. Mild cephalalgia, vertigo, vestibular dysfunction, ataxia, cognitive impairment, memory deficits, irritability, fatigue, and sleep disturbance. Additional clinical notes include disorientation, nausea, and impaired thought
mTBI-19	Occipital: Insula/ Cingulate:	Lingual Gyrus Posterior Cingulate Isthmus, Cingulate	+2.9 +3.2 +3.8	Moderate cognitive impairment, concentration issues, fatigue, and sleep disturbance. Mild cephalalgia, photophobia, memory deficits, confusion. Additional clinical notes include being dazed at time of injury
mTBI-27	Frontal: Parietal: Temporal: Occipital: Insula/ Cingulate: 	Pars Triangularis Caudal mPFC Pars Opercularis Superior Frontal Precentral Superior Parietal Inferior Parietal Supramarginal Precuneus STS Transverse Temporal LOC Insula Rostral ACC	+3.6 +3.3 +3.4 +3.1 +4.6 +3.3 +4.0 +5.4 +4.9 +2.9 +2.9 +4.6 +2.9 +3.7	Severe fatigue and sleep disturbance. Moderate cognitive impairment. Mild cephalalgia, photophobia, phonophobia, vestibular dysfunction, memory deficits and concentration issues. Additional clinical notes include anxiety
mTBI-28	Frontal:	Caudal mPFC Pars Opercularis Superior Frontal	+3.7 +3.5 +3.1	Moderate cephalalgia, photophobia, phonophobia, restlessness, fatigue and sleep disturbance. Mild cervicalgia, vertigo, vestibular dysfunction, ataxia, cognitive impairment, concentration issues, and memory deficits. Additional clinical notes include nausea, reduced tolerance to physical and cognitive exertion, and impaired coordination
mTBI-32	Frontal: Temporal:	Lateral OFC Middle Temporal	+7.2 +4.6	Moderate cephalalgia, cervicalgia, phonophobia, cognitive impairment, confusion, concentration issues, memory deficit, restlessness, and fatigue. Mild photophobia, vertigo, vestibular dysfunction, visual disturbance, ataxia, irritability, and sleep disturbance. Additional clinical notes include being dazed

Note. Presenting symptoms are primarily derived from BIST injury severity assessments and supplemented with additional clinical patient notes made upon presentation of participants to Axis Sports Medicine clinics. Only participants with abnormal iron profiles are included for brevity and relevance. ID = unique identifier; ROI = region of interest; OFC = orbitofrontal cortex; mPFC = middle prefrontal cortex; STS = superior temporal sulcus; LOC = lateral occipital cortex; ACC = anterior cingulate cortex.

8.4.1.1 *Symptoms and cortical iron-related markers*

To provide a descriptive overview of cortical iron profiles and corresponding symptomatology, it should be noted that cognitive, arousal, vestibulo-ocular/movement, and sensory complaints were commonly reported, whereas mood-related issues appeared less frequently (see Table 8.1). Observational relationships between specific cortical regions and abnormal iron markers suggest that abnormalities in the lingual gyrus (four participants) consistently co-occurred with cephalalgia, photophobia, cognitive impairment (including confusion), concentration issues, memory deficits, and sleep disturbances. The middle temporal region (three participants) appeared to be linked to a broader symptom profile, including cognitive impairment (with confusion), concentration issues, memory deficits, fatigue, sleep disturbances, cephalalgia, phonophobia, photophobia, vertigo, ataxia, and visual disturbances. Although other ROIs were less commonly affected ($\leq$ two participants), some descriptive inferences include the involvement of the superior temporal region (including the superior temporal sulcus and its bank) with cognitive impairment, headaches, photophobia, phonophobia, vestibular dysfunction, memory deficits, concentration issues, fatigue, sleep disturbances, and, in one participant, severe tinnitus and severe irritability.

8.4.2 *Secondary depth- and curvature-specific individualised iron profiles*

Secondary exploratory analyses sensitive to six cortical depths and three curvatures further highlighted the heterogeneity of iron deposition in mTBI. Only 17% (6/35) of participants retained normal iron profiles; the remaining 83% (29/35) showed elevated susceptibility in at least one ROI, for at least one depth and for at least one curvature. Isolated instances of negative z-scores (indicating lower iron compared to HC) were observed in seven of the 29 participants but were typically limited to a single ROI/depth combination. Overall, abnormal iron markers were most pronounced in the sulcal fundus, followed by the sulcal bank, and was least evident in the gyral crown. However, there was significant inter-individual variability in ROI/curvature/depth combinations (see Fig. 8.4).

For the 11 participants who previously demonstrated increased iron markers in the initial whole-ROI analyses, a similar ROI-wise distribution of elevated iron markers was observed in depth- and curvature-specific analyses. For example, in whole-ROI analyses mTBI-28 showed elevated susceptibility in the caudal mPFC, pars opercularis, and superior frontal gyrus (see Table 8.1 and Fig. 8.2), which was localised to specific depths and curvatures in the secondary analyses. In addition, regions that did not appear in the initial analyses, including the insula, lateral occipital cortex, pars triangularis, posterior cingulate, precentral and superior parietal areas, exhibited elevated iron scores in depth- and curvature-specific analyses (see Fig. 8.4). Conversely, mTBI-24 exemplifies a case where no abnormal iron profiles were detected in the whole-ROI analysis, but became evident with analyses sensitive to anatomical morphology (see Fig. 8.4).

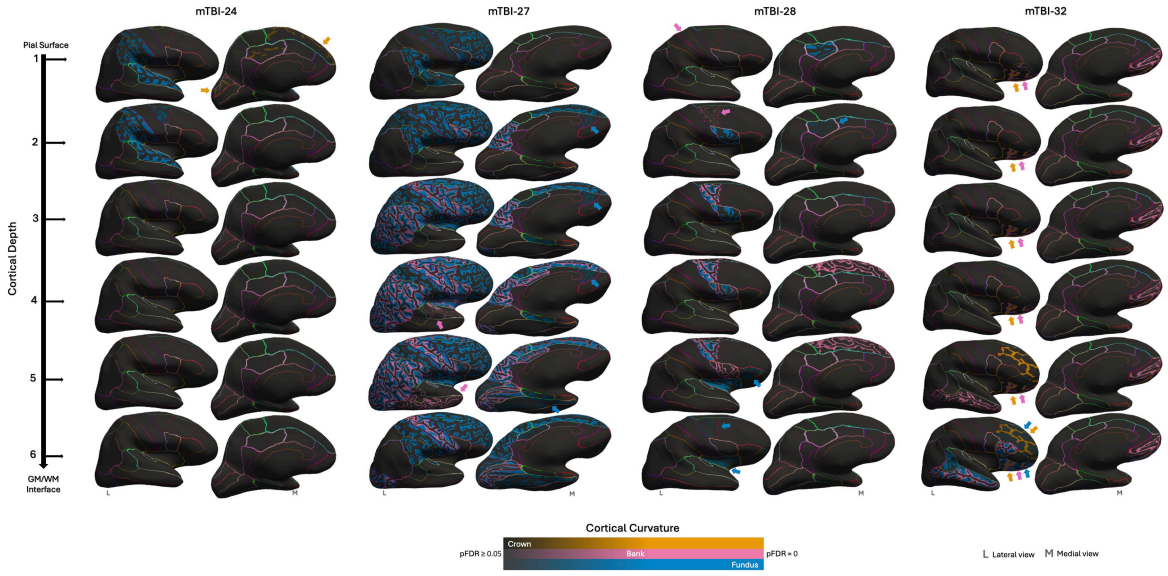

Figure 8.4: Cortical depth- and curvature-specific profiles of mTBI-related abnormal iron markers

Cortical depth- and curvature-specific iron profiles across five representative sr-mTBI participants. Inflated surfaces show each of the six cortical depths, from the pial surface (depth 1) to the GM/WM interface (depth 6). Regions of abnormal iron deposition are colour-coded according to cortical curvature (crown = pink, bank = yellow, and fundus = blue). Colour intensity shows level of statistical significance (pFDR < 0.05). Regions with lower statistical significance are harder to visually distinguish, and are indicated by arrows in the colour of the correspondent cortical curvature. Lateral (L) and medial (M) views are used to visualise the whole brain. Boundaries between ROIs are delineated using coloured lines. pFDR = statistical significance (p-value) after false discovery rate (FDR) correction.

After grouping mTBI participants by iron status based on exploratory depth- and curvature-specific analysis results, a Mann-Whitney U test revealed no significant difference in BIST scores between iron-abnormal (M = 40.6, SD = 33.5) and iron-normal (M = 26.3, SD = 22.4) mTBI participants, U = 63, p = 0.35. An ANOVA showed no significant difference in age between these groups and controls, $F(2, 15) = 1.11$, p = 0.36.

8.5 DISCUSSION

Of the two previous investigations inclusive of cortical ROIs (Gong et al., 2018; Pinky et al., 2022), none have accounted for anatomical variations in cortical depth and curvature, or the influence of inter-individual heterogeneity. The standard group-wise statistical approaches dominating the extant literature may obscure individual brain changes due to the subtle nature of cell damage associated with mTBI. In this chapter, I conducted the first investigation of individual differences in cortical magnetic susceptibility after sr-mTBI across 34 cortical ROIs, using a healthy population template as a reference. Secondary exploratory analyses of individual differences in susceptibility distribution at different cortical depths and curvatures were included to better characterise injury profiles for each participant.

These findings revealed that a substantial subset of individuals with mTBI exhibit elevated levels of cortical positive magnetic susceptibility, indicating injury-related iron accumulation. The primary investigation evidenced abnormal iron profiles in just under one-third (31%; 11/35) of participants relative to the HC population. Additionally, mTBI participants with abnormal iron profiles identified in primary ROI-wise analyses experienced more severe symptoms. In these 11 iron-abnormal clinical participants, elevated iron

profiles were predominantly focal to specific lobes or bi-focal (affecting two lobes). Only one participant exhibited multi-focal cortex-wide elevated z-scores. The high density of affected temporal lobe ROIs indicates that, despite significant inter-subject variability, individual iron-like susceptibility changes following mTBI are preferential to temporal regions. Taken together, these findings support an iron-related mechanism of secondary injury that, in the cortex, modulates symptom severity and may influence symptom presentation.

8.5.1 *Individualised cortical analyses can identify at-risk sub-cohorts*

Iron dyshomeostasis in the basal nuclei is known to impair cognitive function after mTBI (Lu et al., 2015; Raz et al., 2011), however, little is known about the effect of *cortical* iron aggregation on mTBI symptomatology or severity. In Chapter 6 few correlations were apparent between regions of cortical iron accumulation and BIST scores, a measure of injury severity and dominant symptom cluster. In Chapter 6, I posited that this lack of correlation may be accounted for by known variability in the accuracy of symptom reporting or purposeful underreporting of symptoms which is a common phenomenon among sports players (Kroshus et al., 2015; Meier et al., 2015). However, group-level examinations may also obscure individual differences in addition to inhibiting the implementation of more appropriate statistical approaches. Assessing the effect of mTBI at the individual level facilitated more precise between-group analyses of injury severity by differentiating between iron-normal and iron-abnormal mTBI participants for comparison. Results from this primary analysis revealed a significantly higher symptom burden for participants with mTBI when their cortical iron-related profiles were also abnormal.

The field generally lacks reliable correlations between subjective assessments of injury severity and objective measures of brain injury and recovery (McCrea et al., 2017), as well as alignment between cognitive or clinical findings and neuroimaging results (Shenton et al., 2012). Identifying reliable, objective markers of structural changes that are related to subjective self-reported symptoms is crucial because individual variations in brain injury location and severity can lead to vastly different clinical presentations and recovery trajectories but may be missed in group-level analyses (Rosenbaum et al., 2012). Although research indicates that most individuals recover well from mTBI, between 15% (Walker et al., 2013) and 30% (Rosenbaum et al., 2012) of patients experience significant, and in some cases life-changing, long-term clinical sequelae. Understanding the underlying pathophysiological drivers of these poorer outcomes is essential for enabling precise, patient-specific clinical interventions. The finding that 31% of participants exhibited abnormal iron profiles substantial enough to be detected in the primary ROI-wise analyses, which were linked to poorer outcomes, aligns with evidence of structural brain changes detected using advanced MRI in up to 30% of mTBI cases (Maas et al., 2022). In addition, these results support evidence from individualised studies reporting a similar percentage (28%) of ms-TBI cases linked to white matter anomalies in the subacute phase, which are associated with worse cognitive outcomes (Jolly et al., 2021). Standardised susceptibility values in the basal nuclei are also reported to correlate with mTBI symptom duration, but

only in a sub-group of participants with persistent symptomatology for at least a week (Koch et al., 2021).

The results presented here not only reinforce the importance of individualised analyses in revealing associations between the extent of microstructural pathology and negative outcomes following mTBI and the importance of investigating *cortical* ROIs, but also contribute to the sparse literature linking symptomatology to brain changes detectable with advanced neuroimaging. Here, the value of personalised approaches to understanding mild brain injury and differentiating at-risk sub-cohorts becomes strikingly apparent. Further longitudinal studies that track participants through recovery could help to determine whether elevated ROI-wise cortical iron levels are associated with prolonged recovery, persistent post-concussive symptoms, or adverse outcomes later in life. Such research may offer insights into why a subset of individuals with mTBI fail to recover fully.

The promise of individualised assessments to identify biomarkers for mild brain injury is particularly salient given the current absence of objective markers for mTBI diagnosis. Diagnostic decisions are limited to subjective self-report and assessments of physiological function (Lunkova et al., 2021; McCrea et al., 2017), as the heterogeneity of mTBI complicates efforts to identify reliable biomarkers or imaging signatures that can be applied universally across patients. Whether cortical iron accumulation reflects inflammatory processes, BBB disruption (Gozt et al., 2021a), ferroptosis (H. Ma et al., 2022; Tang et al., 2020), or other cytotoxic processes is beyond the scope of the current research. However, the significantly higher symptom burden (BIST score) observed in the iron-abnormal mTBI cohort, as identified via whole-ROI analyses, supports an iron-mediated mechanism of brain changes related to injury severity and functional impairment, and marks cortical iron dyshomeostasis as a promising mTBI biomarker.

8.5.2 *Abnormal regional cortical iron markers and symptom phenotype*

Many of the symptoms observed in mTBI resemble those seen in other iron-mediated neurodegenerative processes, such as cognitive decline in normal ageing (Ghadery et al., 2015), and the cognitive and motor dysfunctions characteristic of diseases like AD, HD, PD, and FRDA, as well as MS, where iron dysregulation is a hallmark feature (Gozt et al., 2021a; Stankiewicz et al., 2007). Genetic disorders of iron overload, such as neuroferritinopathy, also present with cognitive and motor symptoms (Wills et al., 2002). For example, the vulnerability of the temporal lobe to iron accumulation post-mTBI, evident in this individualised study and the results observed in Chapter 6, aligns with the memory impairments characteristic of mTBI (Mckee et al., 2015). Individual-level data from this mTBI sample emphasises the link between high temporal iron accumulation and memory deficits, as exemplified by BIST scores related to memory (see Table 8.1). In addition, dizziness has been related to high strain concentration in the frontal and temporal lobe during sr-mTBI (Viano et al., 2005), potentially accounting for common symptoms related to vertigo and vestibular dysfunction in the present sample.

The diverse range of mechanistic antecedents, pathological mechanisms, and clinical outcomes associated with mTBI reflects the complexity of the underlying pathophysiology (Rosenbaum et al., 2012). mTBI is not a uniform injury, and structural indicators, such as those commonly observed in other forms of TBI, do not always correlate with clinical symptoms or outcomes (Bigler et al., 2012). Here, I speculate that abnormal iron accumulation in specific cortical ROIs may be related to participant symptomatology. For instance, the superior temporal sulcus plays a key role in social cognition, empathy, mentalising about others' emotional states, and "theory of mind" (Basil et al., 2017; Beauchamp, 2015; Deen et al., 2015). Structural changes to this region may explain the severe irritability reported by mTBI-01 (see Table 8.1), along with complaints of severe tinnitus (Leaver et al., 2011). As a hub for audiovisual integration (Hein et al., 2008), the superior temporal region could also be involved in phonophobia (sound sensitivity), visual disturbances, and vestibular dysfunction (Dieterich et al., 2008); symptoms experienced by both mTBI participants whose profiles indicated local elevations in cortical iron. Similarly, the lingual gyrus is active during migraine episodes and responds to luminous stimuli, suggesting its involvement in photophobia, visual processing anomalies, and cephalalgia (headache) (Boulloche et al., 2010). These symptoms were observed in all clinical participants with abnormal iron markers in this region (see Table 8.1). These findings allude to specific areas of cortical iron accumulation that show a relationship to clinical sequelae, suggesting that regions with higher iron burden may be evidence of microstructural cell damage that disrupts normal function.

Here, it should be noted that multiple cortical regions with abnormal iron markers were observed for most mTBI participants, making it challenging to delineate a one-to-one relationship between a specific ROI and symptoms reported. As such, future research should integrate functional MRI to improve the mapping of structural changes to deficits in functional connectivity and well-established brain networks, that may overlap with abnormalities in cortical grey matter regions. Without additional research, observations about regions of iron accumulation and symptom presentation are speculative and much less convincing than case-matching between brain lesions in gross TBI and neurobehavioural symptom presentation (Levin et al., 1987).

8.5.3 *Dominant spatial distributions of abnormal regional cortical iron markers*

Cranial morphology and injury biodynamics once again provide fertile ground for understanding the aggregate distribution of abnormal z-scores across the cortical regions. Iron-related abnormalities were most concentrated in the temporal lobe region, followed by the occipital and then frontal lobes, with fewer occurrences in the insular and cingulate cortices, and only a singular incidence in the parietal cortex. Previous chapters (Chapter 6 and Chapter 7) have examined the significance of the middle cranial fossa morphology to the specific spatial locations of significant findings. This bony hollow cradles the temporal lobe surface and features irregular bony protrusions including, but not limited to, the sphenoid ridge at the intersection of the anterior and middle cranial fossa which ex-

poses the anterior and medial aspects of the temporal lobe to injury (Bigler, 2007). However, this does not represent the sole instance of close brain-skull contact. The anterior cranial fossa hugs the entire frontal lobe surface, with the exception of the medial aspect. The sphenoid ridge, bridging the frontal and temporal skull base, is thus uniquely positioned to expose the posteroinferior frontal lobe deformation and contusion (Bigler, 2007). Although mild TBI typically does not involve severe tissue damage, contact with the skull base may cause microstructural disruption in these regions, potentially accounting for observed spatial distributions of abnormal iron markers in this sample. A post-mortem examination of the effects of mTBI, in which the individual died from causes unrelated to the injury, reinforces the hypothesis that these regions are focal sites of injury. In this case, brain tissue extracted from both frontal and temporal regions exhibited abnormal accumulations of haemosiderin-laden macrophages (Bigler, 2004), suggesting microvascular dysfunction and breaches of the BBB (Mckee et al., 2015) that likely initiate a microhaemorrhage-induced immune response (Nisenbaum et al., 2014).

In this context, the detection of abnormal iron markers in only two regions of the occipital cortex is particularly compelling. Here, the lingual gyrus corresponded to the highest recorded incidence rate of abnormal z-scores across the entire sample (four participants), suggesting that this region may be uniquely vulnerable to injury-related iron dyshomeostasis. Situated on the medial inferior surface of the occipital lobe, the anterior portion of the lingual gyrus gradually merges with the parahippocampal gyrus along the tentorial surface (Palejwala et al., 2021). The connection between these regions, where fibers originating in the lingual gyrus terminate in the parahippocampal gyrus, suggests continuity between the whole-group findings reported in Chapter 6 and these individual-level results. Connections with the temporal lobe also characterise the lateral occipital cortex; the sulcus of this region is nearly continuous with the superior temporal sulcus (Palejwala et al., 2020). This reinforces a relationship between high concentrations of abnormal iron markers observed in temporal, followed by occipital, regions. However, whether the abnormal iron markers observed in these regions result from focal excitotoxicity, compromised integrity of interconnected fiber projections due to DAI, disruption of afferent or efferent targets, a combination of these factors or other as-yet-unexplored injury mechanisms is beyond the scope of the current study.

Head kinematics involved in mTBI may also be relevant, however speculation is hindered by a complex and sometimes contradictory literature (A. I. King et al., 2003). The movement of the brain is influenced by diverse inertial forces with considerable inter-individual variability, though a growing consensus identifies accelerational loading on the brain as a common denominator (Meaney et al., 2011). These forces comprise linear (translational) and rotational acceleration. While rotational acceleration is more frequently associated with both focal and diffuse injuries, linear acceleration is often cited as a precursor in focal injury only (A. I. King et al., 2003). However, both appear to be nearly universal to mTBI events (Meaney et al., 2011). Coupled with limitations imposed by an absence of representative data and a diverse range of possible mechanisms leading to sr-mTBI, inference regarding specific inertial forces is precluded. Nonetheless, at a more macroscopic level the

aggregate distribution of abnormal iron markers in cortical regions is congruent with evidence from finite element analysis. Data from these simulations indicate that lateral impacts tend to produce more severe injury-induced pathology relative to frontal impacts. This decreased injury tolerance is attributed to larger skull deformations, increased intracranial pressure, and heightened exposure to shear stress (L. Zhang et al., 2001).

While frontal head impacts, side impacts, and backward falls are primary factors in the genesis of head injuries in sr-mTBI (Pellman et al., 2003), this regional vulnerability hypothesis may offer an explanation for the higher incidence of abnormal iron markers in the temporal cortex. Extending observations from the study cited above, this hypothesis is further supported by additional finite element analyses using dummy reconstructions from National Football League games to simulate sr-mTBI impacts (Viano et al., 2005). Here, initial “hot spots" of focal strain and increased deformation were localised to the temporal lobe adjacent to the site of impact at 8 ms, but migrated to the opposite temporal lobe at 18 ms, representing potential evidence of coup-contrecoup injuries in bilateral temporal cortices. Less damaging mechanisms of injury in sports participation may also be consistent with the secondary incidence of abnormal iron markers observed in the occipital cortex, followed by the frontal cortex. As contrecoup injuries may be more severe than coup injuries (Drew et al., 2004), a higher incidence of abnormal iron markers in the occipital cortex hints at a higher prevalence of frontal impacts in this sample.

8.5.4 *Depth- and curvature-specific alterations in positive susceptibility: a common feature of mTBI?*

Secondary exploratory analyses revealed significant inter-individual heterogeneity in depth- and curvature-specific cortical iron markers. Prior research has noted associations between both injuries at the pial surface (McKee et al., 2013) and closer to the GM/WM border (Pankatz et al., 2023) with adverse outcomes after mTBI. Although these subtle effects were not associated with injury severity, they corroborate extant evidence of depth-specific, mTBI-induced cellular disruption, and suggest that widespread minor tissue alterations may characterise mTBI. Across participants, a consistent trend for abnormal iron markers was observed in the sulci, with the highest concentrations at the fundus, followed by the sulcal bank. This is aligned with speculations made in Chapter 6 that dominant curvature-specific alterations to positive susceptibility may be attributed to the heightened vulnerability of the sulcal fundus. To briefly revisit the precise injury mechanisms, the sulcal fundus is particularly vulnerable to mechanical deformation (Bakhtiarydavijani et al., 2021; Ghajari et al., 2017) and the “water hammer" effect, where the movement of non-compressible CSF concentrates forces at the base of the sulcus (Kornguth et al., 2017). Conversely, in more severe TBI, contusions are often concentrated at the gyri (Mckee et al., 2015), suggesting that gyral iron accumulation in *mild* TBI may represent a less severe version of this type of injury. An understanding of injury biomechanics may thus prove crucial to explaining variance in loci of neuropathological changes.

Histological studies, including Perls iron staining and ultrahigh-field (7T) R_2^* mapping of tissue samples (Fukunaga et al., 2010) have localised iron deposition to specific cortical layers, reflecting distinct cyto- and myelo-architectural features with layer-specific distributions that show congruence with *in vivo* QSM (Shin et al., 2021). In healthy populations, iron concentrations typically increase from the pial surface toward the GM/WM boundary; deviations away from baselines for each layer suggest an injury-specific model of cortical cellular trauma. For instance, layer I primarily contains axons and dendrites, with the cell bodies in deeper layers (Miyashita, 2022); iron accumulation in different layers may point to diverse pathologies affecting different parts of the cell. Depth-wise patterns may also be related to injury biomechanics: superficial iron accumulation may be a result of perivascular trauma, which is often linked to microhaemorrhages and microglial activation after mTBI (Huang et al., 2021; Mckee et al., 2015; Nisenbaum et al., 2014), whereas deeper iron deposition may reflect more severe shear forces, which are known to cause significant damage near the GM/WM interface in mTBI (Pankatz et al., 2023). This is supported by computational modelling showing shear forces are concentrated in this region (Ghajari et al., 2017), which is also a common site of microbleeds (J. Liu et al., 2014). Tying this in with investigations of cortical curvature, these effects would likely be concentrated at the sulcal fundus (Ghajari et al., 2017; Kornguth et al., 2017; McKee et al., 2013). However, evidence from TBI research also supports the presence of gyral contusions that often follow a layer-specific pattern, with damage prominent at the superficial crest but extending through the cortical mantle to the GM/WM boundary in a “wedge" of haemorrhage and necrotic tissue (Mckee et al., 2015). As iron is also implicated in cell death (H. Ma et al., 2022; Tang et al., 2020), a similar mechanism could plausibly account for instances of iron-related gyral pathology in mTBI that exhibit similar depth-specific patterns.

The predilection for abnormal iron markers concentrated in the temporal regions and in the sulcal fundus (Bieniek et al., 2021; McKee et al., 2023; Murray et al., 2022) reinforces the concerns raised in Chapter 6 and Chapter 7 regarding the speculative relationship between acute iron dysregulation and degenerative cascades culminating in later-life pathology in some cases (Bouras et al., 1997; Yamamoto et al., 2002; Zecca et al., 2004). Such patterns may not only provide insights into the distribution of cellular excitotoxicity experienced by individual participants during the acute stage, but may also serve as a preliminary marker for worse short-term clinical symptomatology and long-term health outcomes. Exploration of the interplay between acute elevations in positive susceptibility, symptom burden, temporal recovery dynamics, and long-term brain health outcomes is warranted; elucidating this link should be a focus for future research.

8.5.5 *Limitations and future research*

Resolution and depth-related constraints, along with the potential for PVE addressed in Chapter 6 apply equally to the present study. Similarly, the limitations related to filtering, confounds related to known age-related increases in cortical susceptibility within this age range (Hallgren et al., 1958), generalisability, small and unequal sample sizes for between-

group comparisons, and the inability to perform one-to-one symptom mapping, as discussed in Chapter 7, are also relevant. However, limitations specific to this individualised cortical approach remain.

As previously discussed in Chapter 6, depth-wise sampling at comparable resolutions (Y. Ma et al., 2023) has been shown to preserve cortical features similar to those investigated in ultrahigh-field (11.7T) depth-specific studies (Aggarwal et al., 2015). However, the model presented here adopts a more conservative approach compared to the 21-depth method employed in Chapter 6 and prior research (Y. Ma et al., 2023; Merenstein et al., 2024; Northall et al., 2023), as well as the 10-depth approach described by Sui et al. (2022). Sampling even fewer depths (e.g., three versus six) could arguably capture overall thickness of the ∼1-4.5 mm wide cerebral cortex (Fischl et al., 2000) and avoid redundancy; however, sampling fewer depths appears to forfeit distinct susceptibility features uniquely revealed by a six-depth model (see Fig. 8.5 and Appendix A). Given potential inter-individual variability in cortical thickness, there is a need for individualised approaches that are sensitive to such heterogeneity.

In addition, this study does not address the precise mechanisms by which different types of mechanical strain contribute to depth- and curvature-specific patterns of potential iron accumulation. Whether these patterns are driven by depth-wise shear forces near the GM/WM interface (Ghajari et al., 2017; Pankatz et al., 2023) or reflect superficial perivascular damage (Huang et al., 2021; Mckee et al., 2015; Nisenbaum et al., 2014), or whether curvature-related deposition may be due to the "water hammer" effect at the sulcal fundus (Kornguth et al., 2017) or contusions of the gyri (Mckee et al., 2015), or a combination of all of these factors, remains unclear. To address this, future research should track athletes throughout the sporting season to better understand how specific injury biomechanics may be related to patterns of iron markers across different cortical depths and layers. Tracking athletes over an extended time-frame could also provide valuable insight into the relationship between potential iron accumulation, symptom progression, and the risk of neurodegeneration.

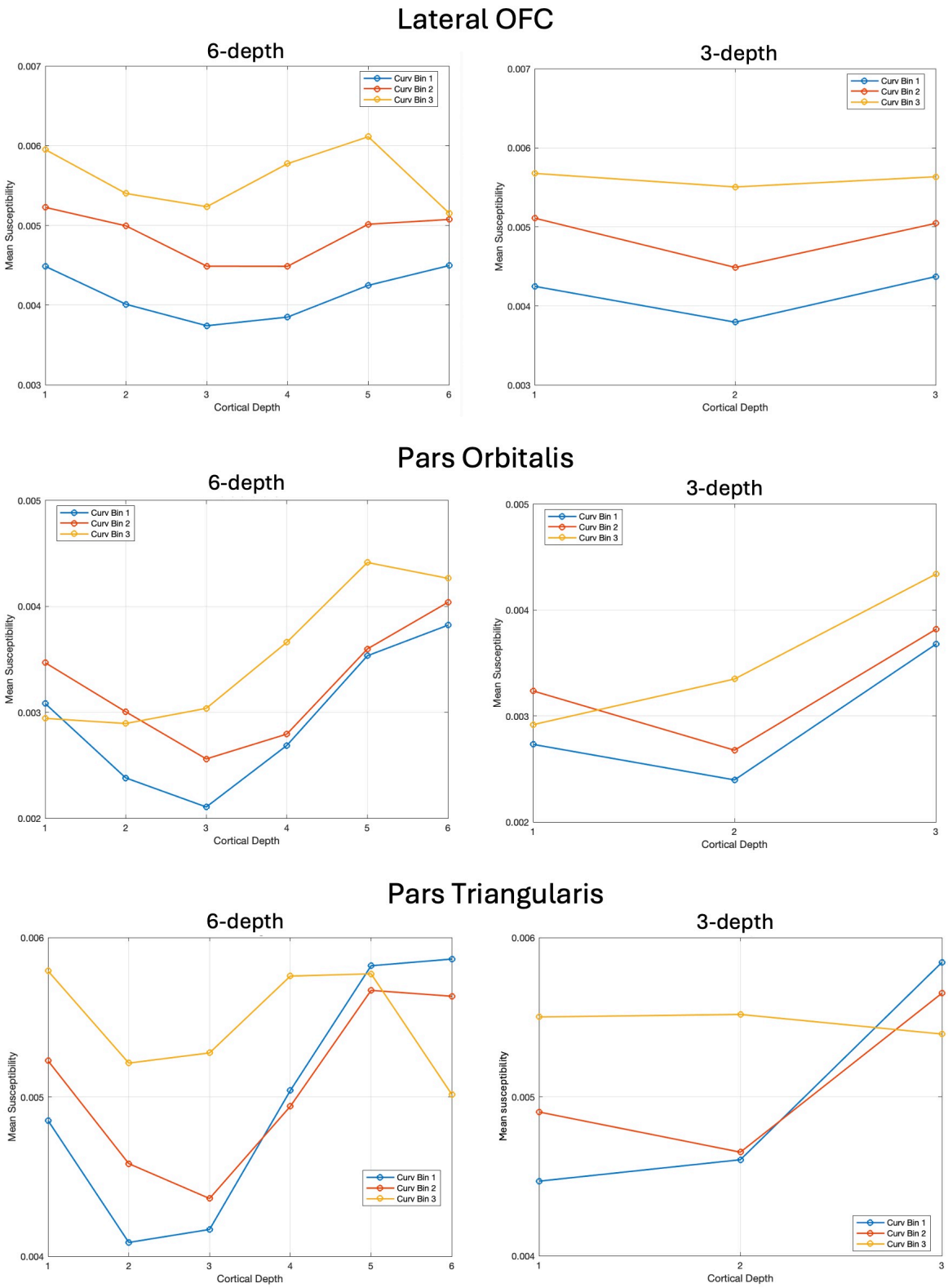

Figure 8.5: Comparison of three- and six-depth models for susceptibility localisation

This figure shows comparative graphs illustrating the effects of sampling at six (left) versus three (right) cortical depths for each curvature bin (crown = blue; bank = orange; fundus = yellow) across three representative cortical ROIs examined in this individualised study. While sampling at six depths may introduce some redundancy into the model, the overall susceptibility patterns remain similar. Restricting the analysis to three depths appears to risk overlooking subtle yet informative differences that only emerge at finer depth granularity. Susceptibility is measured in ppm, and each ROI is scaled to the most appropriate reference range. OFC = orbitofrontal cortex.

8.6 CONCLUSIONS

The results presented here suggest that iron-mediated cell damage in the cerebral cortex may play a key role in mTBI pathology, and that individualised approaches can further elucidate the clinical relevance of iron markers in mTBI. In keeping with the heterogeneity of mTBI, the location of abnormal iron markers after injury was person-specific and may have been influenced by cortical morphology. Differences in injury severity between iron-normal and iron-abnormal mTBI participants highlight why precise investigation is required to understand the link between objective changes in the brain and subjective symptomatology. These results highlight the importance of examining mTBI at an individual level rather than relying on group analyses. This variability likely also complicates the search for universal biomarkers, further underscoring the need for personalised, objective approaches that integrate advanced imaging and detailed symptom profiling.

General Discussion

9

GENERAL DISCUSSION

"Truth... is much too complicated to allow anything but approximations."

John von Neumann

The research conducted in this thesis was designed to address the current under utilisation of QSM in mTBI research, overcome specific limitations of the extant literature, and contribute to a deeper understanding of the microstructural brain tissue alterations occurring as a result of this complex yet subtle injury. This was achieved through three overarching aims that guided development of each of the interrelated QSM-based studies comprising this thesis. The first aim was to *advance the current understanding of mTBI-related changes to brain tissue composition.* The second aim was to *refine and apply techniques that enhance sensitivity to injury-related changes in the brain.* Finally, the third aim sought to *elucidate the differing utilities of traditional group-level analyses versus individualised analytic approaches.* This final discussion first restates the central findings of the research conducted in this thesis. Next, the utility of a threshold-based approach to QSM analysis is discussed. Findings from both the group-level and individualised analytic approaches employed across the studies are then synthesised and their individual and aggregate contributions to the broader scientific literature explored; an approach not possible for each chapter in isolation. This facilitates a comparison of the respective strengths and limitations of different analytic techniques, highlighting the contexts within which each model can be most effectively applied to deepen the current understanding of mTBI. Following this, a unified framework predicated on the findings of each of the respective studies is presented, which serves to highlight common features of brain tissue dyshomeostasis in mTBI and how these central findings represent a critique of the narrow methodologies that constitute the prevailing approach to QSM-based investigations. The limitations applicable to all studies are discussed, and followed by recommendations for future research directions aimed at augmenting and extending the methodologies and findings presented in this work. The thesis is concluded with some final thoughts and closing remarks in § 9.8.

9.1 A SUMMARY OF THE RESULTS OF THESIS

These investigations mark the first application of QSM to characterise depth- and curvature-specific alterations in the cerebral cortex and hippocampal subfields following mTBI, as well as the most extensive examination of the basal ganglia and related nuclei. The alignment of both group- and individual-level findings throughout this thesis with established regional and cellular vulnerabilities suggests that failure to detect similar effects in the wider QSM-mTBI literature may stem from insufficient spatial specificity rather than an absence of pathology. In comparing these results with the extant literature, the findings presented here highlight the importance of incorporating enhanced modelling of cortical and subcortical regions, along with a vulnerability-based framework for ROI selection and analysis. These contributions provide both a rationale and foundational framework for extending investigations in future quantitative MRI studies of mTBI. The results also reinforce recent critiques highlighting the neglect of the hippocampal subfields and other critical regions in QSM-based mTBI research (Gozt et al., 2021a). These central findings and the interrelated nature of results across the studies comprising this thesis are discussed in detail in the subsequent sections of this chapter. Below is a summary of the primary findings upon which the following discussion is based:

- **Inter-voxel thresholding is a viable approach to single-echo QSM analysis in mTBI.**
- **Anatomical specificity is both useful and likely necessary in QSM-based analysis in the context of mTBI.**
- **The spatial distribution of microstructural tissue content alterations may correspond with known injury mechanisms.**
- **Dyshomeostasis of biomagnetic substrates in the medial temporal region may represent a common feature of microstructural mTBI-related pathophysiology.** This finding was supported by the results of all investigations presented in this thesis.
- **Cortical regions are vulnerable to tissue disruption and adverse clinical outcomes following mTBI.** This finding was exemplified in the significantly higher symptom burden for mTBI participants with abnormal regional cortical iron markers relative to mTBI participants exhibiting no such deviation from the healthy normal distribution.
- **Analytic strategy choices should be tailored to the research objective.**
- **Group-level analyses are effective at identifying spatial patterns of tissue disruption that may constitute a shared feature of mTBI.**
- **Individualised analytic approaches are essential for capturing the heterogeneity of mTBI.** Evidence for this is supported by prevalence of individual-specific paramagnetic alterations that were not apparent in group-level analyses.

9.2 INTER-VOXEL THRESHOLDING IS A VIABLE APPROACH TO SINGLE-ECHO QSM ANALYSIS IN MTBI

To date, no QSM-based studies have differentiated magnetic sources in mTBI, either by thresholding (Merenstein et al., 2025; Merenstein et al., 2024) or magnetic source separation (Ahmed et al., 2023; J. Chen et al., 2021; Emmerich et al., 2021; J. Lee et al., 2024; Z. Li et al., 2023; Shin et al., 2021). Though not the focus of this thesis, it is nonetheless essential to understanding the relevance of the collective findings, and serves as a precursor to the general discussion provided in this chapter. In Fig. 9.1 below, I illustrate how thresholding can refine the estimation of magnetic susceptibility in two regions, the subcortical hippocampal CA4 and cortical parahippocampal gyrus, both of which exhibited significant group-level effects in the corresponding research investigations (Chapter 5 and Chapter 6, respectively). Compared with a thresholded approach, analysis of raw QSM effectively averages the susceptibility contributions from positive and negative voxels within these ROIs, diminishing the contrast between them. As a result, mean positive and negative susceptibility values in both the parahippocampal gyrus and the CA4 region are more pronounced in thresholded maps; in raw maps, the contributions are markedly attenuated. Although a significant increase in susceptibility remains evident in the superficial sulcal regions of the parahippocampal gyrus when using raw QSM, significant negative effects disappear in cortical and subcortical regions. Consequently, potential alterations in myelin integrity (Bradl et al., 2010; Hametner et al., 2013; Lassmann et al., 2012) or indicators of cellular stress responses, possibly reflecting early phagocytic activity (Yu et al., 2022), may be masked by stronger iron-related paramagnetic signals. This underscores the value of thresholding for mitigating certain confounding factors and the potential for improving biological interpretations. It is, however, important to acknowledge the limitations of thresholding, which are addressed in detail in the corresponding section of this discussion.

9.3 ANATOMICAL SPECIFICITY IS BOTH USEFUL AND LIKELY NECESSARY IN QSM-BASED ANALYSIS IN MTBI

The works included in thesis collectively reinforce the hypothesis that reliance on narrow methodologies that lack anatomical specificity may, at least in part, account for the general paucity of significant findings that characterise the extant literature (see Chapter 3 for additional details). To date, no studies have reported significant increases in grey matter magnetic susceptibility in an mTBI cohort in any region of the cerebrum (Bell et al., 2024; Gong et al., 2018; Koch et al., 2018; Pinky et al., 2022; Wright et al., 2022; Zivadinov et al., 2018a). One study (Koch et al., 2021) has reported significantly decreased susceptibility in total deep grey matter sub-compartments, however, the validity of this finding is limited by the lack of anatomical specificity and related PVE both from susceptibility sampled across multiple subcortical nuclei to derive an aggregate value and the use of data acquired with anisotropic voxel resolutions (Karsa et al., 2019a). Pinky et al. (2022) have been the only investigators, prior to the current works comprising this thesis, to report significantly in-

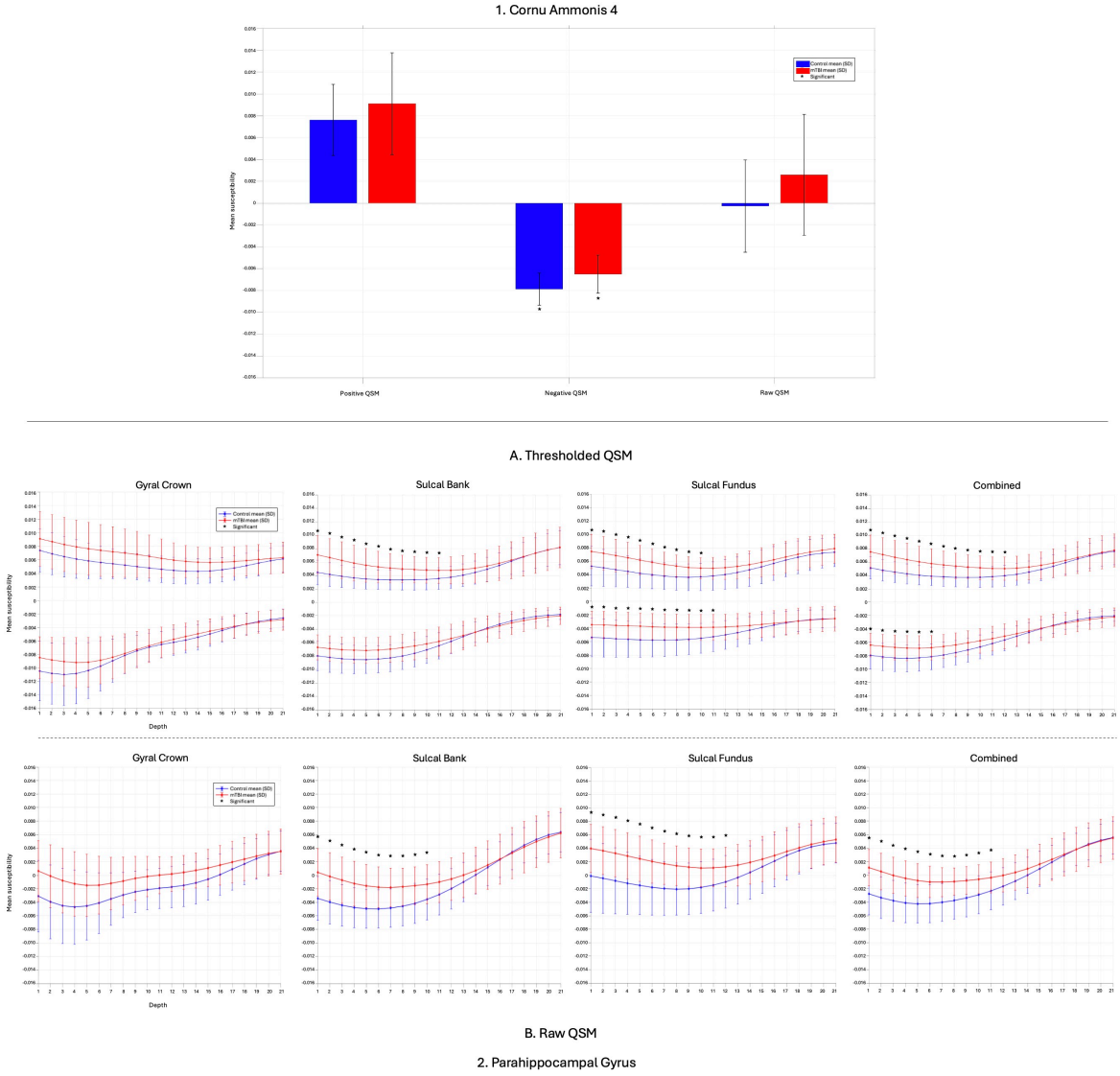

Figure 9.1: The effect of thresholding on susceptibility estimation

⋆ = significant differences between groups after FDR correction ($pFDR < 0.05$).

1. Shows susceptibility estimation for mTBI (red) versus HC (blue) using thresholded (QSM^{+} and QSM^{-}) as well as raw maps in the CA4 region 2. Provides an isolated view of depth- and curvature-specific cortical susceptibility estimation in the parahippocampal gyrus for mTBI (red lines) versus HC (blue line) participants for thresholded positive and negative susceptibility (A) and raw (B) QSM maps at each depth for each curvature. Both figures highlight the averaging effect and loss of detail when using raw QSM for analysis. Susceptibility is measured in ppm between +0.016 and -0.016. Standard deviation (SD) is depicted for both figures to show the spread of the data.

creased grey matter magnetic susceptibility after mTBI using QSM, which was localised exclusively to the cerebellum. In light of the known vulnerability of the cerebellum to injury from proximity to the occipital cranial fossa (Bigler, 2007) these results are particularly interesting. This, like the medial temporal lobe region exhibiting similar anatomical vulnerability (Bigler, 2007), is potentially subject to a more extreme tissue response.

This regional vulnerability is underscored by the persistence of significant increases in susceptibility in the superficial parahippocampal gyrus in Fig. 9.1, even in the presence of potentially more extreme inter-voxel averaging when using raw QSM. The only two QSM-mTBI studies to include cortical grey matter ROIs were either constrained by a mac-

roscopic voxel-wise approach (Gong et al., 2018), or limited to gross segmentations of a small number of cortical ROIs (Pinky et al., 2022). Here, identification of increased susceptibility using a depth- and curvature-specific analytic approach applied to unprocessed QSM enables a more analogous comparison with the singular investigation of the parahippocampal gyrus as a homogeneous cortical parcel conducted by Pinky et al. (2022), which reported no difference between mTBI and controls in this region. These results highlight the importance of anatomical specificity in cortical investigations where the distinct cyto- and myelo-architectural features characterising different layers of the cortical mantle (Brodmann, 2005; Waehnert et al., 2016) may influence topographically heterogeneous tissue content changes after injury.

There is also large variation in mechanical forces acting on different cortical layers, for example, potential impact with the skull at the cortical surface (Bigler, 2007) and shear/strain at the GM/WM interface (Pankatz et al., 2023) which may further amplify layer-specific heterogeneity. As such, MRI methodologies should be responsive to these variables while also accounting for data constraints. In the absence of ultrahigh-field imaging ($\geq$7T) and sub-millimetre voxel resolutions, both of which are crucial for discerning specific cortical laminae (Trampel et al., 2019), column-based analytic techniques (Y. Ma et al., 2023; Merenstein et al., 2024; Northall et al., 2023; Sui et al., 2022; Waehnert et al., 2014) that enable depth-wise investigations of cortical susceptibility should be used to investigate mTBI, as demonstrated here.

The importance of spatial specificity in investigations of mTBI is equally important for subcortical structures. Although several neuroimaging studies have evidenced iron dyshomeostasis in major basal structures such as the thalamus (Raz et al., 2011) and related nuclei (Chong et al., 2023; Lu et al., 2015), as well as in the hippocampus (Lu et al., 2015; Nikolova et al., 2022), QSM-based investigations have not consistently reported similar associations. This inconsistency may partly reflect a predominant focus on global susceptibility estimation in total deep grey matter or on major basal substructures such as the thalamus, caudate, putamen, and undifferentiated globus pallidus (Bell et al., 2024; Gong et al., 2018; Koch et al., 2018; Koch et al., 2021; Pinky et al., 2022; Wright et al., 2022; Zivadinov et al., 2018a). Even in studies extending their analyses to additional subcortical areas, including the nucleus accumbens, amygdala, and hippocampus, the reliance on gross segmentation techniques precludes differentiation of related nuclei and the hippocampal subfields (Pinky et al., 2022; Zivadinov et al., 2018a).

Not only does this approach risk overlooking potentially informative tissue content alterations in discrete subcortical nuclei, but it also fails to account for the extensive variability in cellular architecture, connectivity, and function that characterise the basal ganglia and hippocampal structures (Ding et al., 2015; Lanciego et al., 2012). In particular, conventional approaches neglect the well-documented subfield-specific vulnerabilities in the hippocampus, which result from differences in neurochemical properties and the presence of injury-sensitive cell populations (Geddes et al., 2003; Lowenstein et al., 1992; Santhakumar et al., 2000; Scharfman, 2016), as well as biomechanical factors related to cranial-dural morphology (Bigler, 2007). Overlooking these regions constrains our understanding of mTBI

pathophysiology at scale and may inhibit reliable association between specific loci of susceptibility changes, mechanisms of injury, and distinct clinical phenotypes.

9.4 THE SPATIAL DISTRIBUTION OF MICROSTRUCTURAL TISSUE CONTENT ALTERATIONS MAY CORRESPOND WITH KNOWN INJURY MECHANISMS

Across both group-level and individualised analyses, the findings in this thesis consistently demonstrate the vulnerability of the cerebral cortex and hippocampus to mTBI-related tissue content disruptions detected via QSM. In this work, the more commonly investigated basal ganglia appeared relatively spared in comparison. This heightened vulnerability is especially pronounced in the temporal lobe, and more specifically within the inferior medial temporal region. Within the cortex, sulcal regions, especially the sulcal fundus, were repeatedly identified as focal sites of tissue disruption. Taken together, these convergent data highlight discrete loci of tissue dyshomeostasis that align with established regional vulnerabilities where fluid dynamics, head kinematics, injury biomechanics, cranial-dural morphology, or inherently vulnerable cell populations confer an elevated injury risk. To synthesise these observations, I present a unified framework that offers a more holistic perspective than is possible when examining each region and analytic approach in isolation.

9.4.1 *Dyshomeostasis of biomagnetic substrates in the medial temporal region may represent a common feature of microstructural mTBI-related pathophysiology*

Each study presented in this thesis highlights the temporal lobe's heightened susceptibility to mTBI-related tissue alterations, potentially reflecting the more severe effects of lateral impacts and a lower injury threshold in this region (Viano et al., 2005; L. Zhang et al., 2001). This was empirically supported by the high concentration of abnormal iron markers identified within the temporal lobe when aggregating individualised cortical data across mTBI participants. Secondary incidences were identified in the occipital, followed by the frontal lobes, with minimal evidence of iron-related tissue disruptions in the insular/cingulate and parietal cortices. Such distribution patterns align with established variations in lobe-specific susceptibility and the differential effects of head kinematics that vary along a continuum of severity (Pellman et al., 2003; Viano et al., 2005).

In particular, the medial temporal region appeared to be disproportionately affected across the wider sample. Group-level cortical analyses highlighted the parahippocampal gyrus, situated on the inferior anteromedial surface of the temporal lobe, as a locus of significant positive and negative susceptibility differences between the mTBI cohort and controls, potentially reflecting concomitant iron increases and disruption to neuronal components including myelin. The vulnerability of the medial temporal region was further supported by the singular finding of reduced negative susceptibility in the hippocampal CA4 identified by group-level subcortical analyses, as well as by the prevalence of iron-related abnormalities in the hippocampus, relative to the basal ganglia and associated nuclei, when examined at the individual level. When hippocampal iron markers were

aggregated across mTBI participants, they clustered primarily within the parasubiculum in the anteromedial head of the hippocampus, with fewer observed in more lateral and posterior regions.

The anatomical vulnerability of both the hippocampus and the parahippocampal gyrus encircling it (Webb, 2017), can be attributed to their proximity to the sphenoid ridge, located at the junction of the anterior and middle cranial fossae (Bigler, 2007). The free edge of the tentorium cerebelli transverses the length of the medial temporal lobe, offering reduced structural support and heightening the risk of impact (Bigler, 2007). The morphology of the parahippocampal gyrus is such that as curves upward, it is pressed against the tentorial notch and unprotected by dura. In addition, the hippocampal head lies less than 2 cm from this bony peninsula. Both the hippocampal head and parahippocampal gyrus have been identified as focal sites of tissue pathology in TBI as a result of this anatomical alignment (Bigler, 2007).

In sr-mTBI, the parahippocampal gyrus has demonstrated reductions in volume and cortical thickness (Arciniega et al., 2024) and has been identified as a "hot spot" for impact in simulations of mTBI events during sports games (Viano et al., 2005). Hyper-excitable parasubicular neurons (Sullenberger et al., 2019) may further exacerbate metabolic toxicity in mTBI; a known risk factor for iron overload (Huang et al., 2021). Evidence of extensive neurodegeneration and NFT formation in both the parahippocampal gyrus (Van Hoesen et al., 2000) and parasubiculum (Van Hoesen et al., 1990) in AD highlights the vulnerability of these regions and their cell populations not only to traumatic injury but degenerative processes, for which iron may serve as a mediating factor. This is particularly concerning in the context of mTBI given the risk of later-life neuropathology including CTE, which shares tauopathy as a common pathological feature with AD (Turner et al., 2016). The spatial alignment of abnormal susceptibility markers observed across individual- and group-level analyses further corroborates these regional vulnerabilities.

Although the temporal lobe emerged as a the most frequent site of abnormal iron markers in individual-level cortical analyses, the occipital lingual gyrus was the single most common locus of abnormal z-scores among mTBI participants in the primary analysis. This important caveat nonetheless serves as an indirect confirmation of the overarching region-of-risk hypothesis centred on the medial temporal region. Situated on the inferior anteromedial surface of the occipital lobe, the lingual gyrus extends anteriorly to merge with the parahippocampal gyrus along the tentorial surface (Palejwala et al., 2021). This anatomical continuity, which is also reflected in their shared role in certain aspects of spatial memory (Sulpizio et al., 2013), suggests a common pathway for mTBI-induced susceptibility changes. Rather than isolated events, disruptions in one region may affect downstream targets or extend to structurally connected regions, giving rise to tissue alterations that reflect common injury mechanisms or biomechanical stressors.

This vulnerability to disruption and degeneration of the temporal lobe region is also reflected in a range of neurological conditions, including as a hallmark feature of AD (Braak et al., 1991; Migliaccio et al., 2022; Ravikumar et al., 2024), lobar degeneration with TPD-43-immunoreactive pathology type-C (Peet et al., 2021), and temporal lobe epilepsy

(Kiersnowski et al., 2023). The temporal lobe region as a nexus across pathologies suggests that despite differences in aetiology and mechanism, certain characteristics of this region may predispose it to selective vulnerability. Indeed, the unique cytoarchitecture (Braak et al., 1991), extensive connectivity and cellular excitability (Palop et al., 2006; Palop et al., 2007), as well as altered metabolic function (Mosconi, 2005) have been noted in multiple neurological conditions. In the context of mTBI, these features may exacerbate neuropathology, further corroborating the likelihood of a medial temporal lobe-centric region-of-risk hypothesis reflected in focal tissue disruption across cortical and subcortical investigations in this thesis.

Discrepancies between the group and individual-level cortical findings, namely the general absence of parahippocampal abnormalities identified by individualised analyses, likely stems from differences in methodology and statistical thresholds. It is reasonable to suggest that parahippocampal gyrus disruptions were sufficiently consistent across participants to reach statistical significance in depth- and curvature-specific group-level analyses. In contrast, the z-test method applied to individual-level data used more stringent FDR corrections (21 vs. 34 ROIs, respectively) and the primary ROI-wise analyses treated each cortical region as a homogeneous parcel, potentially reducing sensitivity to parahippocampal susceptibility alterations. In addition, abnormal iron markers in the lingual gyrus were present in only four participants, suggesting altered susceptibility in this region may not be as prevalent.

The high incidence of iron-related abnormalities in the fimbria of the fornix and the mammillary nucleus, observed in individual-level subcortical analyses, illustrates that structural and functional interconnectedness, particularly with the medial temporal lobe, may be a risk factor for focal pathology. This phenomenon has been reported in severe TBI, where post-injury pathology in these downstream regions is thought to stem from medial temporal lobe trauma (Bigler, 2007). Both structures may also be susceptible to mechanical strain during impact (Viano et al., 2005), potentially exacerbating focal excitotoxicity. Interconnection of the mammillary nucleus with the parasubiculum (Rich, 2018), the two structures with the highest recurrence and concomitance of iron-related abnormalities across participants, further exemplifies how shared vulnerabilities may amplify secondary injury cascades.

Aside from the mammillary nucleus, the major nuclei of the basal ganglia and related structures exhibited a conspicuous lack of significant findings across studies. This observation is consistent with other QSM-based investigations that have universally reported no evidence of susceptibility increases in these deep structures following mTBI (Bell et al., 2024; Gong et al., 2018; Koch et al., 2018; Pinky et al., 2022; Wright et al., 2022; Zivadinov et al., 2018a). It is possible that imaging methods other than QSM, for instance MFC (Raz et al., 2011), SWI (Lu et al., 2015), and T_2^* (Chong et al., 2023; Nikolova et al., 2022), may be more sensitive to detecting potentially subtler changes in the basal ganglia. However, the basal ganglia and related nuclei, located deep within the cerebrum (Webb, 2017), may be relatively shielded from inertial forces that are most pronounced in superficial and anterior

brain regions (McAllister, 2011), and impact with the skull base is likely absorbed first by the underlying hippocampus and anteromedial temporal cortex (Bigler, 2007).

Indeed, experimental TBI models repeatedly demonstrate that the cortex and hippocampus are selectively vulnerable to injury whereas other brain regions that appear to be relatively spared (Geddes et al., 2003). In these models, the mechanical impact is often most severe in the cortex; however, the hippocampus is also prone to deformation and adverse biochemical cascades. Hippocampal neurons exhibit a heightened, but shorter-lived, trauma-induced membrane permeability and are also a site of cell death (Geddes et al., 2003) and intensified inflammatory response (Tweedie et al., 2020). Inflammatory cascades have been linked to excessive iron accumulation (Huang et al., 2021; Nisenbaum et al., 2014; Orr et al., 2024), possibly explaining the mechanisms driving the higher incidence rates of abnormal iron markers in the hippocampal subfields. Cortical neurons appear to sustain a longer stretch-induced membrane permeability phase, although this observation has only been verified up to 24 hours post-injury (Geddes et al., 2003). As such, the hippocampus may experience a more acute and intense injury response, but prolonged cellular disruption in the cortex could contribute to more severe clinical outcomes at $\leq$14 days post-injury as observed in this sample.

Morphometric studies of ms-TBI paediatric have similarly reported that the hippocampus undergoes some of the most pronounced volumetric reductions, followed by the frontal and temporal cortices, while basal structures exhibit comparatively milder changes (Wilde et al., 2007). This pattern broadly aligns with the incidence rates of abnormalities observed at the individual level: 13 mTBI participants demonstrated hippocampal alterations, nine in temporal cortical regions (of 11 total), and nine in the basal ganglia or related nuclei. It is important to note that most of the basal abnormalities were localised to the mammillary nucleus, an area infrequently investigated in this context, and only four participants had abnormal iron markers in other basal nuclei. Although differences in statistical thresholds across these regions preclude direct comparison, agreement between these relative incidence rates and the broader literature nonetheless highlight the hippocampus and surrounding temporal cortex as regions disproportionately affected by mTBI. These observations further support the application of vulnerability-based ROI selection frameworks in QSM investigations of mTBI.

Here, the singular group-level finding of decreased negative susceptibility in the CA4 is also interesting, particularly given the relative under representation of abnormal iron markers in this region at the individual level. This suggests that the CA4 is uniquely vulnerable to disruption of negative susceptibility sources but iron dyshomeostasis in this region may be less prevalent. As discussed in Chapter 5, hilar cells are selectively vulnerable across multiple neurological conditions, including head injury (Grovola et al., 2020; Lowenstein et al., 1992; Maxwell et al., 2003a; Santhakumar et al., 2000) and temporal lobe epilepsy (Scharfman, 2016). Decreased negative susceptibility in the CA4 may thus represent a common feature of mTBI that reflects the vulnerability of this region to excitotoxicity, changes to myelin components, or even cell death after injury (see Fig. 9.2). This also highlights the utility of thresholding prior to analysis, whereby these more subtle negative susceptibility

effects would be obscured by the dominant signals from paramagnetic sources of positive susceptibility, as demonstrated in Fig. 9.1 above.

9.4.2 *Cortical regions are vulnerable to tissue disruption and adverse clinical outcomes following mTBI*

The selective vulnerability of the cortex may be of importance to understanding the pathophysiology of mTBI, in addition to the genesis of severe symptomatology. The primary individualised analyses that treated cortical regions as homogeneous parcels demonstrated that mTBI participants with abnormal iron markers exhibited more severe clinical symptoms than mTBI participants with no significant deviations from the HC distribution. This vulnerability may not only reflect prolonged metabolic disruption relative to other brain regions (Geddes et al., 2003) but the presence of subtle degenerative effects or altered synaptic signalling in cortical neurons. Supporting this interpretation, murine models of mild cortical impact have demonstrated cell death and marked reductions in dendritic and synaptic density within the cortex (Gao et al., 2011), suggesting that disruptions to cortical synapses may impair normal neuronal function and manifest as neurological deficits. The high concentration of abnormal iron markers in the temporal cortices also converge with SWI findings linking temporal cortical microhaemorrhages to unfavourable functional outcomes in mTBI (de Haan et al., 2017).

Secondary exploratory analyses that accounted for variations in cortical depth and curvature revealed that the sulcal fundus exhibited the most pronounced susceptibility-related differences, followed by the sulcal bank and, to a lesser extent, the gyral crown. Exposure to shear forces (Bakhtiarydavijani et al., 2021; Ghajari et al., 2017; McKee et al., 2013), or the forcible displacement of non-compressible CSF (Kornguth et al., 2017), preferentially affects the cortical sulci under traumatic conditions which may lead to focal tissue dyshomeostasis. Susceptibility alterations at the gyral crown could indicate the presence of mild contusion (Mckee et al., 2015) that may be occurring less frequently than sulcal injury. The marked heterogeneity of the depth-specific tissue disruption suggests a spectrum of underlying injury mechanisms: altered susceptibility at the pial surface may result from skull contact (Bigler, 2007), whereas shear and strain forces typically impact the GM/WM junction (McKee et al., 2013; Pankatz et al., 2023) potentially leading to disruptions at deeper depths. Susceptibility differences at intermediate depths could plausibly reflect transitional injury processes. Although these depth- and curvature-specific abnormalities were not associated with worse clinical symptom burden, they nonetheless indicate that most mTBI participants (83% in this cohort) exhibit some degree of cortical iron dyshomeostasis, reinforcing the vulnerability of the cortex to a broad spectrum of injury mechanisms.

At the group level, reduced negative susceptibility in the superficial depths of the sulcal fundus was observed alongside concomitant increases in positive susceptibility in distinct voxel populations in the superficial sulcal bank and fundus, suggesting a dual pathology of iron increases accompanied by degeneration of cellular components including myelin. This group-level finding also appears to capture a singular spatial nexus of multiple mTBI

injury mechanisms: the inherent vulnerability of the cerebral cortex, sulci, and antero-medial temporal lobe. The convergence of these findings on a single site highlights the advantage of employing dual analytic strategies where individualised approaches capture subject-specific, clinically relevant information and provide insight into injury heterogeneity, whereas group-level analyses identify features that may be generalisable across participants. As such, susceptibility alterations in the superficial cortical sulci of the parahippocampal gyrus, like decreases in negative susceptibility in CA4, could indicate a shared marker of mTBI (see Fig. 9.2) and may be a promising target for future investigations attempting to identify an imaging-based signature.

9.5 ALL MODELS ARE APPROXIMATIONS OF THE TRUTH

Although the findings of this thesis are novel and interesting, they serve to reinforce that every model offers only an approximation of the underlying biological mechanisms, particularly given the millimetre scale of MRI. This principle applies equally to QSM as an analytic tool, thresholding, anatomical specificity, interpretations of tissue responses through the lens of regional vulnerability and injury biodynamics, and to the spectrum of analytic approaches ranging from individualised to group-level. It is important to remember that a model's value, therefore, depends on the context in which it is used and the specific questions it is employed to answer. Acknowledging that no single framework is universally applicable allows for the selection, or combination, of the approaches best suited to addressing the problem at hand. This perspective is particularly relevant to the interrelated research components of the thesis, which ultimately seek to highlight the complementary nature of group-level and individualised methods, each of which bring unique insights to the study of mTBI. As such, this thesis emphasises that *analytic strategy choices should be tailored to the research objective*.

No single structural imaging marker of mTBI has yet been identified. However, the use of multi-modal neuroimaging methods combined with group-level analyses is advancing the field toward establishing a biomarker(s) (for a recent review, see Lunkova et al., 2021). In the context of QSM, the group-level findings presented in this thesis indicate that this analytic strategy is effective for *identifying spatial patterns of tissue disruption that may constitute a shared feature of mTBI*, as illustrated in Fig. 9.2. When applied with sufficient anatomical specificity, QSM may serve as a valuable addition to the existing suite of complementary neuroimaging tools aimed at addressing this ongoing challenge.

However, the ultimate *clinical* value of neuroimaging techniques depends not only on broad generalisability, but the ability to capture brain alterations that are individually relevant within a given context, such as in mTBI. The precise characteristics and locations of these alterations may not only be relevant to the development and presentation of specific symptoms, but can also inform the selection of appropriate interventions (Marquand et al., 2019). mTBI is characterised by significant inter-individual heterogeneity in injury mechanisms, location and extent of neural tissue disruption (ranging from focal to diffuse patterns), and secondary injury cascades (see Chapter 2). This variability is further

compounded by pre-existing factors, including age, gender, and IQ, that, among others, that contribute to differences in injury severity (Rosenbaum et al., 2012). In this context, *individualised analytic approaches are essential for capturing the heterogeneity of mTBI.*

Individual-level techniques are increasingly being employed to characterise both mTBI (Attyé et al., 2021; Bedggood et al., 2024) and TBI (Clemente et al., 2023; Domínguez et al., 2024; Imms et al., 2022; Jolly et al., 2021), with promising results. The two individualised studies presented here further emphasise the potential of this approach. While preliminary, the overlap between the presence of abnormal iron markers and regions associated with cellular vulnerability and injury mechanisms, as well as the potential for identifying cohorts at risk of more severe symptom burden, highlight the promise of these techniques for advancing research and suggest a possible role for individualised QSM in clinical practice.

While QSM for iron mapping and quantification has been validated through multimodal (Deistung et al., 2013a), *ex vivo* (Langkammer et al., 2012) and histological comparisons (Gillen et al., 2025), substantial barriers remain in integrating QSM into everyday clinical MRI. Variations in scanner hardware, acquisition parameters, and reconstruction algorithms significantly influence the estimation of susceptibility values (Bilgic et al., 2021; Langkammer et al., 2018), and while magnitude and phase images are readily acquired, QSM reconstruction requires significant technical proficiency (Borzage et al., 2022). These challenges are particularly salient in mTBI, where subtle deviations in susceptibility values risk being misinterpreted as evidence of tissue disruption. Although efforts have been made to address these issues, including consensus statements on best-practice acquisition and reconstruction (Bilgic et al., 2024) as well as the development of inline reconstruction pipelines by scanner vendors (Borzage et al., 2022), further logistical refinement and validation is needed before QSM can be reliably applied in the clinic.

Within a research context, where methodological constraints and clinical implications are somewhat minimised, the findings of this thesis provide a proof-of-concept model. First, they demonstrate the utility of adherence to best-practice reconstruction guidelines to enhance the reliability of results (see Chapter 4). Second, they demonstrate that individualised QSM is a viable tool for elucidating tissue disruptions associated with mTBI that may be overlooked in traditional group-level analyses. Third, they exemplify how group-level analyses can be used to identify features that may reflect common features of mTBI across participants. And, finally, they highlight how the use of both group-level and individualised analytic strategies along with tailored methodologies can be harnessed to address specific research objectives. Nonetheless, future research investigations should prioritise the use of advanced sequences with higher spatial resolution and multi-echo acquisitions to enhance biological interpretation, and seek to advance standardisation of individualised methodologies (see *Limitations* in Chapter 7).

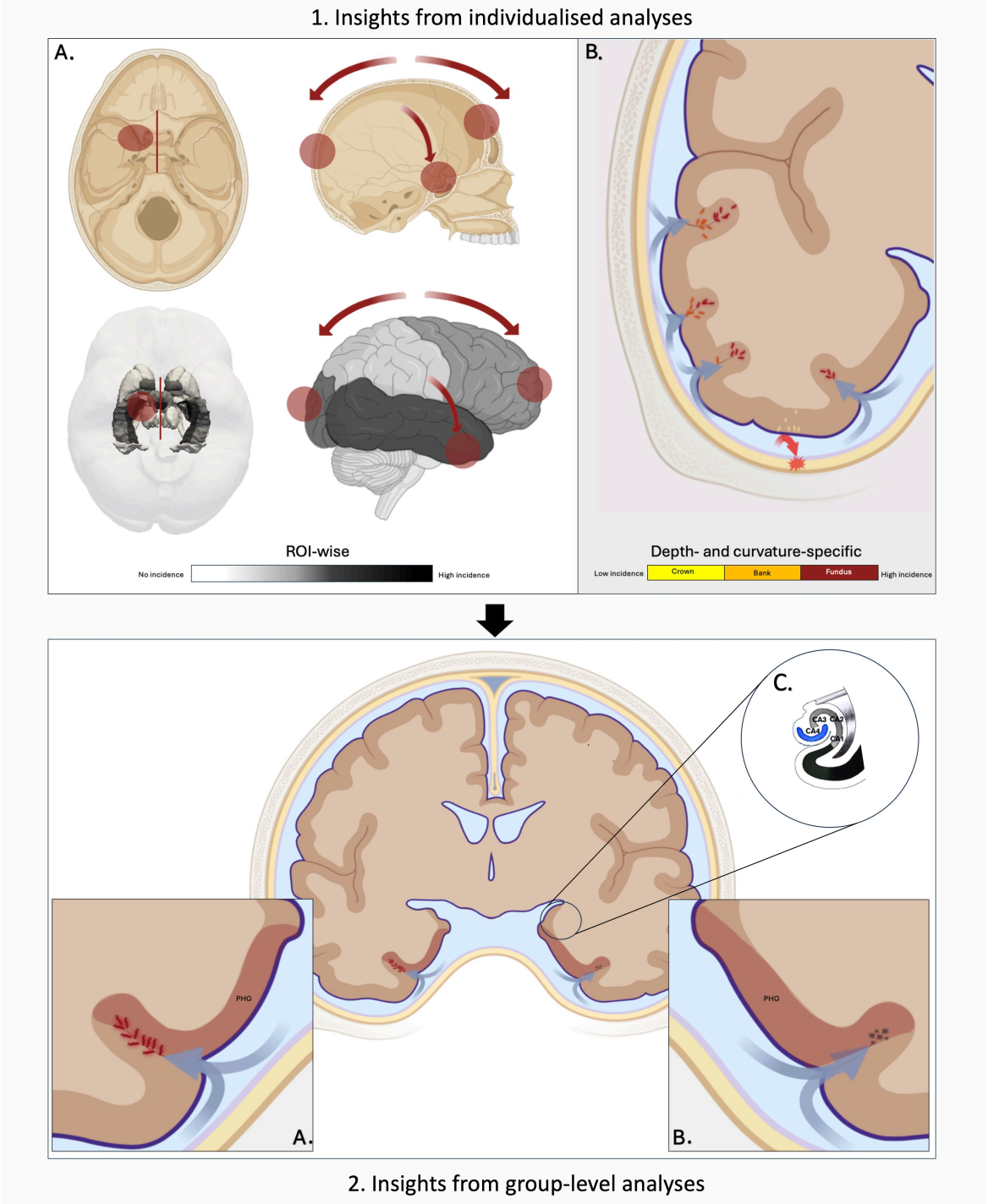

Figure 9.2: Divergent and convergent spatial distributions of susceptibility differences

1. Shows likely injury mechanisms and inter-individual variability in the loci of abnormal cortical and subcortical iron markers for mTBI participants. A) Highlights how brain movement may result in abnormal iron marker variability; impact with the sphenoid and midline strain for markers in the parasubiculum and mammillary nucleus relative to other deep structures; lateral impacts or proximity to the sphenoid for abnormal iron markers in the temporal cortices; head kinematics for secondary involvement of the occipital and frontal cortices. B) Shows the relationship between CSF dynamics, shear/strain forces, and abnormal iron markers primarily at the sulcal fundus and less pronounced in the sulcal bank. Less frequent involvement of the gyral crown may be related to mild contusive forces. Differences in susceptibility at varying cortical depths likely reflects distinct injury mechanisms at the pial surface versus the GM/WM junction. 2. Presents the results of group-level analyses, where increases in positive susceptibility in the parahippocampal gyrus (PHG) concomitant with decreases in negative susceptibility in PHG and CA4 appear to converge on a common spatial nexus for multiple injury mechanisms: the medial temporal lobe. Here, CA4 may be vulnerable to excitotoxicity and anteromedial PHG and sulci vulnerable to mechanical forces. Depiction of ammon's horn (panel 2.C.) reused with permission from Parkin (1996).

9.6 CLINICAL IMPLICATIONS

In an acute mTBI cohort, increased positive susceptibility may reflect early iron dysregulation, contributing to the generation of ROS and localised inflammatory responses (Daglas et al., 2018; Gozt et al., 2021a; Huang et al., 2021; Kruszewski, 2003; Nisenbaum et al., 2014). Significantly decreased positive susceptibility likely indicates iron deficiency and potential neuron loss (Levi et al., 2024). Elevations in negative susceptibility, on the other hand, might indicate higher concentrations of calcium or certain proteins such as Aβ and tau, while decreased negative susceptibility is likely indicative of myelin degradation or cell loss (Chary et al., 2021; Duyn et al., 2017; Gong et al., 2019; Jang et al., 2021; S. Kim et al., 2020; O'Callaghan et al., 2017; Y. Wang et al., 2017; Z. Zhao et al., 2021). Collectively, these pathological processes have been documented across the full spectrum of TBI (Bramlett et al., 2002; Flavin et al., 2023; Giza et al., 2014; Lu et al., 2015; Mahoney et al., 2022; Maxwell et al., 2003b; Nisenbaum et al., 2014; Raz et al., 2011; Weber et al., 2018). In a clinical context, identifying the specific pathophysiological mechanisms that occur shortly after injury, and quantifying their severity, are essential for assessing the extent of mTBI-related damage, guiding targeted interventions, and informing return-to-play decisions for athletes (Maas et al., 2017).

Of particular concern is the risk of a persistent burden and neurodegenerative processes catalysed by even mild brain injuries and repetitive sub-concussive events (Maas et al., 2017). For some individuals, mTBI can induce chronic cognitive deficits, increased susceptibility to mental health disorders, and even premature morbidity (De Beaumont et al., 2009; Guskiewicz et al., 2007; Mackay et al., 2019; McInnes et al., 2017). This risk is elevated in cases of repetitive mTBI, as commonly observed in sports participation, where a clear dose-response relationship exists. Cumulative insults may also trigger progressive cellular and structural deterioration, initiating a cascade of neurobiological events that can culminate in the development of CTE (McKee et al., 2023). Whilst the precise relationship between iron overload and the downstream hyperphosphorylation of tau proteins remains an active area of research, a growing body of evidence suggests that early iron dysregulation may facilitate tau phosphorylation, NFT formation, and necrosis (Juan et al., 2023; Levi et al., 2024; Nisenbaum et al., 2014) and may be implicated in CTE (Bouras et al., 1997; Zecca et al., 2004) and other neurodegenerative disorders including AD, PD, and MS (Daglas et al., 2018; Ghaderi et al., 2024; Levi et al., 2024; Mohammadi et al., 2024a, 2024b; Rouault, 2013; Stephenson et al., 2014; Yamamoto et al., 2002).

The widespread elevations of iron markers in this acute mTBI cohort, especially in regions where tauopathy is present in CTE, raises important questions about the role of iron in both acute secondary injury and subsequent tissue degeneration. In CTE, pathognomonic lesions are characterised by the presence of p-tau at the depth of the cortical sulcus, often involving, but not limited to, the subpial and superficial layers. Moreover, NFTs in the superficial cortical layers, hippocampal CA4 with dendritic swellings, and in the entorhinal cortex and mammillary bodies are diagnostic of CTE and CTE burden (high

versus low) (Bieniek et al., 2021). Extensive atrophy, including neuron loss, gliosis, and NFT accumulation in the medial temporal lobe are also features of CTE.

Regions implicated in these pathological processes show considerable spatial overlap with the findings presented throughout this thesis. This includes a high burden of abnormal iron markers in the mammillary nucleus (Chapter 7); significant involvement of the temporal and medial temporal lobes, including the hippocampus (Chapter 6, Chapter 7, and Chapter 8); pronounced alterations in the cortical sulci (Chapter 6 and Chapter 8); and evidence of parahippocampal and entorhinal cortical involvement (Chapter 6 and Chapter 8). Additionally, decreased negative susceptibility in the hippocampal CA4 (Chapter 5) may reflect myelin degradation or damage to the vulnerable cell populations in this region. Given the established associations between iron overload and tauopathy, the young age of the mTBI cohort, and the disproportionate development of CTE pathology in males (Bieniek et al., 2020), these data indicate that follow-up regarding potential effects to long-term brain health are warranted.

Coupled with the established associations between abnormal iron levels and cognitive decline (Schröder et al., 2013), and the relationship between abnormal cortical iron markers, which were particularly dense in the temporal lobe, and clinical symptomatology (Chapter 8), the collective findings of this thesis also reinforce concerns about the role of iron dysregulation in mTBI pathology. QSM has shown promise in identifying iron dyshomeostasis in AD and PD, as well a putative relationship with tau and Aβ aggregation (Acosta-Cabronero et al., 2013; Ahmed et al., 2023; Gong et al., 2019; H. G. Kim et al., 2017; Merenstein et al., 2024; Mohammadi et al., 2024a; Nikparast et al., 2022b; O'Callaghan et al., 2017; Uchida et al., 2022; Z. Zhao et al., 2021), suggesting that it may similarly enhance our understanding of acute regional iron dyshomeostasis following mTBI and its involvement in the cascade that may, for some individuals, culminate in CTE as a downstream pathophysiological event. Ultimately, improving our understanding of disease catalysts could pave the way for early, targeted therapeutic interventions aimed at mitigating these initial effects.

Here, follow-up investigations will be of importance. A better understanding of iron and other neurobiological correlates, such as myelin damage or protein aggregation, is essential for developing effective care and targeted treatments at the acute stage of mTBI, which could protect against adverse consequences later in life. Recent research has explored the possibility of using heavy metal chelation as a therapeutic target for iron in AD (Mazur et al., 2024) and TBI (Daglas et al., 2018). In AD, this approach has had limited success, perhaps due to the accumulation of iron over a long time course; once iron overload becomes apparent, cell death has already occurred (Levi et al., 2024). However, mechanisms of acute injury-related iron overload may be distinct from long-term aggregation. Murine models using iron chelators such as Deferoxamine (Jia et al., 2023; Long et al., 1996; Panter et al., 1992; J. Zhao et al., 2014) and *N*,*N*′-Di(2-hydroxybenzyl)ethylenediamine-*N*,*N*′-diacetic acid monohydrochloride (Khalaf et al., 2019) have shown promise in reducing TBI symptomatology, likely through inhibition of ferroptosis and reductions in neuroinflammation, ROS, and gliosis. More research is needed to understand efficacy in humans, but this re-

mains a possible avenue for limiting the effects of acute iron dyshomeostasis which may contribute to degenerative effects evident in later life.

9.7 LIMITATIONS AND FUTURE RESEARCH

The first major limitation of the research in this thesis is related to the sequence parameters for magnitude and phase data acquisition used to reconstruct QSM. Here, it is important to point out that while the QSM *reconstruction* algorithm was congruent with recent consensus guidelines, the use of a single-echo GRE *acquisition* was not (Bilgic et al., 2024) and limited the separation of susceptibility sources to a more rudimentary *between* voxels approach. While acquisitions of $\leq$1 mm isotropic resolution are recommended to mitigate potential susceptibility underestimation (Bilgic et al., 2024; Karsa et al., 2019a), acquisitions of $\sim$1 mm voxel resolution nonetheless contain a combination of paramagnetic and diamagnetic susceptibility sources at the molecular level (J. Chen et al., 2021). As a result, thresholding the susceptibility maps can introduce ambiguity regarding the interpretation of the underlying biological substrates. For instance, if a voxel exhibits a negative net susceptibility (indicating diamagnetic dominance), a reduction in the magnitude of this negativity could result either from a loss of diamagnetic material (such as myelin) or from an increase in paramagnetic material (such as iron deposition) that is insufficient to shift the net value to positive but would nonetheless contribute to an overall increase in positive susceptibility when analysed as part of a raw, continuous map (this is also demonstrated in Fig. 9.1). In addition, this approach can lead to indeterminate values in an ROI comprised predominantly of a single susceptibility sign, resulting in indeterminate values for the non-dominant sign. This phenomenon is more likely in smaller ROIs comprised of a more limited number of voxels (see Chapter 5). Lastly, voxels with a net susceptibility of zero likely contain biologically informative data, but were omitted from analysis,

True magnetic source separation, as currently defined by the standing literature, involves isolating the distinct susceptibility contributions *within* individual voxels, effectively deconvolving the bulk voxel-wise susceptibility into its sub-voxel para- and dia-magnetic constituent elements (Ahmed et al., 2023; J. Chen et al., 2021; Emmerich et al., 2021; J. Lee et al., 2024; Z. Li et al., 2023; Shin et al., 2021). Multi-echo sequences not only align with best-practice guidelines for data acquisition (Bilgic et al., 2024), but enable intra-voxel source separation, such as DECOMPOSE-QSM (J. Chen et al., 2021), χ-separation (Shin et al., 2021), and APART-QSM (Z. Li et al., 2023). These source separation techniques would allow robust distinction of disparate susceptibilities within all voxels for a given map, mitigate the issue of zero-value voxels and indeterminate values, and should be adopted by future studies to better elucidate the complex interplay of biological substrates in mTBI.

The second major limitation of this thesis is the inherent challenge in using neuroimaging modalities to directly infer underlying biological processes. This limitation arises from spatial constraints and the reliance on indirect markers to assess tissue composition. Even though the relationship between QSM and iron is well established, QSM remains a surrogate measure. In addition, QSM can provide insight into other biological substrates includ-

ing calcium and protein accumulation as well as changes to myelin content. Integrating a multi-modal MRI protocol enables a more comprehensive understanding of mTBI-related brain alterations. Combining dMRI and fMRI can elucidate both the structural disruptions in white matter pathways and broader network-level functional disruptions, thereby augmenting susceptibility-based findings in grey matter. Additional complementary modalities such as quantitative T_2w imaging analysis, where the presence of paramagnetic substances shortens the T_2 relaxation time (Onyszchuk et al., 2009), would improve inference about iron deposition in brain tissue. Moreover, incorporating PET imaging would offer critical insights into cellular metabolism and other neurobiological processes related to mTBI, thereby enabling more biologically informed interpretations of observed differences. For example, by using tracers sensitive to neuroinflammatory processes including ROS (ROStrace), Aβ (e.g., Pittsburgh Compound B, Florbetapir, Florbetaben, and Flutafuranol) or tau (Flortaucipir and Florquinitau) (Dybing et al., 2023; R. Zhou et al., 2021) which may co-localise with regions of abnormal susceptibility indicating potential iron overload, protein aggregation, or damage to cellular components. Including blood-based biomarker assays would also enhance the interpretation of the neurobiological consequences of mTBI, providing a clearer link between neuroimaging results and molecular pathology. However, the timing of sample collection is critical due to variations in the kinetic profiles of different biomarkers. For instance, in this sample, only neurofilament light chain and p-tau would be reliably detectable in the days to weeks following injury (for consensus guidelines, see Backus et al., 2024).

The third major limitation of this thesis is the exclusive focus on bilateral brain regions. This approach risks masking region-specific or lateralised anomalies that could be critical for understanding mTBI pathophysiology, regional vulnerability, and injury mechanisms. Analysing only bilateral differences may obscure important hemispheric disparities, especially since lateralised effects are well documented in mTBI. These effects are evident in impact distribution (Viano et al., 2005), numerous MRI-based studies (for a review, see Lunkova et al., 2021), as well as in research on iron deposition in chronic mTBI (Lu et al., 2015), murine models of impact-related iron deposition observed using T_2w imaging (Onyszchuk et al., 2009), and dendritic degeneration with Golgi staining (Gao et al., 2011). Future studies should explicitly examine hemispheric differences, and prospective research designs should incorporate data that directly reflects injury mechanisms. For example, helmet tracking data (Saikia et al., 2024; Zhuang et al., 2021) or gameplay recording, to correlate biomechanical forces with observed imaging changes. This approach would enable a more targeted exploration of the causal links between impact dynamics, regional tissue disruption, and clinical outcomes.

In addition, several confounding variables were not accounted for in this research, including number of previous injuries and potential genetic vulnerabilities (Rosenbaum et al., 2012), data regarding the injury environment, mechanical loading, injury biodynamics, and variations in cranial morphology (Knutsen et al., 2020; Orr et al., 2024) which may confound or support results. Representative data should be collected where possible in future research. Given that this study was conducted exclusively in a male cohort that cap-

tures data from adolescence and early adulthood (i.e., ages 16-33), the generalisability of the findings to older or younger athletes is limited. Future studies should aim to include a broader age spectrum to further explore the interaction between age and susceptibility in mTBI, which has been cited throughout the studies presented in this thesis as a potential confounding variable. Age-related regional cortical and subcortical iron accumulation is generally most pronounced up until the third decade of life (Hallgren et al., 1958) and research using cohorts with a broader age range should incorporate statistical modelling that accounts for differential iron deposition with age. In addition, the limited external validity is also relevant to the translation of findings reported here to female athletes. To mitigate these issues and limitations, future research should consider building large control cohorts over time, with standardised imaging acquisition and sequence protocols, which would facilitate the use of more robust normative modelling (Marquand et al., 2016). As opposed to the more basic z-score comparisons when analysing data at the individual level, normative models require hundreds-to-thousands of control subjects, but allow for covariate adjustments and thus data collection and statistical inference across a wider clinical population rather than within the narrow samples often seen in clinical research.

The tightly phenotyped participant cohort used in this thesis also resulted in a limited sample size, and it remains challenging to conduct *a priori* calculations for sufficient statistical power in QSM studies. However, this cohort is in line with other neuroimaging research, as exemplified by an investigation of 388 fMRI papers which reported a median sample size of 33 participants (Yeung, 2018) and an analysis of 270 papers from apex neuroimaging journals published in 2017 and 2018 that reported a median sample of 23 and 24, respectively (Szucs et al., 2020). Szucs et al. (2020) also noted that only four of the 131 papers published in 2017 and five of the 142 papers published in 2018 involved any pre-study power calculations, which were mostly conducted in instances where single t-tests and correlations were used. The cohort(s) used in the studies comprising thesis are also comparable to, or larger than, most previous QSM-mTBI investigations where sample sizes have been reported (Bell et al., 2024; Koch et al., 2021; Pinky et al., 2022; Wright et al., 2022; Zivadinov et al., 2018a). In addition, calculating statistical power for analyses that span multiple ROIs and, in particular, thousands of parcel × curvature × depth combinations is prohibitively exhaustive, and further complicated by the use of z-tests, but may in future be made possible by machine learning algorithms developed for QSM. Nonetheless, it is important to note that the sample sizes used in neuroimaging research are recognised as underpowered for detecting true effects, have low positive predictive value when an effect is identified, and are associated with an amplified estimate of the effect size in the presence of real effects (Button et al., 2013). As such, it is important to acknowledge that the findings in this thesis need to be replicated in larger and more generalisable cohorts.

The focus of the individualised studies on net positive voxels left net negative voxels unexplored. Previous research in AD (Merenstein et al., 2024) has suggested interactions between iron deposition and changes in negative susceptibility in the cerebral cortex on QSM. Future exploratory research designs may thus benefit from inclusion of both susceptibility signs, thereby enabling broader, and potentially concomitant, characterisation

of individualised tissue changes following injury. In addition, because negative susceptibility was not examined at the individual level, it remains unclear whether group-level reductions in the parahippocampal gyrus and CA4 are also reflected across individual participants when z-tests are employed.

Lastly, given the limitations of inferring long-term consequences of sr-mTBI from data collected at the acute stage, future research should prioritise longitudinal studies tracking athletes over time. This prospective approach would yield more precise information compared to retrospective studies, providing valuable insights into the relationships between the number of mTBIs sustained, susceptibility alterations, recovery trajectories, and long-term outcomes. Here, a combination of both group-level and individualised analytic approaches should be used, as exemplified by the works presented in this thesis. The former to identify potentially diagnostic injury signatures, and the latter to understand neuropathology at the individual level and inform individualised interventions, return-to-play pathways, and treatment strategies.

9.8 CONCLUSIONS

The studies comprising this thesis investigated mTBI-related differences in quantitative susceptibility values as a proxy for tissue disruption across the human brain, from the cerebral cortex to deep nuclei, and introduced several novel approaches to the application of QSM in mTBI research. Group-level analyses revealed macroscopic effects that may represent a shared feature of mTBI and a convergence point for multiple injury mechanisms. Individualised analyses exemplified the utility of z-tests in capturing the inherent heterogeneity of mTBI, localising inter-individual differences to distinct cortical and subcortical regions, and identifying their respective relevance to symptom burden and potential injury mechanisms. The findings presented in this thesis suggest that QSM, when applied with sufficient anatomical specificity, may be a valuable addition to the suite of MRI-based imaging techniques currently being leveraged to identify signatures of mTBI and micropathology. The results further suggest that individualised approaches may be a valuable tool in elucidating the clinical relevance of iron in mTBI. Collectively, these data underscore the need for significant improvements in anatomical specificity to characterise alterations to tissue susceptibility using QSM, and suggest that the prevailing focus on major basal ganglia substructures is limiting and should be revised in favour of vulnerability-based frameworks when selecting ROIs for analysis. The use of complementary analytic approaches provides compelling evidence of microstructural brain changes in mTBI that have been largely absent from the QSM literature, laying the groundwork for refining the application of QSM in mTBI. Finally, these data suggest that a deeper understanding of regional tissue disruptions, coupled with comprehensive follow-up investigations, could significantly advance our insight into both the short- and long-term effects of mTBI, including the potential contribution of brain iron to injury-induced degenerative tissue cascades.

BIBLIOGRAPHY

Abbott, N. J., Patabendige, A. A., Dolman, D. E., Yusof, S. R. & Begley, D. J. (2010). Structure and function of the blood-brain barrier. https://doi.org/10.1016/j.nbd.2009.07.030

Ábrahám, H., Vincze, A., Jewgenow, I., Veszprémi, B., Kravják, A., Gömöri, É. & Seress, L. (2010). Myelination in the human hippocampal formation from midgestation to adulthood. *International Journal of Developmental Neuroscience*, *28*(5), 401–410. https://doi.org/10.1016/j.ijdevneu.2010.03.004

Absinta, M., Sati, P., Masuzzo, F., Nair, G., Sethi, V., Kolb, H., Ohayon, J., Wu, T., Cortese, I. C. & Reich, D. S. (2019). Association of Chronic Active Multiple Sclerosis Lesions with Disability in Vivo. *JAMA Neurology*, *76*(12), 1474–1483. https://doi.org/10.1001/jamaneurol.2019.2399

Acosta-Cabronero, J., Betts, M. J., Cardenas-Blanco, A., Yang, S. & Nestor, P. J. (2016). In vivo MRI mapping of brain iron deposition across the adult lifespan. *Journal of Neuroscience*, *36*(2), 364–374. https://doi.org/10.1523/JNEUROSCI.1907-15.2016

Acosta-Cabronero, J., Williams, G. B., Cardenas-Blanco, A., Arnold, R. J., Lupson, V. & Nestor, P. J. (2013). In vivo quantitative susceptibility mapping (QSM) in Alzheimer's disease. *PLoS ONE*, *8*(11). https://doi.org/10.1371/journal.pone.0081093

Aggarwal, M., Li, X., Gröhn, O. & Sierra, A. (2018). Nuclei-specific deposits of iron and calcium in the rat thalamus after status epilepticus revealed with quantitative susceptibility mapping (QSM). *Journal of Magnetic Resonance Imaging*, *47*(2), 554–564. https://doi.org/10.1002/jmri.25777

Aggarwal, M., Nauen, D. W., Troncoso, J. C. & Mori, S. (2015). Probing region-specific microstructure of human cortical areas using high angular and spatial resolution diffusion MRI. *NeuroImage*, *105*, 198–207. https://doi.org/10.1016/j.neuroimage.2014.10.053

Aggleton, J. P., Pralus, A., Nelson, A. J. & Hornberger, M. (2016). Thalamic pathology and memory loss in early Alzheimer's disease: Moving the focus from the medial temporal lobe to Papez circuit. https://doi.org/10.1093/brain/aww083

Ahmed, M., Chen, J., Arani, A., Senjem, M. L., Cogswell, P. M., Jack, C. R. & Liu, C. (2023). The diamagnetic component map from quantitative susceptibility mapping (QSM) source separation reveals pathological alteration in Alzheimer's disease-driven neurodegeneration. *NeuroImage*, *280*. https://doi.org/10.1016/j.neuroimage.2023.120357

Alberts, B., Johnson, A., Lewis, J. & et al. (2002). *Molecular biology of the cell*. Garland Science.

Aminoff, E. M., Kveraga, K. & Bar, M. (2013). The role of the parahippocampal cortex in cognition. https://doi.org/10.1016/j.tics.2013.06.009

Ansari, M. A., Roberts, K. N. & Scheff, S. W. (2008). Oxidative stress and modification of synaptic proteins in hippocampus after traumatic brain injury. *Free Radical Biology and Medicine*, *45*(4), 443–452. https://doi.org/10.1016/j.freeradbiomed.2008.04.038

Arciniega, H., Baucom, Z. H., Tuz-Zahra, F., Tripodis, Y., Carrington, H., Kim, N., Knyazhanskaya, E. E., Jung, L. B., Breedlove, K., T Wiegand, T. L., Daneshvar, D. H., Jarrett Rushmore, R., Billah, T., Pasternak, O., Coleman, M. J. & Adler, C. H. (2024). Brain morphometry in former American football players: 1 findings from the DIAGNOSE CTE research project. *Oxford University Press*, *22*. https://doi.org/10.1093/brain/awae098/7635729

Ashraf, A., Clark, M. & So, P. W. (2018). The aging of iron man. *Frontiers in Aging Neuroscience*, *10*. https://doi.org/10.3389/fnagi.2018.00065

Attyé, A., Renard, F., Baciu, M., Roger, E., Lamalle, L., Dehail, P., Cassoudesalle, H. & Calamante, F. (2021). TractLearn: A geodesic learning framework for quantitative analysis of brain bundles. *NeuroImage*, *233*. https://doi.org/10.1016/j.neuroimage.2021.117927

Avants, B. B., Tustison, N. J., Song, G., Cook, P. A., Klein, A. & Gee, J. C. (2011). A reproducible evaluation of ANTs similarity metric performance in brain image registration. *NeuroImage*, *54*(3), 2033–2044. https://doi.org/10.1016/j.neuroimage.2010.09.025

Azhar, S. & Chong, L. R. (2023). Clinician's guide to the basic principles of MRI. *Postgraduate Medical Journal*, *99*(1174), 894–903. https://doi.org/10.1136/pmj-2022-141998

Azuma, M., Maekawa, K., Yamashita, A., Yokogami, K., Enzaki, M., Khant, Z. A., Takeshima, H., Asada, Y., Wang, Y. & Hirai, T. (2020). Characterization of carotid plaque components by quantitative susceptibility mapping. *American Journal of Neuroradiology*, *41*(2), 310–317. https://doi.org/10.3174/ajnr.A6374

Backus, B. E., Moustafa, F., Skogen, K., Sapin, V., Rane, N., Moya-Torrecilla, F., Biberthaler, P. & Tenovuo, O. (2024). Consensus paper on the assessment of adult patients with traumatic brain injury with Glasgow Coma Scale 13-15 at the emergency department: A multidisciplinary overview. https://doi.org/10.1097/MEJ.0000000000001140

Bai, Y., Wang, M. Y., Han, Y. H., Dou, S. W., Lin, Q., Guo, Y., Li, W., Ding, D. G., Dai, J. P., Qin, W., Shi, D. P., Tian, J. & Dai, Y. M. (2013). Susceptibility Weighted Imaging: A New Tool in the Diagnosis of Prostate Cancer and Detection of Prostatic Calcification. *PLoS ONE*, *8*(1). https://doi.org/10.1371/journal.pone.0053237

Bailes, J. E., Petraglia, A. L., Omalu, B. I., Nauman, E. & Talavage, T. (2013). Role of subconcussion in repetitive mild traumatic brain injury. *Journal of Neurosurgery*, *119*(5), 1235–1245. https://doi.org/10.3171/2013.7.JNS121822

Baker-Nigh, A., Vahedi, S., Davis, E. G., Weintraub, S., Bigio, E. H., Klein, W. L. & Geula, C. (2015). Neuronal amyloid-β accumulation within cholinergic basal forebrain in ageing and Alzheimer's disease. *Brain*, *138*, 1722–1737. https://doi.org/10.1093/brain/awv097

Bakhtiarydavijani, A., Khalid, G., Murphy, M. A., Johnson, K. L., Peterson, L. E., Jones, M., Horstemeyer, M. F., Dobbins, A. C. & Prabhu, R. K. (2021). A mesoscale finite element modeling approach for understanding brain morphology and material heterogeneity effects in chronic traumatic encephalopathy. *Computer Methods in Biomechanics and Biomedical Engineering*, *24*(11), 1169–1183. https://doi.org/10.1080/10255842.2020.1867851

Ballabh, P., Braun, A. & Nedergaard, M. (2004). The blood-brain barrier: An overview: Structure, regulation, and clinical implications. https://doi.org/10.1016/j.nbd.2003.12.016

Bandt, S. K., de Rochefort, L., Chen, W., Dimov, A. V., Spincemaille, P., Kopell, B. H., Gupta, A. & Wang, Y. (2019). Clinical Integration of Quantitative Susceptibility Mapping Magnetic Resonance Imaging into Neurosurgical Practice. *World Neurosurgery*, *122*, e10–e19. https://doi.org/10.1016/j.wneu.2018.08.213

Basil, R. A., Westwater, M. L., Wiener, M. & Thompson, J. C. (2017). A Causal Role of the Right Superior Temporal Sulcus in Emotion Recognition From Biological Motion. *Open Mind*, *2*(1), 26–36. https://doi.org/10.1162/opmi{_}a{_}00015

Beauchamp, M. S. (2015). The social mysteries of the superior temporal sulcus. *Trends in Cognitive Sciences*, *19*(9), 489–490. https://doi.org/10.1016/j.tics.2015.07.002

Bechler, E., Stabinska, J., Thiel, T., Jasse, J., Zukovs, R., Valentin, B., Wittsack, H. J. & Ljimani, A. (2021). Feasibility of quantitative susceptibility mapping (QSM) of the human kidney. *Magnetic Resonance Materials in Physics, Biology and Medicine*, *34*(3), 389–397. https://doi.org/10.1007/s10334-020-00895-9

Bedggood, M. J., Essex, C. A., Theadom, A., Holdsworth, S. J., Faull, R. L. & Pedersen, M. (2024). Individual-level analysis of MRI T2 relaxometry in mild traumatic brain injury: Possible indications of brain inflammation. *NeuroImage: Clinical*, *43*. https://doi.org/10.1016/j.nicl.2024.103647

Bell, T. K., Ansari, M., Joyce, J. M., Mercier, L. J., Gobbi, D. G., Frayne, R., Debert, C. & Harris, A. D. (2024). Quantitative Susceptibility Mapping in Adults with Persistent-Post Concussion Symptoms after Mild Traumatic Brain Injury: An Exploratory Study. *American Journal of Neuroradiology*, ajnr.A8454. https://doi.org/10.3174/ajnr.a8454

Benjamini, Y. & Hochberg, Y. (1995). Controlling the False Discovery Rate: A Practical and Powerful Approach to Multiple Testing. *Journal of the Royal Statistical Society. Series B (Methodological)*, *57*(1), 289–300.

Bhattacharyya, K. (2017). James wenceslaus papez, his circuit, and emotion. *Annals of Indian Academy of Neurology*, *20*(3), 207–210. https://doi.org/10.4103/aian.AIAN{_}487{_}16

Biel, D., Steiger, T. K. & Bunzeck, N. (2021). Age-related iron accumulation and demyelination in the basal ganglia are closely related to verbal memory and executive functioning. *Scientific Reports*, *11*(1). https://doi.org/10.1038/s41598-021-88840-1

Bieniek, K. F., Blessing, M. M., Heckman, M. G., Diehl, N. N., Serie, A. M., Paolini, M. A., Boeve, B. F., Savica, R., Reichard, R. R. & Dickson, D. W. (2020). Association between contact sports participation and chronic traumatic encephalopathy: a retrospective cohort study. *Brain Pathology*, *30*(1), 63–74. https://doi.org/10.1111/bpa.12757

Bieniek, K. F., Cairns, N. J., Crary, J. F., Dickson, D. W., Folkerth, R. D., Keene, C. D., Litvan, I., Perl, D. P., Stein, T. D., Vonsattel, J. P., Stewart, W., Dams-O'connor, K., Gordon, W. A., Tripodis, Y., Alvarez, V. E., Mez, J., Alosco, M. L., Mckee, A. C., Babcock, D., … Koroshetz, W. (2021). The Second NINDS/NIBIB Consensus Meeting to Define Neuropathological Criteria for the Diagnosis of Chronic Traumatic Encephalopathy. *Journal of Neuropathology and Experimental Neurology*, *80*(3), 210–219. https://doi.org/10.1093/jnen/nlab001

Bigler, E. D. (2004). Neuropsychological results and neuropathological findings at autopsy in a case of mild traumatic brain injury. *Journal of the International Neuropsychological Society*, (10), 794–806.

Bigler, E. D. (2007). Anterior and Middle Cranial Fossa in Traumatic Brain Injury: Relevant Neuroanatomy and Neuropathology in the Study of Neuropsychological Outcome. *Neuropsychology*, *21*(5), 515–531. https://doi.org/10.1037/0894-4105.21.5.515

Bigler, E. D., Andersob, C. V. & Blatter, D. D. (2002). Temporal Lobe Morphology in Normal Aging and Traumatic Brain Injury. *AJNR Am J Neuroradiol*, *23*(2), 255–266. http://www.ajnr.org/content/23/2/

Bigler, E. D. & Maxwell, W. L. (2012). Neuropathology of mild traumatic brain injury: Relationship to neuroimaging findings. *Brain Imaging and Behavior*, *6*(2), 108–136. https://doi.org/10.1007/s11682-011-9145-0

Bilgic, B., Fan, A. P., Polimeni, J. R., Cauley, S. F., Bianciardi, M., Adalsteinsson, E., Wald, L. L. & Setsompop, K. (2014). Fast quantitative susceptibility mapping with L1-regularization and automatic parameter selection. *Magnetic Resonance in Medicine*, *72*(5), 1444–1459. https://doi.org/10.1002/mrm.25029

Bilgic, B., Langkammer, C., Marques, J. P., Meineke, J., Milovic, C. & Schweser, F. (2021). QSM reconstruction challenge 2.0: Design and report of results. *Magnetic Resonance in Medicine*, *86*(3), 1241–1255. https://doi.org/10.1002/mrm.28754

Bilgic, B., Pfefferbaum, A., Rohlfing, T., Sullivan, E. V. & Adalsteinsson, E. (2012). MRI estimates of brain iron concentration in normal aging using quantitative susceptibility mapping. *NeuroImage*, *59*(3), 2625–2635. https://doi.org/10.1016/j.neuroimage.2011.08.077

Bilgic, B., Costagli, M., Chan, K. S., Duyn, J., Langkammer, C., Lee, J., Li, X., Liu, C., Marques, J. P., Milovic, C., Robinson, S. D., Schweser, F., Shmueli, K., Spincemaille, P., Straub, S., van Zijl, P. & Wang, Y. (2024). Recommended implementation of quantitative susceptibility mapping for clinical research in the brain: A consensus of the ISMRM electro-magnetic tissue properties study group. *Magnetic Resonance in Medicine*, *91*(5), 1834–1862. https://doi.org/10.1002/mrm.30006

Biondetti, E., Rojas-Villabona, A., Sokolska, M., Pizzini, F. B., Jäger, H. R., Thomas, D. L. & Shmueli, K. (2019). Investigating the oxygenation of brain arteriovenous malformations using quantitative susceptibility mapping. *NeuroImage*, *199*, 440–453. https://doi.org/10.1016/j.neuroimage.2019.05.014

Bird, C. M. & Burgess, N. (2008). The hippocampus and memory: Insights from spatial processing. *Nature Reviews Neuroscience*, *9*(3), 182–194. https://doi.org/10.1038/nrn2335

Bittar, A., Bhatt, N., Hasan, T. F., Montalbano, M., Puangmalai, N., Mcallen, S., Ellsworth, A., Carretero Murillo, M., Taglialatela, G., Lucke-Wold, B., Logsdon, A., Rosen, C., Turner, R. C. & Kayed, R. (2019). Neurotoxic tau oligomers after single versus repetitive mild traumatic brain injury. *Brain Communications*, *1*(1). https://doi.org/10.1093/braincomms/fcz004

Blaylock, R. & Maroon, J. (2011). Immunoexcitotoxicity as a central mechanism in chronic traumatic encephalopathy-A unifying hypothesis. *Surgical Neurology International*, *2*(1), 107. https://doi.org/10.4103/2152-7806.83391

Bloch, F. (1946). Nuclear induction. *Physical review*, *70*(7-8), 460.

Bludau, S., Eickhoff, S. B., Mohlberg, H., Caspers, S., Laird, A. R., Fox, P. T., Schleicher, A., Zilles, K. & Amunts, K. (2014). Cytoarchitecture, probability maps and functions of the human frontal pole. *NeuroImage*, *93*, 260–275. https://doi.org/10.1016/j.neuroimage.2013.05.052

Boccara, C. N., Sargolini, F., Thoresen, V. H., Solstad, T., Witter, M. P., Moser, E. I. & Moser, M. B. (2010). Grid cells in pre-and parasubiculum. *Nature Neuroscience*, *13*(8), 987–994. https://doi.org/10.1038/nn.2602

Bollmann, S., Mattern, H., Bernier, M., Robinson, S. D., Park, D., Speck, O. & Polimeni, J. R. (2022). Imaging of the pial arterial vasculature of the human brain in vivo using highresolution 7T time-of-flight angiography. *eLife*, *11*. https://doi.org/10.7554/eLife.71186

Boré, A., Guay, S., Bedetti, C., Meisler, S. & GuenTher, N. (2023). *Dcm2Bids* (Version 3.1.1). https://doi.org/10.5281/zenodo.8436509

Borzage, M. T., Doyle, E. K., Liu, C. S. J., Nelson, M. D., Blüml, S., Wood, J. C. & Tamrazi, B. (2022). Quantitative Susceptibility Mapping: Translating an Investigative Research Tool into High Volume Clinical Diagnostic Imaging. https://doi.org/10.3390/diagnostics12122962

Boulloche, N., Denuelle, M., Payoux, P., Fabre, N., Trotter, Y. & Géraud, G. (2010). Photophobia in migraine: An interictal PET study of cortical hyperexcitability and its modulation by pain. *Journal of Neurology, Neurosurgery and Psychiatry*, *81*(9), 978–984. https://doi.org/10.1136/jnnp.2009.190223

Bouras, C., Giannakopoulos, P., Good, P. F., Hsu, A., Hof, P. R. & Perl, D. P. (1997). A Laser Microprobe Mass Analysis of Brain Aluminum and Iron in Dementia pugilistica: Comparison with Alzheimer's Disease. *Eur Neurol*, *38*(1), 53–58.

Braak, H. & Braak, E. (1991). Neuropathological stageing of Alzheimer-related changes. *Acta Neuropathol*, *82*, 239–259.

Bradl, M. & Lassmann, H. (2010). Oligodendrocytes: Biology and pathology. https://doi.org/10.1007/s00401-009-0601-5

Bramlett, H. M. & Dietrich, W. D. (2002). Quantitative structural changes in white and gray matter 1 year following traumatic brain injury in rats. *Acta Neuropathologica*, *103*(6), 607–614. https://doi.org/10.1007/s00401-001-0510-8

Branson, H. M. (2013). Normal Myelination. A Practical Pictorial Review. *Neuroimaging Clinics of North America*, *23*(2), 183–195. https://doi.org/10.1016/j.nic.2012.12.001

Braver, T. S. & Bongiolatti, S. R. (2002). The role of frontopolar cortex in subgoal processing during working memory. *NeuroImage*, *15*(3), 523–536. https://doi.org/10.1006/nimg.2001.1019

Brett, B. L., Koch, K. M., Muftuler, L. T., Budde, M., Mccrea, M. A. & Meier, T. B. (2021). Association of Head Impact Exposure with White Matter Macrostructure and Microstructure Metrics. *Journal of Neurotrauma*, *38*(4), 474–484. https://doi.org/10.1089/neu.2020.7376

Brodmann, K. (2005). *Brodmann's localisation in the cerebral cortex*. Springer New York, NY. https://doi.org/https://doi.org/10.1007/b138298

Broux, B., Gowing, E. & Prat, A. (2015). Glial regulation of the blood-brain barrier in health and disease. https://doi.org/10.1007/s00281-015-0516-2

Butler, M. L., Dixon, E., Stein, T. D., Alvarez, V. E., Huber, B., Buckland, M. E., McKee, A. C. & Cherry, J. D. (2022). Tau Pathology in Chronic Traumatic Encephalopathy is Primarily Neuronal. *Journal of Neuropathology and Experimental Neurology*, *81*(10), 773–780. https://doi.org/10.1093/jnen/nlac065

Button, K. S., Ioannidis, J. P., Mokrysz, C., Nosek, B. A., Flint, J., Robinson, E. S. & Munafò, M. R. (2013). Power failure: Why small sample size undermines the reliability of neuroscience. *Nature Reviews Neuroscience*, *14*(5), 365–376. https://doi.org/10.1038/nrn3475

Cacucci, F., Lever, C., Wills, T. J., Burgess, N. & O'Keefe, J. (2004). Theta-modulated place-by-direction cells in the hippocampal formation in the rat. *Journal of Neuroscience*, *24*(38), 8265–8277. https://doi.org/10.1523/JNEUROSCI.2635-04.2004

Calabresi, P., Picconi, B., Tozzi, A., Ghiglieri, V. & Di Filippo, M. (2014). Direct and indirect pathways of basal ganglia: A critical reappraisal. *Nature Neuroscience*, *17*(8), 1022–1030. https://doi.org/10.1038/nn.3743

Callaghan, M. F., Freund, P., Draganski, B., Anderson, E., Cappelletti, M., Chowdhury, R., Diedrichsen, J., FitzGerald, T. H., Smittenaar, P., Helms, G., Lutti, A. & Weiskopf, N. (2014). Widespread age-related differences in the human brain microstructure revealed by quantitative magnetic resonance imaging. *Neurobiology of Aging*, *35*(8), 1862–1872. https://doi.org/10.1016/j.neurobiolaging.2014.02.008

Cammoun, L., Gigandet, X., Meskaldji, D., Thiran, J. P., Sporns, O., Do, K. Q., Maeder, P., Meuli, R. & Hagmann, P. (2012). Mapping the human connectome at multiple scales with diffusion spectrum MRI. *Journal of Neuroscience Methods*, *203*(2), 386–397. https://doi.org/10.1016/j.jneumeth.2011.09.031

Carroll, E. L., Outtrim, J. G., Forsyth, F., Manktelow, A. E., Hutchinson, P. J., Tenovuo, O., Posti, J. P., Wilson, L., Sahakian, B. J., Menon, D. K. & Newcombe, V. F. (2020). Mild traumatic brain injury recovery: a growth curve modelling analysis over 2 years. *Journal of Neurology*, *267*(11), 3223–3234. https://doi.org/10.1007/s00415-020-09979-x

Cassidy, J. D., Carroll, L. J., Peloso, P. M., Borg, J., von Holst, H., Holm, L., Kraus, J. & Coronado, V. G. (2004). Incidence, risk factors and prevention of mild traumatic brain injury: Results of the WHO Collaborating Centre Task Force on Mild Traumatic Brain Injury. https://doi.org/10.1080/16501960410023732

Chai, C., Guo, R., Zuo, C., Fan, L., Liu, S., Qian, T., Mark Haacke, E., Xia, S. & Shen, W. (2017). Decreased susceptibility of major veins in mild traumatic brain injury is correlated with post-concussive symptoms: A quantitative susceptibility mapping study. *NeuroImage: Clinical*, *15*, 625–632. https://doi.org/10.1016/j.nicl.2017.06.008

Chalmers, D. (1996). *The conscious mind: In search of a fundamental theory*. Oxford University Press, Inc.

Chary, K., Nissi, M. J., Nykänen, O., Manninen, E., Rey, R. I., Shmueli, K., Sierra, A. & Gröhn, O. (2021). Quantitative susceptibility mapping of the rat brain after traumatic brain injury. *NMR in Biomedicine*, *34*(2). https://doi.org/10.1002/nbm.4438

Chen, J., Gong, N. J., Chaim, K. T., Otaduy, M. C. G. & Liu, C. (2021). Decompose quantitative susceptibility mapping (QSM) to sub-voxel diamagnetic and paramagnetic components based on gradient-echo MRI data. *NeuroImage*, *242*. https://doi.org/10.1016/j.neuroimage.2021.118477

Chen, W., Gauthier, S. A., Gupta, A., Comunale, J., Liu, T., Wang, S., Pei, M., Pitt, D. & Wang, Y. (2014a). Quantitative susceptibility mapping of multiple sclerosis lesions at various ages. *Radiology*, *271*(1), 183–192. https://doi.org/10.1148/radiol.13130353

Chen, W., Zhu, W., Kovanlikaya, I., Kovanlikaya, A., Liu, T., Wang, S., Salustri, C. & Wang, Y. (2014b). Intracranial calcifications and hemorrhages: Characterization with quantitative susceptibility mapping. *Radiology*, *270*(2), 496–505. https://doi.org/10.1148/radiol.13122640

Cherry, J. D., Babcock, K. J. & Goldstein, L. E. (2020). Repetitive Head Trauma Induces Chronic Traumatic Encephalopathy by Multiple Mechanisms. *Seminars in Neurology*, *40*(4), 430–438. https://doi.org/10.1055/s-0040-1713620

Cherry, J. D., Esnault, C. D., Baucom, Z. H., Tripodis, Y., Huber, B. R., Alvarez, V. E., Stein, T. D., Dickson, D. W. & McKee, A. C. (2021). Tau isoforms are differentially expressed across the hippocampus in chronic traumatic encephalopathy and Alzheimer's disease. *Acta Neuropathologica Communications*, *9*(1). https://doi.org/10.1186/s40478-021-01189-4

Chong, C. D., Nikolova, S., Dumkrieger, G., Wu, T., Berisha, V., Li, J., Ross, K. & Schwedt, T. J. (2023). Thalamic subfield iron accumulation after acute mild traumatic brain injury as a marker of future post-traumatic headache intensity. *Headache*, *63*(1), 156–164. https://doi.org/10.1111/head.14446

Christidi, F., Bigler, E. D., McCauley, S. R., Schnelle, K. P., Merkley, T. L., Mors, M. B., Li, X., Macleod, M., Chu, Z., Hunter, J. V., Levin, H. S., Clifton, G. L. & Wilde, E. A. (2011). Diffusion tensor imaging of the perforant pathway zone and its relation to memory function in patients with severe traumatic brain injury. *Journal of Neurotrauma*, *28*(5), 711–725. https://doi.org/10.1089/neu.2010.1644

Churchill, N. W., Hutchison, M. G., Graham, S. J. & Schweizer, T. A. (2021). Acute and chronic effects of multiple concussions on midline brain structures. *Neurology*, *97*(12), e1170–e1181. https://doi.org/10.1212/WNL.0000000000012580

Churchill, N. W., Hutchison, M. G., Richards, D., Leung, G., Graham, S. J. & Schweizer, T. A. (2017). The first week after concussion: Blood flow, brain function and white matter microstructure. *NeuroImage: Clinical*, *14*, 480–489. https://doi.org/10.1016/j.nicl.2017.02.015

Clemente, A., Attyé, A., Renard, F., Calamante, F., Burmester, A., Imms, P., Deutscher, E., Akhlaghi, H., Beech, P., Wilson, P. H., Poudel, G., Dominguez, J. F. & Caeyenberghs, K. (2023). Individualised Profiling of White Matter Organisation in Moderate-to-Severe Traumatic Brain Injury Patients Using TractLearn: A Proof-of-Concept Study. *Brain Research*, *1806*. https://doi.org/10.1101/2022.03.03.22271839

Connor, J. R. & Menzies, S. L. (1995). Cellular management of iron in the brain. *Journal of the Neurological Sciences*, *34*, 44.

Contarino, V. E., Conte, G., Morelli, C., Trogu, F., Scola, E., Calloni, S. F., Sanmiguel Serpa, L. C., Liu, C., Silani, V. & Triulzi, F. (2020). Toward a marker of upper motor neuron impairment in amyotrophic lateral sclerosis: A fully automatic investigation of the magnetic susceptibility in the precentral cortex. *European Journal of Radiology*, *124*. https://doi.org/10.1016/j.ejrad.2020.108815

Cook, G. A. & Hawley, J. S. (2014). A review of mild traumatic brain injury diagnostics: Current perspectives, limitations, and emerging technology. *Military Medicine*, *179*(10), 1083–1089. https://doi.org/10.7205/MILMED-D-13-00435

Crowe, L. M., Hearps, S., Anderson, V., Borland, M. L., Phillips, N., Kochar, A., Dalton, S., Cheek, J. A., Gilhotra, Y., Furyk, J., Neutze, J., Lyttle, M. D., Bressan, S., Donath, S., Molesworth, C., Oakley, E., Dalziel, S. R. & Babl, F. E. (2018). Investigating the Variability in Mild Traumatic Brain Injury Definitions: A Prospective Cohort Study. *Archives of Physical Medicine and Rehabilitation*, *99*(7), 1360–1369. https://doi.org/10.1016/j.apmr.2017.12.026

Daducci, A., Gerhard, S., Griffa, A., Lemkaddem, A., Cammoun, L., Gigandet, X., Meuli, R., Hagmann, P. & Thiran, J. P. (2012). The Connectome Mapper: An Open-Source Processing Pipeline to Map Connectomes with MRI. *PLoS ONE*, *7*(12). https://doi.org/10.1371/journal.pone.0048121

Daglas, M. & Adlard, P. A. (2018). The Involvement of Iron in Traumatic Brain Injury and Neurodegenerative Disease. *Frontiers in Neuroscience*, *12*. https://doi.org/10.3389/fnins.2018.00981

Dai, Y., Zeng, M., Li, R., Rao, S., Chen, C., Delproposto, Z., Haacke, E. M., Hu, J. & Renate, J. (2011). Improving detection of siderotic nodules in cirrhotic liver with a multi-breath-hold susceptibility-weighted imaging technique. *Journal of Magnetic Resonance Imaging*, *34*(2), 318–325. https://doi.org/10.1002/jmri.22607

De Beaumont, L., Thoret, H., Mongeon, D., Messier, J., Leclerc, S., Tremblay, S., Ellemberg, D. & Lassonde, M. (2009). Brain function decline in healthy retired athletes who sustained their last sports concussion in early adulthood. *Brain*, *132*(3), 695–708. https://doi.org/10.1093/brain/awn347

De Beaumont, L., Tremblay, S., Poirier, J., Lassonde, M. & Théoret, H. (2012). Altered bidirectional plasticity and reduced implicit motor learning in concussed athletes. *Cerebral Cortex*, *22*(1), 112–121. https://doi.org/10.1093/cercor/bhr096

De Rochefort, L., Brown, R., Prince, M. R. & Wang, Y. (2008). Quantitative MR susceptibility mapping using piece-wise constant regularized inversion of the magnetic field. *Magnetic Resonance in Medicine*, *60*(4), 1003–1009. https://doi.org/10.1002/mrm.21710

De Rochefort, L., Liu, T., Kressler, B., Liu, J., Spincemaille, P., Lebon, V., Wu, J. & Wang, Y. (2010). Quantitative susceptibility map reconstruction from MR phase data using bayesian regularization: Validation and application to brain imaging. *Magnetic Resonance in Medicine*, *63*(1), 194–206. https://doi.org/10.1002/mrm.22187

Deen, B., Koldewyn, K., Kanwisher, N. & Saxe, R. (2015). Functional organization of social perception and cognition in the superior temporal sulcus. *Cerebral Cortex*, *25*(11), 4596–4609. https://doi.org/10.1093/cercor/bhv111

Deh, K., Ponath, G. D., Molvi, Z., Parel, G. C. T., Gillen, K. M., Zhang, S., Nguyen, T. D., Spincemaille, P., Ma, Y., Gupta, A., Gauthier, S. A., Pitt, D. & Wang, Y. (2018). Magnetic susceptibility increases as diamagnetic molecules breakdown: Myelin digestion during multiple sclerosis lesion formation contributes to increase on QSM. *Journal of Magnetic Resonance Imaging*, *48*(5), 1281–1287. https://doi.org/10.1002/jmri.25997

de Haan, S., de Groot, J. C., Jacobs, B. & van der Naalt, J. (2017). The association between microhaemorrhages and post - traumatic functional outcome in the chronic phase after mild traumatic brain injury. *Neuroradiology*, *59*(10), 963–969. https://doi.org/10.1007/s00234-017-1898-8

Deistung, A., Schäfer, A., Schweser, F., Biedermann, U., Turner, R. & Reichenbach, J. R. (2013a). Toward in vivo histology: A comparison of quantitative susceptibility mapping (QSM) with magnitude-, phase-, and R2*-imaging at ultra-high magnetic field strength. *NeuroImage*, *65*, 299–314. https://doi.org/10.1016/j.neuroimage.2012.09.055

Deistung, A., Schweser, F. & Reichenbach, J. R. (2017). Overview of quantitative susceptibility mapping. https://doi.org/10.1002/nbm.3569

Deistung, A., Schweser, F., Wiestler, B., Abello, M., Roethke, M., Sahm, F., Wick, W., Nagel, A. M., Heiland, S., Schlemmer, H. P., Bendszus, M., Reichenbach, J. R. & Radbruch, A. (2013b). Quantitative Susceptibility Mapping Differentiates between Blood Depositions and Calcifications in Patients with Glioblastoma. *PLoS ONE*, *8*(3). https://doi.org/10.1371/journal.pone.0057924

Denk, C., Torres, E. H., Mackay, A. & Rauscher, A. (2011). The influence of white matter fibre orientation on MR signal phase and decay. *NMR in Biomedicine*, *24*(3), 246–252. https://doi.org/10.1002/nbm.1581

Dennett, D. C. (1993). *Consciousness explained*. Penguin uk.

Desikan, R. S., Ségonne, F., Fischl, B., Quinn, B. T., Dickerson, B. C., Blacker, D., Buckner, R. L., Dale, A. M., Maguire, R. P., Hyman, B. T., Albert, M. S. & Killiany, R. J. (2006). An automated labeling system for subdividing the human cerebral cortex on MRI scans into gyral based regions of interest. *NeuroImage*, *31*(3), 968–980. https://doi.org/10.1016/j.neuroimage.2006.01.021

Dieterich, M. & Brandt, T. (2008). Functional brain imaging of peripheral and central vestibular disorders. *Brain*, *131*(10), 2538–2552. https://doi.org/10.1093/brain/awn042

Dimov, A. V., Gillen, K. M., Nguyen, T. D., Kang, J., Sharma, R., Pitt, D., Gauthier, S. A. & Wang, Y. (2022). Magnetic Susceptibility Source Separation Solely from Gradient Echo Data: Histological Validation. *Tomography*, *8*(3), 1544–1551. https://doi.org/10.3390/tomography8030127

Dimov, A. V., Gupta, A., Kopell, B. H. & Wang, Y. (2019). High-resolution QSM for functional and structural depiction of subthalamic nuclei in DBS presurgical mapping. *Journal of Neurosurgery*, *131*(2), 360–367. https://doi.org/10.3171/2018.3.JNS172145

Dimov, A. V., Li, J., Nguyen, T. D., Roberts, A. G., Spincemaille, P., Straub, S., Zun, Z., Prince, M. R. & Wang, Y. (2023). QSM Throughout the Body. *Journal of Magnetic Resonance Imaging*, *57*(6), 1621–1640. https://doi.org/10.1002/jmri.28624

Ding, S. L. (2013). Comparative anatomy of the prosubiculum, subiculum, presubiculum, postsubiculum, and parasubiculum in human, monkey, and rodent. https://doi.org/10.1002/cne.23416

Ding, S. L. & Van Hoesen, G. W. (2015). Organization and detailed parcellation of human hippocampal head and body regions based on a combined analysis of Cyto- and chemoarchitecture. *Journal of Comparative Neurology*, *523*(15), 2233–2253. https://doi.org/10.1002/cne.23786

Doherty, C. P., O'Keefe, E., Wallace, E., Loftus, T., Keaney, J., Kealy, J., Humphries, M. M., Molloy, M. G., Meaney, J. F., Farrell, M. & Campbell, M. (2016). Blood-Brain Barrier Dysfunction as a Hallmark Pathology in Chronic Traumatic Encephalopathy. *Journal of Neuropathology and Experimental Neurology*, *75*(7), 656–662. https://doi.org/10.1093/jnen/nlw036

Domínguez, J. F., Stewart, A., Burmester, A., Akhlaghi, H., O'Brien, K., Bollmann, S. & Caeyenberghs, K. (2024). Improving quantitative susceptibility mapping for the identification of traumatic brain injury neurodegeneration at the individual level. *Zeitschrift fur Medizinische Physik*. https://doi.org/10.1016/j.zemedi.2024.01.001

Drachman, D. A. (2005). Do we have brain to spare? *Neurology*, *64*(12), 2004–2005.

Drew, L. B. & Drew, W. E. (2004). The contrecoup-coup phenomenon. *Neurocrit Care*.

Du, G., Liu, T., Lewis, M. M., Kong, L., Wang, Y., Connor, J., Mailman, R. B. & Huang, X. (2016). Quantitative susceptibility mapping of the midbrain in Parkinson's disease. *Movement Disorders*, *31*(3), 317–324. https://doi.org/10.1002/mds.26417

Du, L., Zhao, Z., Cui, A., Zhu, Y., Zhang, L., Liu, J., Shi, S., Fu, C., Han, X., Gao, W., Song, T., Xie, L., Wang, L., Sun, S., Guo, R. & Ma, G. (2018). Increased Iron Deposition on Brain Quantitative Susceptibility Mapping Correlates with Decreased Cognitive Function in Alzheimer's Disease. *ACS Chemical Neuroscience*, *9*(7), 1849–1857. https://doi.org/10.1021/acschemneuro.8b00194

Duyn, J. H. (2013). MR susceptibility imaging. *Journal of Magnetic Resonance*, *229*, 198–207. https://doi.org/10.1016/j.jmr.2012.11.013

Duyn, J. H. & Schenck, J. (2017). Contributions to magnetic susceptibility of brain tissue. *NMR in Biomedicine*, *30*(4). https://doi.org/10.1002/nbm.3546

Dybing, K. M., Vetter, C. J., Dempsey, D. A., Chaudhuri, S., Saykin, A. J. & Risacher, S. L. (2023). Traumatic brain injury and Alzheimer's Disease biomarkers: A systematic review of findings from amyloid and tau positron emission tomography (PET). *medRxiv*, (Preprint). https://doi.org/10.1101/2023.11.30.23298528

Dymerska, B., Eckstein, K., Bachrata, B., Siow, B., Trattnig, S., Shmueli, K. & Robinson, S. D. (2021). Phase unwrapping with a rapid opensource minimum spanning tree algorithm (ROMEO). *Magnetic Resonance in Medicine*, *85*(4), 2294–2308. https://doi.org/10.1002/mrm.28563

Elnekeidy, A. E., Yehia, A. & Elfatatry, A. (2014). Importance of susceptibility weighted imaging (SWI) in management of cerebro-vascular strokes (CVS). *Alexandria Journal of Medicine*, *50*(1), 83–91. https://doi.org/10.1016/j.ajme.2013.05.006

Emmerich, J., Bachert, P., Ladd, M. E. & Straub, S. (2021). On the separation of susceptibility sources in quantitative susceptibility mapping: Theory and phantom validation with an in vivo application to multiple sclerosis lesions of different age. *Journal of Magnetic Resonance*, *330*. https://doi.org/10.1016/j.jmr.2021.107033

Fan, A. P., Bilgic, B., Gagnon, L., Witzel, T., Bhat, H., Rosen, B. R. & Adalsteinsson, E. (2014). Quantitative oxygenation venography from MRI phase. *Magnetic Resonance in Medicine*, *72*(1), 149–159. https://doi.org/10.1002/mrm.24918

Fan, A. P., Evans, K. C., Stout, J. N., Rosen, B. R. & Adalsteinsson, E. (2015a). Regional quantification of cerebral venous oxygenation from MRI susceptibility during hypercapnia. *NeuroImage*, *104*, 146–155. https://doi.org/10.1016/j.neuroimage.2014.09.068

Fan, A. P., Govindarajan, S. T., Kinkel, R. P., Madigan, N. K., Nielsen, A. S., Benner, T., Tinelli, E., Rosen, B. R., Adalsteinsson, E. & Mainero, C. (2015b). Quantitative oxygen extraction fraction from 7-Tesla MRI phase: Reproducibility and application in multiple sclerosis. *Journal of Cerebral Blood Flow and Metabolism*, *35*(1), 131–139. https://doi.org/10.1038/jcbfm.2014.187

Farkas, O., Lifshitz, J. & Povlishock, J. T. (2006). Mechanoporation induced by diffuse traumatic brain injury: An irreversible or reversible response to injury? *Journal of Neuroscience*, *26*(12), 3130–3140. https://doi.org/10.1523/JNEUROSCI.5119-05.2006

Feigin, V. L., Theadom, A., Barker-Collo, S., Starkey, N. J., McPherson, K., Kahan, M., Dowell, A., Brown, P., Parag, V., Kydd, R., Jones, K., Jones, A. & Ameratunga, S. (2013). Incidence of traumatic brain injury in New Zealand: A population-based study. *The Lancet Neurology*, *12*(1), 53–64. https://doi.org/10.1016/S1474-4422(12)70262-4

Feng, W., Neelavalli, J. & Haacke, E. M. (2013). Catalytic multiecho phase unwrapping scheme (CAMPUS) in multiecho gradient echo imaging: Removing phase wraps on a voxel-by-voxel basis. *Magnetic Resonance in Medicine*, *70*(1), 117–126. https://doi.org/10.1002/mrm.24457

Fischl, B. (2012). FreeSurfer. https://doi.org/10.1016/j.neuroimage.2012.01.021

Fischl, B. & Dale, A. M. (2000). Measuring the thickness of the human cerebral cortex from magnetic resonance images. *PNAS*, *20*(97). www.pnas.org

Fiscone, C., Curti, N., Ceccarelli, M., Remondini, D., Testa, C., Lodi, R., Tonon, C., Manners, D. N. & Castellani, G. (2024). Generalizing the Enhanced-DeepSuper-Resolution Neural Network to Brain MR Images: A Retrospective Study on the Cam-CAN Dataset. *eNeuro*, *11*(5). https://doi.org/10.1523/ENEURO.0458-22.2023

Flavin, W. P., Hosseini, H., Ruberti, J. W., Kavehpour, H. P., Giza, C. C. & Prins, M. L. (2023). Traumatic brain injury and the pathways to cerebral tau accumulation. *Frontiers in Neurology*, *14*. https://doi.org/10.3389/fneur.2023.1239653

Fox, R. F. (2004). Origin of Life and Energy. *Encyclopedia of Energy*, *4*, 781–792.

Fukunaga, M., Li, T. Q., Van Gelderen, P., De Zwart, J. A., Shmueli, K., Yao, B., Lee, J., Maric, D., Aronova, M. A., Zhang, G., Leapman, R. D., Schenck, J. F., Merkle, H. & Duyn, J. H. (2010). Layer-specific variation of iron content in cerebral cortex as a source of MRI contrast. *Proceedings of the National Academy of Sciences of the United States of America*, *107*(8), 3834–3839. https://doi.org/10.1073/pnas.0911177107

Gallagher, V., Kramer, N., Abbott, K., Alexander, J., Breiter, H., Herrold, A., Lindley, T., Mjaanes, J. & Reilly, J. (2018). The effects of sex differences and hormonal contraception on outcomes after collegiate sports-related concussion. *Journal of Neurotrauma*, *35*(11), 1242–1247. https://doi.org/10.1089/neu.2017.5453

Gao, X. & Chen, J. (2011). Mild traumatic brain injury results in extensive neuronal degeneration in the cerebral cortex. *Journal of Neuropathology and Experimental Neurology*, *70*(3), 183–191. https://doi.org/10.1097/NEN.0b013e31820c6878

Gardner, R. C. & Yaffe, K. (2015). Epidemiology of mild traumatic brain injury and neurodegenerative disease. https://doi.org/10.1016/j.mcn.2015.03.001

Gayoso, M. J., Al-Majdalawi, A., Garrosa, M., Calvo, B. & Díaz-Flores, L. (2003). Selective calcification of rat brain lesions caused by systemic administration of kainic acid. *Histology and Histopathology*, (18), 855–869. https://doi.org/10.14670/HH-18.855

Geddes, D. M., LaPlaca, M. C. & Cargill, R. S. (2003). Susceptibility of hippocampal neurons to mechanically induced injury. *Experimental Neurology*, *184*(1), 420–427. https://doi.org/10.1016/S0014-4886(03)00254-1

George, K. K., Heithoff, B. P., Shandra, O. & Robel, S. (2022). Mild Traumatic Brain Injury/Concussion Initiates an Atypical Astrocyte Response Caused by Blood-Brain Barrier Dysfunction. *Journal of Neurotrauma*, *39*(1-2), 211–226. https://doi.org/10.1089/neu.2021.0204

Ghaderi, S., Mohammadi, S., Nezhad, N. J., Karami, S. & Sayehmiri, F. (2024). Iron quantification in basal ganglia: quantitative susceptibility mapping as a potential biomarker for Alzheimer's disease – a systematic review and meta-analysis. https://doi.org/10.3389/fnins.2024.1338891

Ghadery, C., Pirpamer, L., Hofer, E., Langkammer, C., Petrovic, K., Loitfelder, M., Schwingenschuh, P., Seiler, S., Duering, M., Jouvent, E., Schmidt, H., Fazekas, F., Mangin, J. F., Chabriat, H., Dichgans, M., Ropele, S. & Schmidt, R. (2015). R2* mapping for brain iron: Associations with cognition in normal aging. *Neurobiology of Aging*, *36*(2), 925–932. https://doi.org/10.1016/j.neurobiolaging.2014.09.013

Ghajari, M., Hellyer, P. J. & Sharp, D. J. (2017). Computational modelling of traumatic brain injury predicts the location of chronic traumatic encephalopathy pathology. *Brain*, *140*(2), 333–343. https://doi.org/10.1093/brain/aww317

Gillen, K. M., Nguyen, T. D., Dimov, A., Kovanlikaya, I., Luu, H. M., Demmon, E., Markowitz, D. M., Bagnato, F., Pitt, D., Gauthier, S. A. & Wang, Y. (2025). Quantitative susceptibility mapping is more sensitive and specific than phase imaging in detecting chronic active multiple sclerosis lesion rims: pathological validation. *Brain Communications*, *7*(1). https://doi.org/10.1093/braincomms/fcaf011

Girard, R., Fam, M. D., Zeineddine, H. A., Tan, H., Mikati, A. G., Shi, C., Jesselson, M., Shenkar, R., Wu, M., Cao, Y., Hobson, N., Larsson, H. B., Christoforidis, G. A. & Awad, I. A. (2017). Vascular permeability and iron deposition biomarkers in longitudinal follow-up of cerebral cavernous malformations. *Journal of Neurosurgery*, *127*(1), 102–110. https://doi.org/10.3171/2016.5.JNS16687

Giza, C. C. & Hovda, D. A. (2001). The Neurometabolic Cascade of Concussion. *Journal of Athletic Training*, *36*(3), 228–235. www.journalofathletictraining.org

Giza, C. C. & Hovda, D. A. (2014). The new neurometabolic cascade of concussion. *Neurosurgery*, *75*, S24–S33. https://doi.org/10.1227/NEU.0000000000000505

Goedert, M., Eisenberg, D. S. & Crowther, R. A. (2017). Propagation of Tau Aggregates and Neurodegeneration. *Annu. Rev. Neurosci.*, *40*, 189–210. https://doi.org/10.1146/annurev-neuro-072116

Gong, N. J., Dibb, R., Bulk, M., van der Weerd, L. & Liu, C. (2019). Imaging beta amyloid aggregation and iron accumulation in Alzheimer's disease using quantitative susceptibility mapping MRI. *NeuroImage*, *191*, 176–185. https://doi.org/10.1016/j.neuroimage.2019.02.019

Gong, N. J., Kuzminski, S., Clark, M., Fraser, M., Sundman, M., Guskiewicz, K., Petrella, J. R. & Liu, C. (2018). Microstructural alterations of cortical and deep gray matter over a season of high school football revealed by diffusion kurtosis imaging. *Neurobiology of Disease*, *119*, 79–87. https://doi.org/10.1016/j.nbd.2018.07.020

Gong, N. J., Wong, C. S., Hui, E. S., Chan, C. C. & Leung, L. M. (2015). Hemisphere, gender and age-related effects on iron deposition in deep gray matter revealed by quantitative susceptibility mapping. *NMR in Biomedicine*, *28*(10), 1267–1274. https://doi.org/10.1002/nbm.3366

Gorgolewski, K. J., Auer, T., Calhoun, V. D., Craddock, R. C., Das, S., Duff, E. P., Flandin, G., Ghosh, S. S., Glatard, T., Halchenko, Y. O., Handwerker, D. A., Hanke, M., Keator, D., Li, X., Michael, Z., Maumet, C., Nichols, B. N., Nichols, T. E., Pellman, J., … Poldrack, R. A. (2016). The brain imaging data structure, a format for organizing and describing outputs of neuroimaging experiments. *Scientific Data*, *3*. https://doi.org/10.1038/sdata.2016.44

Gozt, A., Hellewell, S., Ward, P. G., Bynevelt, M. & Fitzgerald, M. (2021a). Emerging Applications for Quantitative Susceptibility Mapping in the Detection of Traumatic Brain Injury Pathology. *Neuroscience*, *467*, 218–236. https://doi.org/10.1016/j.neuroscience.2021.05.030

Gozt, A., Hellewell, S., Thorne, J., Thomas, E., Buhagiar, F., Markovic, S., Van Houselt, A., Ring, A., Arendts, G., Smedley, B., Van Schalkwyk, S., Brooks, P., Iliff, J., Celenza, A., Mukherjee, A., Xu, D., Robinson, S., Honeybul, S., Cowen, G., … Fitzgerald, M. (2021b). Predicting outcome following mild traumatic brain injury: Protocol for the longitudinal, prospective, observational Concussion Recovery (CREST) cohort study. *BMJ Open*, *11*(5). https://doi.org/10.1136/bmjopen-2020-046460

Graham, A., Livingston, G., Purnell, L. & Huntley, J. (2022). Mild Traumatic Brain Injuries and Future Risk of Developing Alzheimer's Disease: Systematic Review and Meta-Analysis. https://doi.org/10.3233/JAD-220069

Greve, D. N. & Fischl, B. (2009). Accurate and robust brain image alignment using boundary-based registration. *NeuroImage*, *48*(1), 63–72. https://doi.org/10.1016/j.neuroimage.2009.06.060

Grochowski, C., Blicharska, E., Krukow, P., Jonak, K., Maciejewski, M., Szczepanek, D., Jonak, K., Flieger, J. & Maciejewski, R. (2019). Analysis of trace elements in human brain: Its aim, methods, and concentration levels. https://doi.org/10.3389/fchem.2019.00115

Grovola, M. R., Paleologos, N., Wofford, K. L., Harris, J. P., Browne, K. D., Johnson, V., Duda, J. E., Wolf, J. A. & Cullen, D. K. (2020). Mossy cell hypertrophy and synaptic changes in the hilus following mild diffuse traumatic brain injury in pigs. *Journal of Neuroinflammation*, *17*(1). https://doi.org/10.1186/s12974-020-1720-0

Guo, Y., Chen, Y., Zhang, X., Mei, Y., Yi, P., Wang, Y., Feng, Q., Tegola, L. L., Guglielmi, G., Zhang, X. & Feng, Y. (2019). Magnetic Susceptibility and Fat Content in the Lumbar Spine of Postmenopausal Women With Varying Bone Mineral Density. *Journal of Magnetic Resonance Imaging*, *49*(4), 1020–1028. https://doi.org/10.1002/jmri.26279

Guskiewicz, K. M., Marshall, S. W., Bailes, J., McCrea, M., Cantu, R. C., Randolph, C. & Jordan, B. D. (2005). Association between Recurrent Concussion and Late-Life Cognitive Impairment in Retired Professional Football Players. *Neurosurgery*, *57*(4), 719–726. https://doi.org/10.1227/01.neu.0000175725.75780.dd

Guskiewicz, K. M., Marshall, S. W., Bailes, J., Mccrea, M., Harding, H. P., Matthews, A., Mihalik, J. R. & Cantu, R. C. (2007). Recurrent concussion and risk of depression in retired professional football players. *Medicine and Science in Sports and Exercise*, *39*(6), 903–909. https://doi.org/10.1249/mss.0b013e3180383da5

Haacke, M. E., Cheng, N. Y., House, M. J., Liu, Q., Neelavalli, J., Ogg, R. J., Khan, A., Ayaz, M., Kirsch, W. & Obenaus, A. (2005). Imaging iron stores in the brain using magnetic resonance imaging. *Magnetic Resonance Imaging*, *23*(1), 1–25. https://doi.org/10.1016/j.mri.2004.10.001

Haacke, M. E., Delproposto, Z. S., Chaturvedi, S., Sehgal, V., Tenzer, M., Neelavalli, J. & Kido, D. (2007). Imaging Cerebral Amyloid Angiopathy with Susceptibility-Weighted Imaging. *AJNR*, *28*(2), 316–317. www.ajnr.org

Haacke, M. E., Liu, S., Buch, S., Zheng, W., Wu, D. & Ye, Y. (2015). Quantitative susceptibility mapping: Current status and future directions. https://doi.org/10.1016/j.mri.2014.09.004

Haacke, M. E., Xu, Y., Cheng, Y. C. N. & Reichenbach, J. R. (2004). Susceptibility weighted imaging (SWI). *Magnetic Resonance in Medicine*, *52*(3), 612–618. https://doi.org/10.1002/mrm.20198

Hageman, G., Hof, J. & Nihom, J. (2022). Susceptibility-Weighted MRI and Microbleeds in Mild Traumatic Brain Injury: Prediction of Posttraumatic Complaints? https://doi.org/10.1159/000521389

Hagemeier, J., Geurts, J. J. & Zivadinov, R. (2012). Brain iron accumulation in aging and neurodegenerative disorders. *Expert Review of Neurotherapeutics*, *12*(12), 1467–1480. https://doi.org/10.1586/ern.12.128

Hagemeier, J., Zivadinov, R., Dwyer, M. G., Polak, P., Bergsland, N., Weinstock-Guttman, B., Zalis, J., Deistung, A., Reichenbach, J. R. & Schweser, F. (2018). Changes of deep gray matter magnetic susceptibility over 2 years in multiple sclerosis and healthy control brain. *NeuroImage: Clinical*, *18*, 1007–1016. https://doi.org/10.1016/j.nicl.2017.04.008

Haller, S., Haacke, E. M., Thurnher, M. M. & Barkhof, F. (2021). Susceptibility-weighted imaging: Technical essentials and clinical neurologic applications. https://doi.org/10.1148/RADIOL.2021203071

Hallgren, B. & Sourander, P. (1958). The effect of age on the non-haemin iron in the human brain. *Journal of Neurochemistry*, *3*, 41–51.

Hametner, S., Wimmer, I., Haider, L., Pfeifenbring, S., Brück, W. & Lassmann, H. (2013). Iron and neurodegeneration in the multiple sclerosis brain. *Annals of Neurology*, *74*(6), 848–861. https://doi.org/10.1002/ana.23974

Hametner, S., Endmayr, V., Deistung, A., Palmrich, P., Prihoda, M., Haimburger, E., Menard, C., Feng, X., Haider, T., Leisser, M., Köck, U., Kaider, A., Höftberger, R., Robinson, S., Reichenbach, J. R., Lassmann, H., Traxler, H., Trattnig, S. & Grabner, G. (2018). The influence of brain iron and myelin on magnetic susceptibility and effective transverse relaxation - A biochemical and histological validation study. *NeuroImage*, *179*, 117–133. https://doi.org/10.1016/j.neuroimage.2018.06.007

Han, S., Lv, Y., Gao, K., Quan, Q., Lu, H., Liang, H., Zhu, Y., Meng, L. & Luo, Y. (2023). Quantitative Susceptibility Mapping as a Biomarker to Assess Middle Cerebral Artery Thrombus Composition in Acute Ischemic Stroke. *Journal of Vascular Diseases*, *2*(1), 112–121. https://doi.org/10.3390/jvd2010009

Harada, T., Kudo, K., Fujima, N., Yoshikawa, M., Ikebe, Y., Sato, R., Shirai, T., Bito, Y., Uwano, I. & Miyata, M. (2022). Quantitative Susceptibility Mapping: Basic Methods and Clinical Applications. *Radiographics*, *42*(4), 1161–1176. https://doi.org/10.1148/rg.210054

Hardaker, N. J., Hume, P. A. & Sims, S. T. (2024). Differences in Injury Profiles Between Female and Male Athletes Across the Participant Classification Framework: A Systematic Review and Meta-Analysis. https://doi.org/10.1007/s40279-024-02010-7

Hardy, J., Duff, K., Jaunmuktane, Z., Jabbari, E., Phd, M., Square, Q., Thom, M., Lila, R., Institute, W., Lees, A., Morris, H., Duff, K., Langworth-Green, C., Patel, S., Jaunmuktane, Z., Jabbari, E., Morris, H., Thom, M., Lees, A., … Zandi, M. (2023). *Chronic effects of inflammation on tauopathies* (tech. rep.). www.thelancet.com/neurology

He, N., Ling, H., Ding, B., Huang, J., Zhang, Y., Zhang, Z., Liu, C., Chen, K. & Yan, F. (2015). Region-specific disturbed iron distribution in early idiopathic Parkinson's disease measured by quantitative susceptibility mapping. *Human Brain Mapping*, *36*(11), 4407–4420. https://doi.org/10.1002/hbm.22928

Head Injury Interdisciplinary Special Interest Group of the American Congress of Rehabilitation. (1993). Definition of mild traumatic brain injury. *J Head Trauma Rehabil*, *3*(8), 86–87.

Heimer, L. & Van Hoesen, G. W. (2006). The limbic lobe and its output channels: Implications for emotional functions and adaptive behavior. *Neuroscience and Biobehavioral Reviews*, *30*(2), 126–147. https://doi.org/10.1016/j.neubiorev.2005.06.006

Hein, G. & Knight, R. T. (2008). Superior temporal sulcus - It's my area: Or is it? https://doi.org/10.1162/jocn.2008.20148

Hellewell, S. C., Beaton, C. S., Welton, T. & Grieve, S. M. (2020). Characterizing the risk of depression following mild traumatic brain injury: A meta-analysis of the literature comparing chronic mTBI to non-mTBI populations. *Frontiers in Neurology*, *11*, 1–14. https://doi.org/10.3389/fneur.2020.00350

Hellstrøm, T., Westlye, L. T., Kaufmann, T., Trung Doan, N., Søberg, H. L., Sigurdardottir, S., Nordhøy, W., Helseth, E., Andreassen, O. A. & Andelic, N. (2017). White matter microstructure is associated with functional, cognitive and emotional symptoms 12 months after mild traumatic brain injury. *Scientific Reports*, *7*(1). https://doi.org/10.1038/s41598-017-13628-1

Herculano-Houzel, S. (2009). The human brain in numbers: A linearly scaled-up primate brain. https://doi.org/10.3389/neuro.09.031.2009

Hier, D. B., Obafemi-Ajayi, T., Thimgan, M. S., Olbricht, G. R., Azizi, S., Allen, B., Hadi, B. A. & Wunsch, D. C. (2021). Blood biomarkers for mild traumatic brain injury: a selective review of unresolved issues. *Biomarker Research*, *9*(1). https://doi.org/10.1186/s40364-021-00325-5

Hinson, H. E., Rowell, S. & Schreiber, M. (2015). Clinical evidence of inflammation driving secondary brain injury: A systematic review. https://doi.org/10.1097/TA.0000000000000468

Horé, A. & Ziou, D. (2010). Image quality metrics: PSNR vs. SSIM. *Proceedings - International Conference on Pattern Recognition*, 2366–2369. https://doi.org/10.1109/ICPR.2010.579

Howe, E. I., Andelic, N., Fure, S. C., Røe, C., Søberg, H. L., Hellstrøm, T., Spjelkavik, Ø., Enehaug, H., Lu, J., Ugelstad, H., Løvstad, M. & Aas, E. (2022). Cost-effectiveness analysis of combined cognitive and vocational rehabilitation in patients with mild-to-moderate TBI: results from a randomized controlled trial. *BMC Health Services Research*, *22*(1). https://doi.org/10.1186/s12913-022-07585-3

Howell, E. (2022). *How many stars are in the milky way?* Published February 12, 2022 on Space.com.

Huang, S., Li, S., Feng, H. & Chen, Y. (2021). Iron Metabolism Disorders for Cognitive Dysfunction After Mild Traumatic Brain Injury. *Frontiers in Neuroscience*, *15*. https://doi.org/10.3389/fnins.2021.587197

Iglesias, J. E., Augustinack, J. C., Nguyen, K., Player, C. M., Player, A., Wright, M., Roy, N., Frosch, M. P., McKee, A. C., Wald, L. L., Fischl, B. & Van Leemput, K. (2015). A computational atlas of the hippocampal formation using ex vivo, ultra-high resolution MRI: Application to adaptive segmentation of in vivo MRI. *Neuroimage*, (115), 117–137.

Ikebe, Y., Ishimaru, H., Imai, H., Abe, K., Izumo, T., Morofuji, Y., Ideguchi, R., Morikawa, M. & Uetani, M. (2020). Quantitative susceptibility mapping for carotid atherosclerotic plaques: A pilot study. *Magnetic Resonance in Medical Sciences*, *19*(2), 135–140. https://doi.org/10.2463/mrms.mp.2018-0077

Iliff, J. J., Chen, M. J., Plog, B. A., Zeppenfeld, D. M., Soltero, M., Yang, L., Singh, I., Deane, R. & Nedergaard, M. (2014). Impairment of glymphatic pathway function promotes tau pathology after traumatic brain injury. *Journal of Neuroscience*, *34*(49), 16180–16193. https://doi.org/10.1523/JNEUROSCI.3020-14.2014

Imms, P., Clemente, A., Deutscher, E., Radwan, A. M., Akhlaghi, H., Beech, P., Wilson, P. H., Irimia, A., Poudel, G., Domínguez Duque, J. F. & Caeyenberghs, K. (2022). Exploring personalized structural connectomics for moderate to severe traumatic brain injury. *Network Neuroscience*, *1*(7), 160–183. https://doi.org/10.1162/netn{_}a

Inglese, M., Makani, S., Johnson, G., Cohen, B. A., Silver, J. A. & Grossman, R. I. (2005). Diffuse axonal injury in mild traumatic brain injury: a diffusion tensor imaging study. *J. Neurosurg*, *103*, 298–303.

Jafari, R., Hectors, S. J., Koehne de González, A. K., Spincemaille, P., Prince, M. R., Brittenham, G. M. & Wang, Y. (2021). Integrated quantitative susceptibility and R2* mapping for evaluation of liver fibrosis: An ex vivo feasibility study. *NMR in Biomedicine*, *34*(1). https://doi.org/10.1002/nbm.4412

Jafari, R., Sheth, S., Spincemaille, P., Nguyen, T. D., Prince, M. R., Wen, Y., Guo, Y., Deh, K., Liu, Z., Margolis, D., Brittenham, G. M., Kierans, A. S. & Wang, Y. (2019). Rapid automated liver quantitative susceptibility mapping. *Journal of Magnetic Resonance Imaging*, *50*(3), 725–732. https://doi.org/10.1002/jmri.26632

Jahn, H. (2013). Memory loss in Alzheimer's disease. *Dialogues Clin Neurosci.*, (15), 445–454.

Jakimovski, D., Bittner, S., Zivadinov, R., Morrow, S. A., Benedict, R. H., Zipp, F. & Weinstock-Guttman, B. (2024). Multiple sclerosis. *The Lancet*, *403*(10422), 183–202. https://doi.org/10.1016/S0140-6736(23)01473-3

Jang, J., Nam, Y., Jung, S. W., Riew, T. R., Kim, S. H. & Kim, I. B. (2021). Paradoxical paramagnetic calcifications in the globus pallidus: An ex vivo MR investigation and histological validation study. *NMR in Biomedicine*, *34*(10). https://doi.org/10.1002/nbm.4571

Jenkinson, M. (2003). Fast, automated, N-dimensional phase-unwrapping algorithm. *Magnetic Resonance in Medicine*, *49*(1), 193–197. https://doi.org/10.1002/mrm.10354

Jenkinson, M., Bannister, P., Brady, M. & Smith, S. (2002). Improved Optimization for the Robust and Accurate Linear Registration and Motion Correction of Brain Images. *NeuroImage*, *17*(2), 825–841. https://doi.org/10.1006/nimg.2002.1132

Jenkinson, M., Beckmann, C. F., Behrens, T. E., Woolrich, M. W. & Smith, S. M. (2012). FSL. *NeuroImage*, *62*(2), 782–790. https://doi.org/10.1016/j.neuroimage.2011.09.015

Jenkinson, M. & Smith, S. (2001). A global optimisation method for robust affine registration of brain images. *Medical Image Analysis*, *5*, 143–156. www.elsevier.com/locate/media

Jia, H., Liu, X., Cao, Y., Niu, H., Lan Zhang, Li, R. J., Li, F., Sun, D., Shi, M., Wa, L., Liu, X., Yang, G., Chen, F., Zhang, S. & Zhang, J. (2023). Deferoxamine ameliorates neurological dysfunction by inhibiting ferroptosis and neuroinflammation after traumatic brain injury. *Brain Research*, *1812*. https://doi.org/10.1016/j.brainres.2023.148383

Johnson, V. E., Stewart, W. & Smith, D. H. (2010). Traumatic brain injury and amyloid-β pathology: A link to alzheimer's disease? *Nature Reviews Neuroscience*, *11*(5), 361–370. https://doi.org/10.1038/nrn2808

Johnson, V. E., Stewart, W. & Smith, D. H. (2013). Axonal pathology in traumatic brain injury. *Experimental Neurology*, *246*, 35–43. https://doi.org/10.1016/j.expneurol.2012.01.013

Jolly, A. E., Balaet, M., Azor, A., Friedland, D., Sandrone, S., Graham, N. S., Zimmerman, K. & Sharp, D. J. (2021). Detecting axonal injury in individual patients after traumatic brain injury. *Brain*, *144*(1), 92–113. https://doi.org/10.1093/brain/awaa372

Jonkman, L. E., Soriano, A. L., Amor, S., Barkhof, F., van der Valk, P., Vrenken, H. & Geurts, J. J. (2015). Can MS lesion stages be distinguished with MRI? A postmortem MRI and histopathology study. *Journal of Neurology*, *262*(4), 1074–1080. https://doi.org/10.1007/s00415-015-7689-4

Juan, S. M., Daglas, M., Truong, P. H., Mawal, C. & Adlard, P. A. (2023). Alterations in iron content, iron-regulatory proteins and behaviour without tau pathology at one year following repetitive mild traumatic brain injury. *Acta Neuropathologica Communications*, *11*(1). https://doi.org/10.1186/s40478-023-01603-z

Kames, C., Wiggermann, V. & Rauscher, A. (2018). Rapid two-step dipole inversion for susceptibility mapping with sparsity priors. *NeuroImage*, *167*, 276–283. https://doi.org/10.1016/j.neuroimage.2017.11.018

Kan, H., Tsuchiya, T., Yamada, M., Kunitomo, H., Kasai, H. & Shibamoto, Y. (2022). Delineation of prostatic calcification using quantitative susceptibility mapping: Spatial accuracy for magnetic resonance-only radiotherapy planning. *Journal of Applied Clinical Medical Physics*, *23*(2). https://doi.org/10.1002/acm2.13469

Karsa, A., Punwani, S. & Shmueli, K. (2019a). The effect of low resolution and coverage on the accuracy of susceptibility mapping. *Magnetic Resonance in Medicine*, *81*(3), 1833–1848. https://doi.org/10.1002/mrm.27542

Karsa, A. & Shmueli, K. (2019b). SEGUE: A Speedy rEgion-Growing Algorithm for Unwrapping Estimated Phase. *IEEE Transactions on Medical Imaging*, *38*(6), 1347–1357. https://doi.org/10.1109/TMI.2018.2884093

Kataike, V. M., Desmond, P. M., Steward, C., Mitchell, P. J., Davey, C., Yassi, N., Bivard, A., Parsons, M. W., Campbell, B. C., Ng, F. & Venkatraman, V. (2024). Iron changes within infarct tissue in ischemic stroke patients after successful reperfusion quantified using QSM. *Neuroradiology*. https://doi.org/10.1007/s00234-024-03444-6

Katsumoto, A., Takeuchi, H. & Tanaka, F. (2019). Tau Pathology in Chronic Traumatic Encephalopathy and Alzheimer's Disease: Similarities and Differences. https://doi.org/10.3389/fneur.2019.00980

Kee, Y., Liu, Z., Zhou, L., Dimov, A., Cho, J., De Rochefort, L., Keun Seo, J., Wang, Y., Quantita, a. & de Rochefort, L. (2017). Quantitative Susceptibility Mapping (QSM) Algorithms: Mathematical Rationale and Computational Implementations. *64*(11). https://doi.org/10.1109/TBME.2017.2749298{\"{i}}

Kerr, K. M., Agster, K. L., Furtak, S. C. & Burwell, R. D. (2007). Functional neuroanatomy of the parahippocampal region: The lateral and medial entorhinal areas. https://doi.org/10.1002/hipo.20315

Khalaf, S., Ahmad, A. S., Chamara, K. V. & Doré, S. (2019). Unique Properties Associated with the Brain Penetrant Iron Chelator HBED Reveal Remarkable Beneficial Effects after Brain Trauma. *Journal of Neurotrauma*, *36*(1), 43–53. https://doi.org/10.1089/neu.2017.5617

Khan, N., Romila, L., Ciobica, A., Burlui, V., Kamal, F. Z. & Mavroudis, I. (2024). Mild Traumatic Brain Injury as a Risk Factor for Parkinsonism, Tics, and Akathisia: A Systematic Review and Meta-Analysis. https://doi.org/10.3390/life14010032

Kiersnowski, O. C., Winston, G. P., Caciagli, L., Biondetti, E., Elbadri, M., Buck, S., Duncan, J. S., Thornton, J. S., Shmueli, K. & Vos, S. B. (2023). Quantitative susceptibility mapping identifies hippocampal and other subcortical grey matter tissue composition changes in temporal lobe epilepsy. *Human Brain Mapping*, *44*(15), 5047–5064. https://doi.org/10.1002/hbm.26432

Kim, H. G., Park, S., Rhee, H. Y., Lee, K. M., Ryu, C. W., Rhee, S. J., Lee, S. Y., Wang, Y. & Jahng, G. H. (2017). Quantitative susceptibility mapping to evaluate the early stage of Alzheimer's disease. *NeuroImage: Clinical*, *16*, 429–438. https://doi.org/10.1016/j.nicl.2017.08.019

Kim, M. S., Kim, Y. H., Kim, M. S., Kwon, B. S. & Cho, H. R. (2023). Efficacy and Safety of Early Anti-inflammatory Drug Therapy for Secondary Injury in Traumatic Brain Injury. *World Neurosurgery*, *172*, e646–e654. https://doi.org/10.1016/j.wneu.2023.01.110

Kim, S., Lee, Y., Jeon, C. Y., Kim, K., Jeon, Y., Jin, Y. B., Oh, S. & Lee, C. (2020). Quantitative magnetic susceptibility assessed by 7T magnetic resonance imaging in Alzheimer's disease caused by streptozotocin administration. *Quantitative Imaging in Medicine and Surgery*, *10*(3), 789–797. https://doi.org/10.21037/QIMS.2020.02.08

Kim, S., Han, S. C., Gallan, A. J. & Hayes, J. P. (2017). Neurometabolic indicators of mitochondrial dysfunction in repetitive mild traumatic brain injury. *Concussion*, *2*(3), CNC45. https://doi.org/10.2217/cnc-2017-0013

Kim, T. K. & Park, J. H. (2019). More about the basic assumptions of t-test: Normality and sample size. *Korean Journal of Anesthesiology*, *72*(4), 331–335. https://doi.org/10.4097/kja.d.18.00292

King, A. I., Yang, K. H., Zhang, L., Hardy, W. & Viano, D. C. (2003). Is head injury caused by linear or angular acceleration? *IRCOBI Conference*.

King, J. B., Lopez-Larson, M. P. & Yurgelun-Todd, D. A. (2016). Mean cortical curvature reflects cytoarchitecture restructuring in mild traumatic brain injury. *NeuroImage: Clinical*, *11*, 81–89. https://doi.org/10.1016/j.nicl.2016.01.003

Kleiven, S. (2013). Why Most Traumatic Brain Injuries are Not Caused by Linear Acceleration but Skull Fractures are. *Frontiers in Bioengineering and Biotechnology*, *1*. https://doi.org/10.3389/fbioe.2013.00015

Knops, Z. F., Maintz, J. B., Viergever, M. A. & Pluim, J. P. (2006). Normalized mutual information based registration using k-means clustering and shading correction. *Medical Image Analysis*, *10*(3 SPEC. ISS.), 432–439. https://doi.org/10.1016/j.media.2005.03.009

Knutsen, A. K., Gomez, A. D., Gangolli, M., Wang, W. T., Chan, D., Lu, Y. C., Christoforou, E., Prince, J. L., Bayly, P. V., Butman, J. A. & Pham, D. L. (2020). In vivo estimates of axonal stretch and 3D brain deformation during mild head impact. *Brain Multiphysics*, *1*. https://doi.org/10.1016/j.brain.2020.100015

Koch, K. M., Meier, T. B., Karr, R., Nencka, A. S., Muftuler, L. T. & McCrea, M. (2018). Quantitative susceptibility mapping after sports-related concussion. *American Journal of Neuroradiology*, *39*(7), 1215–1221. https://doi.org/10.3174/ajnr.A5692

Koch, K. M., Nencka, A. S., Swearingen, B., Bauer, A., Meier, T. B. & McCrea, M. (2021). Acute Post-Concussive Assessments of Brain Tissue Magnetism Using Magnetic Resonance Imaging. *Journal of Neurotrauma*, *38*(7), 848–857. https://doi.org/10.1089/neu.2020.7322

Koch, K. M., Papademetris, X., Rothman, D. L. & De Graaf, R. A. (2006). Rapid calculations of susceptibility-induced magnetostatic field perturbations for in vivo magnetic resonance. *Physics in Medicine and Biology*, *51*(24), 6381–6402. https://doi.org/10.1088/0031-9155/51/24/007

Kornguth, S., Rutledge, N., Perlaza, G., Bray, J. & Hardin, A. (2017). A Proposed Mechanism for Development of CTE Following Concussive Events: Head Impact, Water Hammer Injury, Neurofilament Release, and Autoimmune Processes. *Brain Sciences*, *7*(12), 164.

Kroshus, E., Garnett, B., Hawrilenko, M., Baugh, C. M. & Calzo, J. P. (2015). Concussion under-reporting and pressure from coaches, teammates, fans, and parents. *Social Science and Medicine*, *134*, 66–75. https://doi.org/10.1016/j.socscimed.2015.04.011

Kruszewski, M. (2003). Labile iron pool: The main determinant of cellular response to oxidative stress. *Mutation Research - Fundamental and Molecular Mechanisms of Mutagenesis*, *531*(1-2), 81–92. https://doi.org/10.1016/j.mrfmmm.2003.08.004

Kudo, K., Liu, T., Murakami, T., Goodwin, J., Uwano, I., Yamashita, F., Higuchi, S., Wang, Y., Ogasawara, K., Ogawa, A. & Sasaki, M. (2016). Oxygen extraction fraction measurement using quantitative susceptibility mapping: Comparison with positron emission tomography. *Journal of Cerebral Blood Flow and Metabolism*, *36*(8), 1424–1433. https://doi.org/10.1177/0271678X15606713

Kuhlmann, T., Ludwin, S., Prat, A., Antel, J., Brück, W. & Lassmann, H. (2017). An updated histological classification system for multiple sclerosis lesions. *Acta Neuropathologica*, *133*(1), 13–24. https://doi.org/10.1007/s00401-016-1653-y

Kupchik, Y. M. & Kalivas, P. W. (2017). The Direct and Indirect Pathways of the Nucleus Accumbens are not what you think. *Neuropsychopharmacology*, *42*, 368–370. https://doi.org/10.1038/npp.2016.210

Laitinen, T., Sierra López, A., Bolkvadze, T., Pitkänen, A. & Gröhn, O. (2015). Diffusion tensor imaging detects chronic microstructural changes in white and grey matter after traumatic brain injury in rat. *Frontiers in Neuroscience*, *9*(MAR). https://doi.org/10.3389/fnins.2015.00128

Lanciego, J. L., Luquin, N. & Obeso, J. A. (2012). Functional neuroanatomy of the basal ganglia. *Cold Spring Harbor Perspectives in Medicine*, *2*(12). https://doi.org/10.1101/cshperspect.a009621

Langkammer, C., Bredies, K., Poser, B. A., Barth, M., Reishofer, G., Fan, A. P., Bilgic, B., Fazekas, F., Mainero, C. & Ropele, S. (2015). Fast quantitative susceptibility mapping using 3D EPI and total generalized variation. *NeuroImage*, *111*, 622–630. https://doi.org/10.1016/j.neuroimage.2015.02.041

Langkammer, C., Liu, T., Khalil, M., Enzinger, C., Jehna, M., Fuchs, S., Fazekas, F., Wang, Y. & Ropele, S. (2013). Quantitative susceptibility mapping in multiple sclerosis. *Radiology*, *267*(2), 551–559. https://doi.org/10.1148/radiol.12120707

Langkammer, C., Schweser, F., Krebs, N., Deistung, A., Goessler, W., Scheurer, E., Sommer, K., Reishofer, G., Yen, K., Fazekas, F., Ropele, S. & Reichenbach, J. R. (2012). Quantitative susceptibility mapping (QSM) as a means to measure brain iron? A post mortem validation study. *NeuroImage*, *62*(3), 1593–1599. https://doi.org/10.1016/j.neuroimage.2012.05.049

Langkammer, C., Schweser, F., Shmueli, K., Kames, C., Li, X., Guo, L., Milovic, C., Kim, J., Wei, H., Bredies, K., Buch, S., Guo, Y., Liu, Z., Meineke, J., Rauscher, A., Marques, J. P. & Bilgic, B. (2018). Quantitative susceptibility mapping: Report from the 2016 reconstruction challenge. *Magnetic Resonance in Medicine*, *79*(3), 1661–1673. https://doi.org/10.1002/mrm.26830

Laskowski, R. A., Creed, J. A. & Raghupathi, R. (2015). Brain neurotrauma: Molecular, neuropsychological, and rehabilitation aspects. Taylor & Francis.

Lassmann, H., Van Horssen, J. & Mahad, D. (2012). Progressive multiple sclerosis: Pathology and pathogenesis. *Nature Reviews Neurology*, *8*(11), 647–656. https://doi.org/10.1038/nrneurol.2012.168

Leaver, A. M., Renier, L., Chevillet, M. A., Morgan, S., Kim, H. J. & Rauschecker, J. P. (2011). Dysregulation of Limbic and Auditory Networks in Tinnitus. *Neuron*, *69*(1), 33–43. https://doi.org/10.1016/j.neuron.2010.12.002

Lee, J. Y., Lee, Y. J., Park, D. W., Nam, Y., Kim, S. H., Park, J., Kim, Y. S., Kim, H. Y. & Oh, K. W. (2017). Quantitative susceptibility mapping of the motor cortex: a comparison of susceptibility among patients with

amyotrophic lateral sclerosis, cerebrovascular disease, and healthy controls. *Neuroradiology*, *59*(12), 1213–1222. https://doi.org/10.1007/s00234-017-1933-9

Lee, J., Ji, S. & Oh, S. H. (2024). So You Want to Image Myelin Using MRI: Magnetic Susceptibility Source Separation for Myelin Imaging. *Magnetic resonance in medical sciences : MRMS : an official journal of Japan Society of Magnetic Resonance in Medicine*, *23*(3), 291–306. https://doi.org/10.2463/mrms.rev.2024-0001

Lee, J., Shmueli, K., Fukunaga, M., Van Gelderen, P., Merkle, H., Silva, A. C. & Duyn, J. H. (2010). Sensitivity of MRI resonance frequency to the orientation of brain tissue microstructure. *Proceedings of the National Academy of Sciences of the United States of America*, *107*(11), 5130–5135. https://doi.org/10.1073/pnas.0910222107

Lefevre-Dognin, C., Cogné, M., Perdrieau, V., Granger, A., Heslot, C., Azouvi, P. & Defi, a. (2021). Definition and epidemiology of mild traumatic brain injury. *Neurochirurgie*, *67*(3), 218–221. https://doi.org/10.1016/j.neuchi.2020.02.002{\"{i}}

Lehto, L. J., Sierra, A., Corum, C. A., Zhang, J., Idiyatullin, D., Pitkänen, A., Garwood, M. & Gröhn, O. (2012). Detection of calcifications in vivo and ex vivo after brain injury in rat using SWIFT. *NeuroImage*, *61*(4), 761–772. https://doi.org/10.1016/j.neuroimage.2012.03.002

Levi, S., Ripamonti, M., Moro, A. S. & Cozzi, A. (2024). Iron imbalance in neurodegeneration. *Molecular Psychiatry*, *29*(4), 1139–1152. https://doi.org/10.1038/s41380-023-02399-z

Levin, H. S., Amparo, E., Eisenberg, H. M., Williams, D. H., High, W. M., McArdle, C. B. & Weiner, R. L. (1987). Magnetic resonance imaging and computerized tomography in relation to the neurobehavioral sequelae of mild and moderate head injuries. *Journal of Neurosurgery*, *66*(5), 706–713. https://doi.org/10.3171/jns.1987.66.5.0706

Lewis, M. M., Du, G., Baccon, J., Snyder, A. M., Murie, B., Cooper, F., Stetter, C., Kong, L., Sica, C., Mailman, R. B., Connor, J. R. & Huang, X. (2018). Susceptibility MRI captures nigral pathology in patients with parkinsonian syndromes. *Movement Disorders*, *33*(9), 1432–1439. https://doi.org/10.1002/mds.27381

Li, G., Tong, R., Zhang, M., Gillen, K. M., Jiang, W., Du, Y., Wang, Y. & Li, J. (2023). Age-dependent changes in brain iron deposition and volume in deep gray matter nuclei using quantitative susceptibility mapping. *NeuroImage*, *269*. https://doi.org/10.1016/j.neuroimage.2023.119923

Li, J., Lin, H., Liu, T., Zhang, Z., Prince, M. R., Gillen, K., Yan, X., Song, Q., Hua, T., Zhao, X., Zhang, M., Zhao, Y., Li, G., Tang, G., Yang, G., Brittenham, G. M. & Wang, Y. (2018). Quantitative susceptibility mapping (QSM) minimizes interference from cellular pathology in R2* estimation of liver iron concentration. *Journal of Magnetic Resonance Imaging*, *48*(4), 1069–1079. https://doi.org/10.1002/jmri.26019

Li, J., Li, Y., Gutierrez, L., Xu, W., Wu, Y., Liu, C., Li, D., Sun, B., Zhang, C. & Wei, H. (2020). Imaging the Centromedian Thalamic Nucleus Using Quantitative Susceptibility Mapping. *Frontiers in Human Neuroscience*, *13*. https://doi.org/10.3389/fnhum.2019.00447

Li, L. & Leigh, J. S. (2004). Quantifying Arbitrary Magnetic Susceptibility Distributions with MR. *Magnetic Resonance in Medicine*, *51*(5), 1077–1082. https://doi.org/10.1002/mrm.20054

Li, W., Liu, C., Duong, T. Q., van Zijl, P. C. & Li, X. (2017). Susceptibility tensor imaging (STI) of the brain. https://doi.org/10.1002/nbm.3540

Li, W., Wang, N., Yu, F., Han, H., Cao, W., Romero, R., Tantiwongkosi, B., Duong, T. Q. & Liu, C. (2015). A method for estimating and removing streaking artifacts in quantitative susceptibility mapping. *NeuroImage*, *108*, 111–122. https://doi.org/10.1016/j.neuroimage.2014.12.043

Li, W., Wu, B., Avram, A. V. & Liu, C. (2012). Magnetic susceptibility anisotropy of human brain in vivo and its molecular underpinnings. *NeuroImage*, *59*(3), 2088–2097. https://doi.org/10.1016/j.neuroimage.2011.10.038

Li, W., Wu, B. & Liu, C. (2011). Quantitative susceptibility mapping of human brain reflects spatial variation in tissue composition. *NeuroImage*, *55*(4), 1645–1656. https://doi.org/10.1016/j.neuroimage.2010.11.088

Li, X., Morgan, P. S., Ashburner, J., Smith, J. & Rorden, C. (2016). The first step for neuroimaging data analysis: DICOM to NIfTI conversion. *Journal of Neuroscience Methods*, *264*, 47–56. https://doi.org/10.1016/j.jneumeth.2016.03.001

Li, Z., Feng, R., Liu, Q., Feng, J., Lao, G., Zhang, M., Li, J., Zhang, Y. & Wei, H. (2023). APART-QSM: An improved sub-voxel quantitative susceptibility mapping for susceptibility source separation using an iterative data fitting method. *NeuroImage*, *274*. https://doi.org/10.1016/j.neuroimage.2023.120148

Lifshitz, J., Kelley, B. J. & Povlishock, J. T. (2007). Perisomatic Thalamic Axotomy After Diffuse Traumatic Brain Injury Is Associated With Atrophy Rather Than Cell Death. *J Neuropathol Exp Neurol*, *66*(3), 218–229. http://jnen.oxfordjournals.org/

Liu, C. (2010). Susceptibility tensor imaging. *Magnetic Resonance in Medicine*, *63*(6), 1471–1477. https://doi.org/10.1002/mrm.22482

Liu, C., Li, W., Tong, K. A., Yeom, K. W. & Kuzminski, S. (2015a). Susceptibility-weighted imaging and quantitative susceptibility mapping in the brain. *Journal of Magnetic Resonance Imaging*, *42*(1), 23–41. https://doi.org/10.1002/jmri.24768

Liu, C., Wei, H., Gong, N.-J., Cronin, M., Dibb, R. & Decker, K. (2015b). Quantitative Susceptibility Mapping: Contrast Mechanisms and Clinical Applications. *Tomography*, *1*(1), 3–17. https://doi.org/10.18383/j.tom.2015.00136

Liu, J., Liu, T., De Rochefort, L., Ledoux, J., Khalidov, I., Chen, W., Tsiouris, J., Wisnieff, C., Spincemaille, P., Prince, M. R. & Wang, Y. (2012). Morphology enabled dipole inversion for quantitative susceptibility mapping using structural consistency between the magnitude image and the susceptibility map. *NeuroImage*, *59*(3), 2560–2568. https://doi.org/10.1016/j.neuroimage.2011.08.082

Liu, J., Kou, Z. F. & Tian, Y. Q. (2014). Diffuse axonal injury after traumatic cerebral microbleeds: An evaluation of imaging techniques. https://doi.org/10.4103/1673-5374.135330

Liu, T., Eskreis-Winkler, S., Schweitzer, A., Chen, W., Kaplitt, M. G., Tsiousir, A. J. & Wang, Y. (2013). Improved subthalamic nucleus depiction with quantitative susceptibility mapping. *Radiology*, *269*, 216–223. https://doi.org/10.1148/radiol.13121991/-/DC1

Liu, T., Khalidov, I., de Rochefort, L., Spincemaille, P., Liu, J., Tsiouris, J. & Wang, Y. (2011a). A novel background field removal method for MRI using projection onto dipole fields (PDF). *NMR in Biomedicine*, *24*(9), 1129–1136. https://doi.org/10.1002/nbm.1670

Liu, T., Liu, J., De Rochefort, L., Spincemaille, P., Khalidov, I., Ledoux, J. & Wang, Y. (2011b). Morphology enabled dipole inversion (MEDI) from a single-angle acquisition: Comparison with COSMOS in human brain imaging. *Magnetic Resonance in Medicine*, *66*(3), 777–783. https://doi.org/10.1002/mrm.22816

Liu, T., Spincemaille, P., De Rochefort, L., Kressler, B. & Wang, Y. (2009). Calculation of susceptibility through multiple orientation sampling (COSMOS): A method for conditioning the inverse problem from measured magnetic field map to susceptibility source image in MRI. *Magnetic Resonance in Medicine*, *61*(1), 196–204. https://doi.org/10.1002/mrm.21828

Liu, T., Surapaneni, K., Lou, M., Cheng, L., Spincemaille, P. & Wang, Y. (2012a). Cerebral microbleeds: Burden assessment by using quantitative susceptibility mapping. *Radiology*, *262*(1), 269–278. https://doi.org/10.1148/radiol.11110251

Liu, T., Xu, W., Spincemaille, P., Avestimehr, S. & Wang, Y. (2012b). Accuracy of the morphology enabled dipole inversion (MEDI) algorithm for quantitative susceptibility mapping in MRI. *IEEE Transactions on Medical Imaging*, *31*(3), 816–824. https://doi.org/10.1109/TMI.2011.2182523

Liu, Y., Dong, J., Song, Q., Zhang, N., Wang, W., Gao, B., Tian, S., Dong, C., Liang, Z., Xie, L. & Miao, Y. (2021). Correlation Between Cerebral Venous Oxygen Level and Cognitive Status in Patients With Alzheimer's Disease Using Quantitative Susceptibility Mapping. *Frontiers in Neuroscience*, *14*. https://doi.org/10.3389/fnins.2020.570848

Livingston, G., Huntley, J., Sommerlad, A., Ames, D., Ballard, C., Banerjee, S., Brayne, C., Burns, A., Cohen-Mansfield, J., Cooper, C., Costafreda, S. G., Dias, A., Fox, N., Gitlin, L. N., Howard, R., Kales, H. C., Kivimäki, M., Larson, E. B., Ogunniyi, A., ... Mukadam, N. (2020). Dementia prevention, intervention, and care: 2020 report of the Lancet Commission. https://doi.org/10.1016/S0140-6736(20)30367-6

Long, D. A., Ghosh, K., Moore, A. N., Dixon, C. E. & Dash, P. K. (1996). *Deferoxamine improves spatial memory performance following experimental brain injury in rats* (tech. rep.).

Łoś, K. & Waszkiewicz, N. (2021). Biological markers in anxiety disorders. https://doi.org/10.3390/jcm10081744

Lowenstein, D. H., Thomas, M. J., Smith, D. H. & Mcintosh2, T. K. (1992). Selective Vulnerability of Dentate Hilar Neurons following Traumatic Brain Injury: A Potential Mechanistic Link between Head Trauma and Disorders of the Hippocampus. *The Journal of Neuroscience*, *12*(12), 4848–4853.

Lu, L., Cao, H., Wei, X., Li, Y. & Li, W. (2015). Iron Deposition Is Positively Related to Cognitive Impairment in Patients with Chronic Mild Traumatic Brain Injury: Assessment with Susceptibility Weighted Imaging. *BioMed Research International*, *2015*. https://doi.org/10.1155/2015/470676

Lunkova, E., Guberman, G. I., Ptito, A. & Saluja, R. S. (2021). Noninvasive magnetic resonance imaging techniques in mild traumatic brain injury research and diagnosis. *Human Brain Mapping*, *42*(16), 5477–5494. https://doi.org/10.1002/hbm.25630

Luo, S., Yang, L. & Wang, L. (2015). Comparison of susceptibility-weighted and perfusion-weighted magnetic resonance imaging in the detection of penumbra in acute ischemic stroke. *Journal of Neuroradiology*, *42*(5), 255–260. https://doi.org/10.1016/j.neurad.2014.07.002

Ma, H., Dong, Y., Chu, Y., Guo, Y. & Li, L. (2022). The mechanisms of ferroptosis and its role in alzheimer's disease. *Frontiers in Molecular Biosciences*, *9*. https://doi.org/10.3389/fmolb.2022.965064

Ma, Y., Bruce, I. P., Yeh, C. H., Petrella, J. R., Song, A. W. & Truong, T. K. (2023). Column-based cortical depth analysis of the diffusion anisotropy and radiality in submillimeter whole-brain diffusion tensor imaging of the human cortical gray matter in vivo. *NeuroImage*, *270*. https://doi.org/10.1016/j.neuroimage.2023.119993

Maas, A. I., Menon, D. K., David Adelson, P. D., Andelic, N., Bell, M. J., Belli, A., Bragge, P., Brazinova, A., Büki, A., Chesnut, R. M., Citerio, G., Coburn, M., Jamie Cooper, D., Tamara Crowder, A., Czeiter, E., Czosnyka, M., Diaz-Arrastia, R., Dreier, J. P., Duhaime, A. C., ... Zemek, R. (2017). Traumatic brain injury: Integrated approaches to improve prevention, clinical care, and research. https://doi.org/10.1016/S1474-4422(17)30371-X

Maas, A. I., Menon, D. K., Manley, G. T., Abrams, M., Åkerlund, C., Andelic, N., Aries, M., Bashford, T., Bell, M. J., Bodien, Y. G., Brett, B. L., Büki, A., Chesnut, R. M., Citerio, G., Clark, D., Clasby, B., Cooper, J. D., Czeiter, E., Czosnyka, M., … Zemek, R. (2022). Traumatic brain injury: progress and challenges in prevention, clinical care, and research. *The Lancet Neurology*, *21*(11), 1004–1060. https://doi.org/10.1016/S1474-4422(22)00309-X

Mackay, D. F., Russell, E. R., Stewart, K., MacLean, J. A., Pell, J. P. & Stewart, W. (2019). Neurodegenerative Disease Mortality among Former Professional Soccer Players. *New England Journal of Medicine*, *381*(19), 1801–1808. https://doi.org/10.1056/nejmoa1908483

Mackenzie, E. L., Iwasaki, K. & Tsuji, Y. (2008). Intracellular iron transport and storage: From molecular mechanisms to health implications. *Antioxidants and Redox Signaling*, *10*(6), 997–1030. https://doi.org/10.1089/ars.2007.1893

Madden, D. J. & Merenstein, J. L. (2023). Quantitative susceptibility mapping of brain iron in healthy aging and cognition. *NeuroImage*, *282*. https://doi.org/10.1016/j.neuroimage.2023.120401

Madden, D. J., Siciliano, R. E., Tallman, C. W., Monge, Z. A., Voss, A. & Cohen, J. R. (2020). Response-level processing during visual feature search: Effects of frontoparietal activation and adult age. *Attention, Perception, and Psychophysics*, *82*(1), 330–349. https://doi.org/10.3758/s13414-019-01823-3

Mahoney, S. O., Chowdhury, N. F., Ngo, V., Imms, P. & Irimia, A. (2022). Mild Traumatic Brain Injury Results in Significant and Lasting Cortical Demyelination. *Frontiers in Neurology*, *13*. https://doi.org/10.3389/fneur.2022.854396

Marner, L., Nyengaard, J. R., Tang, Y. & Pakkenberg, B. (2003). Marked loss of myelinated nerve fibers in the human brain with age. *Journal of Comparative Neurology*, *462*(2), 144–152. https://doi.org/10.1002/cne.10714

Marquand, A. F., Kia, S. M., Zabihi, M., Wolfers, T., Buitelaar, J. K. & Beckmann, C. F. (2019). Conceptualizing mental disorders as deviations from normative functioning. https://doi.org/10.1038/s41380-019-0441-1

Marquand, A. F., Rezek, I., Buitelaar, J. & Beckmann, C. F. (2016). Understanding Heterogeneity in Clinical Cohorts Using Normative Models: Beyond Case-Control Studies. *Biological Psychiatry*, *80*(7), 552–561. https://doi.org/10.1016/j.biopsych.2015.12.023

Marques, J. P. (2021). *Quantitative susceptibility mapping (qsm) challenge 2.0. version*. Radboud University. https://doi.org/https://doi.org/10.34973/m20r-jt17

Marques, J. P. & Bowtell, R. (2005). Application of a fourier-based method for rapid calculation of field inhomogeneity due to spatial variation of magnetic susceptibility. *Concepts in Magnetic Resonance Part B: Magnetic Resonance Engineering*, *25*(1), 65–78. https://doi.org/10.1002/cmr.b.20034

Marques, J. P., Meineke, J., Milovic, C., Bilgic, B., Chan, K. S., Hedouin, R., van der Zwaag, W., Langkammer, C. & Schweser, F. (2021). QSM reconstruction challenge 2.0: A realistic in silico head phantom for MRI data simulation and evaluation of susceptibility mapping procedures. *Magnetic Resonance in Medicine*, *86*(1), 526–542. https://doi.org/10.1002/mrm.28716

Mavroudis, I., Balmus, I.-M., Ciobica, A. & Hogas, M. (2024). A narrative review of risk factors and predictors for poor outcome and prolonged recovery after a mild traumatic brain injury. *International Journal of Neuroscience*, 1–10. https://doi.org/https://doi.org/10.1080/00207454.2024.2328710

Maxwell, W. L., Dhillon, K., Harper, L., Espin, J., Macintosh, T. K., Smith, D. H. & Graham, D. I. (2003a). *There Is Differential Loss of Pyramidal Cells from the Human Hippocampus with Survival after Blunt Head Injury* (tech. rep. No. 3). http://jnen.oxfordjournals.org/

Maxwell, W. L., Domleo, A., Mccoll, G., Jafari, S. S. & Graham, D. I. (2003b). Post-Acute Alterations in the Axonal Cytoskeleton after Traumatic Axonal Injury. *JOURNAL OF NEUROTRAUMA*, *20*(2).

Maxwell, W. L., Kosanlavit, R., Mccreath, B. J., Reid, O. & Graham2, D. I. (1999). Freeze-Fracture and Cytochemical Evidence for Structural and Functional Alteration in the Axolemma and Myelin Sheath of Adult Guinea Pig Optic Nerve Fibers After Stretch Injury. *Journal of Neurotrauma*, *16*(4).

Mazur, T., Malik, M. & Bieńko, D. C. (2024). The impact of chelating compounds on Cu2+, Fe2+/3+, and Zn2+ ions in Alzheimer's disease treatment. https://doi.org/10.1016/j.jinorgbio.2024.112601

McAllister, T. W. (2011). Neurobiological consequences of traumatic brain injury. *Dialogues in Clinical Neuroscience*, *13*(3).

McCrea, M., Meier, T., Huber, D., Ptito, A., Bigler, E., Debert, C. T., Manley, G., Menon, D., Chen, J. K., Wall, R., Schneider, K. J. & McAllister, T. (2017). Role of advanced neuroimaging, fluid biomarkers and genetic testing in the assessment of sport-related concussion: A systematic review. *British Journal of Sports Medicine*, *51*(12), 919–929. https://doi.org/10.1136/bjsports-2016-097447

McInnes, K., Friesen, C. L., MacKenzie, D. E., Westwood, D. A. & Boe, S. G. (2017). Mild Traumatic Brain Injury (mTBI) and chronic cognitive impairment: A scoping review. *PLoS ONE*, *12*(4). https://doi.org/10.1371/journal.pone.0174847

Mckee, A. C. & Daneshvar, D. H. (2015). The neuropathology of traumatic brain injury. *Handbook of clinical neurology* (pp. 45–66). Elsevier B.V. https://doi.org/10.1016/B978-0-444-52892-6.00004-0

McKee, A. C., Stein, T. D., Nowinski, C. J., Stern, R. A., Daneshvar, D. H., Alvarez, V. E., Lee, H. S., Hall, G., Wojtowicz, S. M., Baugh, C. M., Riley, D. O., Kubilus, C. A., Cormier, K. A., Jacobs, M. A., Martin,

B. R., Abraham, C. R., Ikezu, T., Reichard, R. R., Wolozin, B. L., … Cantu, R. C. (2013). The spectrum of disease in chronic traumatic encephalopathy. *Brain*, *136*(1), 43–64. https://doi.org/10.1093/brain/aws307

McKee, A. C., Cairns, N. J., Dickson, D. W., Folkerth, R. D., Dirk Keene, C., Litvan, I., Perl, D. P., Stein, T. D., Vonsattel, J. P., Stewart, W., Tripodis, Y., Crary, J. F., Bieniek, K. F., Dams-O'Connor, K., Alvarez, V. E. & Gordon, W. A. (2016). The first NINDS/NIBIB consensus meeting to define neuropathological criteria for the diagnosis of chronic traumatic encephalopathy. *Acta Neuropathologica*, *131*(1), 75–86. https://doi.org/10.1007/s00401-015-1515-z

McKee, A. C., Stein, T. D., Huber, B. R., Crary, J. F., Bieniek, K., Dickson, D., Alvarez, V. E., Cherry, J. D., Farrell, K., Butler, M., Uretsky, M., Abdolmohammadi, B., Alosco, M. L., Tripodis, Y., Mez, J. & Daneshvar, D. H. (2023). Chronic traumatic encephalopathy (CTE): criteria for neuropathological diagnosis and relationship to repetitive head impacts. *Acta Neuropathologica*, *145*(4), 371–394. https://doi.org/10.1007/s00401-023-02540-w

Meaney, D. F. & Smith, D. H. (2011). Biomechanics of Concussion. https://doi.org/10.1016/j.csm.2010.08.009

Meier, T. B., Brummel, B. J., Singh, R., Nerio, C. J., Polanski, D. W. & Bellgowan, P. S. (2015). The underreporting of self-reported symptoms following sports-related concussion. *Journal of Science and Medicine in Sport*, *18*(5), 507–511. https://doi.org/10.1016/j.jsams.2014.07.008

Merenstein, J. L., Mullin, H. A. & Madden, D. J. (2023). Age-related differences in frontoparietal activation for target and distractor singletons during visual search. *Attention, Perception, and Psychophysics*, *85*(3), 749–768. https://doi.org/10.3758/s13414-022-02640-x

Merenstein, J. L., Zhao, J. & Madden, D. J. (2025). Depthwise cortical iron relates to functional connectivity and fluid cognition in healthy aging. *Neurobiology of Aging*, *148*, 27–40. https://doi.org/10.1016/j.neurobiolaging.2025.01.006

Merenstein, J. L., Zhao, J., Overson, D. K., Truong, T. K., Johnson, K. G., Song, A. W. & Madden, D. J. (2024). Depth- and curvature-based quantitative susceptibility mapping analyses of cortical iron in Alzheimer's disease. *Cerebral Cortex*, *34*(2). https://doi.org/10.1093/cercor/bhad525

Merkel, D. (2014). Docker: Lightweight linux containers for consistent development and deployment. *Linux journal*, *2014*(239), 2.

Meys, K. M., de Vries, L. S., Groenendaal, F., Vann, S. D. & Lequin, M. H. (2022). The Mammillary Bodies: A Review of Causes of Injury in Infants and Children. https://doi.org/10.3174/ajnr.A7463

Migliaccio, R. & Cacciamani, F. (2022). Chapter 25 - the temporal lobe in typical and atypical alzheimer disease. In G. Miceli, P. Bartolomeo & V. Navarro (Eds.), *The temporal lobe* (pp. 449–466). Elsevier. https://doi.org/https://doi.org/10.1016/B978-0-12-823493-8.00004-3

Milovic, C., Lambert, M., Langkammer, C., Bredies, K., Irarrazaval, P. & Tejos, C. (2022). Streaking artifact suppression of quantitative susceptibility mapping reconstructions via L1-norm data fidelity optimization (L1-QSM). *Magnetic Resonance in Medicine*, *87*(1), 457–473. https://doi.org/10.1002/mrm.28957

Milovic, C., Tejos, C., Acosta-Cabronero, J., Özbay, P. S., Schwesser, F., Marques, J. P., Irarrazaval, P., Bilgic, B. & Langkammer, C. (2020). The 2016 QSM Challenge: Lessons learned and considerations for a future challenge design. *Magnetic Resonance in Medicine*, *84*(3), 1624–1637. https://doi.org/10.1002/mrm.28185

Milovic, C., Tejos, C., Silva, J., Shmueli, K. & Irarrazaval, P. (2025). Xsim: A structural similarity index measure optimized for mri qsm. *Magnetic Resonance in Medicine*, *93*(1), 411–421. https://doi.org/10.1002/mrm.30271

Mito, R., Pedersen, M., Pardoe, H., Parker, D., Smith, R. E., Cameron, J., Scheffer, I. E., Berkovic, S. F., Vaughan, D. N. & Jackson, G. D. (2024). Exploring individual fixel-based white matter abnormalities in epilepsy. *Brain Communications*, *6*(1). https://doi.org/10.1093/braincomms/fcad352

Miyashita, Y. (2022). Operating principles of the cerebral cortex as a six-layered network in primates: beyond the classic canonical circuit model. *Proceedings of the Japan Academy Series B: Physical and Biological Sciences*, *98*(3), 93–111. https://doi.org/10.2183/pjab.98.007

Miyata, M., Kakeda, S., Kudo, K., Iwata, S., Tanaka, Y., Wang, Y. & Korogi, Y. (2019). Evaluation of oxygen extraction fraction in systemic lupus erythematosus patients using quantitative susceptibility mapping. *Journal of Cerebral Blood Flow and Metabolism*, *39*(8), 1648–1658. https://doi.org/10.1177/0271678X18764829

Miyata, M., Takahata, K., Sano, Y., Yamamoto, Y., Kurose, S., Kubota, M., Endo, H., Matsuoka, K., Tagai, K., Oya, M., Hirata, K., Saito, F., Mimura, M., Kamagata, K., Aoki, S. & Higuchi, M. (2024). Association between mammillary body atrophy and memory impairment in retired athletes with a history of repetitive mild traumatic brain injury. *Scientific Reports*, *14*(1). https://doi.org/10.1038/s41598-024-57383-6

Mohammadi, S., Ghaderi, S. & Fatehi, F. (2024a). Iron accumulation/overload and Alzheimer's disease risk factors in the precuneus region: A comprehensive narrative review. https://doi.org/10.1002/agm2.12363

Mohammadi, S., Ghaderi, S. & Fatehi, F. (2024b). Putamen iron quantification in diseases with neurodegeneration: a meta-analysis of the quantitative susceptibility mapping technique. https://doi.org/10.1007/s11682-024-00895-6

Möller, H. E., Bossoni, L., Connor, J. R., Crichton, R. R., Does, M. D., Ward, R. J., Zecca, L., Zucca, F. A. & Ronen, I. (2019). Iron, Myelin, and the Brain: Neuroimaging Meets Neurobiology. https://doi.org/10.1016/j.tins.2019.03.009

Monfrini, E., Arienti, F., Rinchetti, P., Lotti, F. & Riboldi, G. M. (2023). Brain Calcifications: Genetic, Molecular, and Clinical Aspects. *International journal of molecular sciences*, *24*(10). https://doi.org/10.3390/ijms24108995

Morey, R. A., Petty, C. M., Xu, Y., Pannu Hayes, J., Wagner, H. R., Lewis, D. V., LaBar, K. S., Styner, M. & McCarthy, G. (2009). A comparison of automated segmentation and manual tracing for quantifying hippocampal and amygdala volumes. *NeuroImage*, *45*(3), 855–866. https://doi.org/10.1016/j.neuroimage.2008.12.033

Morgane, P. J., Galler, J. R. & Mokler, D. J. (2005). A review of systems and networks of the limbic forebrain/limbic midbrain. https://doi.org/10.1016/j.pneurobio.2005.01.001

Mosconi, L. (2005). Brain glucose metabolism in the early and specific diagnosis of Alzheimer's disease: FDG-PET studies in MCI and AD. https://doi.org/10.1007/s00259-005-1762-7

Moulson, M. C. & Nelson, C. A. (2008). *Encyclopedia of Infant and Early Childhood Development: Neurological Development*. Elsevier.

Murdoch, R., Stotesbury, H., Kawadler, J. M., Saunders, D. E., Kirkham, F. J. & Shmueli, K. (2022). Quantitative susceptibility mapping (QSM) and R2* of silent cerebral infarcts in sickle cell anemia. *Frontiers in Neurology*, *13*. https://doi.org/10.3389/fneur.2022.1000889

Murray, H. C., Osterman, C., Bell, P., Vinnell, L. & Curtis, M. A. (2022). Neuropathology in chronic traumatic encephalopathy: a systematic review of comparative post-mortem histology literature. *Acta Neuropathologica Communications*, *10*(1). https://doi.org/10.1186/s40478-022-01413-9

Nakagawa, D., Kudo, K., Awe, O., Zanaty, M., Nagahama, Y., Cushing, C., Magnotta, V., Hayakawa, M., Allan, L., Greenlee, J., Awad, I. A., Carroll, T., Torner, J., Raghavan, M. L. & Hasan, D. M. (2019). Detection of microbleeds associated with sentinel headache using MRI quantitative susceptibility mapping: Pilot study. *Journal of Neurosurgery*, *130*(4), 1391–1397. https://doi.org/10.3171/2018.2.JNS1884

Naumenko, Y., Yuryshinetz, I., Zabenko, Y. & Pivneva, T. (2023). Mild traumatic brain injury as a pathological process. https://doi.org/10.1016/j.heliyon.2023.e18342

Nikolova, S., Schwedt, T. J., Li, J., Wu, T., Dumkrieger, G. M., Ross, K. B., Berisha, V. & Chong, C. D. (2022). T2* reduction in patients with acute post-traumatic headache. *Cephalalgia*, *42*(4-5), 357–365. https://doi.org/10.1177/03331024211048509

Nikparast, F., Ganji, Z., Danesh Doust, M., Faraji, R. & Zare, H. (2022a). Brain pathological changes during neurodegenerative diseases and their identification methods: How does QSM perform in detecting this process? https://doi.org/10.1186/s13244-022-01207-6

Nikparast, F., Ganji, Z. & Zare, H. (2022b). Early differentiation of neurodegenerative diseases using the novel QSM technique: what is the biomarker of each disorder? *BMC Neuroscience*, *23*(1). https://doi.org/10.1186/s12868-022-00725-9

Nisenbaum, E. J., Novikov, D. S. & Lui, Y. W. (2014). The presence and role of iron in mild traumatic brain injury: An imaging perspective. *Journal of Neurotrauma*, *31*, 301–307. https://doi.org/10.1089/neu.2013.3102

Nixon, R. A. (1993). The Regulation of Neurofilament Protein Dynamics by Phosphorylation: Clues to Neurofibrillary Pathobiology. *Brain Pathology*, *3*(1), 29–38. https://doi.org/10.1111/j.1750-3639.1993.tb00723.x

Nomura, J. I., Uwano, I., Sasaki, M., Kudo, K., Yamashita, F., Ito, K., Fujiwara, S., Kobayashi, M. & Ogasawara, K. (2017). Preoperative cerebral oxygen extraction fraction imaging generated from 7t MR quantitative susceptibility mapping predicts development of cerebral hyperperfusion following carotid endarterectomy. *American Journal of Neuroradiology*, *38*(12), 2327–2333. https://doi.org/10.3174/ajnr.A5390

Northall, A., Doehler, J., Weber, M., Vielhaber, S., Schreiber, S. & Kuehn, E. (2023). Layer-specific vulnerability is a mechanism of topographic map aging. *Neurobiology of Aging*, *128*, 17–32. https://doi.org/10.1016/j.neurobiolaging.2023.04.002

O'Callaghan, J., Holmes, H., Powell, N., Wells, J. A., Ismail, O., Harrison, I. F., Siow, B., Johnson, R., Ahmed, Z., Fisher, A., Meftah, S., O'Neill, M. J., Murray, T. K., Collins, E. C., Shmueli, K. & Lythgoe, M. F. (2017). Tissue magnetic susceptibility mapping as a marker of tau pathology in Alzheimer's disease. *NeuroImage*, *159*, 334–345. https://doi.org/10.1016/j.neuroimage.2017.08.003

O'Keeffe, E., Kelly, E., Liu, Y., Giordano, C., Wallace, E., Hynes, M., Tiernan, S., Meagher, A., Greene, C., Hughes, S., Burke, T., Kealy, J., Doyle, N., Hay, A., Farrell, M., Grant, G. A., Friedman, A., Veksler, R., Molloy, M. G., … Campbell, M. (2020). Dynamic Blood-Brain Barrier Regulation in Mild Traumatic Brain Injury. *Journal of Neurotrauma*, *37*(2), 347–356. https://doi.org/10.1089/neu.2019.6483

Onyszchuk, G., LeVine, S. M., Brooks, W. M. & Berman, N. E. (2009). Post-acute pathological changes in the thalamus and internal capsule in aged mice following controlled cortical impact injury: A magnetic resonance imaging, iron histochemical, and glial immunohistochemical study. *Neuroscience Letters*, *452*(2), 204–208. https://doi.org/10.1016/j.neulet.2009.01.049

Oris, C., Kahouadji, S., Durif, J., Bouvier, D. & Sapin, V. (2023). S100B, Actor and Biomarker of Mild Traumatic Brain Injury. https://doi.org/10.3390/ijms24076602

Orr, T. J., Lesha, E., Kramer, A. H., Cecia, A., Dugan, J. E., Schwartz, B. & Einhaus, S. L. (2024). Traumatic Brain Injury: A Comprehensive Review of Biomechanics and Molecular Pathophysiology. https://doi.org/10.1016/j.wneu.2024.01.084

Ost, M., Nylén, K., Csajbok, L., Olssonohrfelt, A., Olssonohrfelt, O., Tullberg, M., Wikkelsö, C., Nellgå Rd, P., Rosengren, L., Blennow, K. & Nellgå Rd, B. (2006). Initial CSF total tau correlates with 1-year outcome in patients with traumatic brain injury. *Neurology*, *9*(69), 1600–1604.

Osterman, C., Hamlin, D., Suter, C. M., Affleck, A. J., Gloss, B. S., Turner, C. P., Faull, R. L., Stein, T. D., McKee, A., Buckland, M. E., Curtis, M. A. & Murray, H. C. (2025). Perivascular glial reactivity is a feature of phosphorylated tau lesions in chronic traumatic encephalopathy. *Acta Neuropathologica*, *149*(1). https://doi.org/10.1007/s00401-025-02854-x

Otsu, N. (1979). A Threshold Selection Method from Gray-level Histograms (OTSU). *IEEE Transactions on Systems, Man, and Cybernetics*, *SMC-9*(1).

Palejwala, A. H., Dadario, N. B., Young, I. M., O'Connor, K., Briggs, R. G., Conner, A. K., O'Donoghue, D. L. & Sughrue, M. E. (2021). Anatomy and White Matter Connections of the Lingual Gyrus and Cuneus. *World Neurosurgery*, *151*, e426–e437. https://doi.org/10.1016/j.wneu.2021.04.050

Palejwala, A. H., O'Connor, K. P., Pelargos, P., Briggs, R. G., Milton, C. K., Conner, A. K., Milligan, T. M., O'Donoghue, D. L., Glenn, C. A. & Sughrue, M. E. (2020). Anatomy and white matter connections of the lateral occipital cortex. *Surgical and Radiologic Anatomy*, *42*(3), 315–328. https://doi.org/10.1007/s00276-019-02371-z

Palop, J. J., Chin, J. & Mucke, L. (2006). A network dysfunction perspective on neurodegenerative diseases. *Nature*, *443*. https://doi.org/10.1038/nature05289

Palop, J. J., Chin, J., Roberson, E. D., Wang, J., Thwin, M. T., Bien-Ly, N., Yoo, J., Ho, K. O., Yu, G. Q., Kreitzer, A., Finkbeiner, S., Noebels, J. L. & Mucke, L. (2007). Aberrant Excitatory Neuronal Activity and Compensatory Remodeling of Inhibitory Hippocampal Circuits in Mouse Models of Alzheimer's Disease. *Neuron*, *55*(5), 697–711. https://doi.org/10.1016/j.neuron.2007.07.025

Pankatz, L., Rojczyk, P., Seitz-Holland, J., Bouix, S., Jung, L. B., Wiegand, T. L., Bonke, E. M., Sollmann, N., Kaufmann, E., Carrington, H., Puri, T., Rathi, Y., Coleman, M. J., Pasternak, O., George, M. S., McAllister, T. W., Zafonte, R., Stein, M. B., Marx, C. E., … Koerte, I. K. (2023). Adverse Outcome Following Mild Traumatic Brain Injury Is Associated with Microstructure Alterations at the Gray and White Matter Boundary. *Journal of Clinical Medicine*, *12*(16). https://doi.org/10.3390/jcm12165415

Panter, S. S., Mark Braughler, J. & Hall, E. D. (1992). Dextran-Coupled Deferoxamine Improves Outcome in a Murine Model of Head Injury. *Journal of Neurotrauma*, *9*(1).

Parkin, A. J. (1996). Human memory: The hippocampus is the key. *Current Biology*, *6*, 1583–1585.

Patricios, J. S., Schneider, K. J., Dvorak, J., Ahmed, O. H., Blauwet, C., Cantu, R. C., Davis, G. A., Echemendia, R. J., Makdissi, M., McNamee, M., Broglio, S., Emery, C. A., Feddermann-Demont, N., Fuller, G. W., Giza, C. C., Guskiewicz, K. M., Hainline, B., Iverson, G. L., Kutcher, J. S., … Meeuwisse, W. (2023). Consensus statement on concussion in sport: The 6th International Conference on Concussion in Sport-Amsterdam, October 2022. *British Journal of Sports Medicine*, *57*(11), 695–711. https://doi.org/10.1136/bjsports-2023-106898

Paul, J., Raj, A., Raghavan, S. & Kesavadas, C. (2024). Comparative analysis of quantitative susceptibility mapping in preclinical dementia detection. https://doi.org/10.1016/j.ejrad.2024.111598

Pauli, W. M., Nili, A. N. & Michael Tyszka, J. (2018). Data Descriptor: A high-resolution probabilistic in vivo atlas of human subcortical brain nuclei. *Scientific Data*, *5*. https://doi.org/10.1038/sdata.2018.63

Pauling, L. & Coryell, C. D. (1936). The Magnetic Properties and Structure of Hemoglobin, Oxyhemoglobin and Carbonmonoxyhemoglobin. *PNAS*, *22*, 210–216. https://www.pnas.org

Pearson, R. C. A., Esirit, M. M., Hiornst, R. W., Wilcock, G. K. & Powell, T. P. S. (1985). *Anatomical correlates of the distribution of the pathological changes in the neocortex in Alzheimer disease (neurofibrillary tangles/lamination/clustering)* (tech. rep.).

Peet, B. T., Spina, S., Mundada, N. & La Joie, R. (2021). Neuroimaging in Frontotemporal Dementia: Heterogeneity and Relationships with Underlying Neuropathology. *Neurotherapeutics*, *18*(2), 728–752. https://doi.org/10.1007/s13311-021-01101-x

Pellman, E. J., Viano, D. C., Tucker, A., Casson, I. R. & Waeckerle, J. F. (2003). Concussion in professional football: Reconstruction of game impacts and injuries. *Neurosurgery*, *53*(4), 799–814.

Persson, N., Wu, J., Zhang, Q., Liu, T., Shen, J., Bao, R., Ni, M., Liu, T., Wang, Y. & Spincemaille, P. (2015). Age and sex related differences in subcortical brain iron concentrations among healthy adults. *NeuroImage*, *122*, 385–398. https://doi.org/10.1016/j.neuroimage.2015.07.050

Pessoa, L. (2017). A Network Model of the Emotional Brain. *Trends in Cognitive Sciences*, *21*(5), 357–371. https://doi.org/10.1016/j.tics.2017.03.002

Piantino, J. A., Iliff, J. J. & Lim, M. M. (2022). The Bidirectional Link Between Sleep Disturbances and Traumatic Brain Injury Symptoms: A Role for Glymphatic Dysfunction? https://doi.org/10.1016/j.biopsych.2021.06.025

Pienaar, R., Fischl, B., Caviness, V., Makris, N. & Grant, P. E. (2008). A Methodology for analyzing curvature in the developing brain from preterm to adult. *International Journal of Imaging Systems and Technology*, *18*(1). https://doi.org/10.1002/ima.v18:1

Pierpoint, L. A. & Collins, C. (2021). Epidemiology of Sport-Related Concussion. https://doi.org/10.1016/j.csm.2020.08.013

Pinky, N. N., Debert, C. T., Dukelow, S. P., Benson, B. W., Harris, A. D., Yeates, K. O., Emery, C. A. & Goodyear, B. G. (2022). Multimodal magnetic resonance imaging of youth sport-related concussion reveals acute changes in the cerebellum, basal ganglia, and corpus callosum that resolve with recovery. *Frontiers in Human Neuroscience*, *16*. https://doi.org/10.3389/fnhum.2022.976013

Pizzagalli, D. A. (2011). Frontocingulate dysfunction in depression: Toward biomarkers of treatment response. https://doi.org/10.1038/npp.2010.166

Poeta, D. L. & Burwell, R. D. (2022). Parahippocampal cortex (phc). In J. Vonk & T. K. Shackelford (Eds.), *Encyclopedia of animal cognition and behavior* (pp. 4941–4945). Springer International Publishing. https://doi.org/10.1007/978-3-319-55065-7_1272

Preiss-Farzanegan, S. J., Chapman, B., Wong, T. M., Wu, J. & Bazarian, J. J. (2009). The Relationship Between Gender and Postconcussion Symptoms After Sport-Related Mild Traumatic Brain Injury. *PM and R*, *1*(3), 245–253. https://doi.org/10.1016/j.pmrj.2009.01.011

Prins, M., Greco, T., Alexander, D. & Giza, C. C. (2013). The pathophysiology of traumatic brain injury at a glance. *DMM Disease Models and Mechanisms*, *6*(6), 1307–1315. https://doi.org/10.1242/dmm.011585

Probst, J., Rohner, M., Zahn, M., Piccirelli, M., Pangalu, A., Luft, A., Deistung, A., Klohs, J. & Wegener, S. (2021). Quantitative susceptibility mapping in ischemic stroke patients after successful recanalization. *Scientific Reports*, *11*(1). https://doi.org/10.1038/s41598-021-95265-3

Purcell, E. M., Torrey, H. C. & Pound, R. V. (1946). Resonance absorption by nuclear magnetic moments in a solid. *Physical review*, *69*(1-2), 37.

Qu, Z., Yang, S., Xing, F., Tong, R., Yang, C., Guo, R., Huang, J., Lu, F., Fu, C., Yan, X., Hectors, S., Gillen, K., Wang, Y., Liu, C., Zhan, S. & Li, J. (2021). Magnetic resonance quantitative susceptibility mapping in the evaluation of hepatic fibrosis in chronic liver disease: A feasibility study. *Quantitative Imaging in Medicine and Surgery*, *11*(4), 1170–1183. https://doi.org/10.21037/qims-20-720

Ranson, S. W. & Clark, S. L. (1995). *The anatomy of the nervous system: Its development and function* (10th Edition). W. B. Saunders Co.

Raslau, F. D., Mark, I. T., Klein, A. P., Ulmer, J. L., Mathews, V. & Mark, L. P. (2015). Memory Part 2: The Role of the Medial Temporal Lobe. *American Journal of Neuroradiology*, *36*(5), 846–849. https://doi.org/10.3174/AJNR.A4169

Rasouli, J., Ramdhani, R., Panov, F. E., Dimov, A., Zhang, Y., Cho, C., Wang, Y. & Kopell, B. H. (2018). Utilization of quantitative susceptibility mapping for direct targeting of the subthalamic nucleus during deep brain stimulation surgery. *Operative Neurosurgery*, *14*(4), 412–419. https://doi.org/10.1093/ons/opx131

Ratcliff, R. (2008). Modeling Aging Effects on Two-Choice Tasks: Response Signal and Response Time Data. *Psychology and Aging*, *23*(4), 900–916. https://doi.org/10.1037/a0013930

Rathbone, A. T. L., Tharmaradinam, S., Jiang, S., Rathbone, M. P. & Kumbhare, D. A. (2015). A review of the neuro- and systemic inflammatory responses in post concussion symptoms: Introduction of the "post-inflammatory brain syndrome" PIBS. https://doi.org/10.1016/j.bbi.2015.02.009

Ravanfar, P., Loi, S. M., Syeda, W. T., Van Rheenen, T. E., Bush, A. I., Desmond, P., Cropley, V. L., Lane, D. J., Opazo, C. M., Moffat, B. A., Velakoulis, D. & Pantelis, C. (2021). Systematic Review: Quantitative Susceptibility Mapping (QSM) of Brain Iron Profile in Neurodegenerative Diseases. *Frontiers in Neuroscience*, *15*. https://doi.org/10.3389/fnins.2021.618435

Ravikumar, S., Denning, A. E., Lim, S., Chung, E., Sadeghpour, N., Ittyerah, R., Wisse, L. E., Das, S. R., Xie, L., Robinson, J. L., Schuck, T., Lee, E. B., Detre, J. A., Tisdall, M. D., Prabhakaran, K., Mizsei, G., de Onzono Martin, M. M. I., Arroyo Jiménez, M. d. M., Mũnoz, M., … Yushkevich, P. A. (2024). Postmortem imaging reveals patterns of medial temporal lobe vulnerability to tau pathology in Alzheimer's disease. *Nature Communications*, *15*(1). https://doi.org/10.1038/s41467-024-49205-0

Raz, E., Jensen, J. H., Ge, Y., Babb, J. S., Miles, L., Reaume, J., Grossman, R. I. & Inglese, M. (2011). Brain iron quantification in mild traumatic brain injury: A magnetic field correlation study. *American Journal of Neuroradiology*, *32*(10), 1851–1856. https://doi.org/10.3174/ajnr.A2637

Reeves, T. M., Lyeth, B. G. & Povlishock, J. T. (1995). *Long-term potentiation deficits and excitability changes following traumatic brain injury* (tech. rep.). Springer-Verlag.

Reichenbach, J. R., Schweser, F., Serres, B. & Deistung, A. (2015). Quantitative Susceptibility Mapping: Concepts and Applications. *Clinical Neuroradiology*, *25*, 225–230. https://doi.org/10.1007/s00062-015-0432-9

Reichenbach, J. R. (2012). The future of susceptibility contrast for assessment of anatomy and function. *NeuroImage*, *62*(2), 1311–1315. https://doi.org/10.1016/j.neuroimage.2012.01.004

Renton, A. I., Dao, T. T., Johnstone, T., Civier, O., Sullivan, R. P., White, D. J., Lyons, P., Slade, B. M., Abbott, D. F., Amos, T. J., Bollmann, S., Botting, A., Campbell, M. E., Chang, J., Close, T. G., Dörig, M., Eckstein, K., Egan, G. F., Evas, S., … Bollmann, S. (2024). Neurodesk: an accessible, flexible and portable data analysis environment for reproducible neuroimaging. *Nature Methods*. https://doi.org/10.1038/s41592-023-02145-x

Rich, J. B. (2018). Mammillary bodies. In J. S. Kreutzer, J. DeLuca & B. Caplan (Eds.), *Encyclopedia of clinical neuropsychology* (pp. 2076–2080). Springer International Publishing. https://doi.org/10.1007/978-3-319-57111-9_1133

Rink, C. & Khanna, S. (2011). Significance of Brain Tissue Oxygenation and the Arachidonic Acid Cascade in Stroke. *Antioxidants & Redox Signalling*, *14*(10), 1889–1903. 10.1089=ars.2010.3474

Robinson, S., Bredies, K., Khabipova, D., Dymerska, B., Marques, J. & Schweser, F. (2017). An illustrated comparison of processing methods for MR phase imaging and QSM: combining array coil signals and phase unwrapping. *NMR in Biomedicine*, *30*(4). https://doi.org/10.1002/nbm.3601

Robinson, S., Schödl, H. & Trattnig, S. (2014). A method for unwrapping highly wrapped multi-echo phase images at very high field: UMPIRE. *Magnetic Resonance in Medicine*, *72*(1), 80–92. https://doi.org/10.1002/mrm.24897

Rodrigue, K. M., Haacke, E. M. & Raz, N. (2011). Differential effects of age and history of hypertension on regional brain volumes and iron. *NeuroImage*, *54*(2), 750–759. https://doi.org/10.1016/j.neuroimage.2010.09.068

Rodrigue, K. M., Kennedy, K. M. & Park, D. C. (2009). Beta-amyloid deposition and the aging brain. *Neuropsychology Review*, *19*(4), 436–450. https://doi.org/10.1007/s11065-009-9118-x

Rolls, E. T. & Mills, W. P. C. (2017). Computations in the deep vs superficial layers of the cerebral cortex. *Neurobiology of Learning and Memory*, *145*, 205–221. https://doi.org/10.1016/j.nlm.2017.10.011

Romeu-Mejia, R., Giza, C. C. & Goldman, J. T. (2019). Concussion Pathophysiology and Injury Biomechanics. https://doi.org/10.1007/s12178-019-09536-8

Root, D. H., Melendez, R. I., Zaborszky, L. & Napier, T. C. (2015). The ventral pallidum: Subregion-specific functional anatomy and roles in motivated behaviors. *Progress in Neurobiology*, *130*, 29–70. https://doi.org/10.1016/j.pneurobio.2015.03.005

Ropper, A. H. & Gorson, K. C. (2007). Clinical practice. concussion. *The New England Journal of Medicine*, *356*(2), 166–172. https://doi.org/10.1056/NEJMcp064645

Rosenbaum, S. B. & Lipton, M. L. (2012). Embracing chaos: The scope and importance of clinical and pathological heterogeneity in mTBI. *Brain Imaging and Behavior*, *6*(2), 255–282. https://doi.org/10.1007/s11682-012-9162-7

Rouault, T. A. (2013). Iron metabolism in the CNS: Implications for neurodegenerative diseases. https://doi.org/10.1038/nrn3453

Rubenstein, R., Chang, B., Yue, J. K., Chiu, A., Winkler, E. A., Puccio, A. M., Diaz-Arrastia, R., Yuh, E. L., Mukherjee, P., Valadka, A. B., Gordon, W. A., Okonkwo, D. O., Davies, P., Agarwal, S., Lin, F., Sarkis, G., Yadikar, H., Yang, Z., Manley, G. T., … Vassar, M. J. (2017). Comparing plasma phospho tau, total tau, and phospho tau–total tau ratio as acute and chronic traumatic brain injury biomarkers. *JAMA Neurology*, *74*(9), 1063–1072. https://doi.org/10.1001/jamaneurol.2017.0655

Ruetten, P. P., Cluroe, A. D., Usman, A., Priest, A. N., Gillard, J. H. & Graves, M. J. (2020). Simultaneous MRI water-fat separation and quantitative susceptibility mapping of carotid artery plaque pre- and post-ultrasmall superparamagnetic iron oxide-uptake. *Magnetic Resonance in Medicine*, *84*(2), 686–697. https://doi.org/10.1002/mrm.28151

Saade, C., Najem, E., Asmar, K., Salman, R., Achkar, B. E. & Naffaa, L. (2019). Intracranial calcifications on CT: An updated review. *Journal of Radiology Case Reports*, *13*(8), 1–18. https://doi.org/10.3941/jrcr.v13i8.3633

Saatman, K. E., Duhaime, A. C., Bullock, R., Maas, A. I., Valadka, A., Manley, G. T., Brody, D., Contant, C., Dash, P., Diaz-Arrastia, R., Fertig, S., Gean, A., Goodman, C., Gordon, W., Hayes, R., Hicks, R., Langloi, J., Marmarou, A., Moore, D., … Wright, D. (2008). Classification of traumatic brain injury for targeted therapies. *Journal of Neurotrauma*, *25*(7), 719–738. https://doi.org/10.1089/neu.2008.0586

Sagan, C. (1980). Cosmos.

Sahyouni, R., Gutierrez, P., Gold, E., Robertson, R. T. & Cummings, B. J. (2017). Effects of concussion on the blood–brain barrier in humans and rodents. *Journal of Concussion*, *1*, 205970021668451. https://doi.org/10.1177/2059700216684518

Saikia, M. J. & Alkhader, A. S. (2024). Smart Textile Impact Sensor for e-Helmet to Measure Head Injury. *Sensors*, *24*(9). https://doi.org/10.3390/s24092919

Salomir, R., De Senneville, B. D. & Moonen, C. T. (2003). A fast calculation method for magnetic field inhomogeneity due to an arbitrary distribution of bulk susceptibility. *Concepts in Magnetic Resonance Part B: Magnetic Resonance Engineering*, *19*(1), 26–34. https://doi.org/10.1002/cmr.b.10083

Sammons, R. P., Parthier, D., Stumpf, A. & Schmitz, D. (2019). Electrophysiological and molecular characterization of the parasubiculum. *Journal of Neuroscience*, *39*(45), 8860–8876. https://doi.org/10.1523/JNEUROSCI.0796-19.2019

Sandsmark, D. K., Bashir, A., Wellington, C. L. & Diaz-Arrastia, R. (2019). Cerebral Microvascular Injury: A Potentially Treatable Endophenotype of Traumatic Brain Injury-Induced Neurodegeneration. *Neuron*, *103*(3), 367–379. https://doi.org/10.1016/j.neuron.2019.06.002

Santhakumar, V., Bender, R., Frotscher, M., Ross, S. T., Hollrigel, G. S., Toth, Z. & Soltesz, I. (2000). Granule cell hyperexcitability in the early post-traumatic rat dentate gyrus: the 'irritable mossy cell' hypothesis. *Journal of Physiology*, (524), 117–134.

Sapin, V., Gaulmin, R., Aubin, R., Walrand, S., Coste, A. & Abbot, M. (2021). Blood biomarkers of mild traumatic brain injury: State of art. https://doi.org/10.1016/j.neuchi.2021.01.001

Schäfer, A., Wharton, S., Gowland, P. & Bowtell, R. (2009). Using magnetic field simulation to study susceptibility-related phase contrast in gradient echo MRI. *NeuroImage*, *48*(1), 126–137. https://doi.org/10.1016/j.neuroimage.2009.05.093

Scharfman, H. E. (2016). The enigmatic mossy cell of the dentate gyrus. *Nature Reviews Neuroscience*, *17*(9), 562–575. https://doi.org/10.1038/nrn.2016.87

Schell, M., Foltyn-Dumitru, M., Bendszus, M. & Vollmuth, P. (2023). Automated hippocampal segmentation algorithms evaluated in stroke patients. *Scientific Reports*, *13*(1). https://doi.org/10.1038/s41598-023-38833-z

Schenck, J. F. (1996). The role of magnetic susceptibility in magnetic resonance imaging: MRI magnetic compatibility of the first and second kinds. *Medical Physics*, *23*(6), 815–850. https://doi.org/10.1118/1.597854

Schenck, J. F. & Zimmerman, E. A. (2004). High-field magnetic resonance imaging of brain iron: Birth of a biomarker? https://doi.org/10.1002/nbm.922

Schmidt, M. A., Engelhorn, T., Marxreiter, F., Winkler, J., Lang, S., Kloska, S., Goelitz, P. & Doerfler, A. (2017). Ultra high-field SWI of the substantia nigra at 7T: Reliability and consistency of the swallow-tail sign. *BMC Neurology*, *17*(1). https://doi.org/10.1186/s12883-017-0975-2

Schofield, M. A. & Zhu, Y. (2003). *Fast phase unwrapping algorithm for interferometric applications* (tech. rep. No. 14).

Schöll, M., Lockhart, S. N., Schonhaut, D. R., O'Neil, J. P., Janabi, M., Ossenkoppele, R., Baker, S. L., Vogel, J. W., Faria, J., Schwimmer, H. D., Rabinovici, G. D. & Jagust, W. J. (2016). PET Imaging of Tau Deposition in the Aging Human Brain. *Neuron*, *89*(5), 971–982. https://doi.org/10.1016/j.neuron.2016.01.028

Schröder, N., Figueiredo, L. S. & De Lima, M. N. M. (2013). Role of brain iron accumulation in cognitive dysfunction: Evidence from animal models and human studies. https://doi.org/10.3233/JAD-121996

Schweser, F., Herrmann, K.-H., Deistung, A., Atterbury, M., Baltzer, P. A., Burmeister, H. P., Kaiser, W. A. & Reichenbach, J. R. (2011a). Quantitative magnetic susceptibility mapping (QSM) in breast disease reveals additional information for MR-based characterization of carcinoma and calcification. *Proc. Intl. Soc. Mag. Reson. Med.*, *19*.

Schweser, F., Deistung, A., Lehr, B. W. & Reichenbach, J. R. (2010). Differentiation between diamagnetic and paramagnetic cerebral lesions based on magnetic susceptibility mapping. *Medical Physics*, *37*(10), 5165–5178. https://doi.org/10.1118/1.3481505

Schweser, F., Deistung, A., Lehr, B. W. & Reichenbach, J. R. (2011b). Quantitative imaging of intrinsic magnetic tissue properties using MRI signal phase: An approach to in vivo brain iron metabolism? *NeuroImage*, *54*(4), 2789–2807. https://doi.org/10.1016/j.neuroimage.2010.10.070

Schweser, F., Deistung, A. & Reichenbach, J. R. (2016). Foundations of MRI phase imaging and processing for Quantitative Susceptibility Mapping (QSM). *Zeitschrift fur Medizinische Physik*, *26*(1), 6–34. https://doi.org/10.1016/j.zemedi.2015.10.002

Schweser, F., Robinson, S. D., de Rochefort, L., Li, W. & Bredies, K. (2017). An illustrated comparison of processing methods for phase MRI and QSM: removal of background field contributions from sources outside the region of interest. https://doi.org/10.1002/nbm.3604

Scopaz, K. A. & Hatzenbuehler, J. R. (2013). Risk Modifiers for Concussion and Prolonged Recovery. *Sports Health*, *5*(6), 537–541. https://doi.org/10.1177/1941738112473059

Seger, C. A. (2006). The basal ganglia in human learning. *Neuroscientist*, *12*(4), 285–290. https://doi.org/10.1177/1073858405285632

Seifert, T. & Shipman, V. (2015). The Pathophysiology of Sports Concussion. *Current Pain and Headache Reports*, *19*(8). https://doi.org/10.1007/s11916-015-0513-0

Senova, S., Fomenko, A., Gondard, E. & Lozano, A. M. (2020). Anatomy and function of the fornix in the context of its potential as a therapeutic target. https://doi.org/10.1136/jnnp-2019-322375

Setnik, L. & Bazarian, J. J. (2007). The characteristics of patients who do not seek medical treatment for traumatic brain injury. *Brain Injury*, *21*(1), 1–9. https://doi.org/10.1080/02699050601111419

Shandra, O., Winemiller, A. R., Heithoff, B. P., Munoz-Ballester, C., George, K. K., Benko, M. J., Zuidhoek, I. A., Besser, M. N., Curley, D. E., Franklin Edwards, G., Mey, A., Harrington, A. N., Kitchen, J. P. & Robel, S. (2019). Repetitive diffuse mild traumatic brain injury causes an atypical astrocyte response and spontaneous recurrent seizures. *Journal of Neuroscience*, *39*(10), 1944–1963. https://doi.org/10.1523/JNEUROSCI.1067-18.2018

Sharma, S. D., Fischer, R., Schoennagel, B. P., Nielsen, P., Kooijman, H., Yamamura, J., Adam, G., Bannas, P., Hernando, D. & Reeder, S. B. (2017). MRI-based quantitative susceptibility mapping (QSM) and R2* mapping of liver iron overload: Comparison with SQUID-based biomagnetic liver susceptometry. *Magnetic Resonance in Medicine*, *78*(1), 264–270. https://doi.org/10.1002/mrm.26358

Sharma, S. D., Hernando, D., Horng, D. E. & Reeder, S. B. (2015). Quantitative susceptibility mapping in the abdomen as an imaging biomarker of hepatic iron overload. *Magnetic Resonance in Medicine*, *74*(3), 673–683. https://doi.org/10.1002/mrm.25448

Shaw, N. A. (2002). The neurophysiology of concussion. *Progress in Neurobiology*, *67*, 281–344.

Shenton, M. E., Hamoda, H. M., Schneiderman, J. S., Bouix, S., Pasternak, O., Rathi, Y., Vu, M. A., Purohit, M. P., Helmer, K., Koerte, I., Lin, A. B. P., Westin, C. F., Kikinis, R., Kubicki, M., Stern, R. A. & Zafonte, R. (2012). A review of magnetic resonance imaging and diffusion tensor imaging findings in mild traumatic brain injury. *Brain Imaging and Behavior*, *6*(2), 137–192. https://doi.org/10.1007/s11682-012-9156-5

Shin, H. G., Lee, J., Yun, Y. H., Yoo, S. H., Jang, J., Oh, S. H., Nam, Y., Jung, S., Kim, S., Fukunaga, M., Kim, W., Choi, H. J. & Lee, J. (2021). χ-separation: Magnetic susceptibility source separation toward iron and myelin mapping in the brain. *NeuroImage*, *240*. https://doi.org/10.1016/j.neuroimage.2021.118371

Shlosberg, D., Benifla, M., Kaufer, D. & Friedman, A. (2010). Blood-brain barrier breakdown as a therapeutic target in traumatic brain injury. https://doi.org/10.1038/nrneurol.2010.74

Shukla, D. & Devi, B. (2010). Mild traumatic brain injuries in adults. *Journal of Neurosciences in Rural Practice*, *1*(2), 82–88. https://doi.org/10.4103/0976-3147.71723

Shultz, S. R., Bao, F., Weaver, L. C., Cain, D. P. & Brown, A. (2013). *Treatment with an anti-CD11d integrin antibody reduces neuroinflammation and improves outcome in a rat model of repeated concussion* (tech. rep.). http://www.jneuroinflammation.com/content/10/1/26

Sick, T. J., Perez-Pinzon, M. A., Feng´´, Z.-Z. & Feng´´, F. (1998). *Impaired expression of long-term potentiation in hippocampal slices 4 and 48 h following mild fluid-percussion brain injury in vivo* (tech. rep.).

Silverberg, N. D., Iverson, G. L., Cogan, A., Dams-O-Connor, K., Delmonico, R., Graf, M. J. P., Iaccarino, M. A., Kajankova, M., Kamins, J., McCulloch, K. L., McKinney, G., Nagele, D., Panenka, W. J., Rabinowitz, A. R., Reed, N., Wethe, J. V., Whitehair, V., Anderson, V., Arciniegas, D. B., … Zemek, R. (2023). The American Congress of Rehabilitation Medicine Diagnostic Criteria for Mild Traumatic Brain Injury. https://doi.org/10.1016/j.apmr.2023.03.036

Smith, D. H., Johnson, V. E. & Stewart, W. (2013). Chronic neuropathologies of single and repetitive TBI: Substrates of dementia? *Nature Reviews Neurology*, *9*(4), 211–221. https://doi.org/10.1038/nrneurol.2013.29

Smith, S. M. (2002). Fast robust automated brain extraction. *Human Brain Mapping*, *17*(3), 143–155. https://doi.org/10.1002/hbm.10062

Smith, S. M., Jenkinson, M., Woolrich, M. W., Beckmann, C. F., Behrens, T. E., Johansen-Berg, H., Bannister, P. R., De Luca, M., Drobnjak, I., Flitney, D. E., Niazy, R. K., Saunders, J., Vickers, J., Zhang, Y., De Stefano, N., Brady, J. M. & Matthews, P. M. (2004). Advances in functional and structural MR image analysis and implementation as FSL. *NeuroImage*, *23*(SUPPL. 1). https://doi.org/10.1016/j.neuroimage.2004.07.051

Snyder-Keller, A., Bolivar, V. J., Zink, S. & Kramer, L. D. (2020). Brain iron accumulation and the formation of calcifications after developmental zika virus infection. *Journal of Neuropathology and Experimental Neurology*, *79*(7), 767–776. https://doi.org/10.1093/jnen/nlaa043

Spitz, G., Maller, J. J., Ng, A., O'Sullivan, R., Ferris, N. J. & Ponsford, J. L. (2013). Detecting lesions after traumatic brain injury using susceptibility weighted imaging: A comparison with fluid-attenuated inversion recovery and correlation with clinical outcome. *Journal of Neurotrauma*, *30*(24), 2038–2050. https://doi.org/10.1089/neu.2013.3021

Stankiewicz, J., Panter, S. S., Neema, M., Arora, A., Batt, C. E. & Bakshi, R. (2007). Iron in Chronic Brain Disorders: Imaging and Neurotherapeutic Implications. *Neurotherapeutics: The Journal of the American Society for Experimental NeuroTherapeutics*, *4*, 371–386.

Stephenson, E., Nathoo, N., Mahjoub, Y., Dunn, J. F. & Yong, V. W. (2014). Iron in multiple sclerosis: Roles in neurodegeneration and repair. https://doi.org/10.1038/nrneurol.2014.118

Stewart, A. W. & Bollman, S. (2022a). *QSMxT/QSMxT*. GitHuB. https://doi.org/https://github.com/QSMxT/QSMxT

Stewart, A. W., Robinson, S. D., O'Brien, K., Jin, J., Widhalm, G., Hangel, G., Walls, A., Goodwin, J., Eckstein, K., Tourell, M., Morgan, C., Narayanan, A., Barth, M. & Bollmann, S. (2022b). QSMxT: Robust masking and artifact reduction for quantitative susceptibility mapping. *Magnetic Resonance in Medicine*, *87*(3), 1289–1300. https://doi.org/10.1002/mrm.29048

Straub, S., El-Sanosy, E., Emmerich, J., Sandig, F. L., Ladd, M. E. & Schlemmer, H. P. (2023). Quantitative magnetic resonance imaging biomarkers for cortical pathology in multiple sclerosis at 7 T. *NMR in Biomedicine*, *36*(3). https://doi.org/10.1002/nbm.4847

Straub, S., Knowles, B. R., Flassbeck, S., Steiger, R., Ladd, M. E. & Gizewski, E. R. (2019). Mapping the human brainstem: Brain nuclei and fiber tracts at 3 T and 7 T. *NMR in Biomedicine*, *32*(9). https://doi.org/10.1002/nbm.4118

Straub, S., Schneider, T. M., Emmerich, J., Freitag, M. T., Ziener, C. H., Schlemmer, H. P., Ladd, M. E. & Laun, F. B. (2017a). Suitable reference tissues for quantitative susceptibility mapping of the brain. *Magnetic Resonance in Medicine*, *78*(1), 204–214. https://doi.org/10.1002/mrm.26369

Straub, S., Laun, F. B., Emmerich, J., Jobke, B., Hauswald, H., Katayama, S., Herfarth, K., Schlemmer, H. P., Ladd, M. E., Ziener, C. H., Bonekamp, D. & Röthke, M. C. (2017b). Potential of quantitative susceptibility mapping for detection of prostatic calcifications. *Journal of Magnetic Resonance Imaging*, *45*(3), 889–898. https://doi.org/10.1002/jmri.25385

Stüber, C., Pitt, D. & Wang, Y. (2016). Iron in multiple sclerosis and its noninvasive imaging with quantitative susceptibility mapping. https://doi.org/10.3390/ijms17010100

Stüber, C., Morawski, M., Schäfer, A., Labadie, C., Wähnert, M., Leuze, C., Streicher, M., Barapatre, N., Reimann, K., Geyer, S., Spemann, D. & Turner, R. (2014). Myelin and iron concentration in the human brain: A quantitative study of MRI contrast. *NeuroImage*, *93*(P1), 95–106. https://doi.org/10.1016/j.neuroimage.2014.02.026

Subramanian, K., Utriainen, D., Ramasamy, D. P., Sethi, S. K., Schweser, F., Beaver, J., Hagemeier, J., Weinstock-Guttman, B., Rajagovindan, R., Zivadinov, R. & Haacke, E. M. (2020). Longitudinal magnetic resonance imaging of cerebral microbleeds in multiple sclerosis patients. *Diagnostics*, *10*(11). https://doi.org/10.3390/diagnostics10110942

Sui, Y. V., Masurkar, A. V., Rusinek, H., Reisberg, B. & Lazar, M. (2022). Cortical myelin profile variations in healthy aging brain: A T1w/T2w ratio study. *NeuroImage*, *264*. https://doi.org/10.1016/j.neuroimage.2022.119743

Sullenberger, T., Don, H. & Kumar, S. S. (2019). Functional Connectivity of the Parasubiculum and Its Role in Temporal Lobe Epilepsy. *Neuroscience*, *410*, 217–238. https://doi.org/10.1016/j.neuroscience.2019.05.008

Sulpizio, V., Committeri, G., Lambrey, S., Berthoz, A. & Galati, G. (2013). Selective role of lingual/parahippocampal gyrus and retrosplenial complex in spatial memory across viewpoint changes relative to the environmental reference frame. *Behavioural Brain Research*, *242*(1), 62–75. https://doi.org/10.1016/j.bbr.2012.12.031

Swanson, L. W. & Cowan, W. M. (1975). *Hippocampo-Hypothalamic Connections: Origin in Subicular Cortex, Not Ammon's Horn* (tech. rep. No. 4199).

Szucs, D. & Ioannidis, J. P. (2020). Sample size evolution in neuroimaging research: An evaluation of highly-cited studies (1990–2012) and of latest practices (2017–2018) in high-impact journals. *NeuroImage*, *221*. https://doi.org/10.1016/j.neuroimage.2020.117164

Tagge, C. A., Fisher, A. M., Minaeva, O. V., Gaudreau-Balderrama, A., Moncaster, J. A., Zhang, X. L., Wojnarowicz, M. W., Casey, N., Lu, H., Kokiko-Cochran, O. N., Saman, S., Ericsson, M., Onos, K. D., Veksler, R., Senatorov, V. V., Kondo, A., Zhou, X. Z., Miry, O., Vose, L. R., ... Goldstein, L. E. (2018). Concussion, microvascular injury, and early tauopathy in young athletes after impact head injury and an impact concussion mouse model. *Brain*, *141*(2), 422–458. https://doi.org/10.1093/brain/awx350

Tang, S., Gao, P., Chen, H., Zhou, X., Ou, Y. & He, Y. (2020). The Role of Iron, Its Metabolism and Ferroptosis in Traumatic Brain Injury. *Frontiers in Cellular Neuroscience*, *14*. https://doi.org/10.3389/fncel.2020.590789

Taube, J. S. (2007). The head direction signal: Origins and sensory-motor integration. https://doi.org/10.1146/annurev.neuro.29.051605.112854

Telling, N. D., Everett, J., Collingwood, J. F., Dobson, J., van der Laan, G., Gallagher, J. J., Wang, J. & Hitchcock, A. P. (2017). Iron Biochemistry is Correlated with Amyloid Plaque Morphology in an Established Mouse Model of Alzheimer's Disease. *Cell Chemical Biology*, *24*(10), 1205–1215. https://doi.org/10.1016/j.chembiol.2017.07.014

Theadom, A., Mahon, S., Hume, P., Starkey, N., Barker-Collo, S., Jones, K., Majdan, M. & Feigin, V. L. (2020). Incidence of Sports-Related Traumatic Brain Injury of All Severities: A Systematic Review. *Neuroepidemiology*, *54*(2), 192–199. https://doi.org/10.1159/000505424

Theadom, A., Hardaker, N., Bray, C., Siegert, R., Henshall, K., Forch, K., Fernando, K., King, D., Fulcher, M., Jewell, S., Shaikh, N., Gottgtroy, R. B. & Hume, P. (2021). The Brain Injury Screening Tool (BIST): Tool development, factor structure and validity. *PLoS ONE*, *16*(2 February). https://doi.org/10.1371/journal.pone.0246512

Thibault, O., Gant, J. C. & Landfield, P. W. (2007). Expansion of the calcium hypothesis of brain aging and Alzheimer's disease: Minding the store. https://doi.org/10.1111/j.1474-9726.2007.00295.x

Tierney, R. T., Sitler, M. R., Swanik, C. B., Swanik, K. A., Higgins, M. & Torg, J. (2005). Gender differences in head-neck segmnet dynamic stabilization during head accelaration. *Medicine and Science in Sports and Exercise*, *37*(2), 272–279. https://doi.org/10.1249/01.MSS.0000152734.47516.AA

Tikhonov, A. N., Goncharsky, A. V., Stepanov, V. V. & Yagola, A. G. (1995). *Numerical Methods for the Solution of Ill-Posed Problems*. Kluwer Academic Publishers. https://doi.org/10.1007/978-94-015-8480-7

Tipirneni-Sajja, A., Loeffler, R. B., Hankins, J. S., Morin, C. & Hillenbrand, C. M. (2021). Quantitative Susceptibility Mapping Using a Multispectral Autoregressive Moving Average Model to Assess Hepatic Iron Overload. *Journal of Magnetic Resonance Imaging*, *54*(3), 721–727. https://doi.org/10.1002/jmri.27584

To, X. V., Cumming, P. & Nasrallah, F. (2024). From impact to recovery: tracking mild traumatic brain injury with MRI—a pilot study and case series. *BMJ Open Sport & Exercise Medicine*, *10*(3), e002010. https://doi.org/10.1136/bmjsem-2024-002010

Tohka, J. (2014). Partial volume effect modeling for segmentation and tissue classification of brain magnetic resonance images: A review. *World Journal of Radiology*, *6*(11), 855. https://doi.org/10.4329/wjr.v6.i11.855

Tournier, D. J., Smith, R., Raffelt, D., Tabbara, R., Dhollander, T., Pietsch, M., Christiaens, D., Jeurissen, B., Yeh, C. H. & Connelly, A. (2019). MRtrix3: A fast, flexible and open software framework for medical image processing and visualisation. *NeuroImage*, *202*. https://doi.org/10.1016/j.neuroimage.2019.116137

Trampel, R., Bazin, P. L., Pine, K. & Weiskopf, N. (2019). In-vivo magnetic resonance imaging (MRI) of laminae in the human cortex. *NeuroImage*, *197*, 707–715. https://doi.org/10.1016/j.neuroimage.2017.09.037

Tran, H. T., LaFerla, F. M., Holtzman, D. M. & Brody, D. L. (2011). Controlled cortical impact traumatic brain injury in 3xTg-AD mice causes acute intra-axonal amyloid-β accumulation and independently accelerates the development of tau abnormalities. *Journal of Neuroscience*, *31*(26), 9513–9525. https://doi.org/10.1523/JNEUROSCI.0858-11.2011

Treit, S., Naji, N., Seres, P., Rickard, J., Stolz, E., Wilman, A. H. & Beaulieu, C. (2021). R2* and quantitative susceptibility mapping in deep gray matter of 498 healthy controls from 5 to 90 years. *Human Brain Mapping*, *42*(14), 4597–4610. https://doi.org/10.1002/hbm.25569

Tukey, J. W. (1977). *Exploratory data analysis*. Addison-Wesley Publishing Company.

Turner, R. C., Lucke-Wold, B. P., Robson, M. J., Lee, J. M. & Bailes, J. E. (2016). Alzheimer's disease and chronic traumatic encephalopathy: Distinct but possibly overlapping disease entities. https://doi.org/10.1080/02699052.2016.1193631

Tustison, N. J., Avants, B. B., Cook, P. A., Zheng, Y., Egan, A., Yushkevich, P. A. & Gee, J. C. (2010). N4ITK: Improved N3 bias correction. *IEEE Transactions on Medical Imaging*, *29*(6), 1310–1320. https://doi.org/10.1109/TMI.2010.2046908

Tuzzi, E., Balla, D. Z., Loureiro, J. R., Neumann, M., Laske, C., Pohmann, R., Preische, O., Scheffler, K. & Hagberg, G. E. (2020). Ultra-High Field MRI in Alzheimer's Disease: Effective Transverse Relaxation Rate and Quantitative Susceptibility Mapping of Human Brain in Vivo and Ex Vivo compared to Histology. *Journal of Alzheimer's Disease*, *73*(4), 1481–1499. https://doi.org/10.3233/JAD-190424

Tweedie, D., Karnati, H. K., Mullins, R., Pick, C. G., Hoffer, B. J., Goetzl, E. J., Kapogiannis, D. & Greig, N. H. (2020). Time-dependent cytokine and chemokine changes in mouse cerebral cortex following a mild traumatic brain injury. *eLife*, *9*, 1–29. https://doi.org/10.7554/ELIFE.55827

Uchida, Y., Kan, H., Kano, Y., Onda, K., Sakurai, K., Takada, K., Ueki, Y., Matsukawa, N., Hillis, A. E. & Oishi, K. (2024). Longitudinal Changes in Iron and Myelination Within Ischemic Lesions Associate with Neurological Outcomes: A Pilot Study. *Stroke*, *55*(4), 1041–1050. https://doi.org/10.1161/STROKEAHA.123.044606

Uchida, Y., Kan, H., Sakurai, K., Oishi, K. & Matsukawa, N. (2022). Quantitative susceptibility mapping as an imaging biomarker for Alzheimer's disease: The expectations and limitations. https://doi.org/10.3389/fnins.2022.938092

Uwano, I., Sasaki, M., Kudo, K., Sato, Y., Ogasaware, Y., Saura, H., Ogasaware, K., Harada, T., Ito, K., Yamashita, F., Goodwin, J. & Higuchi, S. (2015). Measurement of the Oxygen Extraction Fraction in Patients with Steno-occlusive Cerebrovascular Diseases using Quantitative Susceptibility Mapping at 7T. *Proc. Intl. Soc. Mag. Reson. Med.*, 0282.

Van Essen, D. C., Smith, S. M., Barch, D. M., Behrens, T. E., Yacoub, E. & Ugurbil, K. (2013). The WU-Minn Human Connectome Project: An overview. *NeuroImage*, *80*, 62–79. https://doi.org/10.1016/j.neuroimage.2013.05.041

Van Hoesen, G. W., Augustinack, J. C., Dierking, J., Redman, S. J. & Thangavel, R. (2000). The Parahippocampal Gyrus in Alzheimer's Disease Clinical and Preclinical Neuroanatomical Correlates. *Annals New York Academy of Sciences*, *911*(1), 254–274.

Van Hoesen, G. W. & Hyman, B. T. (1990). Hippocampal formation: anatomy and the patterns of pathology in Alzheimer's disease. *Progress in Brain Research*, (83), 445–457.

Vann, S. D. & Aggleton, J. P. (2004). The mammillary bodies: Two memory systems in one? https://doi.org/10.1038/nrn1299

Venkatraman, A., Edlow, B. L. & Immordino-Yang, M. H. (2017). The brainstem in emotion: A review. https://doi.org/10.3389/fnana.2017.00015

Viano, D. C., Casson, I. R., Pellman, E. J., Zhang, L. & King, A. I. (2005). Concussion in professional football: Brain responses by finite element analysis: Part 9. *Neurosurgery*, *57*(5), 891–916. https://doi.org/10.1227/01.NEU.0000186950.54075.3B

Vinayagamani, S., Sheelakumari, R., Sabarish, S., Senthilvelan, S., Ros, R., Thomas, B. & Kesavadas, C. (2021). Quantitative Susceptibility Mapping: Technical Considerations and Clinical Applications in Neuroimaging. *Journal of Magnetic Resonance Imaging*, *53*(1), 23–37. https://doi.org/10.1002/jmri.27058

Waehnert, M. D., Dinse, J., Schäfer, A., Geyer, S., Bazin, P. L., Turner, R. & Tardif, C. L. (2016). A subject-specific framework for in vivo myeloarchitectonic analysis using high resolution quantitative MRI. *NeuroImage*, *125*, 94–107. https://doi.org/10.1016/j.neuroimage.2015.10.001

Waehnert, M. D., Dinse, J., Weiss, M., Streicher, M. N., Waehnert, P., Geyer, S., Turner, R. & Bazin, P.-L. (2014). Anatomically motivated modeling of cortical laminae. *NeuroImage*, *93*, 210–220. https://doi.org/10.1016/j.neuroimage.2013.03.078

Walker, K. R. & Tesco, G. (2013). Molecular mechanisms of cognitive dysfunction following traumatic brain injury. *Frontiers in Aging Neuroscience*, *5*. https://doi.org/10.3389/fnagi.2013.00029

Waltzman, D., Black, L. I., Daugherty, J., Peterson, A. B. & Zablotsky, B. (2025). Prevalence of traumatic brain injury among adults and children. *Annals of Epidemiology*, *103*, 40–47. https://doi.org/10.1016/j.annepidem.2025.02.005

Wang, C., Zhang, Y., Du, J., Huszár, I. N., Liu, S., Chen, Y., Buch, S., Wu, F., Liu, Y., Jenkinson, M., Hsu, C. C. T., Fan, Z., Haacke, E. M. & Yang, Q. (2020). Quantitative Susceptibility Mapping for Characterization of Intraplaque Hemorrhage and Calcification in Carotid Atherosclerotic Disease. *Journal of Magnetic Resonance Imaging*, *52*(2), 534–541. https://doi.org/10.1002/jmri.27064

Wang, M., Dai, Y., Han, Y., Haacke, E. M., Dai, J. & Shi, D. (2011). Susceptibility weighted imaging in detecting hemorrhage in acute cervical spinal cord injury. *Magnetic Resonance Imaging*, *29*(3), 365–373. https://doi.org/10.1016/j.mri.2010.10.016

Wang, Y. & Liu, T. (2015). Quantitative susceptibility mapping (QSM): Decoding MRI data for a tissue magnetic biomarker. *Magnetic Resonance in Medicine*, *73*(1), 82–101. https://doi.org/10.1002/mrm.25358

Wang, Y., Spincemaille, P., Liu, Z., Dimov, A., Deh, K., Li, J., Zhang, Y., Yao, Y., Gillen, K. M., Wilman, A. H., Gupta, A., Tsiouris, A. J., Kovanlikaya, I., Chiang, G. C. Y., Weinsaft, J. W., Tanenbaum, L., Chen, W., Zhu, W., Chang, S., … Prince, M. R. (2017). Clinical quantitative susceptibility mapping (QSM): Biometal imaging and its emerging roles in patient care. *Journal of Magnetic Resonance Imaging*, *46*(4), 951–971. https://doi.org/10.1002/jmri.25693

Wang, Z., Bovik, A. C., Sheikh, H. R. & Simoncelli, E. P. (2004). Image quality assessment: From error visibility to structural similarity. *IEEE Transactions on Image Processing*, *13*(4), 600–612. https://doi.org/10.1109/TIP.2003.819861

Ward, A. M., Schultz, A. P., Huijbers, W., Van Dijk, K. R., Hedden, T. & Sperling, R. A. (2014). The parahippocampal gyrus links the default-mode cortical network with the medial temporal lobe memory system. *Human Brain Mapping*, *35*(3), 1061–1073. https://doi.org/10.1002/hbm.22234

Ward, R. J., Zucca, F. A., Duyn, J. H., Crichton, R. R. & Zecca, L. (2014). The role of iron in brain ageing and neurodegenerative disorders. *The Lancet Neurology*, *13*(10), 1045–1060. https://doi.org/10.1016/S1474-4422(14)70117-6

Wasserman, E. B., Herzog, M. M., Collins, C. L., Morris, S. N. & Marshall, S. W. (2018). Fundamentals of Sports Analytics. https://doi.org/10.1016/j.csm.2018.03.007

Webb, W. G. (2017). 2 - organization of the nervous system i. In W. G. Webb (Ed.), *Neurology for the speech-language pathologist* (Sixth Edition, pp. 13–43). Mosby. https://doi.org/https://doi.org/10.1016/B978-0-323-10027-4.00002-6

Weber, A. M., Pukropski, A., Kames, C., Jarrett, M., Dadachanji, S., Taunton, J., Li, D. K. & Rauscher, A. (2018). Pathological insights from quantitative susceptibility mapping and diffusion tensor imaging in ice hockey players pre and post-concussion. *Frontiers in Neurology*, *9*. https://doi.org/10.3389/fneur.2018.00575

Wegiel, J., Kuchna, I., Wisniewski, T., de Leon, M. J., Reisberg, B., Pirttila, T., Kivimaki, T. & Lehtimaki, T. (2002). Vascular fibrosis and calcification in the hippocampus in aging, Alzheimer disease, and Down syndrome. *Acta Neuropathologica*, *103*(4), 333–343. https://doi.org/10.1007/s00401-001-0471-y

Wei, H., Zhang, C., Wang, T., He, N., Li, D., Zhang, Y., Liu, C., Yan, F. & Sun, B. (2020). Precise targeting of the globus pallidus internus with quantitative susceptibility mapping for deep brain stimulation surgery. *Journal of Neurosurgery*, *133*(5), 1605–1611. https://doi.org/10.3171/2019.7.JNS191254

Wen, Y., Weinsaft, J. W., Nguyen, T. D., Liu, Z., Horn, E. M., Singh, H., Kochav, J., Eskreis-Winkler, S., Deh, K., Kim, J., Prince, M. R., Wang, Y. & Spincemaille, P. (2019). Free breathing three-dimensional cardiac quantitative susceptibility mapping for differential cardiac chamber blood oxygenation - Initial validation in patients with cardiovascular disease inclusive of direct comparison to invasive catheterization. *Journal of Cardiovascular Magnetic Resonance*, *21*(1). https://doi.org/10.1186/s12968-019-0579-7

White, E. R., Pinar, C., Bostrom, C. A., Meconi, A. & Christie, B. R. (2017). Mild Traumatic Brain Injury Produces Long-Lasting Deficits in Synaptic Plasticity in the Female Juvenile Hippocampus. *Journal of Neurotrauma*, *34*(5), 1111–1123. https://doi.org/10.1089/neu.2016.4638

Wilde, E. A., Mccauley, S. R., Hunter, J. V., Bigler, E. D., Chu, Z., Wang, Z. J., Hanten, G. R., Troyanskaya, M., Yallampalli, R., Li, B. X., Chia, J. & Levin, H. S. (2008). *Diffusion tensor imaging of acute mild traumatic brain injury in adolescents Background: Despite normal CT imaging and neurologic functioning, many individuals report* (tech. rep.).

Wilde, E. A., Bigler, E. D., Hunter, J. V., Fearing, M. A., Scheibel, R. S., Newsome, M. R., Johnson, J. L., Bachevalier, J., Li, X. & Levin, H. S. (2007). Hippocampus, amygdala, and basal ganglia morphometrics in children after moderate-to-severe traumatic brain injury. *Developmental Medicine and Child Neurology*, *49*(4), 294–299. https://doi.org/10.1111/j.1469-8749.2007.00294.x

Wills, A. J., Sawle, G. V., Guilbert, P. R. & Curtis, A. R. J. (2002). Palatal tremor and cognitive decline in neuroferritinopathy. *Journal of Neurology, Neurosurgery & Psychiatry*, *73*(1), 91–92. https://doi.org/10.1136/jnnp.73.1.91

Wintermark, M., Sanelli, P. C., Anzai, Y., Tsiouris, A. J. & Whitlow, C. T. (2015). Imaging evidence and recommendations for traumatic brain injury: Advanced neuro- and neurovascular imaging techniques. *American Journal of Neuroradiology*, *36*(2), E1–E11. https://doi.org/10.3174/ajnr.A4181

Wisnieff, C., Ramanan, S., Olesik, J., Gauthier, S., Wang, Y. & Pitt, D. (2015). Quantitative susceptibility mapping (QSM) of white matter multiple sclerosis lesions: Interpreting positive susceptibility and the presence of iron. *Magnetic Resonance in Medicine*, *74*(2), 564–570. https://doi.org/10.1002/mrm.25420

Woolrich, M. W., Jbabdi, S., Patenaude, B., Chappell, M., Makni, S., Behrens, T., Beckmann, C., Jenkinson, M. & Smith, S. M. (2009). Bayesian analysis of neuroimaging data in FSL. *NeuroImage*, *45*(1). https://doi.org/10.1016/j.neuroimage.2008.10.055

Wozniak, J. R., Krach, L., Ward, E., Mueller, B. A., Muetzel, R., Schnoebelen, S., Kiragu, A. & Lim, K. O. (2007). Neurocognitive and neuroimaging correlates of pediatric traumatic brain injury: A diffusion tensor imaging (DTI) study. *Archives of Clinical Neuropsychology*, *22*(5), 555–568. https://doi.org/10.1016/j.acn.2007.03.004

Wright, D. K., O'Brien, T. J. & Shultz, S. R. (2022). Sub-acute Changes on MRI Measures of Cerebral Blood Flow and Venous Oxygen Saturation in Concussed Australian Rules Footballers. *Sports Medicine - Open*, *8*(1). https://doi.org/10.1186/s40798-022-00435-w

Wu, Q. & Wu, Y. (2017). Clinical detection of cerebral microbleeds with quantitative susceptibility mapping in essential hypertension. *Biomedical Research*, *22*(28), 9971–9975. www.biomedres.info

Wu, Y., Wu, H., Guo, X., Pluimer, B. & Zhao, Z. (2020). Blood–Brain Barrier Dysfunction in Mild Traumatic Brain Injury: Evidence From Preclinical Murine Models. *Frontiers in Physiology*, *11*. https://doi.org/10.3389/fphys.2020.01030

Wunderle, K., Hoeger, K. M., Wasserman, E. & Bazarian, J. J. (2014). Menstrual phase as predictor of outcome after mild traumatic brain injury in women. *Journal of Head Trauma Rehabilitation*, *29*(5), E1–E8. https://doi.org/10.1097/HTR.0000000000000006

Xiong, X. Y., Wang, J., Qian, Z. M. & Yang, Q. W. (2014). Iron and Intracerebral Hemorrhage: From Mechanism to Translation. https://doi.org/10.1007/s12975-013-0317-7

Yablonskiy, D. A. & Haacke, E. M. (1994). *Theory of NMR Signal Behavior in Inhomogeneous Tissues: The Static* (tech. rep.).

Yager, R. R. & Alajlan, N. (2014). A note on mean absolute deviation. *Information Sciences*, *279*, 632–641. https://doi.org/10.1016/j.ins.2014.04.016

Yamamoto, A., Shin, R.-W., Hasegawa, K., Naiki, H., Sato, H., Yoshimasu, F. & Kitamoto, T. (2002). *Iron (III) induces aggregation of hyperphosphorylated s and its reduction to iron (II) reverses the aggregation: implications in the formation of neurofibrillary tangles of Alzheimer's disease* (tech. rep.).

Yang, J., Lv, M., Han, L., Li, Y., Liu, Y., Guo, H., Feng, H., Wu, Y. & Zhong, J. (2024). Evaluation of brain iron deposition in different cerebral arteries of acute ischaemic stroke patients using quantitative susceptibility mapping. *Clinical Radiology*, *79*(4), e592–e598. https://doi.org/10.1016/j.crad.2024.01.007

Ye, Y., Zhou, F., Zong, J., Lyu, J., Chen, Y., Zhang, S., Zhang, W., He, Q., Li, X., Li, M., Zhang, Q., Qing, Z. & Zhang, B. (2019). Seed prioritized unwrapping (SPUN) for MR phase imaging. *Journal of Magnetic Resonance Imaging*, *50*(1), 62–70. https://doi.org/10.1002/jmri.26606

Yeung, A. W. (2018). An updated survey on statistical thresholding and sample size of fMRI studies. *Frontiers in Human Neuroscience*, *12*. https://doi.org/10.3389/fnhum.2018.00016

Yu, F., Wang, Y., Stetler, A. R., Leak, R. K., Hu, X. & Chen, J. (2022). Phagocytic microglia and macrophages in brain injury and repair. *CNS Neuroscience and Therapeutics*, *28*(9), 1279–1293. https://doi.org/10.1111/cns.13899

Zecca, L., Youdim, M. B., Riederer, P., Connor, J. R. & Crichton, R. R. (2004). Iron, brain ageing and neurodegenerative disorders. *Nature Reviews Neuroscience*, *5*(11), 863–873. https://doi.org/10.1038/nrn1537

Zech, A., Hollander, K., Junge, A., Steib, S., Groll, A., Heiner, J., Nowak, F., Pfeiffer, D. & Rahlf, A. L. (2022). Sex differences in injury rates in team-sport athletes: A systematic review and meta-regression analysis. https://doi.org/10.1016/j.jshs.2021.04.003

Zeineddine, H. A., Girard, R., Cao, Y., Hobson, N., Fam, M. D., Stadnik, A., Tan, H., Shen, J., Chaudagar, K., Shenkar, R., Thompson, R. E., McBee, N., Hanley, D., Carroll, T., Christoforidis, G. A. & Awad, I. A. (2018). Quantitative susceptibility mapping as a monitoring biomarker in cerebral cavernous malformations with recent hemorrhage. *Journal of Magnetic Resonance Imaging*, *47*(4), 1133–1138. https://doi.org/10.1002/jmri.25831

Zetterberg, H., Morris, H. R., Hardy, J. & Blennow, K. (2016). Update on fluid biomarkers for concussion. https://doi.org/10.2217/cnc-2015-0002

Zhang, J., Liu, T., Gupta, A., Spincemaille, P., Nguyen, T. D. & Wang, Y. (2015). Quantitative mapping of cerebral metabolic rate of oxygen (CMRO2) using quantitative susceptibility mapping (QSM). *Magnetic Resonance in Medicine*, *74*(4), 945–952. https://doi.org/10.1002/mrm.25463

Zhang, L., Yang, K. H. & King, A. I. (2001). *Comparison of Brain Responses Between Frontal and Lateral Impacts by Finite Element Modeling* (tech. rep. No. 1). Mary Ann Liebert, Inc.

Zhang, S., Nguyen, T. D., Zhao, Y., Gauthier, S. A., Wang, Y. & Gupta, A. (2018). Diagnostic accuracy of semiautomatic lesion detection plus quantitative susceptibility mapping in the identification of new and enhancing multiple sclerosis lesions. *NeuroImage: Clinical*, *18*, 143–148. https://doi.org/10.1016/j.nicl.2018.01.013

Zhao, J., Chen, Z., Xi, G., Keep, R. F. & Hua, Y. (2014). Deferoxamine Attenuates Acute Hydrocephalus After Traumatic Brain Injury in Rats. *Translational Stroke Research*, *5*(5), 586–594. https://doi.org/10.1007/s12975-014-0353-y

Zhao, R., Velikina, J., Reeder, S. B., Vasanawala, S., Jeng, M. & Hernando, D. (2023). Validation of liver quantitative susceptibility mapping across imaging parameters at 1.5 T and 3.0 T using SQUID susceptometry as reference. *Magnetic Resonance in Medicine*, *89*(4), 1418–1428. https://doi.org/10.1002/mrm.29529

Zhao, Z., Nelson, A. R., Betsholtz, C. & Zlokovic, B. V. (2015). Establishment and Dysfunction of the Blood-Brain Barrier. https://doi.org/10.1016/j.cell.2015.10.067

Zhao, Z., Zhang, L., Wen, Q., Luo, W., Zheng, W., Liu, T., Zhang, Y., Zhu, K. & Wu, D. (2021). The effect of beta-amyloid and tau protein aggregations on magnetic susceptibility of anterior hippocampal laminae in Alzheimer's diseases. *NeuroImage*, *244*. https://doi.org/10.1016/j.neuroimage.2021.118584

Zhou, D., Liu, T., Spincemaille, P. & Wang, Y. (2014). Background field removal by solving the Laplacian boundary value problem. *NMR in Biomedicine*, *27*(3), 312–319. https://doi.org/10.1002/nbm.3064

Zhou, L., Choi, J. K., Kee, Y., Wang, Y. & Seo, J. K. (2017). Dipole Incompatibility Related Artifacts in Quantitative Susceptibility Mapping. *arXiv*.

Zhou, R., Ji, B., Kong, Y., Qin, L., Ren, W., Guan, Y. & Ni, R. (2021). PET Imaging of Neuroinflammation in Alzheimer's Disease. *Frontiers in Immunology*, *12:739130*. https://doi.org/10.3389/fimmu.2021.739130

Zhu, Z., Naji, N., Esfahani, J. H., Snyder, J., Seres, P., Emery, D. J., Noga, M., Blevins, G., Smyth, P. & Wilman, A. H. (2024). MR Susceptibility Separation for Quantifying Lesion Paramagnetic and Diamagnetic Evolution in Relapsing–Remitting Multiple Sclerosis. *Journal of Magnetic Resonance Imaging*. https://doi.org/10.1002/jmri.29266

Zhuang, Y., Yang, Q., Han, T., O'Malley, R., Kumar, A., Gerald, R. E. & Huang, J. (2021). Fiber optic sensor embedded smart helmet for real-time impact sensing and analysis through machine learning. *Journal of Neuroscience Methods*, *351*. https://doi.org/10.1016/j.jneumeth.2021.109073

Zivadinov, R., Polak, P., Schweser, F., Bergsland, N., Hagemeier, J., Dwyer, M. G., Ramasamy, D. P., Baker, J. G., Leddy, J. J. & Willer, B. S. (2018a). Multimodal Imaging of Retired Professional Contact Sport Athletes Does Not Provide Evidence of Structural and Functional Brain Damage. *Journal of Head Trauma Rehabilitation*, *33*(5), E24–E32. https://doi.org/10.1097/HTR.0000000000000422

Zivadinov, R., Tavazzi, E., Bergsland, N., Hagemeier, J., Lin, F., Dwyer, M. G., Carl, E., Kolb, C., Hojnacki, D., Ramasamy, D., Durfee, J., Weinstock-Guttman, B. & Schweser, F. (2018b). Brain iron at quantitative MRI is associated with disability in multiple sclerosis. *Radiology*, *289*(2), 487–496. https://doi.org/10.1148/radiol.2018180136

A

APPENDIX A: DEPTH-WISE COMPARISONS

Appendix A depicts the full 34 cortical ROIs for which comparative graphs were generated to illustrate the sensitivity of sampling at six cortical depths (left) in Chapter 8 compared to a more conservative three-depth model (right). Susceptibility values are shown at each depth, for each of the three curvature bins (crown = blue; bank = orange; fundus = yellow), for each ROI. Susceptibility is measured in ppm, and scaled appropriately for the range of each ROI. OFC = orbitofrontal cortex; mPFC = medial prefrontal cortex; STS = superior temporal sulcus; LOC = lateral occipital cortex; ACC = anterior cingulate cortex.

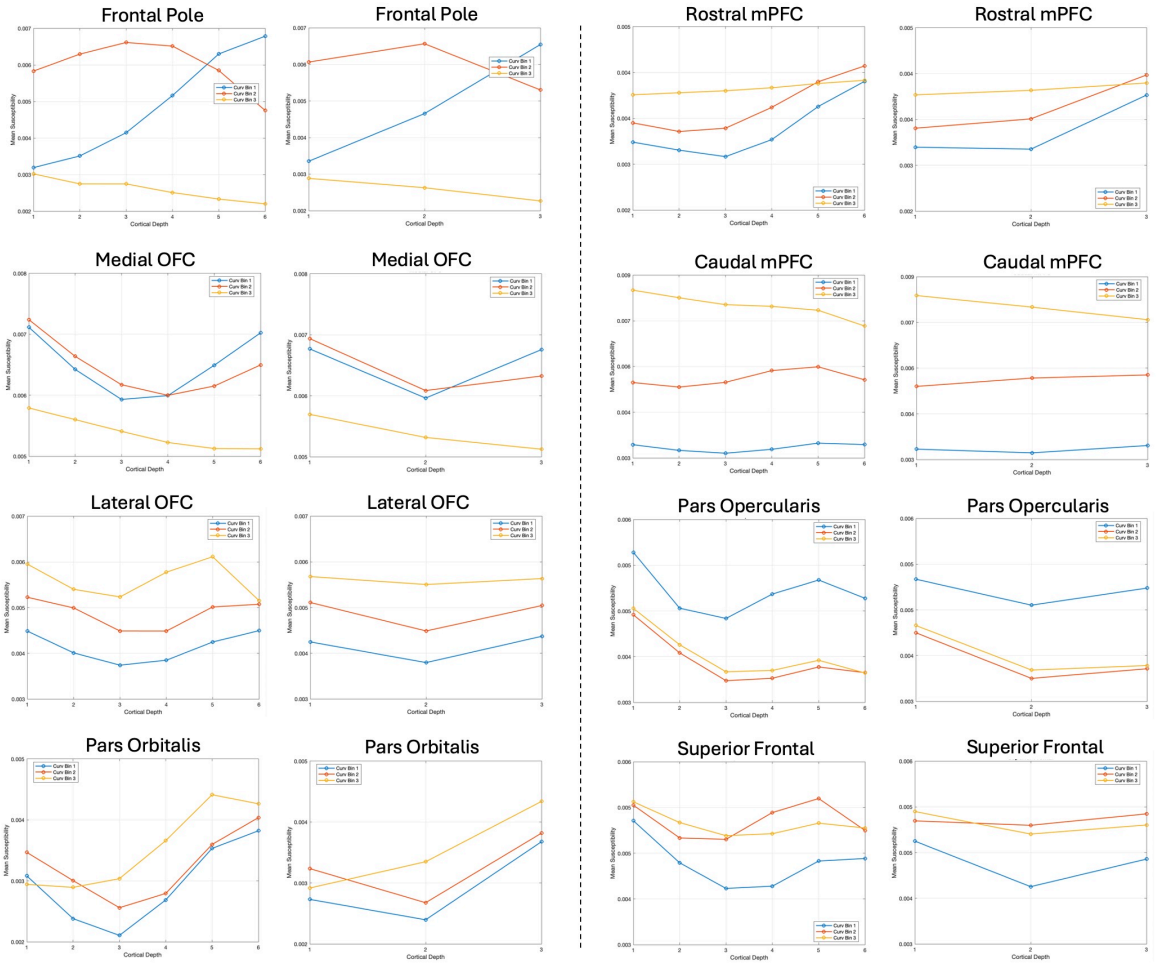

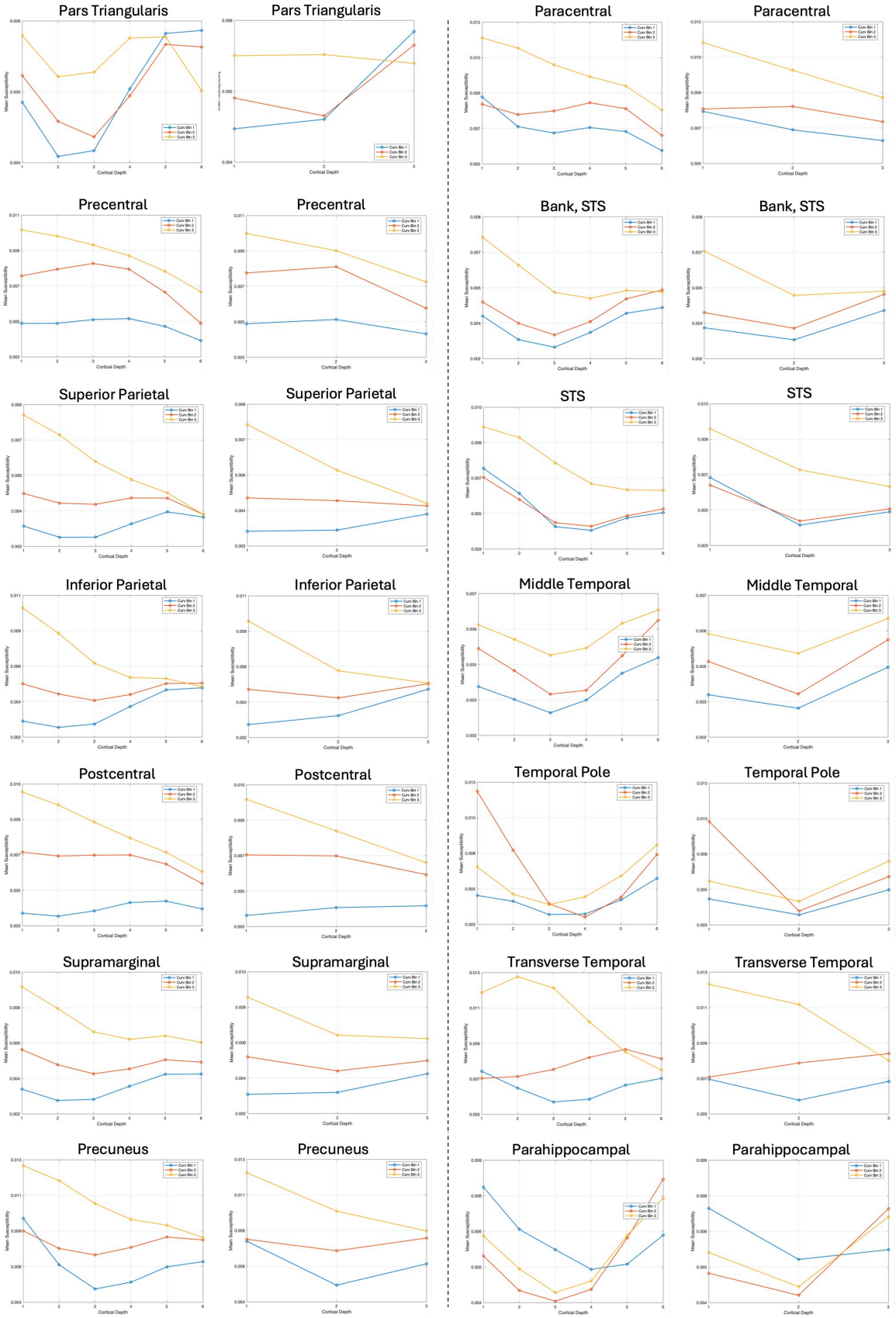
Pars Triangularis
Pars Triangularis
Paracentral
Paracentral
Precentral
Precentral
Bank, STS
Bank, STS
Superior Parietal
Superior Parietal
STS
STS
Inferior Parietal
Inferior Parietal
Middle Temporal
Middle Temporal
Postcentral
Postcentral
Temporal Pole
Temporal Pole
Supramarginal
Supramarginal
Transverse Temporal
Transverse Temporal
Precuneus
Precuneus
Parahippocampal
Parahippocampal
Mean Susceptibility
Cortical Depth
Curv Bin 1
Curv Bin 2
Curv Bin 3

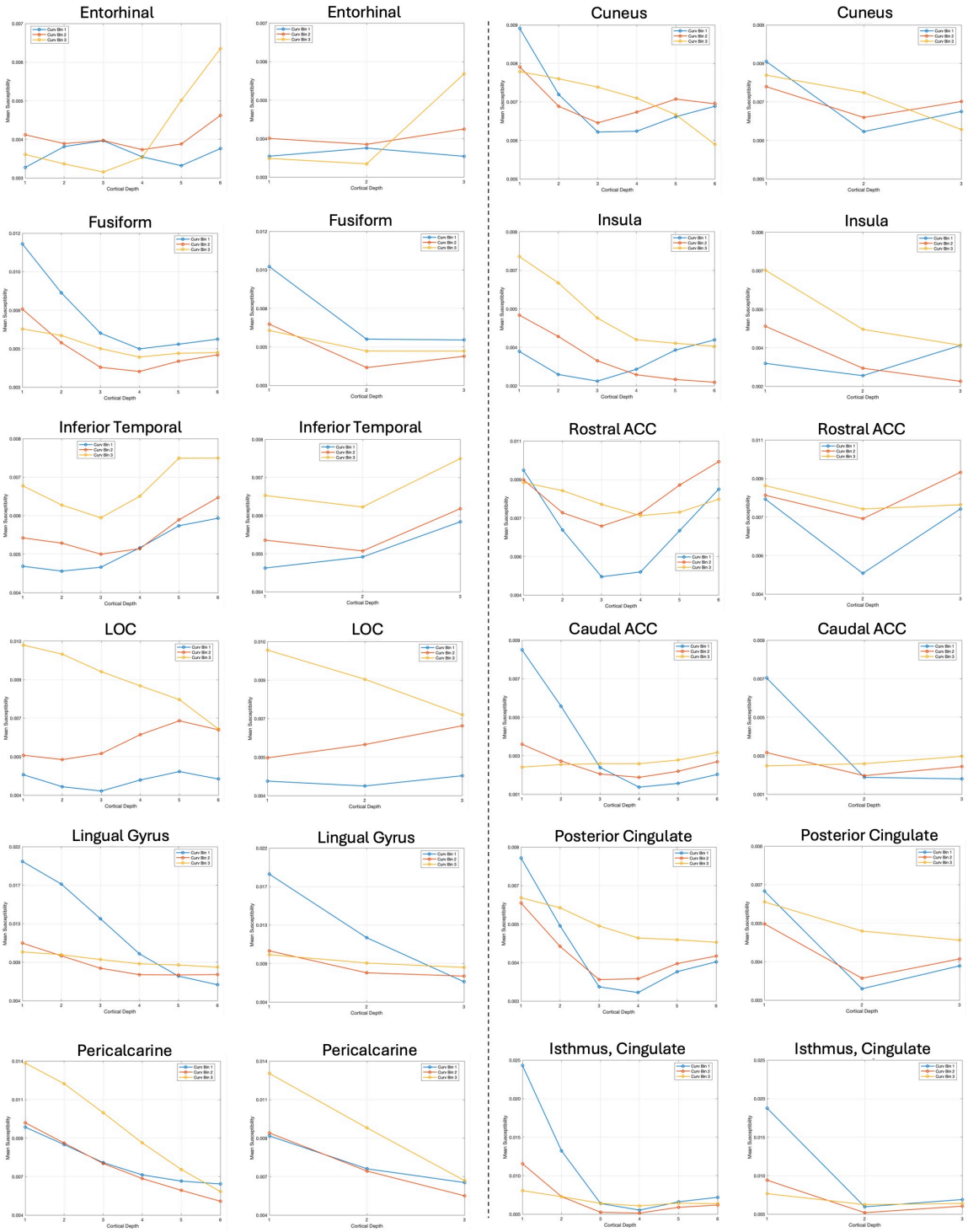
Entorhinal
Entorhinal
Cuneus
Cuneus
Fusiform
Fusiform
Insula
Insula
Inferior Temporal
Inferior Temporal
Rostral ACC
Rostral ACC
LOC
LOC
Caudal ACC
Caudal ACC
Lingual Gyrus
Lingual Gyrus
Posterior Cingulate
Posterior Cingulate
Pericalcarine
Pericalcarine
Isthmus, Cingulate
Isthmus, Cingulate
Mean Susceptibility
Cortical Depth
Curv Bin 1
Curv Bin 2
Curv Bin 3

B

APPENDIX B: PUBLICATIONS

OXFORD

Cerebral Cortex, 2025, **35**, bhaf059
https://doi.org/10.1093/cercor/bhaf059
Advance access publication date 18 March 2025
Original Article

Characterizing positive and negative quantitative susceptibility values in the cortex following mild traumatic brain injury: a depth- and curvature-based study

Christi A. Essex[1,*], Jenna L. Merenstein[2], Devon K. Overson[2], Trong-Kha Truong[2], David J. Madden[2], Mayan J. Bedggood[1], Helen Murray[3], Samantha J. Holdsworth[4], Ashley W. Stewart[5], Catherine Morgan[6], Richard L.M. Faull[3], Patria Hume[7], Alice Theadom[1], and Mangor Pedersen[1]

[1]Department of Psychology and Neuroscience, Auckland University of Technology, 90 Akoranga Drive, Northcote, Auckland 0627, New Zealand
[2]Brain Imaging and Analysis Center, Duke University Medical Center, 40 Duke Medicine Cir #414, Durham, NC 27710, United States
[3]Center for Brain Research, The University of Auckland, 85 Park Road, Grafton, Auckland 1023, New Zealand
[4]Mâtai Medical Research Institute, 466 Childers Road, Te Hapara, Gisborne 4010, New Zealand
[5]Center for Advanced Imaging, The University of Queensland, Building 57 of, University Dr, St Lucia QLD 4067, Australia
[6]Center for Advanced MRI, The University of Auckland, 85 Park Road, Grafton, Auckland 1023, New Zealand
[7]Sports Performance Research Institute New Zealand, Auckland University of Technology, 17 Antares Place, Rosedale, Auckland 0632, New Zealand
*Corresponding author: Christi A. Essex, Department of Psychology and Neuroscience, Auckland University of Technology, 90 Akoranga Drive, Northcote, Auckland 0627, New Zealand. Email: Christi.essex@aut.ac.nz

Evidence has linked head trauma to increased risk factors for neuropathology, including mechanical deformation of the sulcal fundus and, later, perivascular accumulation of hyperphosphorylated tau adjacent to these spaces related to chronic traumatic encephalopathy. However, little is known about microstructural abnormalities and cellular dyshomeostasis in acute mild traumatic brain injury in humans, particularly in the cortex. To address this gap, we designed the first architectonically motivated quantitative susceptibility mapping study to assess regional patterns of net positive (iron-related) and net negative (myelin-, calcium-, and protein-related) magnetic susceptibility across 34 cortical regions of interest following mild traumatic brain injury. Bilateral, between-group analyses sensitive to cortical depth and curvature were conducted between 25 males with acute (<14 d) sports-related mild traumatic brain injury and 25 age-matched male controls. Results suggest a trauma-induced increase in net positive susceptibility focal to superficial, perivascular-adjacent spaces in the parahippocampal sulcus. Decreases in net negative susceptibility values in distinct voxel populations within the same region indicate a potential dual pathology of neural substrates. These mild traumatic brain injury–related patterns were distinct from age-related processes revealed by correlation analyses. Our findings suggest depth- and curvature-specific deposition of biological substrates in cortical tissue convergent with features of misfolded proteins in trauma-related neurodegeneration.

Keywords: brain iron; cerebral cortex; magnetic resonance imaging; mild traumatic brain injury; quantitative susceptibility mapping.

Introduction

Mild traumatic brain injury (mTBI) is responsible for up to 90% of the estimated 50 to 60 million annual incidents of traumatic brain injury worldwide, which represents a ~$400 USD billion global economic burden (Howe et al. 2022; Maas et al. 2022). In addition to economic impacts, exposure to mild head trauma is a major public health concern. mTBI is associated with adverse mental health effects, cognitive decline, increased risk of neurodegenerative disease (Guskiewicz et al. 2007; McInnes et al. 2017), and premature mortality (Mackay et al. 2019). Repeated instances of brain trauma are a well-documented risk factor for the progressive tauopathy known as chronic traumatic encephalopathy (CTE), most often observed in athletes as a result of participation in contact sports, or in military veterans from exposure to blast impacts (McKee et al. 2013, 2023; Bieniek et al. 2015; Ling et al. 2017; Mez et al. 2017, 2020; Bieniek et al. 2020). mTBI is characterized by a primary insult to the brain, affecting tissue microstructure and inducing a cascade of secondary cellular processes, transient states of metabolic distress, and cellular dyshomeostasis (Giza and Hovda 2014). The absence of discernible focal lesions or other macroscopic morphological abnormalities means standard neuroimaging approaches are often insufficiently sensitive to detect mTBI pathology. Advanced neuroimaging methods extending beyond the scope of conventional medical practices may be used to identify the subtle, diffuse (Hier et al. 2021; Lunkova et al. 2021), and heterogeneous changes in brain

Received: October 15, 2024. **Revised:** February 17, 2025. **Accepted:** February 19, 2025

structure (Cook and Hawley 2014; Wintermark et al. 2015). Despite promising advances toward discovery of mTBI biomarkers, to date, no specific markers of structural brain injury have been identified and assessments are thus restricted to clinical evaluations and self-reported impairments in cognitive and physiological function (McCrea et al. 2017; Lunkova et al. 2021). These assessments may not accurately reflect objective measures of brain injury or recovery status, which can constrain intervention efficacy (Shenton et al. 2012; McCrea et al. 2017).

Investigating the role of biomaterials involved in preserving neuronal homeostasis, including trace elements such as brain iron, represents a promising direction for biomarker research. Iron is essential for proper brain function and is a cofactor in various neuronal processes including neurotransmitter-, myelin-, and DNA synthesis, energy metabolism, and oxidative phosphorylation (Ward et al. 2014b). Cellular concentrations are tightly regulated within neural tissue, and dyshomeostasis has been linked to oxidative stress, DNA and protein damage, inflammation, and ferroptosis (a form of iron-regulated cell death) (Mackenzie et al. 2008; Nisenbaum et al. 2014; Ma et al. 2022). Evidence suggests that iron overload is implicated in both secondary injury and the emergence of pathology downstream (Gozt et al. 2021) including hyperphosphorylation of tau (p-tau) (Yamamoto et al. 2002), highlighting the direct interplay between elevated levels of iron and CTE-like processes. Histologically validated colocalization of iron with abnormal protein accumulations in progressive tauopathies has distinguished brain iron as a hallmark feature of degenerative disorders such as Alzheimer's and Parkinson's diseases (AD and PD, respectively) (Zecca et al. 2004; Stankiewicz et al. 2007) and has been cited within neurofibrillary tangles in CTE (Bouras et al. 1997). Despite evidence linking head trauma to increased risk factors for premature iron-related neuropathology (Daglas and Adlard 2018) and increased levels of brain iron in humans following mTBI (Nisenbaum et al. 2014), the association between brain iron accumulation and the pathophysiology of acute sports-related mild traumatic brain injury (sr-mTBI) remains unclear.

Quantitative susceptibility mapping (QSM), an advanced magnetic resonance imaging (MRI) method, measures intrinsic magnetic properties and spatial distributions of biomaterials and molecules (including iron, calcium, protein, and myelin) that are related to brain tissue composition (Duyn and Schenck 2017; Wang et al. 2017; Gong et al. 2019; Kim et al. 2020; Jang et al. 2021; Zhao et al. 2021). The magnetic susceptibility of these materials is proportional to the degree of magnetization exhibited in response to an external magnetic field, such as the main magnetic field of an MRI scanner (B_0) (Schweser et al. 2016). Differences in magnetic field perturbation from dia- and para-magnetic compounds in brain tissue create inhomogeneities in the phase maps of gradient-recalled echo (GRE) MRI sequences (Marques and Bowtell 2005; De Rochefort et al. 2010; Langkammer et al. 2015). This mechanism generates contrast in QSM, thereby providing insights into the architecture of the brain and enabling more accurate delineation of many structural boundaries than the corresponding GRE magnitude images (Liu et al. 2015b). Unlike traditional susceptibility-weighted imaging (SWI) from which QSM is derived, this approach can be used to directly quantify the susceptibility of tissue within regions of interest (ROIs), serving as a close approximation of the constituent elements (Liu et al. 2015a; Deistung et al. 2017). Already integral to dementia research (Ravanfar et al. 2021; Nikparast et al. 2022; Uchida et al. 2022; Ghaderi et al. 2024; Mohammadi et al. 2024; Paul et al. 2024), QSM can be extended to investigate potential susceptibility-related pathology resulting from acute sr-mTBI.

A limited number of studies have used QSM to quantify magnetic susceptibility in white matter (WM) and/or subcortical or global gray matter (GM) (Gong et al. 2018; Koch et al. 2018, 2021; Weber et al. 2018; Zivadinov et al. 2018; Brett et al. 2021; Pinky et al. 2022; Wright et al. 2022; Bell et al. 2025) or as a marker of cerebral venous oxygen saturation ($Sv0_2$) (Chai et al. 2017; Wright et al. 2022; To et al. 2024). QSM investigations of mTBI-related GM alterations have focused almost exclusively on deep gray nuclei as a proxy for injury effects and cellular degeneration. This is due to the high density of iron in these nuclei related to elevated metabolic demand (Gozt et al. 2021), particularly in the globus pallidus, red nucleus, substantia nigra, putamen, dentate, caudate, and thalamus, relative to the cortical GM (Hallgren and Sourander 1958). These deep GM sites are vulnerable to not only iron-mediated disorders (Haacke et al. 2005) but also damage in mTBI (Raz et al. 2011). However, studies using QSM to investigate mTBI effects have largely overlooked the cortex. This complex structure is characterized by ridges (gyri) and grooves (sulci); curvatures corresponding to the base (fundus) of these sulci are exposed to the greatest force during mTBI, including shear stress (Bakhtiarydavijani et al. 2021) and movement of noncompressible CSF in a phenomenon referred to as the "water hammer effect" (Kornguth et al. 2017).

These cortical, microvascular-adjacent, regions most susceptible to mechanical deformation and injury in mTBI are also the primary loci of degeneration and tauopathy in CTE (Smith et al. 2013; Bieniek et al. 2021; McKee et al. 2023) and warrant careful investigation. The two mTBI-QSM studies to include cortical GM ROIs were either constrained by a macroscopic voxel-wise approach (Gong et al. 2018) or limited to gross segmentations of a small number of cortical ROIs (Pinky et al. 2022). Significantly more anatomical precision is needed to detect depth- or curvature-specific differences in magnetic susceptibility within the cortical mantle after mTBI. The cortex is likely excluded from investigation due to several methodological challenges primarily related to complex cortical architectonics. Firstly, differentiating myeloarchitecture, cytoarchitecture, and cortical laminae using ultrahigh-field, ultrahigh-resolution MRI (such as that acquired at 7T or higher) is a developing area in neuroimaging research (Waehnert et al. 2016). Currently, however, ultrahigh-field MRI is not as widely available, and clinical MRI data are more typically acquired on scanners of lower field strengths such as 3T or 1.5T (Straub et al. 2019). Secondly, standard voxel-wise comparisons and gross segmentations are naïve to the architectonics and distribution of cellular elements within the cortical layers; here, advanced analytic techniques are essential. At magnetic field strengths of 3T or lower, and supra-millimeter voxel resolutions, analysis of specific cortical laminae is inhibited; however, column-based analytic techniques (Waehnert et al. 2014; Ma et al. 2023; Northall et al. 2023; Merenstein et al. 2024) enable depth-wise investigations of magnetic susceptibility in the cerebral cortex and are already producing promising results in AD research (Merenstein et al. 2024).

To address these research gaps, we conducted the first architectonically motivated QSM analysis of cortical mTBI effects. This study aimed to: (i) assess regional patterns of positive (iron-related) and negative (myelin-, protein-, and calcium-related) net magnetic susceptibility as a marker of acute cortical pathology after sr-mTBI and (ii) understand the relationship between magnetic susceptibility in the cerebral cortex and variables such as age, injury latency, and severity. Based on prior literature, we hypothesized that differences in susceptibility would likely be evident in the frontal and temporal cortices, which are reported

to be vulnerable to injury in mTBI and are among the first to show degenerative effects of brain injury. We expected this distribution to be most prominent in the sulcal fundus due to increased vulnerability to trauma-induced deformation. Based on known effects of age on cortical iron deposition in this age range (Hallgren and Sourander 1958), net positive susceptibility values were hypothesized to show a positive relationship with age; however, correlation analyses remained largely exploratory and without specific a priori hypotheses.

Materials and methods

Approval for this study was granted by both The Auckland University of Technology Ethics Committee ([AUTEC] Date: 2022 February 18, Ref: 22/12) and the Health and Disabilities Ethics Committee ([HDEC] Date: 2022 February 18, Ref: 2022 EXP 11078). The study was conducted following the Declaration of Helsinki, and all participants provided written informed consent prior to data collection. All participants were provisioned a $50NZD food voucher to acknowledge their contribution as well as a $20NZD fuel voucher or taxi chit to cover travel expenses related to MRI scan attendance.

Participants

Data from 25 male contact sports players (M = 21.10 years old [16 to 32], SD = 4.59) with acute sr-mTBI (<14 d; M = 10.40 d, SD = 3.03) and 25 age-matched male controls (M = 21.10 years old [16 to 32], SD = 4.35) were used for this observational, case–control study (see Table 1). Ages were not significantly different between groups (t (48) = 0.00, P = 1.00). Clinical (sr-mTBI) participants were recruited through three Axis Sports Medicine clinics (Auckland, New Zealand) and through community-based pathways including referrals from healthcare professionals and sports team management. All clinical participants received a confirmed diagnosis of sr-mTBI by a licensed physician as a prerequisite for study inclusion and symptom severity was assessed with the Brain Injury Screening Tool (BIST) (Theadom et al. 2021) upon presentation to Axis clinics or electronically after recruitment. Healthy controls were recruited through print and social media advertisements and word-of-mouth. A history of significant medical or neurological conditions unrelated to the scope of this study or contraindication for MRI precluded study participation. Additionally, controls were excluded if they had any recent history of mTBI events (<12 months) or were living with any long-term effects of previous mTBI. All participants completed a 1-h MRI scan and a short demographic questionnaire. All MRI testing was conducted at the Centre for Advanced MRI (CAMRI), Auckland, New Zealand, and relevant scans were reviewed for clinically significant findings by a certified radiologist to ensure participant safety.

Neuroimaging

Acquisition

Advanced MRI data were acquired on a 3T Siemens MAGNETOM Vida Fit scanner (Siemens Healthcare, Erlangen, Germany) equipped with a 20-channel head coil. A 3D flow-compensated single-echo GRE sequence was used to obtain magnitude and phase images for QSM reconstruction at 1 mm isotropic resolution (TR = 30 ms; TE = 20 ms; flip angle (FA) = 15°; slice thickness = 1.0 mm; field of view (FoV) = 180 mm [LR] × 224 mm [AP]; matrix size = 180 × 224 × 160; bandwidth = 101 Hz/px) for a total acquisition time of ∼3.43 min. Additional acquisition parameters included a transversal orientation with right-to-left phase encoding. Wave-CAIPI acceleration was applied (in-plane = 2, 3D = 2) with 30 calibration reference lines in both phase-encode and 3D directions. For each participant, a high-resolution 3D T1-weighted (T1w) anatomical image volume was acquired for coregistration, parcellation and segmentation using a Magnetization-Prepared Rapid Acquisition Gradient Echo (MPRAGE) sequence (TR = 1,940.0 ms; TE = 2.49 ms, FA = 9°; slice thickness = 0.9 mm; FoV = 230 mm; matrix size = 192 × 512 × 512 mm; GRAPPA = 2; voxel size 0.45 × 0.45 × 0.90 mm) for a total acquisition time of ∼4.31 min. T2 maps, resting-state functional MRI data, diffusion-weighted images, and susceptibility-weighted images were also acquired as part of a larger study and analyzed separately. Participant Digital Imaging and Communications in Medicine (DICOM) images were converted to Neuroimaging Informatics Technology Initiative (NIfTI) files and transformed into brain imaging data structure (BIDS) (Gorgolewski et al. 2016) for further processing using *Dcm2Bids* (Boré et al. 2023) version 3.1.1, which is a wrapper for *dcm2niix* (Li et al. 2016) (v1.0.20230411).

Anatomical image processing

First, bias field correction was performed on the T1w images for each subject using the *N4* algorithm (Tustison et al. 2010) from ANTs (Avants et al. 2011). The bias field–corrected T1w images were processed in FreeSurfer (Fischl 2012) to (i) delineate pial and GM/WM boundary meshes and (ii) generate estimates of cortical thickness and curvature for each vertex (Merenstein et al. 2024). Skull stripping was rerun with additional arguments, including *-gcut* and adjustments to the watershed threshold as needed, to improve the accuracy of the original FreeSurfer (Fischl 2012) pial surface mesh. The pipeline for T1w and QSM image processing is summarized in Fig. 1.

QSM processing

QSM images were reconstructed using QSMxT (Stewart et al. 2022) v6.4.2 (https://qsmxt.github.io/QSMxT/) available as a container via NeuroDesk (Renton et al. 2024) (v2024-03-27), a lightweight virtual environment. QSMxT integrates and automates phase unwrapping using a rapid open-source minimum spanning tree algorithm (Dymerska et al. 2021), background field removal with projection onto dipole fields (Liu et al. 2011), and sparsity-based rapid two-step dipole inversion (Kames et al. 2018); a pipeline congruent with recent consensus statement recommendations for best-practice QSM reconstruction (Bilgic et al. 2023). In this study, QSM was quantified using the average whole-brain susceptibility as the reference. While the selection of an appropriate reference region in QSM remains a topic of ongoing debate (Straub et al. 2017), with each approach involving inherent trade-offs, consensus guidelines support the use of whole-brain susceptibility as a stable and reproducible reference (Bilgic et al. 2023). QSMxT also enables a two-pass combination method for hole filling and artifact reduction (Stewart et al. 2022) which performs parallel QSM masking and reconstruction on susceptibility sources identified as reliable and less reliable. Dual QSM images are then combined into a final integrated image more robust to reconstruction errors and streaking artifacts than those produced using a single-pass approach (Stewart et al. 2022). A brain mask was also generated using FSL's *BET* (Smith 2002) to improve masking and hole-filling of the threshold-based selection algorithm (Otsu 1979) used for two-pass QSM.

Subsequent processing was performed locally using FSL (Smith et al. 2004; Woolrich et al. 2009; Jenkinson et al. 2012). For each subject, the raw magnitude image was skull-stripped using FSL's *BET* (Smith 2002) with robust brain center estimation and a fractional intensity threshold of between 0.3 and 0.6. Binary masks were derived from the skull-stripped magnitude image and applied to the susceptibility maps to erode non-brain noise

Table 1. Summary of sr-mTBI participant clinical characteristics with reference to healthy controls.

ID	Age	DSI (days)	BIST score	MOI	MRI findings
mTBI-01	<20	5	140	Rugby	None
mTBI-02	<20	5	12	Rugby	None
mTBI-03	20s	6	78	Rugby	None
mTBI-04	<20	13	18	Rugby	Small fluid signal spaces in R peritrigonal WM—normal. R caudate cleft along ventricular surface—possibly developmental or from old ischaemic insult
mTBI-05	<20	12	61	Rugby	None
mTBI-06	20s	13	42	Rugby	None
mTBI-07	20s	13	13	Football	Minor artifactual T1 signal in pons
mTBI-08	20s	12	6	Hockey	None
mTBI-09	20s	6	56	Rugby	Minor R orbital fracture (old)
mTBI-10	<20	12	54	Rugby	None
mTBI-11	20s	10	52	Rugby	None
mTBI-12	30s	13	13	Football	None
mTBI-13	<20	5	79	Rugby	None
mTBI-14	20s	13	2	Rugby	Small focus of susceptibility in L superior frontal gyrus, possibly vascular or nonspecific hemosiderin
mTBI-15	<20	13	22	Rugby	None
mTBI-16	<20	8	117	Futsal	Tiny cleft of fluid signal in R cingulate gyrus—minor developmental anomaly or mature gliosis
mTBI-17	20s	13	*	Rugby	None
mTBI-18	20s	10	34	Gymnastics	None
mTBI-19	20s	13	28	Jiu-jitsu	Some artifactual DWI signal in pons
mTBI-20	20s	11	69	Surfing	Tiny susceptibility site in R temporal lobe—may be vascular
mTBI-21	<20	7	14	Rugby	Minor susceptibility in transverse sulcus in R mid temporal lobe—nonspecific, may be vascular or reflect hemosiderin deposition from prior small volume hemorrhage
mTBI-22	<20	13	39	Judo	None
mTBI-23	<20	9	34	Rugby	None
mTBI-24	<20	12	68	Rugby	None
mTBI-25	20s	12	17	Rugby	7 mm pineal cyst—normal limits. Some T1 hyperintensity in R cerebellum—artifact compatible
Mean	21.10 years	10.4	44.5 /160		No findings considered clinically relevant
Mean HC	21.10 years				No findings considered clinically relevant

Note. Diagnostic assessment is limited to the volume T1, SWI, and DWI sequences with only limited interpretation of the multi-echo T2 stack. Clinical assessments are relevant to identification of micro-hemorrhages, areas of siderosis, T1 appearance, gliosis, volume, ventricular volumes, and non-neurological findings. Age is given in a range to prevent re-identification of participants. Possible range of BIST scores is 0 (min) to 160 (max). Clinical group data correspondent to date at MRI only with the exception of the BIST acquired >24 h postinjury prior to MRI scanning (<14 days post). Abbreviations are as follows: ID, unique identifier; DSI, days since injury; BIST, Brain Injury Screening Tool; MOI, mechanism of injury; MRI, magnetic resonance imaging; L, left; R, right; *, missing data.

around the brain perimeter using *fslmaths*. Skull-stripped T1w images were used for the linear coregistration of the magnitude image using FMRIB's Linear Image Registration Tool (*FLIRT*) (Jenkinson and Smith 2001; Jenkinson et al. 2002; Greve and Fischl 2009) with 12 degrees of freedom (DoF). Due to variability in acquisition parameters, FoV, and matrix size between subject images, the 12 DoF linear registration provided more accurate alignment compared to the 6 DoF alternative, allowing for better compensation of nonrigid anatomical variations upon visual inspection. The resulting transformation matrix was used for spatial normalization of the QSM images to T1w space, effectively upsampling the QSM images. As the analyses are based on cortical depth rather than voxel-wise comparisons, upsampling was not considered a concern. In line with prior research that has used a binary intervoxel thresholding approach (Merenstein et al. 2024), net QSM maps were then thresholded into separate maps of dominant voxel-wise sign with *fslmaths*. This approach separates values across voxel boundaries above (QSM^{+}) and below (QSM^{-}) zero, thereby isolating predominantly positive (iron-related) voxels from predominantly negative (myelin-, calcium-, and protein-related) voxels (Duyn and Schenck 2017; O'Callaghan et al. 2017; Wang et al. 2017; Gong et al. 2019; Kim et al. 2020; Jang et al. 2021; Zhao et al. 2021) prior to ROI-wise analysis. Traditional QSM maps represent an aggregate of the susceptibility within voxels (Reichenbach 2012), and this intra-voxel averaging can obscure individual susceptibility sources within a voxel. While intra-voxel susceptibility source separation necessitates the acquisition of multi-echo data (Chen et al. 2021; Emmerich et al. 2021; Shin et al. 2021; Ahmed et al. 2023; Li et al. 2023; Lee et al. 2024), a more rudimentary intervoxel thresholding approach can be applied with single-echo data to separate voxels of dominant sign.

Cortical column generation

To generate cortical columns and sample signed susceptibility values, we used a pipeline previously applied to DWI data analysis (Ma et al. 2023) and recently adapted for use with QSM (Merenstein et al. 2024). First, the T1w FreeSurfer (Fischl 2012) recon served as an input into the *easy_lausanne* tool (https://github.com/mattcieslak/easy_lausanne.git). This stripped-down

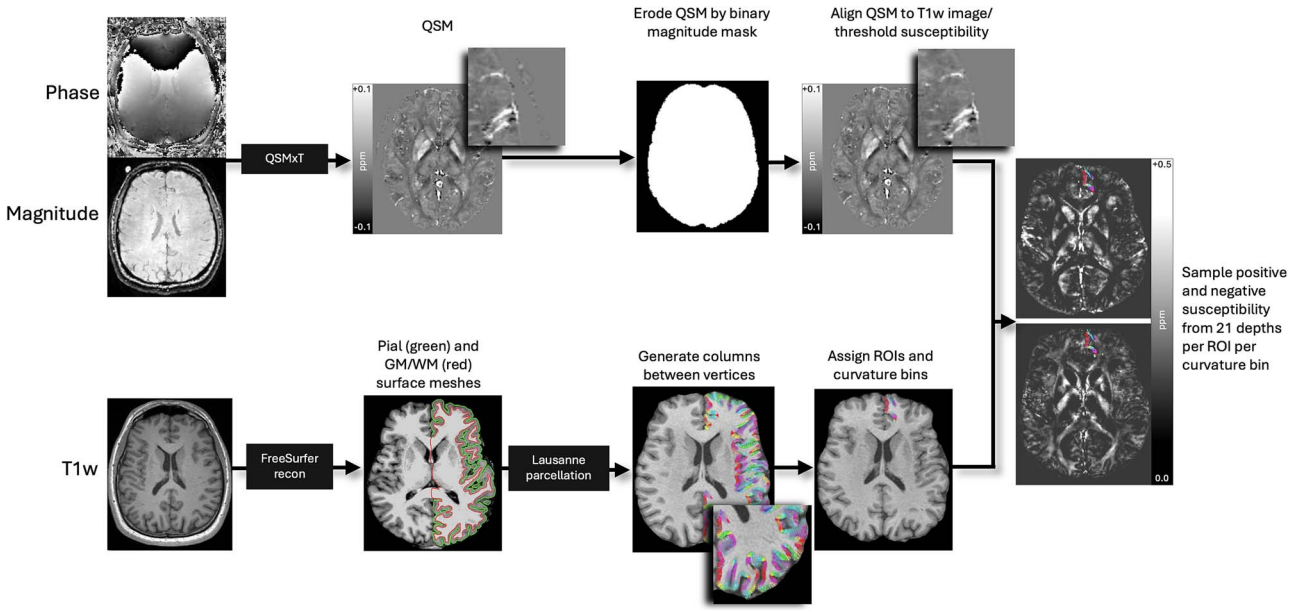

Fig. 1. Image processing pipeline. Steps are performed independently and in parallel for each participant. Quantitative susceptibility maps were reconstructed from magnitude and phase images using QSMxT, and eroded by the skull-stripped, binarized magnitude image mask to remove nonbrain sources of susceptibility. QSM images were then aligned to T1w images and thresholded into net positive and net negative susceptibility maps. FreeSurfer recon was used on bias field–corrected T1w images to produce pial and GM/WM boundary surface meshes, and vertex pairs were then joined to create cortical columns. Parcellations of the cortical GM were estimated by feeding the T1w FreeSurfer recon into *easy_lausanne*. Columns were then assigned specific ROIs and curvature bins and used to sample susceptibility from thresholded QSM maps.

fork of the open-source Connectome Mapper (Daducci et al. 2012) separates the cortex into five atlases, ranging from 34 to 250 ROIs per hemisphere, according to the Lausanne multiscale atlas (Cammoun et al. 2012). For subsequent analyses, we focused on the atlas with 34 ROIs per hemisphere, which is equivalent to the Desikan–Killiany atlas (Desikan et al. 2006) native to FreeSurfer (Fischl 2012).

Cortical columns were created for each hemisphere in T1w space with *write_mrtrix_tracks* (Tournier et al. 2019) in MATLAB (version R2024a), which was used to connect vertex pairs between the pial and GM/WM boundary surface meshes. As such, use of the term "column" in this context denotes a straight line orthogonal to the cortical surface (Merenstein et al. 2024), extending from the pial surface to the GM/WM boundary, rather than implying distinct cortical cytoarchitecture (Brodmann 1909). Each cortical column was segmented into 21 equidistant depths, each with a step size of 5% of the cortical thickness (Waehnert et al. 2014, 2016), from the pial surface to the GM/WM boundary using MRtrix3 *tckresample* (Tournier et al. 2019). Here, the step-wise depths represent the 21 equidistant segmentations rather than specific cellular laminae (LI to LVI) of the cortex. It is important to distinguish results produced using this approach from ultrahigh field investigations of cyto- and myelo-architecture in the cerebral cortex; results described herein are related to cortical "depth" rather than "layer." The columns were categorized based on cortical curvature, derived from FreeSurfer's (Fischl 2012) Gaussian curvature values at each GM/WM boundary vertex (Pienaar et al. 2008) and quantified in units of $1/mm^2$. The categories included the gyral crown (curvature values: −0.6 to −0.1), sulcal bank (−0.1 to 0.1), and sulcal fundus (0.1 to 0.6) (Merenstein et al. 2024). Positive curvature values indicated sulci, while negative values indicated gyri, with higher values corresponding to deeper curvatures (Merenstein et al. 2024). Only columns ranging from 0.5 to 6 mm in length were included in the analysis to capture plausible cortical morphology (Fischl and Dale 2000). Depth was measured in percentage of cortical thickness rather than absolute metrics (mm) to mitigate any variability between control and clinical participants.

Statistical analyses

To provide a detailed analysis of microstructural differences associated with sr-mTBI while maintaining result granularity, we performed analyses at the bilateral regional level using MATLAB (2024a). Average net positive and net negative susceptibility values were extracted from 21 cortical depths for all 34 ROIs. Each ROI was analyzed by an independent curvature bin (gyral crown, sulcal bank, and sulcal fundus) as well as combined curvature as a whole-ROI measure. Between-group analyses were conducted using two-tailed independent-sample *t*-tests. To control for multiple comparisons and align with prior research (Merenstein et al. 2024), we applied a false discovery rate (FDR) correction (Benjamini and Hochberg 1995) to the *P*-values for 21 comparisons (one for each depth) for each ROI/curvature profile. Due to precise age-matching of participants, age was not considered a covariate or confounding variable of interest for between-group comparisons. However, to explore the relationship between QSM values and age in the entire sample, two-tailed partial Pearson correlation coefficients were calculated between age and both net positive and net negative susceptibility values independently for all 34 curvature-combined ROIs, at each depth, while controlling for group effects. To explore the relationship between susceptibility values and other sr-mTBI-related variables, two-tailed Pearson correlation coefficients were also calculated between BIST scores and injury latency (days since injury [DSI]) and both net positive and net negative susceptibility values independently for the sr-mTBI sample only. Net negative susceptibility values were multiplied by −1 to convert them to absolute values, ensuring a consistent directional interpretation in all correlational analyses and more intuitive visualization. mTBI-17 was excluded from correlations between BIST and both

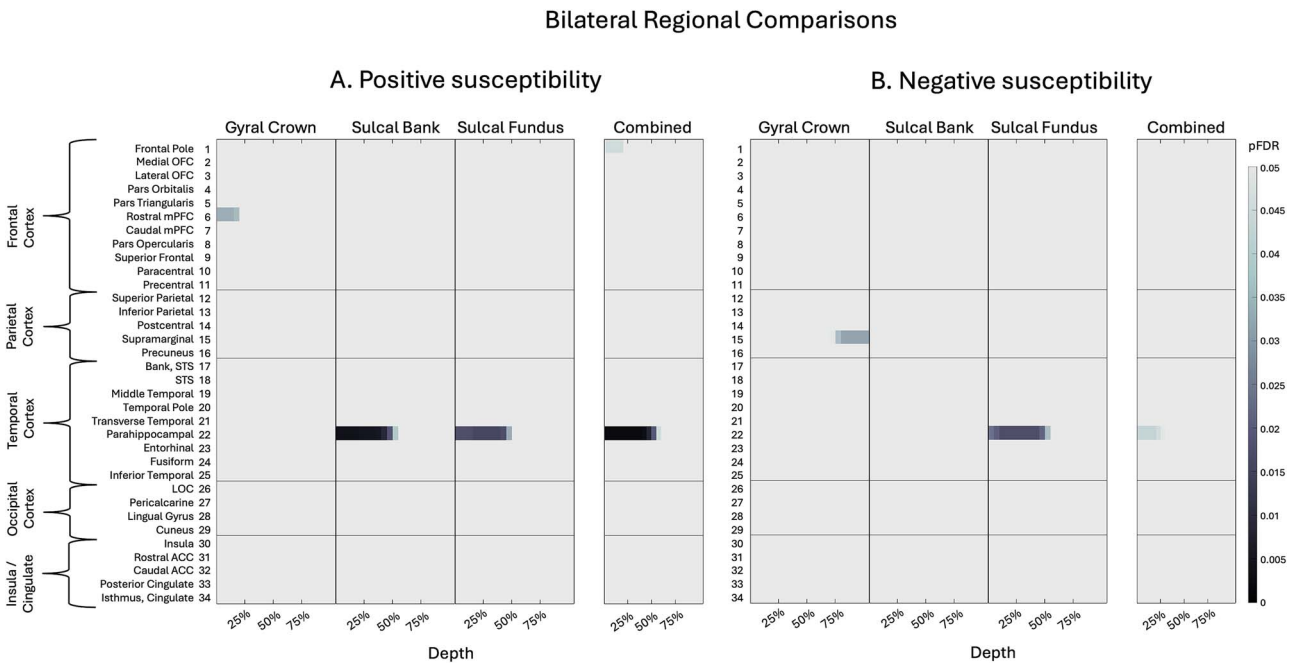

Fig. 2. Bilateral regional curvature and depth results. Color maps demonstrate differences in magnetic susceptibility at each cortical depth (where 0% depth is proximal to the pial surface and increases toward the GM/WM boundary at 100% depth), separately for each curvature bin (crown, bank, fundus) as well as combined curvature as a whole-ROI measure. Two-tailed independent-sample *t*-tests examined group differences in net susceptibility at each depth, for each curvature, at each ROI. *P*-values were corrected for multiple comparisons across 21 cortical depths using FDR. A) Net positive susceptibility values were significantly more positive for participants with sr-mTBI than healthy controls in temporal ROIs and significantly less positive in frontal regions only. B) Net negative susceptibility values were significantly less negative for sr-mTBI participants than controls in temporal ROIs and significantly more negative in parietal ROIs. OFC = orbitofrontal cortex; mPFC = middle prefrontal cortex; STS = superior temporal sulcus; LOC = lateral occipital cortex; ACC = anterior cingulate cortex. Figure based on Merenstein et al. (2024).

net susceptibility signs due to missing data. Correlations were also corrected for 21 depth-wise comparisons using FDR procedures (Benjamini and Hochberg 1995). Given the limited sample size and the need to conserve degrees of freedom in this exploratory study, regression analyses were deliberately omitted.

Results

Regional depth and curvature

Net positive susceptibility

Across bilateral depth profiles, participants with sr-mTBI exhibited significantly higher net positive susceptibility than controls in the temporal lobe only (see Fig. 2A), specifically in superficial depths of the sulcal bank and fundus of the parahippocampal gyrus, a finding that was conserved when curvature was combined as a whole-ROI measure (see also Fig. 3.1A and Fig. 3.2A). Susceptibility was decreased following sr-mTBI in the superficial gyral crown of the rostral medial prefrontal cortex (mPFC) and superficially in the frontal pole when curvature was combined. No significant differences between groups were found in bilateral susceptibility values in parietal, occipital, or insular lobes.

Net negative susceptibility

Across bilateral depth profiles, participants with sr-mTBI exhibited significantly less net negative susceptibility than controls in the temporal lobe only (see Fig. 2B). This finding was focal to the superficial depths of the fundus in the parahippocampal gyrus, as well as when curvature was combined (see also Fig. 3.1B and Fig. 3.2B). Net negative susceptibility was more negative for participants with sr-mTBI deep in the supramarginal gyral crown of the parietal cortex only. No significant differences between groups for curvature were found in the sulcal bank (see Fig. 3B). No significant differences were found in bilateral frontal, occipital, or insular lobes.

Age and bilateral regional net susceptibility

Net positive susceptibility

We observed significant positive correlations between age and iron-related net positive susceptibility distributions exclusively at deeper cortical depths near the GM/WM interface (see Fig. 4A(i)). In the frontal cortex, regions with statistically significant age-related increases in net positive susceptibility values included the pars orbitalis, pars triangularis, superior frontal gyrus, paracentral lobule, and precentral gyrus. In the parietal cortex, significant regions were the superior and inferior parietal lobules, supramarginal gyrus, and precuneus. In the temporal lobe, significant positive correlations were found in the parahippocampal gyrus and inferior temporal gyrus. The only cingulate region to exhibit a positive age-related correlation was the isthmus. No significant positive correlations with age were identified in any ROIs within the occipital cortex. Conversely, we identified significant negative correlations between age and net positive susceptibility exclusively at superficial cortical depths near the pial surface, demonstrating an inverse pattern to the positive correlations. In the frontal cortex, the areas showing significant negative correlations were the pars orbitalis, pars triangularis, superior frontal gyrus, paracentral lobule, and precentral gyrus. In the parietal cortex, the postcentral region exhibited significant negative correlations. No significant negative correlations between net positive susceptibility and age were apparent in temporal, occipital, or insular ROIs.

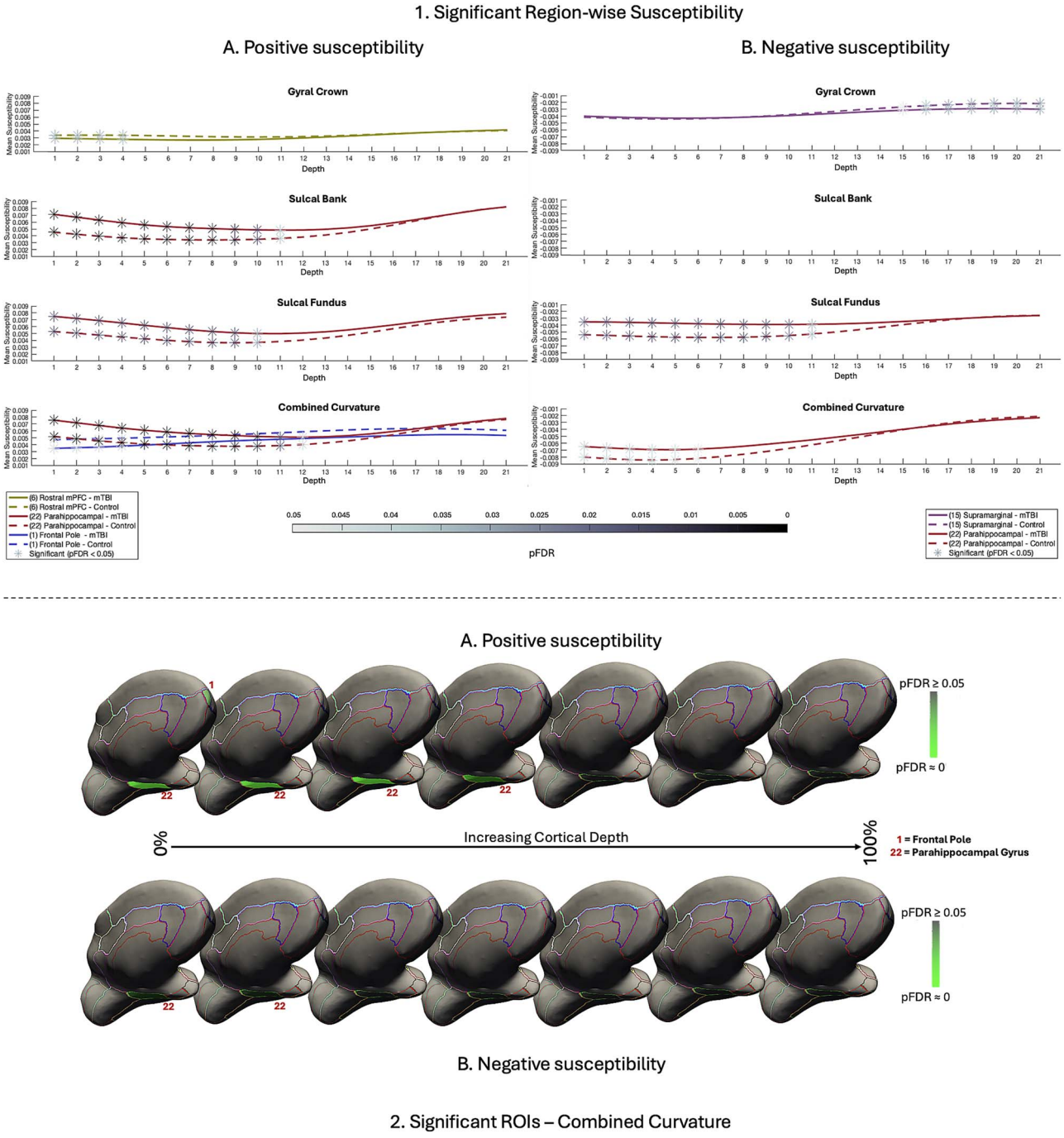

Fig. 3. Significant region-wise susceptibility values. 1) Differences in net sign-wise susceptibility values between mTBI participants and controls for significant regions of interest only. A) Net positive susceptibility values were significantly higher for participants with mTBI than healthy controls in superficial depths of the sulcal bank and fundus of the parahippocampal gyrus, as well as when curvature was combined. Values were significantly less positive for mTBI participants superficially in the gyral crown of the rostral mPFC and the superficial frontal pole when curvature was combined. B) Net negative susceptibility values were significantly less negative for mTBI participants than controls in the superficial depths of sulcal fundus in the parahippocampal gyrus, as well as when curvature was combined. Values were significantly more negative after mTBI deep in the supramarginal gyral crown. Susceptibility is measured in parts per million (ppm). mPFC = middle prefrontal cortex. 2) Medial visualization of significant ROIs after mTBI for both net positive A) and net negative B) susceptibility maps when curvature was combined as a whole-ROI measure. Surface lines demarcate borders between ROIs, projected onto an inflated surface. Significant ROIs are filled; intensity values relate directly to pFDR significance level. For visualization purposes, depth was reduced from 21 to 7 by averaging pFDR values every 3 consecutive depths where 0% is proximal to the pial surface and 100% to the GM/WM interface.

Net negative susceptibility

Significant positive relationships were observed between absolute net negative susceptibility values and age, primarily in the superficial depths of ROIs across all lobes, which at times extended to the GM/WM border (see Fig. 4B(i)). In the frontal lobe, ROIs exhibiting significant positive correlations between age and net negative susceptibility included the frontal pole, rostral mPFC, caudal mPFC, pars opercularis, superior frontal gyrus, and precentral gyrus. All examined ROIs in the parietal cortex exhibited significant positive relationships, namely, in the superior

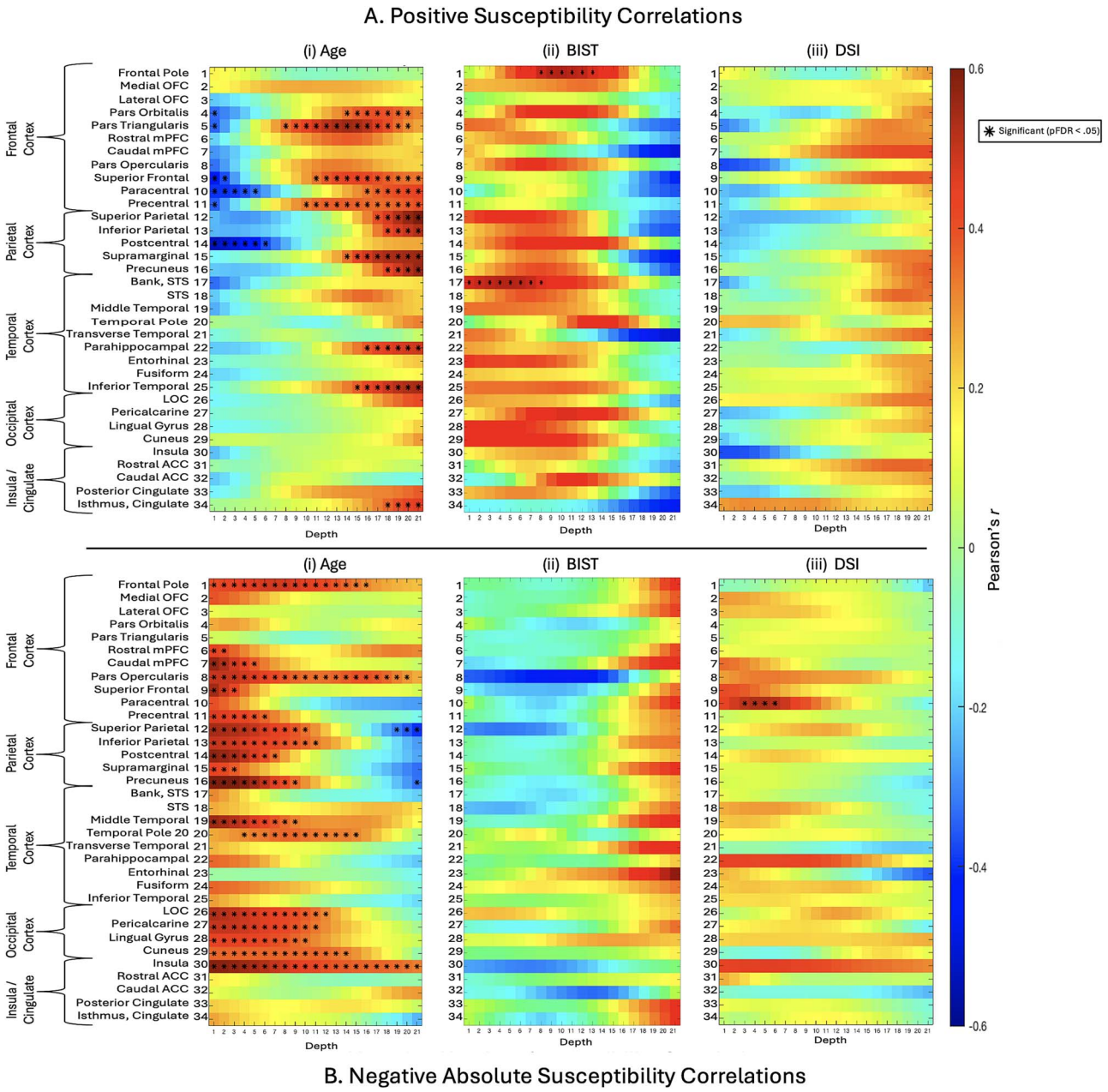

Fig. 4. Correlations between positive or negative net susceptibilities and variables of interest. i) The relationship between age and net positive A) and net negative B) susceptibility values was assessed for each depth for combined curvature as a whole-ROI measure using partial correlations to control for the effects of group status. ii) The relationship between BIST scores as a marker for injury severity and net susceptibility sign values was explored, along with. iii) The relationship between net susceptibility sign values and DSI at the time of MRI scan as a marker of injury latency. Net negative B) susceptibility was transformed into absolute values to better represent the relationship between variables. BIST = brain injury screening tool; DSI = days since injury (at time of MRI scan).

parietal lobule, inferior parietal lobule, postcentral gyrus, supramarginal gyrus, and precuneus. In the temporal cortex, significant positive correlations were found in the middle temporal gyrus and temporal pole. All occipital ROIs showed significant positive correlations, including the lateral occipital cortex, pericalcarine cortex, lingual gyrus, and cuneus. Within the insular cortex, only net negative susceptibilities in the insula demonstrated a significant positive relationship with age. In contrast, significant negative correlations with age were observed only in the deeper cortical layers closer to the GM/WM junction of parietal regions, specifically in the superior parietal lobule and precuneus.

Injury severity and bilateral regional net susceptibility

We observed significant positive correlations between BIST scores and net positive susceptibility values in the mid-depths of the frontal pole and in superficial depths of the bank of the superior temporal sulcus (see Fig. 4A(ii)). No significant correlations were observed between net negative susceptibility and BIST scores (see Fig. 4B(ii)).

Injury latency and bilateral regional net susceptibility

No significant correlations between DSI at time of MRI and net positive susceptibility values were observed for any ROI (see

Fig. 4A(iii)). Net negative susceptibility and DSI were positively correlated in superficial depths of the bilateral paracentral gyrus in the frontal cortex only (see Fig. 4B(iii)).

Discussion

Previous research seeking to understand the role of brain iron following mTBI has focused primarily on susceptibility distributions in subcortical or global GM and/or WM, largely neglecting the vulnerability of cortical regions to microstructural damage following an mTBI. The two investigations inclusive of cortical ROIs were constrained either by macroscopic voxel-wise techniques or a limited number of gross segmentations, which lack the anatomical precision necessary to detect depth- or curvature-specific differences in magnetic susceptibility. To address this gap in the literature, we adapted a new analytic technique already demonstrating efficacy in AD research to perform the first investigation of sr-mTBI-related differences in magnetic susceptibility as a function of cortical depth and curvature. In line with prior QSM research (Merenstein et al. 2024), we thresholded net QSM maps into separate maps of dominant voxel-wise sign to isolate net voxel-wise sign values for analysis.

Our findings revealed increased net positive susceptibility exclusive to the temporal lobe, specifically in the superficial depths at sulcal curvatures in the bilateral parahippocampal gyrus. This pattern was conserved when curvature was aggregated as a whole-ROI measure. In contrast, age-related net positive susceptibility indicative of iron deposition was observed at deep cortical depths, closer to the interface with the white matter, in the overall sample. These findings suggest that increases in net positive susceptibility close to the cortical surface indicate abnormal, injury-related iron accumulation after mTBI. Results corresponded with analyses of net negative susceptibility, which was less negative in the superficial depths of the sulcal parahippocampal gyrus after mild brain trauma. In addition, net negative susceptibility was positively correlated with age in superficial depths only, suggesting possible age-related calcification processes occurring in superficial cortical layers; a pattern opposite to mTBI-related net negative susceptibility effects. Fewer correlations were found between subjective injury status or time elapsed since injury and susceptibility, supporting a body of research demonstrating little relationship between objective injury measures and subjective self-report.

Depth

In vitro histological studies have demonstrated variations in iron distribution relative to specific cortical laminae (e.g., Perls iron staining), where concentrations are lowest at the pial surface and increase progressively through GM toward its junction with WM (Fukunaga et al. 2010). These findings have been corroborated by iron-sensitive R_2* mapping of ex vivo tissue samples using ultrahigh-field (7T) MRI (Fukunaga et al. 2010), which also exhibit high congruence with in vivo QSM (Shin et al. 2021). Taken together, these studies suggest that iron density in the cortex reflects distinct cyto- and myelo-architecture, with variance between layers. In healthy populations, iron density should be sparse at the pial surface and increase with depth. Conversely, our findings indicate an abnormal distribution pattern of net positive susceptibility related to iron deposition exclusively in superficial depths of the parahippocampal gyrus in the temporal cortex following injury (see Fig. 2A, Fig. 3.1A, and Fig. 3.2A). This increased net positive susceptibility at the acute stage of mTBI is directly inverted for depth comparative to healthy layer–specific variation (Fukunaga et al. 2010; Shin et al. 2021) and patterns related to normal aging in this range of the lifespan (see Fig. 4A(i)), suggesting an injury-specific model of cortical microstructural trauma (see Fig. 5).

The focal nature of increased net positive susceptibility in superficial depths suggests iron accumulation near small blood vessels (McKee et al. 2013). Concordantly, microhemorrhage and aggregation of activated microglia around perivascular sites are well documented after mTBI (Nisenbaum et al. 2014; Mckee and Daneshvar 2015; Huang et al. 2021). Here, it is tempting to speculate about potential mechanisms of iron overload following mTBI. Nonheme iron (i.e., bound to proteins such as ferritin and transferrin) generally enters the brain through active transport across the blood–brain barrier (BBB) via vascular endothelial cells; a constant process that is closely regulated within the central nervous system to ensure homeostasis (Gozt et al. 2021). Injury-induced acute cerebral microvascular dysfunction and increased permeability of the BBB (Sandsmark et al. 2019; Wu et al. 2020) likely increase iron transport into these superficial cortical layers (Ward et al. 2014b; Levi et al. 2024), which could result in a perivascular accumulation of iron. Notably, redox reactions involving nonheme iron are a significant source of reactive oxygen species (ROS) (Nisenbaum et al. 2014); when labile iron accumulates to pathological levels, it can exceed the capacity of storage proteins inducing oxidative stress, protein and DNA damage, and ferroptosis (Kruszewski 2003; Nisenbaum et al. 2014; Ward et al. 2014b). This labile iron is frequently considered a critical contributor to secondary injury mechanisms (Nisenbaum et al. 2014; Gozt et al. 2021; Huang et al. 2021) and represents the primary source of paramagnetic susceptibility in the brain on QSM (Langkammer et al. 2012). As such, iron accumulation acting as a catalyst for auto-toxic circuits (Levi et al. 2024) is a candidate hypothesis by which iron dyshomeostasis after mTBI could account for the increased net positive magnetic susceptibility of these compromised perivascular regions on QSM. Iron overload may represent a promising early marker of acute cell damage and mTBI-related neuropathology as well as degeneration of neural tissue downstream. However, as the precise mechanisms by which iron is released in the brain are still under investigation (Zecca et al. 2004; Gozt et al. 2021), these mechanisms cannot yet be disambiguated.

While the relationship between positive susceptibility and paramagnetic iron is well established, the mechanisms underlying diamagnetic sources of contrast are less well understood and more challenging to elucidate (Madden and Merenstein 2023; Northall et al. 2023; Merenstein et al. 2024). Recent research indicates that the primary source of diamagnetic contrast is myelin (Deh et al. 2018), but contributions are also made by calcium (Wang et al. 2017; Kim et al. 2020; Jang et al. 2021) and the deposition of proteins such as amyloid-beta (Aβ) and tau (Gong et al. 2019; Zhao et al. 2021). Our results suggest that net negative susceptibility is decreased in the parahippocampal gyrus at superficial depths following mTBI. Myeloarchitecture studies indicate that Layer I of the cerebral cortex consists primarily of axons, dendrites, and axon terminals, the cell bodies of which are located in deeper layers (Miyashita 2022). Although the cerebral cortex is not well known for high myelin content (Northall et al. 2023), decreased net negative susceptibility at these superficial depths could indicate changes to surface axons. This pattern coincided with increased net positive susceptibility in the superficial parahippocampal gyrus, suggesting a dual model of perivascular microstructural trauma focal to this region. The majority of iron present in the human brain parenchyma is stored

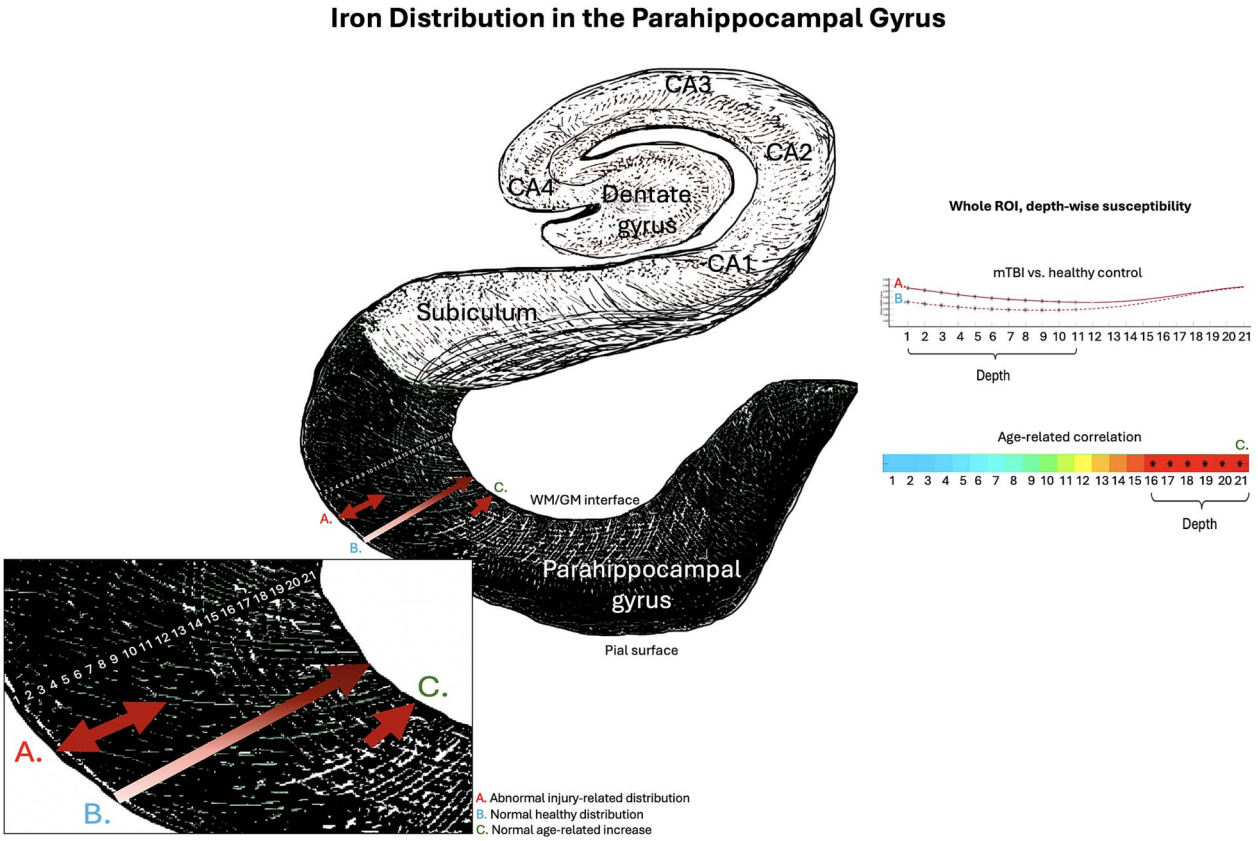

Fig. 5. Iron and net positive susceptibility distributions in the parahippocampal gyrus. Visualization of depth-specific net positive (iron-related) susceptibility distributions. A) Depicts increased net positive susceptibility following mTBI relative to healthy controls restricted to superficial depths of the parahippocampal gyrus. This pattern does not overlap with B) validated patterns of lower iron concentration proximal to the pial surface and increasing toward the GM/WM interface as a pattern of normal layer-specific distributions, or C) normal age-related increases in net positive susceptibility in this population (16 to 32 years) restricted to the deeper cortical depths closer to the GM/WM boundary. Depiction of the hippocampal formation inspired by the illustration in Ranson and Clark (1959).

as nonheme iron within myelin-maintaining oligodendroglia and in myelin itself (Connor and Menzies 1995); pathological iron levels have been known to damage both (Bradl and Lassmann 2010; Lassmann et al. 2012; Hametner et al. 2013). Mechanisms leading to concurrent increases in net positive susceptibility and decreases in net negative susceptibility in distinct voxel populations within the same ROI, as observed in this study, are further supported by research into pathogenesis of multiple sclerosis, which indicates that neuroinflammation and altered BBB permeability can result in iron accumulation in macrophages and other iron-related cytotoxic events, such as oxidative stress, causing degradation of oligodendrocytes and axons (Bradl and Lassmann 2010; Lassmann et al. 2012; Ward et al. 2014b). Research leveraging multi-echo QSM and contemporary magnetic source separation to investigate cortical pathology in MS has also linked decreased negative susceptibility to demyelination, reinforcing the potential role in disease pathology (Straub et al. 2023). Conversely, increased net negative susceptibility was mostly observed at deeper cortical depths closer to the GM/WM junction, which might reflect aggregation of Aβ or tau inherent to AD (Braak and Braak 1991) and CTE (McKee et al. 2023), or calcifications known to negatively affect cognition (Thibault et al. 2007). Notably, the injury-related accumulation patterns did not overlap with age-related changes in net negative susceptibility, which increased at superficial depths (see Fig. 4B(i)). This suggests that both decreased net negative susceptibility in superficial depths and increased net negative susceptibility at deeper cortical depths may result from abnormal, injury-related, neuropathological processes.

Curvature and ROI

Prior research has noted that the sulcal fundus is particularly vulnerable to injury in mTBI due to increased susceptibility to mechanical deformation (Smith et al. 2013; Bakhtiarydavijani et al. 2021; McKee et al. 2023) and the "water hammer effect" (Kornguth et al. 2017). The current study supports a fundus-specific model of damage in mTBI; the only persistent differences between groups in both net positive and net negative susceptibility were observed in sulcal regions of the bilateral parahippocampal gyrus (net positive susceptibility: sulcal bank and fundus; net negative susceptibility: sulcal fundus [see Figs. 2 and 3]). The focal nature of injury to these concave regions extends prior work noting increased mean cortical curvature in the sulcus (King et al. 2016) and sulcal widening (Kornguth et al. 2017) after mTBI. Results are also consistent with observations of mTBI-related vascular injury and microhemorrhage in the sulcal fundus on SWI (Kornguth et al. 2017). Additionally, the inferior medial temporal lobe is a notable site of injury in sr-mTBI (Mckee and Daneshvar 2015) and the parahippocampal gyrus proximal to the sphenoid ridge in TBI (Bigler 2007). Impact with this uneven portion of the skull base combined with reduced protection from dura where this region overlaps with the free edge of the tentorium cerebelli (Bigler 2007), could plausibly explain the differences in net susceptibility values focal to the parahippocampal gyrus. Previous

research has also highlighted associations between sr-mTBI and loss of cortical thickness in the parahippocampal gyrus along with reductions in parahippocampal volume (Arciniega et al. 2024).

Contextually, the parahippocampal cortex acts as a hub region in a network connecting areas of the frontal, parietal, and temporal lobes (Raslau et al. 2015) and represents a vital link between the default-mode network and the medial temporal lobe memory system, as evidenced by resting-state fMRI studies (Ward et al. 2014a). As such, it is integral to various cognitive processes including visuospatial processing and episodic memory (Aminoff et al. 2013) and the facilitation of contextual associations fundamental to higher-order cognitive performance (Raslau et al. 2015). The co-occurrence of iron-related net positive susceptibility values and net negative susceptibility values in different voxels within the same ROI, indicating potential myelin changes, particularly in the integrative superficial depths of the temporal parahippocampal gyrus, is consistent with the memory impairments symptomatic of sr-mTBI (Mckee and Daneshvar 2015).

Age and clinical correlates

Increasing iron in deep GM nuclei and some regions of the cortex is a hallmark of normal aging (Hallgren and Sourander 1958; Zecca et al. 2004). Research indicates that age-related iron increases occur primarily in the motor and premotor cortices, as well as the superior prefrontal and parietal cortices (Hallgren and Sourander 1958; Acosta-Cabronero et al. 2016). Additionally, these increases have been reported in the insula (Acosta-Cabronero et al. 2016) and hippocampus (Hagemeier et al. 2012). Histological evidence suggests that normal increases in cortical nonheme iron may be especially pronounced in younger individuals, sharply increasing during childhood and plateauing at around 30 years of age, depending on region (Hallgren and Sourander 1958; Schenck and Zimmerman 2004). These observations are supported by some (Callaghan et al. 2014; Acosta-Cabronero et al. 2016) but not other (Rodrigue et al. 2011) cross-sectional iron-sensitive MRI findings in adjacent age groups. Our findings support age-related cortical iron increases in a youthful population. In line with prior research, ROIs with age-related increases in likely iron content were most dense in frontal and parietal lobes, in addition to two loci in the temporal lobe and one in the insular cortex (see Fig. 4A(i)). Of all cortical regions, the motor system is particularly affected by age-related iron deposition (Acosta-Cabronero et al. 2016), a pattern mirrored in our findings that shows a notable density in the primary motor cortex. Our results suggest that age-related increases are restricted to deeper cortical depths closer to the GM/WM junction, which is known to naturally express higher iron levels in the healthy population (Fukunaga et al. 2010; Shin et al. 2021). These deeper layers contain large pyramidal cells (Miyashita 2022), which could speculatively accumulate iron differently. Indeed, previous research (Merenstein et al. 2024) has suggested that because age is more predictive of delayed response time rather than difficulties in decision-making (Ratcliff 2008; Madden et al. 2020; Merenstein et al. 2023), age-related iron accumulation should show a preference for deeper layers responsible for output rather than more integrative superficial regions (Rolls and Mills 2017).

In addition, we observed age-related increases in net negative magnetic susceptibility exclusively close to the pial surface. Previous studies utilizing negative QSM have shown similar distributions at superficial depths (Northall et al. 2023). This pattern aligns well with research indicating more common occurrences of calcifications in areas with high vascularization and metabolic activity (Jang et al. 2021), such as the cortical surface serviced by the pial arterial vasculature (Bollmann et al. 2022). Taken together, our findings indicate that age-related increases in iron are likely restricted to deep cortical depths, while diamagnetic calcifications are likely to occur at superficial depths. Both observations are supported by strong biological plausibility and well-documented scientific evidence. This reinforces the conclusion that observed differences in both net positive and net negative susceptibility following sr-mTBI reflect pathological processes distinct from those associated with normal aging.

The general lack of correlation between net positive or net negative susceptibilities and BIST scores may be attributed to the under-reporting of symptoms notorious in sr-mTBI (Meier et al. 2015), which would preclude accurate correlations. While iron negatively correlates with cognitive symptoms in mTBI (Lu et al. 2015), it is well documented that subjective assessments of injury severity do not reliably reflect objective brain injury or recovery status (McCrea et al. 2017) and cognitive/clinical symptoms do not align with neuroimaging findings (Shenton et al. 2012). However, the use of an intervoxel thresholding approach applied to traditional QSM maps may still be insensitive to the more subtle changes in tissue composition, which are better estimated using contemporary susceptibility source separation techniques (see, for example, Emmerich et al. 2021 and Shin et al. 2021). Additionally, the lack of correlation between net positive or net negative susceptibilities and injury latency suggests that acute neuropathology may persist into the subacute and chronic stages, necessitating further research to elucidate the time course of secondary injury in sr-mTBI.

Implications

The role of iron in acute responses following cytotrauma, as well as its colocalization with, and involvement in, misfolded proteins in neurodegenerative diseases, including CTE, identifies it as a potential marker of early degenerative processes (Bouras et al. 1997; Zecca et al. 2004). Interestingly, the temporal lobe and hippocampus are primary loci of atrophy and tau deposition in CTE (Murray et al. 2022; McKee et al. 2023), and iron has been found in neurofibrillary tangles within these regions (Bouras et al. 1997). A pathognomonic CTE lesion is characterized by the presence of p-tau in the cortical sulcus and, while this is not restricted to the subpial regions, supportive features of CTE include the presence of neurofibrillary tangles in superficial cortical layers (II/III), primarily in the temporal lobe (Bieniek et al. 2021; McKee et al. 2023). This laminar predilection is not seen in other tauopathies, like AD, where tau phosphorylation generally occurs in deeper layers (V/VI) (Pearson et al. 1985). Notwithstanding the short-term effects of iron overload, which have been linked to secondary injury in mTBI (Nisenbaum et al. 2014; Huang et al. 2021), the association between iron-mediated oxidative stress and hyperphosphorylation of tau (Yamamoto et al. 2002) coupled with the similarity of iron distributions observed in this study to hallmark distributions of tauopathy and degeneration in CTE raises important questions about the disease path from acute injury to eventual tissue degeneration. The precise mechanisms underlying CTE remain an active area of research, but these findings allude to the potential involvement of acute iron dyshomeostasis in degenerative cascades, warranting further investigation. Until such a time, any parallels drawn between the pattern of iron distribution in this study and the features of CTE tauopathy can, at this stage, only be speculative.

Here, follow-up investigations will be of paramount importance. A better understanding of iron and other neurobiological correlates, such as myelin damage or protein aggregation, may

be essential for developing effective care and targeted treatments at the acute stage of mTBI, which could protect against adverse consequences later in life. Recent research has explored the possibility of using heavy metal chelation as a therapeutic target for iron in AD (Mazur et al. 2024) and TBI (Daglas and Adlard 2018). In AD, this approach has had limited success, perhaps due to the accumulation of iron over a long time course; once iron overload becomes apparent, cell death has already occurred (Levi et al. 2024). However, mechanisms of acute injury-related iron overload may be distinct from long-term aggregation. Murine models using iron chelators such as deferoxamine (Panter et al. 1992; Long et al. 1996; Zhao et al. 2014; Jia et al. 2023) and *N*,*N*-Di(2-hydroxybenzyl)ethylenediamine-*N*,*N*-diacetic acid monohydrochloride (HBED) (Khalaf et al. 2019) have shown promise in reducing TBI symptomatology, likely through inhibition of ferroptosis and reductions in neuroinflammation, ROS, and gliosis. More research is needed to understand efficacy in humans, but this remains a possible avenue for limiting the effects of acute iron dyshomeostasis, which may contribute to degenerative effects evident in later life.

Limitations and future research

While QSM offers valuable insights into iron content and distribution, at lower field strengths (i.e., 3T), voxel resolution is restricted and does not reflect specific architectonics of cortical tissue. Cortical column analyses were thus constrained to investigations of depth rather than susceptibility distribution specific to cortical laminae. Future research could benefit from applying cortical column analysis to images with higher resolutions, for example, those collected on high field scanners, or by pushing images to sub-1 mm resolutions insofar as signal-to-noise ratios and acquisition times correspondent to increased participant burden are not overly compromised (for a comparison of data acquired at 3T and 7T, see Straub et al. 2019). The present study utilized a single-echo QSM sequence, limiting thresholding of susceptibility sources to a more rudimentary "between" (versus "within") voxels approach. It should be noted that this approach can introduce ambiguity regarding the interpretation of the underlying biological substrates. For instance, if a voxel exhibits a net negative susceptibility (indicating diamagnetic dominance), a reduction in the magnitude of this negativity could result either from a loss of diamagnetic material (such as myelin) or from an increase in paramagnetic material (such as iron deposition) that is insufficient to shift the net value to positive but would nonetheless contribute to an overall increase in positive susceptibility when analyzed as part of a raw, continuous map. To address this limitation, we suggest that future studies use multi-echo sequences to enable magnetic source separation "within" individual voxels (Chen et al. 2021; Emmerich et al. 2021; Shin et al. 2021; Ahmed et al. 2023; Li et al. 2023; Lee et al. 2024), thereby enhancing the biological interpretation of the findings and ensuring better alignment with guidelines for best-practice data acquisition (Bilgic et al. 2023).

Incorporating complementary modalities, such as positron emission tomography, would provide a more comprehensive understanding of cellular metabolism and neurobiological processes, potentially linking these to the observed mTBI-related differences and enabling more biologically informed inferences. Inclusion of protein assays, such as blood-based biomarkers, would also aid in creating a more comprehensive picture of the biological consequences of sr-mTBI. A range of potential confounds were not controlled for in this study including prior injuries, genetic predispositions, and environmental influences, which may affect injury severity and presentation (Rosenbaum and Lipton 2012), and future research should consider including additional measures to control for these variables. Given that this study was conducted exclusively in a male cohort that captures data from adolescence and early adulthood (i.e., ages 16 to 32), the generalizability of the findings to older or younger athletes and females may be limited. Sex differences in injury effects are reportedly influenced by a range of factors, including hormonal variations (Wunderle et al. 2014), the use of oral contraceptives (Gallagher et al. 2018), and differences in neck musculature (Tierney et al. 2005). Future research should extend investigations to female athletes and consider comparisons by sex. Future studies should also aim to include a broader age spectrum to further explore the interaction between age and susceptibility in mTBI. Here, it should be noted that age-related regional cortical iron accumulation is generally most pronounced up until the third decade of life (Hallgren and Sourander 1958) and research using cohorts with a broader age range should incorporate statistical modeling that accounts for differential iron deposition with age. Finally, given the limitations of inferring long-term consequences of sr-mTBI from data collected at the acute stage, future research should prioritize longitudinal studies tracking athletes over time. This prospective approach would yield more precise information compared to retrospective studies, providing valuable insights into the relationships between the number of mTBIs sustained, iron accumulation, recovery trajectories, and long-term outcomes. In lieu of longitudinal research, planned upcoming studies will utilize comparison of individual z-scores relative to healthy population norms to better clarify the prevalence of adverse outcomes following sr-mTBI. This approach will aim to enhance our understanding of the impact of sr-mTBI at the individual level, which may be obscured by group-level analyses (Bedggood et al. 2024; Domínguez et al. 2024).

Conclusions

To better characterize the mechanisms of mild traumatic brain injury at the acute stage, we conducted the first QSM study to assess depth- and curvature-specific regional patterns of positive (iron-related) and negative (myelin-, calcium-, and protein-related) magnetic susceptibility in the cerebral cortex following injury. We observed concurrent instances of increased positive susceptibility with decreased negative susceptibility in discrete voxel populations within the parahippocampal gyrus, indicating a possible accumulation of iron concomitant with myelin changes after injury. This distribution pattern was observed in the superficial depths of the sulcus, suggesting perivascular trauma due to mechanical forces. The pattern appeared distinct from age-related differences in positive and negative susceptibility and was reminiscent of supporting features of tau pathology in CTE, which is known to colocalize with iron. These results support a complex, dual-pathology model of trauma after mild head injury and have implications for understanding microstructural brain tissue damage following mTBI.

Acknowledgments

We extend thanks to Aria Courtney, Amabelle Voice-Powell, and Cassandra McGregor for their contribution to the data collection and Tania Ka'ai for bringing her perspective to cultural considerations in this study. In addition, we thank Axis Sports Concussion Clinics, particularly Dr Stephen Kara, for their assistance with recruiting sr-mTBI participants and personnel at the Centre for

Advanced Magnetic Resonance Imaging (CAMRI) for their assistance in collecting MRI data. We also acknowledge Dr Tim Elliot for radiological reporting of all participants and Siemens Healthcare/Siemens Healthineers for the use of a work-in-progress (WIP) sequence for the acquisition of magnitude and phase images.

Author contributions

Christi A. Essex (Conceptualization, Methodology, Project Administration, Validation, Software, Formal Analysis, Investigation, Resources, Data Curation, Writing—Original Draft, Writing—Review & Editing, Visualization), Jenna L. Merenstein (Methodology, Writing—Review & Editing, Visualization), Devon K. Overson (Methodology, Software, Visualization, Validation, Writing—Review & Editing), Trong-Kha Truong (Methodology, Software, Writing—Review & Editing), David J. Madden (Methodology, Software, Writing—Review & Editing), Mayan J. Bedggood (Writing—Review & Editing, Project administration, Investigation), Helen Murray (Writing—Review & Editing), Samantha J. Holdsworth (Writing—Review & Editing), Ashley W. Stewart (Writing—Review & Editing), Catherine Morgan (Writing—Review & Editing), Richard L.M. Faull (Writing—Review & Editing), Patria Hume (Writing—Review & Editing), Alice Theadom (Conceptualization, Methodology, Writing—Review & Editing, Funding acquisition, Supervision), and Mangor Pedersen (Conceptualization, Methodology, Writing—Review & Editing, Funding acquisition, Supervision).

Funding

This work was supported by a grant from the Health Research Council of New Zealand (grant number 21/622).

Conflict of interest statement: None declared.

Data availability

De-identified MRI data and code used for image processing and statistical analysis can be made available upon request to the corresponding author. Parent codes for cortical column generation can be made available upon request from co-authors (J.L.M., T.K.T.) based at the Brain Imaging and Analysis Center at Duke University Medical Center.

References

Acosta-Cabronero J, Betts MJ, Cardenas-Blanco A, Yang S, Nestor PJ. 2016. In vivo MRI mapping of brain iron deposition across the adult lifespan. *J Neurosci*. 36:364–374. https://doi.org/10.1523/JNEUROSCI.1907-15.2016.

Ahmed M et al. 2023. The diamagnetic component map from quantitative susceptibility mapping (QSM) source separation reveals pathological alteration in Alzheimer's disease-driven neurodegeneration. *NeuroImage*. 280:120357. https://doi.org/10.1016/j.neuroimage.2023.120357.

Aminoff EM, Kveraga K, Bar M. 2013. The role of the parahippocampal cortex in cognition. *Trends Cogn Sci*. 17:379–390. https://doi.org/10.1016/j.tics.2013.06.009.

Arciniega H et al. 2024. Brain morphometry in former American football players: 1 findings from the DIAGNOSE CTE research project. *Brain*. 147:3590–3610. https://doi.org/10.1093/brain/awae098.

Avants BB et al. 2011. A reproducible evaluation of ANTs similarity metric performance in brain image registration. *NeuroImage*. 54:2033–2044. https://doi.org/10.1016/j.neuroimage.2010.09.025.

Bakhtiarydavijani A et al. 2021. A mesoscale finite element modeling approach for understanding brain morphology and material heterogeneity effects in chronic traumatic encephalopathy. *Comput Methods Biomech Biomed Engin*. 24:1169–1183. https://doi.org/10.1080/10255842.2020.1867851.

Bedggood MJ et al. 2024. Individual-level analysis of MRI T2 relaxometry in mild traumatic brain injury: possible indications of brain inflammation. *NeuroImage Clin*. 43:103647. https://doi.org/10.1016/j.nicl.2024.103647.

Bell TK et al. 2025. Quantitative susceptibility mapping in adults with persistent-post concussion symptoms after mild traumatic brain injury: an exploratory study. *Am J Neuroradiol*. 46:435–442. https://doi.org/10.3174/ajnr.A8454.

Benjamini Y, Hochberg Y. 1995. Controlling the false discovery rate: a practical and powerful approach to multiple testing. *J Royal Stat Soc: Series B*. 57:289–300. https://doi.org/10.1111/j.2517-6161.1995.tb02031.x.

Bieniek KF et al. 2015. Chronic traumatic encephalopathy pathology in a neurodegenerative disorders brain bank. *Acta Neuropathol*. 130:877–889. https://doi.org/10.1007/s00401-015-1502-4.

Bieniek KF et al. 2020. Association between contact sports participation and chronic traumatic encephalopathy: a retrospective cohort study. *Brain Pathol*. 30:63–74. https://doi.org/10.1111/bpa.12757.

Bieniek KF et al. 2021. The second NINDS/NIBIB consensus meeting to define neuropathological criteria for the diagnosis of chronic traumatic encephalopathy. *J Neuropathol Exp Neurol*. 80:210–219. https://doi.org/10.1093/jnen/nlab001.

Bigler ED. 2007. Anterior and middle cranial fossa in traumatic brain injury: relevant neuroanatomy and neuropathology in the study of neuropsychological outcome. *Neuropsychology*. 21:515–531. https://doi.org/10.1037/0894-4105.21.5.515.

Bilgic B et al. 2023. Recommended implementation of quantitative susceptibility mapping for clinical research in the brain: a consensus of the ISMRM electro-magnetic tissue properties study group. *Magn Reson Med*. 91:1834–1862. https://doi.org/10.1002/mrm.30006.

Bollmann S et al. 2022. Imaging of the pial arterial vasculature of the human brain in vivo using highresolution 7T time-of-flight angiography. *elife*. 11:e71186. https://doi.org/10.7554/eLife.71186.

Boré A, Guay S, Bedetti C, Meisler S. 2023. GuenTher N. Dcm2Bids (Version 3.1.1) [Computer software]. https://doi.org/10.5281/zenodo.8436509.

Bouras C et al. 1997. A laser microprobe mass analysis of brain Aluminum and iron in dementia pugilistica: comparison with Alzheimer's disease. *Eur Neurol*. 38:53–58. https://doi.org/10.1159/000112903.

Braak H, Braak E. 1991. Neuropathological stageing of Alzheimer-related changes. *Acta Neuropathol*. 82:239–259. https://doi.org/10.1007/BF00308809.

Bradl M, Lassmann H. 2010. Oligodendrocytes: biology and pathology. *Acta Neuropathol*. 119:37–53. https://doi.org/10.1007/s00401-009-0601-5.

Brett BL et al. 2021. Association of Head Impact Exposure with white matter macrostructure and microstructure metrics. *J Neurotrauma*. 38:474–484. https://doi.org/10.1089/neu.2020.7376.

Brodmann K. 1909. Localization in the cerebral cortex. In: *Vergleichende Lokalisationslehre der Grosshirnrinde in ihren Prinzipien dargestellt auf Grund des Zellenbaues* . Barth, Leipzig.

Callaghan MF et al. 2014. Widespread age-related differences in the human brain microstructure revealed by quantitative magnetic resonance imaging. *Neurobiol Aging*. 35:1862–1872. https://doi.org/10.1016/j.neurobiolaging.2014.02.008.

Cammoun L et al. 2012. Mapping the human connectome at multiple scales with diffusion spectrum MRI. *J Neurosci Methods*. 203: 386–397. https://doi.org/10.1016/j.jneumeth.2011.09.031.

Chai C et al. 2017. Decreased susceptibility of major veins in mild traumatic brain injury is correlated with post-concussive symptoms: a quantitative susceptibility mapping study. *NeuroImage Clin*. 15:625–632. https://doi.org/10.1016/j.nicl.2017.06.008.

Chen J, Gong NJ, Chaim KT, Otaduy MCG, Liu C. 2021. Decompose quantitative susceptibility mapping (QSM) to sub-voxel diamagnetic and paramagnetic components based on gradient-echo MRI data. *NeuroImage*. 242:118477. https://doi.org/10.1016/j.neuroimage.2021.118477.

Connor JR, Menzies SL. 1995. Cellular management of iron in the brain. *J Neurol Sci*. 134:33–44. https://doi.org/10.1016/0022-510x(95)00206-h.

Cook GA, Hawley JS. 2014. A review of mild traumatic brain injury diagnostics: current perspectives, limitations, and emerging technology. *Mil Med*. 179:1083–1089. https://doi.org/10.7205/MILMED-D-13-00435.

Daducci A et al. 2012. The connectome mapper: an open-source processing pipeline to map connectomes with MRI. *PLoS One*. 7:e48121. https://doi.org/10.1371/journal.pone.0048121.

Daglas M, Adlard PA. 2018. The involvement of iron in traumatic brain injury and neurodegenerative disease. *Front Neurosci*. 12:981. https://doi.org/10.3389/fnins.2018.00981.

De Rochefort L et al. 2010. Quantitative susceptibility map reconstruction from MR phase data using bayesian regularization: validation and application to brain imaging. *Magn Reson Med*. 63:194–206. https://doi.org/10.1002/mrm.22187.

Deh K et al. 2018. Magnetic susceptibility increases as diamagnetic molecules breakdown: myelin digestion during multiple sclerosis lesion formation contributes to increase on QSM. *J Magn Reson Imaging*. 48:1281–1287. https://doi.org/10.1002/jmri.25997.

Deistung A, Schweser F, Reichenbach JR. 2017. Overview of quantitative susceptibility mapping. *NMR Biomed*. 30:e3569. https://doi.org/10.1002/nbm.3569.

Desikan RS et al. 2006. An automated labeling system for subdividing the human cerebral cortex on MRI scans into gyral based regions of interest. *NeuroImage*. 31:968–980. https://doi.org/10.1016/j.neuroimage.2006.01.021.

Domínguez JF et al. 2024. Improving quantitative susceptibility mapping for the identification of traumatic brain injury neurodegeneration at the individual level. *Z Med Phys*. https://doi.org/10.1016/j.zemedi.2024.01.001.

Duyn JH, Schenck J. 2017. Contributions to magnetic susceptibility of brain tissue. *NMR Biomed*. 30:10.1002/nbm.3546. https://doi.org/10.1002/nbm.3546.

Dymerska B et al. 2021. Phase unwrapping with a rapid opensource minimum spanning tree algorithm (ROMEO). *Magn Reson Med*. 85:2294–2308. https://doi.org/10.1002/mrm.28563.

Emmerich J, Bachert P, Ladd ME, Straub S. 2021. On the separation of susceptibility sources in quantitative susceptibility mapping: theory and phantom validation with an in vivo application to multiple sclerosis lesions of different age. *J Magn Reson*. 330:107033. https://doi.org/10.1016/j.jmr.2021.107033.

Fischl B. 2012. *FreeSurfer NeuroImage*. 62:774–781. https://doi.org/10.1016/j.neuroimage.2012.01.021.

Fischl B, Dale AM. 2000. Measuring the thickness of the human cerebral cortex from magnetic resonance images. *PNAS*. 20: 11050–11055. https://doi.org/10.1073/pnas.200033797.

Fukunaga M et al. 2010. Layer-specific variation of iron content in cerebral cortex as a source of MRI contrast. *Proc Natl Acad Sci USA*. 107:3834–3839. https://doi.org/10.1073/pnas.0911177107.

Gallagher V et al. 2018. The effects of sex differences and hormonal contraception on outcomes after collegiate sports-related concussion. *J Neurotrauma*. 35:1242–1247. https://doi.org/10.1089/neu.2017.5453.

Ghaderi S, Mohammadi S, Nezhad NJ, Karami S, Sayehmiri F. 2024. Iron quantification in basal ganglia: quantitative susceptibility mapping as a potential biomarker for Alzheimer's disease – a systematic review and meta-analysis. *Front Neurosci*. 18. https://doi.org/10.3389/fnins.2024.1338891.

Giza CC, Hovda DA. 2014. The new neurometabolic cascade of concussion. *Neurosurgery*. 75 Suppl 4(04):S24–S33. https://doi.org/10.1227/NEU.0000000000000505.

Gong NJ et al. 2018. Microstructural alterations of cortical and deep gray matter over a season of high school football revealed by diffusion kurtosis imaging. *Neurobiol Dis*. 119:79–87. https://doi.org/10.1016/j.nbd.2018.07.020.

Gong NJ, Dibb R, Bulk M, van der Weerd L, Liu C. 2019. Imaging beta amyloid aggregation and iron accumulation in Alzheimer's disease using quantitative susceptibility mapping MRI. *NeuroImage*. 191:176–185. https://doi.org/10.1016/j.neuroimage.2019.02.019.

Gorgolewski KJ et al. 2016. The brain imaging data structure, a format for organizing and describing outputs of neuroimaging experiments. *Sci Dat*. 3:160044. https://doi.org/10.1038/sdata.2016.44.

Gozt A, Hellewell S, Ward PG, Bynevelt M, Fitzgerald M. 2021. Emerging applications for quantitative susceptibility mapping in the detection of traumatic brain injury pathology. *Neuroscience*. 467:218–236. https://doi.org/10.1016/j.neuroscience.2021.05.030.

Greve DN, Fischl B. 2009. Accurate and robust brain image alignment using boundary-based registration. *NeuroImage*. 48:63–72. https://doi.org/10.1016/j.neuroimage.2009.06.060.

Guskiewicz KM et al. 2007. Recurrent concussion and risk of depression in retired professional football players. *Med Sci Sports Exerc*. 39:903–909. https://doi.org/10.1249/mss.0b013e3180383da5.

Haacke ME et al. 2005. Imaging iron stores in the brain using magnetic resonance imaging. *Magn Reson Imaging*. 23:1–25. https://doi.org/10.1016/j.mri.2004.10.001.

Hagemeier J, Geurts JJ, Zivadinov R. 2012. Brain iron accumulation in aging and neurodegenerative disorders. *Expert Rev Neurother*. 12:1467–1480. https://doi.org/10.1586/ern.12.128.

Hallgren B, Sourander P. 1958. The effect of age on the non-haemin iron in the human brain. *J Neurochem*. 3:41–51. https://doi.org/10.1111/j.1471-4159.1958.tb12607.x.

Hametner S et al. 2013. Iron and neurodegeneration in the multiple sclerosis brain. *Ann Neurol*. 74:848–861. https://doi.org/10.1002/ana.23974.

Hier DB et al. 2021. Blood biomarkers for mild traumatic brain injury: a selective review of unresolved issues. *Biomark Res*. 9. https://doi.org/10.1186/s40364-021-00325-5.

Howe EI et al. 2022. Cost-effectiveness analysis of combined cognitive and vocational rehabilitation in patients with mild-to-moderate TBI: results from a randomized controlled trial. *BMC Health Serv Res*. 22:185. https://doi.org/10.1186/s12913-022-07585-3.

Huang S, Li S, Feng H, Chen Y. 2021. Iron metabolism disorders for cognitive dysfunction after mild traumatic brain injury. *Front Neurosci*. 15:587197. https://doi.org/10.3389/fnins.2021.587197.

Jang J et al. 2021. Paradoxical paramagnetic calcifications in the globus pallidus: an ex vivo MR investigation and histological validation study. *NMR Biomed*. 34:e4571. https://doi.org/10.1002/nbm.4571.

Jenkinson M, Smith S. 2001. A global optimisation method for robust affine registration of brain images. *Med Image Anal*. 5:143–156. https://doi.org/10.1016/S1361-8415(01)00036-6.

Jenkinson M, Bannister P, Brady M, Smith S. 2002. Improved optimization for the robust and accurate linear registration and motion correction of brain images. *NeuroImage*. 17:825–841. https://doi.org/10.1006/nimg.2002.1132.

Jenkinson M, Beckmann CF, Behrens TE, Woolrich MW, Smith SM. 2012. *FSL NeuroImage*. 62:782–790. https://doi.org/10.1016/j.neuroimage.2011.09.015.

Jia H et al. 2023. Deferoxamine ameliorates neurological dysfunction by inhibiting ferroptosis and neuroinflammation after traumatic brain injury. *Brain Res*. 1812:148383. https://doi.org/10.1016/j.brainres.2023.148383.

Kames C, Wiggermann V, Rauscher A. 2018. Rapid two-step dipole inversion for susceptibility mapping with sparsity priors. *NeuroImage*. 167:276–283. https://doi.org/10.1016/j.neuroimage.2017.11.018.

Khalaf S, Ahmad AS, Chamara KV, Doré S. 2019. Unique properties associated with the brain penetrant iron chelator HBED reveal remarkable beneficial effects after brain trauma. *J Neurotrauma*. 36:43–53. https://doi.org/10.1089/neu.2017.5617.

Kim S et al. 2020. Quantitative magnetic susceptibility assessed by 7T magnetic resonance imaging in Alzheimer's disease caused by streptozotocin administration. *Quant Imaging Med Surg*. 10:789–797. https://doi.org/10.21037/qims.2020.02.08.

King JB, Lopez-Larson MP, Yurgelun-Todd DA. 2016. Mean cortical curvature reflects cytoarchitecture restructuring in mild traumatic brain injury. *Neuroimage Clin*. 11:81–89. https://doi.org/10.1016/j.nicl.2016.01.003.

Koch KM et al. 2018. Quantitative susceptibility mapping after sports-related concussion. *Am J Neuroradiol*. 39:1215–1221. https://doi.org/10.3174/ajnr.A5692.

Koch KM et al. 2021. Acute post-concussive assessments of brain tissue magnetism using magnetic resonance imaging. *J Neurotrauma*. 38:848–857. https://doi.org/10.1089/neu.2020.7322.

Kornguth S, Rutledge N, Perlaza G, Bray J, Hardin A. 2017. A proposed mechanism for development of CTE following concussive events: head impact, water hammer injury, neurofilament release, and autoimmune processes. *Brain Sci*. 7:164. https://doi.org/10.3390/brainsci7120164.

Kruszewski M. 2003. Labile iron pool: the main determinant of cellular response to oxidative stress. *Mutat Res*. 531:81–92. https://doi.org/10.1016/j.mrfmmm.2003.08.004.

Langkammer C et al. 2012. Quantitative susceptibility mapping (QSM) as a means to measure brain iron? A post mortem validation study. *Neuroimage*. 62:1593–1599. https://doi.org/10.1016/j.neuroimage.2012.05.049.

Langkammer C et al. 2015. Fast quantitative susceptibility mapping using 3D EPI and total generalized variation. *NeuroImage*. 111:622–630. https://doi.org/10.1016/j.neuroimage.2015.02.041.

Lassmann H, Van Horssen J, Mahad D. 2012. Progressive multiple sclerosis: pathology and pathogenesis. *Nat Rev Neurol*. 8:647–656. https://doi.org/10.1038/nrneurol.2012.168.

Lee J, Ji S, Oh SH. 2024. So you want to image myelin using MRI: magnetic susceptibility source separation for myelin imaging. *Magn Reson Med Sci*. 23:291–306. https://doi.org/10.2463/mrms.rev.2024-0001.

Levi S, Ripamonti M, Moro AS, Cozzi A. 2024. Iron imbalance in neurodegeneration. *Mol Psychiatry*. 29:1139–1152. https://doi.org/10.1038/s41380-023-02399-z.

Li X, Morgan PS, Ashburner J, Smith J, Rorden C. 2016. The first step for neuroimaging data analysis: DICOM to NIfTI conversion. *J Neurosci Methods*. 264:47–56. https://doi.org/10.1016/j.jneumeth.2016.03.001.

Li Z et al. 2023. APART-QSM: an improved sub-voxel quantitative susceptibility mapping for susceptibility source separation using an iterative data fitting method. *NeuroImage*. 274:120148. https://doi.org/10.1016/j.neuroimage.2023.120148.

Ling H et al. 2017. Mixed pathologies including chronic traumatic encephalopathy account for dementia in retired association football (soccer) players. *Acta Neuropathol*. 133:337–352. https://doi.org/10.1007/s00401-017-1680-3.

Liu T et al. 2011. A novel background field removal method for MRI using projection onto dipole fields (PDF). *NMR Biomed*. 24:1129–1136. https://doi.org/10.1002/nbm.1670.

Liu C, Li W, Tong KA, Yeom KW, Kuzminski S. 2015a. Susceptibility-weighted imaging and quantitative susceptibility mapping in the brain. *J Magn Reson Imaging*. 42:23–41. https://doi.org/10.1002/jmri.24768.

Liu C et al. 2015b. Quantitative susceptibility mapping: contrast mechanisms and clinical applications. *Tomography*. 1:3–17. https://doi.org/10.18383/j.tom.2015.00136.

Long DA, Ghosh K, Moore AN, Dixon CE, Dash PK. 1996. Deferoxamine improves spatial memory performance following experimental brain injury in rats. *Brain Res*. 717:109–117. https://doi.org/10.1016/0006-8993(95)01500-0.

Lu L, Cao H, Wei X, Li Y, Li W. 2015. Iron deposition is positively related to cognitive impairment in patients with chronic mild traumatic brain injury: assessment with susceptibility weighted imaging. *Biomed Res Int*. 2015:470676. https://doi.org/10.1155/2015/470676.

Lunkova E, Guberman GI, Ptito A, Saluja RS. 2021. Noninvasive magnetic resonance imaging techniques in mild traumatic brain injury research and diagnosis. *Hum Brain Mapp*. 42:5477–5494. https://doi.org/10.1002/hbm.25630.

Ma H, Dong Y, Chu Y, Guo Y, Li L. 2022. The mechanisms of ferroptosis and its role in alzheimer's disease. *Front Mol Biosci*. 9:965064. https://doi.org/10.3389/fmolb.2022.965064.

Ma Y et al. 2023. Column-based cortical depth analysis of the diffusion anisotropy and radiality in submillimeter whole-brain diffusion tensor imaging of the human cortical gray matter in vivo. *NeuroImage*. 270:119993. https://doi.org/10.1016/j.neuroimage.2023.119993.

Maas AI et al. 2022. Traumatic brain injury: progress and challenges in prevention, clinical care, and research. *Lancet Neurol*. 21:1004–1060. https://doi.org/10.1016/S1474-4422(22)00309-X.

Mackay DF et al. 2019. Neurodegenerative disease mortality among former professional soccer players. *N Engl J Med*. 381:1801–1808. https://doi.org/10.1056/NEJMoa1908483.

Mackenzie EL, Iwasaki K, Tsuji Y. 2008. Intracellular iron transport and storage: from molecular mechanisms to health implications. *Antioxid Redox Signal*. 10:997–1030. https://doi.org/10.1089/ars.2007.1893.

Madden DJ, Merenstein JL. 2023. Quantitative susceptibility mapping of brain iron in healthy aging and cognition. *NeuroImage*. 282:120401. https://doi.org/10.1016/j.neuroimage.2023.120401.

Madden DJ et al. 2020. Response-level processing during visual feature search: effects of frontoparietal activation and adult age. *Atten Percept Psychophys*. 82:330–349. https://doi.org/10.3758/s13414-019-01823-3.

Marques JP, Bowtell R. 2005. Application of a fourier-based method for rapid calculation of field inhomogeneity due to spatial variation of magnetic susceptibility. *Concept Magn Reson B*. 25:65–78. https://doi.org/10.1002/cmr.b.20034.

MATLAB [Computer software]. *Natick*, Massachusetts: The MathWorks Inc.; 2024a.

Mazur T, Malik M, Bieńko DC. 2024. The impact of chelating compounds on Cu2+, Fe2+/3+, and Zn2+ ions in Alzheimer's disease treatment. *J Inorg Biochem*. 257:112601. https://doi.org/10.1016/j.jinorgbio.2024.112601.

McCrea M et al. 2017. Role of advanced neuroimaging, fluid biomarkers and genetic testing in the assessment of sport-related concussion: a systematic review. *Br J Sports Med*. 51:919–929. https://doi.org/10.1136/bjsports-2016-097447.

McInnes K, Friesen CL, MacKenzie DE, Westwood DA, Boe SG. 2017. Mild traumatic brain injury (mTBI) and chronic cognitive impairment: a scoping review. *PLoS One*. 14:e021842. https://doi.org/10.1371/journal.pone.0218423.

Mckee AC, Daneshvar DH. 2015. The neuropathology of traumatic brain injury. *Handb Clin Neurol*. 127:45–66. https://doi.org/10.1016/B978-0-444-52892-6.00004-0.

McKee AC et al. 2013. The spectrum of disease in chronic traumatic encephalopathy. *Brain*. 136:43–64. https://doi.org/10.1093/brain/aws307.

McKee AC et al. 2023. Chronic traumatic encephalopathy (CTE): criteria for neuropathological diagnosis and relationship to repetitive head impacts. *Acta Neuropathol*. 145:371–394. https://doi.org/10.1007/s00401-023-02540-w.

Meier TB et al. 2015. The underreporting of self-reported symptoms following sports-related concussion. *J Sci Med Sport*. 18:507–511. https://doi.org/10.1016/j.jsams.2014.07.008.

Merenstein JL, Mullin HA, Madden DJ. 2023. Age-related differences in frontoparietal activation for target and distractor singletons during visual search. *Atten Percept Psychophys*. 85:749–768. https://doi.org/10.3758/s13414-022-02640-x.

Merenstein JL et al. 2024. Depth- and curvature-based quantitative susceptibility mapping analyses of cortical iron in Alzheimer's disease. *Cereb Cortex*. 34. https://doi.org/10.1093/cercor/bhad525.

Mez J et al. 2017. Clinicopathological evaluation of chronic traumatic encephalopathy in players of American football. *JAMA*. 318:360–370. https://doi.org/10.1001/jama.2017.8334.

Mez J et al. 2020. Duration of American football play and chronic traumatic encephalopathy. *Ann Neurol*. 87:116–131. https://doi.org/10.1002/ana.25611.

Miyashita Y. 2022. Operating principles of the cerebral cortex as a six-layered network in primates: beyond the classic canonical circuit model. *Proc Japan Acad Ser B Phys Biol Sci*. 98:93–111. https://doi.org/10.2183/pjab.98.007.

Mohammadi S, Ghaderi S, Fatehi F. 2024. Putamen iron quantification in diseases with neurodegeneration: a meta-analysis of the quantitative susceptibility mapping technique. *Brain Imaging Behav*. 18:1239–1255. https://doi.org/10.1007/s11682-024-00895-6.

Murray HC, Osterman C, Bell P, Vinnell L, Curtis MA. 2022. Neuropathology in chronic traumatic encephalopathy: a systematic review of comparative post-mortem histology literature. *Acta Neuropathol Commun*. 10:108. https://doi.org/10.1186/s40478-022-01413-9.

Nikparast F, Ganji Z, Danesh Doust M, Faraji R, Zare H. 2022. Brain pathological changes during neurodegenerative diseases and their identification methods: how does QSM perform in detecting this process? *Insights Imaging*. 13:74. https://doi.org/10.1186/s13244-022-01207-6.

Nisenbaum EJ, Novikov DS, Lui YW. 2014. The presence and role of iron in mild traumatic brain injury: an imaging perspective. *J Neurotrauma*. 31:301–307. https://doi.org/10.1089/neu.2013.3102.

Northall A et al. 2023. Layer-specific vulnerability is a mechanism of topographic map aging. *Neurobiol Aging*. 128:17–32. https://doi.org/10.1016/j.neurobiolaging.2023.04.002.

O'Callaghan J et al. 2017. Tissue magnetic susceptibility mapping as a marker of tau pathology in Alzheimer's disease. *NeuroImage*. 159:334–345. https://doi.org//10.1016/j.neuroimage.2017.08.003.

Otsu N. 1979. A threshold selection method from gray-level histograms. *IEEE Trans Syst Man Cybern*. 9:62–66. https://doi.org/10.1109/TSMC.1979.4310076.

Panter SS, Braughler JM, Hall ED. 1992. Dextran-coupled deferoxamine improves outcome in a murine model of head injury. *J Neurotrauma*. 9:47–53. https://doi.org/10.1089/neu.1992.9.47.

Paul J, Raj A, Raghavan S, Kesavadas C. 2024. Comparative analysis of quantitative susceptibility mapping in preclinical dementia detection. *Eur J Radiol*. 178:111598. https://doi.org/10.1016/j.ejrad.2024.111598.

Pearson RCA, Esirit MM, Hiornst RW, Wilcock GK, Powell TPS. 1985. Anatomical correlates of the distribution of the pathological changes in the neocortex in Alzheimer disease (neurofibrillary tangles/lamination/clustering). *Proc Natl Acad Sci USA*. 82:4531–4534. https://doi.org/10.1073/pnas.82.13.453.

Pienaar R, Fischl B, Caviness V, Makris N, Grant PE. 2008. A methodology for analyzing curvature in the developing brain from preterm to adult. *Int J Imaging Syst Technol*. 18:42–68. https://doi.org/10.1002/ima.v18:1.

Pinky NN et al. 2022. Multimodal magnetic resonance imaging of youth sport-related concussion reveals acute changes in the cerebellum, basal ganglia, and corpus callosum that resolve with recovery. *Front Hum Neurosci*. 16:976013. https://doi.org/10.3389/fnhum.2022.976013.

Ranson SW, Clark SL. *Anatomy of the Nervous System*. 10th ed. Philadelphia: W. B. Saunders Co.; 1959.

Raslau FD et al. 2015. Memory part 2: the role of the medial temporal lobe. *Am J Neuroradiol*. 36:846–849. https://doi.org/10.3174/ajnr.A4169.

Ratcliff R. 2008. Modeling aging effects on two-choice tasks: response signal and response time data. *Psychol Aging*. 23:900–916. https://doi.org/10.1037/a0013930.

Ravanfar P et al. 2021. Systematic review: quantitative susceptibility mapping (QSM) of brain iron profile in neurodegenerative diseases. *Front Neurosci*. 15. https://doi.org/10.3389/fnins.2021.618435.

Raz E et al. 2011. Brain iron quantification in mild traumatic brain injury: a magnetic field correlation study. *Am J Neuroradiol*. 32:1851–1856. https://doi.org/10.3174/ajnr.A2637.

Reichenbach JR. 2012. The future of susceptibility contrast for assessment of anatomy and function. *NeuroImage*. 62:1311–1315. https://doi.org/10.1016/j.neuroimage.2012.01.004.

Renton AI et al. 2024. Neurodesk: an accessible, flexible and portable data analysis environment for reproducible neuroimaging. *Nat Methods*. 21:804–808. https://doi.org/10.1038/s41592-023-02145-x.

Rodrigue KM, Haacke EM, Raz N. 2011. Differential effects of age and history of hypertension on regional brain volumes and iron. *NeuroImage*. 54:750–759. https://doi.org/10.1016/j.neuroimage.2010.09.068.

Rolls ET, Mills WPC. 2017. Computations in the deep vs superficial layers of the cerebral cortex. *Neurobiol Learn Mem*. 145:205–221. https://doi.org/10.1016/j.nlm.2017.10.011.

Rosenbaum SB, Lipton ML. 2012. Embracing chaos: the scope and importance of clinical and pathological heterogeneity in mTBI. *Brain Imaging Behav*. 6:255–282. https://doi.org/10.1007/s11682-012-9162-7.

Sandsmark DK, Bashir A, Wellington CL, Diaz-Arrastia R. 2019. Cerebral microvascular injury: a potentially treatable endophenotype of traumatic brain injury-induced neurodegeneration. *Neuron*. 103:367–379. https://doi.org/10.1016/j.neuron.2019.06.002.

Schenck JF, Zimmerman EA. 2004. High-field magnetic resonance imaging of brain iron: birth of a biomarker? *NMR Biomed*. 17: 433–445. https://doi.org/10.1002/nbm.922.

Schweser F, Deistung A, Reichenbach JR. 2016. Foundations of MRI phase imaging and processing for quantitative susceptibility mapping (QSM). *Z Med Phys*. 26:6–34. https://doi.org/10.1016/j.zemedi.2015.10.002.

Shenton ME et al. 2012. A review of magnetic resonance imaging and diffusion tensor imaging findings in mild traumatic brain injury. *Brain Imaging Behav*. 6:137–192. https://doi.org/10.1007/s11682-012-9156-5.

Shin HG et al. 2021. χ-Separation: magnetic susceptibility source separation toward iron and myelin mapping in the brain. *NeuroImage*. 240:118371. https://doi.org/10.1016/j.neuroimage.2021.118371.

Smith SM. 2002. Fast robust automated brain extraction. *Hum Brain Mapp*. 17:143–155. https://doi.org/10.1002/hbm.10062.

Smith SM et al. 2004. Advances in functional and structural MR image analysis and implementation as FSL. *NeuroImage*. 23: S208–S219. https://doi.org/10.1016/j.neuroimage.2004.07.051.

Smith DH, Johnson VE, Stewart W. 2013. Chronic neuropathologies of single and repetitive TBI: substrates of dementia? *Nat Rev Neurol*. 9:211–221. https://doi.org/10.1038/nrneurol.2013.29.

Stankiewicz J et al. 2007. Iron in chronic brain disorders: imaging and neurotherapeutic implications. *Neurotherapeutics*. 4:371–386. https://doi.org/10.1016/j.nurt.2007.05.006.

Stewart AW et al. 2022. QSMxT: robust masking and artifact reduction for quantitative susceptibility mapping. *Magn Reson Med*. 87:1289–1300. https://doi.org/10.1002/mrm.29048.

Straub S et al. 2017. Suitable reference tissues for quantitative susceptibility mapping of the brain. *Magn Reson Med*. 78:204–214. https://doi.org/10.1002/mrm.26369.

Straub S et al. 2019. Mapping the human brainstem: brain nuclei and fiber tracts at 3 T and 7 T. *NMR Biomed*. 32:e4118. https://doi.org/10.1002/nbm.4118.

Straub S et al. 2023. Quantitative magnetic resonance imaging biomarkers for cortical pathology in multiple sclerosis at 7 T. *NMR Biomed*. 36:e4847. https://doi.org/10.1002/nbm.4847.

Theadom A et al. 2021. The brain injury screening tool (BIST): tool development, factor structure and validity. *PLoS One*. 16:e0246512. https://doi.org/10.1371/journal.pone.0246512.

Thibault O, Gant JC, Landfield PW. 2007. Expansion of the calcium hypothesis of brain aging and Alzheimer's disease: minding the store. *Aging Cell*. 6:307–317. https://doi.org/10.1111/j.1474-9726.2007.00295.x.

Tierney RT et al. 2005. Gender differences in head-neck segment dynamic stabilization during head acceleration. *Med Sci Sports Exerc*. 37:272–279. https://doi.org/10.1249/01.mss.0000152734.47516.aa.

To XV, Cumming P, Nasrallah F. 2024. From impact to recovery: tracking mild traumatic brain injury with MRI—a pilot study and case series. *BMJ Open Sport Exerc Med*. 10:e002010. https://doi.org/10.1136/bmjsem-2024-002010.

Tournier DJ et al. 2019. MRtrix3: a fast, flexible and open software framework for medical image processing and visualisation. *NeuroImage*. 202:116137. https://doi.org/10.1016/j.neuroimage.2019.116137.

Tustison NJ et al. 2010. N4ITK: improved N3 bias correction. *IEEE Trans Med Imaging*. 29:1310–1320. https://doi.org/10.1109/TMI.2010.2046908.

Uchida Y, Kan H, Sakurai K, Oishi K, Matsukawa N. 2022. Quantitative susceptibility mapping as an imaging biomarker for Alzheimer's disease: the expectations and limitations. *Front Neurosci*. 16:938092. https://doi.org/10.3389/fnins.2022.938092.

Waehnert MD et al. 2014. Anatomically motivated modeling of cortical laminae. *NeuroImage*. 93:210–220. https://doi.org/10.1016/j.neuroimage.2013.03.078.

Waehnert MD et al. 2016. A subject-specific framework for in vivo myeloarchitectonic analysis using high resolution quantitative MRI. *NeuroImage*. 125:94–107. https://doi.org/10.1016/j.neuroimage.2015.10.001.

Wang Y et al. 2017. Clinical quantitative susceptibility mapping (QSM): biometal imaging and its emerging roles in patient care. *J Magn Reson Imaging*. 46:951–971. https://doi.org/10.1002/jmri.25693.

Ward RJ, Zucca FA, Duyn JH, Crichton RR, Zecca L. 2014a. The role of iron in brain ageing and neurodegenerative disorders. *Lancet Neurol*. 13:1045–1060. https://doi.org/10.1016/S1474-4422(14)70117-6.

Ward AM et al. 2014b. The parahippocampal gyrus links the default-mode cortical network with the medial temporal lobe memory system. *Hum Brain Mapp*. 35:1061–1073. https://doi.org/10.1002/hbm.22234.

Weber AM et al. 2018. Pathological insights from quantitative susceptibility mapping and diffusion tensor imaging in ice hockey players pre and post-concussion. *Front Neurol*. 9:575. https://doi.org/10.3389/fneur.2018.00575.

Wintermark M, Sanelli PC, Anzai Y, Tsiouris AJ, Whitlow CT. 2015. Imaging evidence and recommendations for traumatic brain injury: advanced neuro- and neurovascular imaging techniques. *Am J Neuroradiol*. 36:E1–E11. https://doi.org/10.3174/ajnr.A4181.

Woolrich MW et al. 2009. Bayesian analysis of neuroimaging data in FSL. *NeuroImage*. 45:S173–S186. https://doi.org/10.1016/j.neuroimage.2008.10.055.

Wright DK, O'Brien TJ, Shultz SR. 2022. Sub-acute changes on MRI measures of cerebral blood flow and venous oxygen saturation in concussed Australian rules footballers. *Sports Med Open*. 8. https://doi.org/10.1186/s40798-022-00435-w.

Wu Y, Wu H, Guo X, Pluimer B, Zhao Z. 2020. Blood–brain barrier dysfunction in mild traumatic brain injury: evidence from preclinical murine models. *Front Physiol*. 11. https://doi.org/10.3389/fphys.2020.01030.

Wunderle K, Hoeger KM, Wasserman E, Bazarian JJ. 2014. Menstrual phase as predictor of outcome after mild traumatic brain injury in women. *J Head Trauma Rehabil*. 29:E1–E8. https://doi.org/10.1097/HTR.0000000000000006.

Yamamoto A et al. 2002. Iron (III) induces aggregation of hyperphosphorylated tau and its reduction to iron (II) reverses the aggregation: implications in the formation of neurofibrillary tangles of Alzheimer's disease. *J Neurochem*. 82:1137–1147. https://doi.org/10.1046/j.1471-4159.2002.t01-1-01061.x.

Zecca L, Youdim MBH, Riederer P, Connor JR, Crichton RR. 2004. Iron, brain ageing and neurodegenerative disorders. *Nat Rev Neurosci*. 5:863–873. https://doi.org/10.1038/nrn1537.

Zhao J et al. 2014. Deferoxamine attenuates acute hydrocephalus after traumatic brain injury in rats. *Transl Stroke Res*. 5:586–594. https://doi.org/10.1007/s12975-014-0353-y.

Zhao Z et al. 2021. The effect of beta-amyloid and tau protein aggregations on magnetic susceptibility of anterior hippocampal laminae in Alzheimer's diseases. *NeuroImage*. 244:118584. https://doi.org/10.1016/j.neuroimage.2021.118584.

Zivadinov R et al. 2018. Multimodal imaging of retired professional contact sport athletes does not provide evidence of structural and functional brain damage. *J Head Trauma Rehabil*. 33:E24–E32. https://doi.org/10.1097/HTR.0000000000000422.

Cerebral Cortex, 2025, **35**, bhaf059
https://doi.org/10.1093/cercor/bhaf059
Original Article

BRAIN COMMUNICATIONS

Mild traumatic brain injury increases cortical iron: evidence from individual susceptibility mapping

Christi A. Essex,[1] Devon K. Overson,[2] Jenna L. Merenstein,[2] Trong-Kha Truong,[2] David J. Madden,[2] Mayan J. Bedggood,[1] Catherine Morgan,[3,4,5] Helen C. Murray,[5] Samantha J. Holdsworth,[5,6,7] Ashley W. Stewart,[8] Richard L. M. Faull,[5] Patria Hume,[9] Alice Theadom[1] and Mangor Pedersen[1]

Quantitative susceptibility mapping has been applied to map brain iron distribution after mild traumatic brain injury to understand properties of neural tissue which may be related to cellular dyshomeostasis. However, this is a heterogeneous injury associated with microstructural brain changes, and 'traditional' group-wise statistical approaches may lead to a loss of clinically relevant information, as subtle alterations at the individual level can be obscured by averages and confounded by within-group variability. More precise and individualized approaches are needed to characterize mild traumatic brain injury better and elucidate potential cellular mechanisms to improve intervention and rehabilitation. To address this issue, we use quantitative MRI to build individualized profiles of regional positive (iron-related) magnetic susceptibility across 34 bilateral cortical ROIs following mild traumatic brain injury. Healthy population templates were constructed for each cortical area using standardized *Z*-scores derived from 25 age-matched male controls aged between 16 and 32 years ($M = 21.10$, SD = 4.35), serving as a reference against which *Z*-scores of 35 males with acute (<14 days) sports-related mild traumatic brain injury were compared [$M = 21.60$ years (range: 16–33), SD = 4.98]. Secondary analyses sensitive to cortical depth and curvature were also generated to approximate the location of iron accumulation in the cortical laminae and the effect of gyrification. Primary analyses indicated that approximately one-third (11/35; 31%) of injured participants exhibited elevated positive susceptibility indicative of abnormal iron profiles relative to the healthy population, a finding that was mainly concentrated in regions within the temporal lobe. Injury severity was significantly higher ($P = 0.02$) for these participants than their iron-normal counterparts, suggesting a link between injury severity, symptom burden, and elevated cortical iron. Secondary exploratory analyses of cortical depth and curvature profiles revealed abnormal iron accumulation in 83% (29/35) of mild traumatic brain injury participants, enabling better localization of injury-related changes in iron content to specific loci within each region and identifying effects that may be more subtle and lost in region-wise averaging. Our findings suggest that individualized approaches can further elucidate the clinical relevance of iron in mild head injury. Differences in injury severity between iron-normal and iron-abnormal mild traumatic brain injury participants identified in our primary analysis highlight not only why precise investigation is required to understand the link between objective changes in the brain and subjective symptomatology, but also identify iron as a candidate biomarker for tissue pathology after mild traumatic brain injury.

1 Department of Psychology and Neuroscience, Auckland University of Technology, Auckland 0627, New Zealand
2 Brain Imaging and Analysis Center, Duke University Medical Center, Durham, NC 27710, USA
3 Center for Advanced MRI, The University of Auckland, Auckland 1023, New Zealand
4 School of Psychology, The University of Auckland, Auckland 1142, New Zealand
5 Center for Brain Research, The University of Auckland, Auckland 1023, New Zealand
6 Mātai Medical Research Institute, Gisborne 4010, New Zealand
7 Faculty of Medical and Health Sciences, The University of Auckland, Auckland 1023, New Zealand
8 Center for Advanced Imaging, The University of Queensland, Queensland 4067, Australia

Received November 24, 2024. Revised February 18, 2025. Accepted March 10, 2025. Advance access publication March 12, 2025

9 School of Sport and Recreation, Faculty of Health and Environmental Science, Sports Performance Research Institute New Zealand, Auckland University of Technology, Auckland 0627, New Zealand

Correspondence to: Christi A. Essex
Department of Psychology and Neuroscience, Auckland University of Technology
Auckland 0627, New Zealand
E-mail: christi.essex@aut.ac.nz

Keywords: brain iron; cerebral cortex; individualized profiles; mild traumatic brain injury; quantitative susceptibility mapping

Graphical Abstract

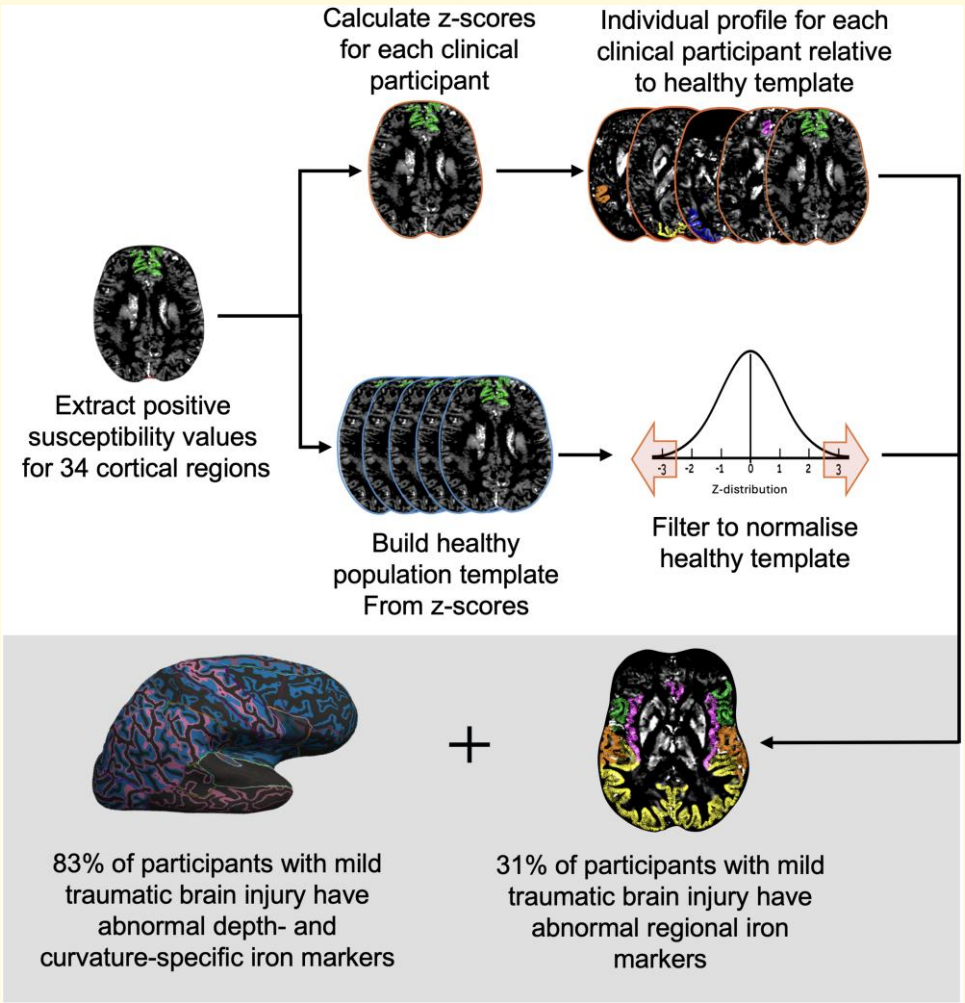

Introduction

Exposure to mild traumatic brain injury (mTBI) is a significant public and personal health concern, accounting for ~90% of the 50–60 million annual cases of traumatic brain injury (TBI) worldwide.[1] Global financial losses related to TBI are estimated at ~USD $400 billion per year,[1,2] however, beyond the economic impacts mTBI can increase the risk of neurodegeneration, dementia[3,4] and premature death.[5] In the short term, mTBI can result in a range of symptoms with significant inter-individual variability, including cognitive, emotional and physiological disturbances such as sleep disruption, light sensitivity, fatigue, headaches, vertigo, vestibular problems, depression and anxiety, which significantly impact quality of life and participation in day-to-day activities for many.[4] In some cases, these symptoms can persist up to three decades post-injury.[6,7] Numerous factors contribute to differences in injury severity,

symptom burden, *in vivo* brain tissue pathology and even autopsy findings. These include individual differences prior to injury such as genetic predispositions, age, gender, IQ, psychiatric history, prior mTBI exposure and substance use history, as well as differences in the mechanisms and loci of injury.[8] In sports-related mTBI (sr-mTBI), for example, variability in the sport and even player position can affect injury severity, lead to diverse effects on brain structure and function, and divergence in symptom burden and cluster.[8]

The heterogeneity of mTBI is apparent at even the cellular level. The rapid changes in inertia (acceleration/deceleration/rotation) or exogenous skull impact associated with mTBI cause the transmission of mechanical forces to the brain, resulting in a mechanistically specific primary insult and microstructural tissue damage.[8,9] This initiates a variable cascade of secondary cellular processes, including disruption of the blood–brain barrier (BBB), cerebrovascular dysfunction, oxidative stress, axonal degeneration and neuroinflammation[9,10] which can propagate for months after the initial impact.[11] However, the pathophysiology of mTBI remains poorly understood, and specific biomarkers indicative of mTBI remain, to date, elusive. Unlike moderate-to-severe TBI (ms-TBI), where lesions, haemorrhages or macroscopic morphological abnormalities can be detected, routine MRI methods are often insensitive to mTBI-related neuropathology.[12,13] This limitation necessitates the use of advanced MRI techniques not typically employed in conventional medical settings to identify the subtle changes in brain structure characteristic of this 'mild' injury.[14,15] Integrating these advanced imaging modalities into routine patient care requires further validation and the establishment of clinically and individually relevant biomarkers for mTBI diagnosis and treatment.

Iron accumulation is increasingly recognized as a component of neuropathology following mTBI, contributing not only to acute-phase secondary injury and later cell death,[9] but also cognitive dysfunction after mTBI.[16,17] Quantitative susceptibility mapping (QSM) is an advanced MRI technique that can be used to estimate the magnetic susceptibility of tissue, such as paramagnetism exhibited by iron in response to an applied magnetic field.[18-23] Non-heme iron (particularly ferritin-bound iron), is the main source of paramagnetism on QSM[18,24-26] and widely recognized as the form of iron most involved in secondary injury after mTBI.[9,27,28] Iron dyshomeostasis can trigger auto-toxic circuits that drive neurodegenerative processes,[29] including the generation of reactive oxygen species, which at high levels can lead to cytotoxic oxidative stress,[30] lipid damage and increased permeability of the cell membrane,[9] as well as iron-regulated cell death (ferroptosis).[31] As such, elevated levels of iron in cortical regions would suggest localization of injury-related pathological processes and changes in brain structure. These changes may be related, but not limited to, mTBI-induced permeability of the BBB[32] and neuroinflammation,[33] both of which are known to be involved in iron accumulation.[9,30] Iron has also been implicated in the hyperphosphorylation of tau proteins (p-tau)[28] observed in mTBI-related tauopathies; its co-localization with p-tau thus identifies it as a promising early indicator of neurodegeneration.[34,35]

A limited number of studies have employed QSM to investigate the role of brain iron in microstructural tissue damage following mTBI, focusing mainly on subcortical nuclei or global grey and/or white matter (WM),[36-44] with only a few studies including cortical regions of interest (ROIs)[38,41] or investigating the relevance of cortical morphology.[45] However, the diversity of mTBI effects may not be discernible at the group level, which currently constitutes the standard statistical approach. Individual-level investigations of injury-specific effects may better characterize mTBI-related neuropathology, and are increasingly recognized as providing more biologically informative data than group-level studies, especially in clinical populations where targeted interventions are both useful and necessary,[46] such as mTBI. Personalized profiles can be generated by leveraging *Z*-scores to compare the results of individual quantitative measures to the distribution of a healthy normative population. This approach allows for a clearer understanding of where the individual falls relative to normal ranges for selected metrics.[47] Individual analytic approaches have been successfully applied in the context of mTBI using T2 relaxometry as a marker of neuroinflammation,[48] and diffusion-weighted imaging (DWI) to investigate WM fibre tracts.[49] Under the TBI umbrella more broadly, individual analyses have been applied to fixel-based analysis of diffusion MRI[50] and diffusion tensor imaging (DTI)[51] to investigate WM integrity, as well as structural connectomics,[52] in ms-TBI. One study has used QSM to generate individualized profiles of iron deposition in ms-TBI,[47] however, dedicated personalized investigations of iron deposition at the individual level following *mild* TBI are, to the authors knowledge, lacking.

To address these research gaps, we conducted the first dedicated individual-level investigation of iron-related mTBI effects. This study aimed to: (i) generate individual profiles of cortical iron deposition following sr-mTBI, and; (ii) extend these findings by deriving profiles sensitive to cortical architectonics (depth and curvature) as a supplemental, secondary approach. Our prior research suggests that elevated magnetic susceptibility should be most evident in ROIs in the temporal lobe.[45] However, given the preliminary and exploratory nature of this study, we did not have specific *a priori* hypotheses about the direction of effects in all cortical regions.

Materials and methods

Ethical approval for this research was obtained from the Health and Disabilities Ethics Committee (HDEC) (Date: 18/02/2022, Reference: 2022 EXP 11078) and institutional approval was also obtained from the Auckland University of Technology Ethics Committee (AUTEC) (Date: 18/02/2022, Reference: 22/12). In accordance with the Declaration of Helsinki, all participants provided written informed consent prior to data collection.

Participants

Thirty-five male contact sports players [$M = 21.60$ years (range: 16–33), SD = 4.98] with acute sr-mTBI [sustained within 14 days of MRI scanning ($M = 10.40$ days, SD = 3.01)] and 25 age-matched male controls [$M = 21.10$ years (range: 16–32), SD = 4.35] were recruited for this observational study (see Table 1). To mitigate potential age-related confounds, we ensured that ages were not significantly different between groups [$t(58) = -0.44$, $P = 0.66$]. Clinical (sr-mTBI) participants were recruited through three Axis Sports Medicine Clinics (Auckland, New Zealand), via print and social media advertisements, word-of-mouth and through community-based referrals from healthcare professionals and sports team management. Each clinical participant was required to have a confirmed sr-mTBI diagnosis by a licensed physician as a prerequisite for study inclusion, and symptom severity was assessed using the Brain Injury Screening Tool (BIST)[53] either upon presentation to Axis Clinics or electronically following recruitment. Healthy controls (HC) were recruited through print and social media advertisements, and word-of-mouth. Exclusion criteria for all the participants included a history of significant medical or neurological conditions unrelated to the study's objectives and contraindications for MRI. Additionally, controls were excluded if they had any recent history of mTBI events (<12 months) or were living with any long-term effects of previous mTBI. All participants completed a brief demographic questionnaire and attended a 1-h MRI scan at The Centre for Advanced MRI (CAMRI), Auckland, New Zealand. All scans were reviewed by a certified neuroradiologist consultant for clinically significant findings. No findings from MRI in either group were considered clinically significant (see Table 1).

Neuroimaging

Details on image acquisition and processing have been previously reported,[45] and are summarized here for brevity.

Acquisition

MRI data were acquired on a 3T Siemens MAGNETOM Vida Fit scanner (Siemens Healthcare, Erlangen, Germany) equipped with a 20-channel head coil. A 3D flow-compensated Gradient Echo sequence was used to obtain magnitude and unfiltered phase images for QSM reconstruction. Data were collected at 1 mm isotropic voxel size with matrix size = 180 × 224 × 160 mm, Repetition Time (TR) = 30 ms; Echo Time (TE) = 20 ms; Flip Angle (FA) = 15°; Field of View (FoV) = 180 mm (Left-Right)×224 mm (Anterior-Posterior), in a total acquisition time of ~3.43 min. For each participant, a high-resolution 3D T1-weighted (T1w) anatomical image volume was acquired for coregistration and parcellation using a Magnetization-Prepared Rapid Acquisition Gradient Echo (MPRAGE) sequence (TR = 1940.0 ms; TE = 2.49 ms, FA = 9°; slice thickness = 0.9 mm; FoV = 230 mm; matrix size = 192 × 512 × 512 mm; GRAPPA = 2; voxel size 0.45 × 0.45 × 0.90 mm) for a total acquisition time of ~4.31 min. Digital Imaging and Communications in Medicine files were converted to Neuroimaging Informatics Technology Initiative (NIfTI) files and transformed to brain imaging data structure[54] for further processing using *Dcm2Bids*[55] version 3.1.1, which is a wrapper for *dcm2niix*[56] (v1.0.20230411).

Image processing

Bias field-corrected[57,58] T1w images were processed in FreeSurfer[59] to: (i) delineate pial and grey matter/WM (GM/WM) boundary meshes and (ii) generate estimates of cortical thickness and curvature for each vertex.[60] QSM images were reconstructed using a rapid open-source minimum spanning tree algorithm (ROMEO),[61] background field removal with projection onto dipole fields[62] and sparsity-based rapid two-step dipole inversion[63]; a pipeline congruent with recent consensus statement recommendations for best-practice QSM reconstruction.[64] Whilst the optimal reference region for susceptibility estimation remains debated,[65] recent consensus guidelines recommend quantifying QSM relative to a specific reference structure.[64] To comply with these guidelines and ensure stability and reproducibility, QSM was referenced to whole-brain susceptibility as smaller regions can be more vulnerable to artefacts, distortions and inhomogeneities, affecting the final brain map.[64] All QSM reconstruction was carried out via QSM×T[66] v6.4.2 (https://qsmxt.github.io/QSMxT/) and used a robust two-pass combination method for artefact reduction.[67]

Subsequent processing was performed using the Functional Neuroimaging Research Group (FMRIB) Software Library.[68-70] For each subject, the raw magnitude image was skull-stripped[71] and binarised. These binary masks were used to erode non-brain signal around the brain perimeter using *fslmaths*. Magnitude images were linearly coregistered to the T1w image using FMRIB's Linear Transformation Tool (*FLIRT*)[72-74] with 12 degrees of freedom (DoF). Due to variability in acquisition type, field-of-view and matrix size between subjects' QSM and T1w images, the 12 DoF linear registrations provided more accurate alignment compared to the six DoF alternative, allowing for better compensation of non-rigid anatomical variations upon visual inspection. The resulting transformation matrix was used for spatial normalization of the QSM images to T1w space. In line with prior research,[60] QSM maps were thresholded into separate inter-voxel sign (positive and negative) maps with *fslmaths*. Traditional QSM maps represent average intra-voxel susceptibility values,[75] which may obscure individual susceptibility sources. Further confounding effects may be introduced via inter-voxel averaging during analysis. This thresholding approach may help address the latter limitation by isolating voxels containing predominantly paramagnetic substrates, such as iron, which could enable more targeted analyses of susceptibility sources. Only positive sign maps were used in analyses to target cortical iron distribution.

Cortical column generation

To generate cortical columns and sample positive susceptibility values, we adapted a pipeline previously applied to DWI[76] and

Table 1 Summary of sr-mTBI participant clinical characteristics

ID	Age	DSI	BIST	MOI	MRI findings
mTBI-01	<20	5	140	Rugby	None
mTBI-02	<20	5	12	Rugby	None
mTBI-03	20s	6	78	Rugby	None
mTBI-04	<20	13	18	Rugby	Small fluid signal spaces in R peritrigonal WM—normal. R caudate cleft along ventricular surface—possibly developmental or from old ischaemic insult
mTBI-05	20s	13	42	Football	None
mTBI-06	20s	13	13	Hockey	Minor artifactual T1 signal in pons
mTBI-07	20s	12	6	Rugby	None
mTBI-08	20s	6	56	Rugby	Minor R orbital fracture (old)
mTBI-09	<20	12	54	Rugby	None
mTBI-10	20s	10	52	Rugby	None
mTBI-11	30s	13	13	Football	None
mTBI-12	<20	5	79	Rugby	None
mTBI-13	20s	13	2	Rugby	Small focus of susceptibility in L superior frontal gyrus possibly vascular or nonspecific haemosiderin
mTBI-14	<20	13	22	Rugby	None
mTBI-15	<20	8	117	Futsal	Tiny cleft of fluid signal in R cingulate gyrus—minor developmental anomaly or mature gliosis
mTBI-16	20s	13	[a]	Rugby	None
mTBI-17	20s	10	34	Gymnastics	None
mTBI-18	20s	13	28	Jiu-jitsu	Some artifactual DWI signal in pons
mTBI-19	20s	11	69	Surfing	Tiny susceptibility site in R temporal lobe—may be vascular
mTBI-20	<20	7	14	Rugby	Minor susceptibility in transverse sulcus in R mid temporal lobe—nonspecific, may be vascular or reflect haemosiderin deposition from prior small volume haemorrhage
mTBI-21	20s	14	47	Rugby	None
mTBI-22	<20	12	28	Football	None
mTBI-23	<20	13	39	Judo	None
mTBI-24	<20	9	34	Rugby	None
mTBI-25	<20	12	68	Rugby	None
mTBI-26	20s	12	17	Rugby	7 mm pineal cyst—normal limits. Some T1 hyperintensity in R cerebellum—artifact compatible
mTBI-27	<20	12	12	Rugby	None
mTBI-28	20s	12	25	Rugby	Mildly prominent cisterna magna
mTBI-29	30s	7	30	Football	A few mildly prominent biparietal and L cerebral peduncle perivascular spaces—normal variant
mTBI-30	30s	12	51	Swimming	None
mTBI-31	20s	5	6	Rugby	None
mTBI-32	<20	12	2	Rugby	Some DWI signal disturbance anterior to pons—likely artifactual
mTBI-33	<20	14	22	Rugby	2–3 tiny foci of susceptibility in R frontal lobe—nonspecific, possible site of prior microhaemorrhage. A punctate focus of T1 hypointensity/T2 hyperintensity superolateral to the frontal horn of R lateral ventricle
mTBI-34	20s	8	58	Football	Bifrontal developmental venous anomaly noted—normal variants
mTBI-35	<20	8	8	Rugby	Minuscule foci of susceptibility in R cerebellar hemisphere/posterior to R aspect of the splenium of CC—non-specific. Minor susceptibility in R sylvian fissure—vascular
Mean mTBI	21.60 (4.98) years of age	10.4 (3.01) DSI	38.1 (32.0)/ 160 BIST		No findings considered clinically relevant
Mean HC	21.10 (4.35) years of age				No findings considered clinically relevant

Diagnostic assessment is limited to the volume T1, SWI and DWI sequences with only limited interpretation of the multi-echo T2 stack. Clinical assessments are relevant to the identification of micro-haemorrhages, areas of siderosis, T1 appearance, gliosis, volume, ventricular volumes and non-neurological findings. The possible range of BIST scores is 0 (min)–160 (max). Clinical group data correspond to the date of MRI only, except for BIST scores acquired >24 h post-injury and prior to MRI (<14 days post). ID, unique identifier; DSI, days since injury; BIST, Brain Injury Screening Tool; MOI, mechanism of injury; WM, white matter; CC, corpus callosum; DWI, diffusion-weighted imaging; L, left; R, right. [a]Missing data (BIST incomplete on the Axis Sport Medicine Clinic patient portal, reason unknown).

QSM[45,60] for depth- and curvature-specific cortical analysis. First, the T1w FreeSurfer[59] recon served as an input into the *easy_lausanne* tool (https://github.com/mattcieslak/easy_lausanne.git), based on the open-source Connectome Mapper,[77] to separate the cortex into 34 ROIs per hemisphere according to the Lausanne multi-scale atlas (equivalent to the Desikan-Killiany atlas[78] native to FreeSurfer).[59]

Depth

Cortical columns were created for each hemisphere in T1w space with *write_mrtrix_tracks*[79] in MATLAB (version R2024a), which was used to connect vertex pairs between pial and GM/WM boundary surface meshes. Each cortical column was segmented into six equidistant depths extending from the pial surface to the GM/WM boundary using

MRtrix3 *tckresample*.[79] This approach differs from previous studies using a 21-depth approach.[45,60,76] Here, we used six depths to decrease the number of depth-wise comparisons, and to better approximate the structure of the intracortical layers.[80,81] It should be noted that these depths represent equidistant segmentations rather than specific cellular laminae (layers I–VI) of the cortex, differing from ultra-high-field investigations of cortical cyto- and myelo-architecture. Results described here are related to cortical *depth*, rather than *layer*.

Curvature

The columns were also categorized based on cortical curvature, derived from FreeSurfer's[59] Gaussian curvature values at each GM/WM boundary vertex[82] and quantified in units of $1/mm^2$. The categories included the gyral crown (curvature values: −0.6 to −0.1), sulcal bank (−0.1 to 0.1), sulcal fundus (0.1–0.6), or whole ROI (−0.6 to 0.6).[60] Positive curvature values indicated sulci, while negative values indicated gyri, with higher values corresponding to deeper curvatures.[60] Only columns ranging from 0.5 to 6 mm in length were included in the analysis to capture plausible cortical morphology.[83] Depth was measured in percentage of cortical thickness rather than absolute metrics (millimetre) to mitigate variability between the participants.

Personalized QSM profiles

We generated individual QSM profiles for each ROI at the bilateral level using MATLAB (2024a) (see Fig. 1 for visualization). Mean positive susceptibility values were extracted across the whole ROI (curvature and depth combined), as well as three curvature bins (gyral crown, sulcal bank and sulcal fundus) and six cortical depths independently for all 34 ROIs. For the whole-ROI profiles, *Z*-scores were calculated for all participants (HC and mTBI), by subtracting the HC group mean from each individual's susceptibility value and dividing by the HC group SD; a method commonly used in prior research.[47,48,51,52] To bring the HC data closer to a normal distribution, outlier scores for the HC group were filtered[47] if they fell outside two times the interquartile range (IQR); a more stringent criterion than methods used to identify mild outliers at 1.5 times the IQR, but less extreme than the more conservative filter of three times the IQR.[84] As a result, data from $N = 1$ HC participants were excluded in three of the 34 ROIs, and data from $N = 2$ HC participants were excluded in one of the 34 ROIs. After filtering, the Shapiro–Wilk normality test yielded an average *W*-value of $M = 0.96$ (SD = 0.02) across *Z*-distributions for all ROIs, indicating that the data distribution within each ROI was close to normal. The final equation for deriving the whole-ROI *Z*-scores for individual mTBI participants was as follows:

$$Z_{\mathrm{mTBI}} = \frac{X_{\mathrm{mTBI}} - \mu_{\mathrm{HCnorm}}}{\sigma \mathrm{HC}_{\mathrm{norm}}},$$

where Z_{mTBI} represents the ROI-wise *Z*-score for each mTBI participant; X_{mTBI} is the ROI-wise mean QSM value for each mTBI participant; μ_{HCnorm} is the mean ROI-wise QSM value of the HC group after outlier filtering, and; σ_{HCnorm} is the ROI-wise SD of the HC group QSM values after filtering. This approach ensures that mTBI participants' susceptibility values are directly comparable to the healthy range reflecting a normalized distribution. The same process was repeated for each depth at each curvature bin, however, the IQR filter was omitted due to the number of comparison points.

Statistical analysis

To assess statistical significance for whole-ROI mTBI *Z*-scores, two-tailed *P*-values were calculated from the *Z*-scores using the cumulative distribution function of the standard normal distribution. A false discovery rate (FDR) correction[85] was applied to the *P*-values for 34 ROI-wise comparisons.

To conduct exploratory statistical tests, we divided the mTBI group into two subgroups: those whose *Z*-scores significantly deviated from HC norms (i.e. iron-abnormal) and those whose scores did not (i.e. iron-normal) as identified via primary and secondary analyses, respectively. Although there was no statistically significant difference in age between mTBI participants and controls, we performed an ANOVA for the new groupings to confirm that age was not driving the results. Additionally, we used nonparametric Mann–Whitney U-tests to assess whether injury severity (BIST[53] scores) differed significantly between iron-abnormal and iron-normal mTBI participants, excluding mTBI-16 for these analyses only due to missing injury severity data.

Results

Regional individualized cortical iron profiles

We calculated personalized profiles of iron-related differences in positive susceptibility across 34 cortical ROIs for each mTBI participant, to understand the effects of mild brain trauma at the individual level. Of the 35 mTBI participants, 11 (31%) exhibited significantly elevated positive susceptibility for at least one ROI relative to the HC population template (see Table 2), likely indicating elevated iron. No clinical participants' *Z*-scores were significantly lower than the HC population.

In these 11 clinical participants, injury-related elevated susceptibility was evident across all cortical lobes, however, these were predominantly localized to either a single lobe (45%) or two lobes (45%). Only one participant (9%) exhibited widespread, multi-focal abnormalities across the cortex (see Table 2 and Fig. 2). Notably, a high density of affected ROIs was observed in the temporal lobe for 82% (9 out of 11) of participants with abnormal iron profiles (see Table 2). In contrast, 45% (5/11) had abnormal iron in occipital ROIs, 27% (3/11) in frontal ROIs, 18% (2/11)

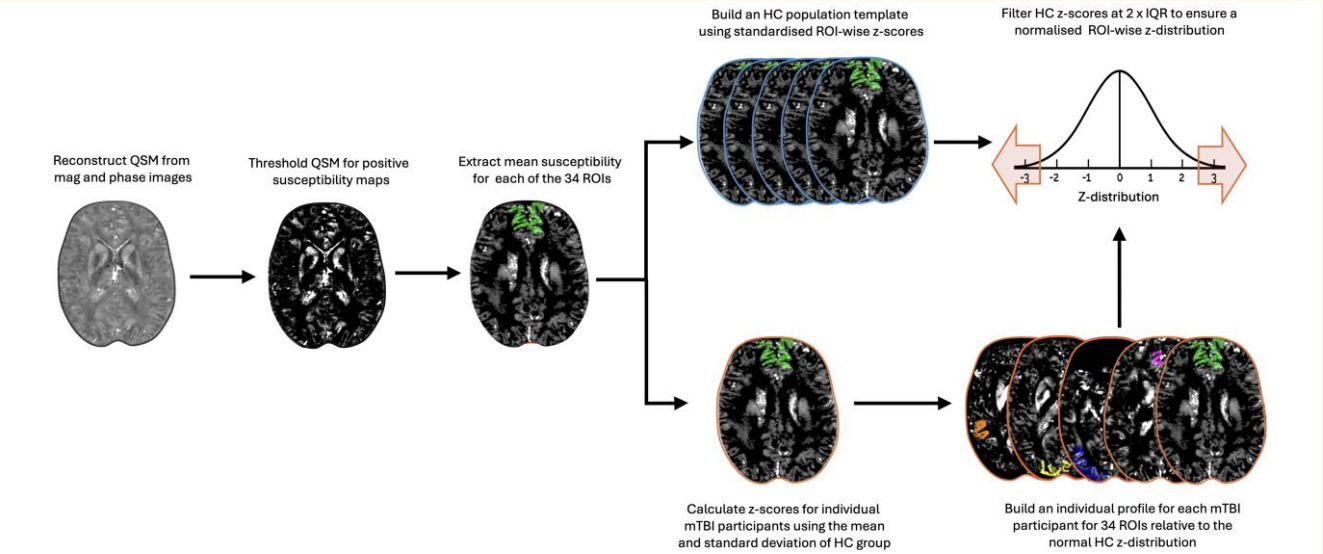

Figure 1 QSM post-processing and generation of individual iron profiles. Steps are performed after QSM image reconstruction using QSM×T. QSM images were thresholded to create a positive sign map, and mean susceptibility values were extracted for each ROI, as well as for each cortical depth (1–6) and curvature (crown, bank, and fundus). Z-scores were calculated using the mean and SD of the HC group, and standardized around a mean of zero. The HC distribution was then filtered to remove outliers exceeding two times IQR, normalizing the distribution. Individual profiles for mTBI participants were constructed by comparing each participant's *Z*-scores to the healthy normal distribution, while controlling for multiple comparisons across the 34 cortical ROIs. Abbreviations are as follows: QSM, quantitative susceptibility mapping; ROI, region of interest; HC, healthy control; IQR, interquartile range.

in the insula or cingulate and only one participant (9%) had an abnormal profile inclusive of parietal ROIs.

After subdividing the mTBI participants into iron-normal (24/35; 69%) and iron-abnormal (11/35; 31%) based on their individual ROI-wise profiles, a one-way ANOVA showed no significant effect of age between these groups and controls, $F(2, 26) = 2.0$, $P = 0.2$. The Mann–Whitney U-test revealed that injury severity (BIST[53]) scores were significantly worse for the iron-abnormal mTBI group ($M = 59.6$, SD = 40.5) than the iron-normal mTBI group ($M = 29.2$, SD = 23.3), $U = 57$, $P = 0.02$ (see Fig. 3).

Symptoms and cortical iron-related markers

To provide a descriptive overview of cortical iron profiles and corresponding symptomatology (see Table 2), we note observational relationships between abnormalities in the lingual gyrus (four participants) and cephalalgia, photophobia, cognitive impairment (including confusion), concentration issues, memory deficits and sleep disturbances. The middle temporal region (three participants) appeared to be linked to a broader symptom profile, including cognitive impairment (with confusion), concentration issues, memory deficits, fatigue, sleep disturbances, cephalalgia, phonophobia, photophobia, vertigo, ataxia and visual disturbances. Although other ROIs were less commonly affected (less than or equal to two participants), some descriptive inferences include the involvement of the superior temporal region [including the superior temporal sulcus (STS) and its bank] with cognitive impairment, headaches, photophobia, phonophobia, vestibular dysfunction, memory deficits, concentration issues, fatigue, sleep disturbances, and in one participant, severe tinnitus and irritability.

Secondary depth- and curvature-specific iron profiles

Secondary exploratory analyses sensitive to six cortical depths and three curvatures further highlighted the heterogeneity of iron deposition in mTBI. Only 17% (6/35) of participants retained normal iron profiles; the remaining 83% (29/35) showed elevated susceptibility in at least one ROI, for at least one depth and for at least one curvature. Isolated instances of negative *Z*-scores (indicating lower iron compared to HC) were observed in 7 of the 29 participants but were typically limited to a single ROI/depth combination. Overall, abnormal iron accumulation was most pronounced in the sulcal fundus, followed by the sulcal bank, and was least evident in the gyral crown. However, there was significant inter-individual variability in ROI/curvature/depth combinations (see Fig. 4).

For the 11 participants who demonstrated increased iron in the whole-ROI analyses, a similar ROI-wise distribution of elevated iron was observed in depth- and curvature-specific analyses. For example, in the whole-ROI analysis mTBI-30 showed elevated susceptibility in the caudal mPFC, pars opercularis and superior frontal gyrus (see Table 2 and Fig. 2), which was localized to specific depths and curvatures in the secondary analyses. In addition,

Table 2 Summary of affected ROI, *Z*-score, and symptomatology for iron-abnormal sr-mTBI participants

ID	Lobe(s)	ROI	*Z*-score	pFDR	Presenting symptoms
mTBI-01	Temporal:	Bank, STS	+3.1	0.036	Initial emesis. Severe tinnitus and phonophobia, vertigo, cephalalgia, cervicalgia, photophobia, visual disturbances, cognitive impairment with confusion, concentration issues, memory deficits, irritability, restlessness, fatigue, sleep disturbances. Moderate vestibular dysfunction and ataxia noted.
	Occipital:	Lingual gyrus	+4.1	0.002	
mTBI-03	Temporal:	Parahippocampal	+3.7	0.008	Moderate cervicalgia, cephalalgia, photophobia, phonophobia, vertigo, vestibular dysfunction, cognitive impairment with confusion, concentration issues, memory deficits, irritability, restlessness, fatigue, sleep disturbances. Mild visual disturbance and ataxia present. Additional clinical notes include myalgia.
mTBI-04	Temporal:	Fusiform	+3.0	0.039	Moderate cervicalgia and photophobia. Mild cephalalgia, ataxia, mild cognitive impairment with confusion, concentration issues, memory deficits, sleep disturbance. Clinical notes include vertigo and confusion at onset.
	Occipital:	Lingual gyrus	+6.0	5×10^{-8}	
mTBI-05	Temporal:	Middle temporal	+3.5	0.007	Moderate cognitive impairment, concentration issues, memory deficits, fatigue, sleep disturbance. Mild cephalalgia, phonophobia, photophobia, visual disturbance, ataxia, confusion. Clinical notes include mild vertigo with visuomotor sensitivity and light cranial pressure.
	Occipital:	LOC	+3.5	0.007	
		Lingual gyrus	+3.2	0.014	
mTBI-15	Temporal:	Middle temporal	+3.0	0.047	Severe phonophobia, photophobia, vestibular dysfunction, cognitive impairment with confusion, concentration issues, memory deficits, irritability, fatigue, sleep disturbance. Moderate cephalalgia, cervicalgia, vertigo, restlessness. Mild visual disturbance and ataxia.
		Entorhinal	+5.7	3×10^{-6}	
mTBI-16	Temporal:	Temporal pole	+3.7	0.009	No BIST. Clinical notes include transient mental fog, bradyphrenia, indecisiveness, vestibular dysfunction.
mTBI-17	Temporal:	Temporal pole	+3.4	0.020	Moderate phonophobia, photophobia, visual disturbance, concentration issues. Mild cephalalgia, vertigo, vestibular dysfunction, ataxia, cognitive impairment, memory deficits, irritability, fatigue, sleep disturbance. Clinical notes include disorientation, nausea, and impaired thought.
mTBI-18	Occipital:	Lingual gyrus	+2.9	0.045	Moderate cognitive impairment, concentration issues, fatigue, sleep disturbance. Mild cephalalgia, photophobia, memory deficits, confusion. Clinical notes include being dazed at time of injury.
	Cingulate:	Posterior cingulate	+3.2	0.021	
		Isthmus, Cingulate	+3.8	0.005	
mTBI-29	Frontal:	Pars triangularis	+3.6	0.001	Severe fatigue and sleep disturbance. Moderate cognitive impairment. Mild cephalalgia, photophobia, phonophobia, vestibular dysfunction, memory deficits, concentration issues. Clinical notes include anxiety.
	Parietal:	Caudal mPFC	+3.3	0.004	
	Temporal:	Pars opercularis	+3.4	0.003	
	Occipital:	Superior frontal	+3.1	0.006	
	Insula/cingulate:	Precentral	+4.6	4×10^{-5}	
		Superior parietal	+3.3	0.004	
		Inferior parietal	+4.0	4×10^{-4}	
		Supramarginal	+5.4	3×10^{-6}	
		Precuneus	+4.9	2×10^{-5}	
		STS	+2.9	0.011	
		Transverse temporal	+2.9	0.010	
		LOC	+4.6	4×10^{-5}	
		Insula	+2.9	0.010	
		Rostral ACC	+3.7	0.001	
mTBI-30	Frontal:	Caudal mPFC	+3.7	0.007	Moderate cephalalgia, photophobia, phonophobia, restlessness, fatigue, sleep disturbance. Mild cervicalgia, vertigo, vestibular dysfunction, ataxia, cognitive impairment, concentration issues, memory deficits. Clinical notes include nausea, reduced tolerance to physical/cognitive exertion, and impaired coordination.
		Pars opercularis	+3.5	0.007	
		Superior frontal	+3.1	0.021	
mTBI-34	Frontal:	Lateral OFC	+7.2	3×10^{-12}	Moderate cephalalgia, cervicalgia, phonophobia, cognitive impairment, confusion, concentration issues, memory deficits, restlessness, fatigue. Mild photophobia, vertigo, vestibular dysfunction, visual disturbance, ataxia, irritability, sleep disturbance. Clinical notes include being dazed.
	Temporal:	Middle temporal	+4.6	7×10^{-5}	

Presenting symptoms are derived from BIST injury severity assessments and supplemented with additional clinical patient notes made upon presentation of participants to Axis Sports Medicine clinics. Only participants with abnormal iron profiles are included for brevity and relevance. ID, unique identifier; BIST, Brain Injury Screening Tool; ROI, region of interest; OFC, orbitofrontal cortex; mPFC, middle prefrontal cortex; STS, superior temporal sulcus; LOC, lateral occipital cortex; ACC, anterior cingulate cortex; *p*FDR, statistical significance (*P*-value) after FDR correction.

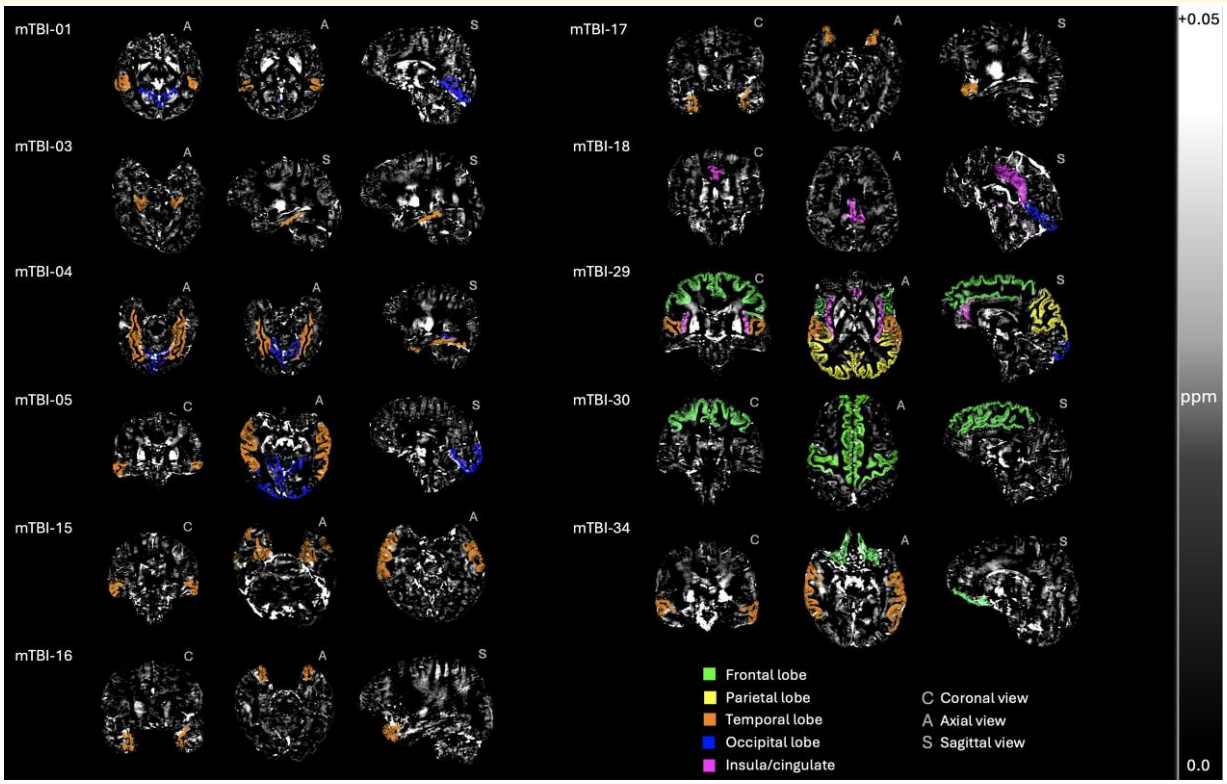

Figure 2 Individualized profiles of abnormal iron accumulation sites following mTBI. Visualization of the specific ROIs and lobes where mTBI participants' ($N = 1$) *Z*-scores significantly deviate from the HC population ($N = 25$–23), highlighting the individualized profiles of iron accumulation following mTBI. The selected orientations (C, coronal; A, axial; S, sagittal) are for best visualization of each participants' result. These maps have been threshold for positive susceptibility values (iron-related) and are expressed in parts per million (ppm) from 0.0 to +0.05. Z-scores and correspondent *P*-values (after FDR correction: *p*FDR) are detailed in Table 2.

regions that did not appear in the initial analyses, including the insula, lateral occipital cortex (LOC), pars triangularis, posterior cingulate, precentral and superior parietal areas, exhibited elevated iron scores in depth- and curvature-specific analyses (see Fig. 4). Conversely, mTBI-25 exemplifies a case where no abnormal iron profile was detected in the whole-ROI analysis but became evident in the analyses sensitive to anatomical morphology (see Fig. 4).

After grouping mTBI participants by iron status based on secondary depth- and curvature-specific results, a Mann–Whitney U-test revealed no significant difference in BIST scores between iron-abnormal ($M = 40.6$, $SD = 33.5$) and iron-normal ($M = 26.3$, $SD = 22.4$) mTBI participants, $U = 63$, $P = 0.35$. An ANOVA showed no significant difference in age between these groups and controls, $F(2, 15) = 1.11$, $P = 0.36$.

Discussion

Previous studies using QSM to examine the role of brain iron following mTBI have primarily focused on subcortical brain areas or global grey and/or WM.[36-44] Only three investigations have included cortical ROIs and, of these, only our previous work[45] accounted for anatomical variations in cortical depth and curvature. However, these studies relied on group-level statistical analyses, which can obscure individual brain changes due to the subtle nature of cell damage associated with mTBI. This approach may limit our understanding of this heterogeneous injury, hindering the implementation of individualized rehabilitation strategies and treatments. We believe, therefore, that research incorporating comparisons of individual clinical participant data to healthy normative ranges can play a key role in informing targeted neural and pharmacological interventions. We conducted the first investigation of individual differences in cortical magnetic susceptibility after sr-mTBI across 34 cortical ROIs, using a healthy population template as a reference. Secondary exploratory analyses sensitive to cortical depth and curvature were included to better characterize injury profiles for each participant.

Our findings revealed that a substantial subset of individuals with mTBI exhibit elevated levels of cortical magnetic susceptibility, indicating injury-related iron accumulation. Our primary investigation evidenced abnormal iron profiles in just under one-third (31%; 11/35) of participants relative to the HC population. Additionally, we found that mTBI participants with abnormal iron accumulation identified in primary ROI-wise analyses experienced more severe symptoms. In these 11 iron-abnormal clinical participants, elevated iron profiles were predominantly focal to specific

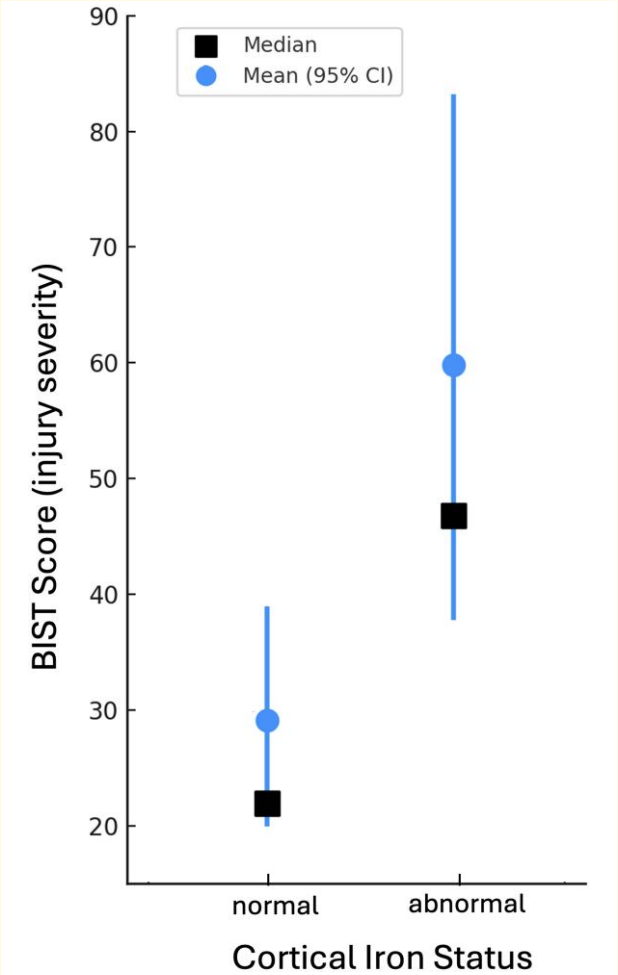

Figure 3 BIST scores by cortical iron status. A Mann–Whitney U-test revealed that injury severity scores were significantly higher for iron-abnormal ($N = 10$; $M = 59.6$, SD = 40.5) than iron-normal ($N = 24$; $M = 29.2$, SD = 23.3) mTBI participants, $U = 57$, $P = 0.02$. Median and mean scores are depicted alongside 95% CI.

lobes or bi-focal (affecting two lobes). Only one participant exhibited multi-focal cortex-wide elevated *Z*-scores. The high density of affected temporal lobe ROIs indicates that, despite significant inter-subject variability, iron accumulation following mTBI is preferential to temporal regions. Taken together, our findings support an iron-related mechanism of secondary injury that modulates symptom severity and may influence symptom presentation.

Iron dyshomeostasis in the basal nuclei is known to impair cognitive function after mTBI,[16,17] however, little is known about the effect of 'cortical' iron aggregation on mTBI symptomatology or severity. In our previous work,[45] we reported few correlations between regions of cortical iron accumulation and BIST[53] scores, a measure of injury severity and dominant symptom cluster. This may be accounted for by variability in the accuracy of symptom reporting or purposeful underreporting of symptoms, a common phenomenon among sports players.[86] However, group-level examinations may also obscure individual differences and inhibit the implementation of more targeted statistical approaches. By assessing the effect of mTBI at the individual level, we were able to facilitate precise between group analyses of injury severity that differentiated between iron-normal and iron-abnormal mTBI participants. Results from our primary analysis revealed a significantly higher symptom burden for participants with mTBI when their iron profiles were also abnormal.

The field generally lacks reliable correlations between subjective assessments of injury severity and objective measures of brain injury and recovery,[87] as well as alignment between cognitive or clinical findings and neuroimaging results.[88] Identifying reliable, objective markers of structural changes that are related to subjective self-reported symptoms is crucial because individual variations in brain injury location and severity can lead to disparate clinical presentations and recovery trajectories but may be missed in group-level analyses.[8] Although research indicates that most individuals recover well from mTBI, between 15[11] and 30%[8] of patients experience significant, and in some cases life-changing, long-term clinical sequelae. Understanding the underlying pathophysiological drivers of these poorer outcomes is essential for enabling precise, patient-specific clinical interventions. Our finding that 31% of participants exhibited abnormal iron profiles substantial enough to be detected in the primary ROI-wise analyses, which were linked to poorer outcomes, aligns with both evidence of structural brain changes detected with advanced MRI in up to 30% of mTBI cases,[1] as well as evidence from individualized studies reporting a similar percentage (28%) of subacute-phase WM anomalies and associations with worse cognitive outcomes in ms-TBI.[51] In addition, standardized susceptibility values in the basal nuclei are reported to correlate with mTBI symptom duration, but only in a sub-group of participants with persistent symptomatology for at least a week.[40] In keeping with these findings, our results reinforce the importance of individualized analyses in revealing not only associations between the extent of microstructural pathology and negative outcomes following mTBI, but for identifying at-risk cohorts. Here, the value of personalized approaches to understanding mTBI becomes strikingly apparent. Further longitudinal studies that track participants through recovery could help to determine whether elevated ROI-wise cortical iron levels are associated with prolonged recovery, persistent post-concussive symptoms, or adverse outcomes later in life. Such research may offer insights into why a subset of individuals with mTBI fails to recover fully.

The promise of individualized assessments to identify biomarkers for mild brain injury is particularly salient given the current absence of objective markers for mTBI diagnosis. Diagnostic decisions are limited to subjective self-report and assessments of physiological function,[13,87] as the heterogeneity of mTBI complicates efforts to identify reliable biomarkers or imaging signatures that can be applied universally across patients. Whether cortical iron accumulation reflects inflammatory processes, BBB disruption,[9]

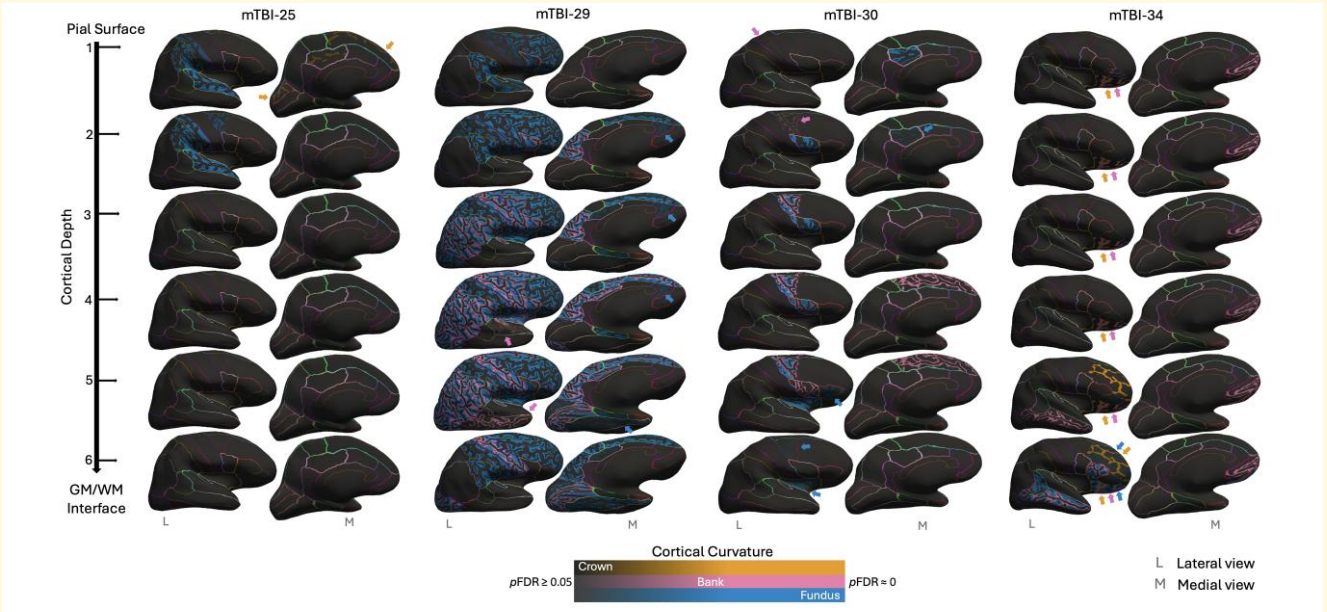

Figure 4 Cortical depth- and curvature-specific profiles of mTBI-related abnormal iron accumulation. Cortical depth- and curvature-specific iron profiles across five representative sr-mTBI participants. Inflated surfaces show each of the six cortical depths, from the pial surface (depth 1) to the GM/WM interface (depth 6). Regions of abnormal iron deposition are colour-coded according to cortical curvature. Colour intensity shows level of statistical significance (pFDR < 0.05). Regions with lower statistical significance that are harder to visually distinguish are indicated by arrows in the colour of the correspondent cortical curvature. Lateral (L) and medial (M) views are used to visualize the whole brain. Boundaries between ROIs are delineated using coloured lines. To derive Z-scores, individual ($N = 1$) mTBI participants' data were compared to the HC normal distribution ($N = 25$), at each depth ($N = 6$), for each curvature ($N = 3$), within each ROI ($N = 34$). Full statistical results, including Z-scores and P-values (after FDR correction) are available in Supplementary Data 1. Abbreviations are as follows: pFDR = statistical significance (P-value) after FDR correction.

ferroptosis,[31,89] or other cytotoxic processes is beyond the scope of the current research. However, we posit that the significantly higher symptom burden (BIST[53] score) observed in the iron-abnormal mTBI cohort, as identified via whole-ROI analyses, supports an iron-mediated mechanism of brain changes related to injury severity and functional impairment, and marks iron as a promising mTBI biomarker. Of particular note, many of the symptoms observed in mTBI resemble those seen in other iron-mediated neurodegenerative processes, such as cognitive decline in normal aging,[90] and the cognitive and motor dysfunctions characteristic of diseases like Alzheimer's, Huntington's, Parkinson's and Friedrich's ataxia, as well as multiple sclerosis, where iron dysregulation is a hallmark feature.[9,91] Genetic disorders of iron overload, such as neuroferritinopathy, also present with cognitive and motor symptoms.[92]

The susceptibility of the temporal lobe to iron accumulation post-mTBI, evident in this and previous research,[45] aligns with the memory impairments characteristic of mTBI.[93] Individual-level data from our mTBI sample emphasizes the link between high temporal iron accumulation and memory deficits, as exemplified by BIST[53] scores related to memory (see Table 2). In addition, specific distributions of p-tau focal to temporal (and frontal) cortex are considered features of chronic traumatic encephalopathy (CTE),[94,95] an mTBI-related neurodegenerative disorder. Of particular concern, co-localization of iron with p-tau in CTE has been highlighted in histological examinations.[34] Whilst the precise relationship between iron overload and the downstream hyperphosphorylation of tau proteins remains an active area of research, further exploration of the interplay between acute cortical iron elevation, symptom burden, temporal recovery dynamics and long-term brain health outcomes is warranted.

The diversity of mechanistic antecedents, pathological mechanisms and clinical outcomes associated with mTBI reflects the complex underlying pathophysiology.[8] mTBI is not a uniform injury and structural indicators, such as those commonly observed in other forms of TBI, do not always correlate with clinical symptoms or outcomes.[96] Here, we speculate that abnormal iron accumulation in specific cortical ROIs may be related to participant symptomatology. For instance, the STS plays a key role in social cognition, empathy, mentalising about others' emotional states and 'theory of mind.'[97-99] Structural changes to this region may explain the severe irritability reported by mTBI-01 (see Table 2), along with complaints of severe tinnitus.[100] As a hub for audiovisual integration,[101] the superior temporal region could also be involved in phonophobia (sound sensitivity), visual disturbances and vestibular dysfunction[102]; symptoms experienced by both mTBI participants whose profiles indicated local iron elevation. Similarly, the lingual

gyrus is active during migraine episodes and responds to luminous stimuli, suggesting its involvement in photophobia, visual processing anomalies and cephalalgia (headache).[103] These symptoms were observed in all clinical participants with iron aggregation in this region (see Table 2). Our findings allude to specific areas of cortical iron accumulation that show a relationship to clinical sequelae, suggesting that regions with higher iron burden may be evidence of microstructural cell damage that disrupts normal function. Here, it should be noted that multiple cortical regions with abnormal iron markers were observed for most mTBI participants, making it challenging to delineate a one-to-one relationship between a specific ROI and symptoms reported. As such, future research should integrate functional MRI to improve the mapping of structural changes to deficits in functional connectivity and well-established brain networks that may overlap with abnormalities in cortical grey matter regions. Without additional research, observations about regions of iron accumulation and symptom presentation are speculative and less convincing than case-matching between brain lesions in gross TBI and neurobehavioural symptom presentation.[104]

Depth- and curvature-specific iron accumulation

Secondary exploratory analyses revealed significant inter-individual heterogeneity in depth- and curvature-specific cortical iron accumulation. Although these subtle effects were not associated with injury severity, they provide evidence of widespread minor tissue alterations following mTBI. A consistent trend for iron deposition was observed in the sulci, with the highest concentration at the fundus, followed by the sulcal banks. This pattern may be attributed to the heightened vulnerability of the fundus to mTBI-related injury, which is susceptible to mechanical deformation due to the 'water hammer effect,' where CSF is forced into the depths of the sulci, causing local damage.[105] Supporting this, previous research has demonstrated that mTBI increases cortical curvature in the sulcus,[106] as well as widens the sulci and causes focal vascular injury and microhaemorrhages in the fundus, as evidenced by susceptibility-weighted imaging.[105] Conversely, in more severe TBI, contusions are often concentrated at the gyri,[93] suggesting that gyral iron accumulation in 'mild' TBI may represent a less severe version of this type of injury. An understanding of injury biomechanics may thus prove crucial to explaining variance in loci of neuropathological changes. Research shows that different types of head impacts can result in varying brain deformations and injury patterns, with sulci being particularly vulnerable to mechanical strain, which is consistent with, and can be predicted by, patterns of tauopathy observed in neurodegenerative conditions.[107] Personalized iron accumulation patterns may provide insight into the specific injury mechanisms and related cellular disruption experienced by each individual participant at the acute stage. Elucidating this link, as well as how this may be related to mTBI-induced neuropathology in later life, should be a focus for future research.

Histological studies, including Perl's iron staining and ultra-high-field (7T) R_2* mapping of tissue samples[108] have localized iron deposition to specific cortical layers, reflecting distinct cyto- and myelo-architectural features with layer-specific distributions that show congruence with *in vivo* QSM.[109] In healthy populations, iron concentrations typically increase from the pial surface towards the GM/WM boundary; deviations away from baselines for each layer suggest an injury-specific model of cortical cellular trauma. For instance, layer I primarily contains axons and dendrites, with the cell bodies in deeper layers[110]; iron accumulation in different layers may point to diverse pathologies affecting different parts of the cell. Depth-wise patterns may also be related to injury biomechanics: superficial iron accumulation may be a result of perivascular trauma, which is often linked to microhaemorrhages and microglial activation after mTBI,[27,28,93] whereas deeper iron deposition may reflect more severe shear forces, which are known to cause significant damage near the GM/WM interface in mTBI.[111] This is supported by computational modelling showing that shear forces are concentrated in this region,[107] which is also a common site of microbleeds.[112] Tying this in with investigations of cortical curvature, these effects would likely be concentrated at the sulcal fundus.[105,107,113] However, evidence from TBI research supports contusions of the gyri that often follow a layer-specific pattern, with damage prominent at the superficial crest but extending through the cortical mantle to the GM/WM boundary in a 'wedge' of haemorrhage and necrotic tissue.[93] Iron-dependent cell death, ferroptosis,[31,89] could plausibly account for instances of iron-related gyral pathology in mTBI that exhibit similar depth-specific patterns.

It is important to note that both injuries at the pial surface[113] and closer to the GM/WM border[111] have been related to adverse outcomes after mTBI. However, subpial iron deposition near small blood vessels in the fundus is congruent with distributions of sulcal tauopathy seen in CTE,[113] which may be related to breaches in the BBB.[107] Injury-induced microvascular dysfunction may increase BBB permeability[114,115] which likely increases active transport of non-heme iron via vascular endothelial cells into the superficial layers of the cortex[9,29,116] which could account for perivascular accumulations.[93,94] The potential long-term effects of iron deposition in this young cohort warrants further investigation, given the known relationship between iron accumulation and tau pathology.[34]

Limitations and future research

The ability of neuroimaging modalities to infer underlying biological processes is limited by spatial constraints and inference about tissue composition from indirect markers. While the use of QSM can provide insight into potential iron accumulation, it remains a surrogate measure of iron-tissue content. Integrating complementary modalities such

as PET, or protein assays, would offer a more comprehensive understanding of the underlying neurobiology. Additionally, because analyses related to cortical thickness involve sampling multiple tissue types across a small cross-section, higher resolutions become particularly important.[117] Although ≤1 mm isotropic resolution is recommended to mitigate partial volume effects,[64] such artefacts may be problematic at the cortical surface and GM/WM tissue interface. While erosion steps were used to reduce non-brain signals around the outer cortex, acquiring higher-resolution images, assuming an adequate field-of-view,[60] may further reduce partial volume effects. It is worth noting that QSM studies conducted at similar resolution found that discarding the outer depths did not significantly alter susceptibility measurements,[60] suggesting that the influence of partial volume-induced distortions may be relatively modest under these conditions. The 1 mm isotropic voxel resolution also inherently restricts depth-wise analysis of the ∼1–4.5 mm thick cerebral cortex.[83] However, studies employing comparable depth-specific methodologies have utilized data from QSM,[60] DTI,[76] T1w/T2w imaging[118] and quantitative T1 and QSM,[119] to sample between 10 and 21 cortical depths with meaningful results. In addition, the DTI-based study[76] reported the identification of features with 0.9 mm isotropic resolution, single-shell data similar to those found with 92 µm isotropic, high-angular-resolution data,[120] underscoring the ability of these technique to conserve features even at coarser resolutions. Whilst the model presented here is more conservative than previous approaches, sampling fewer depths (e.g. three) could arguably capture overall cortical thickness and avoid redundancy; however, sampling fewer depths appears to forfeit distinct susceptibility features uniquely revealed by a six-depth model (see Supplementary Figs 1–34). Given inter-individual variability in cortical thickness, there is need for individualized approaches that are sensitive to heterogeneity. These inherent constraints should nonetheless be considered when interpreting the presented data.

It should be noted that this study did not control for several potential confounding factors, including prior injuries, genetic predispositions and environmental influences, all known to affect injury severity and recovery trajectories.[8] Moreover, natural age-related increases in cortical iron are particularly pronounced within this specific age range.[121] In principle, within a sample so closely age-matched, the normal distribution reflects typical variation in cortical susceptibility values, but age effects may still not be fully accounted for. The power of *Z*-scores to regress these variables is limited, particularly at small sample sizes and future research should consider recruiting large control cohorts that enable more robust approaches, such as normative modelling.[122] This would also confer the added benefit of sampling across broader populations, simultaneously improving generalizability. This is particularly salient for female athletes, for whom hormonal variations,[123] the use of oral contraceptives[124] and differences in neck musculature[125] lend themselves to further heterogeneity in injury severity and outcome. In lieu of normative modelling, investigations using female cohorts are planned to address this gap. Lastly, the current study relied on a single-echo QSM sequence, constraining susceptibility thresholding to 'between' voxels. Multi-echo sequences enable the separation of susceptibility sources 'within' voxels,[109,126,127] and should be considered for future research.

To conclude, our results suggest that iron-mediated cell damage plays a key role in mTBI pathology. In keeping with the heterogeneity of mTBI, accumulation of cortical iron after injury is person-specific and may be influenced by cortical morphology. These results highlight the importance of examining mTBI at an individual level rather than relying on group-level analyses. This variability likely also complicates the search for universal biomarkers, further underscoring the need for personalized approaches that integrate advanced imaging and detailed symptom profiling.

Supplementary material

Supplementary material is available at *Brain Communications* online.

Acknowledgements

We extend thanks to Amabelle Voice-Powell and Cassandra McGregor for their contribution to the data collection, and Tania Ka'ai for bringing her perspective to cultural considerations on this study. In addition, we thank Axis Sports Concussion Clinics, particularly Dr Stephen Kara, for their assistance with recruiting sr-mTBI participants and personnel at the Centre for Advanced Magnetic Resonance Imaging (CAMRI) for their assistance in collecting MRI data. We also acknowledge Dr Tim Elliot for radiological reporting of all participants and Siemens Healthineers for the use of a work-in-progress (WIP) prototype sequence for the acquisition data used to perform QSM.

Funding

This project was funded by a grant from the Health Research Council of New Zealand (HRC; grant #21/622).

Competing interests

The authors report no competing interests.

Data availability

De-identified MRI data can be made available upon request to the corresponding author (C.A.E.). Codes used for *Z*-score generation and analysis are available on the GitHub of the corresponding author (https://github.com/

ChristiEssex/QSMindividualised). Parent codes for cortical column generation are hosted on GitHub (https://github.com/devonko) and can be available upon request from co-authors (J.L.M. and T.-K.T.) based at the Brain Imaging and Analysis Center at Duke University Medical Center. QSM data were generated using QSMxT (https://qsmxt.github.io/QSMxT/). Additional data processing, including pial surface estimation, was conducted with FreeSurfer (https://surfer.nmr.mgh.harvard.edu).

References

1. Maas AI, Menon DK, Manley GT, *et al.* Traumatic brain injury: Progress and challenges in prevention, clinical care, and research. *Lancet Neurol*. 2022;21(11):1004-1060.
2. Howe EI, Andelic N, Fure SC, *et al.* Cost-effectiveness analysis of combined cognitive and vocational rehabilitation in patients with mild-to-moderate TBI: Results from a randomized controlled trial. *BMC Health Serv Res*. 2022;22(1):185.
3. Guskiewicz KM, Marshall SW, Bailes J, *et al.* Recurrent concussion and risk of depression in retired professional football players. *Med Sci Sports Exerc*. 2007;39(6):903-909.
4. McInnes K, Friesen CL, MacKenzie DE, *et al.* Mild traumatic brain injury (mTBI) and chronic cognitive impairment: A scoping review. *PLoS One*. 2017;12(4):e0174847.
5. Mackay DF, Russell ER, Stewart K, *et al.* Neurodegenerative disease mortality among former professional soccer players. *N Engl J Med*. 2019;381:1801-1808.
6. De Beaumont L, Thoret H, Mongeon D, *et al.* Brain function decline in healthy retired athletes who sustained their last sports concussion in early adulthood. *Brain*. 2009;132(3):695-708.
7. Guskiewicz KM, Marshall SW, Bailes J, *et al.* Association between recurrent concussion and late-life cognitive impairment in retired professional football players. *Neurosurgery*. 2005;57(4):719-726.
8. Rosenbaum SB, Lipton ML. Embracing chaos: The scope and importance of clinical and pathological heterogeneity in mTBI. *Brain Imaging Behav*. 2012;6(2):255-282.
9. Gozt A, Hellewell S, Ward PG, *et al.* Emerging applications for quantitative susceptibility mapping in the detection of traumatic brain injury pathology. *Neuroscience*. 2021;467:218-236.
10. Giza CC, Hovda DA. The new neurometabolic cascade of concussion. *Neurosurgery*. 2014;75(Suppl 4):S24-S33.
11. Walker KR, Tesco G. Molecular mechanisms of cognitive dysfunction following traumatic brain injury. *Front Aging Neurosci*. 2013;5:29.
12. Hier DB, Obafemi-Ajayi T, Thimgan MS, *et al.* Blood biomarkers for mild traumatic brain injury: A selective review of unresolved issues. *Biomark Res*. 2021;9(1):70.
13. Lunkova E, Guberman GI, Ptito A, *et al.* Noninvasive magnetic resonance imaging techniques in mild traumatic brain injury research and diagnosis. *Hum Brain Mapp*. 2021;42(16):5477-5494.
14. Cook GA, Hawley JS. A review of mild traumatic brain injury diagnostics: Current perspectives, limitations, and emerging technology. *Mil Med*. 2014;179(10):1083-1089.
15. Wintermark M, Sanelli PC, Anzai Y, *et al.* Imaging evidence and recommendations for traumatic brain injury: Advanced neuro- and neurovascular imaging techniques. *AJNR Am J Neuroradiol*. 2015;36(2):E1-E11.
16. Lu L, Cao H, Wei X, *et al.* Iron deposition is positively related to cognitive impairment in patients with chronic mild traumatic brain injury: Assessment with susceptibility weighted imaging. *Biomed Res Int*. 2015;2015:470676.
17. Raz E, Jensen JH, Ge Y, *et al.* Brain iron quantification in mild traumatic brain injury: A magnetic field correlation study. *AJNR Am J Neuroradiol*. 2011;32(10):1851-1856.
18. Duyn JH, Schenck J. Contributions to magnetic susceptibility of brain tissue. *NMR Biomed*. 2017;30(4):10.1002/nbm.3546.
19. Jang J, Nam Y, Jung SW, *et al.* Paradoxical paramagnetic calcifications in the globus pallidus: An ex vivo MR investigation and histological validation study. *NMR Biomed*. 2021;34(10):e4571.
20. Kim S, Lee Y, Jeon CY, *et al.* Quantitative magnetic susceptibility assessed by 7T magnetic resonance imaging in Alzheimer's disease caused by streptozotocin administration. *Quant Imaging Med Surg*. 2020;10(3):789-797.
21. Wang Y, Spincemaille P, Liu Z, *et al.* Clinical quantitative susceptibility mapping (QSM): Biometal imaging and its emerging roles in patient care. *J Magn Reson Imaging*. 2017;46(4):951-971.
22. Gong NJ, Dibb R, Bulk M, *et al.* Imaging beta amyloid aggregation and iron accumulation in Alzheimer's disease using quantitative susceptibility mapping MRI. *NeuroImage*. 2019;191:176-185.
23. Zhao Z, Zhang L, Wen Q, *et al.* The effect of beta-amyloid and tau protein aggregations on magnetic susceptibility of anterior hippocampal laminae in Alzheimer's diseases. *NeuroImage*. 2021;244:118584.
24. Langkammer C, Schweser F, Krebs N, *et al.* Quantitative susceptibility mapping (QSM) as a means to measure brain iron? A post mortem validation study. *NeuroImage*. 2012;62(3):1593-1599.
25. Liu C, Li W, Tong KA, *et al.* Susceptibility-weighted imaging and quantitative susceptibility mapping in the brain. *J Magn Reson Imaging*. 2015;42(1):23-41.
26. Ravanfar P, Loi SM, Syeda WT, *et al.* Systematic review: Quantitative susceptibility mapping (QSM) of brain iron profile in neurodegenerative diseases. *Front Neurosci*. 2021;15:618435.
27. Huang S, Li S, Feng H, *et al.* Iron metabolism disorders for cognitive dysfunction after mild traumatic brain injury. *Front Neurosci*. 2021;15:587197.
28. Nisenbaum EJ, Novikov DS, Lui YW. The presence and role of iron in mild traumatic brain injury: An imaging perspective. *J Neurotrauma*. 2014;31(4):301-307.
29. Levi S, Ripamonti M, Moro AS, *et al.* Iron imbalance in neurodegeneration. *Mol Psychiatry*. 2024;29:1139-1152.
30. Daglas M, Adlard PA. The involvement of iron in traumatic brain injury and neurodegenerative disease. *Front Neurosci*. 2018;12:981.
31. Tang S, Gao P, Chen H, *et al.* The role of iron, its metabolism and ferroptosis in traumatic brain injury. *Front Cell Neurosci*. 2020;14:590789.
32. Neuwelt E, Abbott J, Abrey L, *et al.* Strategies to advance translational research into brain barriers. *Lancet Neurol*. 2008;7(1):84-96.
33. Morganti-Kossmann MC, Satgunaseelan L, Bye N, *et al.* Modulation of immune response by head injury. *Injury*. 2007;38(12):1392-1400.
34. Bouras C, Giannakopoulos P, Good PF, *et al.* A laser microprobe mass analysis of brain aluminum and iron in dementia pugilistica: Comparison with Alzheimer's disease. *Eur Neurol*. 1997;38(1):53-58.
35. Zecca L, Youdim MB, Riederer P, *et al.* Iron, brain ageing and neurodegenerative disorders. *Nat Rev Neurosci*. 2004;5:863-873.
36. Bell TK, Ansari M, Joyce JM, *et al.* Quantitative susceptibility mapping in adults with persistent-post concussion symptoms after mild traumatic brain injury: An exploratory study. *AJNR Am J Neuroradiol*. 2025;46(2):435-442.
37. Brett BL, Koch KM, Muftuler LT, *et al.* Association of head impact exposure with white matter macrostructure and microstructure metrics. *J Neurotrauma*. 2021;38(4):474-484.
38. Gong NJ, Kuzminski S, Clark M, *et al.* Microstructural alterations of cortical and deep gray matter over a season of high school football revealed by diffusion kurtosis imaging. *Neurobiol Dis*. 2018;119:79-87.
39. Koch KM, Meier TB, Karr R, *et al.* Quantitative susceptibility mapping after sports-related concussion. *AJNR Am J Neuroradiol*. 2018;39(7):1215-1221.

40. Koch KM, Nencka AS, Swearingen B, *et al.* Acute post-concussive assessments of brain tissue magnetism using magnetic resonance imaging. *J Neurotrauma*. 2021;38(7):848-857.
41. Pinky NN, Debert CT, Dukelow SP, *et al.* Multimodal magnetic resonance imaging of youth sport-related concussion reveals acute changes in the cerebellum, basal ganglia, and corpus callosum that resolve with recovery. *Front Hum Neurosci*. 2022;16:976013.
42. Weber AM, Pukropski A, Kames C, *et al.* Pathological insights from quantitative susceptibility mapping and diffusion tensor imaging in ice hockey players pre and post-concussion. *Front Neurol*. 2018;9:575.
43. Wright DK, O'Brien TJ, Shultz SR. Sub-acute changes on MRI measures of cerebral blood flow and venous oxygen saturation in concussed Australian rules footballers. *Sports Med Open*. 2022;8:45.
44. Zivadinov R, Polak P, Schweser F, *et al.* Multimodal imaging of retired professional contact sport athletes does not provide evidence of structural and functional brain damage. *J Head Trauma Rehabil*. 2018;33(5):E24-E32.
45. Essex CA, Merenstein JL, Overson DK, *et al.* Characterizing positive and negative quantitative susceptibility values in the cortex following mild traumatic brain injury: a depth- and curvature-based study. *Cereb Cortex*. 2025;35(3):bhaf059. https://doi.org/10.1093/cercor/bhaf059
46. Mito R, Pedersen M, Pardoe H, *et al.* Exploring individual fixel-based white matter abnormalities in epilepsy. *Brain Commun*. 2023;6(1):fcad352.
47. Domínguez JF, Stewart A, Burmester A, *et al.* Improving quantitative susceptibility mapping for the identification of traumatic brain injury neurodegeneration at the individual level. *Z Med Phys*. Published online 8 February 2024. doi: 10.1016/j.zemedi.2024.01.001
48. Bedggood MJ, Essex CA, Theadom A, *et al.* Individual-level analysis of MRI T2 relaxometry in mild traumatic brain injury: Possible indications of brain inflammation. *Neuroimage Clin*. 2024;43:103647.
49. Attyé A, Renard F, Baciu M, *et al.* TractLearn: A geodesic learning framework for quantitative analysis of brain bundles. *NeuroImage*. 2021;233:117927.
50. Clemente A, Attyé A, Renard F, *et al.* Individualised profiling of white matter organisation in moderate-to-severe traumatic brain injury patients using TractLearn: A proof-of-concept study. *Brain Res*. 2023;1806:48289.
51. Jolly AE, Bălăeț M, Azor A, *et al.* Detecting axonal injury in individual patients after traumatic brain injury. *Brain*. 2021;144(1):92-113.
52. Imms P, Clemente A, Deutscher E, *et al.* Exploring personalized structural connectomics for moderate to severe traumatic brain injury. *Network Neurosci*. 2023;1(7):160-183.
53. Theadom A, Hardaker N, Bray C, *et al.* The brain injury screening tool (BIST): Tool development, factor structure and validity. *PLoS One*. 2021;16(2):e0246512.
54. Gorgolewski KJ, Auer T, Calhoun VD, *et al.* The brain imaging data structure, a format for organizing and describing outputs of neuroimaging experiments. *Sci Data*. 2016;3:160044.
55. Bore A, Guay S, Bedetti C, *et al.* 2023. https://github.com/cbedetti/Dcm2Bids
56. Li X, Morgan PS, Ashburner J, *et al.* The first step for neuroimaging data analysis: DICOM to NIfTI conversion. *J Neurosci Methods*. 2016;264:47-56.
57. Avants BB, Tustison NJ, Song G, *et al.* A reproducible evaluation of ANTs similarity metric performance in brain image registration. *NeuroImage*. 2011;54(3):2033-2044.
58. Tustison NJ, Avants BB, Cook PA, *et al.* N4ITK: Improved N3 bias correction. *IEEE Trans Med Imaging*. 2010;29(6):1310-1320.
59. Fischl B. FreeSurfer. *NeuroImage*. 2012;62(2):774-781.
60. Merenstein JL, Zhao J, Overson DK, *et al.* Depth- and curvature-based quantitative susceptibility mapping analyses of cortical iron in Alzheimer's disease. *Cereb Cortex*. 2024;34(2):bhad525.
61. Dymerska B, Eckstein K, Bachrata B, *et al.* Phase unwrapping with a rapid open-source minimum spanning tree algorithm (ROMEO). *Magn Reson Med*. 2020;85(4):2294-2308.
62. Liu T, Khalidov I, de Rochefort L, *et al.* A novel background field removal method for MRI using projection onto dipole fields (PDF). *NMR Biomed*. 2011;24(9):1129-1136.
63. Kames C, Wiggermann V, Rauscher A. Rapid two-step dipole inversion for susceptibility mapping with sparsity priors. *NeuroImage*. 2018;167:276-283.
64. Bilgic B, Costagli M, Chan KS, *et al.* Recommended implementation of quantitative susceptibility mapping for clinical research in the brain: A consensus of the ISMRM Electro-Magnetic Tissue Properties Study Group. *Magn Reson Med*. 2024;91(5):1834-1862.
65. Straub S, Schneider TM, Emmerich J, *et al.* Suitable reference tissues for quantitative susceptibility mapping of the brain. *Magn Reson Med*. 2017;78(1):204-214.
66. Stewart AW, Bollman S. 2022. https://qsmxt.github.io/QSMxT/
67. Stewart AW, Robinson SD, O'Brien K, *et al.* QSMxT: Robust masking and artifact reduction for quantitative susceptibility mapping. *Magn Reson Med*. 2022;87(3):1289-1300.
68. Jenkinson M, Beckmann CF, Behrens TE, *et al.* FSL. *NeuroImage*. 2012;62(2):782-790.
69. Smith SM, Jenkinson M, Woolrich MW, *et al.* Advances in functional and structural MR image analysis and implementation as FSL. *NeuroImage*. 2004;23(Suppl 1):S208-S219.
70. Woolrich MW, Jbabdi S, Patenaude B, *et al.* Bayesian analysis of neuroimaging data in FSL. *NeuroImage*. 2009;45(Suppl 1):S173-S185.
71. Smith SM. Fast robust automated brain extraction. *Hum Brain Mapp*. 2002;17(3):143-155.
72. Greve DN, Fischl B. Accurate and robust brain image alignment using boundary-based registration. *NeuroImage*. 2009;48(1):63-72.
73. Jenkinson M, Bannister P, Brady M, *et al.* Improved optimization for the robust and accurate linear registration and motion correction of brain images. *NeuroImage*. 2002;17(2):825-841.
74. Jenkinson M, Smith S. A global optimization method for robust affine registration of brain images. *Med Image Anal*. 2001;5(2):143-156.
75. Reichenbach JR. The future of susceptibility contrast for assessment of anatomy and function. *NeuroImage*. 2012;62(2):1311-1315.
76. Ma Y, Bruce IP, Yeh CH, *et al.* Column-based cortical depth analysis of the diffusion anisotropy and radiality in submillimeter whole-brain diffusion tensor imaging of the human cortical gray matter in vivo. *NeuroImage*. 2023;270:119993.
77. Daducci A, Gerhard S, Griffa A, *et al.* The connectome mapper: An open-source processing pipeline to map connectomes with MRI. *PLoS One*. 2012;7(12):e48121.
78. Desikan RS, Segonne F, Fischl B, *et al.* An automated labeling system for subdividing the human cerebral cortex on MRI scans into gyral based regions of interest. *NeuroImage*. 2006;31(3):968-980.
79. Tournier DJ, Smith R, Raffelt D, *et al.* MRtrix3: A fast, flexible and open software framework for medical image processing and visualisation. *NeuroImage*. 2019;202:116137.
80. Waehnert MD, Dinse J, Weiss M, *et al.* Anatomically motivated modeling of cortical laminae. *NeuroImage*. 2014;93(Pt 2):210-220.
81. Waehnert MD, Dinse J, Schäfer A, *et al.* A subject-specific framework for in vivo myeloarchitectonic analysis using high resolution quantitative MRI. *NeuroImage*. 2016;125:94-107.
82. Pienaar R, Rojczyk P, Seitz-Holland J, *et al.* A methodology for analyzing curvature in the developing brain from preterm to adult. *Int J Imaging Syst Technol*. 2008;18(1):42-68.
83. Fischl B, Dale AM. Measuring the thickness of the human cerebral cortex from magnetic resonance images. *Proc Natl Acad Sci U S A*. 2000;97(20):11050-11055.
84. Tukey JW. *Exploratory data analysis*. Addison-Wesley Publishing Company; 1977.

85. Benjamini Y, Hochberg Y. Controlling the false discovery rate: A practical and powerful approach to multiple testing. *J R Stat Soc Ser B (Methodol)*. 1995;57(1):289-300.
86. Kroshus E, Garnett B, Hawrilenko M, *et al.* Concussion underreporting and pressure from coaches, teammates, fans, and parents. *Soc Sci Med*. 2015;134:66-75.
87. McCrea M, Meier T, Huber D, *et al.* Role of advanced neuroimaging, fluid biomarkers and genetic testing in the assessment of sport-related concussion: A systematic review. *Br J Sports Med*. 2017;51(12):919-929.
88. Shenton ME, Hamoda HM, Schneiderman JS, *et al.* A review of magnetic resonance imaging and diffusion tensor imaging findings in mild traumatic brain injury. *Brain Imaging Behav*. 2012;6(2):137-192.
89. Ma H, Dong Y, Chu Y, *et al.* The mechanisms of ferroptosis and its role in Alzheimer's disease. *Front Mol Biosci*. 2022;9:965064.
90. Ghadery C, Pirpamer L, Hofer E, *et al.* R2* mapping for brain iron: Associations with cognition in normal aging. *Neurobiol Aging*. 2015;36(2):925-932.
91. Stankiewicz J, Panter SS, Neema M, *et al.* Iron in chronic brain disorders: Imaging and neurotherapeutic implications. *Neurotherapeutics*. 2007;4(3):371-386.
92. Wills AJ, Sawle GV, Guilbert PR, *et al.* Palatal tremor and cognitive decline in neuroferritinopathy. *J Neurol Neurosurg Psychiatry*. 2002;73:91-92.
93. McKee AC, Daneshvar DH. The neuropathology of traumatic brain injury. In: Connolly ES Jr, ed. *Handbook of clinical neurology*. Elsevier B.V.; 2015:45-66.
94. Murray HC, Osterman C, Bell P, *et al.* Neuropathology in chronic traumatic encephalopathy: A systematic review of comparative post-mortem histology literature. *Acta Neuropathol Commun*. 2022;10:109.
95. McKee AC, Stein TD, Huber BR, *et al.* Chronic traumatic encephalopathy (CTE): Criteria for neuropathological diagnosis and relationship to repetitive head impacts. *Acta Neuropathol*. 2023;145(4):371-394.
96. Bigler ED, Maxwell WL. Neuropathology of mild traumatic brain injury: Relationship to neuroimaging findings. *Brain Imaging Behav*. 2012;6(2):108-136.
97. Basil RA, Westwater ML, Wiener M, *et al.* A causal role of the right superior temporal sulcus in emotion recognition from biological motion. *Open Mind (Camb)*. 2017;2(1):26-36.
98. Beauchamp MS. The social mysteries of the superior temporal sulcus. *Trends Cogn Sci*. 2015;19(9):489-490.
99. Deen B, Koldewyn K, Kanwisher N, *et al.* Functional organization of social perception and cognition in the superior temporal sulcus. *Cereb Cortex*. 2015;25(11):4596-4609.
100. Leaver AM, Renier L, Chevillet MA, *et al.* Dysregulation of limbic and auditory networks in tinnitus. *Neuron*. 2011;69(1):33-43.
101. Hein G, Knight RT. Superior temporal sulcus - It's my area: Or is it? *J Cogn Neurosci*. 2008;20(12):2125-2136.
102. Dieterich M, Brandt T. Functional brain imaging of peripheral and central vestibular disorders. *Brain*. 2008;131(10):2538-2552.
103. Boulloche N, Denuelle M, Payoux P, *et al.* Photophobia in migraine: An interictal PET study of cortical hyperexcitability and its modulation by pain. *J Neurol Neurosurg Psychiatry*. 2010;81(9):978-984.
104. Levin HS, Amparo E, Eisenberg HM, *et al.* Magnetic resonance imaging and computerized tomography in relation to the neurobehaviorial sequelae of mild and moderate head injuries. *J Neurosurg*. 1987;66(5):706-713.
105. Kornguth S, Rutledge N, Perlaza G, *et al.* A proposed mechanism for development of CTE following concussive events: Head impact, water hammer injury, neurofilament release, and autoimmune processes. *Brain Sci*. 2017;7(12):164.
106. King JB, Lopez-Larson MP, Yurgelun-Todd DA. Mean cortical curvature reflects cytoarchitecture restructuring in mild traumatic brain injury. *NeuroImage Clin*. 2016;11:81-89.
107. Ghajari M, Hellyer PJ, Sharp DJ. Computational modelling of traumatic brain injury predicts the location of chronic traumatic encephalopathy pathology. *Brain*. 2017;140(2):333-343.
108. Fukunaga M, Li TQ, Van Gelderen P, *et al.* Layer-specific variation of iron content in cerebral cortex as a source of MRI contrast. *Proc Natl Acad Sci U S A*. 2010;107(8):3834-3839.
109. Shin HG, Lee J, Yun YH, *et al.* χ-separation: Magnetic susceptibility source separation toward iron and myelin mapping in the brain. *NeuroImage*. 2021;240:118371.
110. Miyashita Y. Operating principles of the cerebral cortex as a six-layered network in primates: Beyond the classic canonical circuit model. *Proc Japan Acad B*. 2022;98(3):93-111.
111. Pankatz L, Rojczyk P, Seitz-Holland J, *et al.* Adverse outcome following mild traumatic brain injury is associated with microstructure alterations at the gray and white matter boundary. *J Clin Med*. 2023;12(16):5415.
112. Liu J, Kou ZF, Tian YQ. Diffuse axonal injury after traumatic cerebral microbleeds: An evaluation of imaging techniques. *Brain Inj*. 2014;9(12):1222-1230.
113. McKee AC, Stein TD, Nowinski CJ, *et al.* The spectrum of disease in chronic traumatic encephalopathy. *Brain*. 2013;136(Pt 1):43-64.
114. Sandsmark DK, Bashir A, Wellington CL, *et al.* Cerebral microvascular injury: A potentially treatable endophenotype of traumatic brain injury-induced neurodegeneration. *Neuron*. 2019;103(3):367-379.
115. Wu Y, Wu H, Guo X, *et al.* Blood–brain barrier dysfunction in mild traumatic brain injury: Evidence from preclinical murine models. *Front Physiol*. 2020;11:1030.
116. Ward RJ, Zucca FA, Duyn JH, *et al.* The role of iron in brain ageing and neurodegenerative disorders. *Lancet Neurol*. 2014;13(10):1045-1060.
117. Tohka J. Partial volume effect modeling for segmentation and tissue classification of brain magnetic resonance images: A review. *World J Radiol*. 2014;6(11):855-864.
118. Sui YV, Masurkar AV, Rusinek H, *et al.* Cortical myelin profile variations in healthy aging brain: A T1w/T2w ratio study. *NeuroImage*. 2022;264:119743.
119. Northall A, Doehler J, Weber M, *et al.* Layer-specific vulnerability is a mechanism of topographic map aging. *Neurobiol Aging*. 2023;128:17-32.
120. Aggarwal M, Nauen DW, Troncoso JC, *et al.* Probing region-specific microstructure of human cortical areas using high angular and spatial resolution diffusion MRI. *NeuroImage*. 2015;105:198-207.
121. Hallgren B, Sourander P. The effect of age on the non-haemin iron in the human brain. *J Neurochem*. 1958;3(1):41-51.
122. Marquand AF, Rezek I, Buitelaar J, *et al.* Understanding heterogeneity in clinical cohorts using normative models: Beyond case-control studies. *Biol Psychiatry*. 2016;80(7):552-561.
123. Wunderle K, Hoeger KM, Wasserman E, *et al.* Menstrual phase as predictor of outcome after mild traumatic brain injury in women. *J Head Trauma Rehabil*. 2014;29(5):E1-E8.
124. Gallagher V, Kramer N, Abbott K, *et al.* The effects of sex differences and hormonal contraception on outcomes after collegiate sports-related concussion. *J Neurotrauma*. 2018;35(11):1242-1247.
125. Tierney RT, Sitler MR, Swanik CB, *et al.* Gender differences in head-neck segment dynamic stabilization during head acceleration. *Med Sci Sports Exerc*. 2005;37(2):272-279.
126. Lee J, Ji S, Oh SH. So you want to image myelin using MRI: Magnetic susceptibility source separation for myelin imaging. *Magn Reson Med Sci*. 2024;23(3):291-306.
127. Li Z, Feng R, Liu Q, *et al.* APART-QSM: An improved sub-voxel quantitative susceptibility mapping for susceptibility source separation using an iterative data fitting method. *NeuroImage*. 2023;274:120148.

Magnetic susceptibility of the hippocampal subfields and basal ganglia in acute mild traumatic brain injury

Christi A. Essex[a,*], Mayan J. Bedggood[a], Jenna L. Merenstein[b], Catherine Morgan[c, d], Helen C. Murray[e], Samantha J. Holdsworth[f], Richard L. M. Faull[e], Patria Hume[g], Alice Theadom[a], Mangor Pedersen[a]

[a]Department of Psychology and Neuroscience, Auckland University of Technology, Auckland 0627, New Zealand
[b]Brain Imaging and Analysis Center, Duke University Medical Center, Durham, NC 27710, United States
[c]Center for Advanced MRI, The University of Auckland, Auckland 1023, New Zealand
[d]School of Psychology and Centre for Brain Research, The University of Auckland, Auckland 1023, New Zealand
[e]Center for Brain Research, The University of Auckland, Auckland 1023, New Zealand
[f]Mātai Medical Research Institute, Gisborne 4010, New Zealand
[g]Sports Performance Research Institute New Zealand, Auckland University of Technology, Auckland 0627, New Zealand

*Christi A. Essex: christi.essex@autuni.ac.nz

Abstract. Despite vulnerability to microstructural tissue damage following mild traumatic brain injury (mTBI), key subcortical brain regions have been overlooked in quantitative susceptibility mapping (QSM) studies. Alterations to tissue composition in the functionally and structurally distinct hippocampal subfields and basal ganglia regions may reflect distinct symptomatology, and better characterisation of these regions is needed to increase our understanding of mTBI pathophysiology. To address this issue, we analysed differences in positive and negative QSM values between 25 males with acute (< 14 days) sports-related mTBI (sr-mTBI) and 25 age-matched male controls across 10 hippocampal subfields and 16 basal nuclei. Additional variables of interest including age, injury severity, and days since injury at time of the magnetic resonance imaging (MRI) scan were also correlated with both positive and negative susceptibility values. Primary analyses indicated no significant difference in positive susceptibility values between sr-mTBI participants and controls for hippocampal and basal ganglia ROIs. For negative sign values, susceptibility was significantly less negative for sr-mTBI participants in the cornu ammonis 4 (CA4) region only (pFDR = 0.04). In line with the known linear relationship between iron deposition and age in deep grey matter, particularly within the first three decades of life, significant positive relationships were observed between net positive susceptibility and age in the putamen, caudate, red nucleus, parabrachial pigmented nucleus, and ventral pallidum (pFDR < 0.05). Positive relationships were also observed between absolute negative susceptibility values and age in the hippocampal fimbria, caudate, and extended amygdala (pFDR < 0.05), suggesting age-related calcifications in these regions. A negative relationship was observed between absolute negative values and age in the ventral pallidum (pFDR = 0.04), indicating potential changes to myelin content in this region. No significant associations were observed between any other variable and signed susceptibility values. The results of this study contribute to, and extend, prior literature regarding the temporal kinetics of biomagnetic substrates as a function of ageing. Decreased negative susceptibility after mTBI in the CA4 region also suggests potential injury-related effects on myelin content or neuron loss; a particularly interesting finding in light of the well-established vulnerability of cell populations in this region and susceptibility to pathology in chronic traumatic encephalopathy (CTE). The lack of other significant between-group differences suggest that alterations to tissue content may not be quantifiable at the acute stage of injury in subcortical ROIs or may be masked by age-related tissue susceptibility changes as a common feature across all participants in this young cohort. Future research should consider the use of longitudinal study designs to mitigate the influence of these factors.

Keywords: basal ganglia; brain iron; concussion; hippocampal subfields; mild traumatic brain injury; quantitative susceptibility mapping.

Introduction

Whilst participation in sports can have many physical and psychological benefits, there is a non-negligible risk of sustaining a mild traumatic brain injury (mTBI). This is the most common form of traumatic brain injury (TBI),[1] and reports suggest that up to 30% of all TBI cases are mild head injuries resulting from sports participation.[2] The related changes to cognition, mental health, and physiology can be far from what categorisation as a "mild" injury would suggest, significantly degrading quality of life and participation in activities of daily living.[3] These symptoms are generally associated with the acute and subacute stages, but may persist for decades after injury.[4–6] In addition, repeated instances of mild head trauma expose individuals to a mTBI-related form of progressive neurodegeneration, chronic traumatic encephalopathy (CTE),[3,7] and increased risk of premature mortality.[8] Given the popularity of sports the world over, the issue of mTBI warrants careful consideration.

A mTBI is induced by either impact or inertial forces[9] which transmit mechanical energy to the brain[10] causing primary and secondary injury.[11] Primary injury occurs at the time of the incident when the brain is displaced within the skull, damaging the neurons, glia, and blood vessels of the cerebral tissues.[12] mTBI is most often associated with a diffuse primary injury, specifically diffuse axonal injury, whereby the cellular nerve fibers are stretched, causing cytoskeletal damage.[11,13,14] Secondary injury refers to the resultant dynamic physiological processes catalysed by the

primary injury; this complex and self-perpetuating cascade of biomechanical and metabolic disturbance within the affected tissues can propagate for months after the initial impact.[15] This includes, but is by no means limited to, altered neurotransmitter signalling, changes to cerebral blood flow, mitochondrial dysfunction, blood-brain barrier (BBB) disruption, oxidative stress, demyelination, and neuroinflammatory responses.[9,11,16] However, the underlying pathophysiology of mTBI remains poorly understood.[14]

Iron is an essential co-factor for many neuronal processes including mitochondrial respiration, oxygen transport, cellular metabolism, and synthesis of neurotransmitters, myelin, and DNA.[17,18] However, iron overload, particularly in non-heme form (i.e., iron bound to proteins like ferritin and transferrin rather than heme groups), is increasingly recognised as a driver of secondary neurotoxic events[11,19] including oxidative stress, cellular degeneration, and inflammation.[20–22] Non-heme iron is also the primary source of paramagnetic signals assessed by quantitative susceptibility mapping (QSM), an analytical technique of magnetic resonance imaging (MRI) data that enables quantification of biomagnetic substances in neural tissue.[23–26] As such, mapping distributions of positive susceptibility across the brain as a proxy for iron load represents a promising avenue for investigating potential biomarkers of neuropathology following mTBI. Myelin constitutes the primary source of diamagnetic contrast on QSM,[27] but calcium[28–30] and certain proteins such as beta-amyloid (Aβ) and tau also contribute[31–33] and concentrations of all aforementioned biomagnetic substrates may change as a function of injury-related processes in mTBI.[11,16,22,34] Isolation of these susceptibility sources may therefore provide crucial insight into the subtle biodynamics and injury cascades occurring shortly after injury.

Research using QSM to examine alterations to grey matter after mTBI have focused on markers of iron accumulation in the basal ganglia as a proxy for secondary injury processes. Iron, as a fundamental component of neurotransmitter synthesis, is more abundant in these deep regions compared to cortical grey matter[35] which supports the high metabolic demand related to signal processing.[11] Dense concentrations of iron are particularly noteworthy in the globus pallidus, red nucleus, substantia nigra, putamen, caudate, and thalamus[35] and may predispose these regions to iron-mediated disorders.[36] Additional vulnerability to shear and strain damage in mTBI[37] due to axons originating from, terminating in, or intersecting with these nuclei,[11,38,39] for example thalamo-cortical projections,[40] may further increase the risk of iron-driven secondary injury.

Within this existing body of research, a focus on either total deep grey matter,[41,42] basal ganglia segmentations,[43–45] or a combination of the two,[46,47] have predominated. Where segmentations have been employed, the analyses are typically confined to major subcortical structures such as the caudate, putamen, thalamus, and globus pallidus,[43,44,46] potentially overlooking the susceptibility of many other deep grey matter regions to cytotrauma. To date, only two studies[45,47] have extended their investigations to include additional subcortical structures such as the nucleus accumbens, amygdala, and hippocampus, which exhibit similar iron-related vulnerability as the basal nuclei. However, even these more comprehensive examinations have lacked the anatomical specificity needed to identify distinct structural and functional subregions that may be differentially affected by mTBI, representing a crucial oversight in the QSM-mTBI literature.[11] These include distinct pallidal substructures, limbic structures, and other associated nuclei. Examining these additional subregions may be critical for identifying potentially more subtle mTBI-related changes to biomagnetic substrates that could otherwise be washed out when examining entire regions-of-interest (ROI), as we have previously demonstrated in the cortical grey matter.[48]

Pathological changes in these deep brain structures responsible for motor control,[49,50] emotional regulation,[51] learning,[52] and memory,[53] may also drive the heterogeneity of mTBI symptomatology. Iron overload in the deep grey matter in particular may significantly alter cognitive function after mTBI.[54] The convergent evidence indicates that more comprehensive assessments of the subcortical nuclei are warranted. In addition, examining the hippocampus using a whole-ROI approach neglects the structural and functional distinctions between its subfields. The hippocampus

is particularly vulnerable to injury,[55] and as a central hub for memory[56] damage to this area may be related to the memory impairments characteristic of mTBI.[57] Macroscopic methods may thus risk masking specific hippocampal pathologies that are likely related to mTBI symptomatology. In addition, temporal regions, including the hippocampus, also exhibit region-specific atrophy and tau hyperphosphorylation (p-tau) in CTE,[58–60] which may be related to iron dyshomeostasis.[22,61,62]

Taken together, these studies suggest that investigations differentiating between distinct brain regions and their substructures are necessary to better understand the pathology of mTBI, and may assist in elucidating the genesis of specific injury-related deficits. To contribute to the sparse extant literature, we conducted the first QSM analysis of mTBI effects in the hippocampal subfields alongside the most detailed segmentation of the basal ganglia to date. This study aimed to: 1) assess the effects of mTBI on positive (iron-related) and negative (myelin-, protein-, calcium-related) net magnetic susceptibility to better understand acute pathology in, a) 16 segmentations of the basal ganglia, and b) 10 segmentations of the hippocampus, and; 2) elucidate the relationship between magnetic susceptibility in these regions and potentially moderating variables including age, and injury latency and severity. Although many of these regions are both high in iron and susceptible to mTBI-related pathology, the limited prior literature has produced mixed results regarding the direction of iron-related effects, if any. Furthermore, the absence of QSM thresholded for inter-voxel sign in previous studies precludes the development of robust hypotheses regarding the directionality of negative susceptibility effects in grey matter. As such, there were no specific *a priori* hypotheses related to either susceptibility sign, nor secondary correlational analyses.

Materials and Methods

Ethical approval for this research was obtained from the Health and Disabilities Ethics Committee (HDEC) (Date: 18/02/2022, Reference: 2022 EXP 11078) and institutional approval was also obtained from the Auckland University of Technology Ethics Committee (AUTEC) (Date: 18/02/2022, Reference: 22/12). In accordance with the Declaration of Helsinki, all participants provided written informed consent prior to data collection.

Participants

Data from 25 male contact sports players (M = 21.10 years old [16-32], SD = 4.59) with acute sports-related mTBI (sr-mTBI) ($<$ 14 days; M = 10.40 days, SD = 3.03) and 25 age-matched male controls (M = 21.10 years old [16-32], SD = 4.35) were used for this observational study (see Table 1). To mitigate any potential confounding effects due to the known linear relationship between brain iron content and age,[17,35,63–67] particularly in this young cohort, we ensured that ages were not significantly different between groups ($t(48) = 0.00$, $p = 1.00$). Clinical sr-mTBI participants were recruited through three Axis Sports Medicine clinics (Auckland, New Zealand), via print and social media advertisements, word-of-mouth, and through community-based pathways including referrals from healthcare professionals and sports team management. Each clinical participant was required to have a confirmed sr-mTBI diagnosis by a licensed physician as a prerequisite for study inclusion, and symptom severity was assessed using the Brain Injury Screening Tool (BIST)[68] either upon presentation to Axis clinics or electronically following recruitment. Healthy controls (HC) were recruited through print and social media advertisements, and word-of-mouth. Exclusion criteria for all participants included a history of significant medical or neurological conditions unrelated to the study's objectives and contraindications for MRI. Additionally, controls were excluded if they had any recent history of mTBI events ($<$ 12 months) or were living with any long-term effects of previous mTBI. All participants completed a brief demographic questionnaire and attended a 1-hour MRI scan at The Centre for Advanced MRI (CAMRI), Auckland, New Zealand. All scans were reviewed by a certified neuroradiologist consultant for clinically significant findings. While some incidental findings were identified,

none were considered to be clinically significant and required no follow-up. MRI findings for this cohort are reported in extensive detail in previous publications.[48]

Table 1: Summary of sr-mTBI participant clinical characteristics

ID	Age	DSI	BIST Score	MOI
mTBI-01	< 20	5 days	140	Rugby
mTBI-02	< 20	5 days	12	Rugby
mTBI-03	20s	6 days	78	Rugby
mTBI-04	< 20	13 days	18	Rugby
mTBI-05	< 20	12 days	61	Rugby
mTBI-06	20s	13 days	42	Rugby
mTBI-07	20s	13 days	13	Football
mTBI-08	20s	12 days	6	Hockey
mTBI-09	20s	6 days	56	Rugby
mTBI-10	< 20	12 days	54	Rugby
mTBI-11	20s	10 days	52	Rugby
mTBI-12	30s	13 days	13	Football
mTBI-13	< 20	5 days	79	Rugby
mTBI-14	20s	13 days	2	Rugby
mTBI-15	< 20	13 days	22	Rugby
mTBI-16	< 20	8 days	117	Futsal
mTBI-17	20s	13 days	*	Rugby
mTBI-18	20s	10 days	34	Gymnastics
mTBI-19	20s	13 days	28	Jiu-jitsu
mTBI-20	20s	11 days	69	Surfing
mTBI-21	< 20	7 days	14	Rugby
mTBI-22	< 20	13 days	39	Judo
mTBI-23	< 20	9 days	34	Rugby
mTBI-24	< 20	12 days	68	Rugby
mTBI-25	20s	12 days	17	Rugby
Mean mTBI	21.10 (4.59) years	10.4 (3.03) days	44.5 (35.0) /160	
Mean HC	21.10 (4.35) years			

Note. Diagnostic assessment was limited to the volume T1, SWI and DWI sequences with only limited interpretation of the multi-echo T2 stack. Clinical assessments were relevant to the identification of micro-haemorrhages, areas of siderosis, T1 appearance, gliosis, volume, ventricular volumes and non-neurological findings. Age is reported in a range to prevent re-identification of participants. The possible range of BIST scores is 0 (min) to 160 (max). Clinical group data corresponded to date at MRI only with the exception of the BIST[68] acquired >24 hours post-injury prior to MRI scanning (<14 days post). Abbreviations are: mTBI = mild traumatic brain injury; HC = healthy control; ID = unique identifier; DSI = days since injury; BIST = Brain Injury Screening Tool[68]; MOI = mechanism of injury; MRI = magnetic resonance imaging; L = Left; R = right; * = missing data (BIST incomplete on the Axis Sport Medicine Clinic patient portal, reason unknown).

Neuroimaging

Details on image acquisition and processing have been previously reported,[48] and are summarised here for brevity.

Acquisition

MRI data were acquired on a 3T Siemens MAGNETOM Vida Fit scanner (Siemens Healthcare, Erlangen, Germany) equipped with a 20-channel head coil. A 3D flow-compensated single-echo gradient-recalled echo (GRE) sequence was used to obtain magnitude and unfiltered phase images suitable for QSM reconstruction. Data were collected at 1 mm isotropic voxel size with matrix size = 180 x 224 x 160 mm, TR = 30 ms; TE = 20 ms; FA = 15°; FoV = 180 mm (LR) × 224 mm (AP) in a total acquisition time of ∼3.43 minutes. For each participant, a high-resolution 3D T_1-weighted (T_1w) anatomical image volume was acquired for coregistration, parcellation and segmentation using a Magnetisation-Prepared Rapid Acquisition Gradient Echo (MPRAGE) sequence (TR = 1940.0 ms; TE = 2.49 ms, FA = 9°; slice thickness = 0.9 mm; FoV = 230 mm; matrix size = 192 x 512 x 512 mm; GRAPPA = 2; voxel size 0.45 x 0.45 x 0.90 mm) for a total acquisition time of ∼4.31 minutes. DICOMs were converted to NIfTI files and transformed to brain imaging data structure (BIDS)[69] for further processing using *Dcm2Bids*[70] version 3.1.1, which is a wrapper for *dcm2niix*[71] (v1.0.20230411).

QSM processing

QSM images were reconstructed using QSMxT[72] v6.4.2 and used a robust two-pass combination method for artefact reduction,[73] rapid open-source minimum spanning tree algorithm (ROMEO) for phase unwrapping,[74] background field removal with projection onto dipole fields (PDF),[75] sparsity-based rapid two-step dipole inversion (RTS),[76] and whole-brain susceptibility referencing; a pipeline congruent with recent consensus statement recommendations for best-practice QSM reconstruction.[77]

For each participant, the raw magnitude image was skull-stripped using FSL's *BET*[78] with robust brain centre estimation and a fractional intensity threshold of between 0.3 and 0.6. Binary masks were derived from the skull-stripped magnitude image and applied to the susceptibility maps to erode non-brain signal around the brain perimeter using *fslmaths*. Skull-stripped magnitude images were linearly registered to the California Institute of Technology's 168 (CIT168) T_1w template[79] in Montreal Neurological Institute 152 (MNI152) space using FMRIB's Linear Transformation Tool (FLIRT)[80–82] with 12 degrees of freedom (DoF) suitable for atlas-based registration. The resulting transformation matrix was then used for spatial normalisation of the QSM images using FLIRT.[80–82] Using inter-voxel thresholding methods,[83,84] QSM maps were then thresholded into separate maps of net positive voxels (QSM^+) and net negative (QSM^-) voxels with *fslmaths*, by separating values across voxel boundaries above (QSM^+) and below (QSM^-) zero. This approach may enable more targeted analyses of specific susceptibility sources without the confounding effects of inter-voxel averaging. Both QSM^+ and QSM^- susceptibility maps were used in subsequent analyses.

Basal ganglia segmentation

The CIT168 basal ganglia mask, available in MNI152 space, provides a detailed 16-part probabilistic atlas of the basal nuclei.[79] Derived from T_1w and T_2-weighted *in vivo* structural images of 168 participants from the Human Connectome Project,[85] this atlas is openly accessible via the NeuroVault Collection (No. 3145). The segmentations included: the striatum, comprised of the putamen (Pu), caudate (Ca), and nucleus accumbens (NAC); the pallidum, which includes the globus pallidus externus (GPe), globus pallidus internus (GPi), and ventral pallidum (VeP); and the substantia nigra, including the substantia nigra pars compacta (SNc) and substantia nigra pars reticulata (SNr). Additional segmentations covered the extended amygdala (EXA) and other limbic structures including the hypothalamus (HTH) and mammillary nucleus (MN), the mesolimbic ventral tegmental area (VTA) and the associated parabrachial pigmented nucleus (PBP), the epithalamic habenular nuclei (HN), the subthalamic nucleus (STH), and the red nucleus (RN) (see Fig. 1 for reference).

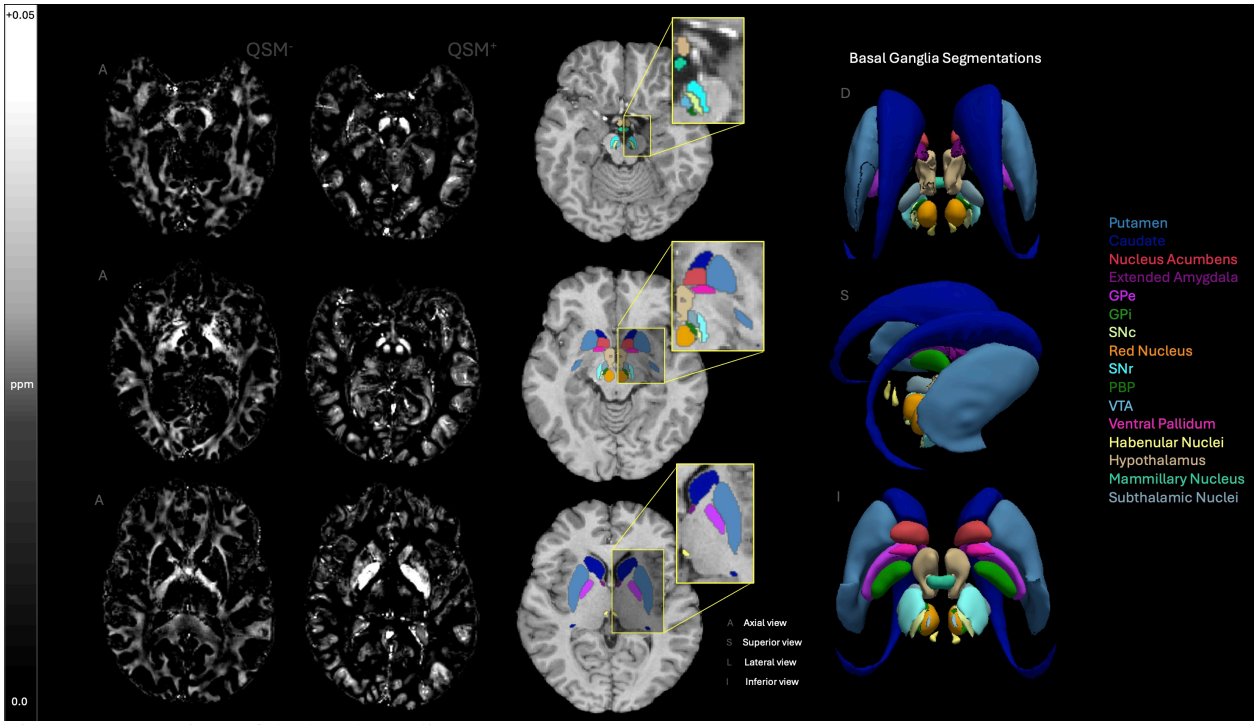

Fig 1: Segmentations of the basal ganglia

Sixteen bilateral segmentations of the basal ganglia are displayed across axial (A) slices of the T_1w CIT168-MNI152 brain template, as well as 3D renderings from superior (S), inferior (I), and lateral (L) perspectives for both the CIT168-MNI152 brain template and corresponding basal ganglia mask. The key for each basal nuclei is provided in the respective colour of that region. Axial slices for signed maps (QSM^- and QSM^+) are shown at comparable depths for visual reference. Susceptibility values are expressed in parts per million (ppm) ranging from 0.0 to +0.05, and negative maps are multiplied by -1 for better visualisation. GPe = globus pallidus externus; GPi = globus pallidus internus; SNc = substantia nigra pars compacta; SNr = substantia nigra pars reticulata; PBP = parabrachial pigmented nucleus; VTA = ventral tegmental area.

Hippocampal segmentation

Prior to hippocampal segmentation, bias field correction was applied to each participants' T_1w images using the *N4* algorithm[86] from the Advanced Normalisation Tools (ANTs) library.[87] The bias field-corrected T_1w images were then processed with FreeSurfer's *recon-all* pipeline.[88] Subsequent unilateral segmentation of the hippocampal subfields was conducted using an automated, FreeSurfer-based pipeline.[89] This hippocampal segmentation leverages a probabilistic atlas derived from ultrahigh-field, *ex vivo* MRI data with approximately 0.1 mm isotropic voxel resolution to automate the delineation of hippocampal substructures for each hemisphere. Three resulting hippocampal segmentation schemes were produced, a macroscopic head/body/tail segmentation (denoted as "HBT"), a detailed scheme where molecular subregions are merged with the nearest neighbours, specifically the CA subfields (labeled "CA"), and a detailed segmentation where molecular subregions are not merged (referred to as "FS60"). Of these, the mid-detail segmentation (the "CA" scheme) was selected for use in statistical analysis, balancing the level of segmentation detail with the need to mitigate the multiple comparisons problem. The hippocampal subregion masks included in this segmentation: the parasubiculum, presubiculum, subiculum, cornu ammonis (CA) regions CA1, CA3 (which includes CA2), and CA4, the hippocampal-amygdala transition area (HATA), fimbria, hippocampal tail, and hippocampal fissure. For full segmentation details, refer to Table 2, and for visual representation see Fig. 2.

Table 2: Hippocampal subfields and their closest anatomical structures in "CA" segmentation

Parasubiculum	Parasubiculum
Presubiculum head	Presubiculum
Presubiculum body	
Subiculum head	Subiculum
Subiculum body	
CA1 head	CA1
CA1 body	
CA3 head	CA3
CA3 body	
CA4 head	CA4
CA4 body	
GC-ML-DG head	
GC-ML-DG body	
Molecular layer HP-head	Closest structure*
Molecular layer HP-body	
HATA	HATA
Fimbria	Fimbria
Hippocampal tail	Hippocampal tail
hippocampal fissure	hippocampal fissure

* = voxels in the molecular layer are assigned the label of the closest voxel that is neither molecular layer nor background.

Note. This table details the unilateral segmentations of hippocampal subfields within the volume labelled as "CA", along with associated hippocampal structures. Subfield CA2 is incorporated into CA3. Table is also available at the FreeSurfer Wiki.

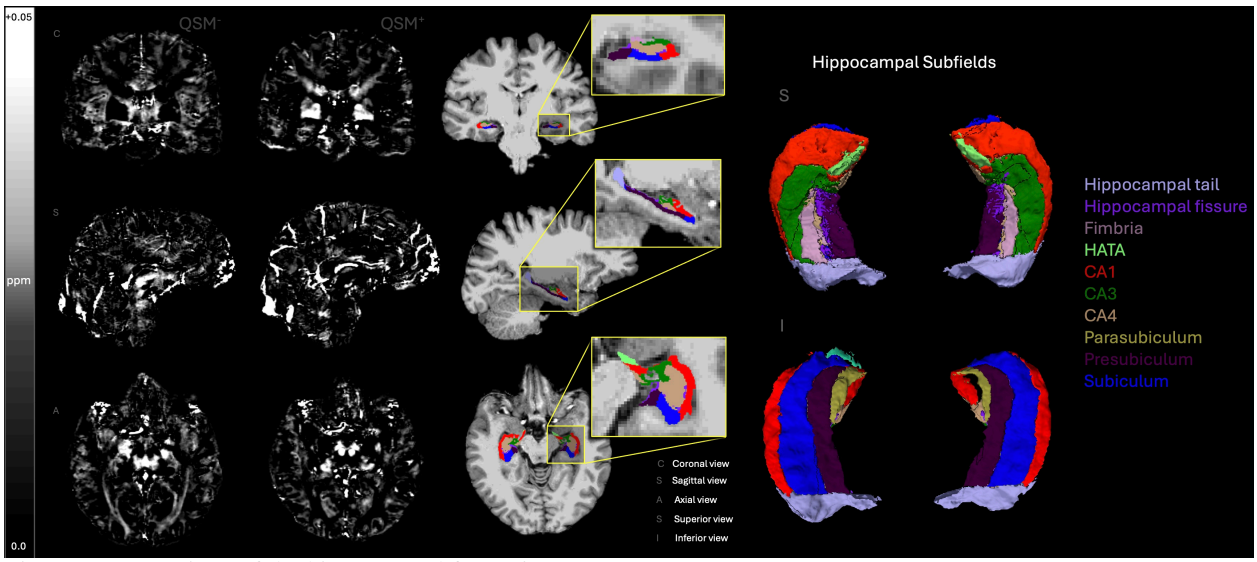

Fig 2: Segmentations of the hippocampal formation

Visual representation of the unilateral hippocampal segmentations provided by FreeSurfer under the "CA" scheme, displayed across coronal (C), axial (A), and sagittal (S) views as well as a 3D rendering from the inferior (I) and superior (S) views. The key for each hippocampal region is provided in the respective colour of that region. Signed maps (QSM^- and QSM^+) from which susceptibility values are sampled for each hippocampal region are shown for each orientation (C, A, S). Susceptibility values are expressed in ppm ranging from 0.0 to +0.05, and negative maps are multiplied by -1 for better visualisation. HATA = hippocampal-amygdala transition area; CA 1-4 = cornu ammonis regions 1-4 (Note: CA2 is included in CA3).

To standardise each of the hippocampal subfield masks for data analysis, each subjects' skull-stripped T_1w brain image and left and right hemisphere hippocampal masks were converted from FreeSurfer's .mgz format to NIfTI format (.nii.gz) using MRtrix3 *mrconvert*.[90] After format conversion, each subjects' T_1w brain image was registered to the CIT168 T_1w template in MNI152 space[79] using FLIRT[80–82] with 12 DoF. The resulting transformation matrix was then applied to both the left and right hemisphere hippocampal masks using nearest-neighbour interpolation to maintain the integrity of discrete hippocampal label boundaries during transformation. These steps ensured spatial alignment between each of the hippocampal masks, the signed susceptibility maps, and the CIT168 segmentations of the basal ganglia provided in MNI152 space.[79]

Statistical analyses

Statistical analyses were conducted at the bilateral level using MATLAB (2024a). Average positive and negative susceptibility values from both QSM^+ and QSM^- maps were extracted from the 16 bilateral segmentations of the basal ganglia. For the 10 hippocampal regions, left and right hemisphere susceptibility values were extracted and averaged to yield a bilateral measure. Any ROIs in which zero values were present for any participant were omitted from subsequent analysis (the PBP for QSM^- analyses, and the HN for QSM^+ analyses). There were no zero values for any participants for any hippocampal ROIs. To evaluate the effects of sr-mTBI compared to healthy controls, two-tailed independent sample t-tests were performed for each subcortical ROI, assessing group differences in susceptibility values. To control for multiple comparisons, a Benjamini-Hochberg false discovery rate (FDR) correction[91] was applied separately to the 15 p-values corresponding to the remaining basal nuclei (all nuclei except the PBP for QSM^- and HN for QSM^+) and the 10 p-values for the hippocampal regions, for each signed susceptibility map. Since participants were precisely age-matched, age was not treated as a covariate or confounding factor in the between-group comparisons. However, to examine the associations between QSM values and age across the entire cohort, partial Pearson correlation coefficients were computed. These analyses assessed the potential linear relationship between age and both positive and negative susceptibility values across all subcortical ROIs, controlling for group status. Additional relationships were explored between susceptibility values and sr-mTBI-related variables using Pearson correlation coefficients, including BIST[68] scores and injury latency (days since injury; DSI) variables, for clinical participants only. Due to missing BIST[68] data, mTBI-17 was excluded from analyses related to injury severity. Correlations were also corrected for 15 and 10 ROI-wise comparisons, respectively, using FDR procedures.[91]

Results

Regional analyses

Using two-tailed independent sample t-tests, differences in bilateral regional susceptibility (positive and negative) were examined for each of the hippocampal subfields and basal nuclei. P-values were corrected for 10 and 15 comparisons, respectively, using FDR procedures.[91]

Basal nuclei

Results showed no significant differences in positive or negative susceptibility between sr-mTBI participants and HC for any of the basal nuclei (pFDR > 0.05; see Fig. 3).

Hippocampal subfields

There were no significant differences in positive susceptibility between groups for any of the 10 hippocampal subfields (see Fig. 3). Negative susceptibility values were significantly less negative for sr-mTBI participants (M = -0.007, SD = 0.002) than HC (M = -0.008, SD = 0.001) in the CA4 only ($t(48)$ = -2.99, pFDR = 0.04). No significant differences between groups for negative susceptibility values were observed for any other hippocampal ROI.

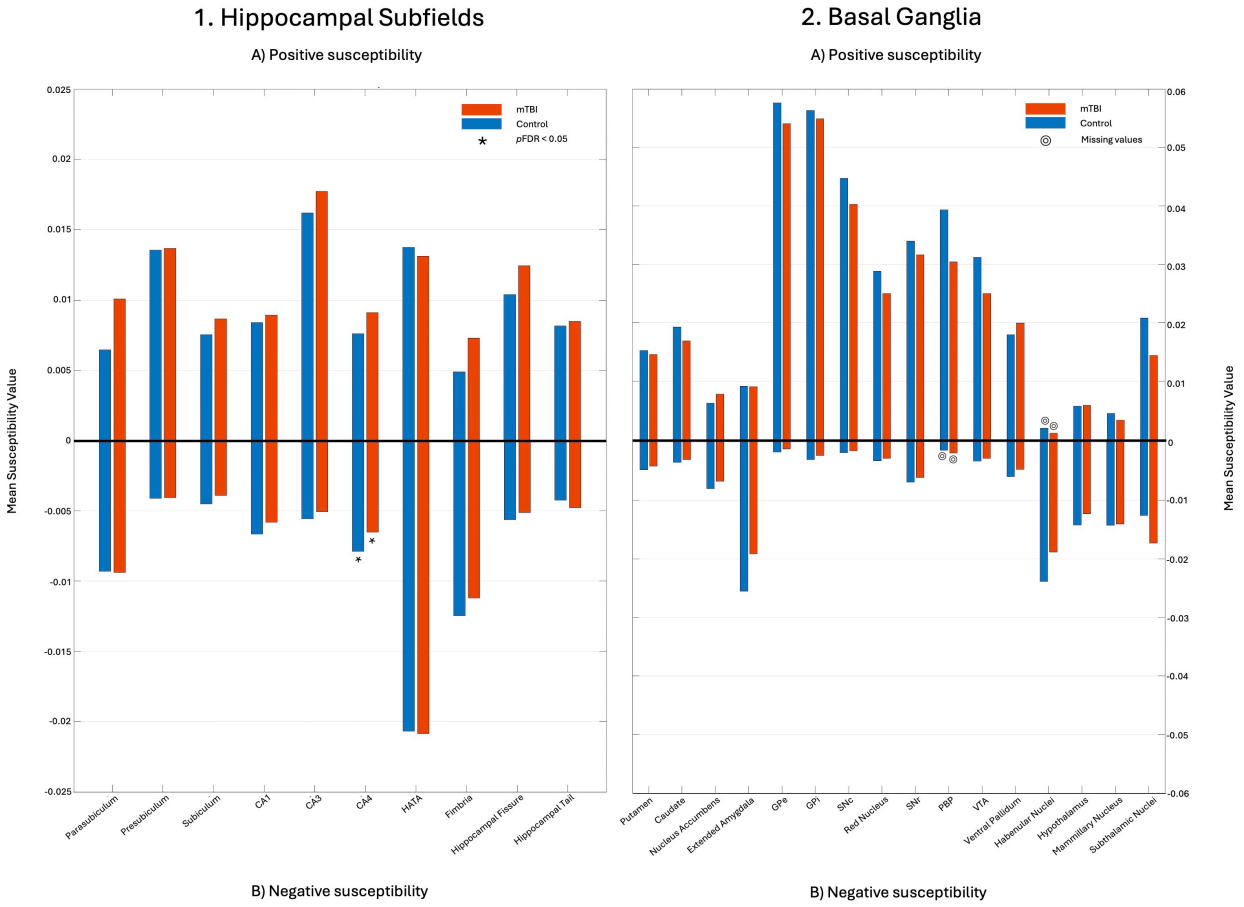

Fig 3: Mean susceptibility values in the hippocampal and basal ROIs

Bar plots showing the mean susceptibility values for mTBI (red bars) versus HC (blue bars) for: 1. Hippocampal subfields, and; 2. Basal banglia, for both A) positive and B) negative susceptibility maps. Susceptibility is measured in ppm. ⋆ = significant differences between groups; ⊙ = regions omitted from further analysis due to zero ROI-wise values for any participant.

Bilateral regional correlations

Partial Pearson correlation coefficients were used to assess the relationship between age and both positive and negative susceptibility for the 10 hippocampal and 15 viable basal segmentations, controlling for group status. Additionally, correlations between both susceptibility signs and 1) BIST scores[68] as an indicator of injury severity, and; 2) DSI at the time of the MRI scan as a marker of injury latency, were conducted for the mTBI sample only. Negative susceptibility was transformed into absolute values to more clearly illustrate relationships between variables. P-values were adjusted separately for the 10 hippocampal subfields and 15 segmentations of the basal nuclei using FDR methods.[91]

Age

No statistically significant correlations were observed between age and positive susceptibility values for any hippocampal ROI, however, a significant positive correlation between age and absolute negative susceptibility in the fimbria ($r(48) = 0.42$, pFDR = 0.03) was observed, suggesting age-related increases in negative susceptibility (i.e., susceptibility becomes more negative with age) (see Fig. 4).

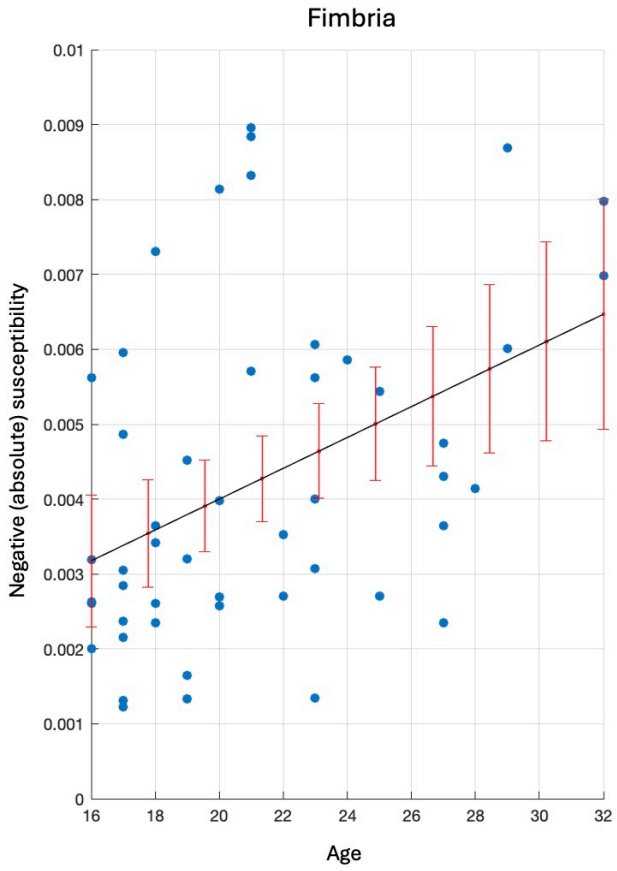

Fig 4: Significant correlations: Age and negative susceptibility in the fimbria

Scatter plot illustrating the statistically significant correlation between negative (absolute) susceptibility values in the hippocampal fimbria and age. A line of best fit (black) highlights the trend. 95% confidence interval bars (red) indicate the predicted range for true values, providing a measure of uncertainty in the model.

Results indicated significant age-related increases in positive susceptibility values in several basal regions, including the putamen ($r(48) = 0.64$, pFDR < 0.001), caudate ($r(48) = 0.50$, pFDR = 0.001), red nucleus ($r(48) = 0.66$, pFDR < 0.001), PBP ($r(48) = 0.40$, pFDR < 0.02), and ventral pallidum ($r(48) = 0.35$, pFDR = 0.04) (see Fig. 5).

Significant positive correlations were also evident between age and absolute negative susceptibility in the caudate ($r(48) = 0.39$, pFDR = 0.04) and extended amygdala ($r(48) = 0.51$, pFDR = 0.002) suggesting that susceptibility in these regions tends to increase (become more negative) with age. Significant negative correlations were also observed between age and absolute negative susceptibility values in the ventral pallidum ($r(48) = -0.37$, pFDR = 0.04), suggesting that susceptibility tends to decrease (become less negative) with age (see Fig. 5).

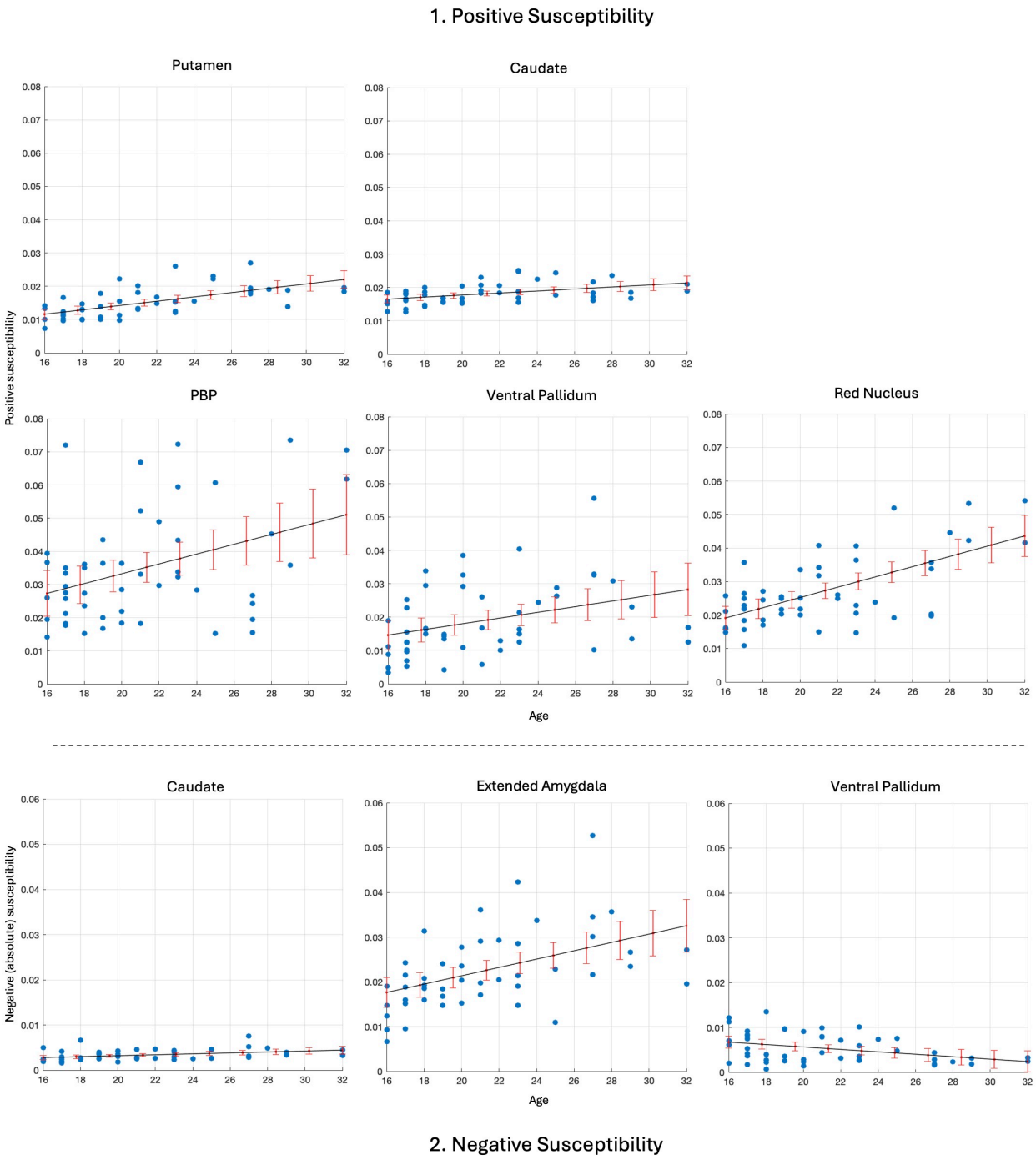

Fig 5: Significant correlations: Age and susceptibility values in the basal ganglia

Scatter plots illustrating the statistically significant correlations between both 1. Positive and 2. Negative (absolute) susceptibility values and age in basal ROIs. A line of best fit (black) highlights the trend. 95% confidence interval bars (red) indicate the predicted range for true values, providing a measure of uncertainty in the model.

Injury severity and injury latency

No statistically significant correlations were observed between both positive and absolute negative susceptibility values and either DSI or BIST scores, for any basal nuclei or hippocampal subfield.

Discussion

Despite the vulnerability of the striatum and other deep nuclei to mechanical strain, cytoskeletal damage, and secondary metabolic disruptions after mTBI, all of which are risk factors for iron accumulation, previous QSM research has not yet achieved the anatomical specificity necessary to extensively characterise mTBI-related alterations to tissue content in the subcortical grey matter. To address this limitation, we performed a highly detailed segmentation of the basal ganglia alongside the first QSM analysis of the distinct hippocampal subfields in mTBI. QSM images were thresholded for inter-voxel sign prior to analysis. Between-group comparisons showed no significant differences between mTBI participants and controls for either susceptibility sign in the basal ganglia, or for positive sign in the hippocampal subfields. However, the hippocampal CA4 region exhibited significantly decreased (less negative) negative susceptibility values for the mTBI group relative to healthy controls. Correlational analyses also revealed no significant associations between either susceptibility sign and injury latency or severity in the mTBI group within any ROI. Congruent with expected age-related trends, positive susceptibility values in the putamen, caudate, PBP, ventral pallidum, and red nucleus increased with age. Age-related increases in negative susceptibility were also apparent in the hippocampal fimbria, the caudate, and the extended amygdala, but decreased with age in the ventral pallidum.

Negative susceptibility is decreased in CA4 after mTBI

The hippocampal CA4 region is particularly susceptible to both tau pathology in CTE[59,92] and associated local dendritic swelling which are considered supporting features for diagnosis.[58,93] As a microtubule-associated protein, tau is a promising early indicator of axonal injury in mTBI.[94] While focal accumulation of tau would likely result in increased negative susceptibility on QSM,[32,33] the observation of decreased negative susceptibility in CA4 reported here nonetheless supports an axonal-injury model. This type of injury is characteristic of both TBI[95] and mTBI,[96] and is associated with disruptions of the myelin sheath[97,98] or demyelination as demonstrated in both animal models[99] and human QSM studies investigating sr-mTBI.[100] Although density of myelinated fibers is relatively low in the hilus (CA4),[101] disruptions to myelination in this region could plausibly account for localised decreases in negative susceptibility, suggesting this area could be vulnerable to axonal damage during mTBI and could speculatively represent an acute component of the injury cascade that culminates in tauopathy as a downstream pathological event later in life for some people.

Other plausible explanations for decreased negative susceptibility after mTBI could be related to phagocytosis of stressed cells and their components, including myelin. Microglia and macrophages are known to target and phagocytose distressed but still viable cells, even in the absence of cell death.[102] This could result in a reduction in negative susceptibility if cells within a ROI are particularly sensitive to even mild injury and resultant distress signalling. Indeed, research suggests that the CA4 region is selectively vulnerable to sustained cell loss after head injury.[103,104] Of particular relevance to this hypothesis, the hilus contains glutamatergic mossy cells and GABA-ergic somatostatin-expressing hilar interneurons which are highly vulnerable to damage and excitotoxicity in temporal lobe epilepsy, TBI, and mTBI.[105–107] Indeed, murine models demonstrate irreversible loss of somatostatin-expressing hilar interneurons within just four hours of injury.[103]

In addition, mossy cells, unique to the hilus, are especially predisposed to metabolic disruptions and excitotoxicity, as well as premature neurodegenerative processes.[107] Murine models also demonstrate the link between TBI and damage to hilar mossy cells, the "irritable mossy cell" hypothesis, which may account for the memory-related impairments observed after TBI.[106,107] Mossy cells also express proteins that may be implicated in depression, and reductions in mossy cells may increase levels of anxiety[107]; both of which are mood-related symptoms of mTBI.[108]

Whilst speculation is interesting, in the absence of histological analysis, the precise pathological mechanisms cannot be accurately characterised. However, at minimum the results presented here support prior research noting the vulnerability of the hippocampus, and in particular the CA4, to mTBI-related pathology.

Positive susceptibility in subcortical grey matter and mTBI

This, and other,[41–47] QSM investigations have found no significant evidence of iron accumulation in the basal nuclei or hippocampus after mTBI. However, iron accumulation as a pathologic feature of mTBI in many of these regions is well documented, contradicting the lack of iron-related findings reported here. For example, an iron-sensitive magnetic field correlation (MFC) study[37] reported iron accumulation in the globus pallidus and thalamus following mTBI. Investigations using susceptibility weighted imaging (SWI) have also identified iron deposition in the caudate, thalamus, right substantia nigra, red nucleus, lenticular nucleus, splenium of the corpus callosum, and hippocampus in chronic mTBI, concomitantly linking accumulations in the substantia nigra with cognitive dysfunction.[54] Studies using T_2^* imaging have identified iron deposition in cortical, subcortical (left putamen, bilateral hippocampal), and brainstem regions,[109] along with reports of accumulation in the lateral geniculate nucleus of the thalamus,[110] with both studies citing associations between elevated iron and post-mTBI headache symptomatology.

Additionally, animal models of controlled cortical impact TBI have demonstrated iron deposition in the thalamus ipsilateral to the impact site upon histological examination, with focal depositions co-localising T_2 hypointensity on MRI.[111] Murine models also report the vulnerability of the hippocampus to oxidative stress and synaptic protein modification, underscoring not only the regional susceptibility to traumatic injury mechanisms, but also identifying a potential role of iron in the generation of cytotoxic free radicals.[112] Post-mortem studies have provided evidence of iron accumulation in hippocampal neurofibrillary tangles (NFTs) in CTE,[61] as well as abnormal hemosiderin-laden macrophages near small vessels in the frontal and temporal lobes less than one year post-injury, indicating ferritin-bound non-heme iron deposition[113] which is corroborated by recent research noting the presence of L-ferritin-positive astrocytes proximal to CTE lesions.[114]

Despite these studies highlighting the vulnerability of the basal nuclei and hippocampus to iron-mediated pathology at multiple stages post-injury, an absence of significant group differences in positive susceptibility observed in this study may suggest a general protective effect conferred by the deep subcortical location of these regions. In contrast, our prior work has demonstrated that the cortex, particularly the parahippocampal gyrus, is susceptible to iron-mediated pathology following mTBI.[48] In more targeted, individualised analyses, cortical iron pathology has been observed in one-third of mTBI participants (rising to 83% when accounting for cortical depth and curvature) across various cortical ROIs, which was related to more severe injury-related symptoms.[115]

It is also reasonable to suggest that the absence of between-group differences in iron markers may reflect the influence of normal age-related increases in iron (for a review, see Madden and Merenstein[17]), which could obscure subtle mTBI-specific effects. Age-related iron deposition is particularly pronounced in the basal nuclei and most evident within the age range of participants in this study, as discussed in more detail further below. This shared characteristic among younger individuals may explain the lack of significant group differences in iron-related markers. In contrast, the general lack of age effects in hippocampal regions and the resultant sensitivity to disruptions in negative susceptibility in the CA4 region supports the hypothesis that changes to biomagnetism which are common to all participants may obscure injury-related susceptibility effects. Consequently, the unique alteration to negative susceptibility values in the hippocampal CA4 thus likely reflect specific pathological consequences of mTBI.

In keeping with these observations, thresholding bulk magnetic susceptibility likely enabled the isolation and identification of weaker negative susceptibility effects, which could otherwise have been diluted or overshadowed by stronger positive susceptibility signals during analysis.[26] This could also account for the lack of significant differences reported in previous studies where neither more rudimentary thresholding or true magnetic source separation techniques were employed to generate separate sign-wise maps,[41–47] providing support for intra- or inter-voxel susceptibility separation techniques, depending on the data acquisition parameters.

mTBI and negative susceptibility in subcortical grey matter

We found no evidence of increased negative susceptibility in the subcortical grey matter following mTBI. However, alterations to varying biomagnetic substrates following TBI have previously been characterised in murine models using QSM and R_2^* imaging alongside histological examinations to assess changes not only to iron, but also myelin and calcium.[116] These models have demonstrated concurrent iron and calcium accumulation, as well as demyelination after impact. These findings are reinforced by additional *in vivo* and *ex vivo* murine models of TBI also reporting significant calcifications, which are proposed as an indirect measure of inflammation[117] and microglia activation[118] following injury. Of particular interest, studies have noted that calcifications often co-localise with paramagnetic iron in TBI.[116] This finding underscores the complex interplay of tissue components affected by mTBI and highlights the contribution of both paramagnetic and diamagnetic substrates to injury pathology. This further validates the need for either source separation, if data are acquired with multi-echo sequences,[119–124] or single-echo-compatible voxel-wise thresholding,[83,84] in QSM research to differentiate these overlapping effects and better elucidate underlying biological mechanisms.

Aβ and tau, two proteins with potentially diamagnetic properties,[31–33] have been associated with both acute injury pathology and later neurodegenerative processes, and are known to co-localise with iron in Alzheimer's disease (AD)[17] and CTE.[61] Tau is a promising fluid biomarker for axonal injury in mTBI[94] and both fluid tau[125,126] and Aβ levels can accumulate at the acute stage of TBI.[127] Focal accumulations may be present in the entorhinal cortex, hippocampus, and striatum (caudate and putamen) as evidenced by PET studies of TBI.[128] The aggregation of both proteins would likely produce differences in negative susceptibility on QSM. However, systematic reviews have noted inconsistencies between studies regarding the presence or absence of Aβ as a pathologic feature of TBI,[128] and similar conflicting evidence exists regarding the biodynamics of tau in mTBI, with some studies suggesting elevations within hours-to-days, and others indicating no difference between individuals with mTBI and controls acutely after injury.[94] These factors may have contributed to the absence of quantifiable increases in negative susceptibility in the present study. Alternatively, and perhaps more plausibly, the results presented here indicate that Aβ and tau are not present in this young cohort[129,130] imaged at the acute stage of a mild head injury.

Temporal biodynamics of positive susceptibility

Iron increases throughout the lifespan as a function of normal ageing.[17,63] Particularly steep increases in brain iron content are present in the red nucleus and substantia nigra within the first 20 years of life, the globus pallidus at approximately 30 years, with maximal values reached in the putamen and caudate at approximately five to six decades after birth.[35] This histological study is supported by extensive QSM investigations,[17] for example, QSM and R_2^* mapping have demonstrated susceptibility increases in the putamen and globus pallidus throughout adulthood, with values in the caudate peaking in the third decade.[66] Other QSM studies have evidenced increased susceptibility values in the caudate, putamen, globus pallidus, red nucleus, and substantia nigra in healthy older populations relative to younger samples.[64] Both imaging and histological studies support the biological plausibility of correlational results presented here, particularly within the caudate, putamen, and red nucleus.[17] This study

also extends the existing literature through the observation of additional age-related positive susceptibility increases in the PBP and ventral pallidum. Our correlational findings, and evidence from the literature more broadly, suggest that a younger cohort is particularly prone to iron deposition as a shared characteristic, irrespective of mTBI status. For hippocampal regions, on the other hand, age-related iron accumulation apparent in previous research[17,63,65,67] was not reflected in the results of this study, potentially due to a likelihood of more subtle effects in these regions, coupled with the limited age range of this sample.

Temporal biodynamics of negative susceptibility

The temporal dynamics of diamagnetic substrates are relatively under-investigated in QSM, making inferences far less substantive than those related to paramagnetism and iron. Although myelin is the main source of negative susceptibility on QSM[27] it is unlikely that increases in negative susceptibility reflect age-related increases in myelin content. Whilst developmental myelination of axons is apparent up until approximately 30 years of age, this protraction of normal processes is generally restricted to prefrontal cortical regions.[131] In other brain regions, steep increases in myelin content are most apparent in the first months of life, after which time any disparities between age groups are unlikely to produce noticeable differences in tissue contrast on MRI.[132] Age-related kinetics of Aβ and tau aggregation point toward similar conclusions. While deposits of Aβ have been detected in the brains of individuals as young as 20 years old,[133] it is typically a feature associated with older age, and has been noted in both the presence and absence of cognitive dysfunction[129]; a similar pattern to that observed in tau accumulation.[130] As such, trends for increasing negative susceptibility with age are unlikely to be related to proteinopathy. Here, reasonable speculation suggests that the positive relationship between negative susceptibility and age in the caudate, extended amygdala, and hippocampal fimbria may be related instead to calcifications in these regions. This is supported by a body of work highlighting age-related calcifications in the basal ganglia[134,135] and hippocampus[136] in healthy individuals. However, the paucity of granular segmentations in the wider literature makes drawing parallels with the present research more difficult.

Conversely, the decrease in negative susceptibility as a function of age in the ventral pallidum may be related to myelin changes. The ventral pallidum contains both neuronal cell bodies and myelinated axons for rapid signal transmission.[137–139] Although literature related to age-induced demyelination specific to this region does not abound, investigations of myelin biodynamics more broadly suggests a 10% decrease per decade between the ages of 20 and 80,[140] which may account for the moderate effects evident here.

Injury latency and severity do not affect subcortical tissue magnetic susceptibility

While research suggests a negative correlation between iron deposition and cognitive ability following mTBI,[54] self-reported injury severity is often misaligned with objective markers of pathology, including on neuroimaging.[141,142] Alongside the under-reporting of symptoms that often occurs following a sr-mTBI,[143,144] these factors could confound results and contribute to the lack of correlation between positive or negative susceptibilities and both BIST scores and injury latency variables observed here. However, results from a previous investigation have suggested a link between injury severity and *cortical* iron dyshomeostasis.[115] The cortex is particularly vulnerable to a diverse range of injury mechanisms and downstream pathology in mTBI, including acute mechanical deformation and sulcal "water hammer" injury, which may be implicated in cortical atrophy and tauopathy in CTE.[60,145,146] It is therefore not unreasonable to suggest that cortical, rather than subcortical, brain tissue content changes may be more predictive of adverse symptomatology after mTBI. Finally, the lack of correlation between positive or negative susceptibilities and injury latency suggests that mTBI-related neuropathology may be time-dependent and more evident at subacute and chronic stages. Additional longitudinal research may be needed to better represent associations between injury latency and alterations to brain tissue content.

Limitations

The absence of elevations in positive or negative net magnetic susceptibility following mTBI suggest that iron deposition, calcifications, or focal aggregation of proteins such as tau and Aβ may not be present at the acute stage of injury. However, aforementioned research provides strong evidence that head injury more broadly, and even mild instances, can lead to diverse changes across biomagnetic substrates. Several factors may have inhibited the detection of changes in this research. Firstly, focal accumulations of iron, calcium, or proteins may better characterise chronic or later-life effects rather than acute pathophysiology, as evidenced by neuroimaging studies where differences in iron deposition were apparent at an average of 559 days post-injury.[37] Secondly, tau elevations are most commonly reported in cases of repeated exposure to head injuries[94] and tau oligomer polymorphisms are expressed differently in single versus repetitive mTBI.[147] However, in the absence of prior injury data, the study design precluded stratification of mTBI participants according to prior mTBI exposure. Without this information, detection of negative susceptibility changes and the potential relationship with tau pathology may be inhibited. Future studies should consider longitudinal research designs tracking athletes' exposure to head injury to better elucidate the cumulative and temporal effect of mTBI on biomagnetic substrates.

Notwithstanding the detail of the segmentations used in this study relative to previous more macroscopic investigations, the spatial resolution of the susceptibility maps may still limit detection of microstructural alterations. Because the susceptibility value at each voxel in a QSM image is obtained by convolving the susceptibilities of neighbouring voxels with a dipole kernel, each voxels susceptibility value is influenced by the surrounding susceptibility distribution,[148] and thus resolutions of 1 mm and above may hinder the detection of the subtle pathophysiological changes associated with mTBI. However, it should be noted that a 1 mm isotropic voxel resolution still meets the minimum criteria for best-practice QSM.[77]

Additionally, the use of single-echo QSM restricted voxel thresholding to an inter-voxel approach. As a result, the presence of multiple biological substrates with opposing magnetic properties *within* voxels may have confounded results by representing an aggregate of all susceptibility sources. These bipolar contributions within voxels cannot be disambiguated, and thus analysed, without multi-echo acquisitions.[119–124] This was also a likely cause of missing values in certain ROIs comprised primarily of either positive or negative susceptibility sources, such as the habenular nuclei or PBP (see Fig. 3). Thresholding these extremely polarised regions may result in zero values for the non-dominant sign for some participants, which may be further exacerbated by the size of ROIs, like the relatively small habenular nuclei. The use of multi-echo acquisitions would likely also resolve this limitation. In addition, group-level analyses may obscure individual neuropathology and inter-individual heterogeneity[115,149,150] and less macroscopic statistical approaches are currently planned for future research.

While the hippocampal[89] and basal ganglia[79] atlases offer robust segmentations, several limitations are associated with these approaches. First, the hippocampal segmentations provided via FreeSurfer[88] were developed from a small number of donors (10 for healthy controls, up to 15 when including mild cognitive impairment and AD subjects), with advanced age at death (60–91 years), which may result in hippocampal atrophy influencing the delineations. Furthermore, even with ultrahigh resolution MRI, some regional boundaries are not clearly visible in the training data. Similarly, for the basal ganglia atlas, some fine anatomical details may be lost, potentially leading to inaccuracies in boundary delineation. Although manual delineation is considered the gold standard, it requires extensive anatomical expertise and is prohibitively time-consuming.[151] Recent advances in deep-learning-based hippocampal segmentation have shown promise[152]; however, given that the current cohort is unlikely to exhibit gross hippocampal atrophy or other dramatic structural alterations, these advanced approaches may be more beneficial in samples where such abnormalities are expected.

Lastly, this research was conducted on a sample exclusively comprised of males, limiting external validity. This is particularly relevant to the translation of findings reported here to female sports players. Sex can influence time-dependence of the neuroinflammatory response,[94] and fluctuating sex hormone profiles,[153] oral contraceptive use,[154] and variability in neck muscle morphology[155] can contribute to differences in injury severity and outcome. Further research is planned within this demographic, and will ensure generalisability to female athletes of this age range.

Conclusions

This research builds upon previous QSM studies of mTBI by presenting the first assessment of mild injury effects specifically in the hippocampal subfields, and offers the most detailed segmentation of the basal ganglia to date. Here, both positive (iron-related) and negative (myelin-, calcium-, and protein-related) net susceptibility maps were utilised to better understand the impact of mTBI on biological substrates with differing biomagnetic profiles. Results revealed mTBI-related decreased negative susceptibility in the hippocampal CA4, indicating potential disruption to myelin or vulnerable cell populations in this region which may represent a component of the degenerative injury cascade. The absence of significant increases in either susceptibility sign as a marker of mTBI pathophysiology may reflect a general protective effect of subcortical location within the brain, or the confounding effect of age-related susceptibility changes common to all participants. Finally, results from correlational analyses support and extend prior literature regarding age-related iron deposition in subcortical grey matter and contributes to the sparse literature on the relationship between negative susceptibility values and age.

Author Contributions

Christi A. Essex (Conceptualisation, Methodology, Project Administration, Validation, Software, Formal Analysis, Investigation, Resources, Data Curation, Writing - Original Draft, Writing - Review & Editing, Visualisation); **Mayan J. Bedggood** (Writing - Review & Editing, Project administration, Investigation); **Jenna L. Merenstein** (Writing - Review & Editing); **Catherine Morgan** (Methodology, Writing - Review & Editing); **Helen Murray** (Writing - Review & Editing); **Samantha J. Holdsworth** (Writing - Review & Editing); **Richard L.M. Faull** (Writing - Review & Editing); **Patria Hume** (Writing - Review & Editing); **Alice Theadom** (Conceptualisation, Methodology, Writing - Review & Editing, Funding acquisition, Supervision); **Mangor Pedersen** (Conceptualisation, Methodology, Writing - Review & Editing, Funding acquisition, Supervision)

Acknowledgements

We extend thanks to Amabelle Voice-Powell and Cassandra McGregor for their contribution to the data collection, and Tania Ka'ai for bringing her perspective to cultural considerations on this study. In addition, we thank Axis Sports Concussion Clinics, particularly Dr Stephen Kara, for their assistance with recruiting sr-mTBI participants and personnel at the Centre for Advanced Magnetic Resonance Imaging (CAMRI) for their assistance collecting MRI data. We also acknowledge Dr Tim Elliot for radiological reporting of all participants and Siemens Healthineers for the use of a work-in-progress (WIP) prototype sequence for the acquisition data used to perform QSM.

Funding

This project was funded by a grant from the Health Research Council of New Zealand (HRC), grant #21/622.

The first author (CE) is supported by a Dame Dorothy Winstone Doctoral Completion Award from the Kate Edger Foundation of New Zealand.

Competing Interests

The authors report no competing interests.

Data availability

De-identified MRI data and code used for image processing and statistical analysis can be made available upon request to the corresponding author.

References

1 A. I. Maas, D. K. Menon, G. T. Manley, *et al.*, "Traumatic brain injury: progress and challenges in prevention, clinical care, and research," *The Lancet Neurology* **21**, 1004–1060 (2022).

2 A. Theadom, S. Mahon, P. Hume, *et al.*, "Incidence of Sports-Related Traumatic Brain Injury of All Severities: A Systematic Review," *Neuroepidemiology* **54**(2), 192–199 (2020).

3 K. McInnes, C. L. Friesen, D. E. MacKenzie, *et al.*, "Mild Traumatic Brain Injury (mTBI) and chronic cognitive impairment: A scoping review," *PLoS ONE* **12** (2017).

4 L. De Beaumont, H. Thoret, D. Mongeon, *et al.*, "Brain function decline in healthy retired athletes who sustained their last sports concussion in early adulthood," *Brain* **132**(3), 695–708 (2009).

5 K. M. Guskiewicz, S. W. Marshall, J. Bailes, *et al.*, "Association between Recurrent Concussion and Late-Life Cognitive Impairment in Retired Professional Football Players," *Neurosurgery* **57**(4), 719–726 (2005).

6 S. C. Hellewell, C. S. Beaton, T. Welton, *et al.*, "Characterizing the risk of depression following mild traumatic brain injury: A meta-analysis of the literature comparing chronic mTBI to non-mTBI populations," *Frontiers in Neurology* **11**, 1–14 (2020).

7 K. M. Guskiewicz, S. W. Marshall, J. Bailes, *et al.*, "Recurrent concussion and risk of depression in retired professional football players," *Medicine and Science in Sports and Exercise* **39**(6), 903–909 (2007).

8 D. F. Mackay, E. R. Russell, K. Stewart, *et al.*, "Neurodegenerative Disease Mortality among Former Professional Soccer Players," *New England Journal of Medicine* **381**(19), 1801–1808 (2019).

9 Y. Naumenko, I. Yuryshinetz, Y. Zabenko, *et al.*, "Mild traumatic brain injury as a pathological process," (2023).

10 C. B. Jeter, G. W. Hergenroeder, M. J. Hylin, *et al.*, "Biomarkers for the diagnosis and prognosis of mild traumatic brain injury/concussion," *Journal of Neurotrauma* **30**, 657–670 (2013).

11 A. Gozt, S. Hellewell, P. G. Ward, *et al.*, "Emerging Applications for Quantitative Susceptibility Mapping in the Detection of Traumatic Brain Injury Pathology," *Neuroscience* **467**, 218–236 (2021).

12 M. Prins, T. Greco, D. Alexander, *et al.*, "The pathophysiology of traumatic brain injury at a glance," *DMM Disease Models and Mechanisms* **6**, 1307–1315 (2013).

13 K. E. Saatman, A. C. Duhaime, R. Bullock, *et al.*, "Classification of traumatic brain injury for targeted therapies," in *Journal of Neurotrauma*, **25**, 719–738 (2008).

14 T. Seifert and V. Shipman, "The Pathophysiology of Sports Concussion," *Current Pain and Headache Reports* **19**(8) (2015).

15 K. R. Walker and G. Tesco, "Molecular mechanisms of cognitive dysfunction following traumatic brain injury," *Frontiers in Aging Neuroscience* **5** (2013).

16 C. C. Giza and D. A. Hovda, "The new neurometabolic cascade of concussion," *Neurosurgery* **75**, S24–S33 (2014).

17 D. J. Madden and J. L. Merenstein, "Quantitative susceptibility mapping of brain iron in healthy aging and cognition," *NeuroImage* **282** (2023).

18 R. J. Ward, F. A. Zucca, J. H. Duyn, *et al.*, "The role of iron in brain ageing and neurodegenerative disorders," *The Lancet Neurology* **13**(10), 1045–1060 (2014).

19 S. Huang, S. Li, H. Feng, *et al.*, "Iron Metabolism Disorders for Cognitive Dysfunction After Mild Traumatic Brain Injury," *Frontiers in Neuroscience* **15** (2021).

20 H. Ma, Y. Dong, Y. Chu, *et al.*, "The mechanisms of ferroptosis and its role in alzheimer's disease," *Frontiers in Molecular Biosciences* **9** (2022).

21 E. L. Mackenzie, K. Iwasaki, and Y. Tsuji, "Intracellular iron transport and storage: From molecular mechanisms to health implications," *Antioxidants and Redox Signaling* **10**(6), 997–1030 (2008).

22 E. J. Nisenbaum, D. S. Novikov, and Y. W. Lui, "The presence and role of iron in mild traumatic brain injury: An imaging perspective," *Journal of Neurotrauma* **31**, 301–307 (2014).

23 J. H. Duyn and J. Schenck, "Contributions to magnetic susceptibility of brain tissue," *NMR in Biomedicine* **30**(4) (2017).

24 C. Langkammer, F. Schweser, N. Krebs, *et al.*, "Quantitative susceptibility mapping (QSM) as a means to measure brain iron? A post mortem validation study," *NeuroImage* **62**(3), 1593–1599 (2012).

25 C. Liu, W. Li, K. A. Tong, *et al.*, "Susceptibility-weighted imaging and quantitative susceptibility mapping in the brain," *Journal of Magnetic Resonance Imaging* **42**(1), 23–41 (2015).

26 P. Ravanfar, S. M. Loi, W. T. Syeda, *et al.*, "Systematic Review: Quantitative Susceptibility Mapping (QSM) of Brain Iron Profile in Neurodegenerative Diseases," *Frontiers in Neuroscience* **15** (2021).

27 K. Deh, G. D. Ponath, Z. Molvi, *et al.*, "Magnetic susceptibility increases as diamagnetic molecules breakdown: Myelin digestion during multiple sclerosis lesion formation contributes to increase on QSM," *Journal of Magnetic Resonance Imaging* **48**, 1281–1287 (2018).

28 J. Jang, Y. Nam, S. W. Jung, *et al.*, "Paradoxical paramagnetic calcifications in the globus pallidus: An ex vivo MR investigation and histological validation study," *NMR in Biomedicine* **34**(10) (2021).

29 S. Kim, Y. Lee, C. Y. Jeon, *et al.*, "Quantitative magnetic susceptibility assessed by 7T magnetic resonance imaging in Alzheimer's disease caused by streptozotocin administration," *Quantitative Imaging in Medicine and Surgery* **10**(3), 789–797 (2020).

30 Y. Wang, P. Spincemaille, Z. Liu, *et al.*, "Clinical quantitative susceptibility mapping (QSM): Biometal imaging and its emerging roles in patient care," *Journal of Magnetic Resonance Imaging* **46**(4), 951–971 (2017).

31 N. J. Gong, R. Dibb, M. Bulk, *et al.*, "Imaging beta amyloid aggregation and iron accumulation in Alzheimer's disease using quantitative susceptibility mapping MRI," *NeuroImage* **191**, 176–185 (2019).

32 J. O'Callaghan, H. Holmes, N. Powell, *et al.*, "Tissue magnetic susceptibility mapping as a marker of tau pathology in Alzheimer's disease," *NeuroImage* **159**, 334–345 (2017).

33 Z. Zhao, L. Zhang, Q. Wen, *et al.*, "The effect of beta-amyloid and tau protein aggregations on magnetic susceptibility of anterior hippocampal laminae in Alzheimer's diseases," *NeuroImage* **244** (2021).

34 M. Daglas and P. A. Adlard, "The Involvement of Iron in Traumatic Brain Injury and Neurodegenerative Disease," *Frontiers in Neuroscience* **12** (2018).

35 B. Hallgren and P. Sourander, "The effect of age on the non-haemin iron in the human brain," *Journal of Neurochemistry* **3**, 41–51 (1958).

36 M. E. Haacke, N. Y. Cheng, M. J. House, *et al.*, "Imaging iron stores in the brain using magnetic resonance imaging," *Magnetic Resonance Imaging* **23**(1), 1–25 (2005).

37 E. Raz, J. H. Jensen, Y. Ge, *et al.*, "Brain iron quantification in mild traumatic brain injury: A magnetic field correlation study," *American Journal of Neuroradiology* **32**(10), 1851–1856 (2011).

38 J. Lifshitz, B. J. Kelley, and J. T. Povlishock, "Perisomatic Thalamic Axotomy After Diffuse Traumatic Brain Injury Is Associated With Atrophy Rather Than Cell Death," *J Neuropathol Exp Neurol* **66**(3), 218–229 (2007).

39 A. H. Ropper and K. C. Gorson, "Clinical practice. concussion," *The New England Journal of Medicine* **356**(2), 166–172 (2007).

40 N. A. Shaw, "The neurophysiology of concussion," *Progress in Neurobiology* **67**, 281–344 (2002).

41 K. M. Koch, A. S. Nencka, B. Swearingen, *et al.*, "Acute Post-Concussive Assessments of Brain Tissue Magnetism Using Magnetic Resonance Imaging," *Journal of Neurotrauma* **38**(7), 848–857 (2021).

42 D. K. Wright, T. J. O'Brien, and S. R. Shultz, "Sub-acute Changes on MRI Measures of Cerebral Blood Flow and Venous Oxygen Saturation in Concussed Australian Rules Footballers," *Sports Medicine - Open* **8**(1) (2022).

43 T. K. Bell, M. Ansari, J. M. Joyce, *et al.*, "Quantitative susceptibility mapping in adults with persistent-post concussion symptoms after mild traumatic brain injury: An exploratory study," *American Journal of Neuroradiology* (2024).

44 N. J. Gong, S. Kuzminski, M. Clark, *et al.*, "Microstructural alterations of cortical and deep gray matter over a season of high school football revealed by diffusion kurtosis imaging," *Neurobiology of Disease* **119**, 79–87 (2018).

45 N. N. Pinky, C. T. Debert, S. P. Dukelow, *et al.*, "Multimodal magnetic resonance imaging of youth sport-related concussion reveals acute changes in the cerebellum, basal ganglia, and corpus callosum that resolve with recovery," *Frontiers in Human Neuroscience* **16** (2022).

46 K. M. Koch, T. B. Meier, R. Karr, *et al.*, "Quantitative susceptibility mapping after sports-related concussion," *American Journal of Neuroradiology* **39**(7), 1215–1221 (2018).

47 R. Zivadinov, P. Polak, F. Schweser, *et al.*, "Multimodal Imaging of Retired Professional Contact Sport Athletes Does Not Provide Evidence of Structural and Functional Brain Damage," *Journal of Head Trauma Rehabilitation* **33**(5), E24–E32 (2018).

48 C. A. Essex, J. L. Merenstein, D. K. Overson, *et al.*, "Characterizing positive and negative quantitative susceptibility values in the cortex following mild traumatic brain injury: a depth- and curvature-based study," *Cerebral Cortex* **35** (2025).

49 P. Calabresi, B. Picconi, A. Tozzi, *et al.*, "Direct and indirect pathways of basal ganglia: A critical reappraisal," *Nature Neuroscience* **17**(8), 1022–1030 (2014).

50 J. L. Lanciego, N. Luquin, and J. A. Obeso, "Functional neuroanatomy of the basal ganglia," *Cold Spring Harbor Perspectives in Medicine* **2**(12) (2012).

51 L. Pessoa, "A Network Model of the Emotional Brain," *Trends in Cognitive Sciences* **21**(5), 357–371 (2017).

52 C. A. Seger, "The basal ganglia in human learning," *Neuroscientist* **12**(4), 285–290 (2006).

53 C. M. Bird and N. Burgess, "The hippocampus and memory: Insights from spatial processing," *Nature Reviews Neuroscience* **9**(3), 182–194 (2008).

54 L. Lu, H. Cao, X. Wei, *et al.*, "Iron Deposition Is Positively Related to Cognitive Impairment in Patients with Chronic Mild Traumatic Brain Injury: Assessment with Susceptibility Weighted Imaging," *BioMed Research International* **2015** (2015).

55 H. Arciniega, Z. H. Baucom, F. Tuz-Zahra, *et al.*, "Brain morphometry in former American football players: 1 findings from the DIAGNOSE CTE research project," *Oxford University Press* **22** (2024).

56 F. D. Raslau, I. T. Mark, A. P. Klein, *et al.*, "Memory Part 2: The Role of the Medial Temporal Lobe," *American Journal of Neuroradiology* **36**, 846–849 (2015).

57 A. C. Mckee and D. H. Daneshvar, "The neuropathology of traumatic brain injury," in *Handbook of Clinical Neurology*, **127**, 45–66, Elsevier B.V. (2015).

58 K. F. Bieniek, N. J. Cairns, J. F. Crary, *et al.*, "The Second NINDS/NIBIB Consensus Meeting to Define Neuropathological Criteria for the Diagnosis of Chronic Traumatic Encephalopathy," *Journal of Neuropathology and Experimental Neurology* **80**, 210–219 (2021).

59 J. D. Cherry, C. D. Esnault, Z. H. Baucom, *et al.*, "Tau isoforms are differentially expressed across the hippocampus in chronic traumatic encephalopathy and Alzheimer's disease," *Acta Neuropathologica Communications* **9** (2021).

60 A. C. McKee, T. D. Stein, B. R. Huber, *et al.*, "Chronic traumatic encephalopathy (CTE): criteria for neuropathological diagnosis and relationship to repetitive head impacts," *Acta Neuropathologica* **145**(4), 371–394 (2023).

61 C. Bouras, P. Giannakopoulos, P. F. Good, *et al.*, "A Laser Microprobe Mass Analysis of Brain Aluminum and Iron in Dementia pugilistica: Comparison with Alzheimer's Disease," *Eur Neurol* **38**(1), 53–58 (1997).

62 A. Yamamoto, R.-W. Shin, K. Hasegawa, *et al.*, "Iron (III) induces aggregation of hyperphosphorylated s and its reduction to iron (II) reverses the aggregation: implications in the formation of neurofibrillary tangles of Alzheimer's disease," tech. rep. (2002).

63 A. Ashraf, M. Clark, and P. W. So, "The aging of iron man," *Frontiers in Aging Neuroscience* **10** (2018).

64 B. Bilgic, A. Pfefferbaum, T. Rohlfing, *et al.*, "MRI estimates of brain iron concentration in normal aging using quantitative susceptibility mapping," *NeuroImage* **59**(3), 2625–2635 (2012).

65 J. Hagemeier, J. J. Geurts, and R. Zivadinov, "Brain iron accumulation in aging and neurodegenerative disorders," *Expert Review of Neurotherapeutics* **12**(12), 1467–1480 (2012).

66 S. Treit, N. Naji, P. Seres, *et al.*, "R2* and quantitative susceptibility mapping in deep gray matter of 498 healthy controls from 5 to 90 years," *Human Brain Mapping* **42**, 4597–4610 (2021).

67 L. Zecca, M. B. Youdim, P. Riederer, *et al.*, "Iron, brain ageing and neurodegenerative disorders," *Nature Reviews Neuroscience* **5**(11), 863–873 (2004).

68 A. Theadom, N. Hardaker, C. Bray, *et al.*, "The Brain Injury Screening Tool (BIST): Tool development, factor structure and validity," *PLoS ONE* **16**(2 February) (2021).

69 K. J. Gorgolewski, T. Auer, V. D. Calhoun, *et al.*, "The brain imaging data structure, a format for organizing and describing outputs of neuroimaging experiments," *Scientific Data* **3** (2016).

70 A. Boré, S. Guay, C. Bedetti, *et al.*, "Dcm2Bids," (2023).

71 X. Li, P. S. Morgan, J. Ashburner, *et al.*, "The first step for neuroimaging data analysis: DICOM to NIfTI conversion," *Journal of Neuroscience Methods* **264**, 47–56 (2016).

72 A. W. Stewart and S. Bollman, "QSMxT/QSMxT," (2022).

73 A. W. Stewart, S. D. Robinson, K. O'Brien, *et al.*, "QSMxT: Robust masking and artifact reduction for quantitative susceptibility mapping," *Magnetic Resonance in Medicine* **87**(3), 1289–1300 (2022).

74 B. Dymerska, K. Eckstein, B. Bachrata, *et al.*, "Phase unwrapping with a rapid opensource minimum spanning tree algorithm (ROMEO)," *Magnetic Resonance in Medicine* **85**(4), 2294–2308 (2021).

75 T. Liu, I. Khalidov, L. de Rochefort, *et al.*, "A novel background field removal method for MRI using projection onto dipole fields (PDF)," *NMR in Biomedicine* **24**(9), 1129–1136 (2011).

76 C. Kames, V. Wiggermann, and A. Rauscher, "Rapid two-step dipole inversion for susceptibility mapping with sparsity priors," *NeuroImage* **167**, 276–283 (2018).

77 B. Bilgic, M. Costagli, K. S. Chan, *et al.*, "Recommended implementation of quantitative susceptibility mapping for clinical research in the brain: A consensus of the ISMRM electro-magnetic tissue properties study group," *Magnetic Resonance in Medicine* **91**, 1834–1862 (2024).

78 S. M. Smith, "Fast robust automated brain extraction," *Human Brain Mapping* **17**(3), 143–155 (2002).

79 W. M. Pauli, A. N. Nili, and J. Michael Tyszka, "Data Descriptor: A high-resolution probabilistic in vivo atlas of human subcortical brain nuclei," *Scientific Data* **5** (2018).

80 D. N. Greve and B. Fischl, "Accurate and robust brain image alignment using boundary-based registration," *NeuroImage* **48**(1), 63–72 (2009).

81 M. Jenkinson, P. Bannister, M. Brady, *et al.*, "Improved Optimization for the Robust and Accurate Linear Registration and Motion Correction of Brain Images," *NeuroImage* **17**(2), 825–841 (2002).

82 M. Jenkinson and S. Smith, "A global optimisation method for robust affine registration of brain images," *Medical Image Analysis* **5**, 143–156 (2001).

83 J. L. Merenstein, J. Zhao, D. K. Overson, *et al.*, "Depth- and curvature-based quantitative susceptibility mapping analyses of cortical iron in Alzheimer's disease," *Cerebral Cortex* **34**(2) (2024).

84 J. L. Merenstein, J. Zhao, and D. J. Madden, "Depthwise cortical iron relates to functional connectivity and fluid cognition in healthy aging," *Neurobiology of Aging* **148**, 27–40 (2025).

85 D. C. Van Essen, S. M. Smith, D. M. Barch, *et al.*, "The WU-Minn Human Connectome Project: An overview," *NeuroImage* **80**, 62–79 (2013).

86 N. J. Tustison, B. B. Avants, P. A. Cook, *et al.*, "N4ITK: Improved N3 bias correction," *IEEE Transactions on Medical Imaging* **29**(6), 1310–1320 (2010).

87 B. B. Avants, N. J. Tustison, G. Song, *et al.*, "A reproducible evaluation of ANTs similarity metric performance in brain image registration," *NeuroImage* **54**(3), 2033–2044 (2011).

88 B. Fischl, "FreeSurfer," (2012).

89 J. E. Iglesias, J. C. Augustinack, K. Nguyen, *et al.*, "A computational atlas of the hippocampal formation using ex vivo, ultra-high resolution MRI: Application to adaptive segmentation of in vivo MRI," *Neuroimage* (115), 117–137 (2015).

90 D. J. Tournier, R. Smith, D. Raffelt, *et al.*, "MRtrix3: A fast, flexible and open software framework for medical image processing and visualisation," *NeuroImage* **202** (2019).

91 Y. Benjamini and Y. Hochberg, "Controlling the False Discovery Rate: A Practical and Powerful Approach to Multiple Testing," *Journal of the Royal Statistical Society. Series B (Methodological)* **57**(1), 289–300 (1995).

92 H. C. Murray, C. Osterman, P. Bell, *et al.*, "Neuropathology in chronic traumatic encephalopathy: a systematic review of comparative post-mortem histology literature," *Acta Neuropathologica Communications* **10**(1) (2022).

93 A. C. McKee, N. J. Cairns, D. W. Dickson, *et al.*, "The first NINDS/NIBIB consensus meeting to define neuropathological criteria for the diagnosis of chronic traumatic encephalopathy," *Acta Neuropathologica* **131**(1), 75–86 (2016).

94 W. P. Flavin, H. Hosseini, J. W. Ruberti, *et al.*, "Traumatic brain injury and the pathways to cerebral tau accumulation," *Frontiers in Neurology* **14** (2023).

95 V. E. Johnson, W. Stewart, and D. H. Smith, "Axonal pathology in traumatic brain injury," *Experimental Neurology* **246**, 35–43 (2013).

96 M. Inglese, S. Makani, G. Johnson, *et al.*, "Diffuse axonal injury in mild traumatic brain injury: a diffusion tensor imaging study," *J. Neurosurg* **103**, 298–303 (2005).

97 W. L. Maxwell, A. Domleo, G. Mccoll, *et al.*, "Post-Acute Alterations in the Axonal Cytoskeleton after Traumatic Axonal Injury," *JOURNAL OF NEUROTRAUMA* **20**(2) (2003).

98 W. L. Maxwell, R. Kosanlavit, B. J. Mccreath, *et al.*, "Freeze-Fracture and Cytochemical Evidence for Structural and Functional Alteration in the Axolemma and Myelin Sheath of Adult Guinea Pig Optic Nerve Fibers After Stretch Injury," *Journal of Neurotrauma* **16**(4) (1999).

99 H. M. Bramlett and W. D. Dietrich, "Quantitative structural changes in white and gray matter 1 year following traumatic brain injury in rats," *Acta Neuropathologica* **103**(6), 607–614 (2002).

100 A. M. Weber, A. Pukropski, C. Kames, *et al.*, "Pathological insights from quantitative susceptibility mapping and diffusion tensor imaging in ice hockey players pre and post-concussion," *Frontiers in Neurology* **9** (2018).

101 H. Ábrahám, A. Vincze, I. Jewgenow, *et al.*, "Myelination in the human hippocampal formation from midgestation to adulthood," *International Journal of Developmental Neuroscience* **28**, 401–410 (2010).

102 F. Yu, Y. Wang, A. R. Stetler, *et al.*, "Phagocytic microglia and macrophages in brain injury and repair," *CNS Neuroscience and Therapeutics* **28**(9), 1279–1293 (2022).

103 D. H. Lowenstein, M. J. Thomas, D. H. Smith, *et al.*, "Selective Vulnerability of Dentate Hilar Neurons following Traumatic Brain Injury: A Potential Mechanistic Link between Head Trauma and Disorders of the Hippocampus," *The Journal of Neuroscience* **12**(12), 4848–4853 (1992).

104 W. L. Maxwell, K. Dhillon, L. Harper, *et al.*, "There Is Differential Loss of Pyramidal Cells from the Human Hippocampus with Survival after Blunt Head Injury," Tech. Rep. 3 (2003).

105 M. R. Grovola, N. Paleologos, K. L. Wofford, *et al.*, "Mossy cell hypertrophy and synaptic changes in the hilus following mild diffuse traumatic brain injury in pigs," *Journal of Neuroinflammation* **17** (2020).

106 V. Santhakumar, R. Bender, M. Frotscher, *et al.*, "Granule cell hyperexcitability in the early post-traumatic rat dentate gyrus: the 'irritable mossy cell' hypothesis," *Journal of Physiology* (524), 117–134 (2000).

107 H. E. Scharfman, "The enigmatic mossy cell of the dentate gyrus," *Nature Reviews Neuroscience* **17**(9), 562–575 (2016).

108 S. B. Rosenbaum and M. L. Lipton, "Embracing chaos: The scope and importance of clinical and pathological heterogeneity in mTBI," *Brain Imaging and Behavior* **6**(2), 255–282 (2012).

109 S. Nikolova, T. J. Schwedt, J. Li, *et al.*, "T2* reduction in patients with acute post-traumatic headache," *Cephalalgia* **42**(4-5), 357–365 (2022).

110 C. D. Chong, S. Nikolova, G. Dumkrieger, *et al.*, "Thalamic subfield iron accumulation after acute mild traumatic brain injury as a marker of future post-traumatic headache intensity," *Headache* **63**, 156–164 (2023).

111 G. Onyszchuk, S. M. LeVine, W. M. Brooks, *et al.*, "Post-acute pathological changes in the thalamus and internal capsule in aged mice following controlled cortical impact injury: A magnetic resonance imaging, iron histochemical, and glial immunohistochemical study," *Neuroscience Letters* **452**, 204–208 (2009).

112 M. A. Ansari, K. N. Roberts, and S. W. Scheff, "Oxidative stress and modification of synaptic proteins in hippocampus after traumatic brain injury," *Free Radical Biology and Medicine* **45**, 443–452 (2008).

113 E. D. Bigler, "Neuropsychological results and neuropathological findings at autopsy in a case of mild traumatic brain injury," *Journal of the International Neuropsychological Society* (10), 794–806 (2004).

114 C. Osterman, D. Hamlin, C. M. Suter, *et al.*, "Perivascular glial reactivity is a feature of phosphorylated tau lesions in chronic traumatic encephalopathy," *Acta Neuropathologica* **149** (2025).

115 C. A. Essex, D. K. Overson, J. L. Merenstein, *et al.*, "Mild traumatic brain injury increases cortical iron: evidence from individual susceptibility mapping," *Brain Communications* **7**(2) (2025).

116 K. Chary, M. J. Nissi, O. Nykänen, *et al.*, "Quantitative susceptibility mapping of the rat brain after traumatic brain injury," *NMR in Biomedicine* **34** (2021).

117 L. J. Lehto, A. Sierra, C. A. Corum, *et al.*, "Detection of calcifications in vivo and ex vivo after brain injury in rat using SWIFT," *NeuroImage* **61**, 761–772 (2012).

118 M. J. Gayoso, A. Al-Majdalawi, M. Garrosa, *et al.*, "Selective calcification of rat brain lesions caused by systemic administration of kainic acid," *Histology and Histopathology* (18), 855–869 (2003).

119 M. Ahmed, J. Chen, A. Arani, *et al.*, "The diamagnetic component map from quantitative susceptibility mapping (QSM) source separation reveals pathological alteration in Alzheimer's disease-driven neurodegeneration," *NeuroImage* **280** (2023).

120 J. Chen, N. J. Gong, K. T. Chaim, *et al.*, "Decompose quantitative susceptibility mapping (QSM) to sub-voxel diamagnetic and paramagnetic components based on gradient-echo MRI data," *NeuroImage* **242** (2021).

121 J. Emmerich, P. Bachert, M. E. Ladd, *et al.*, "On the separation of susceptibility sources in quantitative susceptibility mapping: Theory and phantom validation with an in vivo application to multiple sclerosis lesions of different age," *Journal of Magnetic Resonance* **330** (2021).

122 J. Lee, S. Ji, and S. H. Oh, "So You Want to Image Myelin Using MRI: Magnetic Susceptibility Source Separation for Myelin Imaging," *Magnetic resonance in medical sciences : MRMS : an official journal of Japan Society of Magnetic Resonance in Medicine* **23**(3), 291–306 (2024).

123 Z. Li, R. Feng, Q. Liu, *et al.*, "APART-QSM: An improved sub-voxel quantitative susceptibility mapping for susceptibility source separation using an iterative data fitting method," *NeuroImage* **274** (2023).

124 H. G. Shin, J. Lee, Y. H. Yun, *et al.*, "χ-separation: Magnetic susceptibility source separation toward iron and myelin mapping in the brain," *NeuroImage* **240** (2021).

125 M. Ost, K. Nylén, L. Csajbok, *et al.*, "Initial CSF total tau correlates with 1-year outcome in patients with traumatic brain injury," *Neurology* **9**(69), 1600–1604 (2006).

126 R. Rubenstein, B. Chang, J. K. Yue, *et al.*, "Comparing plasma phospho tau, total tau, and phospho tau–total tau ratio as acute and chronic traumatic brain injury biomarkers," *JAMA Neurology* **74**, 1063–1072 (2017).

127 V. E. Johnson, W. Stewart, and D. H. Smith, "Traumatic brain injury and amyloid-β pathology: A link to alzheimer's disease?," *Nature Reviews Neuroscience* **11**(5), 361–370 (2010).

128 K. M. Dybing, C. J. Vetter, D. A. Dempsey, *et al.*, "Traumatic brain injury and Alzheimer's Disease biomarkers: A systematic review of findings from amyloid and tau positron emission tomography (PET)," *medRxiv* (Preprint) (2023).

129 K. M. Rodrigue, K. M. Kennedy, and D. C. Park, "Beta-amyloid deposition and the aging brain," *Neuropsychology Review* **19**(4), 436–450 (2009).

130 M. Schöll, S. N. Lockhart, D. R. Schonhaut, *et al.*, "PET Imaging of Tau Deposition in the Aging Human Brain," *Neuron* **89**, 971–982 (2016).

131 M. C. Moulson and C. A. Nelson, *Encyclopedia of Infant and Early Childhood Development: Neurological Development*, Elsevier (2008).

132 H. M. Branson, "Normal Myelination. A Practical Pictorial Review," *Neuroimaging Clinics of North America* **23**(2), 183–195 (2013).

133 A. Baker-Nigh, S. Vahedi, E. G. Davis, *et al.*, "Neuronal amyloid-β accumulation within cholinergic basal forebrain in ageing and Alzheimer's disease," *Brain* **138**, 1722–1737 (2015).

134 E. Monfrini, F. Arienti, P. Rinchetti, *et al.*, "Brain Calcifications: Genetic, Molecular, and Clinical Aspects," *International journal of molecular sciences* **24**(10) (2023).

135 C. Saade, E. Najem, K. Asmar, *et al.*, "Intracranial calcifications on CT: An updated review," *Journal of Radiology Case Reports* **13**, 1–18 (2019).

136 J. Wegiel, I. Kuchna, T. Wisniewski, *et al.*, "Vascular fibrosis and calcification in the hippocampus in aging, Alzheimer disease, and Down syndrome," *Acta Neuropathologica* **103**(4), 333–343 (2002).

137 L. Heimer and G. W. Van Hoesen, "The limbic lobe and its output channels: Implications for emotional functions and adaptive behavior," *Neuroscience and Biobehavioral Reviews* **30**(2), 126–147 (2006).

138 Y. M. Kupchik and P. W. Kalivas, "The Direct and Indirect Pathways of the Nucleus Accumbens are not what you think," *Neuropsychopharmacology* **42**, 368–370 (2017).

139 D. H. Root, R. I. Melendez, L. Zaborszky, *et al.*, "The ventral pallidum: Subregion-specific functional anatomy and roles in motivated behaviors," *Progress in Neurobiology* **130**, 29–70 (2015).

140 L. Marner, J. R. Nyengaard, Y. Tang, *et al.*, "Marked loss of myelinated nerve fibers in the human brain with age," *Journal of Comparative Neurology* **462**(2), 144–152 (2003).

141 M. McCrea, T. Meier, D. Huber, *et al.*, "Role of advanced neuroimaging, fluid biomarkers and genetic testing in the assessment of sport-related concussion: A systematic review," *British Journal of Sports Medicine* **51**(12), 919–929 (2017).

142 M. E. Shenton, H. M. Hamoda, J. S. Schneiderman, *et al.*, "A review of magnetic resonance imaging and diffusion tensor imaging findings in mild traumatic brain injury," *Brain Imaging and Behavior* **6**(2), 137–192 (2012).

143 E. Kroshus, B. Garnett, M. Hawrilenko, *et al.*, "Concussion under-reporting and pressure from coaches, teammates, fans, and parents," *Social Science and Medicine* **134**, 66–75 (2015).

144 T. B. Meier, B. J. Brummel, R. Singh, *et al.*, "The underreporting of self-reported symptoms following sports-related concussion," *Journal of Science and Medicine in Sport* **18**, 507–511 (2015).

145 S. Kornguth, N. Rutledge, G. Perlaza, *et al.*, "A Proposed Mechanism for Development of CTE Following Concussive Events: Head Impact, Water Hammer Injury, Neurofilament Release, and Autoimmune Processes," *Brain Sciences* **7**(12), 164 (2017).

146 D. H. Smith, V. E. Johnson, and W. Stewart, "Chronic neuropathologies of single and repetitive TBI: Substrates of dementia?," *Nature Reviews Neurology* **9**, 211–221 (2013).

147 A. Bittar, N. Bhatt, T. F. Hasan, *et al.*, "Neurotoxic tau oligomers after single versus repetitive mild traumatic brain injury," *Brain Communications* **1**(1) (2019).

148 Y. Wang and T. Liu, "Quantitative susceptibility mapping (QSM): Decoding MRI data for a tissue magnetic biomarker," *Magnetic Resonance in Medicine* **73**(1), 82–101 (2015).

149 M. J. Bedggood, C. A. Essex, A. Theadom, *et al.*, "Individual-level analysis of MRI T2 relaxometry in mild traumatic brain injury: Possible indications of brain inflammation," *NeuroImage: Clinical* **43** (2024).

150 J. F. Domínguez, A. Stewart, A. Burmester, *et al.*, "Improving quantitative susceptibility mapping for the identification of traumatic brain injury neurodegeneration at the individual level," *Zeitschrift fur Medizinische Physik* (2024).

151 R. A. Morey, C. M. Petty, Y. Xu, *et al.*, "A comparison of automated segmentation and manual tracing for quantifying hippocampal and amygdala volumes," *NeuroImage* **45**, 855–866 (2009).

152 M. Schell, M. Foltyn-Dumitru, M. Bendszus, *et al.*, "Automated hippocampal segmentation algorithms evaluated in stroke patients," *Scientific Reports* **13** (2023).

153 K. Wunderle, K. M. Hoeger, E. Wasserman, *et al.*, "Menstrual phase as predictor of outcome after mild traumatic brain injury in women," *Journal of Head Trauma Rehabilitation* **29**(5), E1–E8 (2014).

154 V. Gallagher, N. Kramer, K. Abbott, *et al.*, "The effects of sex differences and hormonal contraception on outcomes after collegiate sports-related concussion," *Journal of Neurotrauma* **35**(11), 1242–1247 (2018).

155 R. T. Tierney, M. R. Sitler, C. B. Swanik, *et al.*, "Gender differences in head-neck segmnet dynamic stabilization during head accelaration," *Medicine and Science in Sports and Exercise* **37**(2), 272–279 (2005).

Individualised quantitative susceptibility mapping reveals abnormal hippocampal iron markers in acute mild traumatic brain injury

Christi A. Essex[a,*], Mayan J. Bedggood[a], Jenna L. Merenstein[b], Catherine Morgan[c, d], Helen C. Murray[e], Samantha J. Holdsworth[e,f,g], Richard L. M. Faull[e], Patria Hume[h], Alice Theadom[a], Mangor Pedersen[a]

[a]Department of Psychology and Neuroscience, Auckland University of Technology, Auckland 0627, New Zealand
[b]Brain Imaging and Analysis Center, Duke University Medical Center, Durham, NC 27710, United States
[c]Center for Advanced MRI, The University of Auckland, Auckland 1023, New Zealand
[d]School of Psychology and Centre for Brain Research, The University of Auckland, Auckland 1023, New Zealand
[e]Center for Brain Research, The University of Auckland, Auckland 1023, New Zealand
[f]Department of Anatomy and Medical Imaging, Faculty of Medical and Health Sciences, The University of Auckland, Auckland 1023, New Zealand
[g]Mātai Medical Research Institute, Gisborne 4010, New Zealand
[h]Sports Performance Research Institute New Zealand, Auckland University of Technology, Auckland 0627, New Zealand

*Christi A. Essex: christi.essex@aut.ac.nz

Abstract. Quantitative susceptibility mapping (QSM) is an advanced post-processing technique of magnetic resonance imaging data that can be leveraged as a surrogate marker of iron accumulation in the brain following mild traumatic brain injury (mTBI). However, subtle tissue content changes characteristic of this complex injury may be lost to group-wise averaging when standard statistical models are employed. To provide more clinically- and individually-relevant information, z-tests can be used to build personalised profiles of positive susceptibility as a marker of abnormal iron homeostasis. Here, we mapped subject-specific deviations in iron-related positive susceptibility across 10 bilateral segmentations of the hippocampal subfields and 15 basal nuclei. The healthy normal susceptibility distribution for each region-of-interest (ROI) was derived from the aggregate data of 25 age-matched male controls (M = 21.10 years [range: 16-32], SD = 4.35) using z-tests. Region-wise z-scores for each of the 35 males aged between 16 and 33 years (M = 21.60, SD = 4.98) with acute ($<$ 14 days) sports-related mTBI (sr-mTBI) were compared against the healthy reference range. Of the sr-mTBI participants, 43% exhibited abnormal iron markers in at least one ROI, which involved the hippocampal subfields in a majority (87%) of cases. Across all ROIs, particularly dense concentrations were observed in the parasubiculum and mammillary nucleus. Injury severity scores were not significantly different between sr-mTBI participants with abnormal iron markers (M = 41.7, SD = 34.5) and those without (M = 35.6, SD = 30.8), p = 0.5, however, abnormal iron markers in certain hippocampal subfields and the mammillary nucleus were observationally linked to clinical symptom phenotype. Taken together, these data allude to a region-of-risk model in which areas of the anteromedial hippocampal head, which is proximal to the sphenoid ridge, and midline structures are vulnerable to iron-mediated pathology. These findings underscore the importance of subject-specific analyses and how these sensitive methods can be used to map regional iron dyshomeostasis against cranial-dural morphology and established injury biomechanics.

Keywords: basal ganglia; brain iron; hippocampal subfields; individualised profiles; mild traumatic brain injury; quantitative susceptibility mapping.

Introduction

As the most prevalent neurological condition, traumatic brain injury (TBI) represents a significant global health concern.[1] Projections estimate that TBI will remain one of the three foremost causes of injury-related death and disability into 2030.[2] However, far from a binary condition, TBI exists along a continuum from mild to severe, with mild TBI (mTBI) accounting for the vast majority ($\sim$90%) of all cases.[1] Unlike severe TBI where lesions are readily identifiable on conventional clinical imaging, such as computed tomography (CT) and magnetic resonance imaging (MRI), the degree of tissue damage is comparatively less extreme for mTBI and standard radiographic methods fail to detect mTBI-related brain alterations in 90-95% of cases.[1] As a result, mTBI diagnosis and prognosis relies almost exclusively on clinical assessment by subjective self-report,[3] introducing a level of ambiguity that has led not only to definitional and diagnostic inconsistencies, but drastic inequities in access to care.[4,5] Here, the identification of objective markers sensitive to the inter-individual heterogeneity of micropathology is critical to advancing the current understanding of mTBI and facilitating targeted, equitable, interventions.

Iron, the most abundant trace metal in the brain, has been implicated in the secondary neurometabolic cascade[6–8] and is associated with cognitive impairments following mTBI,[7,9,10] highlighting its promise as a potential mTBI biomarker. Whilst the precise mechanisms by which

excess iron accumulates in the brain is an area of ongoing research, injury-induced microvascular dysfunction, microbleeds, and increased blood-brain barrier (BBB) permeability likely increase iron transport into neural tissue.[6,7,11,12] Normally sequestered in ferritin to mitigate oxidative stress, supra-physiological levels of iron can overwhelm the capacity of storage proteins, resulting in a labile iron pool which catalyses highly cytotoxic redox reactions.[13,14] The reactive species generated by redox cycling precipitates oxidative stress, lipid peroxidation, increased cell membrane permeability, increased expression of pro-inflammatory cytokines, demyelination, damage to DNA, RNA, carbohydrates, lipids, and proteins, mitochondrial dysfunction, glutamate excitotoxicity, proteinopathy, and iron-regulated cell death.[6,8,11,13–19]

Quantitative susceptibility mapping (QSM), an advanced MRI post-processing technique, leverages the magnetic field perturbations induced by biomagnetic substrates, including non-heme iron, to generate scalar maps for an indirect marker of tissue dyshomeostasis.[20–22] While QSM has been extensively used to characterise iron dyshomeostasis in neurodegenerative disorders,[23–28] this technique remains under-utilised in the context of mTBI.[29] In the relatively small number of QSM investigations of mTBI, the total deep grey matter or major basal ganglia substructures including the thalamus, caudate, putamen, and globus pallidus remain the most commonly targeted subcortical regions of interest (ROIs) due to their high iron load in the brain.[30–36] This high regional iron content also render the basal ganglia particularly amenable to imaging methods sensitive to tissue magnetic susceptibility, such as QSM. While this highlights the prevailing rationale for selecting the basal ganglia as logical targets in QSM-based mTBI research, the limited anatomical specificity may account for the lack of significant results indicative of iron accumulation in the subcortical grey matter.[30–36] Even the two more extensive investigations inclusive of nucleus accumbens and/or amygdala segmentations[34,36] have not differentiated the subdivisions of basal ganglia, for example the internal and external segments of the globus pallidus, nor explored mTBI effects in other associated nuclei. Evidence from susceptibility-weighted imaging (SWI) identifying the substantia nigra and red nucleus as loci of iron dyshomeostasis post-mTBI[9] highlights why exploration of additional structures may enable better characterisation of altered iron signalling in the brain after injury.

Additionally, despite the well-documented vulnerability of the hippocampus to injury,[37,38] inflammatory processes, impaired long-term potentiation,[39,40] increased expression of amyloid precursor protein,[41] and a high expression of transferrin receptor protein 1 (TfR1) on the apical BBB endothelium[42] which may exacerbate abnormal iron transport across this barrier following injury, investigations of this a crucial memory hub[43] remain limited. Of the three extant studies to include the hippocampus as a region-of-interest (ROI),[34,36,44] only our previous work[44] has differentiated the hippocampal subfields. Here, we posited that limited anatomical specificity and treatment of the hippocampus as a homogeneous ROI may mask the iron-related pathology that has been detected by SWI[9] but is absent from the findings of prior QSM-based research. Using an extensive 16-part segmentation of the basal nuclei and 10 hippocampal subfields, we identified decreased negative susceptibility in the cornu ammonis (CA) 4 region consistent demyelination and the selective vulnerability of hilar cell populations to injury.[45–49] However, like prior investigations, we observed no significant increase in positive susceptibility as a marker of iron dyshomeostasis in deep grey matter.

Here, recent research highlighting the utility of subject-specific modelling to capture data that are otherwise lost to group-wise averaging[50–56] is particularly relevant. The vast majority of clinical research employ analytic techniques that assess group averages and treat individual variability primarily as noise.[57] These methods are used in an attempt to identify signatures representative of the “average patient”, and while more standard group-wise statistical approaches have been fundamental identifying disorder-specific neural signatures, such as structural alterations in the amygdala and hippocampus in anxiety[58] and altered rostral anterior cingulate activity in depression,[59] the generalisability at the individual level is limited.[57] These macroscopic approaches likely obscure the individual-level heterogeneity that characterises clinical cohorts; variation that is central

to identifying appropriate and effective intervention.[57] Group-level analytic strategies remain the most common method used in QSM investigations of mTBI. The potential loss of subtle tissue responses to averaging effects could plausibly explain the general lack of significant effects across the extant literature. Indeed, we have previously demonstrated the capacity of individualised investigations to identify individual-level cortical iron markers [60] that are not apparent at the group level.[61] In this individualised study, identification of a significantly higher symptom burden for mTBI participants presenting with abnormal iron markers relative to those exhibiting no evidence of iron dyshomeostasis further underscores the clinical relevance of more sensitive modelling. In the present investigation, we extend this individualised technique to deep grey matter, using the results to facilitate targeted analyses of differences in injury severity scores between mTBI participants with normal and abnormal subcortical iron markers as a secondary measure. Given the novel and exploratory nature of this study, no specific *a priori* hypotheses were made regarding the direction of effects across all basal nuclei and hippocampal subfields.

Materials and Methods

Ethical approval for this research was obtained from the Health and Disabilities Ethics Committee (HDEC) (Date: 18/02/2022, Reference: 2022 EXP 11078) and institutional approval was also obtained from the Auckland University of Technology Ethics Committee (AUTEC) (Date: 18/02/2022, Reference: 22/12). In accordance with the Declaration of Helsinki, all participants provided written informed consent prior to data collection.

Participants

Thirty-five male contact sports players (M = 21.60 years [range: 16-33], SD = 4.98) with acute sports-related mTBI (sr-mTBI) sustained within 14 days of MRI scanning (M = 10.40 days, SD = 3.01) and 25 age-matched male controls (M = 21.10 years [range: 16-32], SD = 4.35) were recruited for this observational study (see Table 1). To minimise confounds related to iron accumulation across the lifespan,[62–68] we ensured ages were not significantly different between groups ($t(58) = -0.44$, $p = 0.66$). Clinical (sr-mTBI) participants were recruited through three Axis Sports Medicine clinics (Auckland, New Zealand), via print and social media advertisements, word-of-mouth, and through community-based pathways including referrals from healthcare professionals and sports team management. Each clinical participant was required to have a confirmed sr-mTBI diagnosis by a licensed physician as a prerequisite for study inclusion, and symptom severity was assessed using the Brain Injury Screening Tool (BIST)[69] either upon presentation to Axis clinics or electronically following recruitment. Healthy controls (HC) were recruited through print and social media advertisements, and word-of-mouth. Exclusion criteria for all participants included a history of significant medical or neurological conditions unrelated to the study's objectives and contraindications for MRI. Additionally, controls were excluded if they had any recent history of mTBI events ($<$ 12 months) or were living with any long-term effects of previous mTBI. All participants completed a brief demographic questionnaire and attended a 1-hour MRI scan at The Centre for Advanced MRI (CAMRI), Auckland, New Zealand. All scans were reviewed by a certified neuroradiologist consultant for clinically significant findings. No clinically significant diagnoses were identified from MRI in either group, and no incidental findings required follow-up (see Table 1).

Table 1: Clinical characteristics of participants with mTBI

ID	Age	DSI	BIST Score	MOI	MRI findings
mTBI-01	< 20	5 days	140	Rugby	None
mTBI-02	< 20	5 days	12	Rugby	None
mTBI-03	20s	6 days	78	Rugby	None
mTBI-04	< 20	13 days	18	Rugby	Small fluid signal spaces in R peritrigonal WM - normal. R caudate cleft along ventricular surface - possibly developmental or from old ischaemic insult
mTBI-05	< 20	12 days	12	Rugby	None
mTBI-06	20s	13 days	42	Rugby	None
mTBI-07	20s	13 days	13	Football	Minor artefactual T1 signal in pons
mTBI-08	20s	12 days	6	Hockey	None
mTBI-09	20s	6 days	56	Rugby	Minor R orbital fracture (old)
mTBI-10	< 20	12 days	54	Rugby	None
mTBI-11	20s	10 days	52	Rugby	None
mTBI-12	30s	13 days	13	Football	None
mTBI-13	< 20	5 days	79	Rugby	None
mTBI-14	20s	13 days	2	Rugby	Small focus of susceptibility in L superior frontal gyrus possibly vascular or nonspecific haemosiderin
mTBI-15	< 20	13 days	22	Rugby	None
mTBI-16	< 20	8 days	117	Futsal	Tiny cleft of fluid signal in R cingulate gyrus - minor developmental anomaly or mature gliosis
mTBI-17	20s	13 days	*	Rugby	None
mTBI-18	20s	10 days	34	Gymnastics	None
mTBI-19	20s	13 days	28	Jiu-jitsu	Some artefactual DWI signal in pons
mTBI-20	20s	11 days	69	Surfing	Tiny susceptibility site in R temporal lobe - may be vascular
mTBI-21	< 20	7 days	14	Rugby	Minor susceptibility in transverse sulcus in R mid temporal lobe - nonspecific, may be vascular or reflect haemosiderin deposition from prior small volume haemorrhage
mTBI-22	< 20	13 days	39	Judo	None
mTBI-23	< 20	9 days	34	Rugby	None
mTBI-24	< 20	12 days	68	Rugby	None
mTBI-25	20s	12 days	17	Rugby	7mm pineal cyst - normal limits. Some T1 hyperintensity in R cerebellum - artefact compatible
mTBI-26	20s	12 days	25	Rugby	Mildly prominent cisterna magna
mTBI-27	30s	7 days	30	Football	A few mildly prominent biparietal and L cerebral peduncle perivascular spaces - normal variant
mTBI-28	30s	12 days	51	Swimming	None
mTBI-29	20s	5 days	6	Rugby	None
mTBI-30	< 20	12 days	2	Rugby	Some DWI signal disturbance anterior to pons - likely artefactual
mTBI-31	< 20	14 days	22	Rugby	2-3 tiny foci of susceptibility in R frontal lobe - nonspecific, possible site of prior microhemorrhage. A punctate focus of T1 hypointensity/T2 hyperintensity superolateral to the frontal horn of R lateral ventricle
mTBI-32	20s	8 days	58	Football	Bifrontal developmental venous anomaly noted - normal variants
mTBI-33	< 20	8 days	8	Rugby	Minuscule foci of susceptibility in R cerebellar hemisphere /posterior to R aspect of the splenium of CC - nonspecific. Minor susceptibility in R sylvian fissure - vascular
mTBI-34	20s	14 days	47	Rugby	None
mTBI-35	< 20	12 days	28	Football	None
Mean mTBI	21.60 (4.98) years	10.4 (3.01) days	38.1 (32.0) /160		No findings considered clinically relevant
Mean HC	21.10 (4.35) years				No findings considered clinically relevant

Note. Diagnostic assessment is limited to the volume T1, SWI and DWI sequences with only limited interpretation of the multi-echo T2 stack. Clinical assessments are relevant to the identification of micro-haemorrhages, areas of siderosis, T1 appearance, gliosis, volume, ventricular volumes and non-neurological findings. Age is given in a range to prevent re-identification of participants. The possible range of BIST scores is 0 (min) to 160 (max). Clinical group data correspondent to date at MRI only with the exception of the BIST[69] acquired >24 hours post-injury prior to MRI scanning (<14 days post). Abbreviations are as follows: mTBI = mild traumatic brain injury; HC = healthy control; ID = unique identifier; DSI = days since injury; BIST = Brain Injury Screening Tool; MOI = mechanism of injury; MRI = magnetic resonance imaging; L = Left; R = right; * = missing data (BIST incomplete on the Axis Sport Medicine Clinic patient portal, reason unknown).

Neuroimaging

Details on image acquisition and processing have been previously reported,[44,61] and are summarised here for brevity.

Acquisition

MRI data were acquired on a 3T Siemens MAGNETOM Vida Fit scanner (Siemens Healthcare, Erlangen, Germany) equipped with a 20-channel head coil. A 3D flow-compensated single-echo gradient-recalled echo (GRE) sequence was used to obtain magnitude and unfiltered phase images for QSM reconstruction. Data were collected at 1 mm isotropic voxel size with matrix size = 180 x 224 x 160 mm, repetition time (TR) = 30 ms; echo time (TE) = 20 ms; flip angle (FA) = 15°; field of view (FoV) = 180 mm (LR) × 224 mm (AP) in a total acquisition time of ∼3.43 minutes. For each participant, a high-resolution 3D T_1-weighted (T_1w) anatomical image volume was acquired for coregistration and segmentation using a Magnetisation-Prepared Rapid Acquisition Gradient Echo (MPRAGE) sequence (TR = 1940.0 ms; TE = 2.49 ms, FA = 9°; slice thickness = 0.9 mm; FoV = 230 mm; matrix size = 192 x 512 x 512 mm; GRAPPA = 2; voxel size 0.45 x 0.45 x 0.90 mm) for a total acquisition time of ∼4.31 minutes.

QSM processing

QSM images were reconstructed using the QSMxT[70] v6.4.2 pipeline with two-pass artefact reduction.[71] The rapid open-source minimum spanning tree algorithm algorithm was used for phase unwrapping,[72] background field removal was performed using projection onto dipole fields,[73] and rapid two-step dipole inversion was used for susceptibility estimation.[74] Susceptibility was referenced to the whole-brain in accordance with recent consensus statement recommendations.[75]

Magnitude images were skull-stripped with FSL's *BET*[76] and used to generate binary masks for signal erosion at the brain perimeter on QSM using *fslmaths*. Skull-stripped magnitude images were linearly registered to the CIT168 T_1w template[77] with 12 degrees of freedom (DoF) suitable for atlas-based registration using FMRIB's Linear Transformation Tool.[78–80] The corresponding transformation matrix was used for spatial normalisation of the QSM images using FLIRT.[78–80] QSM images were then thresholded above and below zero to generate separate maps of net positive (iron-related) and net negative (myelin-, calcium-, and protein-related) voxel-wise susceptibility.[81,82] Only net positive susceptibility maps (QSM^+) were retained for statistical analysis of iron markers.

Basal ganglia segmentation

The 16-part CIT168 bilateral basal ganglia mask[77] in MNI152 space was used for segmentation of the putamen (Pu), caudate (Ca), nucleus accumbens (NAC), globus pallidus externus (GPe), globus pallidus internus (GPi), ventral pallidum (VeP), substantia nigra pars compacta (SNc), substantia nigra pars reticulata (SNr), extended amygdala (EXA), hypothalamus (HTH), mammillary nucleus (MN), ventral tegmental area (VTA), parabrachial pigmented nucleus (PBP), habenular nuclei (HN), subthalamic nucleus (STH), and the red nucleus (RN).

Hippocampal segmentation

Each participants' T_1w structural image was processed using FreeSurfer's *recon-all* pipeline[83] to generate a 10-part unilateral segmentation of the hippocampal subfields.[84] The hippocampal subregion masks include the parasubiculum, presubiculum, subiculum, cornu ammonis (CA) regions CA1, CA3 (which includes CA2), and CA4, the hippocampal-amygdala transition area (HATA), fimbria, hippocampal tail, and hippocampal fissure. To standardise each hippocampal subfield mask for data analysis, each participants' T_1w brain image was registered to the CIT168 T_1w template in MNI152 space[77] with 12 DoF using FLIRT.[78–80] The resulting transformation matrix was then applied to both the left and right hemisphere hippocampal masks using nearest-neighbour interpolation.

Personalised QSM profiles

Individual profiles of positive susceptibility were generated at the bilateral level using MATLAB (2024a). Mean positive susceptibility values were extracted from each of the 16 bilateral basal ROIs and 10 unilateral hippocampal segmentations. To yield a bilateral measure, left and right hemisphere susceptibility values were averaged for each hippocampal subfield. The HN was omitted due to zero values in this ROI for a subset of participants. No zero values were present for any participant within any hippocampal ROI. Z-scores were calculated for all participants (HC and mTBI), by subtracting the HC group mean from each individual's susceptibility value and dividing by the HC group standard deviation in accordance with methods used across different imaging modalities to investigate the effects of TBI and mTBI.[50–55,60] To bring the HC data closer to a normal distribution, outlier scores for the HC group were filtered if they fell outside 2 times the interquartile range (IQR), a more stringent criterion than the methods used to identify mild outliers 1.5 times the IQR, but less extreme than the more conservative filter of 3 times the IQR.[85] HC outliers were filtered in the hippocampal parasubiculum (n = 2), presubiculum (n = 2), and subiculum (n = 1). For basal ROIs, $n = 1$ HC participant was excluded in the EXA and VeP, $n = 2$ participants were excluded in the STH, and $n = 6$ participants were excluded in the MN. Despite the more extensive filtering applied to the MN region, the reduced HC sample size for this region (n = 19) is larger than comparable individualised QSM studies investigating moderate-to-severe TBI that have used a sample size of 12.[53] After filtering, the Shapiro-Wilk normality test yielded an average W value of $M = 0.95$ ($SD = 0.02$) across hippocampal ROIs and an average W value of $M = 0.94$ ($SD = 0.03$) across basal nuclei, indicating that the data distribution within each ROI was close to normal. The pipeline is summarised in Fig. 1 below.

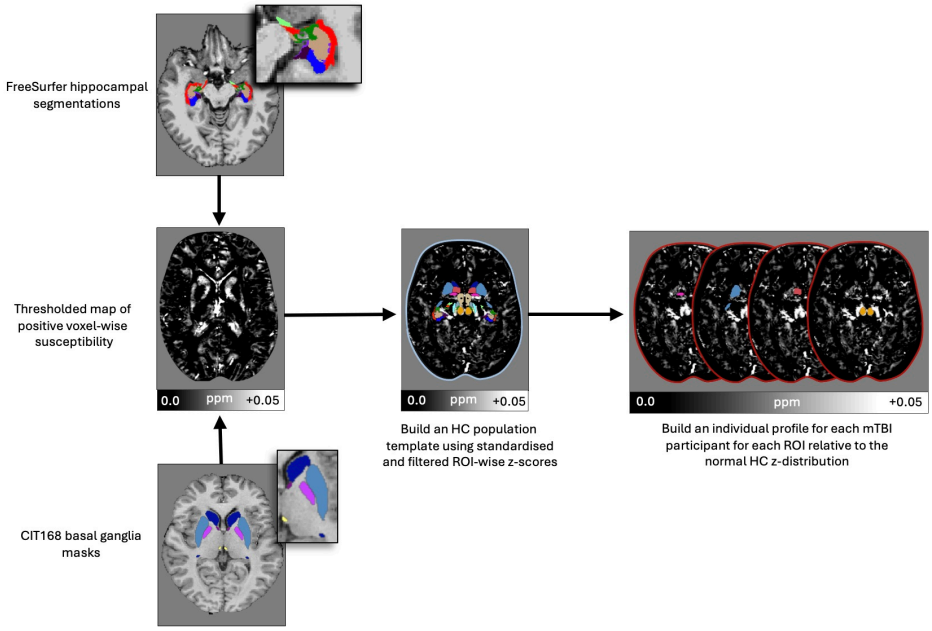

Fig 1: Pipeline for individual subcortical iron profile generation

FreeSurfer was used to generate segmentations of the hippocampal subfields from each participants' T_1w image volume, and the CIT168-MNI152 basal ganglia mask was used to delineate subcortical nuclei. These segmentations are overlaid on a structural T_1w image volume for enhanced visualisation (top left = hippocampal segmentations; bottom left = basal ganglia masks). QSM images were thresholded for net positive susceptibility (QSM^+ = centre left image). After voxel-wise thresholding, mean positive susceptibility values were extracted for each hippocampal and basal ROI. Z-scores were calculated using the mean and standard deviation of the healthy control group, and standardised around a mean of zero. The HC distribution was filtered to remove outliers exceeding two times IQR for a normal distribution. Each mTBI participants' z-score were compared to the healthy ROI-wise normal distribution, while controlling for multiple comparisons. QSM = quantitative susceptibility mapping; ROI = region of interest; mTBI = mild traumatic brain injury; HC = healthy control; IQR = interquartile range.

Statistical analyses

To assess statistical significance for mTBI z-scores, two-tailed p-values were calculated from the z-scores using the cumulative distribution function of the standard normal distribution. A false discovery rate (FDR) correction[86] was separately applied to the p-values for the 10 hippocampal or 15 basal nuclei ROI-wise comparisons.

To conduct secondary exploratory statistical tests, the mTBI group was divided into two subgroups: those whose z-scores significantly deviated from the HC normal distribution for any hippocampal or basal ROI (i.e., iron-abnormal) and those whose scores did not (i.e., iron-normal). Although preliminary analyses indicated no statistically significant difference in age between mTBI and HC participant groups, an ANOVA was performed between these three new subgroups (iron-normal, iron-abnormal, and controls) to confirm that age was not driving the identification of abnormal z-scores. Iron deposition in subcortical nuclei is a recognised feature of healthy ageing, particularly in individuals of a similar age range to this cohort,[62,65,66] thereby necessitating this further analysis to ensure that observed results were not confounded by normative, age-related tissue changes. Additionally, a nonparametric Mann-Whitney U test was used to assess whether injury severity (BIST scores) differed significantly between iron-abnormal and iron-normal mTBI participants, excluding mTBI-17 for this analysis only due to missing BIST data (see Table 1).

Results

Regional individualised subcortical iron profiles

Of the 35 total mTBI participants, 15 (43%) exhibited significantly higher z-scores than the healthy population template in at least one ROI (see Table 2, Fig. 2.2A and Fig. 2.2B). Among these "iron-abnormal" participants, 87% expressed abnormal iron markers inclusive of hippocampal ROIs, which frequently involved the parasubiculum. In contrast, only 60% of participants had abnormal iron markers inclusive of basal ganglia subregions. These abnormal markers were characterised by a relatively narrow distribution of z-scores across the available basal ganglia segmentations, with abnormal z-scores most commonly observed in the mammillary nucleus.

In addition to the high incidence of elevated z-scores in the hippocampal parasubiculum and basal mammillary nucleus, both of which were affected in approximately half of the 15 participants with abnormal iron markers (47%), relatively lower incidences of iron-related abnormalities were apparent in the hippocampal fimbria (27%), presubiculum and HATA (20% each) (see Fig. 2.2A and Fig. 2.2B). Less frequently affected ROIs included the hippocampal CA4 region and hippocampal fissure, as well as the basal nucleus accumbens and ventral pallidum, each with a 13% incidence rate. The basal SNc, PBP, hypothalamus, VTA, subthalamic nucleus, and hippocampal subiculum exhibited only isolated instances of elevated susceptibility across the whole iron-abnormal cohort. Only two hippocampal ROIs exhibited no significant deviations from the healthy normal distribution for any mTBI participant; the hippocampal tail and CA3. In contrast, no abnormal iron profiles were identified for several major basal subregions, including the putamen, caudate, globus pallidus (both internus and externus), red nucleus, SNr, and extended amygdala.

Only one participant (mTBI-18) had a z-score below the healthy control range, showing a z of -2.0 in the CA1 region. This case also represents the sole instance of CA1 involvement (see Table 2, Fig. 2.2A and Fig. 2.2B).

Table 2: Summary of significant ROI-wise z-scores and symptomatology for iron-abnormal sr-mTBI participants in the basal ganglia and hippocampal subfields

ID	Segmentation	ROI	z-score	Presenting symptoms
mTBI-01	Hippocampus: Basal Ganglia:	Parasubiculum Mammillary Nucleus	+3.7 +4.3	Initial emesis, followed by severe tinnitus and phonophobia, vertigo, cephalalgia, cervicalgia, photophobia, visual disturbance, cognitive impairment, confusion, concentration issues, memory deficits, irritability, restlessness, fatigue, and sleep disturbance. Moderate vestibular dysfunction and ataxia were also noted
mTBI-04	Hippocampus:	Parasubiculum	+2.4	Moderate cervicalgia and photophobia. Mild cephalalgia, ataxia, cognitive impairment, confusion, concentration issues, memory deficits, sleep disturbance. Additional clinical notes include vertigo and confusion at onset
mTBI-10	Hippocampus:	Parasubiculum	+5.8	Moderate cephalalgia, photophobia, vertigo, visual disturbance, fatigue, sleep disturbance. Mild cervicalgia, phonophobia, vestibular dysfunction, ataxia, cognitive issues, memory deficits, confusion, concentration issues, irritability, and restlessness. Additional clinical notes include hand numbness, pins and needles
mTBI-11	Hippocampus: Basal Ganglia:	Parasubiculum Mammillary Nucleus	+2.9 +4.1	Severe photophobia. Moderate cervicalgia, restlessness, fatigue, and sleep disturbance. Mild cephalalgia, phonophobia, vertigo, vestibular dysfunction, ataxia, visual disturbance, cognitive impairment, concentration issues, memory deficits, confusion, and irritability
mTBI-12	Hippocampus:	Presubiculum CA4 Fimbria Hippocampal Fissure	+2.8 +2.1 +3.1 +3.6	Mild cephalalgia, cervicalgia, photophobia, phonophobia, cognitive dysfunction, concentration issues, irritability, fatigue
mTBI-17	Hippocampus: Basal Ganglia:	Parasubiculum Mammillary Nucleus	+4.0 +11.0	No BIST. Clinical notes include transient mental fog, bradyphrenia, indecisiveness, and vestibular dysfunction
mTBI-18	Hippocampus: Basal Ganglia:	Presubiculum Subiculum CA1 CA4 Fimbria Hippocampal Fissure Mammillary Nucleus	+3.1 +2.5 -2.0 +2.9 +13.1 +4.0 +3.4	Moderate phonophobia, photophobia, visual disturbance, concentration issues. Mild cephalalgia, vertigo, vestibular dysfunction, ataxia, cognitive impairment, memory deficits, irritability, fatigue, and sleep disturbance. Additional clinical notes include disorientation, nausea, and impaired thought
mTBI-19	Basal Ganglia:	Nucleus Accumbens	+3.4	Moderate cognitive impairment, concentration issues, fatigue, and sleep disturbance. Mild cephalalgia, photophobia, memory deficits, and confusion. Additional clinical notes include being dazed at time of injury
mTBI-21	Hippocampus:	Fimbria	+4.4	Mild cephalalgia, photophobia, vertigo, cognitive impairment, memory deficits, concentration issues, fatigue, and sleep disturbance
mTBI-24	Hippocampus:	Parasubiculum	+6.1	Moderate cervicalgia, photophobia, phonophobia, vertigo, vestibular dysfunction, ataxia, cognitive impairment, memory deficits, confusion, concentration issues, irritability, restlessness, and fatigue. Mild cephalalgia, visual disturbance, sleep disturbance
mTBI-27	Hippocampus: Basal Ganglia:	HATA Nucleus Accumbens Ventral Pallidum	+2.7 +3.2 +2.8	Severe fatigue and sleep disturbance. Moderate cognitive impairment. Mild cephalalgia, photophobia, phonophobia, vestibular dysfunction, memory deficits and concentration issues. Additional clinical notes include anxiety
mTBI-28	Hippocampus: Basal Ganglia:	HATA Mammillary Nucleus	+4.6 +3.3	Moderate cephalalgia, photophobia, phonophobia, restlessness, fatigue and sleep disturbance. Mild cervicalgia, vertigo, vestibular dysfunction, ataxia, cognitive impairment, concentration issues, and memory deficits. Additional clinical notes include nausea, reduced tolerance to physical and cognitive exertion, and impaired coordination
mTBI-30	Basal Ganglia:	Ventral Pallidum Mammillary Nucleus	+2.9 +2.7	Fatigue
mTBI-31	Hippocampus:	Presubiculum HATA Fimbria	+3.3 +2.8 +5.2	Moderate fatigue and sleep disturbance. Mild cephalalgia, photophobia, cognitive impairment, concentration issues, irritability and restlessness
mTBI-32	Hippocampus: Basal Ganglia:	Parasubiculum SNc PBP VTA Hypothalamus Mammillary Nucleus Subthalamic Nuclei	+4.5 +2.9 +3.9 +3.1 +5.2 +3.5 +3.0	Moderate cephalalgia, cervicalgia, phonophobia, cognitive impairment, confusion, concentration issues, memory deficits, restlessness, and fatigue. Mild photophobia, vertigo, vestibular dysfunction, visual disturbance, ataxia, irritability, and sleep disturbance. Additional clinical notes include being dazed

Note. Presenting symptoms are primarily derived from BIST injury severity assessments and supplemented with additional clinical patient notes made upon presentation of participants to Axis Sports Medicine clinics. Only participants with abnormal iron profiles are included for brevity and relevance. ID = unique identifier; ROI = region of interest; CA = cornu ammonis; HATA = hippocampal-amygdala transition area.

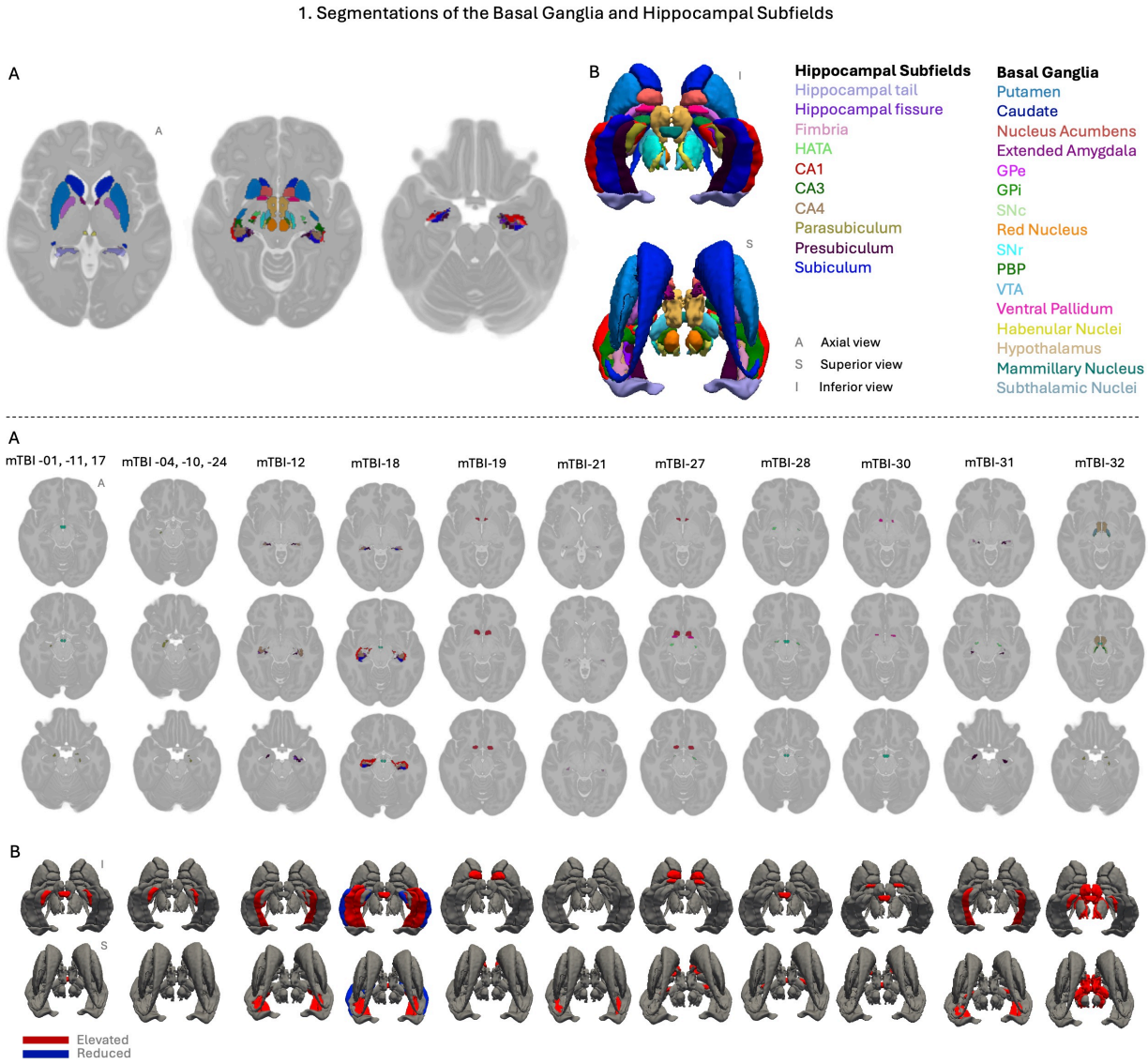

Fig 2: Segmentations and individualised profiles for abnormal subcortical iron markers

1. Visualisation of basal ganglia and hippocampal subfield segmentations. A. Axial (A) slices of the CIT168-MNI152 T_1w brain template depicting segmentations of the basal ganglia and hippocampal subfields, selected to optimise structural visualisation. B. 3D renderings show superior (S) and inferior (I) views of the segmented regions, with key subcortical structures labelled in their respective colours. 2. Significant deviations in subcortical iron markers for each sr-mTBI participant relative to the healthy control population. A. Axial views of the CIT168-MNI152 T_1w template highlight significant subcortical ROIs for each participant, shown in the segmentation colours. B. 3D renderings highlight regions with significantly elevated (red) or reduced (blue) z-scores to show regions with abnormal iron profiles; all other regions are greyed out. CA = cornu ammonis; GP = globus pallidus (GPi = internus; GPe = externus); SN = substantia nigra (SNc = pars compacta; SNr = pars reticulata); PBP = parabrachial pigmented nucleus; VTA = ventral tegmental area.

On aggregate, incidence rates of abnormal iron markers tended to cluster around the midline, in commissural nuclei, and inferior regions (see Fig. 3). A particularly high concentration was observed in the hippocampus, which is located inferior to the basal ganglia. Within the hippocampus, prevalent abnormal iron markers were observed near the anteromedial aspect of the hippocampus (the hippocampal head), decreasing in frequency laterally and toward the distal tail. In contrast, more superior regions, including the dorsal aspect of the hippocampus and the basal ganglia (excluding the mammillary nucleus) appeared to be less affected.

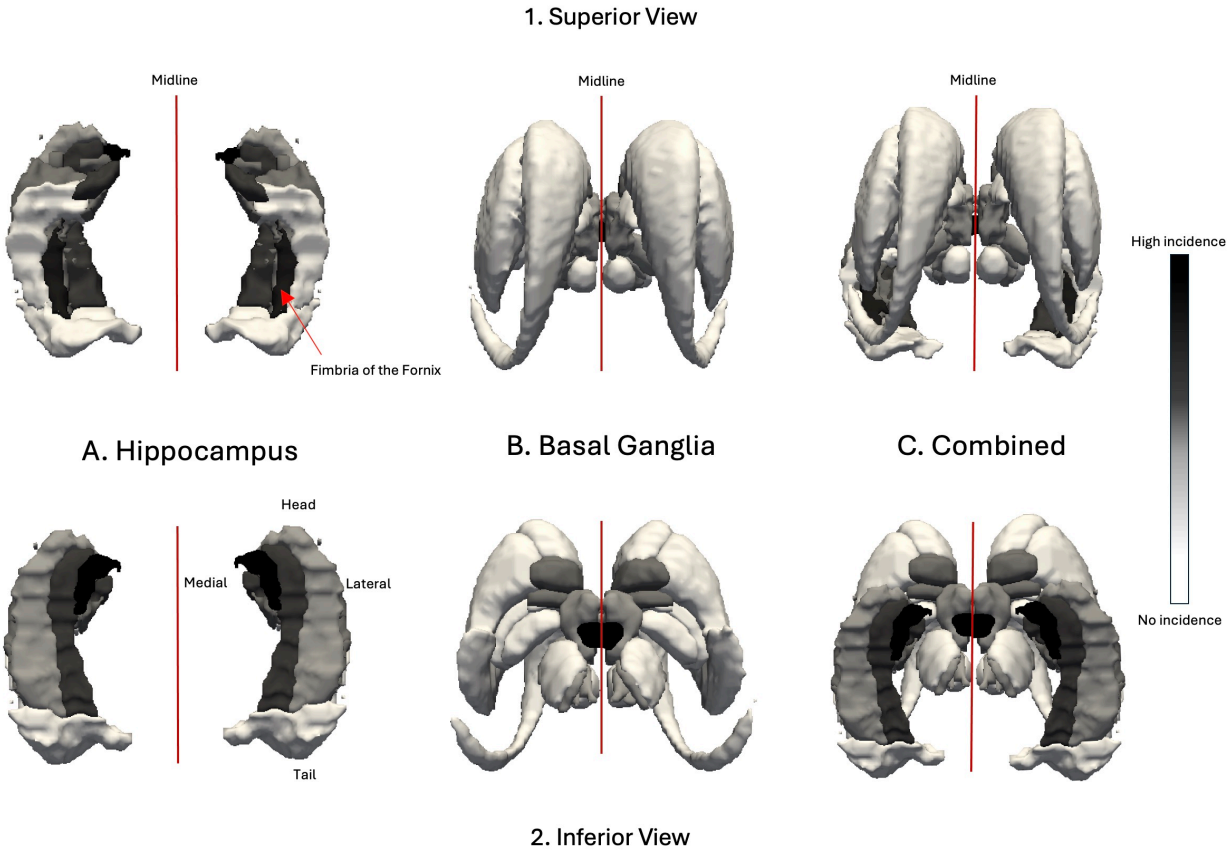

Fig 3: Aggregated regional incidence of abnormal iron markers

This figure presents a 3D model of relative incidence rates aggregated across the "iron-abnormal" mTBI population from a superior (1) and inferior (2) view. Incidence rates are represented in grey scale (high: black; low: white). A. Depicts the hippocampus in isolation. Anteromedial, and commissural (i.e., the fimbria) structures of the more inferior hippocampus show a higher incidence of abnormal z-scores than more superior or lateral structures. The medial aspect of the anterior hippocampal head is more frequently affected than lateral regions or the more distal tail. B. Depicts the basal ganglia in isolation. Substructures of the superiorly-situated basal ganglia show relatively lower rates of abnormal iron markers than the underlying hippocampal formation, with affected regions also primarily located in relatively more inferior and structures near the midline. C. Provides a combined view integrating both hippocampal and basal ganglia regions. The CA1 region has been omitted due to negative z-score.

After subdividing the mTBI participants into iron-normal (20/35; 57%) and iron-abnormal (15/35; 43%) sub-groups based on their individual profiles, a one-way ANOVA showed no significant differences in age between the three groups (iron-normal mTBI, iron-abnormal mTBI, and controls), $F(2, 32) = 1.12$, $p = 0.3$. A Mann-Whitney U test revealed no significant difference in BIST scores between iron-normal ($M = 35.6$, $SD = 30.8$) and iron-abnormal ($M = 41.7$, $SD = 34.5$) mTBI participants, $U = 120$, $p = 0.5$.

Patterns between symptoms and subcortical iron-related markers

This section is included for descriptive purposes, and relates to observations rather than results of inferential statistics. Elevated iron markers with hippocampal involvement presented alongside self-reported cognitive symptoms (including cognitive impairment, memory deficit, concentration issues, confusion, and clinical notes related to mental fog and bradyphrenia). Disturbances in arousal (fatigue and sleep) and sensory sensitivities (including headache, photophobia, and phonophobia) were reported by 92% of participants with hippocampal abnormalities. Vestibulo-ocular dysfunction (including vestibular symptoms, vertigo, ataxia, and visual disturbance) were slightly less common in this cohort (85%), followed by

mood disturbances (77%). Participants with elevated hippocampal iron markers that included the parasubiculum reported cognitive impairment and vestibulo-ocular symptomatology at a 100% incidence rate. Elevated iron markers in the mammillary nucleus, which almost invariably co-occurred with hippocampal regions and rarely with other basal regions, was also associated with high incidences of cognitive symptoms and vestibulo-ocular disturbances, as well as issues related to arousal (86% each). In contrast, relatively lower frequencies of all symptom clusters were reported across participants with abnormal iron markers inclusive of basal ganglia subregions. Cognitive impairment and arousal disturbances occurred in 89% of these participants, vestibulo-ocular and sensory dysfunctions in 78% each, and mood disturbances in 67% (see Table 2 for all symptom/region information).

Discussion

Group-level analytic methods currently dominate the field of clinical research.[57] However, the suitability of this approach for comprehensive understanding of neuropathology, particularly in the context of mTBI, may be limited. By focusing on population-level effects, subtle, yet clinically meaningful, inter-individual differences in pathophysiology may be overlooked. To advance the current understanding of deep grey matter iron aggregation in acute mTBI, we conducted the first dedicated individualised analysis of positive susceptibility in subcortical brain regions. Detailed segmentations of the basal ganglia were integrated with comprehensive delineation of the hippocampal subfields; an approach designed to overcome the anatomical limitations of previous group-level QSM investigations. Iron markers across 15 basal ganglia segmentations and 10 hippocampal subfields for individual mTBI participants were assessed relative to a normative control population using z-scores, enabling identification of subcortical regions where iron markers significantly deviated from a healthy reference range.

Results revealed abnormal subcortical iron profiles in approximately half of the mTBI sample, most of which involved at least one hippocampal subfield. Hippocampal abnormalities were not only observationally linked to a high incidence of cognitive symptoms, but were also associated with more frequent occurrence of all symptom clusters relative to participants whose abnormal profiles involved the basal nuclei. Among the hippocampal subregions, the parasubiculum was both the most prevalent ROI to be affected, and universally accompanied self reported cognitive and vestibulo-ocular symptoms. For iron-abnormal mTBI participants with basal ganglia involvement, elevated iron markers in the mammillary nucleus were also prevalent, occurring at the same incidence rate as markers in the parasubiculum across the entire iron-abnormal cohort. Significant z-scores in the mammillary nucleus most often co-occurred with hippocampal abnormalities or in isolation, rather than concomitant with abnormal z-scores in other basal nuclei. Symptoms related to cognitive, arousal, and vestibulo-ocular dysfunction were the most frequently reported symptoms among mTBI participants with mammillary nucleus involvement. Statistical analysis of injury severity scores between iron-normal and iron-abnormal mTBI participants revealed no significant differences, suggesting that although abnormal subcortical iron profiles may be observationally associated with specific symptom phenotypes, they may not be directly related to injury severity on aggregate.

Regional injury vulnerability in the hippocampus

The extensive white matter connections between the basal ganglia and both cortical and subcortical structures[87,88] increase vulnerability to shear and strain in these regions during mTBI.[10] This excessive biomechanical loading may also alter iron expression via secondary injury mechanisms.[6] In addition, the naturally high levels of iron in these nuclei, which under normal conditions support metabolic functions,[6,14,65] may exacerbate risk of trauma-induced cytotoxicity mediated by iron.[89] However, the higher incidence rates of iron-related abnormalities observed in hippocampal regions compared to the basal ganglia in this individualised study suggest that the prevailing focus on basal structures in the extant literature may

represent a critical oversight. Instead, results presented here indicate that the underlying hippocampus, and possibly the surrounding cerebrum,[60] may instead afford the basal ganglia a relative degree of structural protection from injury (see Fig. 4).

Despite the medial temporal lobe's known vulnerability to traumatic insult,[90,91] the hippocampus remains under-studied in QSM-based investigations of mTBI. Viewed in the context of the broader literature, the general predilection for hippocampal iron-related abnormalities across participants in this study indicate local changes to magnetic susceptibility that may be related to iron-driven secondary injury mechanisms[6,15] congruent with regional vulnerability of the hippocampus to mechanical deformation in TBI.[91] Both acute and chronic pathophysiological sequelae associated with hippocampal regions following mild-to-severe traumatic injury can include cytotoxic secondary injury, disruptions to vascular and metabolic function, diffuse axonal injury of afferent and efferent fibers, and even chronic traumatic encephalopathy (CTE)-associated tauopathy and focal atrophy as a downstream pathological event,[90,92] for which iron overload may be a mediating factor.[6–8,93] On aggregate, the results of the present study suggest that the hippocampus is a primary site of mTBI-related pathophysiological processes.

Towards a region-of-risk model of mTBI

The distinct, subfield-specific patterns that emerged when abnormal iron markers were aggregated across participants highlights not only the hippocampus but also specific subfields and spatial locations as regions with heightened vulnerability to injury. Injury biomechanics and morphology of the skull base may contribute to increased mechanical loading and strain, focal tissue damage, and a resultant dynamic cascade of secondary injury mechanisms which may include altered iron signalling in select vulnerable, and interconnected, regions (see Fig. 4). Specifically, the concentration of iron markers in the parasubiculum, mammillary nucleus, and fimbria support and extend findings from a previous group-wise cortical QSM investigation[61] which demonstrated localisation of abnormal positive susceptibility values to the adjacent parahippocampal gyrus.

Anatomically, the head of the hippocampus is situated approximately 2 cm from the irregular sphenoid ridge at the junction of the anterior and middle cranial fossa, and is particularly susceptible to mechanical deformation over this bony protrusion during impact.[94] The parasubiculum, as part of this region,[95] may thus be more vulnerable to injury than hippocampal substructures located peripherally to this region of heightened injury risk (e.g., the subiculum) or in the more distal hippocampal tail. This observation is supported by a high degree of spatial overlap between areas of varying injury vulnerability, as informed by cranial-dural architecture and injury biomechanics, and the relative incidence rates of abnormal z-scores observed here which cluster at the anterior aspect of the hippocampus (the hippocampal head), and diminish with proximity to this region (see Fig. 4). These results are also congruent with prior research noting the anterior aspect of the medial temporal lobe as a region of risk.[94,96] Data from investigations of temporal lobe epilepsy suggests that parasubicular neurons are hyper-excitable,[97] which may contribute to iron accumulation as a consequence of excitotoxicity in mTBI,[7] further exacerbating regional risk. Additionally, the contribution of iron deficiency to neuron loss[14] provides a plausible explanation for the abnormally low z-score observed in the hippocampal CA1 region of a single participant in this study, reinforcing a hippocampus-specific model of tissue disruption.

Beyond the medial temporal lobe, midline and commissural structures, including the fornix, are increasingly recognised as regions prone to excessive biomechanical loading during sr-mTBI impacts, and have been associated with memory and cognitive impairments in 30-50% of cases and removal from play in 30%.[98] Damage to midline structures has also been cited as a risk factor for subsequent mTBI,[99] and although these observations were not directly related to the structures under investigation in the present study, the incidence of abnormal iron markers in the mammillary nucleus and fimbria observed in this sample is nonetheless noteworthy. The fimbria is a key component of the fornix; a commissural tract not only connecting the bilateral hippocampus, but the hippocampus to the mammillary bodies.[94,100] Evidence of dyshomeostatic

mechanisms focal to this region may be related to head kinematics during impact, whereby rotational forces are a likely cause of strain-related diffuse injury,[101,102] which may be particularly damaging to the fornix[98] and related nuclei. In addition, the mammillary bodies, located on the inferior aspect of the diencephalon, are paired structures that sit on either side of the midline and are connected by the intermammillary sulcus.[103] These nuclei are also related to the commissural fornix, forming the terminals of its anterior pillars.[104]

Degeneration of both the fornix and mammillary bodies has been extensively documented in TBI, which is attributed to medial temporal lobe trauma and disruption of these regions as downstream targets.[94] The mammillary bodies receive projections from the parasubiculum,[104] and abnormal iron markers in this region may represent a more subtle, but pathologically significant, manifestation of degenerative excitotoxic processes that exist on a continuum with more severe TBI. The interconnection of these two regions may not only explain equivalent incidences of iron-related abnormalities in these regions, but their frequent co-occurrence within individual participant results (see Table 2). Taken together, these data not only reinforce the importance of subfield-specific investigations of the hippocampus and granular segmentations of the basal anatomy, but also provide evidence that sites of cellular distress signalling can be mapped to potential injury mechanisms via quantification of positive susceptibility and the use of individualised analytic techniques. This lends support to the utilisation of individualised study designs to detect heterogeneous changes in brain tissue content, and contributes to the current understanding of the relationships between potential iron overload, injury dynamics, and mTBI pathophysiology.

Regional iron dysregulation, symptom cluster, and Papez circuit integration

Disruption to cellular integrity can impede function, resulting in changes to cognition and behaviour that may be related to specific injury biodynamics and loci of neuronal injury.[93] Although elevated subcortical iron markers were not associated with greater self-reported symptom *severity*, and causal inference is precluded in this sample, the universal incidence of symptom clusters within the cognitive domain among participants with abnormal hippocampal iron markers is consistent with extant literature linking memory and cognitive deficits to medial temporal lobe damage[90] and iron dyshomeostasis.[7,9] In addition to the general concentration of abnormal iron markers within the hippocampal subfields broadly, the mammillary nucleus and parasubiculum emerged as consistent sites of abnormal iron loading which could speculatively be related to symptom phenotype.

Although the specific role of the parasubiculum in mTBI-induced pathology and associated symptomatology remains under explored, its involvement in key pathways mediating cognitive and vestibulo-ocular functions may offer a plausible explanation for clinical deficits reported by participants presenting with abnormal iron profiles in this region. Participants with elevated iron markers in the mammillary nucleus also reported similar symptoms, with an additional high incidence of arousal disturbances (see Table 2). Functional and structural connectivity between these two regions[104,105] may account not only for the overlapping symptomatology, but also for the frequent co-occurrence of abnormal iron markers.

As part of the subicular complex, the parasubiculum occupies a central position in the medial temporal lobe memory system, supporting memory formation.[106,107] This is exemplified by observations of pyramidal cell loss and the formation of severe neurofibrillary tangles (NFTs) in the parasubiculum in Alzheimer's disease (AD)[108] with memory loss as a central feature.[109] The parasubiculum also plays a critical role in spatial information processing. [110,111] This region is anatomically and functionally connected to the area prostriata, which projects to visual, motor, and auditory regions,[106] and interfaces with the entorhinal cortex, a region critical for both memory formation and integration of vestibular and directional cues in spatial navigation.[107,112] Directional and spatial orientation signals are further modulated by connections to the mammillary bodies. "Head-direction" cells responsive to head orientation and spatial encoding in the presubicular and parasubicular cortices[110,111,113] transmit signals to the lateral mammillary nucleus to facilitate navigation and orientation.[114]

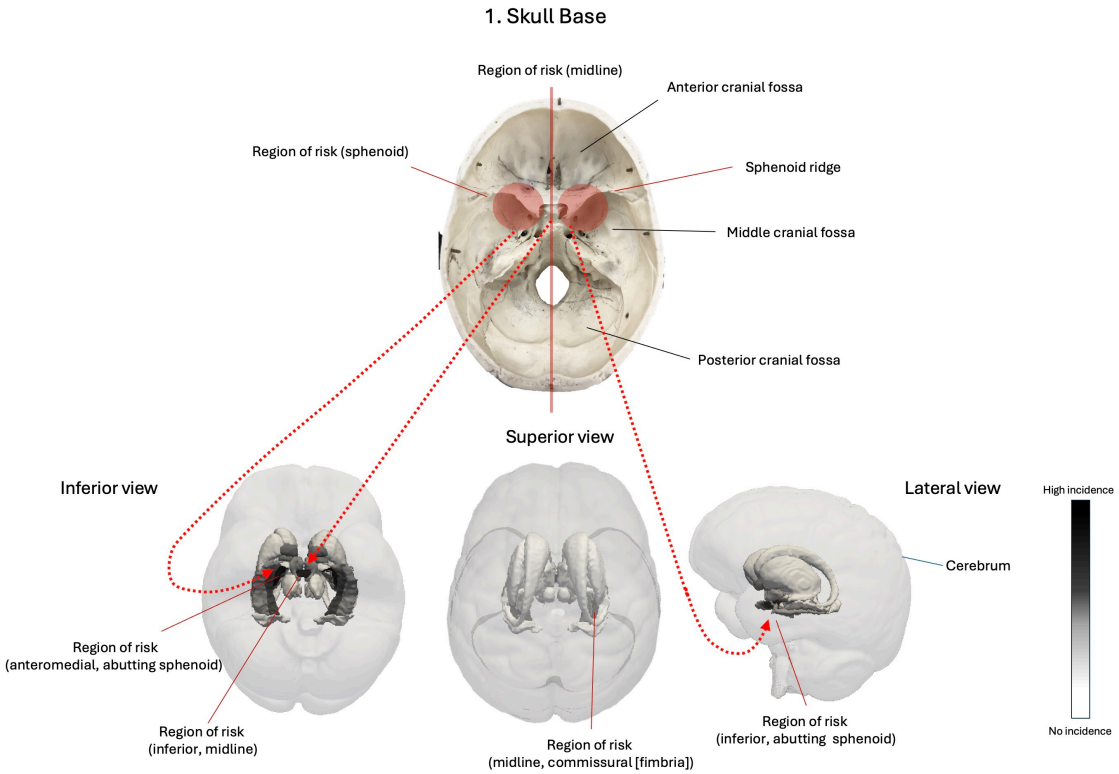

Fig 4: Spatial alignment between regions of heightened injury risk and abnormal iron markers

This figure highlights the anatomical alignment between structural vulnerability and impact biomechanics with aggregate iron markers in subcortical brain regions across "iron-abnormal" mTBI participants. 1. Visualises the cranial base from a superior view. Key regions of mechanical risk, including the sphenoid ridge and midline zones, are highlighted in red. 2. Provides a 3D render showing spatial alignment between regions of risk and incidence rates of abnormal iron markers across the sample. This model provides a visualisation of the vulnerability of inferior structures, particularly in the anterior aspect proximal to the sphenoid ridge, as well as midline and commissural regions, to cranial impact, strain, and force transmission. The basal ganglia, shielded from below by the hippocampus and from above by the cerebrum, may be afforded more protection from injury. The CA1 region has been omitted due to a negative z-score.

The mammillary bodies also serve as a central pathway for memory processes. In addition to receiving hippocampal outputs via the fornix,[100] the mammillary bodies relay these signals to the anterior thalamic nuclei through the mammillothalamic tract.[115] This relay function is a critical component of the Papez circuit central to emotion and memory.[116] Damage to this fundamental network has been associated with a variety of neurological disorders that have cognitive impairment as a defining feature, including AD, Parkinson's disease (PD), semantic dementia, and global amnesia.[116,117] Atrophy of the mammillary bodies is also distinguishing feature of Korsakoff syndrome, a degenerative neurological disorder related to chronic alcohol abuse which is characterised by episodic memory deficits,[114] and linked to dysfunction within Papez circuit.[117] Within the context of mTBI, pathology of the mammillary bodies has been cited as an antecedent of memory impairment stemming from Papez circuit disconnection in retired athletes with a history of repetitive mTBI.[118] By extension, it is plausible that similar symptoms reported by participants with evidence of iron accumulation in these key, highly interconnected, regions might arise from dysfunction of these central circuits.

Finally, the high incidence of issues related to arousal also reported by participants with abnormal iron markers in the mammillary nucleus could speculatively be attributed to disruption of histaminergic neurons within the mammillary bodies that regulate arousal and wakefulness. Damage to these neurons has been identified as a mediating factor in sleep dysregulation following mTBI,[119] corroborating this hypothesis.

The potential of an individualised approach for enhancing research and clinical care

Collectively, the distribution of abnormal iron markers across subcortical nuclei suggests a region-of-risk model informed by injury biomechanics and a complex interplay with cranial and dural architecture (see Fig. 4). It is well-established that different biomechanical forces give rise to heterogeneous and dynamic injury cascades, complicating the study of mTBI pathophysiology.[93,120] The results presented here suggest that characterising dyshomeostatic iron signalling at the individual level may serve as a viable proxy for secondary injury mechanisms occurring in a subset of individuals, and at specific spatial locations. These data indicate that mTBI induces iron overload in at least one subcortical region for 43% of participants with mTBI. Taken together with the lack of identifiable differences in positive susceptibility between mTBI participants and controls in a previous extensive group level investigation[44] and in the literature more broadly,[30–36] this finding suggests that iron dyshomeostasis in the deep grey matter may not constitute a feature of mTBI generalisable to all cases. However, the use of individualised modelling likely enables identification of instances at the single-subject level where iron accumulation may be occurring, providing biologically informative results that are otherwise lost to averages. This suggests that targeted interventions, for example heavy metal chelation therapies,[121–125] may be beneficial for some individuals, emphasising importance of identifying individual variation that could inform the development of future clinical trials and specific treatment strategies.[57] In addition, leveraging inherent tissue susceptibility variations has the potential to identify not only specific injury patterns but also individuals at elevated risk of suboptimal recovery, subsequent injury, or localised tissue pathology, provided that study designs are suitably responsive. The observed relationships between loci of abnormal iron markers and symptom clusters also alludes to the potential of individualised approaches to elucidate how distinct patterns of cellular disruption may be related to specific clinical phenotypes.

As an extension of the same logic, the relative under representation of abnormal iron markers in the CA4 in this sample, coupled with the observation of decreased negative susceptibility for mTBI participants in this region in prior group-level analyses,[44] suggests that while the CA4 may be vulnerable to disruption of negative susceptibility sources, mechanisms of iron dyshomeostasis in this region are less prevalent. This, in turn, highlights the utility of group-wise analyses to identify potential signatures of mTBI that are congruent with established disturbance of hilar cell populations in head injury[45–48] and temporal lobe epilepsy.[49] These convergent data underscore the importance of tailoring the analytic strategy choices to the research objective.

This work also underscores inherent limitations of the standard methodological focus prevalent in contemporary QSM-based mTBI research. Specifically, identifying hippocampal subfields and the mammillary nucleus as primary loci of acute, iron-related mTBI pathophysiology suggests that prior research concentrated only on major basal ganglia structures,[30–33,35] or using gross hippocampal segmentations,[34,36] is likely insensitive to discrete regions differentially affected by injury. At minimum, this work highlights the need to incorporate both individualised analyses and detailed segmentations into future research designs to improve understanding of regional, inter-individual tissue content changes following mTBI, and provides evidence that calls for the scientific community embrace new paradigms that account for injury heterogeneity[120] and more detailed segmentations[6] are well-founded.

Lastly, the congruence between dominant spatial distributions of abnormal iron markers in this sample and diagnostic features of CTE are concerning given the putative relationship between the two.[68,126,127] In particular, the presence of NFTs in the hippocampus and mammillary bodies is diagnostic of CTE and CTE burden (high versus low).[92] Identifying these specific regions as common locations of potential iron dyshomeostasis in mTBI raises further questions about the interrelatedness of acute cascades that may present as later-life pathology in a subset of individuals.

Limitations and future research

There is a lack of any widely established best-practice method to normalise the HC z-distribution and other individualised QSM research has employed less stringent filtering at three times IQR to detect more severe TBI pathology.[53] Future research would benefit from standardised practices for outlier detection. The mammillary nucleus, in particular, was more extensively filtered than other regions. This may have contributed to a greater proportion of abnormal z-scores in this region, despite a residual sample size that is still more robust than other comparable studies.[53] In addition, the use of nonparametric approaches for between-group comparisons of iron-normal and iron-abnormal mTBI participants is limited by the inherent challenges associated with small and unequal sample sizes, which may compromise the statistical power and reliability of these findings; thus, the results of the Mann-Whitney U test to investigated differences in injury severity scores should be interpreted with caution.

Natural age-related increases in subcortical iron can also be particularly pronounced within this specific age range,[65] and although the ages of the HC and mTBI participants were closely matched, some confounding effects may still be introduced. For example, the relative under representation of abnormal iron markers in the basal substructures (with the exception of the mammillary nucleus) may be related to the potential confounding effects of age-related increases in iron. These effects may be particularly relevant in regions known to exhibit elevated iron content during normal ageing such as the red nucleus, substantia nigra, globus pallidus, putamen, and caudate,[62,63,65–67] many of which showed no evidence of abnormal individualised iron markers compared to the HC population. Despite the lack of statistically significant age differences between groups in all relevant analyses, it is still possible that age-related variability in regional iron content may yield an inherently broader normative distribution, thereby confounding identification of abnormal iron markers in the mTBI cohort.

Although this study used detailed segmentations, some structural limitations remain. For instance, the mammillary bodies comprise functionally and structurally distinct subregions. Evidence from murine models suggests that head-direction cells are present in the lateral, but not medial, mammillary nuclei.[114] Future investigations should consider additional segmentation granularity, whilst balancing the need to detect subregion-specific pathophysiology and challenges related to multiple comparisons. In addition, individualised approaches should integrate additional MRI imaging modalities, for example, to investigate white matter pathway integrity as a marker of axonal injury (e.g., by diffusion MRI) and/or functional connectivity via functional MRI. A multi-modal approach would facilitate a deeper understanding of how specific tracts, networks, and nodes are implicated in injury-related pathophysiology and symptomatology, and how this may relate to patterns of cellular disruption in grey matter on QSM.

The use of single-echo data for QSM reconstruction inhibits the application of true intra-voxel magnetic source separation.[128–133] While inter-voxel thresholding has been applied to investigations of AD[81] and healthy ageing[82] with meaningful results, this approach does not distinguish the heterogeneous susceptibility sources within voxels, constraining inference at the biological level. Lastly, the identification of relationships between abnormal regional iron markers and symptomatology made here were observational only; the small sample size and some ambiguity in self-reported symptoms precludes the use of inferential statistics. Additional intra-individual overlap in abnormal z-scores in basal and hippocampal ROIs also inhibits precise delineation of the relationship between basal versus hippocampal z-score clusters and clinical symptom phenotype. The reader should bear in mind that any inferences are speculative, and do not represent a one-to-one symptom-to-ROI mapping.

Conclusions

This study presented the first dedicated individualised QSM investigation of iron-related tissue content changes in subcortical grey matter regions following mTBI. The results highlighted the inter-individual heterogeneity in regional iron markers, and underscored the vulnerability of specific

hippocampal subfields congruent with established regions-of-risk in the TBI literature. Injury severity was not significantly different between mTBI participants presenting with abnormal iron markers and those who did not, however, iron-related markers localised to certain hippocampal subfields and the mammillary nucleus appeared to be related to distinct clinical phenotypes. These results support the use of analytic techniques sensitive to inter-individual variation to identify instances of injury-induced grey matter micropathology, which have been largely absent from the group-wise QSM investigations of mTBI that have been conducted to date.

Author Contributions

Christi A. Essex (Conceptualisation, Methodology, Project Administration, Validation, Software, Formal Analysis, Investigation, Resources, Data Curation, Writing - Original Draft, Writing - Review & Editing, Visualisation); **Mayan J. Bedggood** (Writing - Review & Editing, Project administration, Investigation); **Jenna L. Merenstein** (Writing - Review & Editing); **Catherine Morgan** (Methodology, Writing - Review & Editing); **Helen Murray** (Writing - Review & Editing); **Samantha J. Holdsworth** (Writing - Review & Editing); **Richard L.M. Faull** (Writing - Review & Editing); **Patria Hume** (Writing - Review & Editing); **Alice Theadom** (Conceptualisation, Methodology, Writing - Review & Editing, Funding acquisition, Supervision); **Mangor Pedersen** (Conceptualisation, Methodology, Writing - Review & Editing, Funding acquisition, Supervision)

Acknowledgements

We extend thanks to Amabelle Voice-Powell and Cassandra McGregor for their contribution to the data collection, and Tania Ka'ai for bringing her perspective to cultural considerations on this study. In addition, we thank Axis Sports Concussion Clinics, particularly Dr Stephen Kara, for their assistance with recruiting sr-mTBI participants and personnel at the Centre for Advanced Magnetic Resonance Imaging (CAMRI) for their assistance collecting MRI data. We also acknowledge Dr Tim Elliot for radiological reporting of all participants and Siemens Healthineers for the use of a work-in-progress (WIP) prototype sequence for the acquisition data used to perform QSM.

Funding

This project was funded by a grant from the Health Research Council of New Zealand (HRC), grant #21/622.

The first author (CE) is supported by a Dame Dorothy Winstone Doctoral Completion Award from the Kate Edger Foundation of New Zealand.

Competing Interests

The authors report no competing interests.

Data availability

De-identified MRI data and code used for image processing and statistical analysis can be made available upon request to the corresponding author.

References

1 A. I. Maas, D. K. Menon, G. T. Manley, *et al.*, "Traumatic brain injury: progress and challenges in prevention, clinical care, and research," *The Lancet Neurology* **21**, 1004–1060 (2022).

2 A. I. Maas, D. K. Menon, P. D. David Adelson, *et al.*, "Traumatic brain injury: Integrated approaches to improve prevention, clinical care, and research," (2017).

3 C. Lefevre-Dognin, M. Cogné, V. Perdrieau, *et al.*, "Definition and epidemiology of mild traumatic brain injury," *Neurochirurgie* **67**(3), 218–221 (2021).

4 L. M. Crowe, S. Hearps, V. Anderson, *et al.*, "Investigating the Variability in Mild Traumatic Brain Injury Definitions: A Prospective Cohort Study," *Archives of Physical Medicine and Rehabilitation* **99**, 1360–1369 (2018).

5 N. D. Silverberg, G. L. Iverson, A. Cogan, *et al.*, "The American Congress of Rehabilitation Medicine Diagnostic Criteria for Mild Traumatic Brain Injury," (2023).

6 A. Gozt, S. Hellewell, P. G. Ward, *et al.*, "Emerging Applications for Quantitative Susceptibility Mapping in the Detection of Traumatic Brain Injury Pathology," *Neuroscience* **467**, 218–236 (2021).

7 S. Huang, S. Li, H. Feng, *et al.*, "Iron Metabolism Disorders for Cognitive Dysfunction After Mild Traumatic Brain Injury," *Frontiers in Neuroscience* **15** (2021).

8 E. J. Nisenbaum, D. S. Novikov, and Y. W. Lui, "The presence and role of iron in mild traumatic brain injury: An imaging perspective," *Journal of Neurotrauma* **31**, 301–307 (2014).

9 L. Lu, H. Cao, X. Wei, *et al.*, "Iron Deposition Is Positively Related to Cognitive Impairment in Patients with Chronic Mild Traumatic Brain Injury: Assessment with Susceptibility Weighted Imaging," *BioMed Research International* **2015** (2015).

10 E. Raz, J. H. Jensen, Y. Ge, *et al.*, "Brain iron quantification in mild traumatic brain injury: A magnetic field correlation study," *American Journal of Neuroradiology* **32**(10), 1851–1856 (2011).

11 R. J. Ward, F. A. Zucca, J. H. Duyn, *et al.*, "The role of iron in brain ageing and neurodegenerative disorders," *The Lancet Neurology* **13**(10), 1045–1060 (2014).

12 X. Y. Xiong, J. Wang, Z. M. Qian, *et al.*, "Iron and Intracerebral Hemorrhage: From Mechanism to Translation," (2014).

13 M. Kruszewski, "Labile iron pool: The main determinant of cellular response to oxidative stress," in *Mutation Research - Fundamental and Molecular Mechanisms of Mutagenesis*, **531**, 81–92, Elsevier (2003).

14 S. Levi, M. Ripamonti, A. S. Moro, *et al.*, "Iron imbalance in neurodegeneration," *Molecular Psychiatry* **29**(4), 1139–1152 (2024).

15 M. Daglas and P. A. Adlard, "The Involvement of Iron in Traumatic Brain Injury and Neurodegenerative Disease," *Frontiers in Neuroscience* **12** (2018).

16 H. Ma, Y. Dong, Y. Chu, *et al.*, "The mechanisms of ferroptosis and its role in alzheimer's disease," *Frontiers in Molecular Biosciences* **9** (2022).

17 E. L. Mackenzie, K. Iwasaki, and Y. Tsuji, "Intracellular iron transport and storage: From molecular mechanisms to health implications," *Antioxidants and Redox Signaling* **10**(6), 997–1030 (2008).

18 E. Stephenson, N. Nathoo, Y. Mahjoub, *et al.*, "Iron in multiple sclerosis: Roles in neurodegeneration and repair," (2014).

19 S. Tang, P. Gao, H. Chen, *et al.*, "The Role of Iron, Its Metabolism and Ferroptosis in Traumatic Brain Injury," *Frontiers in Cellular Neuroscience* **14** (2020).

20 A. Deistung, F. Schweser, and J. R. Reichenbach, "Overview of quantitative susceptibility mapping," (2017).

21 C. Langkammer, F. Schweser, N. Krebs, *et al.*, "Quantitative susceptibility mapping (QSM) as a means to measure brain iron? A post mortem validation study," *NeuroImage* **62**(3), 1593–1599 (2012).

22 C. Liu, W. Li, K. A. Tong, *et al.*, "Susceptibility-weighted imaging and quantitative susceptibility mapping in the brain," *Journal of Magnetic Resonance Imaging* **42**(1), 23–41 (2015).

23 S. Ghaderi, S. Mohammadi, N. J. Nezhad, *et al.*, "Iron quantification in basal ganglia: quantitative susceptibility mapping as a potential biomarker for Alzheimer's disease – a systematic review and meta-analysis," (2024).

24 S. Mohammadi, S. Ghaderi, and F. Fatehi, "Putamen iron quantification in diseases with neurodegeneration: a meta-analysis of the quantitative susceptibility mapping technique," (2024).

25 F. Nikparast, Z. Ganji, M. Danesh Doust, *et al.*, "Brain pathological changes during neurodegenerative diseases and their identification methods: How does QSM perform in detecting this process?," (2022).

26 P. Ravanfar, S. M. Loi, W. T. Syeda, *et al.*, "Systematic Review: Quantitative Susceptibility Mapping (QSM) of Brain Iron Profile in Neurodegenerative Diseases," *Frontiers in Neuroscience* **15** (2021).

27 J. Paul, A. Raj, S. Raghavan, *et al.*, "Comparative analysis of quantitative susceptibility mapping in preclinical dementia detection," (2024).

28 Y. Uchida, H. Kan, K. Sakurai, *et al.*, "Quantitative susceptibility mapping as an imaging biomarker for Alzheimer's disease: The expectations and limitations," (2022).

29 A. Gozt, S. Hellewell, J. Thorne, *et al.*, "Predicting outcome following mild traumatic brain injury: Protocol for the longitudinal, prospective, observational Concussion Recovery (CREST) cohort study," *BMJ Open* **11** (2021).

30 T. K. Bell, M. Ansari, J. M. Joyce, *et al.*, "Quantitative Susceptibility Mapping in Adults with Persistent-Post Concussion Symptoms after Mild Traumatic Brain Injury: An Exploratory Study," *American Journal of Neuroradiology* , ajnr.A8454 (2024).

31 N. J. Gong, S. Kuzminski, M. Clark, *et al.*, "Microstructural alterations of cortical and deep gray matter over a season of high school football revealed by diffusion kurtosis imaging," *Neurobiology of Disease* **119**, 79–87 (2018).

32 K. M. Koch, T. B. Meier, R. Karr, *et al.*, "Quantitative susceptibility mapping after sports-related concussion," *American Journal of Neuroradiology* **39**(7), 1215–1221 (2018).

33 K. M. Koch, A. S. Nencka, B. Swearingen, *et al.*, "Acute Post-Concussive Assessments of Brain Tissue Magnetism Using Magnetic Resonance Imaging," *Journal of Neurotrauma* **38**(7), 848–857 (2021).

34 N. N. Pinky, C. T. Debert, S. P. Dukelow, *et al.*, "Multimodal magnetic resonance imaging of youth sport-related concussion reveals acute changes in the cerebellum, basal ganglia, and corpus callosum that resolve with recovery," *Frontiers in Human Neuroscience* **16** (2022).

35 D. K. Wright, T. J. O'Brien, and S. R. Shultz, "Sub-acute Changes on MRI Measures of Cerebral Blood Flow and Venous Oxygen Saturation in Concussed Australian Rules Footballers," *Sports Medicine - Open* **8**(1) (2022).

36 R. Zivadinov, P. Polak, F. Schweser, *et al.*, "Multimodal Imaging of Retired Professional Contact Sport Athletes Does Not Provide Evidence of Structural and Functional Brain Damage," *Journal of Head Trauma Rehabilitation* **33**(5), E24–E32 (2018).

37 H. Arciniega, Z. H. Baucom, F. Tuz-Zahra, *et al.*, "Brain morphometry in former American football players: 1 findings from the DIAGNOSE CTE research project," *Oxford University Press* **22** (2024).

38 D. M. Geddes, M. C. LaPlaca, and R. S. Cargill, "Susceptibility of hippocampal neurons to mechanically induced injury," *Experimental Neurology* **184**(1), 420–427 (2003).

39 T. J. Sick, M. A. Perez-Pinzon, Z.-Z. Feng´´, *et al.*, "Impaired expression of long-term potentiation in hippocampal slices 4 and 48 h following mild fluid-percussion brain injury in vivo," tech. rep. (1998).

40 E. R. White, C. Pinar, C. A. Bostrom, *et al.*, "Mild Traumatic Brain Injury Produces Long-Lasting Deficits in Synaptic Plasticity in the Female Juvenile Hippocampus," *Journal of Neurotrauma* **34**, 1111–1123 (2017).

41 E. A. Wilde, E. D. Bigler, J. V. Hunter, *et al.*, "Hippocampus, amygdala, and basal ganglia morphometrics in children after moderate-to-severe traumatic brain injury," *Developmental Medicine and Child Neurology* **49**, 294–299 (2007).

42 T. A. Rouault, "Iron metabolism in the CNS: Implications for neurodegenerative diseases," (2013).

43 F. D. Raslau, I. T. Mark, A. P. Klein, *et al.*, "Memory Part 2: The Role of the Medial Temporal Lobe," *American Journal of Neuroradiology* **36**, 846–849 (2015).

44 C. A. Essex, M. J. Bedggood, J. L. Merenstein, *et al.*, "Magnetic susceptibility of the hippocampal subfields and basal ganglia in acute mild traumatic brain injury," (2025).

45 M. R. Grovola, N. Paleologos, K. L. Wofford, *et al.*, "Mossy cell hypertrophy and synaptic changes in the hilus following mild diffuse traumatic brain injury in pigs," *Journal of Neuroinflammation* **17** (2020).

46 D. H. Lowenstein, M. J. Thomas, D. H. Smith, *et al.*, "Selective Vulnerability of Dentate Hilar Neurons following Traumatic Brain Injury: A Potential Mechanistic Link between Head Trauma and Disorders of the Hippocampus," *The Journal of Neuroscience* **12**(12), 4848–4853 (1992).

47 W. L. Maxwell, K. Dhillon, L. Harper, *et al.*, "There Is Differential Loss of Pyramidal Cells from the Human Hippocampus with Survival after Blunt Head Injury," Tech. Rep. 3 (2003).

48 V. Santhakumar, R. Bender, M. Frotscher, *et al.*, "Granule cell hyperexcitability in the early post-traumatic rat dentate gyrus: the 'irritable mossy cell' hypothesis," *Journal of Physiology* (524), 117–134 (2000).

49 H. E. Scharfman, "The enigmatic mossy cell of the dentate gyrus," *Nature Reviews Neuroscience* **17**(9), 562–575 (2016).

50 A. Attyé, F. Renard, M. Baciu, *et al.*, "TractLearn: A geodesic learning framework for quantitative analysis of brain bundles," *NeuroImage* **233** (2021).

51 M. J. Bedggood, C. A. Essex, A. Theadom, *et al.*, "Individual-level analysis of MRI T2 relaxometry in mild traumatic brain injury: Possible indications of brain inflammation," *NeuroImage: Clinical* **43** (2024).

52 A. Clemente, A. Attyé, F. Renard, *et al.*, "Individualised Profiling of White Matter Organisation in Moderate-to-Severe Traumatic Brain Injury Patients Using TractLearn: A Proof-of-Concept Study," *Brain Research* **1806** (2023).

53 J. F. Domínguez, A. Stewart, A. Burmester, *et al.*, "Improving quantitative susceptibility mapping for the identification of traumatic brain injury neurodegeneration at the individual level," *Zeitschrift fur Medizinische Physik* (2024).

54 P. Imms, A. Clemente, E. Deutscher, *et al.*, "Exploring personalized structural connectomics for moderate to severe traumatic brain injury," *Network Neuroscience* **1**(7), 160–183 (2022).

55 A. E. Jolly, M. Balaeţ, A. Azor, *et al.*, "Detecting axonal injury in individual patients after traumatic brain injury," *Brain* **144**(1), 92–113 (2021).

56 R. Mito, M. Pedersen, H. Pardoe, *et al.*, "Exploring individual fixel-based white matter abnormalities in epilepsy," *Brain Communications* **6**(1) (2024).

57 A. F. Marquand, S. M. Kia, M. Zabihi, *et al.*, "Conceptualizing mental disorders as deviations from normative functioning," (2019).

58 K. Łoś and N. Waszkiewicz, "Biological markers in anxiety disorders," (2021).

59 D. A. Pizzagalli, "Frontocingulate dysfunction in depression: Toward biomarkers of treatment response," (2011).

60 C. A. Essex, D. K. Overson, J. L. Merenstein, *et al.*, "Mild traumatic brain injury increases cortical iron: evidence from individual susceptibility mapping," *Brain Communications* **7**(2) (2025).

61 C. A. Essex, J. L. Merenstein, D. K. Overson, *et al.*, "Characterizing positive and negative quantitative susceptibility values in the cortex following mild traumatic brain injury: a depth- and curvature-based study," *Cerebral Cortex* **35** (2025).

62 A. Ashraf, M. Clark, and P. W. So, "The aging of iron man," *Frontiers in Aging Neuroscience* **10** (2018).

63 B. Bilgic, A. Pfefferbaum, T. Rohlfing, *et al.*, "MRI estimates of brain iron concentration in normal aging using quantitative susceptibility mapping," *NeuroImage* **59**(3), 2625–2635 (2012).

64 J. Hagemeier, J. J. Geurts, and R. Zivadinov, "Brain iron accumulation in aging and neurodegenerative disorders," *Expert Review of Neurotherapeutics* **12**(12), 1467–1480 (2012).

65 B. Hallgren and P. Sourander, "The effect of age on the non-haemin iron in the human brain," *Journal of Neurochemistry* **3**, 41–51 (1958).

66 D. J. Madden and J. L. Merenstein, "Quantitative susceptibility mapping of brain iron in healthy aging and cognition," *NeuroImage* **282** (2023).

67 S. Treit, N. Naji, P. Seres, *et al.*, "R2* and quantitative susceptibility mapping in deep gray matter of 498 healthy controls from 5 to 90 years," *Human Brain Mapping* **42**, 4597–4610 (2021).

68 L. Zecca, M. B. Youdim, P. Riederer, *et al.*, "Iron, brain ageing and neurodegenerative disorders," *Nature Reviews Neuroscience* **5**(11), 863–873 (2004).

69 A. Theadom, N. Hardaker, C. Bray, *et al.*, "The Brain Injury Screening Tool (BIST): Tool development, factor structure and validity," *PLoS ONE* **16**(2 February) (2021).

70 A. W. Stewart and S. Bollman, "QSMxT/QSMxT," (2022).

71 A. W. Stewart, S. D. Robinson, K. O'Brien, *et al.*, "QSMxT: Robust masking and artifact reduction for quantitative susceptibility mapping," *Magnetic Resonance in Medicine* **87**(3), 1289–1300 (2022).

72 B. Dymerska, K. Eckstein, B. Bachrata, *et al.*, "Phase unwrapping with a rapid opensource minimum spanning tree algorithm (ROMEO)," *Magnetic Resonance in Medicine* **85**(4), 2294–2308 (2021).

73 T. Liu, I. Khalidov, L. de Rochefort, *et al.*, "A novel background field removal method for MRI using projection onto dipole fields (PDF)," *NMR in Biomedicine* **24**(9), 1129–1136 (2011).

74 C. Kames, V. Wiggermann, and A. Rauscher, "Rapid two-step dipole inversion for susceptibility mapping with sparsity priors," *NeuroImage* **167**, 276–283 (2018).

75 B. Bilgic, M. Costagli, K. S. Chan, *et al.*, "Recommended implementation of quantitative susceptibility mapping for clinical research in the brain: A consensus of the ISMRM electro-magnetic tissue properties study group," *Magnetic Resonance in Medicine* **91**, 1834–1862 (2024).

76 S. M. Smith, "Fast robust automated brain extraction," *Human Brain Mapping* **17**(3), 143–155 (2002).

77 W. M. Pauli, A. N. Nili, and J. Michael Tyszka, "Data Descriptor: A high-resolution probabilistic in vivo atlas of human subcortical brain nuclei," *Scientific Data* **5** (2018).

78 D. N. Greve and B. Fischl, "Accurate and robust brain image alignment using boundary-based registration," *NeuroImage* **48**(1), 63–72 (2009).

79 M. Jenkinson, P. Bannister, M. Brady, *et al.*, "Improved Optimization for the Robust and Accurate Linear Registration and Motion Correction of Brain Images," *NeuroImage* **17**(2), 825–841 (2002).

80 M. Jenkinson and S. Smith, "A global optimisation method for robust affine registration of brain images," *Medical Image Analysis* **5**, 143–156 (2001).

81 J. L. Merenstein, J. Zhao, D. K. Overson, *et al.*, "Depth- and curvature-based quantitative susceptibility mapping analyses of cortical iron in Alzheimer's disease," *Cerebral Cortex* **34**(2) (2024).

82 J. L. Merenstein, J. Zhao, and D. J. Madden, "Depthwise cortical iron relates to functional connectivity and fluid cognition in healthy aging," *Neurobiology of Aging* **148**, 27–40 (2025).

83 B. Fischl, "FreeSurfer," (2012).

84 J. E. Iglesias, J. C. Augustinack, K. Nguyen, *et al.*, "A computational atlas of the hippocampal formation using ex vivo, ultra-high resolution MRI: Application to adaptive segmentation of in vivo MRI," *Neuroimage* (115), 117–137 (2015).

85 J. W. Tukey, *Exploratory Data Analysis*, Addison-Wesley Publishing Company (1977).

86 Y. Benjamini and Y. Hochberg, "Controlling the False Discovery Rate: A Practical and Powerful Approach to Multiple Testing," *Journal of the Royal Statistical Society. Series B (Methodological)* **57**(1), 289–300 (1995).

87 J. Lifshitz, B. J. Kelley, and J. T. Povlishock, "Perisomatic Thalamic Axotomy After Diffuse Traumatic Brain Injury Is Associated With Atrophy Rather Than Cell Death," *J Neuropathol Exp Neurol* **66**(3), 218–229 (2007).

88 A. H. Ropper and K. C. Gorson, "Clinical practice. concussion," *The New England Journal of Medicine* **356**(2), 166–172 (2007).

89 M. E. Haacke, N. Y. Cheng, M. J. House, *et al.*, "Imaging iron stores in the brain using magnetic resonance imaging," *Magnetic Resonance Imaging* **23**(1), 1–25 (2005).

90 F. Christidi, E. D. Bigler, S. R. McCauley, *et al.*, "Diffusion tensor imaging of the perforant pathway zone and its relation to memory function in patients with severe traumatic brain injury," *Journal of Neurotrauma* **28**, 711–725 (2011).

91 E. D. Bigler, C. V. Andersob, and D. D. Blatter, "Temporal Lobe Morphology in Normal Aging and Traumatic Brain Injury," *AJNR Am J Neuroradiol* **23**(2), 255–266 (2002).

92 K. F. Bieniek, N. J. Cairns, J. F. Crary, *et al.*, "The Second NINDS/NIBIB Consensus Meeting to Define Neuropathological Criteria for the Diagnosis of Chronic Traumatic Encephalopathy," *Journal of Neuropathology and Experimental Neurology* **80**, 210–219 (2021).

93 T. J. Orr, E. Lesha, A. H. Kramer, *et al.*, "Traumatic Brain Injury: A Comprehensive Review of Biomechanics and Molecular Pathophysiology," (2024).

94 E. D. Bigler, "Anterior and Middle Cranial Fossa in Traumatic Brain Injury: Relevant Neuroanatomy and Neuropathology in the Study of Neuropsychological Outcome," *Neuropsychology* **21**, 515–531 (2007).

95 D. L. Poeta and R. D. Burwell, *Parahippocampal Cortex (PHC)*, 4941–4945. Springer International Publishing, Cham (2022).

96 A. C. Mckee and D. H. Daneshvar, "The neuropathology of traumatic brain injury," in *Handbook of Clinical Neurology*, **127**, 45–66, Elsevier B.V. (2015).

97 T. Sullenberger, H. Don, and S. S. Kumar, "Functional Connectivity of the Parasubiculum and Its Role in Temporal Lobe Epilepsy," *Neuroscience* **410**, 217–238 (2019).

98 D. C. Viano, I. R. Casson, E. J. Pellman, *et al.*, "Concussion in professional football: Brain responses by finite element analysis: Part 9," *Neurosurgery* **57**(5), 891–916 (2005).

99 N. W. Churchill, M. G. Hutchison, S. J. Graham, *et al.*, "Acute and chronic effects of multiple concussions on midline brain structures," *Neurology* **97**(12), e1170–e1181 (2021).

100 S. Senova, A. Fomenko, E. Gondard, *et al.*, "Anatomy and function of the fornix in the context of its potential as a therapeutic target," (2020).

101 A. I. King, K. H. Yang, L. Zhang, *et al.*, "Is head injury caused by linear or angular acceleration?," in *IRCOBI Conference*, (Lisbon) (2003).

102 S. Kleiven, "Why Most Traumatic Brain Injuries are Not Caused by Linear Acceleration but Skull Fractures are," *Frontiers in Bioengineering and Biotechnology* **1** (2013).

103 K. M. Meys, L. S. de Vries, F. Groenendaal, *et al.*, "The Mammillary Bodies: A Review of Causes of Injury in Infants and Children," (2022).

104 J. B. Rich, *Mammillary Bodies*, 2076–2080. Springer International Publishing, Cham (2018).

105 L. W. Swanson and W. M. Cowan, "Hippocampo-Hypothalamic Connections: Origin in Subicular Cortex, Not Ammon's Horn," Tech. Rep. 4199 (1975).

106 S. L. Ding, "Comparative anatomy of the prosubiculum, subiculum, presubiculum, postsubiculum, and parasubiculum in human, monkey, and rodent," (2013).

107 K. M. Kerr, K. L. Agster, S. C. Furtak, *et al.*, "Functional neuroanatomy of the parahippocampal region: The lateral and medial entorhinal areas," (2007).

108 G. W. Van Hoesen and B. T. Hyman, "Hippocampal formation: anatomy and the patterns of pathology in Alzheimer's disease," *Progress in Brain Research* (83), 445–457 (1990).

109 H. Jahn, "Memory loss in Alzheimer's disease," *Dialogues Clin Neurosci.* (15), 445–454 (2013).

110 C. N. Boccara, F. Sargolini, V. H. Thoresen, *et al.*, "Grid cells in pre-and parasubiculum," *Nature Neuroscience* **13**, 987–994 (2010).

111 R. P. Sammons, D. Parthier, A. Stumpf, *et al.*, "Electrophysiological and molecular characterization of the parasubiculum," *Journal of Neuroscience* **39**, 8860–8876 (2019).

112 J. S. Taube, "The head direction signal: Origins and sensory-motor integration," (2007).

113 F. Cacucci, C. Lever, T. J. Wills, *et al.*, "Theta-modulated place-by-direction cells in the hippocampal formation in the rat," *Journal of Neuroscience* **24**, 8265–8277 (2004).

114 S. D. Vann and J. P. Aggleton, "The mammillary bodies: Two memory systems in one?," (2004).

115 Y. Miyashita, "Operating principles of the cerebral cortex as a six-layered network in primates: beyond the classic canonical circuit model," *Proceedings of the Japan Academy Series B: Physical and Biological Sciences* **98**(3), 93–111 (2022).

116 J. P. Aggleton, A. Pralus, A. J. Nelson, *et al.*, "Thalamic pathology and memory loss in early Alzheimer's disease: Moving the focus from the medial temporal lobe to Papez circuit," (2016).

117 K. Bhattacharyya, "James wenceslaus papez, his circuit, and emotion," *Annals of Indian Academy of Neurology* **20**, 207–210 (2017).

118 M. Miyata, K. Takahata, Y. Sano, *et al.*, "Association between mammillary body atrophy and memory impairment in retired athletes with a history of repetitive mild traumatic brain injury," *Scientific Reports* **14** (2024).

119 J. A. Piantino, J. J. Iliff, and M. M. Lim, "The Bidirectional Link Between Sleep Disturbances and Traumatic Brain Injury Symptoms: A Role for Glymphatic Dysfunction?," (2022).

120 S. B. Rosenbaum and M. L. Lipton, "Embracing chaos: The scope and importance of clinical and pathological heterogeneity in mTBI," *Brain Imaging and Behavior* **6**(2), 255–282 (2012).

121 H. Jia, X. Liu, Y. Cao, *et al.*, "Deferoxamine ameliorates neurological dysfunction by inhibiting ferroptosis and neuroinflammation after traumatic brain injury," *Brain Research* **1812** (2023).

122 D. A. Long, K. Ghosh, A. N. Moore, *et al.*, "Deferoxamine improves spatial memory performance following experimental brain injury in rats," tech. rep. (1996).

123 S. Khalaf, A. S. Ahmad, K. V. Chamara, *et al.*, "Unique Properties Associated with the Brain Penetrant Iron Chelator HBED Reveal Remarkable Beneficial Effects after Brain Trauma," *Journal of Neurotrauma* **36**, 43–53 (2019).

124 S. S. Panter, J. Mark Braughler, and E. D. Hall, "Dextran-Coupled Deferoxamine Improves Outcome in a Murine Model of Head Injury," *Journal of Neurotrauma* **9**(1) (1992).

125 J. Zhao, Z. Chen, G. Xi, *et al.*, "Deferoxamine Attenuates Acute Hydrocephalus After Traumatic Brain Injury in Rats," *Translational Stroke Research* **5**(5), 586–594 (2014).

126 C. Bouras, P. Giannakopoulos, P. F. Good, *et al.*, "A Laser Microprobe Mass Analysis of Brain Aluminum and Iron in Dementia pugilistica: Comparison with Alzheimer's Disease," *Eur Neurol* **38**(1), 53–58 (1997).

127 A. Yamamoto, R.-W. Shin, K. Hasegawa, *et al.*, "Iron (III) induces aggregation of hyperphosphorylated s and its reduction to iron (II) reverses the aggregation: implications in the formation of neurofibrillary tangles of Alzheimer's disease," tech. rep. (2002).

128 M. Ahmed, J. Chen, A. Arani, *et al.*, "The diamagnetic component map from quantitative susceptibility mapping (QSM) source separation reveals pathological alteration in Alzheimer's disease-driven neurodegeneration," *NeuroImage* **280** (2023).

129 J. Chen, N. J. Gong, K. T. Chaim, *et al.*, "Decompose quantitative susceptibility mapping (QSM) to sub-voxel diamagnetic and paramagnetic components based on gradient-echo MRI data," *NeuroImage* **242** (2021).

130 J. Emmerich, P. Bachert, M. E. Ladd, *et al.*, "On the separation of susceptibility sources in quantitative susceptibility mapping: Theory and phantom validation with an in vivo application to multiple sclerosis lesions of different age," *Journal of Magnetic Resonance* **330** (2021).

131 J. Lee, S. Ji, and S. H. Oh, "So You Want to Image Myelin Using MRI: Magnetic Susceptibility Source Separation for Myelin Imaging," *Magnetic resonance in medical sciences : MRMS : an official journal of Japan Society of Magnetic Resonance in Medicine* **23**(3), 291–306 (2024).

132 Z. Li, R. Feng, Q. Liu, *et al.*, "APART-QSM: An improved sub-voxel quantitative susceptibility mapping for susceptibility source separation using an iterative data fitting method," *NeuroImage* **274** (2023).

133 H. G. Shin, J. Lee, Y. H. Yun, *et al.*, "χ-separation: Magnetic susceptibility source separation toward iron and myelin mapping in the brain," *NeuroImage* **240** (2021).

...If you can force your heart and nerve and sinew
To serve your turn long after they are gone,
And so hold on when there is nothing in you
Except the Will which says to them: 'Hold on!...' [1]

1 Rudyard Kipling. *If.*